

Redshifting Azobenzenes for Photoswitchable Ion Transport and Catalysis

Aidan J. Kerckhoffs

Supervisor: Matthew J. Langton

Balliol College, University of Oxford





A thesis submitted for the degree of Doctor of Philosophy

Chemistry Research Laboratory

Hillary Term 2023

Redshifting Azobenzenes for Photoswitchable Ion Transport and Catalysis

Aidan J. Kerckhoffs, Balliol College, University of Oxford

Supervisor: Matthew J. Langton

Abstract of Thesis submitted for the degree of Doctor of Philosophy, Trinity Term, 2023

This thesis describes the design of novel redshifted azobenzene scaffolds with tuneable thermal half-lives. These photoswitches are employed within photoswitchable ion transporters and halogen bonding catalysts.

Chapter 1 Outlines the field of ion transport and the design of synthetic ionophores, followed by an introduction to manipulating biological systems with light.

Chapter 2 describes the development of novel, highly redshifted azobenzene scaffolds, showcasing robust periods trends in relation to absorption wavelength, solid-state structure conformations, (*Z*)-isomer half-life and glutathione stability.

Chapter 3 concerns the design, synthesis and transport properties of fully reversible redshifted photoswitchable anion transporters.

Chapter 4 broadens the scope of the explored photoswitches by functionalisation with different receptor groups, showcasing proof-of-principle studies towards achieving halogen bonding photoswitchable catalysis and ion pair binding.

Chapter 5 summarises the conclusions and future work for this thesis

Chapter 6 outlines the experimental procedures conducted during this work.

Acknowledgements

First and foremost, a big thank you to Matt for being an ideal supervisor – you've helped keep me on track so well, and your supervision style has fostered so many great projects that I can be very proud of. I wouldn't change anything about how my DPhil went and that is a testament to the great dynamic that has been cultivated over the years within your group. It has been such a journey watching the group grow into what it is now and I'm excited to see what's next! Next, I would like to thank Andrew Docker for putting me under his wing when I first arrived – we've shared such a good blend of intellectually stimulating conversations and laughs. I attribute a lot of my successes to your mentorship. You've set definitely set the bar high.

Of course, I would like to thank all the Langton and Beer group members - new and old - for being such a kind caring and loving group, and all the meaningful friendships and memories I've formed over the years. It's going to be sad to leave: all of you will always have a special place in my heart. Special shoutout to Aaron for our fun and unorthodox experiences together, Euan for our therapy sessions, Xiangyu for being my spiritual guide and all the meaningful conversations, Martin for the excellent vibes and tunes, Amir for quality company, Charlie for all the silly laughs, (Parma)Shaun for the banter, Kelly for your endless great energy, Toby for your cheeriness, and Elba + Dom for adding an extra dimension of kindness of our group.

To all my Oxford people; Elliot, Yas, Jack, Darius, Katrina, Hollie, Charlie, Henry, Otis, Helene, Cyril, Balliol MCR football boys, and all the weird and wonderful fleeting interactions I've had with every person – each and every moment has had an impact on who I am today. This period of my life has lead to so much growth into the young man I am today. To all my external people; Ben, Chris, Antonio, Patrick, Blair, Sami, Yazan, Ian, Naim, Stefan, Jamal, young Anthony, Yousif, Dawno, Connah, Nick, Sam, Nancy and the chorizo boys back in Spain. I love and treasure you all. Thank you for the timeless memories. Wow. What a fun couple of years.

Thanks to Opa en Oma for your support and emphasis on education, thank you so much to Mama en Papa for making me, and making me who I am; a nice blend of freedom with sensible boundaries has allowed me to pursue my dreams – one of them being this DPhil.

Previously Published work

Some of the work described in this thesis has been published:

1) Photo-switchable anion binding and catalysis with a visible light responsive halogen bonding receptor. A. Kerckhoffs, I. Moss, M. J. Langton, ***Chem. Commun.***, 2023, **59**, 51-54

2) Fast relaxing red and near-IR switchable azobenzenes with chalcogen and halogen substituents: periodic trends, tuneable thermal half-lives and chalcogen bonding. A. Kerckhoffs, K. Christensen, M. J. Langton, *Chem. Sci.,* 2022, **13**, 11551-11559 (*Most popular 2022 organic chemistry articles and 2022 Chemical Science HOT Article Collection*

3) Red-shifted tetra-*ortho*-halo-azobenzenes for photo-regulated transmembrane anion transport. A. Kerckhoffs, Z. Bo, S. E Penty, F. Duarte, M. J. Langton, *Org. Biomol. Chem.*, 2021, **19**, 9058-9067

4) Supramolecular chemistry in lipid bilayer membranes. L. E. Bickerton, T. G. Johnson, A. Kerckhoffs, M. J. Langton, ***Chem. Sci.***, 2021, **12**, 11252-11274 (*Review*)

5) Reversible photo-control over transmembrane anion transport using visible-light responsive supramolecular carriers. A. Kerckhoffs, M. J. Langton, ***Chem. Sci.***, 2020, **11**, 6325-6331

Oral Presentations

September 2022: 36th PGR Heterocyclic and Synthesis symposium (Publication **2**)

June 2022: AstraZeneca/University of Oxford Organic/Chemical Biology graduate symposium winner (Publication **2)**

June 2022: SBM Science Day Talk, (Publication **2**)

June 2020: SBM Science Day (Online), (Publication **5**)

September 2020: Invited Flash Talk at *ChemPlusChem* Young Talents and Mentors Symposium (Online). Publication **5)**

Poster Presentations

December 2022: SICC Singapore. (Publication **2**)

May 2021: ISMSC conference 2021 Poster commendation (Publication **3**)

June 2020: SBM Science Day (Online), (Publication **5**)

May 2020: ISMSC conference 2020 Poster Award (Publication **2**)

Abbreviations

δ: chemical shift; Δ: change in; λ: wavelength; μ: micro; μW: Microwave; br.: Broad; Boc: tert-butyloxycarbonyl; BINAP: (2,2′-bis(diphenylphosphino)-1,1′-binaphthyl); conc.: concentrated; CF: 5(6)-Carboxyfluorescein; CuAAC: Cu(I)-catalysed azide-alkyne cycloaddition; °C: degrees Celcius; *d*: deuterated; d: doublet DBDMH: 1,3-Dibromo-5,5-Dimethylhydantoin; DBU: 1,8-Diazabicyclo[5.4.0]undec-7-ene; DCM: Dichloromethane; DIPEA: N,N-Diisopropylethylamine; DMAP: 4-Dimethylaminopyridine; DMF: *N*,*N*-Dimethylformamide; DMSO: Dimethylsulfoxide; DPPA; Diphenylphosphoryl azide; DPPC: 1,2-dipalmitoyl-sn-glycero-3-phosphocholine; eq.: equivalent; Et: ethyl; EYPG: egg-yolk phosphatidylglycerol; h: hour(s); HB: Hydrogen bond; HEPES: N-(2- hydroxyethyl)piperazine-N'-(2-ethanesulfonic acid); HPTS: 8-hydroxy-1,3,6-pyrenetrisulfonate; HRMS: High resolution mass spectrometry; Hz: hertz; K_a: association constant; KF: Potassium Fluoride; KOH: Potassium hydroxide; L: litre; LUVs: large unilamellar vesicles; m: metre, milli or multiplet; m: meta; M: molar concentration; MeCN: Acetonitrile; MeOH: Methanol; min: minute(s); Ms: methanesulfonyl; MS: mass spectrometry; NBS: *N*-Bromosuccinimide; NCS: *N*-Chlorosuccinimide; NMP: N-Methyl-2-pyrrolidone; *o*: ortho; OAc: Acetate; p: para; PIDA: phenyliodine(III) diacetate; Phth: Phthaloyl; PSS: Photo-stationary state; POPC: 1-palmitoyl-2-oleoyl-sn-glycero-3-phosphocholine; Pr: propyl; q: quartet; Quant: Quantitative; rt: Room temperature; s: singlet or second; sat: saturated; t: tertiary alkyl group; TBA: tetabutylammonium; TFA: Trifluoroacetic acid; THF: Tetrahydrofuran; TLC: thin layer chromatography; TMS: Trimethylsilyl; Ts: toluenesulfonyl; UV-Vis; ultraviolet-visible; X: halogen atom; XB: halogen bond.

Table of contents

Chapter 1: Introduction 1
1.1 Ion transport across lipid bilayer membranes 1
1.1.1 Biological membranes 1
1.1.2 Ion channels, pumps and electrochemical gradients 2
1.1.3. Channelopathies 3
1.2 Small molecule ion transporters 5
1.2.1 Synthetic ion channels 5
1.2.2 Mobile carriers 6
1.2.3 Naturally occurring mobile carriers 7
1.2.4 Synthetic ion transporter design 9
1.2.4.1 Ion transporter Design: association constant and non-covalent interactions 10
1.2.4.2 Synthetic ion transporter design: lipophilicity and lipophilic balance 13
1.2.5 Key examples of synthetic transporters 15
1.2.5 Concluding remarks on ion transporters 17
1.3 Light as an external stimulus 17
1.3.1 Light responsive systems in nature 18
1.3.2 Optogenetics 18
1.3.3 Photodynamic therapy 20
1.3.4 Photopharmacology 21
1.3.4.1 Photoresponsive motifs 21
1.3.4.2 Examples of photoswitches employed in photopharmacology 23
1.3.4.3 Examples of photocages employed in photopharmacology 26
1.3.4.4 Challenges and outlook in photopharmacology 27
1.3.4.5 Challenges and outlook for azobenzenes in photopharmacology 29
1.4 Project aims 32
1.5 References 33
Chapter 2 – Red-shifting and tuning the half-life of azobenzenes 37
2.1 Unsubstituted azobenzenes 37
2.2 Background: redshifting azobenzenes 38
2.2.1 Redshifting Azobenzenes: modifying π → π * transitions 38
2.2.2 Redshifting Azobenzenes: modifying n → π * transitions 39
2.3 Approach towards redshifting azobenzenes and controlling half-life 41
2.4 Synthesis of azobenzene derivatives 43
2.4.1 Synthesis of halogen X_4 derivatives 43
2.4.2 Synthesis of chalcogen X_4 derivatives 45
2.4.3 Synthesis of X_2,*m*-Y_2 derivatives 48

2.5 Photoswitching properties of azobenzene derivatives 51
2.5.1 Optical and electronic properties of simple X_4 derivatives 52
2.5.2 Solid-state structural analysis of simple X_4 derivatives 55
2.5.3 Photoisomerisation and half-lives of stable azobenzenes 58
2.5.4 Unstable azobenzene structures 61
2.6 Glutathione stability 62
2.7 Chapter Conclusions 63
2.8 References 63
Chapter 3 – Photoswitchable transmembrane anion transporters 65
3.1 Stimuli-responsive anion transporters 65
3.1.1 Stimuli-responsive carriers without the use of light 65
3.1.2 Stimuli-responsive carriers responsive to light 67
3.2 Proposed approach towards developing redshifted photoswitchable transporters 68
3.2.1 Initial design and synthesis of photoswitchable anion transporter 69
3.2.2 NMR titrations and anion binding capabilities of initial scaffold 71
3.2.3 Ion transport properties of initial photoswitchable scaffold 73
3.2.4 Control experiments 78
3.2.5 In-situ photo-switching experiments within a lipid bilayer membrane 80
3.3 Attempts to improve cooperativity 82
3.3.1 Synthesis 83
3.3.2 Anion binding studies and cooperativity 86
3.3.3 Ion transport studies 87
3.4 Chapter conclusions 90
3.5 References 91
Chapter 4 – Modifications to the receptor 93
4.1 Attempts to improve the receptor 93
4.1.2 Thioureas 94
4.1.3 Iodotriazoles 95
4.2.1 Background 98
4.2.2 Anion binding properties of photoswitchable catalyst XB-Azo 100
4.2.3 Photoswitchable catalysis 102
4.3 Ion pair transport 104
4.3.1 Proposed ion pair transporters 104
4.3.2 Synthesis of ion pair transporters 106
4.3.3 ^{1}H NMR binding studies of ion pair mobile carriers 108
4.3.4 Transport studies of ion pair mobile carriers 110
4.4 Chapter conclusions and future work 113

4.5 References 114
Chapter 5 – Thesis conclusions and future work 116
5.1 Summary of thesis 116
5.2 Future work 117
6.1 Appendix 119
6.1.1 Materials and methods 119
6.2.1 Synthetic procedures (Chapter 2) 121
6.2.2 UV-Vis spectra (Chapter 2) 170
6.2.3 Photoswitching: PSS and half-Life determination 174
6.2.4 GSH Stability Studies 178
6.2.5 Single crystal X-ray diffraction experiments 179
6.2.6 References (Chapter 2 appendix) 191
6.3.1 Synthetic procedures (Chapter 3) 192
6.3.2 UV Vis spectra (Chapter 3) 216
6.3.3 NMR titration experiments (Chapter 3) 217
6.3.4 Anion transport studies (Chapter 3) 220
6.3.4.1 Vesicle preparation 220
6.3.4.2 Transport assays with HPTS 220
6.3.4.3 Ion selectivity assay (Figure 8B-D; Figure 12C-E) 221
6.3.4.4 Transport data with HPTS 222
6.3.4.5 Calcein leakage assay (Figure 8G, 12F) 223
6.3.4.6 ISE assay vesicle preparation 223
6.3.4.7 Electrode calibration 224
6.3.4.8 Transport assays with ISE (Figure 9F) 225
6.3.5 References (Chapter 3 appendix) 226
6.4.1 Synthetic procedures (Chapter 4) 226
6.4.2 NMR titrations (Chapter 4) 246
6.4.3 Anion transport studies (Chapter 4) 248
6.4.3.1 Lucigenin transport assays 248
6.4.4 ^{1}H NMR kinetics Studies (Chapter 4) 249
6.4.5 References (Chapter 4 appendix) 252

Chapter 1: Introduction

1.1 Ion transport across lipid bilayer membranes

The precise, controlled transport of ions across a lipid bilayer is fundamental to a plethora of biological functions, including cell proliferation and signalling, muscle contraction, and maintaining cellular pH, membrane potential and osmotic balance.[1] Misregulation of ion transport results in diseases collectively known as channelopathies, including cystic fibrosis, short QT syndrome and epileptic seizures.[2] Small molecules capable of facilitating transmembrane ion transport have recently emerged as a promising approach towards treating channelopathies and cancer and studying ion transport processes.[3] This chapter focuses on relevant concepts related to ion transport, channelopathies and mobile ion carriers.

1.1.1 Biological membranes

Lipids are composed of a polar head group and non-polar tails, and serve as the main component of cell membranes.[4] Due to the hydrophobic effect, these amphiphilic molecules self-assemble into lipid bilayers in aqueous media to form two-dimensional bilayers comprising a hydrophobic core of similar polarity to hexane, which subsequently form sealed 3-D cellular compartment to minimise interactions of fatty acid chains with the aqueous environment (Figure 1). *Cis* double bonds within the tails disrupt close packing and result in increased membrane fluidity and permeability, whereas longer fatty chains enhance membrane rigidity and reduce permeability. Synthetic membranes such as large unilamellar vesicles (LUVs, 100 nm to 1 µM in diameter) can conveniently be generated from commercial lipids such as POPC and extrusion methods, with high control over size and internal contents such as fluorescent probes; allowing LUVs to routinely be used to study membrane-bound molecular systems.[5]

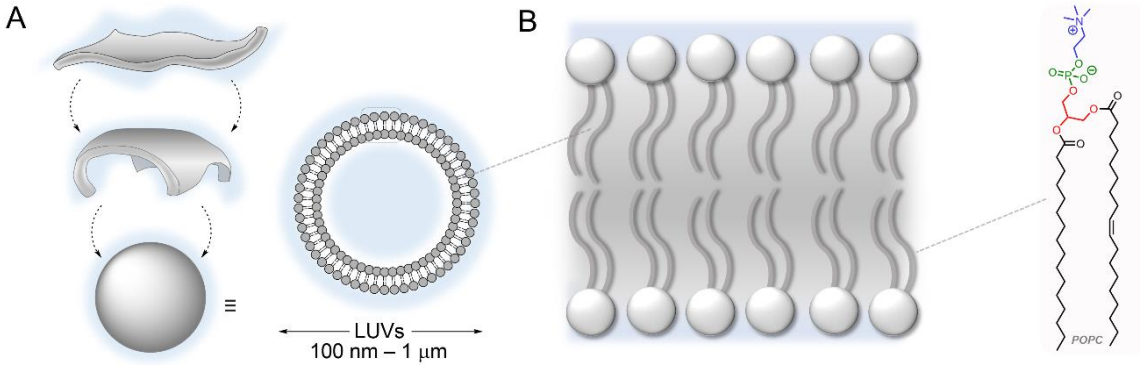


Figure 1. (A) Self-assembly of lipids into vesicles (B) structure of a lipid bilayer membrane and POPC

1.1.2 Ion channels, pumps and electrochemical gradients

Small uncharged or lipophilic molecules can passively diffuse across the plasma membrane *via* passive diffusion down their concentration gradients, whereas charged molecules and ions are virtually impenetrable to the lipid bilayer.[6] This is due to the inherently high hydrophilicity and stable hydration spheres of ions, which must initially become desolvated to cross the hydrophobic bilayer. To overcome this, nature has developed ion pumps, channels, and in some cases, mobile carriers to transport ions across the bilayer, which replace the solvated water with stabilising non-covalent interactions; lowering the energetic barrier of crossing the membrane.[4]

Ion pumps and channels are endogenous proteins that partially or fully span the lipid bilayer (Figure 2). Ion channels allow passive transport along an electrochemical gradient, with transport rates up to the diffusion limit.[7] Channels contain cavities complementary to the charge and spatial requirements of the ion, providing excellent selectivity between ions *via* non-covalent interactions. For instance, potassium channels contain a series of α-helix carbonyl oxygens, capable of forming ion-dipole interactions within a network of dehydrated potassium ions, whilst in chloride channels, selectivity arises from a series of amide hydrogen bond donors along an α-helix (Figure 2B).[8]

In contrast, pumps such as NKCC, KCC and Na^+/K^+ ATPase are enzymes that harness energy to transport ions thermodynamically uphill, the latter, utilising ATP to exchange three Na^+ for two K^+ by pumping the ions against their respective concentration gradients to maintain the resting membrane potential of a cell.[9] Both channels and pumps are typically gated (reversibly switched on and off) by external stimuli such as ligand or ion binding, light, pH, voltage or mechanical stress, allowing precise control of ion concentrations across lipid bilayers.[10]

Cells exhibit an uneven distribution of ions across the lipid bilayer, usually leading to a negative membrane potential (V_m); continually maintained by ion pumps and co-transporters (Figure 2C).[11] At V_m, the equilibrium potentials of ions are generally away from their respective electrochemical equilibrium potential ($V_x \neq V_m$, where V_x is the equilibrium potential of ion x).

Depending on the membrane potential of the cell and concentration gradients of the ions maintained by pumps, this results in a continuous influx or efflux of ions along their electrochemical gradients *via* their respective channels.[12] This electrochemical gradient and thus direction of ion flow are typically in the same direction of the concentration gradients, but the ion flow may be opposed to the concentration gradient if the overall membrane potential is outweighed by the equilibrium potential of the ion. For example, some cells exhibit extremely high chloride channel activity or intracellular chloride concentrations, leading to removal ($V_{Cl} \approx V_m$) or reversal ($V_{Cl} > V_m$) of the electrochemical gradient for chloride.[13]

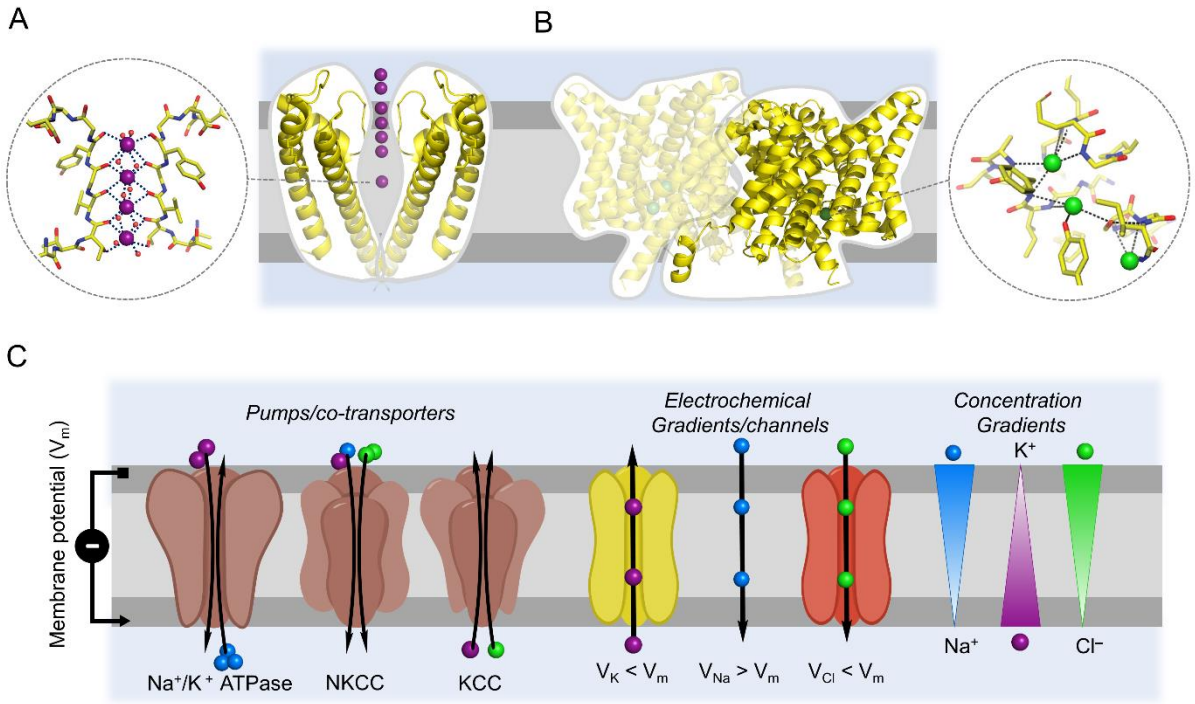


Figure 2. (A) Potassium channel solved by MacKinnon (PDB: 1K4C) (B) Dimeric chloride channel solved by MacKinnon (PDB: 1OTS). Key interactions within selectivity filters are illustrated (C) Schematic diagram illustrating membrane potential, electrochemical gradients and concentration gradients of ions.

1.1.3. Channelopathies

Misregulation of ion transport results in diseases collectively known as channelopathies. For example, mutations in the cystic fibrosis transmembrane conductance regulator (CFTR) channel results in insufficient chloride efflux in epithelial cells (which naturally exhibit a less negative V_{Cl} than the resting membrane potential of the cell).[13] During normal CFTR function,

chloride channel efflux acts as a driving force for water to enter the lung tubes. This salt/water layer is optimally balanced to allow cilia (microscopic hair-like structures) on lung cell surfaces to sweep mucus out of the airways.[14] As a consequence of CFTR channel inactivity, ducts and tubes become blocked with mucus, leading to symptoms such as intestinal blockage, chronic lung infections, male infertility and excessively salty sweat.[15]

It is thus of significant interest to develop systems that can replace or overcome faulty channels as a potential treatment for channelopathies such as cystic fibrosis. Synthetic anion transporters can potentially replace faulty CFTR channels by facilitating chloride and/or bicarbonate efflux to epithelial surfaces, thus significant research efforts have been dedicated to their development.[3] Current CF therapeutics only function in patients with specific mutations, whilst replacement of faulty channels would allow general treatment of the disease, irrespective of the >2000 known CFTR mutations.[16]

Increasing evidence suggests that abnormal activity or expression of ion channels and pumps aids cancer progression, thus cancer may also be regarded as a channelopathy.[17] A hallmark of cancer is a depolarised V_m relative to normal cells, which favours cell proliferation. Aberrations in cancer cell membrane potentials have also been shown to play key roles in cell migration and cell differentiation for reduced apoptosis (programmed cell death).[18] Thus, misregulated ion distributions are directly linked to cancer cell survival. Another hallmark of cancer is the reversal of the pH gradient in cancer cells relative to healthy cells, with higher intracellular pH (pH_i) than extracellular pH (pH_e) due to increased H^+ pump and transporter activity and expression. This inverse pH gradient is key for cancer cell survival, leading to signalling that limits apoptosis, promotes cell proliferation and enhances cell migration.[19]

Consequently, perturbing chemical gradients using small molecules is a promising approach towards triggering cell death of cancer cells. In particular, regulation of chloride, calcium and potassium ions has been shown to promote the onset of apoptosis.[20] Furthermore, membrane hyperpolarisation, pH_i acidification or deacidification of acidic organelles are known to promote apoptotic signalling pathways. [21]

1.2 Small molecule ion transporters

1.2.1 Synthetic ion channels

The use of naturally derived membrane-spanning proteins to artificially control transmembrane ion transport is very expensive and such proteins can be challenging to modify if abiotic function is desired.[22] Furthermore, overexpression of ion channels in bacteria leads to problems with folding and assembly, and often has toxic effects on host cell machinery; limiting preparation of larger quantities.[23] Therefore, a more attractive approach towards mitigating faulty channel activity in a therapeutic context is the development of simpler synthetic ion channels, which are readily modified and prepared from commercial precursors (Figure 3).

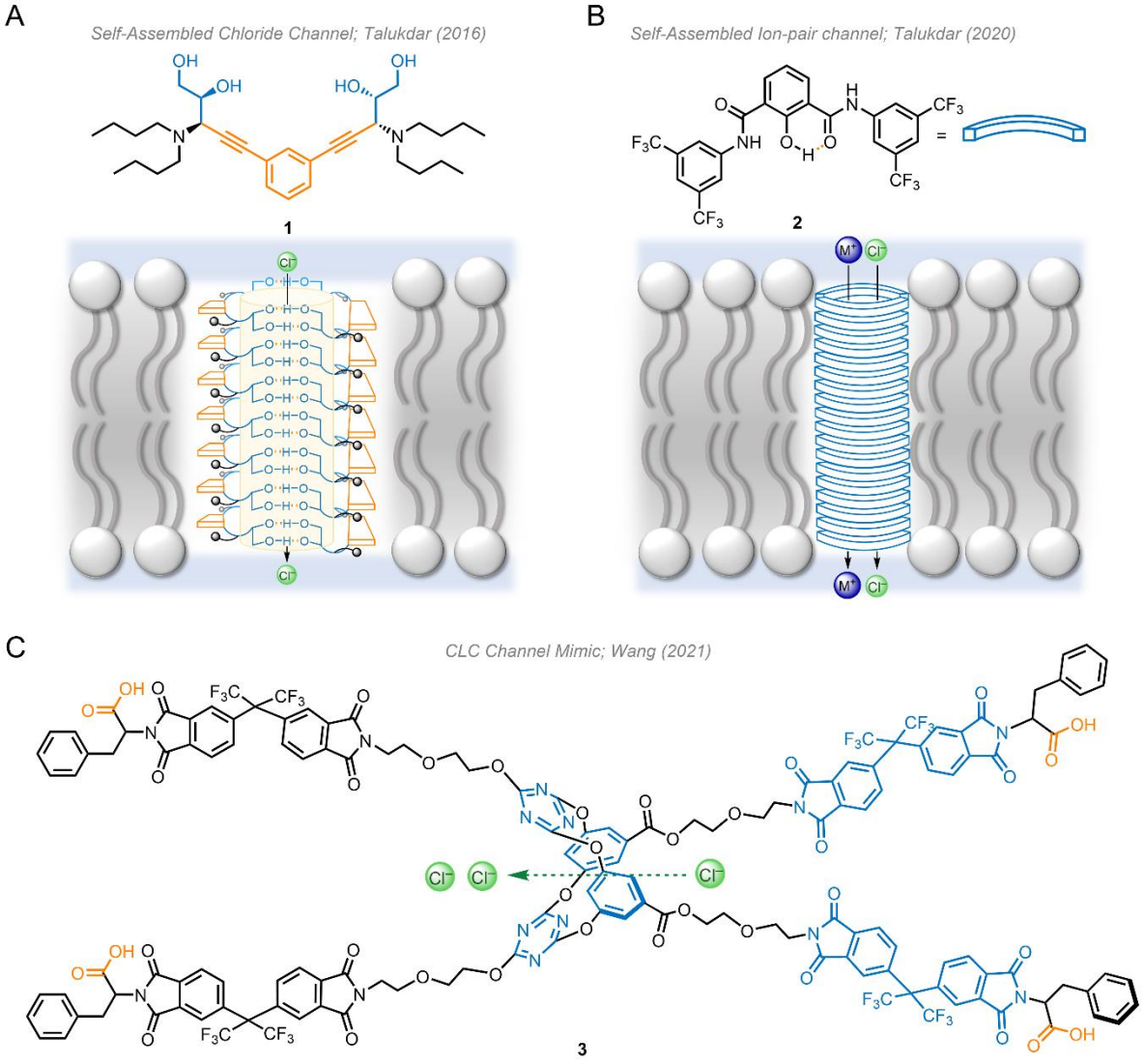


Figure 3. (A) Self-assembled bis-diol chloride channel by Talukdar[24] (B) Self-assembled KCl/NaCl channel by Talukdar[25] (C) CLC chloride channel mimic by Wang[26]

A powerful approach towards generating synthetic membrane-spanning channel is self-assembling monomers. For example, Talukdar and co-workers developed bis-diol **1**, which self-assembles into a channel via intermolecular hydrogen bonding and hydrophobic interactions, allowing high insertion into the lipophilic bilayer (Figure 3A).[24] The authors report high chloride selectivity within the hydrophilic region of the channel. When cells were treated with **1**, a strong correlation with channel-induced chloride transport and apoptosis was observed; thus **1** represents a promising scaffold for cancer therapeutics. The same group also reported isophthalimide **2**, which self assembles into an ion pair channel via H-bonds and π-π interactions to facilitate KCl or NaCl symport. The authors report that both anion and cation transport in cells incubated with **2** were responsible for apoptotic pathways.[25]

Although promising scaffolds, self-assembled channels require relatively high concentrations of monomer to form active structures. In contrast, membrane-spanning molecules such as **3** are less concentration dependent and structurally more similar to natural ion channels. **3** serves as a mimic of the hour-glass shaped nature CLC chloride channel; anchoring itself across the bilayer with the carboxyl groups and polar lipid head groups, whilst the lipophilic regions span the hydrophobic core of the membrane.[26] The authors observed high Cl^- selectivity in the presence of Br^- within the electron-deficient triazine macrocyclic cavity, which they attribute to stronger interactions to the more strongly bound Cl^- anion within the channel. However, the delivery of such large molecules to a membrane within a therapeutic context is challenging and may lead to poor bioavailability.[27] Therefore, a more promising approach towards treating channelopathies would be the development of small molecule mobile carriers.

1.2.2 Mobile carriers

Mobile carrier ionophores show high promise as therapeutics for cancer treatment and channelopathies, or as tools for studying ion transport processes.[3] Mobile carriers are small, hydrophobic receptors that permeate the membrane and form a supramolecular ion complex at the membrane interface. This complex subsequently diffuses across the bilayer and rotates in order to decomplex the ion at the opposite interface (Figure 4).[28]

The stabilising intermolecular interactions within the encapsulated hydrophobic receptor partially compensate for the loss of hydration energies at the membrane interface; significantly lowering the kinetic barrier to crossing and allowing turnover rates of thousands of ions per second. [28] Essentially, mobile carrier transporters are translocation catalysts, as they facilitate ionic diffusion without being consumed in the process.[29] Encouragingly, anion transporters have already been shown to successfully transport chloride within epithelial cells for replacing CFTR function[3] and selectively trigger apoptosis in cancer cells.[30]

Mobile carriers or channels may transport ions across a bilayer either alone or coupled to the transport of another species. If an ion is transported across the bilayer without being coupled to another, this is a uniport process (Figure 4B). Since ions are charged, this represents an electrogenic process, meaning a net charge is translocated across the bilayer and V_m is affected. Symporters co-transport two ions in the same direction across the bilayer, whereas antiporters facilitate the exchange of two ions in opposite directions in an electrogenic fashion with respect to each ion. [31] Both of these latter processes are generally net neutral, as the charge separation is balanced by the coupled ion.

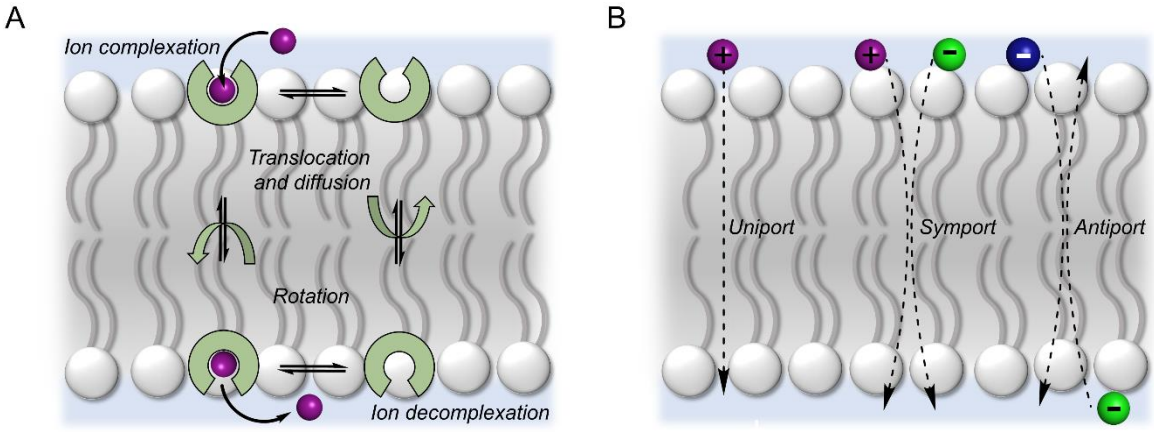


Figure 4. (A) Schematic of mobile carrier-mediated ion transport (B) Outline of main transport mechanisms for ion transporters

1.2.3 Naturally occurring mobile carriers

Nature provides a continuous source of inspiration for chemists when designing bioactive molecules and indeed also transporters. Numerous naturally occurring mobile ionophores with

remarkable selectivities and exquisite structural features are available, and are regularly used as antibiotics or research tools to study ion transport in synthetic bilayers (Figure 5).

Valinomycin is a cyclic depsipeptide secreted by *Streptomyces*, acting as a highly active and selective electrogenic potassium transporter (Figure 5A). Valinomycin functions as a potent bacteriostatic to outgrow other bacteria or fungi, as it rapidly can depolarise mitochondrial membranes.[32] The high selectivity is proposed to arise from a highly ordered intramolecular hydrogen bonding network, which preorganises the carbonyls into a spherical cavity with optimal ion-dipole distances for K^+.[33] The external hydrophobic groups mask the polar binding cavity, allowing high membrane penetration and potassium transport across the bilayer.

Prodigiosin and related derivatives are naturally occurring anticancer, antimalarial, and antibacterial compounds, with their action often proposed to arise from their ionophoric activity (Figure 5B).[34] Various prodiginines have been observed to transport ^-Cl and H^+ into cells[34] or deacidify acidic organelles,[36] in line with the structure of **4** bound to HCl in the solid state.[37] Similar to valinomycin, the binding site is relatively well shielded with hydrophobic groups.

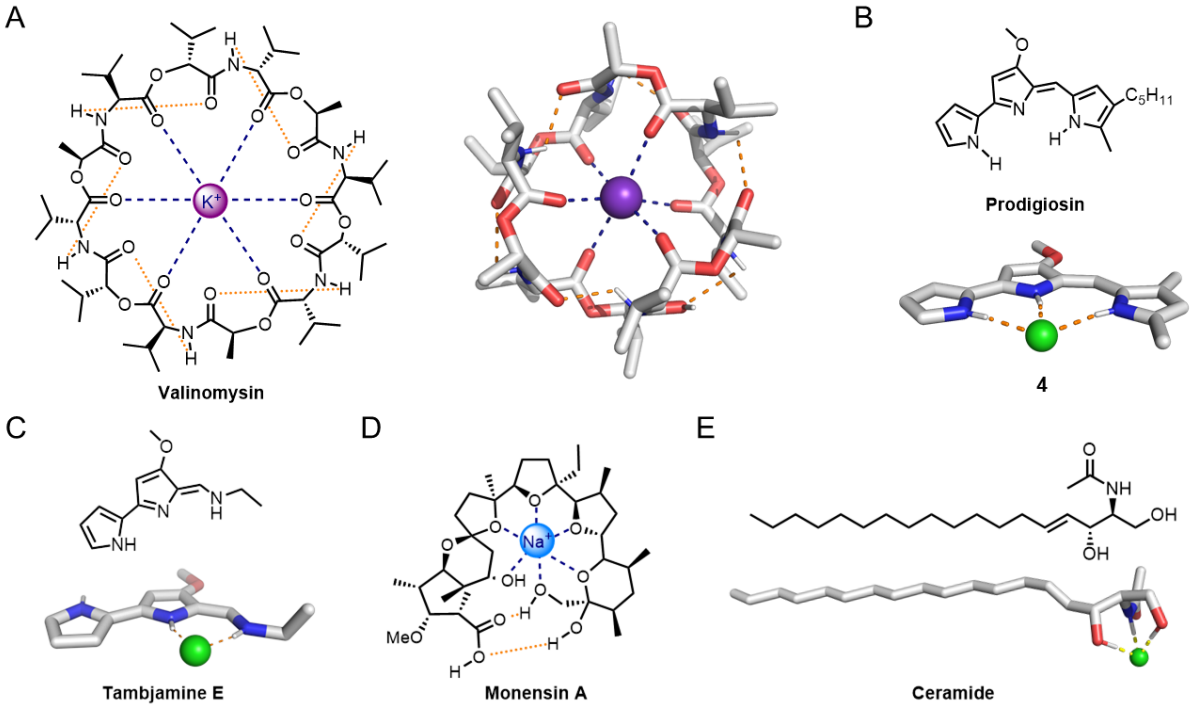


Figure 5. Examples of natural ionophores. (A) Valinomycin with solid-state K^+ bound structure[33] (B) Prodigiosin with solid state chloride-bound derivative **4**.[37] (C) Monensin A (D) Ceramide with chloride-bound model (MM+ force field, HyperChem). (E) Tambjamine E with solid state chloride complex [38]

The **tambjamine** alkaloids are known to dissipate ion and pH gradients in cells, and exhibit potent cytotoxic and antibacterial properties (Figure 5C). Despite previous reports attributing the high biological activity of the tambjamines to HCl symport, Quesada observed that these compounds are efficient Cl^-/HCO_3^- exchangers and poor HCl symporters in vesicles, with anion exchange being insensitive to pH gradients.[38] These results may be rationalised by the higher basicity (pK_a ~ 10) compared to prodigiosin (pK_a ~ 5.4),[36] which significantly attenuates the deprotonation step required for H^+ transport.

Monensin A is a highly active M^+/H^+ exchanger, leading to potent antibacterial and growth promoting properties in livestock such as poultry or cattle (Figure 5D).[39] In bacteria, monensin transports K^+ out of the cell in exchange for protons; leading to membrane depolarisation and internal acidification, followed by Na^+ influx, which disrupts cell homeostasis and eventually leads to cell death.[40] The well shielded yet flexible nature of the binding cavity is key for the efficient binding and transport for a range of monovalent ions.

Ceramide is a fatty acid found within cell membranes, traditionally serving as both a structural component and aiding protein channel formation at high ceramide concentrations (Figure 5E). However, Davis and co-workers reported that at low concentrations, these compounds readily transport chloride in exchange for nitrate or bicarbonate across synthetic bilayers, which may contribute towards various cellular functions ceramide conducts in vivo.[41]

1.2.4 Synthetic ion transporter design

Transmembrane ion transport is a complex multi-step process; involving ion binding and decomplexation at the aqueous interface, and partitioning, diffusion and rotation within the lipid bilayer. Other competing processes such as complexation with other ions or the phospholipid headgroups may impede transport rates, and any substituent of the molecule may influence each of the key transport steps.[42] Therefore, it remains challenging to accurately predict the design criteria for effective transmembrane carriers. However, many trends have been observed, in particular within key parameters such as binding affinity, lipophilicity and molecular shape.[43]

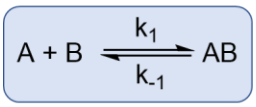
1.2.4.1 Ion transporter Design: association constant and non-covalent interactions

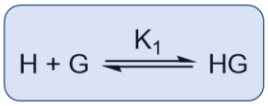
For both channels and mobile carriers, specific non-covalent interactions are essential to stabilise ions within the transporter and compensate for the dehydration penalty. The binding affinity between a receptor (host; H) and ion (guest; G) can be quantified with the association constant K_a, with larger values of K corresponding to stronger binding in a given solvent.[44] The key equations describing the relationship between association/dissociation rates k_1 *and* k_{-1} and binding constant K for 1:1 and 1:2 host : guest binding are:

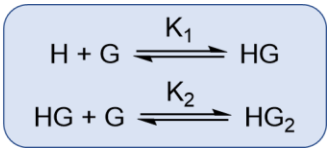
$$K_a = \frac{1}{K_d} = \frac{k_1}{k_{-1}} \quad (1.1)$$

$$K_1 = \frac{[HG]}{[H][G]} \quad (1.2)$$

$$K_2 = \frac{[HG_2]}{[H][HG]} \quad (1.3)$$







where K_a is the association constant, K_d is the dissociation constant, k_1 and k_{-1} are rates of association and dissociation, K_1 is the first binding event, K_2 the second binding event, HG is the 1:1 host-guest complex, and HG_2 is the 1:2 host-guest complex.

Although ion transport is a kinetic effect, whereas K_a is a thermodynamic parameter, transport rates generally improve with increasing binding affinity due to higher proportions of the required ion-carrier complex. In general, it is desirable to achieve strong binding using appropriately preorganised and complementary receptors to adequately extract the ion from the aqueous phase. If a receptor can simultaneously contact and bind anions without generating internal strain or repulsions, it is said to exhibit complementarity, whilst preorganization into its active binding conformation greatly minimises the enthalpic and entropic costs of reorganisation and desolvation, leading to enhanced K_a values.[45] The rigid steroidal framework **5** fulfils these requirements by preorganising the extremely acidic hydrogen bonding NH groups so that they can cooperatively bind the anion (Figure 6A). [46] In some rare cases, such as compound **5**, high binding affinity is detrimental to transport activity because release of the ion on the other side of the membrane becomes rate limiting.

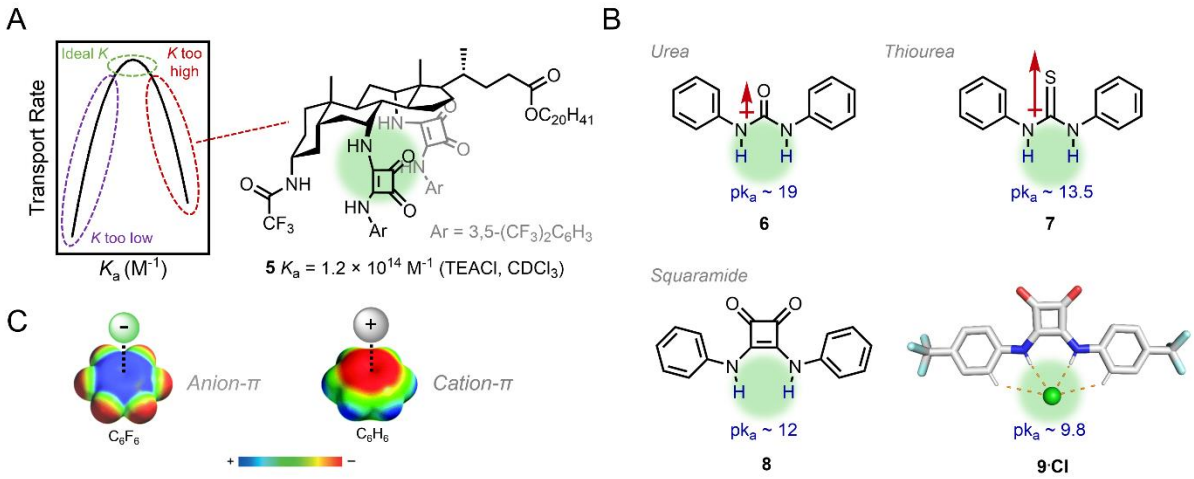


Figure 6. (A) Transport rates generally increase with increasing binding affinity, until decomplexation is rate-limiting, as observed for highly preorganised **5**. (B) Common HB binding motifs, with solid-state squaramide chloride complex[47] (C) Electrostatic potentials of anion and cation π interactions.[48]

Hydrogen bond (HB) donors are the most common binding motifs found in anion transporters, as they are precise, specific, tuneable, and highly directional, with strengths ranging between 4–120 kJ mol^{-1} based on functional group and substituent.[49] Commonly employed motifs include ureas, thioureas and squaramides (Figure 6B). Thioureas are generally more acidic than ureas due to the increased C=S dipole and sulfur's improved ability to stabilize negative charge relative to oxygen.[50] Squaramides feature an additional 10 to 50-fold affinity for halides over thioureas, explained by the more converging N-H donors suitable for spherical anions[46] and increased ortho polarised C-H donation (Figure 6B).[51] The increased acidity has also been rationalised by the enhancement of cyclobutene ring aromaticity upon hydrogen bond formation, and the delocalisation of charge over a larger number of atoms.[52]

In addition to HBs and polarised C-H bonds, anion-π and cation-π interactions can be exploited within receptors for ion recognition. Anion-π interactions are electrostatic interactions between an electron deficient (π-acidic) aromatic ring and anions, arising from the permanent positive quadrupole moment within ring (blue) (Figure 6C).[48] In contrast, benzene exhibits a negative quadrupole (red) more favourable for cation binding. Such motifs have been used in both anion sensing and recognition applications, as well as synthetic transporters.[53]

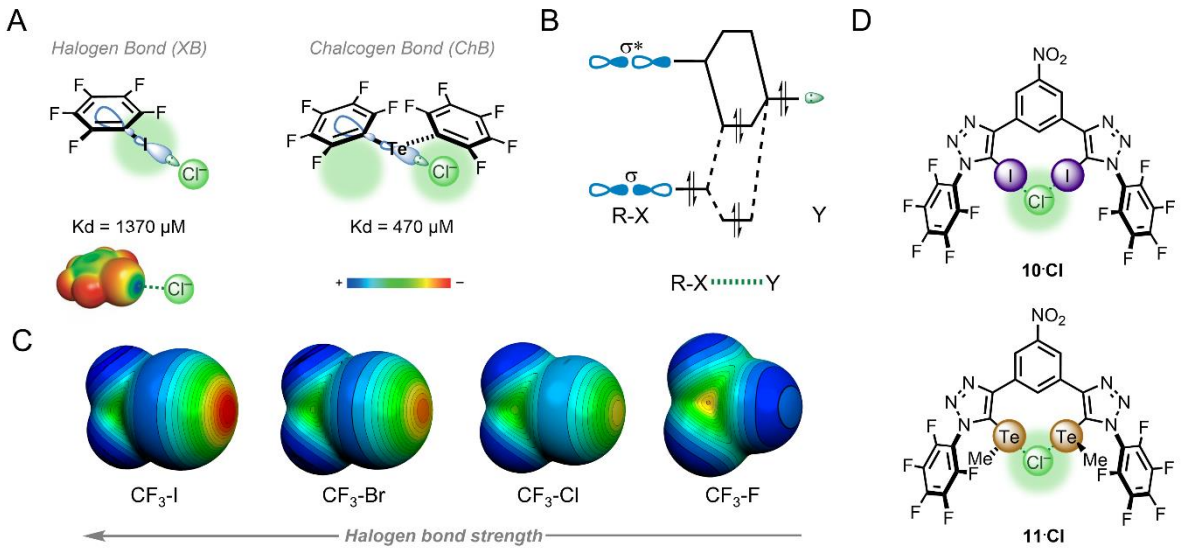


Figure 7. (A) Simple examples of chalcogen and halogen bonding receptors with electrostatic potential map.[54] (B) Generic orbital representation of σ-hole interaction (C) Molecular electrostatic potential maps for the halogen series.[55] (D) Highly active halogen and chalcogen bonding transporters.[56]

Another important class of non-covalent interactions are the chalcogen bond (ChB) and halogen bond (XB), which arise from electron deficient regions, coined 'σ -holes', on group 16 elements and 17 elements bonded to electron-withdrawing functionalities (Figure 7A).[54] Heavy group 16 and 17 elements exhibit an anisotropic electron distribution, resulting in a partially positive charge at the pole of the σ* of the R-X bond, whereas the region orthogonal to the R-X bond represents an 'electronegative belt' of electron density. The positively charged pole can attractively interact with Lewis bases, forming a halogen or chalcogen bond with high directionality (Figure 7B),[57] as the electronegative belt repels the incoming negative charge.

Generally, the larger the halogen or chalcogen, the larger the size of the σ-hole. This effect is also a consequence of the smaller, less polarisable and more electronegative elements sharing a disproportional amount of negative charge, which neutralises the σ-hole (Figure 7C).[55] Relative to hydrogen bonds, XBs and ChBs are more easily tuneable (X can modified as well as R), more directional (~180 ° between the donor and acceptor due to the highly localised σ–hole), and less solvent dependent (due to some degree of charge transfer compared to HB dipole interactions; with similar strength to a metal – halide coordination bond), allowing strong binding even in aqueous media.[58] These desirable features have led

to the development of ionophores such as **10** and **11**, which exploit σ–hole interactions to achieve high ion transport activity (**10**) and selectivity (**11**; preferential binding and transport of the softer Cl^- over ^-OH).[56]

1.2.4.2 Synthetic ion transporter design: lipophilicity and lipophilic balance

Similar to the requirement for small molecule drugs, the correct balance in lipophilicity and hydrophilicity is key for high biological activity in ion transporters. In fact, optimal lipophilicity was found to be the dominant variable in a QSAR study on anion transport activity conducted by Gale, although size and binding affinity also had significant contributions.[43] Transporters must be highly lipophilic to partition within the membrane, but sufficiently hydrophilic to reach the aqueous interface for anion binding, and also be delivered to the bilayer without self-aggregating or precipitating in the aqueous phase.[59] Lipophilicity is quantified by the octanol/water partition coefficient log *P*,[60] where values > 0 represent a higher affinity to the organic phase:

$$\log P = \frac{[A]_{octanol}}{[A]_{water}} \quad (1.4)$$

Thioureas are common replacements for urea groups due to their increased lipophilicity, solubility and binding strength.[61] Similarly, aromatic F and CF_3 groups conjugated to the binding site often improve *K* by inductive effects whilst simultaneously increasing lipophilicity. Although C-F bonds are polar, aromatic C-F and CF_3 groups exhibit reduced polarizability due to the extreme electronegativity of fluorine; making fluorine lone pairs unavailable to hydrogen bond and break the stable HB networks in water. Combined, these effects result in weaker interactions towards water relative to non-polar media, leading to increased lipophilicity and hydrophobicity.[62] In one study, replacement of C-H groups with CF_3 units improved transport by 3 orders of magnitude, which the authors mainly ascribe to the increased log *P*.[63]

Queseda studied the importance of balancing log *P* by varying the alkyl chain lengths of tambjamines whilst keeping chloride binding affinities constant (Figure 8A).[64] Below log *P* = 2, there was limited activity due to poor partitioning. Transport activity peaked at log *P* ≈ 4.2,

with a reduction in activity at high values rationalised by poor deliverability from the aqueous phase (precipitation or aggregation) and lower mobility within the lipid bilayer. A similar trend was observed by Gale in a related study on thioureas, although the maximum was shifted to log*P* ≈ 5-6,[65] highlighting that the optimum log*P* value varies between transporter series.

A. P. Davis and Gale investigated the effects of 'lipophilic balance' by varying the thiourea position between R_1 and R_2 whilst keeping log *P*, *K* and total number of carbons in R_1 + R_2 constant (Figure 9B).[66] Transporters with a centrally located anion binding site ($R_1 \approx R_2$) were considerably more active than peripherally located receptors ($R_1 \neq R_2$). The authors argue that these complexes behave as surfactants, allowing efficient integration within the bilayer and hampering transport. If R_1 and R_2 are balanced, interface interactions are less favourable, leading to faster diffusion across the bilayer. The binding site is more enclosed, which masks

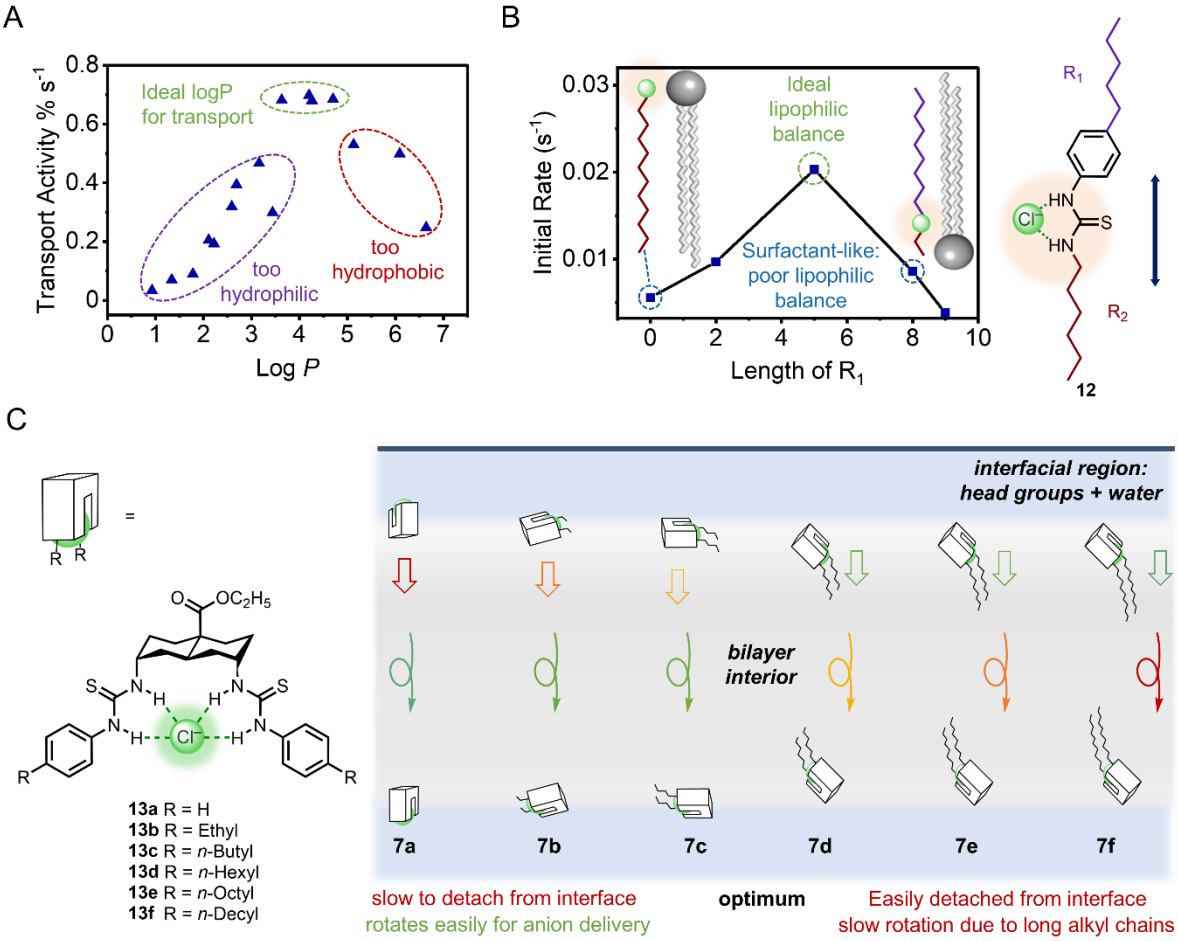


Figure 8. (A) Transport activity vs log P for tambjamine analogues.[64] (B) Impact of lipophilic balance on transport rates.[66] (C) Cartoon representation of transdecalin derivatives **13**, and the impact of lipophilic balance and molecular shape on transport rates.[68]

the polarity and charge from the bilayer and facilitates anion desolvation at the interface. The importance of binding site enclosure towards transmembrane transport is well-established,[67] and may also reduce non-specific binding to other ions and phospholipid head groups.

In a related study by A.P Davis, varying alkyl chain lengths from C_0 – C_{10} in dithioureidodecalins provided a sharp maximum at C_6, consistent with previous studies on receptor encapsulation and lipophilic balance (Figure 9C). MD simulations revealed that shorter alkyl chains form stable interactions between the thioureas and the aqueous interface; impeding transport rates. Longer alkyl chains increase hydrophobic interactions towards the bilayer, leading to binding site reorientation and weaker interface interactions and improved transport. However, these hydrophobic interactions must be broken to rotate the transporter towards the other interface. This barrier to rotation becomes rate determining when the alkyl chain length is too long, resulting in peak transport rates at C_6, where interface interactions and reorientation penalties are balanced.

1.2.5 Key examples of synthetic transporters

Some key examples of transmembrane ion carriers with promising biological activities will be detailed, which generally fulfil the aforementioned design criteria (Figure 9). In a study by Gale and co-workers,[30] **9** and **14** were found promote chloride influx in live cells; coupled to Na^+ influx *via* endogenous channels. Both compounds were reported to promote apoptotic pathways in cells, which was augmented with higher concentrations of external Na+ and Cl^-. **9** was also capable of increasing lysosomal pH, leading to disruption of autophagy (which aids cancer cell survival), representing a unique anti-cancer mechanism.

Calix-pyrroles **15a-b** developed by Gale and Sessler displayed similar properties to the squaramides; promoting Na^+ and Cl^- influx and apoptosis in cells lacking endogenous chloride channels.[20] Intracellular pH remained unaffected in the presence of **15**, whilst inhibiting Na^+ channels attenuated sodium influx and cell death, consistent with an NaCl symport mechanism operating as the mechanism of action for these compounds.

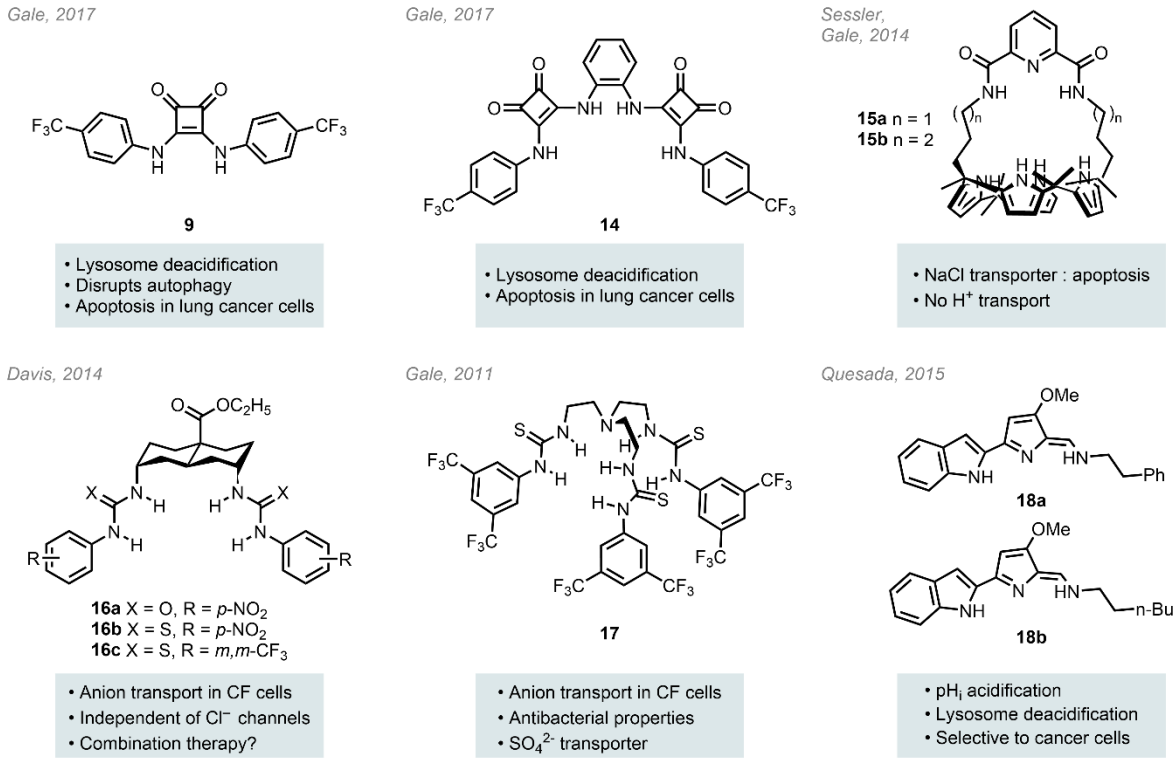


Figure 9. Selected examples of transporters displaying promising biological activities by Gale[30], Sessler and Gale,[20] Davis,[59] Gale,[59] and Quesada.[69]

Recently, Gale, Davis and co-workers screened a library of previously reported anionophores, and **16**-**17** were found to restore chloride transport in cystic fibrosis cells.[59] At lower concentrations, **17** was non-toxic to CF cells but displayed cytotoxicity towards selected cancer lines, whilst at higher concentrations **16b**, **16c** and **17** exhibited mild toxicity to CF cells. Remarkably, **16a** retained potent activity without any cytotoxic effects. The authors also investigated the sensitivity to inhibition of endogenous CaCC (a chloride channel capable of restoring anion transport in CF) and CFTR channels. **16a** and **16b** activity was unaffected by CTFR and CaCC inhibitors, confirming that their transport activity is independent of endogenous chloride channels channels. **17** was inhibited by both CTFR and CaCC inhibitors, whilst remarkably CFTR inhibition increased the transport activity of **16c**. The effects of clinically licenced cystic fibrosis medications were additive in the presence of **16-17**, so these derivatives could potentially be used for combination therapy. In a separate study, **17** and related analogues displayed potent antibacterial activity and were capable of transporting hydrophilic SO_4^{2-} in vesicles.[70]

Finally, synthetic tambjamines **18** were found to acidify pH_i, deacidify lysosomes, and hyperpolarise cells by promoting chloride influx, resulting in selective elimination of cancer cells in the presence of noncancerous cell lines, with more enhanced cytotoxic effects when external chloride concentration was higher.

1.2.5 Concluding remarks on ion transporters

The area of synthetic ion transporters has experienced a burgeoning interest in the last 10-20 years and has become an established area of research; showing promise as potential therapeutics for cystic fibrosis and cancer. Many impressive examples have been reported, displaying promising activities in both vesicles and biological cells, and although not complete by any means, several guidelines exist towards aiding the design of new transporters. However, in nature, ion transport is gated by external stimuli, which allows the precise control of ion flow. Therefore, it would be of interest to develop ionophores that respond to external stimuli such as light; allowing high spatiotemporal control of ion transport using a readily adaptable synthetic system.

1.3 Light as an external stimulus

Light represents an attractive stimulus for manipulating biological systems due to its high spatio-temporal precision, non-invasive nature and wavelength-dependent orthogonality.[71] Light has been demonstrated to image and map information ranging from scales to nanometers (10^{-8} m) to light years (10^{16} m) using super-resolution microscopes or space-based telescopes.[72] To date, a wide range of photoresponsive biological tools have been reported, including naturally occurring systems, optogenetic techniques, photocleavable systems, and photoswitchable peptides, pharmaceuticals, oligonucleotides and channels.[73] The common principle in all these methods is the exploitation of the high spatial selectivity of light, allowing high localisation solely in the region of interest.[74]

1.3.1 Light responsive systems in nature

As previously described, ion channels are typically gated by external stimuli such as ligand or ion binding, light, pH, voltage or mechanical stress, allowing precise control of ion concentrations across lipid bilayers. A key natural example is the halorhodopsin chloride pump, which features a lysine-bound all-*trans* retinal that switches off pump activity in the dark, whilst in the presence of 570 nm light, isomerisation to 13-*cis*-retinal takes place, inducing changes in conformation and polarity and ultimately switching on pump activity (Figure 10).[75] Photon absorption by retinal-derived proteins in the retina and subsequent conversion into electrical signals also forms the basis of vision in animals.[76]

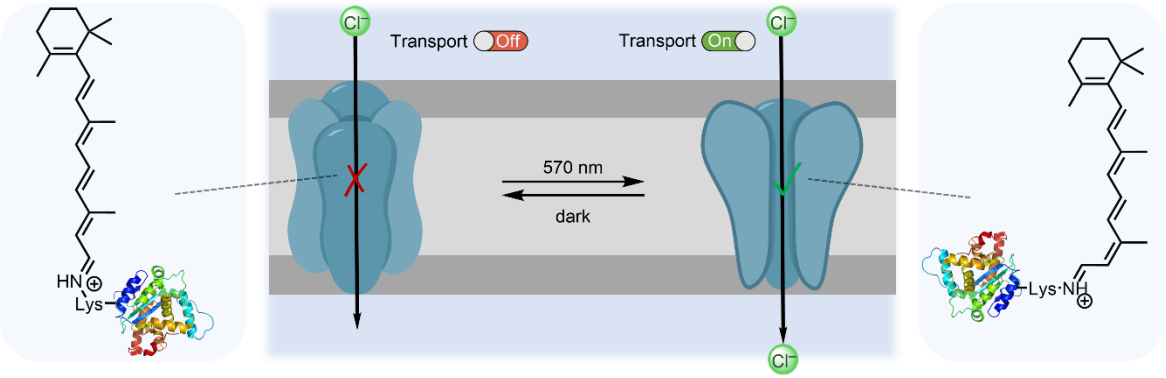


Figure 10. Photoswitchable chloride pump halorhodopsin. Chloride influx is switched on in the presence of 570 nm light by retinal isomerisation.

1.3.2 Optogenetics

The brain is inherently complicated to analyse and understand, as it is made up of an extremely large amount of highly ordered interconnected heterogenous neurons.[77] The field of optogenetics, which involves the expression of light-sensitive proteins in target neurons, allows spatiotemporal control of signalling pathways within the brain, enabling precise mapping of neuronal activity within the brain at the single synapse level (Figure 11).[78]

In brief, light activated channels or pumps coined opsins (analogous to Figure 10) are expressed within a specific neuronal cell type. When activated with light, ion flow hyperpolarizes or depolarizes the cell membrane of the neuron from its resting potential V_m, resulting in inhibition or excitation of adjacent neurons.[79] This allows the excitation and

inhibition of specific neurons and observing the outputs and functions of these neural networks using electrophysiological methods. [78] Optogenetic techniques may be employed in live cells, mice and even humans, and incorporated into any excitable cells (e.g. cardiac or eye).[79]

Since the initial incorporation of opsins within neurons, there has been an explosion of studies utilising optogenic techniques, ranging from individual synaptic scales to the full network of the brain. For instance, local injections of viral vectors or direct creation of transgenic mouse lines has enabled optogenic analysis of neural networks in mice in a study by Petersen and co-workers.[80] The authors studied the synaptic activity within small neuron networks (microcircuits) by comparing responses within different optogenic neuron types. This allowed detailed mapping of these networks, and confirmed the role of FS GABAergic neurons in excitatory neuron inhibition.[81] Many research groups have also demonstrated that optogenetic techniques can stimulate the sensorimotor cortex whilst simultaneously recording motor movements in mice to determine precise cortical function towards motor responses.[80]

Another important feature of optogenetic techniques is the ability to engineer various wavelength-responsive proteins, including blue, green, yellow or red light.[82] This opens up the possibility of developing more complex systems in which multiple photoreceptors can be activated within a single cell to coordinate cellular responses. This enables comparison of different strengths of multiple types of input onto the same neuron, and has been demonstrated to enable quantitative comparison of strengths along multiple pathways across the entire brain.[83]

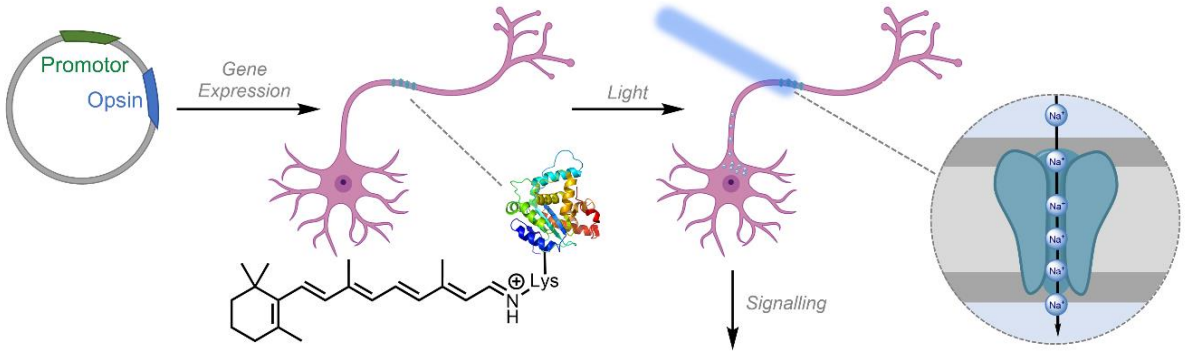


Figure 11. Outline of optogenetic methods to study neuronal networks

Recently, optogenetic techniques have advanced to human trials. Roska and co-workers developed an optogenetic vector that was injected directly into a blind patients eye. Combined with specialised goggles that transform visual stimulus into light pulses, the amber (590 nm) - light responsive channelrhodopsin was successfully employed to restore vision towards simple objects in the patient. This represents the first example of a partial functional recovery in a neurodegenerative disease after optogenetic therapy in humans.[84]

In summary, a plethora of revolutionary discoveries and applications within the field of optogenetics have been developed over the last 20 years. This demonstrates the high versatility of using light to precisely manipulate biological functions, and sets a strong precedent for future endeavours in these highly multidisciplinary overlapping fields.

1.3.3 Photodynamic therapy

Photodynamic therapy is a clinically approved technique used for cancer treatment, exploiting photosensitisers that become excited with specific wavelengths of light. The excited species react with molecule oxygen to generate $^1O_2$ and reactive oxygen species (ROS) within the irradiated tissue, resulting in cell death within relatively specific regions (Figure 12A).[85]

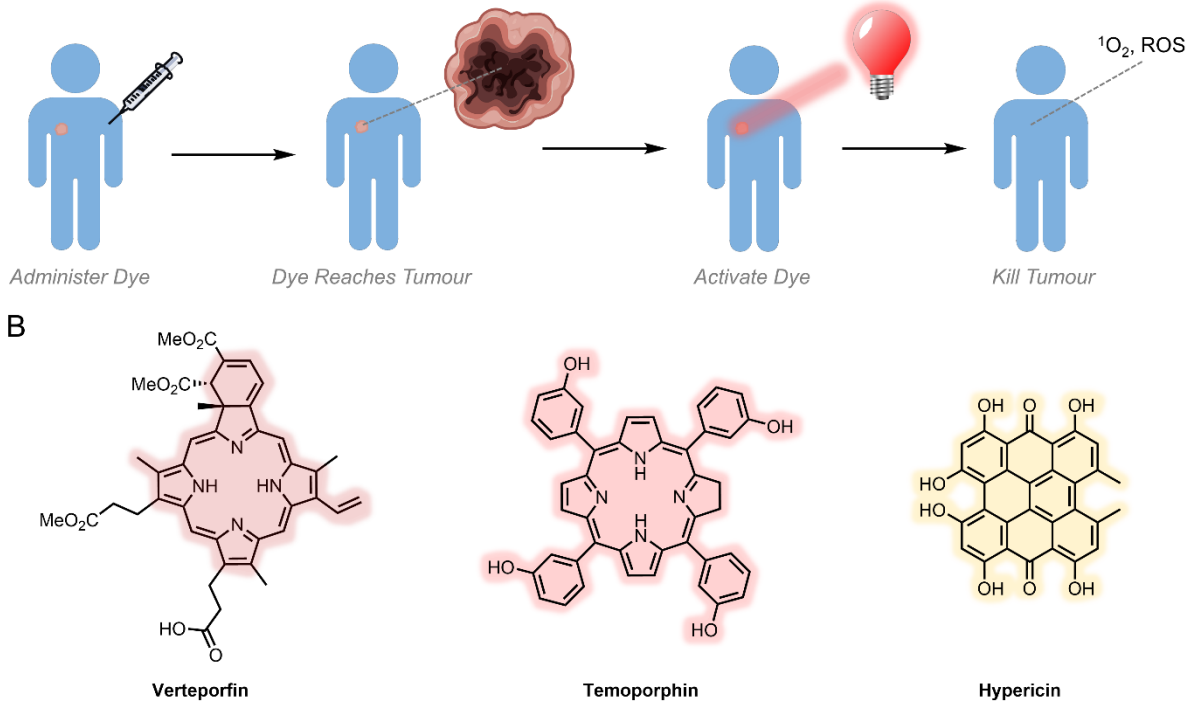


Figure 12. (A) Outline of photodynamic therapy (B) Examples of dyes used in photodynamic therapy

Typically, highly conjugated amphiphilic dyes absorbing between 600 – 800 nm are used with high quantum yields towards singlet oxygen, such as **Verteporphin, Temoporphin** and **Hypericin** (Figure 12B).[86] Although clinically used across the globe as successful cancer treatments, there are still issues with efficient delivery of the photosensitisers to the target site, so recent efforts have been devoted towards tagging the dyes and their delivery systems with specific antibodies and high affinity ligands to target specific regions of tissue.[87]

1.3.4 Photopharmacology

Drug molecules have become an essential component of modern medicine, with yearly spending on medicines by developed countries reaching $ 1.4 trillion in 2021.[88] Although extremely effective at treating enormous ranges of disease states, key issues such as poor selectivity to targets and drug resistance (e.g. the emergence of resistant bacterial strains) result in toxic complications and limit the application of pharmaceuticals.[89] Increasing the selectivity of drug molecules towards their respective targets would lower the therapeutic window and therefore dose of a drug.[90] 85% of promising small-molecule drug candidates are discarded prematurely, often due to limited therapeutic windows and poor selectivity profiles (whether this is binding to single or multiple desired targets simultaneously without interacting to off-targets).[89,91] One promising approach towards overcoming selectivity and drug resistance issues are light-activated drugs, which offer full spatiotemporal control of drug activity. Such compounds typically contain a photoresponsive motif capable of isomerisation.

1.3.4.1 Photoresponsive motifs

Several synthetic photoresponsive motifs have been successfully employed within drug-like molecules and biological tools, and these can be broadly categorised as photoswitches (reversible) or photocages (irreversible). The most commonly employed photoswitches are azobenzenes **19** (chapter 2), [hemi](thio)indigos **20-22**,[92,93] diaryl-ethenes **23**,[89] and stilbenes **24**,[94] which all principally exist as two double bond isomers (Figure 13A-D).

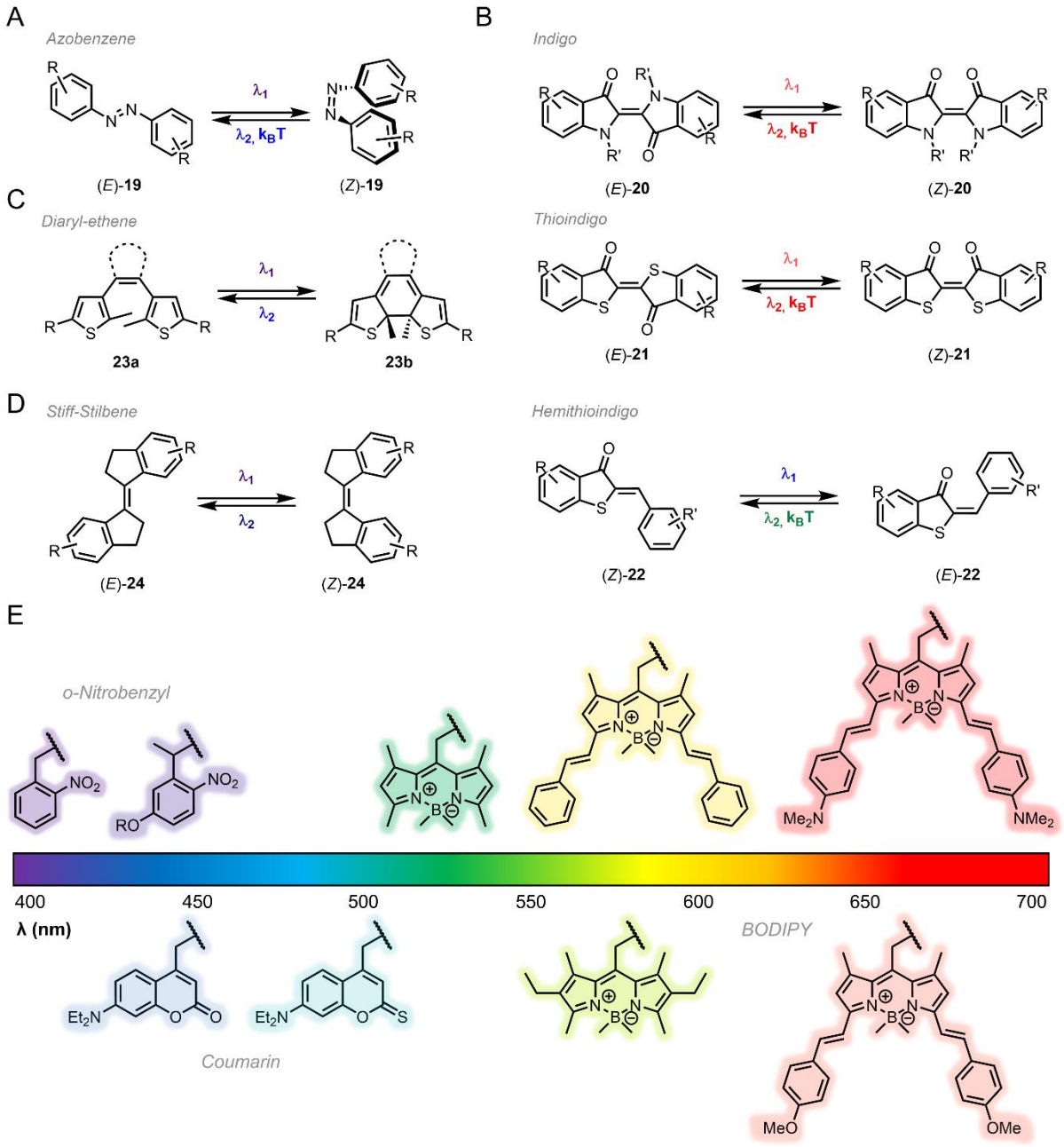


Figure 13. (A-D): Commonly employed photoswitches (E): Commonly employed photocages

In brief, (*E*) → (*Z*) isomerisation of azobenzenes leads to a large geometrical change and polarity (dipole moments changes of ~ 3 D), and this process can be reversed using orthogonal wavelengths of light or thermal decay.[89] N-N, disubstituted Indigos **20** have recently emerged as efficient photoswitches, capable of isomerising with highly redshifted wavelengths of light. It is necessary to functionalise the N-substituent, as the amide hydrogens suppress switching activity *via* excited state H-atom transfers.[92] The analogous thioindigo **21** lacks these hydrogen atoms, so can readily photoisomerise, whereas hemithioindigos **22** can be switched

in a highly bistable fashion with low fatigue.[93] Diaryl-ethenes **23** isomerise via a photochemical cyclisation, from the open (**23a**) to closed (**23b**) form, resulting in large changes in flexibility and conjugation and electronic properties.[89] Stiff-stilbenes **24** are an example of strained alkenes that can reversibly switch using UV and visible light. These derivatives are readily prepared and exhibit high quantum yields for photoisomerization, and have the added benefit that both isomers are isolable, which is convenient when bistable systems are required.

Photocages fundamentally differ from photoswitches in that they irreversibly cleave in the presence of light (Figure 13E).[95] The cleavage and absorption wavelength of the chromophores can be tuned across the entire range of the visible spectrum depending on which motif (*o*-nitrobenzyl, coumarin, BODIPY) and substitution patterns are employed, which opens up opportunities where photoprotecting groups can be orthogonally cleaved selectively in the presence of another.[96] In general, photochemical cleavage of photocages can reveal key pharmophoric features of a molecule, allowing high 'Off' → 'On' control.[74]

1.3.4.2 Examples of photoswitches employed in photopharmacology

In 2011, Trauner and co-workers reported small molecule azobenzene derivative **25** capable of blocking voltage-gated potassium channels in the (*E*)-form (Figure 14A).[97] The authors demonstrated that irradiation with a variety of wavelengths translated into a range of different (*Z*)-isomer percentages, leading to wavelength dependent current traces, whilst in the dark, the system naturally relaxes to the (*E*)-form again to block the channel in the order of seconds. These small molecule inhibitors thus essentially function as a photoswitchable version of the well-known channel blocker lidocaine, which acts as a local anaesthetic. In a follow-up study,[98] these small molecules were shown to restore light sensitivity to the retina in mouse models representing degenerative blinding diseases. Thus, similar to optogenetics, these systems show high promise as a potential strategy to restore vision in these kinds of diseases.

Kuhn and co-workers reported a hemithioindigo system that functions as a photoswitchable 12/15-lipoxygenase inhibitor (Figure 14B).[99] In the 'off state' (*Z*)-**26**, binding was weak (IC_{50} = 0.7 mM), whilst after irradiation with light, the inhibitor bound with 21 μM potency. Together

with *in silico* modelling of known X-ray structures of the enzyme, the authors suggest that upon isomerisation to (*E*)-**26**, binding towards iron within the active site is significantly sterically favourable, leading to the enhanced binding affinity. The authors reason that these compounds could potentially be isomerised within the skin to treat inflammatory skin diseases/ In 2014, Komrov employed a diaryl-ethene motif within antimicrobial peptide gramicidin S (Figure 14C). [100] The hydrazide amide linkage within the structure was essential to maximise air stability, as electron-rich diarylethenes are prone to oxidation. Using molecular dynamics,

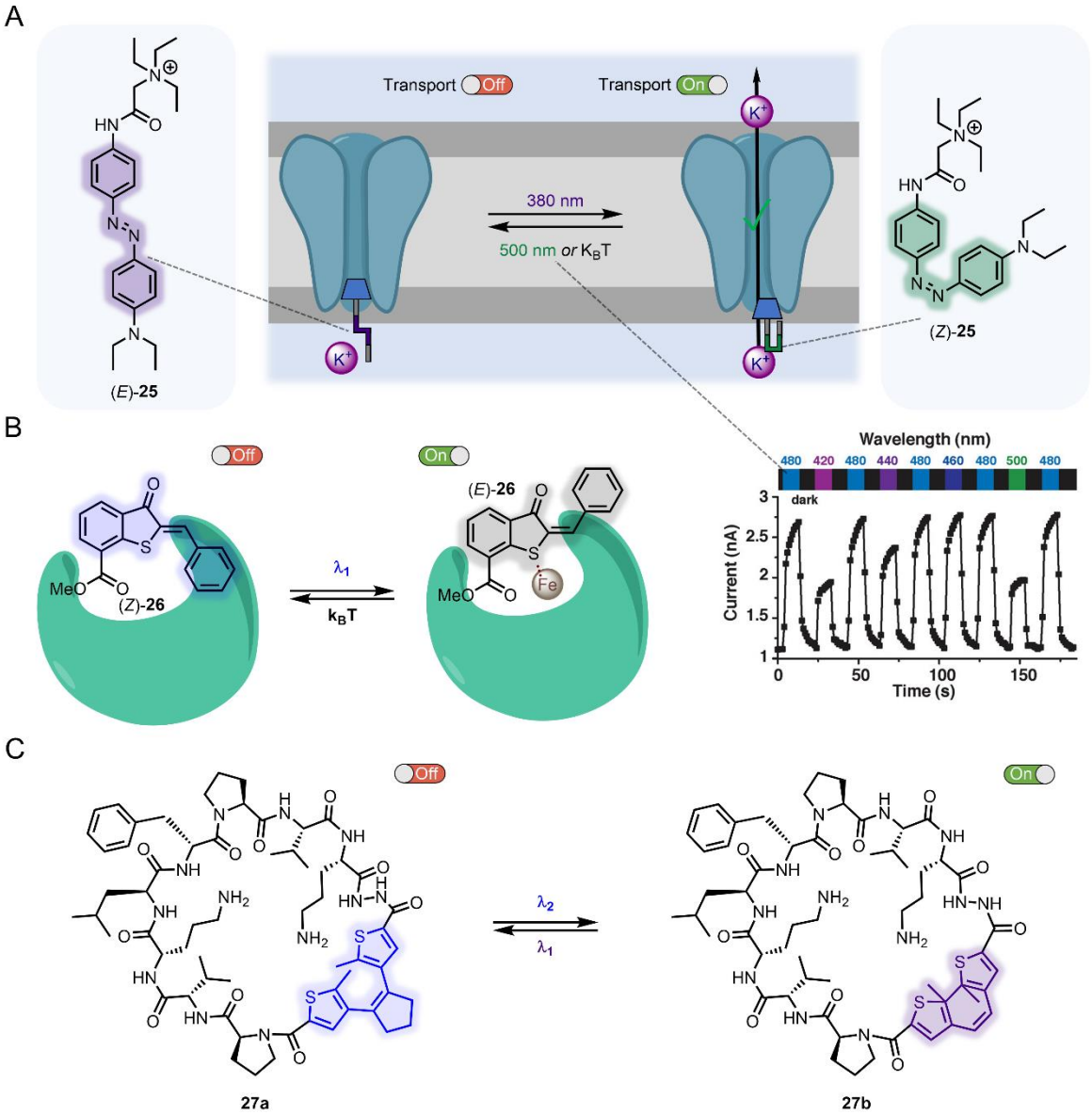


Figure 14. (A) Photoswitchable ion channel blocker by Trauner.[97] Graph reproduced with permission. (B) Photoswitchable Lipoxygenase inhibitor using hemithioindigo by Kuhn.[99] (C) Photoswitchable antimicrobial by Komarov.[100]

the authors anticipated that the amphiphilic side chain pattern required for biological activity would reside in an unfavourable conformation in the more strained 'closed' diarylethene **27a**. Upon isomerisation to the open form **27b**, the conformation was significantly more similar to natural gramicidin. Antimicrobial assays confirmed that the activity could be controlled with light, opening up opportunities towards localised treatment of microbial infections.

In 2017, Tour *et al.* incorporated an axially chiral overcrowded stilbene into a molecular drill **28** (Figure 15).[101] In the presence of UV light, (*E*) → (*Z*) → (*E*) isomerisation proceeds via unidirectional 180° rotations to minimise steric clash with the chiral methyl group.[102] The authors exploited the mechanical force induced by the unidirectional rotor motion to drill pores into membranes with high spatiotemporal precision during irradiation. These pores were shown to induce cell necrosis and facilitate the transport of chemical species across bilayers in live cells. The rotor could be functionalised with peptides to target cell-surface recognition sites, whilst appendage of fluorophores allowed tracking of the compound within cells. In a follow-up publication, the authors report similar derivatives capable of killing both Gram-negative and Gram-negative bacteria within minutes in therapeutic models of burn wounds.

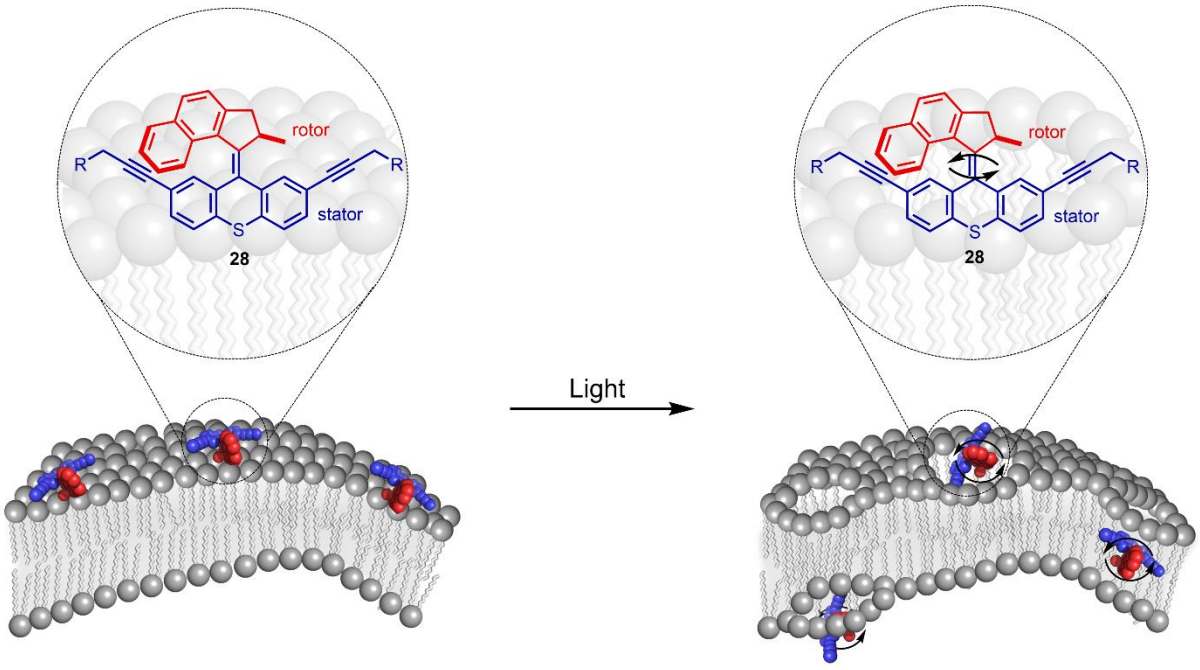


Figure 15. Photoswitchable molecular drill by Tour and co-workers. [101]

This novel broad-spectrum molecular machine-based antibiotic mechanism was shown to not lead to the development of antibacterial resistance that is usually accompanied with conventional small-molecule drugs.[103]

1.3.4.3 Examples of photocages employed in photopharmacology

A wide range of biological functions can be triggered using photocaged drug molecules. For example, Yi and co-workers developed nitrobenzyl caged prodrug **29**, which upon irradiation forms nitroaldehyde **30** and antitumour compound 5-fluorouracil **31,** which currently is the most widely used anticancer drug (Figure 16A).[104] **29** did not display to any cytotoxic effects towards healthy cells, but exhibited antitumour activity when irradiated with UV light, demonstrating high potential for **29** as a selective agent for cancer treatment.

Photoprotecting groups have also been employed within living systems. Jullien *et. al.* developed thiocoumarin **32**, which upon irradiation releases **33** and cyclofen derivative **34,** which can control the activation of proteins and development of embryos.[105] The authors demonstrate that when **32** and **13-*cis*-retinoic acid** were incorporated within zebrafish embryos, orthogonal photoactivation to **34** and **all-*trans*-retinoic acid** was possible, enabling the control of zebrafish embryo development.

Finally, Feringa and co-workers developed BODIPY photocage **35**, which upon illumination with red light affords **36** and dopamine **37**.[106] Dopamine is essential towards regulating cardiac function by increasing heart rate, but clinical use of **37** to treat cardiac function often leads to side effects ranging from anxiety to life-threatening arrythmias. By selectively cleaving **35** inside human cardiomyocytes, the authors demonstrated that the beating frequency and cardiac rhythm could be controlled using light, showcasing that photoprotecting groups display promising potential within a biological and even medical setting.

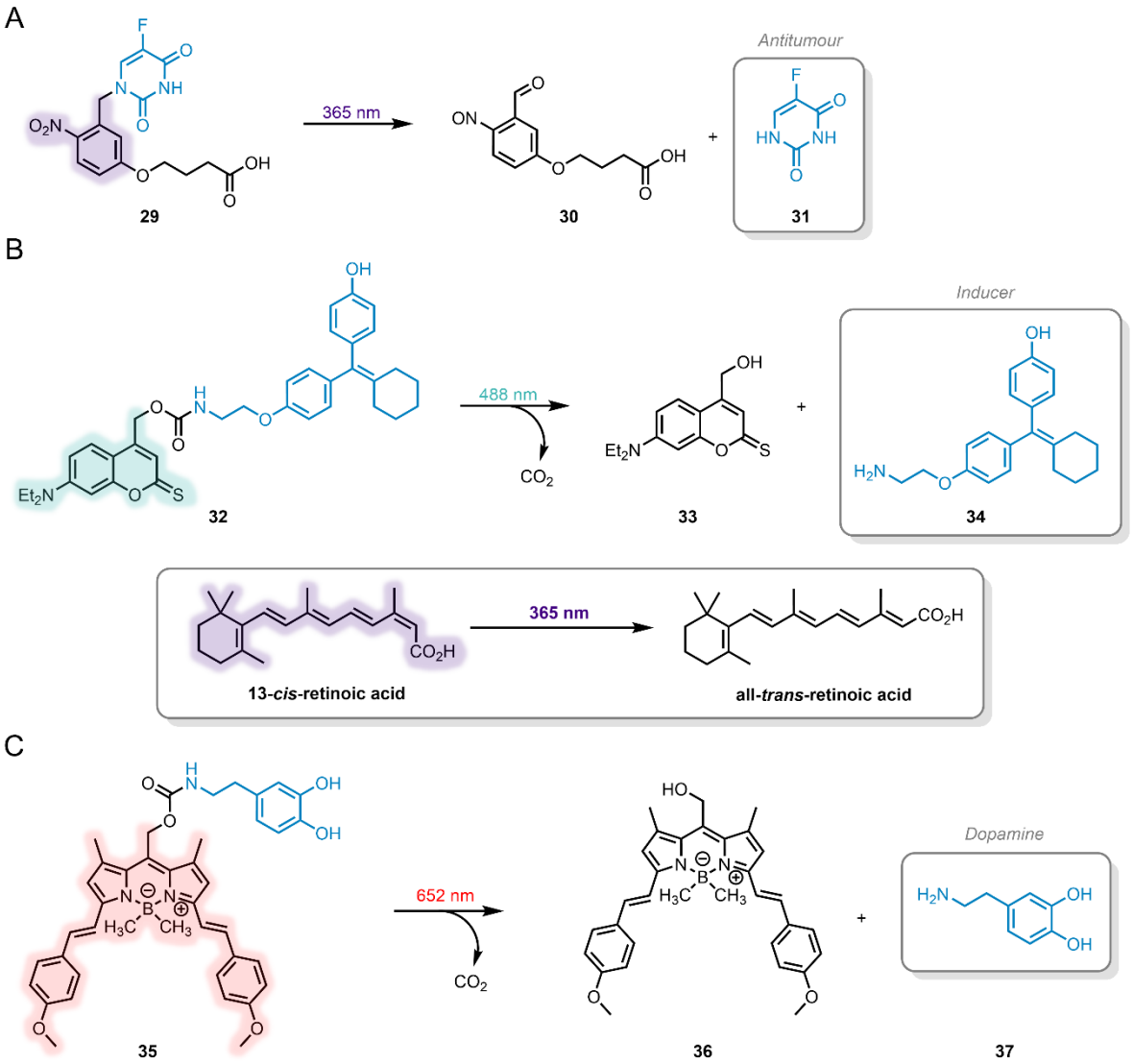


Figure 16. Photocaged biologically active compounds by (A) Yi[104] (B) Jullien[105] (C) Feringa[106]

1.3.4.4 Challenges and outlook in photopharmacology

The field of photopharmacology is still at its infancy, and thus most reports are still at the proof-of-concept stage. However, significant landmark discoveries have been made over recent years, including a large number of examples modulating a range of targets in both cellular models and live animals such as zebrafish; including G-protein coupled receptors, enzymes, cytoskeletons, ion channels, pumps or cytotoxic agents.[107]

There are inherently many challenges when developing photopharmaceuticals, especially as multiple compounds (i.e. both isomers of a photoswitch, or the cage and uncaged compound in photocages) and their metabolites must simultaneously fulfil the criteria required for

generating a successful medicine, and all compounds involved must be approved for clinical use.[74] These criteria include, but are not limited to, desirable absorption, bioavailability, solubility, metabolic stability, clearance, low toxicity, selectivity to off-targets, membrane permeability, favourable pharmacodynamics and high activity.[90]

Current estimates stipulate that one in every 5000 drug candidate that enter preclinical stages become approved drugs, and each of these would have originated from early-stage drug discovery programs, often involving screening in the order of 100,000 compounds.[108] Combined with the added dimension of introducing photoresponsive properties, this process becomes increasingly challenging. This also includes the structural constraints (e.g. the requirement of aromatic rings conjugated to a photoisomerisable bond) or the requirement for substituents essential for efficient switching properties. Not every pharmacophore may exhibit obvious photoswitch attachment sites, making the general design of the system non-trivial,[109] and the interplay of multiple kinetic processes (absorption, clearance, photoswitch thermal half-life etc) make the study of photopharmaceuticals more complicated. [74]

In spite of these challenges, photopharmaceuticals offer distinct benefits over traditional medicines. For example, Feringa and co-workers developed photoswitchable quinoline antibiotic **37** which displays higher antibacterial activity when irradiated with light due to the formation of (*Z*)-**37** (Figure 17A).[110] The half-life of this isomer is ~ 2 hours, which consequently means that the active antibiotic will not accumulate within the system after a significant time delay; within three hours, the antibiotic effects are completely lost (Figure 17B). In many cases, build-up of antibiotics within bacteria lead to resistance, so the authors postulate this can theoretically prevent the development of microbial resistance.[74]

Appropriately tuned thermal half-life or reversible photoswitches can also be used modulate the drugs properties within the body. For example, if both isomers display significantly different metabolic stabilities, clearances or pharmacokinetic profiles, appropriately timed isomerisation and irradiation times may be used to fine-tune the behaviour of the drug to maximise its

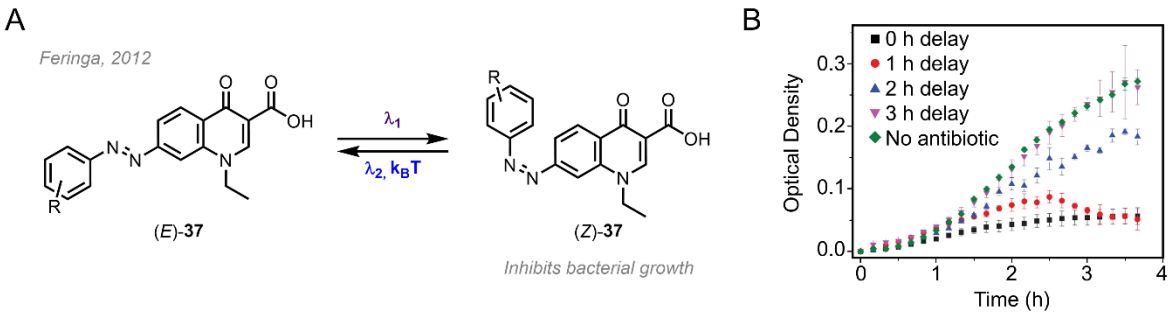


Figure 17. (A) Photoswitchable antibiotic (B) Growth curves of E. coli with varying delay times after irradiation. Samples irradiated 3 h before incubation show similar growth patterns to the control run. Graph reproduced with permission.[110]

therapeutic window.[74] If both isomers of the photoswitch exhibit significantly different polarities and thus absorption and membrane permeabilities, irradiation with light could be used to control these variables when required. Precise timing of when the drug is activated (e.g. after sufficient absorption) and appropriate blood-concentrations again offers unprecedented spatiotemporal control unique to photopharmaceuticals.[89]

In the case of photocages, it is also possible to repurpose clinically approved drugs that have already gone through rigorous medicinal chemistry programs, by modification with a photoswitch.[111] This may shorten the hit-to-lead process, as long as the photocaged drug and its photodecomposition products fulfil the clinical requirements of the drug. Perhaps it may also be necessary to deliver the light-activated drugs via carriers such as hydrogels to improve their biological properties and distribution.[109]

1.3.4.5 Challenges and outlook for azobenzenes in photopharmacology

Azobenzenes are the most commonly employed motifs within photopharmacology, as they are easily tuneable, functionalisable, can switch without detectable fatigue, and exhibit large conformational changes (Chapter 2 discusses azobenzenes in greater detail).[107] However, molecules containing the azo functional group are often flagged as pan-assay interference compounds (PAINS),[74] which are compounds that commonly interfere with assay readings during drug hit screenings, often leading to false positives. This is often due to N=N reduction (usually *via* GSH [glutathione], azo reductases, or NADPH reductases) to the corresponding

hydrazine, which may in reality be the active drug molecule.[112] Azobenzenes are also strongly coloured dyes, which may interfere with the assay readings, and are prone to aggregation. Additionally, azo reduction can lead to toxic and potentially carcinogenic arylamine biproducts, whilst oxidation to the diazonium leads to toxic metabolites.[89] The N=N bond can also potentially form adducts with DNA, leading to potentially harmful side-effects. [74]

However, these issues can be avoided by screening compounds using less reductive assays, or *via* phenotypic screens, although this then requires retrospectively identifying the target protein that elicits the phenotypic response of the lead molecule.[74] Additionally, lower concentrations or less reactive azobenzenes can be used, such as more electron-rich systems that render the diazo bond less electrophilic, or more sterically hindered and weakly basic diazo bonds, which suppress diazo protonation and subsequent reduction (Figure 18A).[74] Another approach is using heteroarylazo systems, which have shown high promise as efficient photoswitches that exhibit high stability under biological conditions, and offer polar interactions that could contribute to ligand binding and maximising lipophilic efficiency.[113] Careful modification of the azobenzene core and understanding of metabolites may allow the generation of structures that exhibit lower toxicity. Furthermore, if doses are appropriately low and activities sufficiently high, toxic effects can be overcome, as observed in animal models of vision restoration.[107]

Gratifyingly, several azo compounds have historically been approved for human use (Figure 18B). For example, Prontosil **38**, originally used as a dye on laboratory rats and rabbits, was found to exhibit potent antibacterial properties without significant toxicity, and was prolifically used within the 20th century.[114] However, **38** actually functioned as a prodrug to **39** *via* azo reduction. Phenazopyridine **40** acts as a local analgesic within the urinary tract, and is still orally prescribed.[115] The side effects are relatively benign, including orange/red coloured urine due to the presence of the azo dye. Furthermore, dyes **41-43** are commonly employed as food colourings and exhibit no toxic side effects.[89]

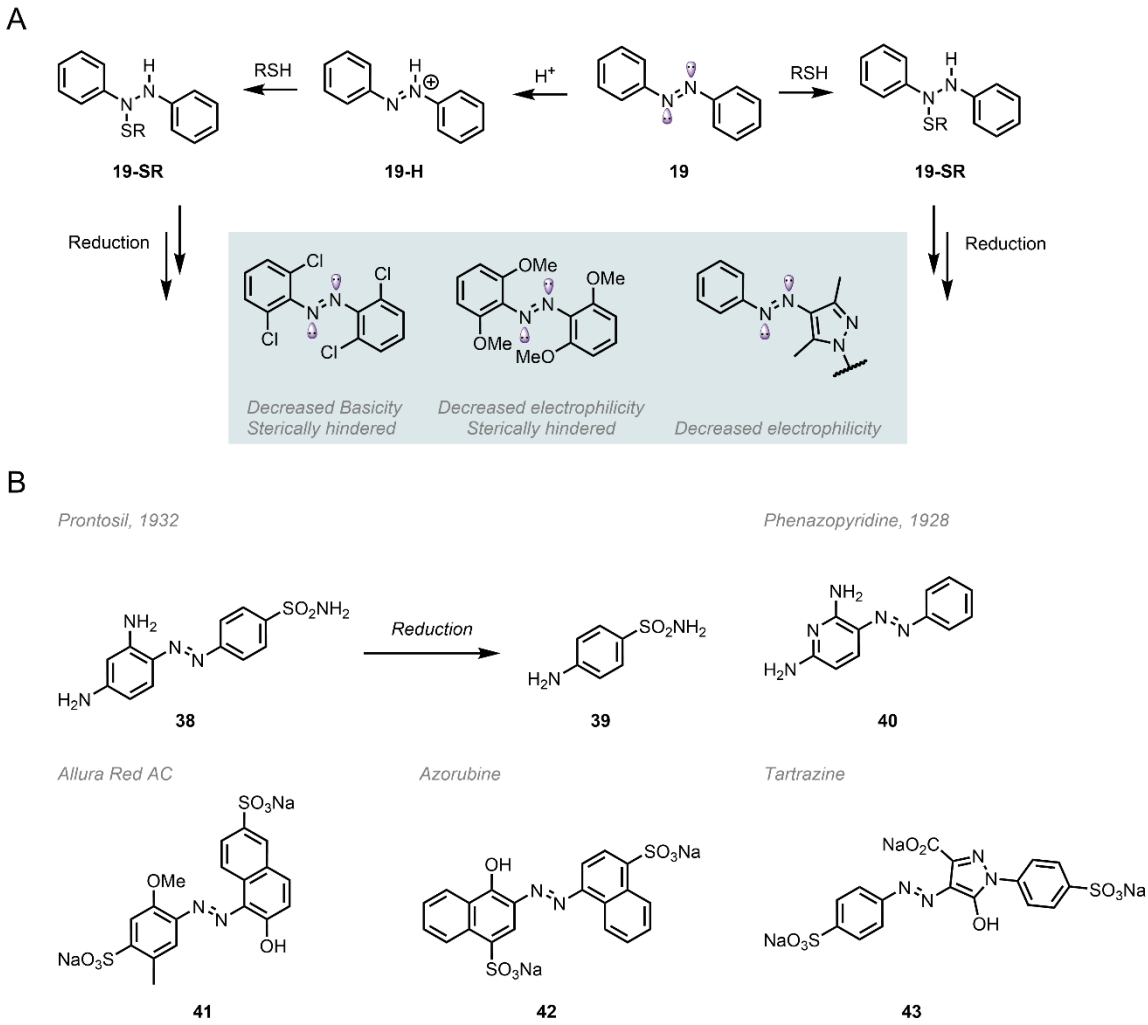


Figure 18. (A) Possible reduction pathways of azo bonds and solutions to supress reduction (B) Azo compounds approved for human use.

One final challenge is the inherent issue of studying both isomers for their drug-like properties. Incomplete photoconversions or short half-lives may provide complications in analysing biological data.[74] This may be overcome by preparing bistable derivatives of the model system,[116] facilitating the ability to study both isomers in detail, and potentially obtain crystal structures of the both photoswitches interacting with their target(s).[89] Another potential caveat is that photoisomerisation may not occur once one isomer is strongly bound to a target, however binding is typically a dynamic effect, so this issue may be overcome. [89]

However challenging, many research groups are actively progressing the field, and combined with the momentum of optogenics and photodynamic therapy, and ever-growing improvements in light sources (LED power and precision),[109] the field of manipulating

biological systems with light represents an exciting and fruitful area of research. Photoswitchable systems show high promise in the context of treating topical conditions or within the retina, but recent work has also employed systems that respond to more redshifted wavelengths of light, allowing photoswitching within deeper tissues.[89]

1.4 Project aims

The following chapters will outline work to build on the library of available azobenzene substitution patterns, with the aim of accessing scaffolds that exhibited improved photoswitching properties, structures that isomerise within more deeply penetrating tissues, and exhibit improved pharmacokinetics, metabolic stability and other relevant properties. These photoswitches will then be employed within the context of photoswitchable ion transporters, which are currently underexplored and show high promise as potential therapeutics.

Chapter 2 describes the development of novel, highly redshifted azobenzene scaffolds, showcasing robust periods trends in relation to absorption wavelength, solid-state structure conformations, (*Z*)-isomer half-life and glutathione stability.

Chapter 3 concerns the design, synthesis and transport properties of fully reversible redshifted photoswitchable anion transporters.

Chapter 4 broadens the scope of the explored photoswitches by functionalisation with different receptor groups, showcasing proof-of-principle studies towards achieving halogen bonding photoswitchable catalysis and ion pair binding.

Chapter 5 outlines the experimental procedures during this work.

1.5 References

[1] D. C. Gadsby, *Nat. Rev. Mol. Cell Biol.,*, 2009, **10**, 344–352.
[2] J.-B. Kim, *Korean J Pediatr.*, 2014, **57**, 1–18.
[3] J. T. Davis, P. A. Gale and R. Quesada, *Chem. Soc. Rev.*, 2020, **49**, 6056–6086.
[4] B. Alberts, A. Johnson, J. Lewis, M. Raff, K. Roberts and P. Walter, *Molecular Biology of the Cell. 4th edition*.
[5] N. Sakai and S. Matile, *J. Phys. Org. Chem.,*, 2006, **19**, 452–460.
[6] N. J. Yang and M. J. Hinner, *Methods Mol Biol*, 2015, **1266**, 29–53.
[7] P. Läuger, *Angew. Chem. Int. Ed.*, 1985, **24**, 905–923.
[8] E. Gouaux and R. Mackinnon, *Science*, 2005, **310**, 1461–1465.
[9] M. V. Clausen, F. Hilbers and H. Poulsen, *Front., Physiol.*, 2017, **8**, 1–16
[10] R. S. Hector and M. S. Gin, *Supramolecul Chem.*, 2005, **17**, 129–134.
[11] S. H. Wright, *Adv Physiol Educ*, 2004, **28**, 139–142.
[12] S. Offermanns and W. Rosenthal, Eds., in *Encyclopedia of Molecular Pharmacology*, Springer, Berlin, Heidelberg, 2008, pp. 457–457.
[13] C.-Y. Tang and T.-Y. Chen, *J Biomed Biotechnol*, 2011, **2011**, 685328.
[14] M. T. Clunes and R. C. Boucher, *Drug Discov. Today Dis. Mec.h*, 2007, **4**, 63–72.
[15] S. Kumar, A. Tana and A. Shankar, *Eur. J. Intern. Med.*, 2014, **25**, 803–807.
[16] E. Hernando, V. Capurro, C. Cossu, M. Fiore, M. García-Valverde, V. Soto-Cerrato, R. Pérez-Tomás, O. Moran, O. Zegarra-Moran and R. Quesada, *Sci. Rep.*, 2018, **8**, 2608.
[17] A. Litan and S. A. Langhans, *Front. Cell Neurosci*, 2015, **9**, 86.
[18] M. Yang and W. Brackenbury, *Front. Physiol*., 2013, **4**, 1-10
[19] B. A. Webb, M. Chimenti, M. P. Jacobson and D. L. Barber, *Nat. Rev. Cancer.*, 2011, **11**, 671–677.
[20] S.-K. Ko, S. K. Kim, A. Share, V. M. Lynch, J. Park, W. Namkung, W. Van Rossom, N. Busschaert, P. A. Gale, J. L. Sessler and I. Shin, *Nat. Chem.*, 2014, **6**, 885–892.
[21] R. Perez-Tomas and M. Vinas, *Curr. Med. Chem.*, **17**, 2222–2231.
[22] L. E. Bickerton, T. G. Johnson, A. Kerckhoffs and M. J. Langton, *Chem. Sci.*, 2021, **12**, 11252–11274.
[23] J. J. Clare, *Disc.y Med.*, 2010, **9**, 253–260.
[24] T. Saha, A. Gautam, A. Mukherjee, M. Lahiri and P. Talukdar, *J. Am. Chem. Soc.*, 2016, **138**, 16443–16451.
[25] J. A. Malla, V. K. Sharma, M. Lahiri and P. Talukdar, *Chem. Eur. J.*, 2020, **26**, 11946–11949.
[26] W.-L. Huang, X.-D. Wang, Y.-F. Ao, Q.-Q. Wang and D.-X. Wang, *J. Am. Chem. Soc.*, 2020, **142**, 13273–13277.
[27] P. D. Leeson and R. J. Young, *ACS Med. Chem. Lett.*, 2015, **6**, 722–725.
[28] B. C. Pressman, *Annu. Rev. Biochem.*, 1976, **45**, 501–530.
[29] T. M. Fyles, *Chem. Soc. Rev.*, 2007, **36**, 335–347.
[30] N. Busschaert, S.-H. Park, K.-H. Baek, Y. P. Choi, J. Park, E. N. W. Howe, J. R. Hiscock, L. E. Karagiannidis, I. Marques, V. Félix, W. Namkung, J. L. Sessler, P. A. Gale and I. Shin, *Nat. Chem.*, 2017, **9**, 667–675.
[31] M. G. Wolfersberger, *J. Exp. Biol.*, 1994, **196**, 5–6.
[32] I. J. Furlong, C. L. Mediavilla, R. Ascaso, A. L. Rivas and M. K. Collins, *Cell. Death. Differ.*, 1998, **5**, 214–221.
[33] K. Neupert-Laves and M. Dobler, *Helvetica. Chimica. Act.a*, 1975, **58**, 432–442.
[34] A. Fürstner, J. Grabowski, C. W. Lehmann, T. Kataoka and K. Nagai, *Chembiochem*, 2001, **2**, 60–68.
[35] T. Sato, H. Konno, Y. Tanaka, T. Kataoka, K. Nagai, H. H. Wasserman and S. Ohkuma, *J.Biol. Chem.*, 1998, **273**, 21455–21462.
[36] J. T. Davis, in *Anion Recognition in Supramolecular Chemistry*, eds. P. A. Gale and W. Dehaen, Springer, Berlin, Heidelberg, 2010, pp. 145–176.
[37] S. Jenkins, C. D. Incarvito, J. Parr and H. H. Wasserman, *CrystEngComm*, 2009, **11**, 242–245.

[38] P. I. Hernández, D. Moreno, A. A. Javier, T. Torroba, R. Pérez-Tomás and R. Quesada, *Chem. Commun.*, 2012, **48**, 1556–1558.
[39] D. Łowicki and A. Huczyński, *BioMed Res. Int.*, 2013, **2013**, e742149.
[40] J. B. Russell, *J. Anim. Sci.*, 1987, **64**, 1519–1525.
[41] J. William A. Harrell, M. L. Bergmeyer, P. Y. Zavalij and J. T. Davis, *Chem. Commun.*, 2010, **46**, 3950–3952.
[42] T. N. Lambert, J. M. Boon, B. D. Smith, M. N. Pérez-Payán and A. P. Davis, *J. Am. Chem. Soc.*, 2002, **124**, 5276–5277.
[43] N. Busschaert, S. J. Bradberry, M. Wenzel, C. J. E. Haynes, J. R. Hiscock, I. L. Kirby, L. E. Karagiannidis, S. J. Moore, N. J. Wells, J. Herniman, G. J. Langley, P. N. Horton, M. E. Light, I. Marques, P. J. Costa, V. Félix, J. G. Frey and P. A. Gale, *Chem. Sci.*, 2013, **4**, 3036.
[44] P. Thordarson, *Chem. Soc. Rev.*, 2011, **40**, 1305–1323.
[45] J. B. Wittenberg and L. Isaacs, in *Supramolecular Chemistry*, John Wiley & Sons, Ltd, 2012.
[46] S. J. Edwards, H. Valkenier, N. Busschaert, P. A. Gale and A. P. Davis, *Angew. Chem. Int. Ed.*, 2015, **54**, 4592–4596.
[47] N. Busschaert, I. L. Kirby, S. Young, S. J. Coles, P. N. Horton, M. E. Light and P. A. Gale, *Angew. Chem.*, 2012, **124**, 4502–4506.
[48] B. L. Schottel, H. T. Chifotides and K. R. Dunbar, *Chem. Soc. Rev.*, 2008, **37**, 68–83.
[49] J. Emsley, *Chem. Soc. Rev.*, 1980, **9**, 91–124.
[50] F. G. Bordwell, D. J. Algrim and J. A. Harrelson, *J. Am. Chem. Soc.*, 1988, **110**, 5903–5904.
[51] V. Amendola, G. Bergamaschi, M. Boiocchi, L. Fabbrizzi and M. Milani, *Chem. Eur. J.*, 2010, **16**, 4368–4380.
[52] D. Quiñonero, A. Frontera, P. Ballester and P. M. Deyà, *Tetrahedron Lett.*, 2000, **41**, 2001–2005.
[53] J. Mareda and S. Matile, *Chem. Eur. J.*, 2009, **15**, 28–37.
[54] P. J. Costa, *Phys. Sci. Rev.*, 2017, **2**, 1–16
[55] T. Clark, M. Hennemann, J. S. Murray and P. Politzer, *J. Mol. Model.*, 2007, **13**, 291–296.
[56] L. E. Bickerton, A. Docker, A. J. Sterling, H. Kuhn, F. Duarte, P. D. Beer and M. J. Langton, *Chem. Eur. J.*, 2021, chem.202101681.
[57] D. A. Decato, E. A. John and O. B. Berryman, in *Halogen Bonding in Solution*, John Wiley & Sons, Ltd, 2021, pp. 1–41.
[58] C. C. Robertson, R. N. Perutz, L. Brammer and C. A. Hunter, *Chem. Sci.*, 2014, **5**, 4179–4183.
[59] H. Li, H. Valkenier, A. G. Thorne, C. M. Dias, J. A. Cooper, M. Kieffer, N. Busschaert, P. A. Gale, D. N. Sheppard and A. P. Davis, *Chem. Sci.*, 2019, **10**, 9663–9672.
[60] A. K. Dash and W. F. Elmquist, in *Analytical Profiles of Drug Substances and Excipients*, ed. H. G. Brittain, Academic Press, 2001, vol. 27, pp. 67–113.
[61] M. J. Spooner and P. A. Gale, *Supramol. Chem.*, 2018, **30**, 514–519.
[62] J. C. Biffinger, H. W. Kim and S. G. DiMagno, *ChemBioChem*., 2004, **5**, 622–627.
[63] N. Busschaert, M. Wenzel, M. E. Light, P. Iglesias-Hernández, R. Pérez-Tomás and P. A. Gale, *J. Am. Chem. Soc.*, 2011, **133**, 14136–14148.
[64] V. Saggiomo, S. Otto, I. Marques, V. Félix, T. Torroba and R. Quesada, *Chem. Commun.*, 2012, **48**, 5274–5276.
[65] M. J. Spooner and P. A. Gale, *Chem. Commun.*, 2015, **51**, 4883–4886.
[66] H. Valkenier, C. J. E. Haynes, J. Herniman, P. A. Gale and A. P. Davis, *Chem. Sci.*, 2014, **5**, 1128.
[67] L. W. Judd and A. P. Davis, *Chem. Commun.*, 2010, **46**, 2227–2229.
[68] S. J. Edwards, I. Marques, C. M. Dias, R. A. Tromans, N. R. Lees, V. Félix, H. Valkenier and A. P. Davis, *Chem. Eur. J.*, 2016, **22**, 2004–2011.
[69] V. Soto-Cerrato, P. Manuel-Manresa, E. Hernando, S. Calabuig-Fariñas, A. Martínez-Romero, V. Fernández-Dueñas, K. Sahlholm, T. Knöpfel, M. García-Valverde, A. M.

Rodilla, E. Jantus-Lewintre, R. Farràs, F. Ciruela, R. Pérez-Tomás and R. Quesada, *J. Am. Chem. Soc.*, 2015, **137**, 15892–15898.
[70] A. I. Share, K. Patel, C. Nativi, E. J. Cho, O. Francesconi, N. Busschaert, P. A. Gale, S. Roelens and J. L. Sessler, *Chem. Commun.*, 2016, **52**, 7560–7563.
[71] M. M. Lerch, M. J. Hansen, W. A. Velema, W. Szymanski and B. L. Feringa, *Nat. Commun.*, 2016, **7**, 12054.
[72] J. Broichhagen, J. A. Frank and D. Trauner, *Acc. Chem. Res.*, 2015, **48**, 1947–1960.
[73] C. Brieke, F. Rohrbach, A. Gottschalk, G. Mayer and A. Heckel, *Angew. Chem. Int. Ed.*, 2012, **51**, 8446–8476.
[74] M. J. Fuchter, *J. Med. Chem.*, 2020, **63**, 11436–11447.
[75] F. Zhang, J. Vierock, O. Yizhar, L. E. Fenno, S. Tsunoda, A. Kianianmomeni, M. Prigge, A. Berndt, J. Cushman, J. Polle, J. Magnuson, P. Hegemann and K. Deisseroth, *Cell*, 2011, **147**, 1446–1457.
[76] K. Palczewski, *J. Biol. Chem.*, 2012, **287**, 1612–1619.
[77] N. Li and P. Miao, *IEEE Pulse*, 2014, **5**, 55–59.
[78] E. S. Boyden, F. Zhang, E. Bamberg, G. Nagel and K. Deisseroth, *Nat. Neurosci.*, 2005, **8**, 1263–1268.
[79] E. A. Ferenczi, X. Tan and C. L.-H. Huang, *Front. Physiol*., 2019, **10**, 1-19
[80] D. Lim, J. LeDue, M. Mohajerani, M. Vanni and T. Murphy, *Front. Neurosci*., 2013, **7**, 1-15
[81] M. Avermann, C. Tomm, C. Mateo, W. Gerstner and C. C. H. Petersen, *J. Neurophysiol,*, 2012, **107**, 3116–3134.
[82] A. Dwijayanti, C. Zhang, C. L. Poh and T. Lautier, *Front. Bioeng. Biotechnol.*, 2022, **9**, 804563.
[83] B. M. Hooks, J. Y. Lin, C. Guo and K. Svoboda, *J. Neurosci.*, 2015, **35**, 4418–4426.
[84] J.-A. Sahel, E. Boulanger-Scemama, C. Pagot, A. Arleo, F. Galluppi, J. N. Martel, S. D. Esposti, A. Delaux, J.-B. de Saint Aubert, C. de Montleau, E. Gutman, I. Audo, J. Duebel, S. Picaud, D. Dalkara, L. Blouin, M. Taiel and B. Roska, *Nat. Med.*, 2021, **27**, 1223–1229.
[85] J. H. Correia, J. A. Rodrigues, S. Pimenta, T. Dong and Z. Yang, *Int. J. Pharm.,*, 2021, **13**, 1332.
[86] R. R. Allison and C. H. Sibata, *Photodiagnosis Photodyn. Ther.*, 2010, **7**, 61–75.
[87] G. Gunaydin, M. E. Gedik and S. Ayan, *Frontiers in Chemistry*.
[88] N. R. Mosteanu, in *2021 5th International Conference on Software and e-Business (ICSEB)*, 2021, pp. 55–60.
[89] W. A. Velema, W. Szymanski and B. L. Feringa, *J. Am. Chem. Soc.*, 2014, **136**, 2178–2191.
[90] G. Thomas, *Fundamentals of Medicinal Chemistry*, John Wiley & Sons, Ltd, 2004
[91] J. A. DiMasi, L. Feldman, A. Seckler and A. Wilson, *Clin. Pharm. Therap.,*, 2010, **87**, 272–277.
[92] C.-Y. Huang, A. Bonasera, L. Hristov, Y. Garmshausen, B. M. Schmidt, D. Jacquemin and S. Hecht, *J. Am. Chem. Soc.*, 2017, **139**, 15205–15211.
[93] S. Wiedbrauk and H. Dube, *Tetrahedron Lett.*, 2015, **56**, 4266–4274.
[94] D. Villarón and S. J. Wezenberg, *Angew. Chem. Int. Ed.*, 2020, **59**, 13192–13202.
[95] R. Weinstain, T. Slanina, D. Kand and P. Klán, *Chem. Rev.*, 2020, **120**, 13135–13272.
[96] W. Szymański, W. A. Velema and B. L. Feringa, *Angew. Chem. Int. Ed.*,, 2014, **53**, 8682–8686.
[97] A. Mourot, M. A. Kienzler, M. R. Banghart, T. Fehrentz, F. M. E. Huber, M. Stein, R. H. Kramer and D. Trauner, *ACS Chem. Neurosci.*, 2011, **2**, 536–543.
[98] A. Polosukhina, J. Litt, I. Tochitsky, J. Nemargut, Y. Sychev, I. De Kouchkovsky, T. Huang, K. Borges, D. Trauner, R. N. Van Gelder and R. H. Kramer, *Neuron*, 2012, **75**, 271–282.
[99] S. Herre, T. Schadendorf, I. Ivanov, C. Herrberger, W. Steinle, K. Rück-Braun, R. Preissner and H. Kuhn, *ChemBioChem*, 2006, **7**, 1089–1095.

[100] O. Babii, S. Afonin, M. Berditsch, S. Reiβer, P. K. Mykhailiuk, V. S. Kubyshkin, T. Steinbrecher, A. S. Ulrich and I. V. Komarov, *Angew. Chem. Int. Ed.*,, 2014, **53**, 3392–3395.
[101] V. García-López, F. Chen, L. G. Nilewski, G. Duret, A. Aliyan, A. B. Kolomeisky, J. T. Robinson, G. Wang, R. Pal and J. M. Tour, *Nature*, 2017, **548**, 567–572.
[102] N. Koumura, R. W. Zijlstra, R. A. van Delden, N. Harada and B. L. Feringa, *Nature*, 1999, **401**, 152–155.
[103] A. L. Santos, D. Liu, A. K. Reed, A. M. Wyderka, A. van Venrooy, J. T. Li, V. D. Li, M. Misiura, O. Samoylova, J. L. Beckham, C. Ayala-Orozco, A. B. Kolomeisky, L. B. Alemany, A. Oliver, G. P. Tegos and J. M. Tour, *Sci. Adv.*, 2022, **8**, eabm2055.
[104] S. Mo, Y. Wen, F. Xue, H. Lan, Y. Mao, G. Lv and T. Yi, *Sci. Bull.*, 2016, **61**, 459–467.
[105] L. Fournier, C. Gauron, L. Xu, I. Aujard, T. Le Saux, N. Gagey-Eilstein, S. Maurin, S. Dubruille, J.-B. Baudin, D. Bensimon, M. Volovitch, S. Vriz and L. Jullien, *ACS Chem. Biol.*, 2013, **8**, 1528–1536.
[106] K. Sitkowska, M. F. Hoes, M. M. Lerch, L. N. Lameijer, P. van der Meer, W. Szymański and B. L. Feringa, *Chem. Commun.*, 2020, **56**, 5480–5483.
[107] K. Hüll, J. Morstein and D. Trauner, *Chem. Rev.*, 2018, **118**, 10710–10747.
[108] S. Kraljevic, P. J. Stambrook and K. Pavelic, *EMBO Rep*, 2004, **5**, 837–842.
[109] B. M. Vickerman, E. M. Zywot, T. K. Tarrant and D. S. Lawrence, *Nat. Rev. Chem.*, 2021, **5**, 816–834.
[110] W. A. Velema, J. P. van der Berg, M. J. Hansen, W. Szymanski, A. J. M. Driessen and B. L. Feringa, *Nat. Chem.*, 2013, **5**, 924–928.
[111] P. S. Dupart, K. Mitra, C. E. Lyons and M. C. T. Hartman, *Chem. Commun.*, 2019, **55**, 5607–5610.
[112] J. B. Baell and J. W. M. Nissink, *ACS Chem. Biol.*, 2018, **13**, 36–44.
[113] J. Calbo, C. E. Weston, A. J. P. White, H. S. Rzepa, J. Contreras-García and M. J. Fuchter, *J. Am. Chem. Soc.*, 2017, **139**, 1261–1274.
[114] F. Chast, in *The Practice of Medicinal Chemistry (Second Edition)*, ed. C. G. Wermuth, Academic Press, London, 2003, pp. 3–28.
[115] John H. eastham and P. Patel, in *StatPearls*, StatPearls Publishing, Treasure Island (FL), 2022.
[116] D. Bléger, J. Schwarz, A. M. Brouwer and S. Hecht, *J. Am. Chem. Soc.*, 2012, **134**, 20597–20600.

Chapter 2 – Red-shifting and tuning the half-life of azobenzenes

2.1 Unsubstituted azobenzenes

Azobenzenes are particularly attractive photoswitches due to their small size, robust switching, large conformational changes, low rate of photo bleaching, and ease of synthesis and derivatization.[1,2,3] Although the UV-vis spectra of the parent azobenzene isomers (*E*)**-1** and (*Z*)**-1** overlap significantly, sufficient separation of excitation bands and differences in extinction coefficients enable photoisomerisation with relatively high photostationary states (PSS) (Figure 1A). Irradiation at 340 nm promotes π → π* excitation into short-lived S_2 states, providing a pathway for (*Z*)**-1** accumulation with an 80% PSS. *Z* → *E* isomerisation proceeds via n → π* transitions to S_1 excited states, leading to a PSS of 95% with 450 nm light (Figure 1B).[4]

The photoisomerisation mechanisms for azobenzene are solvent and substituent dependent, and are still ongoing topics of investigation.[5] However, π → π* transitions generally break the N=N π bond, allowing free rotation to the (*Z*)-isomer, whereas n → π * transitions promote nitrogen inversion *via* an sp-hydridised intermediate in both directions. [3] The usually less thermodynamically stable Z-isomer exhibits a half-life ($\tau_{1/2}$) of 4.7 hours at room temperature. Therefore, complete *Z* → *E* relaxation takes place if sufficient thermal energy is supplied;[6] typically proceeding via an inversion mechanism via a linear Ar-N intermediate.[7]

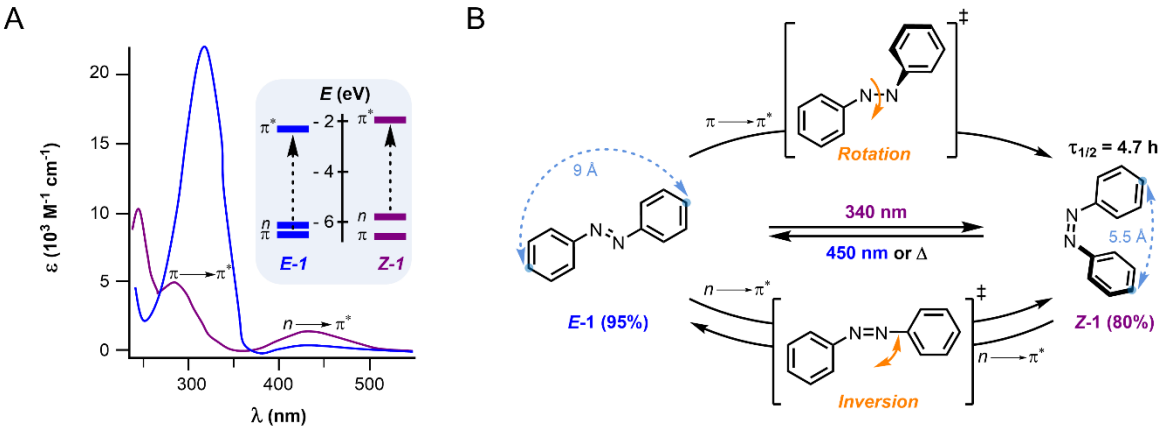


Figure 1. (B) UV-Vis spectrum[4] and orbital energies[8] for **1**. (B) Azobenzene isomerisation mechanisms and photostationary states. End-to-end distances illustrate the magnitude of conformational change.[3]

2.2 Background: redshifting azobenzenes

UV radiation is necessary to form appreciable quantities of (*Z*)**-1**. However, UV light can damage cellular surroundings and exhibits low tissue penetration due to high scattering; limiting its use *in vivo*.[9] Scattering is inversely proportional to the fourth power of wavelength,[10] and the near-IR (NIR) window is limited by tissue type and water/Haemoglobin absorption, leading to optimal tissue penetrance at ~ 730 nm (the phototherapeutic window).[11] Moreover, incomplete photoconversions and relatively mid-range (*Z*)**-1** lifetimes limit applications where either bi-stability or applications relying on (*Z*) thermal decay is required.[8]

These limitations have stimulated the development of azobenzenes that operate towards more red-shifted wavelengths.[12] Ideally, these derivatives are non-toxic and stable to hydrolysis and reduction. It is also preferable for the less stable (usually *Z*) isomer to be the active species to avoid any thermal relaxation causing bioactivity outside the zone of irradiation.[2] Additionally, $\tau_{1/2}$ and PSSs should be maximised if bi-stable photoswitches are required, whereas more rapid thermal relaxation rates around 0.1 – 10 s could allow accumulation of the (*Z)* isomer under constant light irradiation, useful for applications where spatial targeting is desired.[13] However, extremely fast relaxation rates should be avoided as this results in insufficient *cis* content, unless exceptionally bright light sources are used.[2]

2.2.1 Redshifting Azobenzenes: modifying π → π * transitions

The general strategy for redshifting π → π transitions is increasing conjugation, which typically results in higher π and lower π*, energies. Increased conjugation in push-pull systems **2**, **3,** and **4** leads to slightly redshifted π → π* energies, but also significantly shortens *Z* half-lives due to reduced N=N double bond character (Figure 2).[14] Lewis acid-base complexation to BF_2 in the highly conjugated **5** leads to π delocalisation; lowering the π* and raising the π orbital energies to the point where the π orbital is now the HOMO. This facilitates *E* → *Z* isomerisation with low fatigue and high PSS up to the NIR region.[15]. However, these compounds are challenging to functionalise, unstable to hydrolysis and their half-lives significantly decrease in the presence of oxygen, limiting their use *in vivo*.[2]

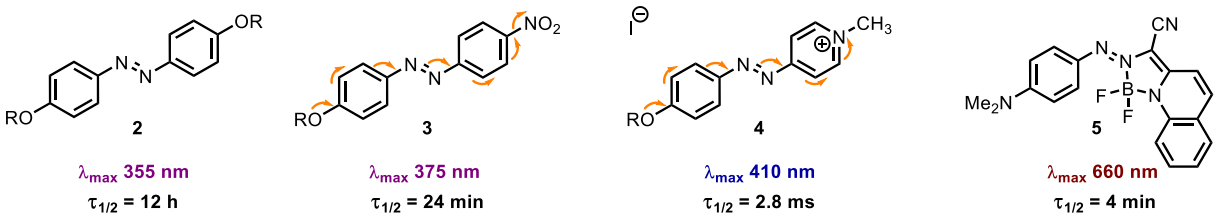


Figure 2. Selected examples of redshifting azobenzenes by modifying π → π * transitions.

2.2.2 Redshifting Azobenzenes: modifying n → π * transitions

A more attractive strategy towards redshifting ABs is perturbing the n → π* transitions, as these are typically excited at higher wavelengths than π → π* transitions, exhibit higher quantum yields for *E* → *Z* isomerisation,[12] and do not require large π systems to increase conjugation. An enticing example is bridged azobenzene ("Diazocene") **6** (Figure 3A), where the geometrical constrains of the *ortho*-ethylene bridge redshifts the n → π * transition of the E isomer by ~ 100 nm, allowing near-quantitative photoconversions with red (*E* → *Z*) and blue light (*Z* → *E*).[16] Unfortunately, red light irradiation produces the more thermally stable *Z* isomer, and analogues are synthetically challenging to access.[17]

Early work by Bisle and Rau suggested that tetra *ortho* methyl substitution in **7** redshifted the n → π* transition by ~ 25 nm relative to **E-1**, which may be due to an increase in n orbital energy due to repulsive interactions.[18] In 2009, Woolley observed that 2,2'-diamino azobenzenes were significantly red-shifted, with more strongly donating groups displaying more red-shifted transitions and shorter half-lives.[19] However, these motifs suffered from instability, perhaps due to competing photo-oxidation processes.[2]

In 2011, Woolley reported tetra-methoxy derivative **9**, featuring unfavourable lone pair repulsions that redshift **E-9** and are relaxed upon E → Z isomerisation.[20] The authors incorporated the motif into a stapled peptide, and could reversibly increase and decrease peptide helicity using red (E → Z, 660 nm, 98% PSS) and blue LEDs (Z → E, 460 nm, 85% PSS) respectively. The use of red light was possible due to broad n → π* tails that absorb up to 650 nm. Azobenzene **9** is stable to photobleaching but is readily reduced by glutathione, limiting the use *in vivo*. This may be attributed to the significant diazo nitrogen protonation,

which catalyses reduction (pK_aH ~ 4 due to intramolecular HB and electron donation.[21] Replacing OMe with SEt groups evades this issue due to decreased diazo basicity. However, sulphur participation results in three large overlapping bands, leading to poor PSS with a variety of wavelengths and difficulty reforming **E-10** using light (without thermal relaxation).[22]

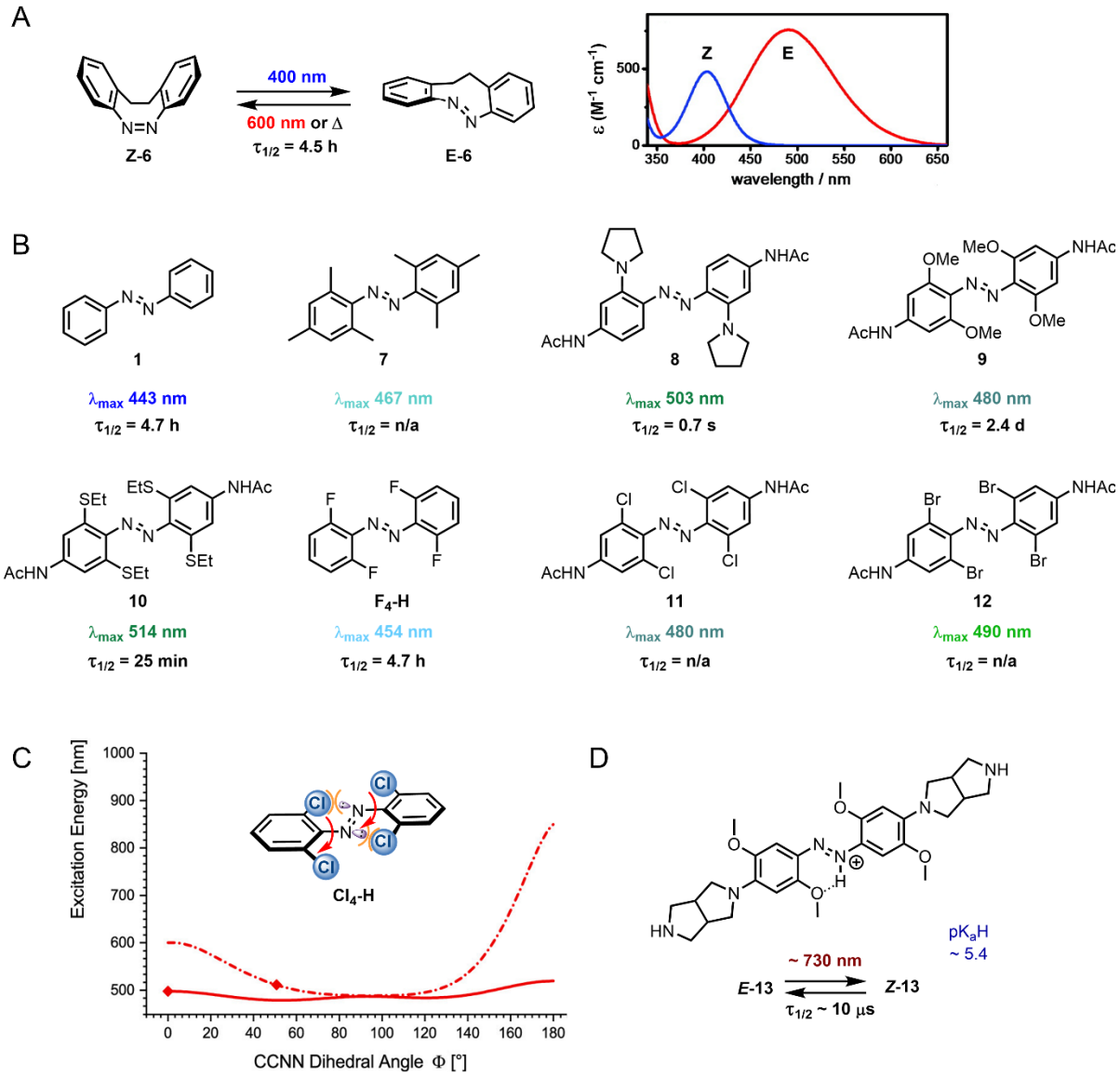


Figure 3. (A) Examples of redshifting azobenzenes by modifying n → π * transitions. (B) Dependence of n → π* energy with dihedral angle. Data reproduced from Trauner *et al*.[1] Planar conformations exhibit more diazo/chlorine repulsion in 1 (dotted) compared to azobenzene (solid). (C) Ortho/meta substitution leads to significant red-shifting (D) Meta methoxy derivative by Woolley.

In seminal work by Hecht in 2012, the authors observed that introduction of four σ-withdrawing ortho fluorines reduces N=N bond lone pair repulsion in **F$_4$**, leading to lowered n orbital energies, *Z* n→ π * blue-shifting and a $\tau_{1/2}$ of two years. *o*-Fluorines also stabilise π* energies

for both isomers, leading to an overall n→ π* redshift in **E-F$_4$** and overall large n→ π* separations and high PSSs in both directions with green (91% Z) and purple light (86% E).

In 2013, Woolley reported that tetra-*ortho* chloro azobenzenes **11** displayed remarkable bistable switching behaviour with high PSSs, low photobleaching, stability to glutathione, and ***E*-1** isomerisation with red light despite a λ_{max} of only <500 nm.[21] E → Z isomerisation was even possible at 652 nm to produce 87% PSS and 8-fold antibacterial activity when the motif was incorporated into a potential drug candidate, although this required 2-3 hours of irradiation.[23] Crystal structures, systematic replacement of Cl for hydrogens, and rotating Ar-N bonds *in silico* revealed that *n* → π* transitions in tetra-chloro derivative **Cl$_4$-H** were sensitive to azobenzene conformation and planarity, in contrast to unsubstituted azobenzene **1** where conformation did not affect absorbance (Figure 3C).[1] These results demonstrated that the deeply red-shifted n → π* tails arise from minor populations of planar conformations, where chlorines directly face the nitrogen lone pairs to destabilise n orbitals. Woolley also reported tetra-ortho bromo azobenzenes **12**, although their properties were not studied in detail.[21]

Finally, meta methoxy substitution in *E*-**13** leads to absorption tails up to 800 nm due to the 'distribution rule of auxochromes', which stipulates that donors *ortho* or *meta* to acceptor groups lead to the strongest bathochromic shifts.[24] This result highlights that only one *ortho* substituent on each side may be necessary to achieve red-shifted photoswitches, as long as there is an electron-donating *meta* substituent on each ring.

2.3 Approach towards redshifting azobenzenes and controlling half-life

As discussed in the previous section, a key feature of redshifted azobenzenes are lone pair containing ortho substituents, which can repulsively interact with the diazo lone pairs, leading to an increase in n orbital energy and redshifting of the n → π* excitation energy, with more planar conformations exhibiting more deeply redshifted tails. Upon isomerisation to the Z-isomer, these repulsive interactions are relieved; separating the n → π* bands of both isomers, which leads to good PSSs. Thus, it was reasoned that larger and heavier ortho substituents (Se, Te, I) would lead to more redshifted systems due to higher average clash between the

diazo lone pairs and substituent. Substituents which increase the average population of planar conformations in the system are also expected to be more redshifted. Thus, we reasoned that heavy chalcogen substituents would result in planar conformations due to intramolecular chalcogen bonding between the diazo lone pair and chalcogen atom sigma hole, whilst simultaneously providing a large substituent that can redshift the system. As discussed in chapter 1, chalcogen bonds are a highly directional non-covalent interaction between a polarised chalcogen atom and a Lewis basic site. Overall, this leads to the general tetra-ortho substituted series **X_4**, where X is the *ortho* atom substituent.

Our second design involved two ortho substituents to retain a balance of destabilising diazo lone pair clash yet high planarity, and introducing meta-donating substituents to maximise redshifting by the 'distribution rule of auxochromes' (**X_2,*m*-Y_2**). Very frequently, published photoswitches lack appendages for further derivatisation and applications, therefore in all derivatives it was key to include para-substituents with reactive functionality.

We also anticipated that these systematic structural changes would provide predictable periodic trends of UV-vis absorption strength and wavelengths, solid state bond angles, and Z-isomer $\tau_{1/2}$ (in particular, we anticipate longer half-lives with more electron withdrawing ortho substituents due to reduced diazo N=N lone pair repulsion). At the beginning of this project, a large amount of such data was not available and consistently reported and normalised; thus, we anticipated that the study should provide valuable information on the design of azobenzenes with predictable switching properties.

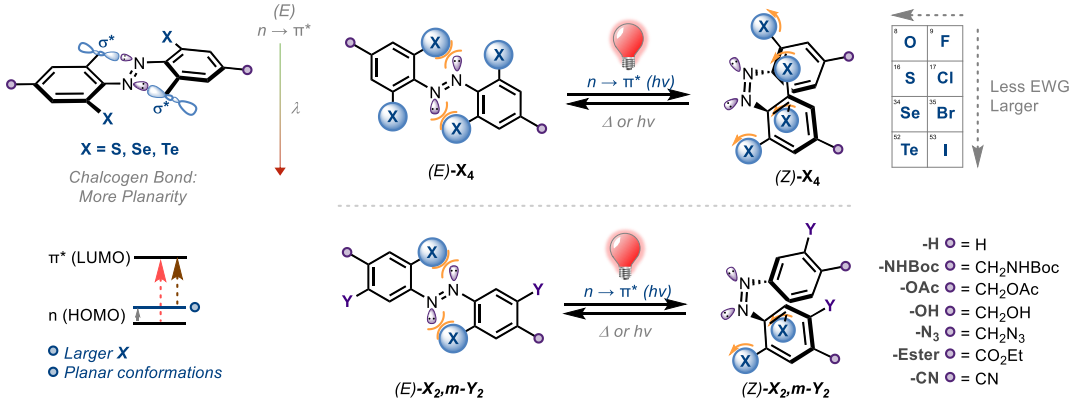
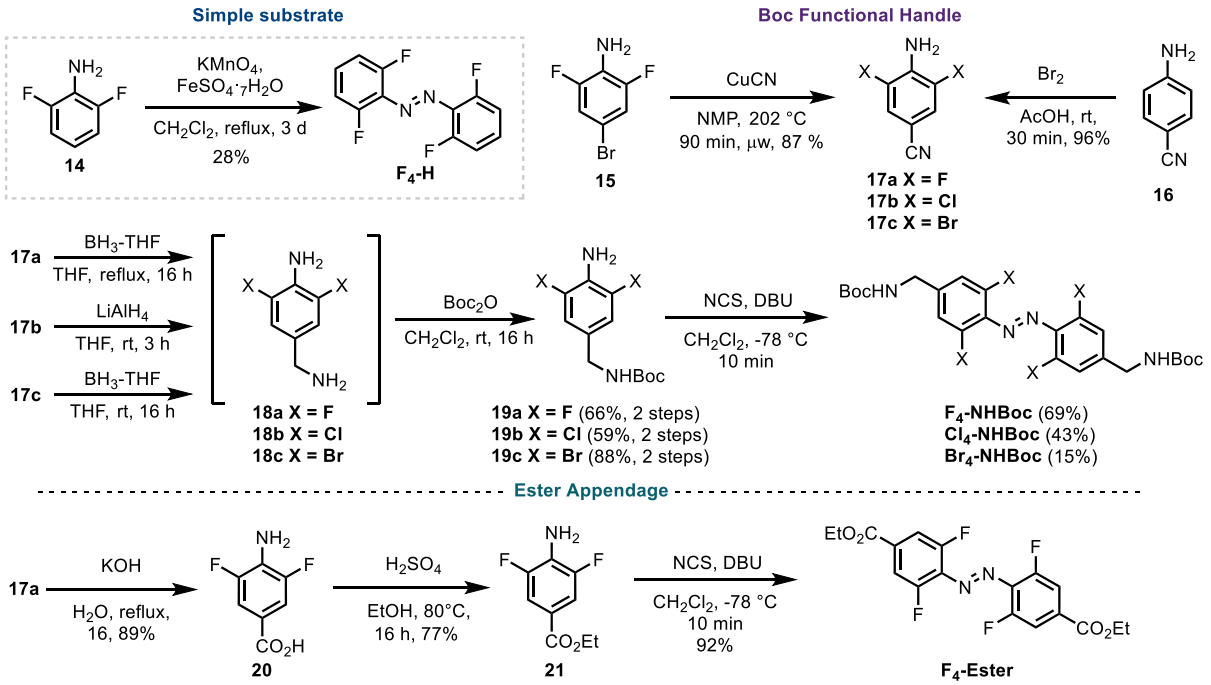


Figure 4. Targetted heavy chalcogen and halogen substituted azobenzenes. Larger X groups and planar conformations should redshift the E-isomer n → π* more due to clash with the *n* lone pair.

2.4 Synthesis of azobenzene derivatives

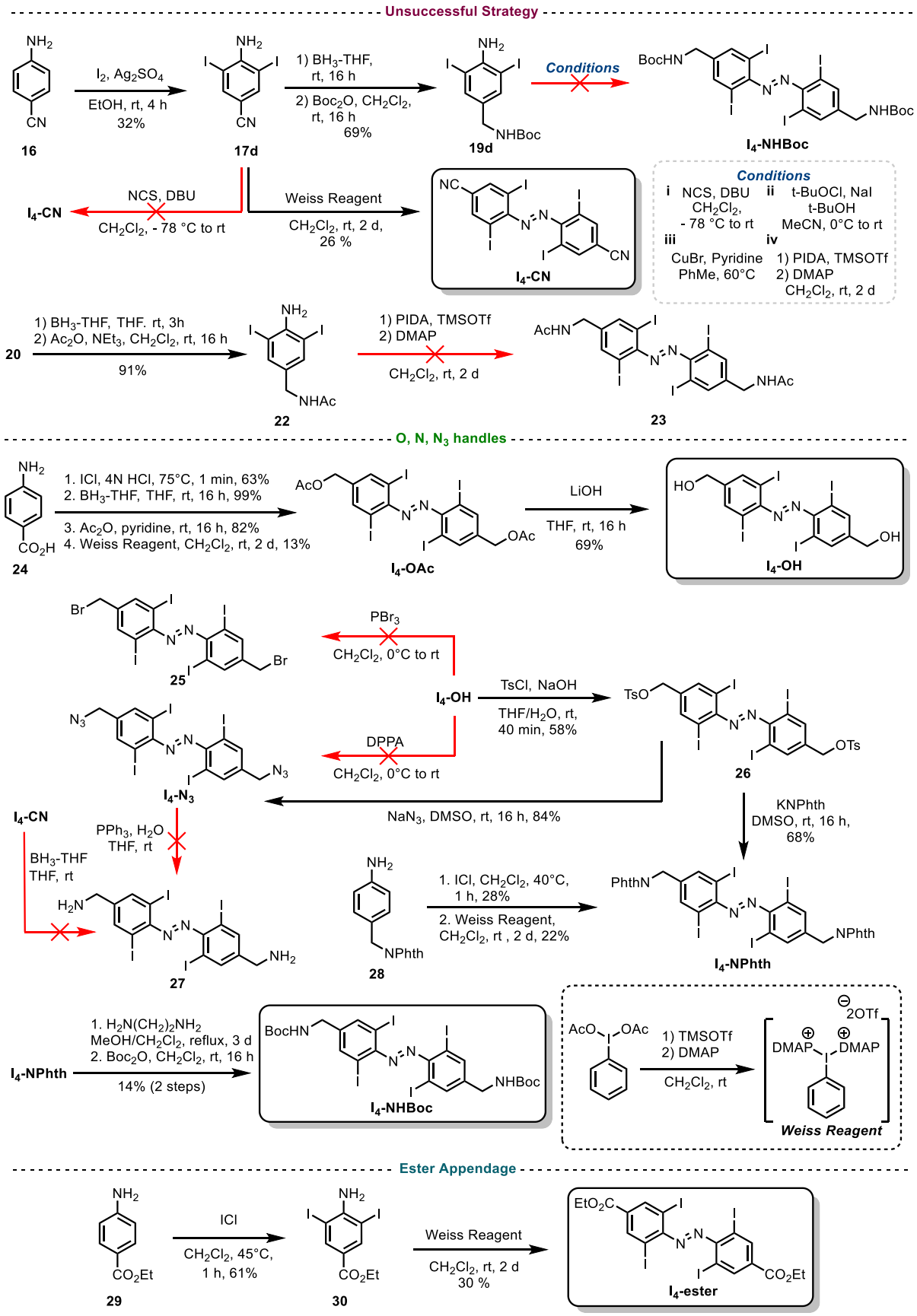
2.4.1 Synthesis of halogen X_4 derivatives



Scheme 1. Preparation of tetra ortho -fluoro, -chloro and -bromo azobenzene derivatives.

The simple **F_4-H** derivative was prepared via a modified literature procedure by oxidative dimerization of aniline **14** (Scheme 1).[8] Dihalo nitrile derivatives **17** were accessed via a Rosenmund-von Braun cyanation of **15** for the fluoro derivative, and direct bromination of aniline **16**, whereas **17b** was commercially available. The nitriles were reduced with a variety of conditions to give rise to amines **18a-c**, which were immediately protected to afford the protected building blocks **19a-c**. These were oxidatively dimerised to furnish the **X_4** derivatives using DBU-Cl^+,[25] with more sterically demanding substrates exhibiting poorer yields. **21** was prepared via a known literature sequence; via hydrolysis of **17a** and esterification of **20**. Oxidative coupling provided the **F_4-ester** in high yields.

The **I_4** substrates were significantly more challenging to access due to the inherently strained bond formed (Scheme 2). Initial attempts involved a similar approach to Scheme 1, by halogenating **16**, followed by reduction and protection to **19d**. Unfortunately, a variety of oxidative coupling conditions afforded complex mixtures without product, in part due to poor solubility of starting material and presumably the sterically demanding transformation.



Scheme 2. Preparation of tetra ortho -iodo derivatives.

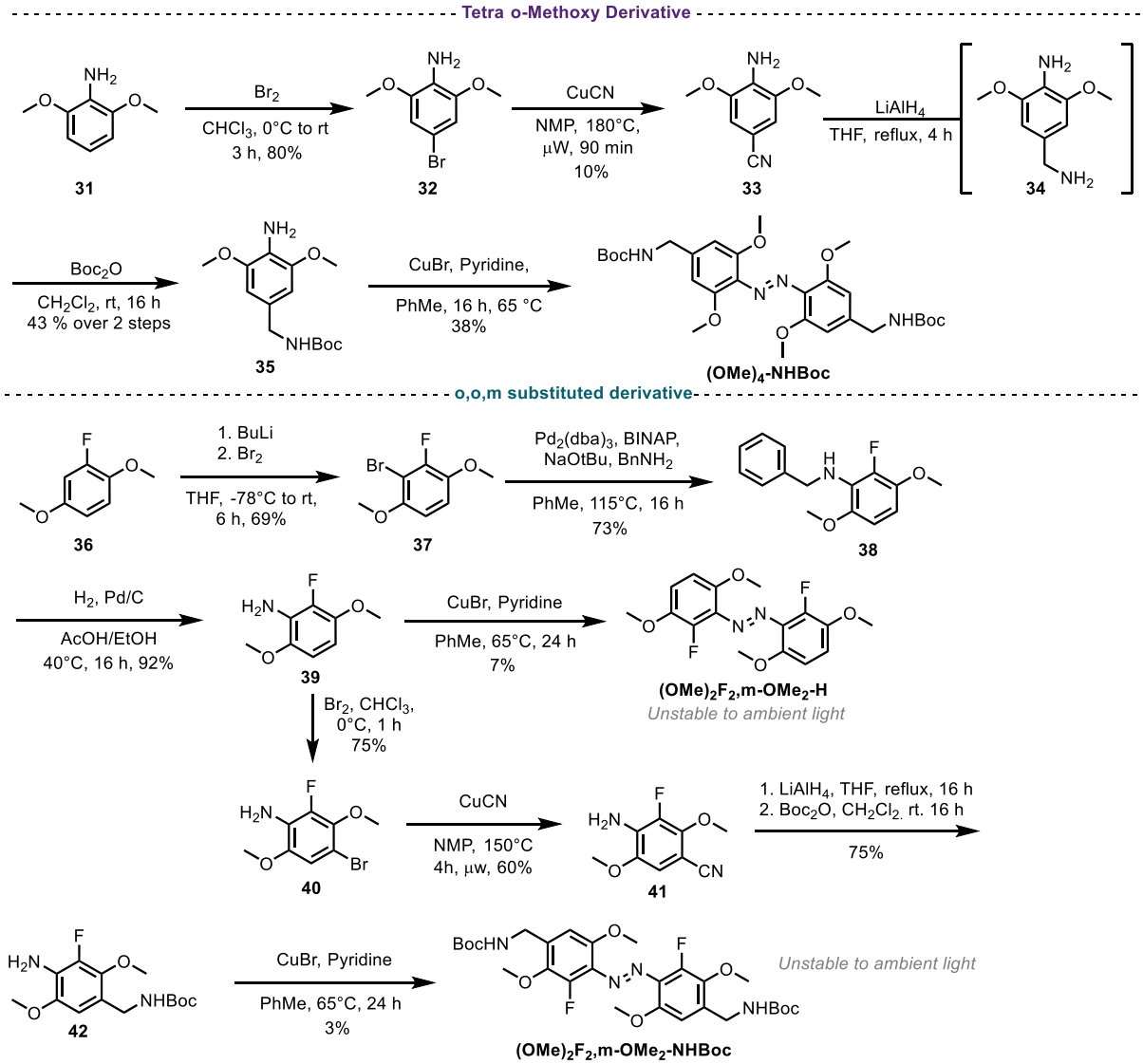
Gratifyingly, it was possible to dimerise **17d** using Weiss reagent (prepared *in situ* from PIDA, TMFOTf and DMAP)[26] to **I_4-CN**, although it was not possible using the NCS/DBU conditions,[25] even when the reaction mixture was heated beyond -78 °C. Therefore, attempts to dimerise **22**; containing a less labile acetamide protecting group were performed with Weiss reagent, but unfortunately this was unsuccessful. Instead, a substrate with an acetyl protected alcohol derived from **24** was successfully dimerised to **I_4-OAc**, albeit in poor yields. The acetyl group was removed to afford key building block **I_4-OH**. It was not possible to convert the alcohol to bromide **28** or azide **29** using phosphorus reagents, perhaps due to potential reduction of the diazo bond. However, tosylation to **26** allowed for the preparation of **I_4-N_3** and phthalimide derivative **I_4-Phth.** Staudinger reduction of **I_4-N_3** to **27** resulted in direct SN_2 substitution of PPh_3 due to the relatively activated N_3 leaving group, whereas borane reduction of **I_4-CN** to **27** was found to preferentially reduced the diazo bond.

Therefore, **I_4-Phth** was used as the amino-derived **I_4** substrate. Interestingly, this could be prepared from direct iodination of **28** and subsequent Weiss reagent coupling, suggesting that the N-H functionality was perhaps responsible for preventing dimerization in previous attempts. Mild deprotection of the phthalimide was possible using ethylene diamine, but it was not possible to isolate **27** due to purification issues. Therefore, the crude mixture was boc protected to afford **I_4-NHBoc** in low yields. The ester appended derivative **I_4-ester** was successfully prepared in moderate yields *via* **29** and **30**.

2.4.2 Synthesis of chalcogen X_4 derivatives

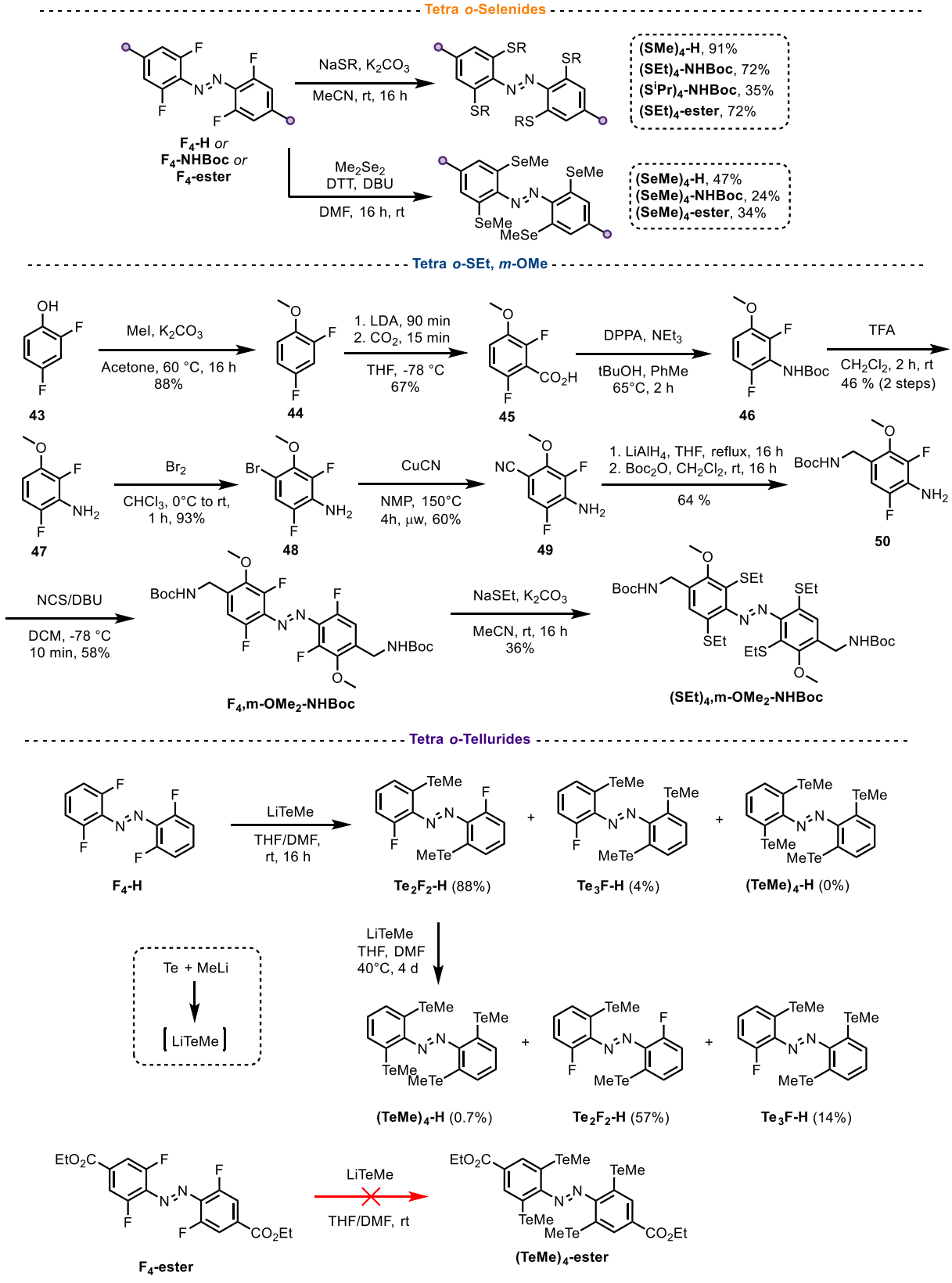
The preparation of methoxy derivatives is outlined in Scheme 3. **32** was prepared via regioselective bromination of **31**. Cyanation to **33** proceeded in poor yields due to heavy emulsion formation during the work-up. The nitrile was reduced to **34** and protected to electron-rich **35**, which only dimerised using CuBr/Pyridine in air to afford the **$(OMe)_4$** photoswitch. We also attempted to combine scaffold **13** with fluoro substituents to develop **$(OMe)_2F_2$,m-OMe_2-NHBoc** in attempt to reduce the $\tau_{1/2}$ and pK_A**.** Regioselective *o*-lithiation of **36** to **37** followed by cross-coupling using benzylamine as the ammonia equivalent afforded

38. Deprotection to **39** and dimerization to **(OMe)$_2$F$_2$,m-OMe$_2$** resulted in a photoswitch sensitive to light. Nevertheless, **39** was brominated to **40**, cyanated to **41** and reduced and protected to generate **42**. Dimerisation resulted in a poor yielding photoswitch sensitive to both ambient light and irradiation using LEDs.



Scheme 3. Preparation of tetra ortho -methoxy derivatives.

The S and Se derivatives were all prepared from the corresponding **F$_4$** derivative by direct displacement with commercial thiolates and in-situ generated selenide nucleophiles (Scheme 4). This afforded a library of **S$_4$** derivatives with varying steric bulk and para functional handles in high yields. This is a significant improvement on previously reported methods where the 2,6-dithio anilines were directly oxidatively coupled, with yields ~ 2%.[22] The previously unprecedented selenide derivatives were found to be stable and easy to handle.



Scheme 4. Preparation of heavy chalcogen $\mathbf{X_4}$ derivatives.

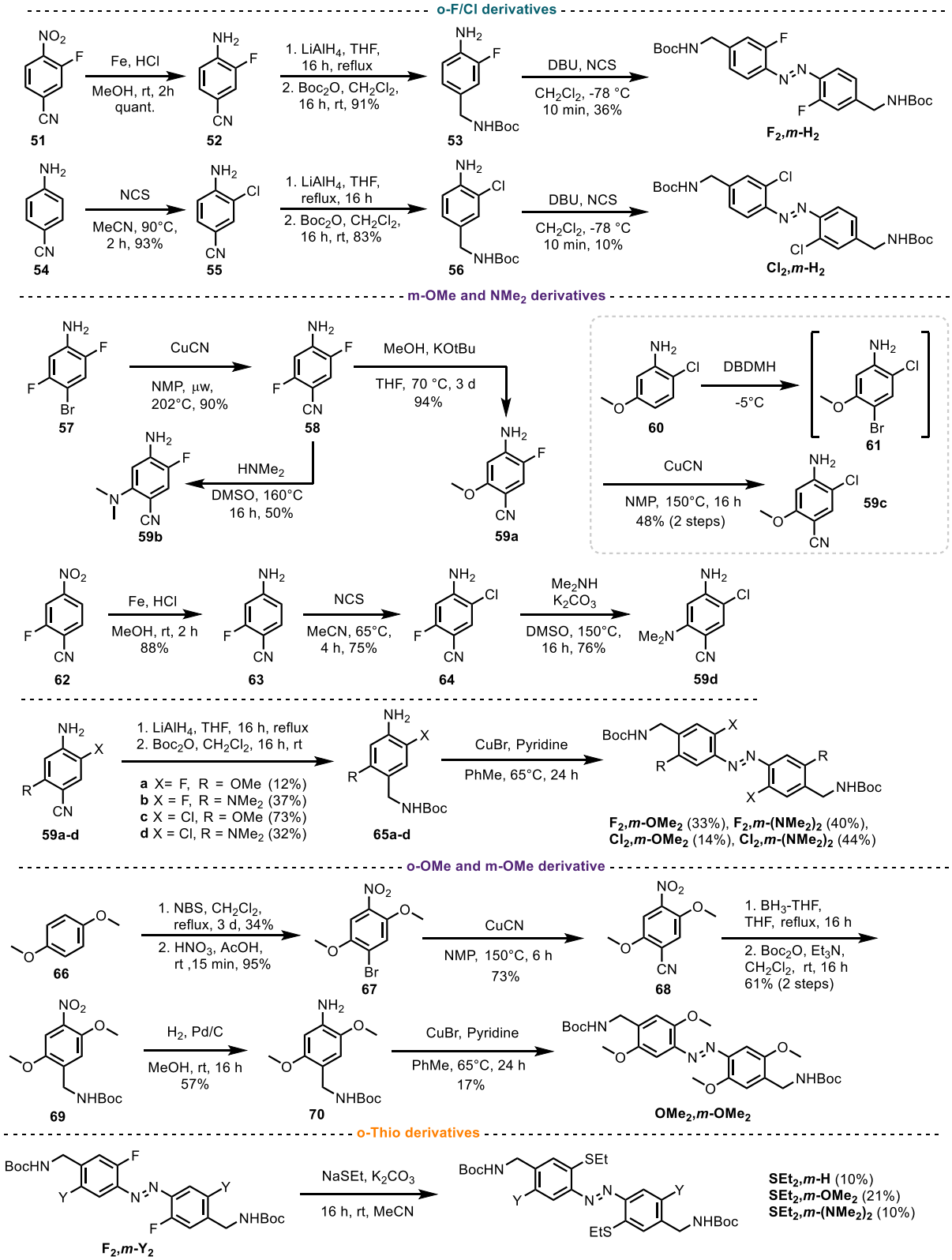
We also sought to prepare photoswitch **$(SEt)_4$,m-OMe_2-NHBoc**, which combined the steric bulk of **S_4** derivatives with *meta*-methoxy substitution, in expectation that the rule of auxochromes would further redshift the derivative. **43** was methylated to **44**, then converted to the carboxylic acid via an *ortho*-lithiation strategy to **45**. This was subjected to a Curtius rearrangement to **46**, and deprotected to **47**. Regioselective bromination to **48** and subsequent cyanation to **49** allowed preparation of the boc-protected building block **50** in good yields. Oxidative dimerization to the azobenzene was successful, and all four fluorine atoms were displaced to afford the desired photoswitch **$(SEt)_4$,m-OMe_2-NHBoc** in good yields.

Finally, the challenging telluride derivatives were prepared via an unprecedented nucleophilic aromatic substitution reaction, with an in-situ prepared TeMe nucleophile from MeLi and elemental tellurium (condition optimisation is found in the appendix (section 6.3.1). It was necessary to prepare the **Te_4** derivative step-wise via **Te_2F_2-H,** which was remarkably stable, presumably due to strong intramolecular chalcogen bonds (*vide infra*) and the difficulty in introducing further steric bulk. We also attempted to prepare **$(TeMe_4)$-ester**, but a mixture of mono and di-substituted telluride was obtained using 20 eq LiTeMe.

2.4.3 Synthesis of X_2,*m*-Y_2 derivatives

The preparation of X_2,*m*-Y_2 derivatives generally proceeded by preparing an aniline building block with the appropriate substitution pattern (Scheme 5). **51** was reduced, then subsequently treated with LAH and selectively boc protected to **53**, which was oxidatively dimerised to **F_2,m-H_2**. Similarly, regioselective chlorination of **54** to **55** and subsequent reduction and protection gave rise to **56**, which was dimerised in poor yields to **Cl_2,m-H_2**, due to competitive aromatic chlorination reactions taking place. The *meta* substituted fluoro derivatives originated from **57**, which was cyanated to **58**. Nucleophilic aromatic substitution *ortho* to the nitrile afforded **59a** and **59b**. The *meta* substituted chloro derivatives were prepared via selective bromination of **60** to **61** and subsequent cyanation to **59c**. **59d** was generated by reduction of **62** to **63**, followed by regioselective chlorination to **64**, which was subjected to nucleophilic aromatic substitution conditions. **59a-d** were successfully reduced and boc protected to provide **65a-d**

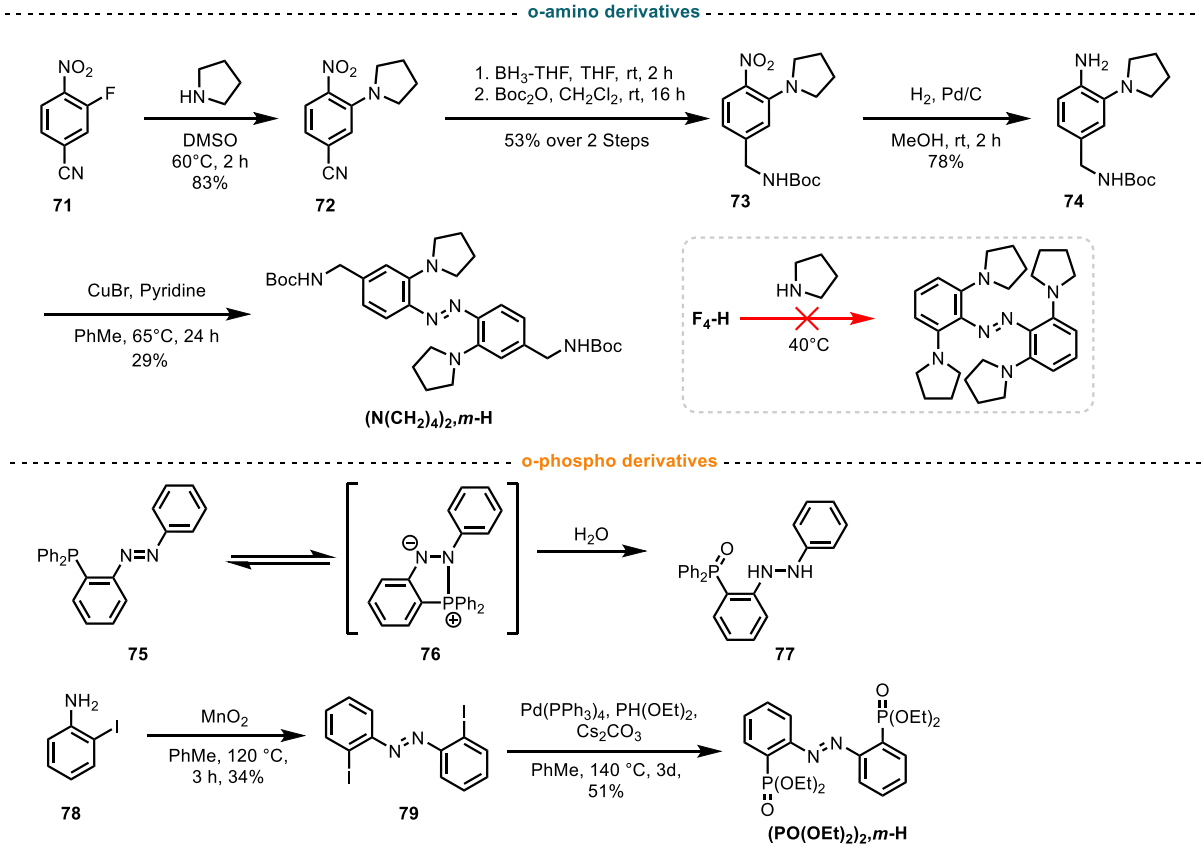
in variable yields (reported in Scheme 5). For these electron-rich substrates, it was necessary to oxidatively couple using CuBr and air to afford the desired **X_2,*m*-Y_2** derivatives.



Scheme 5. Preparation of **X_2,*m*-Y_2 derivatives**

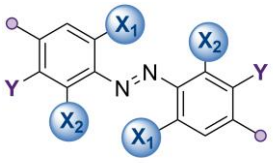
The mixed *o/m* methoxy substitution pattern related to Woolley's derivative **13** was generated by bromination and nitration of **66**. Cyanation to **68** and reduction and boc protection afforded **69**, which was hydrogenated to **70**. The electron-rich aniline was dimerised using CuBr/air to afford photoswitch **OMe_2,*m*-OMe_2**. Finally, the **SEt_2,*m*-OMe_2** derivatives were prepared from the fluorinated derivatives in poor yields, perhaps due to competing diazo bond reduction.

Finally, *o*-pnictogenated azobenzenes were also investigated. **$(N(CH_2)_4)_2$,m-H** was prepared from **51.** The amino functionality was installed via SN_{Ar} to **71**, which was reduced and protected to **72**. Hydrogenation to **73** and oxidative coupling afforded the desired photoswitch, which unfortunately proved to be unstable to ambient light. Attempts to generate the tetra-amino derivative from **F_4** in neat pyrrolidine were unsuccessful due to the extreme instability of the product. Trivalent phospho azobenzenes have previously been studied by Yamamura, who observed that the phosphine of **74** undergoes an intramolecular attack on the diazo bond to formally reduce the bond to **76**, and generation of the P(V) species.[27] Therefore, we prepared the P(V) photoswitch by oxidatively dimerising **77** into **78**, followed by a Hirao coupling.[28]

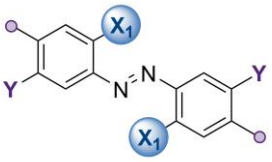


Scheme 6. Preparation of **X_2,*m*-Y_2 derivatives**

2.5 Photoswitching properties of azobenzene derivatives



Entry 1-24



Entry 25-37

Table 1. List of photoswitches studied

	AB	X_1, X_2[a]	Y	Para	Conditions	Yield	$\tau_{1/2}$	λ_{excite}[e] (nm)	λ_{max}[f] (nm)	PSS (% Z)
1	**F_4-H**	F	H	H	$KMnO_4/FeSO_4$	28%	[b]	[b]	[b]	[b]
2	**F_4-NHBoc**	F	H	CH_2NHBoc	NCS/DBU	69%	1.25 y	530	454	84%
3	**F_4-Ester**	F	H	CO_2Et	NCS/DBU	92%	[b]	[b]	[b]	[b]
4	**Cl_4-NHBoc**	Cl	H	CH_2NHBoc	NCS/DBU	43%	160 h	625	462.6	77%
5	**Br_4-NHBoc**	Br	H	CH_2NHBoc	NCS/DBU	15%	12 h	625	465.9	66%
6	**I_4-OAc**	I	H	CH_2OAc	Weiss Reagent	13%	2 m	625	501.3	[b]
7	**I_4-OH**	I	H	CH_2OH	From *entry 6*	-	[b]	[b]	500.3	[b]
8	**I_4-N_3**	I	H	CH_2N_3	From *entry 6*	-	3 m	625	514.4	[b]
9	**I_4-NPhth**	I	H	CH_2NPhth	From *entry 6*	-	3 m	625[g]	511.8	50%
10	**I_4-NHBoc**	I	H	CH_2NHBoc	From *entry 6*	-	5 m	660	514.3	[b]
11	**I_4-CN**	I	H	CN	Weiss Reagent	26%	20 s	660	520.8	[b]
12	**I_4-ester**	I	H	CO_2Et	Weiss Reagent	30%	46 s	660[h]	519.6	[b]
13	**$(OMe)_4$-NHBoc**	OMe	H	CH_2NHBoc	CuBr/Pyridine	38%	8.2 d	625	459.8	95%
14	**$(OMe)_2F_2$,*m*-OMe_2-NHBoc**	OMe, F	OMe	CH_2NHBoc	CuBr/Pyridine	3%	[c]	530	425.4	[b]
15	**$(SMe)_4$-H**	SMe	H	H	S_NAr from *1*	91%	5 m	625	514.2	[b]
16	**$(SEt)_4$-NHBoc**	SEt	H	CH_2NHBoc	S_NAr from *2*	72%	3 m	625	514.5	46%
17	**$(SEt)_4$-ester**	SEt	H	CO_2Et	S_NAr from *3*	44%	52 s	660	558.9	[b]
18	**$(S^iPr)_4$-NHBoc**	S^iPr	H	CH_2NHBoc	S_NAr from *2*	35%	3 m	625	500.4	[b]
19	**$(SEt)_4$,*m*-OMe_2-NHBoc**	SEt	OMe	CH_2NHBoc	S_NAr	36%	[c]	590	512.9	[b]
20	**$(SeMe)_4$-H**	SeMe	H	H	S_NAr from *1*	47%	80 s	625	533.9	[i]
21	**$(SeMe)_4$-NHBoc**	SeMe	H	CH_2NHBoc	S_NAr from *2*	24%	34 s	625	534.3	14%
22	**$(SeMe)_4$-ester**	SeMe	H	CO_2Et	S_NAr from *3*	34%	2.5 s	660	588.8	[i]
23	**Te_2F_2-H**	TeMe, F	H	H	S_NAr from *1*	88%	[d]	n/a	543	[b]
24	**$(TeMe)_4$-H**	TeMe	H	H	S_NAr from *23*	0.7%	[d]	n/a	518.5	[b]
25	**F_2,*m*-H_2**	F	H	CH_2NHBoc	NCS/DBU	36%	75 h	530	452.5	50%
26	**F_2,*m*-OMe_2**	F	OMe	CH_2NHBoc	CuBr/Pyridine	14%	77 h	530	387.1	50%
27	**F_2,*m*-$(NMe_2)_2$**	F	NMe_2	CH_2NHBoc	CuBr/Pyridine	38%	16 h	530	405.5	48%
28	**Cl_2,*m*-H_2**	Cl	H	CH_2NHBoc	NCS/DBU	10%	34 h	530	471.0	50%
29	**Cl_2,*m*-OMe_2**	Cl	OMe	CH_2NHBoc	CuBr/Pyridine	14%	18 h	530	475.0	77%
30	**Cl_2,*m*-$(NMe_2)_2$**	Cl	NMe_2	CH_2NHBoc	CuBr/Pyridine	44%	4 h	530	432.1	50%
31	**OMe_2,*m*-OMe_2**	OMe	OMe	CH_2NHBoc	CuBr/Pyridine	17%	[c]	530	426.6	[b]
33	**$(SEt)_2$,*m*-H_2**	SEt	H	CH_2NHBoc	S_NAr from *25*	10%	44 m	590	431.3	50%
34	**$(SEt)_2$,*m*-OMe_2**	SEt	OMe	CH_2NHBoc	S_NAr from *26*	21%	9 m	590	464.1	[b]
35	**$(SEt)_2$,*m*-$(NMe_2)_2$**	SEt	NMe_2	CH_2NHBoc	S_NAr from *27*	10%	140 s	590	543.0	[b]
36	**$(N(CH_2)_4)_2$,*m*-H**	$N(CH_2)_4$	H	CH_2NHBoc	CuBr/Pyridine	29%	[c]	530	530.2	[b]
37	**$(PO(OEt)_2)_2$,*m*-H**	$PO(OEt)_2$	H	H	Cross coupling	51%	[c]	530	458.2	[b]

[a] $X_1 = X_2$ if one entry. [b] Not determined. [c] Decomposed under irradiation with light. [d] No photo-switching observed. [e] Emission maximum of the LED used for photo-switching. [f] λ_{max} of $n \rightarrow \pi^*$ transition. [g] Switching possible up to 660 nm (43% Z PSS). [h] Switching possible up to 730 nm. [i] Thermal half-life too fast to determine the PSS distribution. All half-life and photo-switching experiments conducted in DMSO at 298 K.

The key structural features, synthetic approaches and photoswitching properties for the studied derivatives are summarised in Table 1. *n* → π* maxima were determined by deconvolution of the recorded UV-vis spectra.[29] The half-lives were determined for all novel derivatives. PSS data were generally acquired for slower relaxing derivatives and key isostructural species. (All spectra, PSS data, half-life data are found in figure S1-S8).

2.5.1 Optical and electronic properties of simple X_4 derivatives

The UV-vis spectra of the simple ***E*-X$_4$** derivatives are summarised in Figure 5A-B. For each derivative, the *p*-CH_2NHBoc derivative is displayed, except for **Te$_4$-H**, as this was the only synthetically available derivative. In general, the halogenated **X$_4$** spectra and **OMe$_4$** derivative

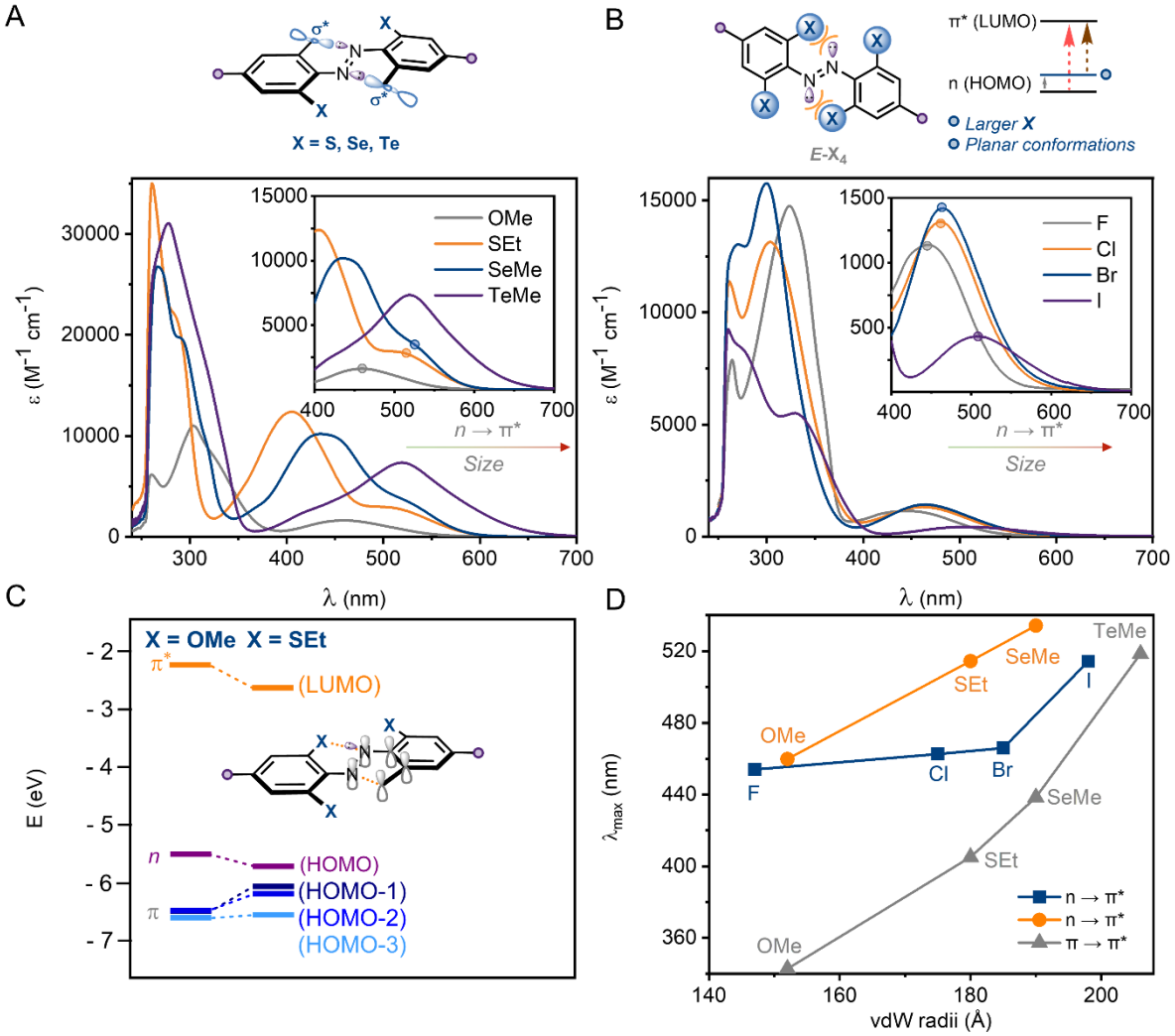


Figure 5. (A-B) UV-vis spectra of *(E)*-**X$_4$** in DMSO at 25°C. Inset: *n* → π* transition; circles: deconvoluted λ_{max} of *n* → π* transition. For TeMe, it was not possible to successfully deconvolute the *n* → π* λ_{max} due to the broad HOMO-1-LUMO transition (C) Calculated orbitals for **13**.[22] (D) In general, increases in atomic radii result in more redshifted *n* → π* transitions.

exhibit visually similar absorption profiles, whereas the derivatives capable of forming chalcogen bonding interactions (S, Se, Te) contain an extra broad peak (HOMO-1 → π*) which presumably arises from chalcogen atom participation (Figure 5C), as previously observed by Woolley for related *ortho*-thio derivatives.[22] This ligand-based π → π* transition is strong relative to the formally symmetry forbidden *n* → π* transition.[3] In the case of TeMe, this signal swamps the *n* → π* peak and was not successfully deconvoluted.

For each row, the heavy chalcogen *n* → π* are more deeply redshifted than the corresponding halogen, which may at first glance appear to be a result of intramolecular chalcogen interactions increasing the average planarity within the system. This is in line with Butcher and co-workers observations that the λ_{max} of *n* → π* transitions of mono-substituted *o*-Seleno azobenzenes was more redshifted when the intramolecular chalcogen bonding interaction was stronger.[30] However, it is also conceivable that the ChB interaction results in π delocalisation over the 5-membered ring (Figure 5C), lowering the π* to a large extent (similar to ortho-boron azobenzene **5**; Figure 2). This is in agreement with DFT calculations performed by Woolley (Figure 5C), where upon switching from OMe to SEt, the n orbital actually decreases in energy due to the stabilising chalcogen binding interaction, whilst the π* energy is decreased to an even larger extent from π delocalisation across the 5-membered π system. [22] This results in a net redshifting of the *n* → π* transition, with the more strongly interacting heavy chalcogens displaying more deeply redshifted *n* → π* transition due to this effect.

Within each group of the $\mathbf{X_4}$ halogen derivatives, larger atoms result in a more redshifted *n* → π* maximum (Figure 5D), presumably due to more destabilising clash resulting in large increase in n orbital energy. Similarly, larger atoms exhibit more deeply redshifted tails arising from planar conformations with increasing steric interactions. Within both groups, the increase in *n* → π* absorption maximum is remarkably linear between row 2-4 elements (Figure 5D). However, there is an anomalously large increase between bromine and iodine, where perhaps a critical point is reached whereby the azobenzene lone pair cannot twist away from the large halogens in any conformation without experiencing destabilising interactions with the iodine.

Between selenium and tellurium, it is conceivable that there is a similarly sharp increase of *n* → π* maximum which is hidden within the larger π → π* peak. This ligand-based π → π* transition of the chalcogens exponentially decreases in energy (Figure 5D), providing further evidence of π delocalisation across the 5-membered ring becoming more pronounced with the more strongly interacting chalcogen atoms. Overall, these deeply redshifted transitions for the heavier **X_4** derivatives are desirable features towards achieving red to near-IR photoswitching in azobenzenes.

In contrast, for the (*E*)-**F_2,m-Y_2,** (*E*)-**Cl_2,m-Y_2** and (*E*)-**$(SEt)_2$,m-Y_2** derivatives it was found that although the meta auxochrome (Y = OMe and NMe_2) broadened and increased the absorbance of the n → π* transition, the absorption tail of the *n* → π* transition does not tend to exceed 600 nm (Figure 6). Akin to the **X_4** derivatives, the *n* → π* λ_{max} follows the trend

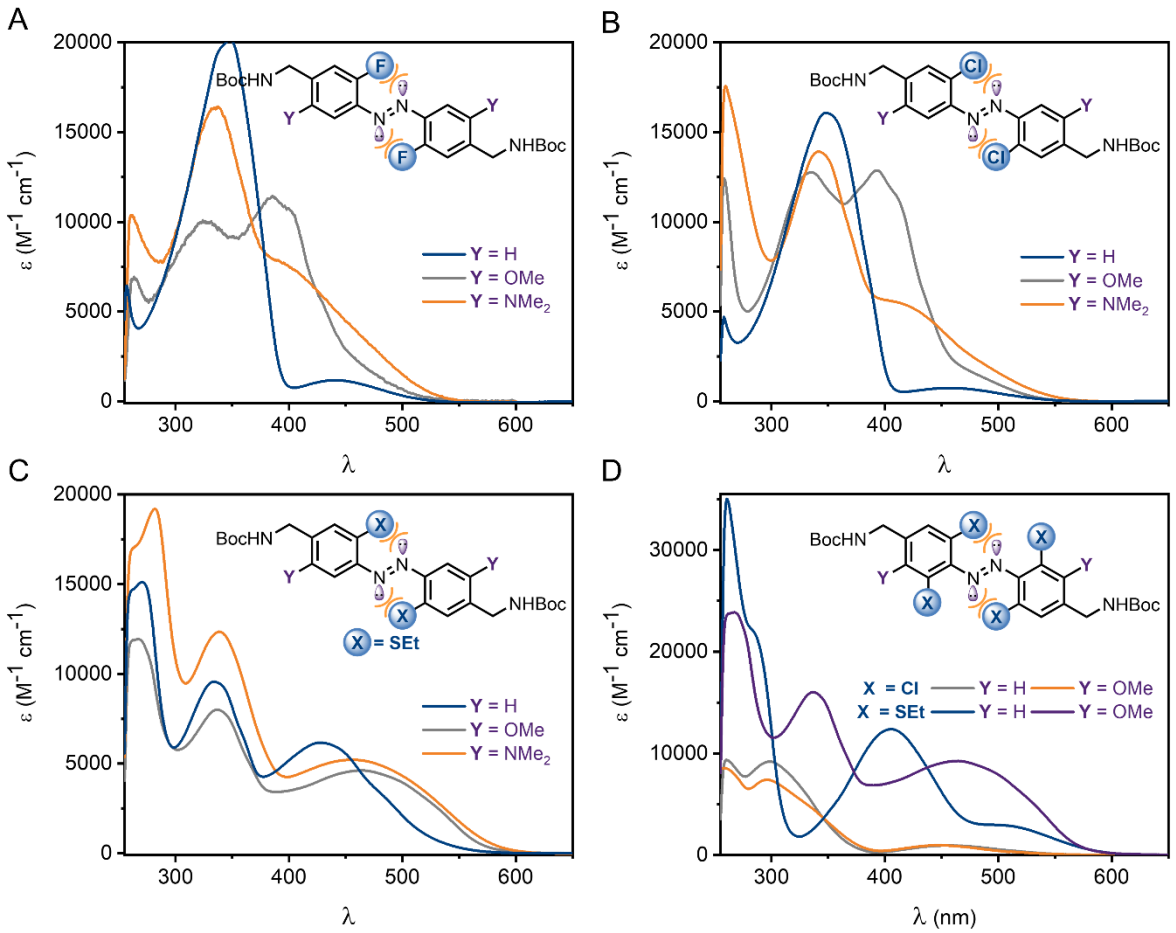


Figure 6. (A-C) UV-vis spectra of **(*E*)-X_2,m-Y_2**, in DMSO at 25°C. D) UV-vis spectra of compounds combining X_4 substitution with meta auxochromes in DMSO at 25°C

ortho-S > Cl > F, consistent with larger atoms displaying more redshifted transitions. In general, there is a poor correlation with electron donating ability of the meta substituent and *n* → π* λ_{max}. However, it is evident that four ortho substituents are necessary to achieve deeply redshifted tails. Combining four ortho substituents with a meta auxochrome broadened and increased the absorbance of the n → π* transition for **$(SEt)_4$,m-OMe_2-NHBoc,** although the *n* → π* λ_{max} is more blueshifted for the m-OMe derivative (Figure 6D). For the **Cl_4** derivative, addition of a m-OMe does not significantly impact the spectrum, suggesting that there is little communication between the diazo bond and the meta substituent, perhaps due to the highly twisted N=N-Ar dihedral angle.

2.5.2 Solid-state structural analysis of simple X_4 derivatives

To explore the role of the ortho-substituents on the azobenzene structure, and how they relate to the UV-vis spectra, single crystals of the novel tetra-ortho derivatives were grown and analysed by X-ray crystallography. Structures for the known **F_4**[31] and **OMe_4**[21] derivatives were accessed from the Cambridge Crystallographic Data Centre (CCDC). Full tabulated data are found in the appendix Table S2-S13. The structures are summarised in Figure 7.

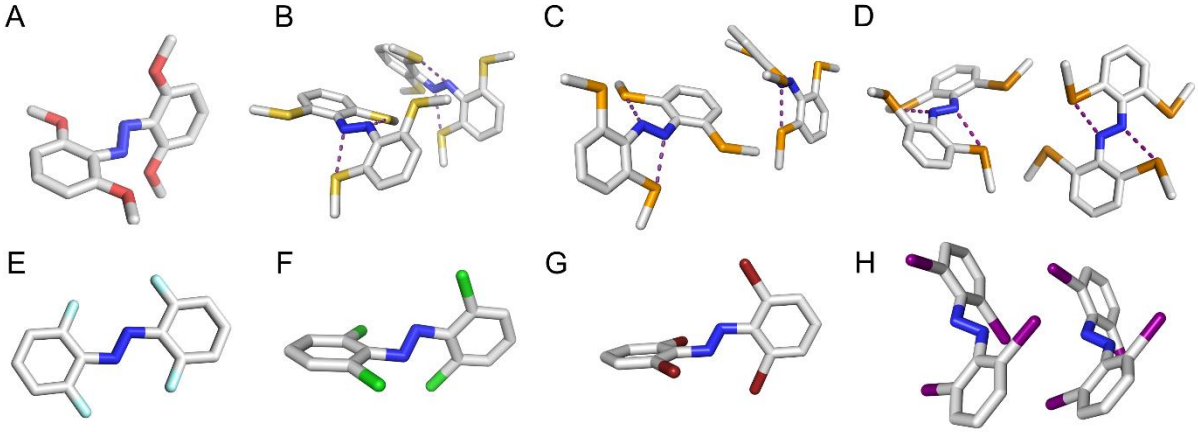


Figure 7. Crystal structures of novel tetra-ortho substituted azobenzene scaffolds (para substituents not shown for clarity). (A) **$(OMe)_4$-Br**[21] (B) **$(SMe)_4$-H** (C) **$(SeMe)_4$-H** (D) **$(TeMe)_4$-H** (E) **F_4-I**[31] (F) **Cl_4-OAc** (G) **Br_4-NHBoc** (H) **I_4-N_3**. Intra-molecular chalcogen bonds forming 5-membered rings between the chalcogen and azo N atoms represented with purple dotted lines. For B, C, D and H two conformations are present within the unit cell. Crystal structures solved in-house by K. Christensen

For B-D and H, multiple conformations were present within one unit cell, as previously observed by Trauner and co-workers for the tetra-chloro azobenzenes.[1] This supports the notion that these photoswitches are conformationally flexible, allowing the possibility for the formation of more planar, redshifted geometries. The geometrical parameters of these structures are summarised in Figure 8. Generally, the N=N diazo bond is twisted for the heavier chalcogens, which is likely to arise from to arise from strict geometrical requirements enforced by the intramolecular chalcogen bond (Figure 8A). However, the most sterically hindered **Te$_4$** N=N bond is relatively close to 180°, which is consistent with maximising π delocalisation across the 5-membered intramolecular chalcogen bond as observed in solution state. In theoretical calculations by Trauner on Cl$_4$ derivatives,[1] increased N=N distortion and longer N-N bonds results in more redshifted *n* → π* transitions. This may be in-part why the chalcogens on average exhibit higher absorbances.

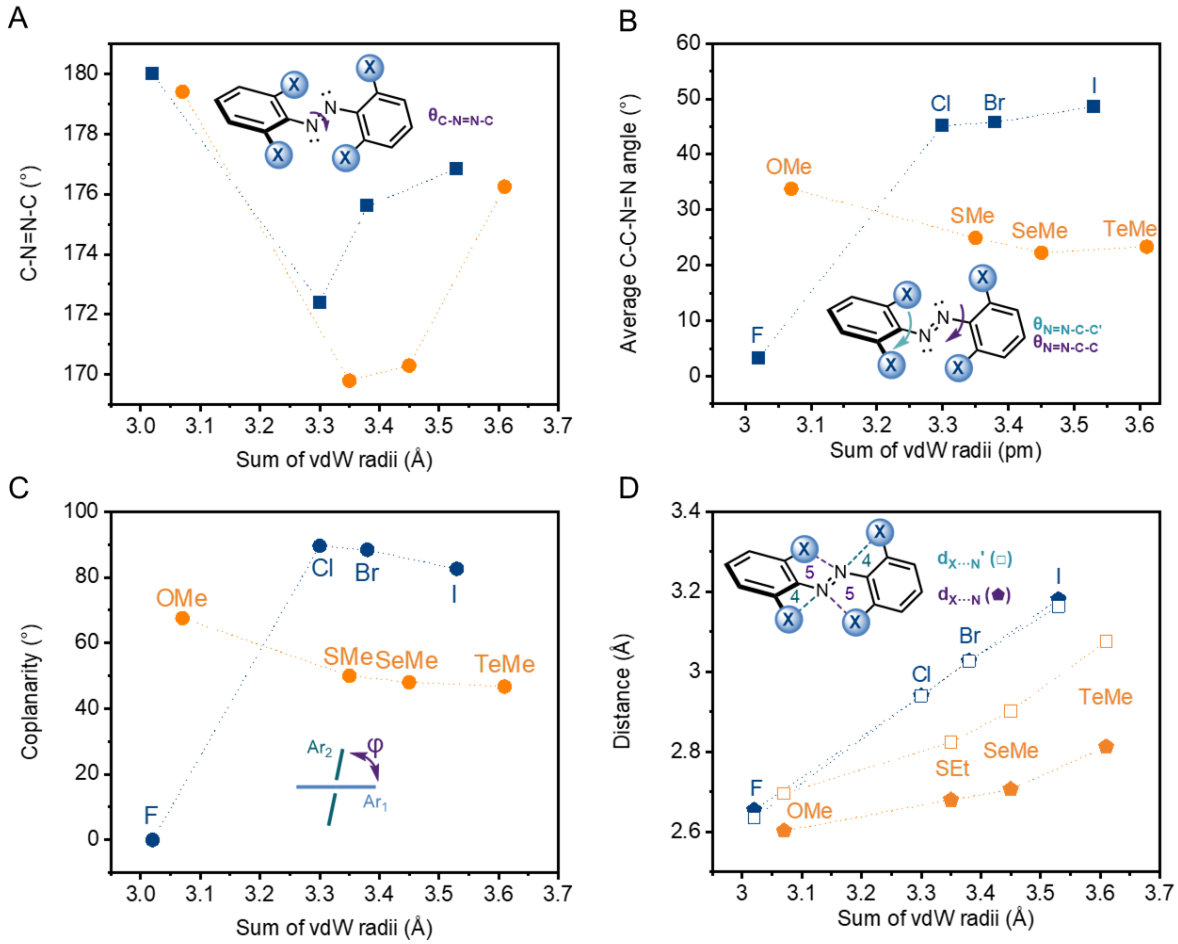


Figure 8. Geometric parameters from single-crystal data for (*E*)-**X$_4$** (A) C-N=N-C dihedral, (B) average N=N-C-C dihedral, (C) coplanarity of rings, (D) distances between diazo lone pair and X-atom (formation of intramolecular 5 (⬟) and 4 (□) membered rings)

In general, each aryl ring is independently twisted away from the diazo bond (dihedral N=N-C-C ≠ N=N-C-C'), consistent with the proposed conformational flexibility of the ***E*-X$_4$** derivatives (Figure 8B-C). The average angle and coplanarity generally increases across the halogens, presumably due to steric effects. In contrast, for the chalcogens this steric effect is outweighed by the chalcogen bond strength increasing across the series, which enforces more planar character for the larger derivatives. Further evidence for this effect is seen in Figure 8D, where the halogens have no inherent preference towards forming 4 or 5-membered interactions with the diazo lone pairs, i.e. where steric clash is minimised (dX···N ≈ dX···N'), as the σ-hole of the halogen is on the pole of the halogen atom and unable to interact with the diazo lone pair. Furthermore, the average distance increases linearly with the sum of vdW radii, consistent with this being a purely steric effect. In contrast, the chalcogens have an inherent preference to form a 5-membered intramolecular X···N interaction via the highly directional chalcogen bond, where good overlap is possible.

It was also possible to obtain a single crystal structure of **Te$_2$-F$_2$-H** (Figure 9B). In the solid state, this structure is completely planar due to the strong 5-membered Te···N chalcogen bond (2.72 Å), well within the sum of the N-Te vdW radii (3.61 Å; 75%). When Te is swapped for Cl (**Cl$_2$F$_2$-H**)[1] or H (**F$_2$H$_2$-NHBoc**), the substituent facing the diazo lone pair is the smallest atom, arising from steric effects to avoid lone pair repulsion. In particular, **Cl$_2$F$_2$-H** is less planar than

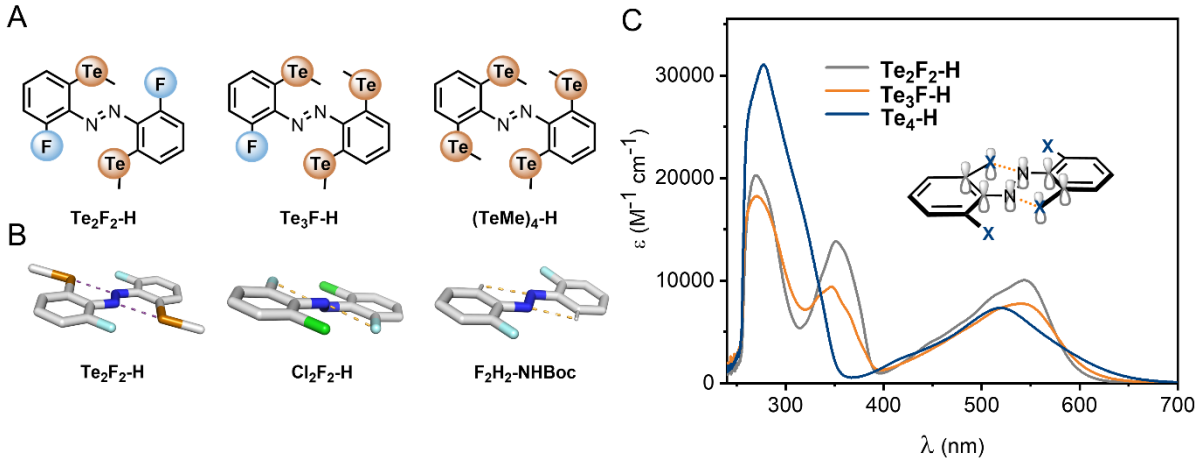


Figure 9. (A) Structures of tellurium-substituted azobenzenes. (B) Crystal structures: **Cl$_2$F$_2$** structure accessed from CCDC[1], **F$_2$H$_2$-NHBoc** determined in-house (para substituent omitted for clarity). (C) UV-vis spectra of Te derivatives

Te_2-F_2-H despite the smaller size of Cl compared to Te, serving as further evidence for the presence of 5-membered ring π delocalisation *via* the chalcogen bonds. This can also be inferred from the UV-vis spectrum, with **Te_2-F_2-H** exhibiting the more red-shifted ligand-based π → π* λ_{max} (Figure 9C). **Te_2-F_2-H** exhibits the optimal balance of intramolecular chalcogen bonds without any destabilising steric interactions from the fluorine atoms, allowing a fully planar structure. Thus, incremental increases in number of ortho-Te atoms results in a blueshift of the λ_{max} arising from less average π overlap, but more deeply redshifted absorption tails; arising from minor populations of planar structures that redshift the *n* → π* transitions.

2.5.3 Photoisomerisation and half-lives of stable azobenzenes

The half-lives for *Z* to *E* thermal relaxation, (Z)-$\tau_{1/2}$ of the all azobenzene derivatives were evaluated (Table 1 and Figure 10). Similar to the subtle changes observed in absorption maxima for (*E*)-**X_2,m-Y_2,** the impact of the meta group for (Z)- **X_2,m-Y_2** $\tau_{1/2}$ were not as drastic as anticipated based on Woolley's observations for compound **13**.[24] The half-lives electron-rich di-halogenated azobenzenes were in the order of hours to days. However, relatively predictable, incremental decreases in half-life were observed: substituting H for OMe typically resulted in a 4-fold drop in $\tau_{1/2}$, whilst switching OMe for NMe_2

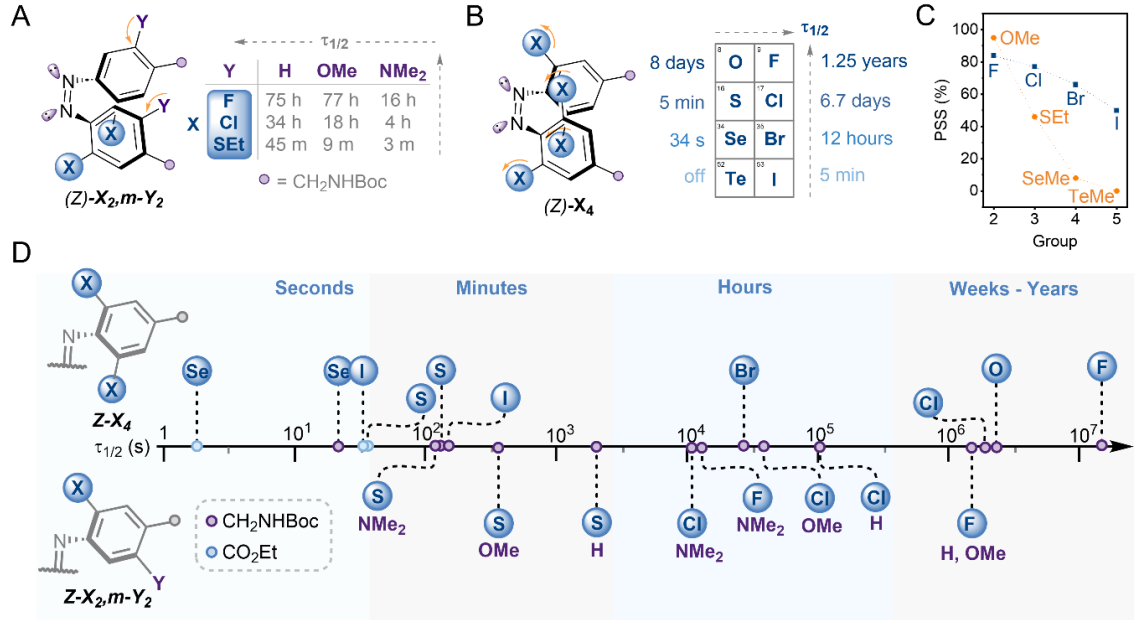


Figure 10. (A) Half-life of (*Z*)-**X_2,m-Y_2** derivatives (B) Half-life of *(Z)*-**X_4** derivatives with *p*-CH_2NHBoc linker (for X=Te, para =H). (C) PSS for **X_4** derivatives (D) Schematic timeline showing the range of half-lives for the Z → E thermal isomerisation, including p-ester derivatives.

afforded a ~ 3-fold decrease. These results suggest that more electron rich aromatic rings exhibit shorter half-lives, perhaps due to more single bond character in the N=N bond facilitating thermal back-relaxation. The nature of the ortho-substituent was more influential on half-life, with more electronegative groups displaying longer lifetimes. This is likely to arise from σ-withdrawing groups alleviating lone pair repulsion of the N=N bond, which lowers the energy of the isomer and results in a longer thermal half-life.[12]

The X_4 derivatives exhibited more robust periodic trends; with $\tau_{1/2}$ decreasing down each group. This is consistent with more electronegative, σ-withdrawing elements alleviating lone pair repulsion of the N=N bond. For X = F, anomalously high Z-isomer stability has previously been attributed to intramolecular C···F interactions further stabilising the structure.[32] Increasing the steric bulk of the alkyl group appended to sulfur from ethyl to iso-propyl blueshifts the switching transition, presumably due to steric clash that distorts from planarity outweighing the chalcogen bonding interactions (Table 1, entry 16 → 18). This structural change does not affect the thermal $\tau_{1/2}$ of the Z-isomer. Across this series of photoswitches, the $\tau_{1/2}$ can be tuned over 7 orders of magnitude within one isostructural series, which opens up applications where precise tuning of photoswitching and thermal relaxation is desired. No switching was observed for the **Te_4** and **Te_2F_2** derivative. This may arise from the $\tau_{1/2}$ being too short to allow significant accumulation of the (*Z*)-isomer under photo-irradiation. However, Haberhauer proposed that strong intramolecular chalcogen bonds could result in large energy differences between the *E* and *Z* isomer; which supresses photoswitching in *o*-PhTe substituted azobenzenes.[33]

The photo-stationary states (PSSs) of **X_4** derivatives ranged from 48 to 77% Z isomer when irradiated with the appropriate LEDs (Table 1, Figure 10C), with heavier atoms exhibiting lower PSSs. This may potentially be a consequence of the Z-isomer also displaying significant n orbital destabilisation, resulting in a more redshifted $n \rightarrow \pi^*$ transition, and thus more overlap of this transition for both isomers. For the chalcogens, the drop in PSS down the group is more dramatic. This may in part be due to the shorter Z isomer-half-lives preventing full conversion

to the Z-isomer (and hence not reaching the true PSS under the experimental conditions), or a consequence of overlapping *E* and *Z* absorption bands.

The para-substituent also has a significant influence on the Z isomer $\tau_{1/2}$ (Table 1). Generally, switching from a para-H substituent to a methylene group results in a 2-fold decrease in half-life, consistent with more electron-rich aromatic rings displaying shorter half-lives due to marginally more single bond character.[34] Switching to an ester group results in ~ 4 − 10-fold decreases in half-life, which may be rationalised by π-acceptors stabilising the linear Ar-N-N-Ar transition state during thermal isomerisation. [12] The presence of an ester group also results in a significant redshifting of the $n \rightarrow \pi^*$ transition, whilst also serving as a potential functional

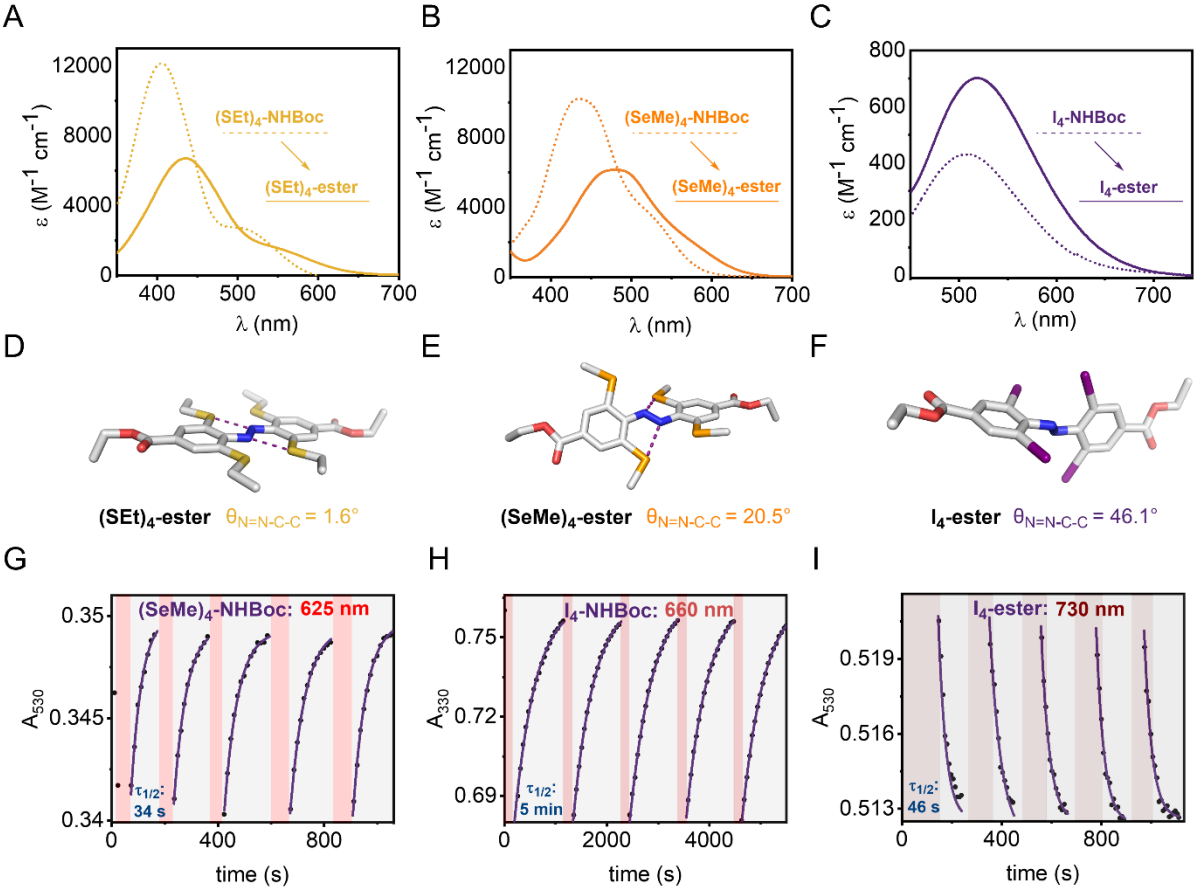


Figure 11. (A-C): Stacked UV-Vis spectra of S, Se and I derivatives (D-F): Solid-state structures of para-ester derivatives with average aryl-N=N dihedral angles. (G-I). Reversible photoswitching for tetra ortho-substituted azobenzene derivatives: (G) **(SeMe)$_4$-NHBoc** with 625 nm, (H) **I$_4$-NHBoc** with 660 nm and (I) **I$_4$-ester** with 730 nm irradiation. Data point: absorbance at the indicated wavelength, solid line: 1st order exponential fit. Red shaded region indicates time period of irradiation with LED: ~100 μM samples were irradiated with LEDs (625 nm, ~0.9 W; 660 nm, ~1.1 W, 730 nm ~0.7 W).

handle (Figure 11A-C). These tails may arise from increased average planarity in the system to maximise π conjugation. Indeed, **SEt$_4$-ester** is essentially planar in the solid state (Figure 11D), unlike the **(SMe$_4$)-H** counterpart. For the seleno and iodo derivatives, the decrease in planarity is less dramatic in the solid-state crystal structures, presumably arising from competing steric effects with the larger atoms (Figure 11E-F).

The **(SeMe)$_4$**, **(SEt)$_4$**, and **I$_4$** derivatives display thermal half-lives in the order useful for spatial targeting applications (second to minute range), allowing reversible switching between both isomers using only red wavelengths of light (E → Z) and thermal isomerisation (Z → E) without any detectable fatigue (Figure 11G-I). Furthermore, it is theoretically possible to selectively photoisomerise one azobenzene in the presence of another. For instance, **(SeMe)$_4$-NHBoc** does not switch with 660 nm light, whereas **I$_4$-NHBoc** or **I$_4$-ester** derivatives isomerise under these conditions. Notably, it was possible to photoswitch **I$_4$-ester** at the phototherapeutic window (730 nm), where there is optimal tissue penetration (Figure 11I).

2.5.4 Unstable azobenzene structures

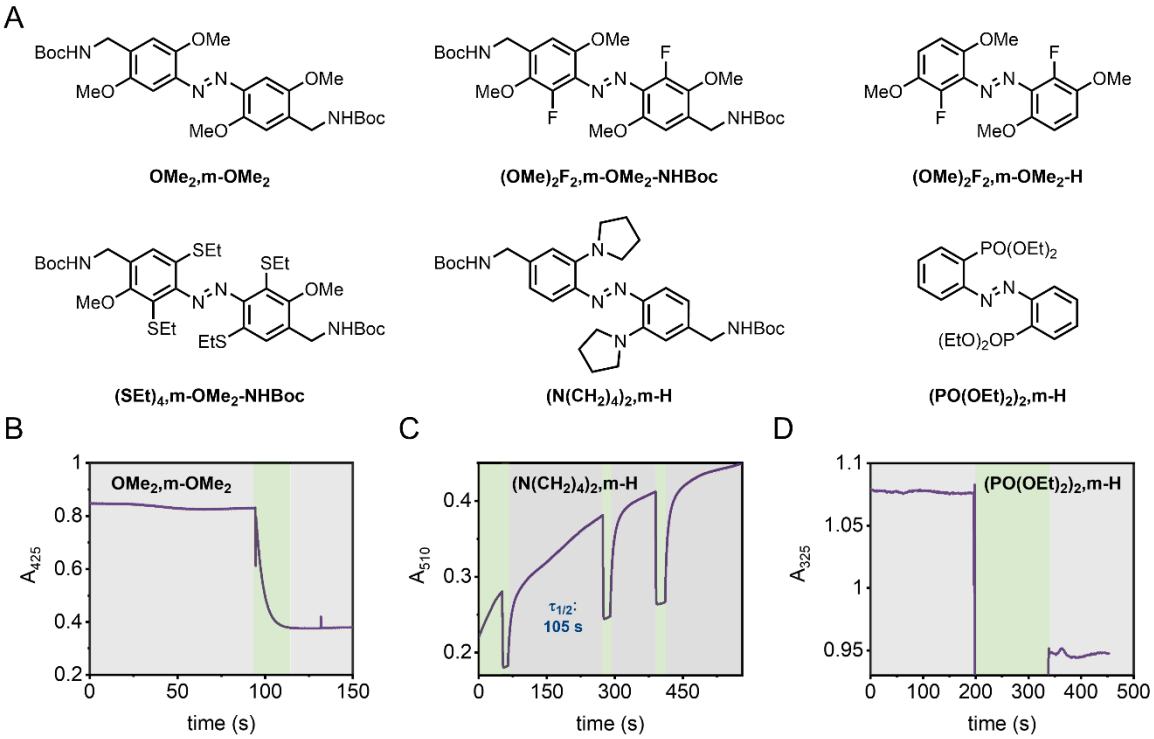


Figure 12. (A): Structures of unstable azobenzenes (B-D): Solid line: absorbance at the indicated wavelength. Green shaded region indicates time period of irradiation with green LED.

In general, photoswitches exhibiting electron-rich aromatic rings were unstable under ambient light perhaps due to competing photooxidation processes (Figure 12A). For the methoxy-containing derivatives, decomposition was observed during irradiation (Figure 12B). For the amino substrate, photoswitching was observed during irradiation, but a gradual general increase absorption with a $\tau_{1/2}$ of 105 s was observed when the light was switched off, indicative of decomposition (Figure 12C). For the phosphonate ester derivative, a similar light-induced decomposition to the methoxy derivatives was observed (Figure 12D), with no observable exponential decays.

2.6 Glutathione stability

Finally, the utility of the photoswitches under reductive biological conditions was accessed by exposure to the highest expected intracellular concentration of glutathione (10 mM).[13] All **X_4**-NHBoc derivatives were deprotected with TFA to afford the corresponding water soluble bis-ammonium derivative. Each compound was dissolved in N_2-degassed 100 mM phosphate buffer at pH 7 containing 10 mM GSH, the changes in absorbance were monitored, and the half-life determined using a 1-st order exponential fit (Figure 13, Figure S9). Generally, the smaller and less electronegative elements exhibited higher stability towards GSH, rationalised by smaller, more electron-withdrawing substituents simultaneously increasing the electrophilicity of the N=N bond and decreasing steric bulk aiding attack of the nucleophilic GSH. The **I_4** derivative may be anomalously unstable due to reduction of the C-I bond. However this derivative still exhibits similar stability to the **F_4** derivative which has previously

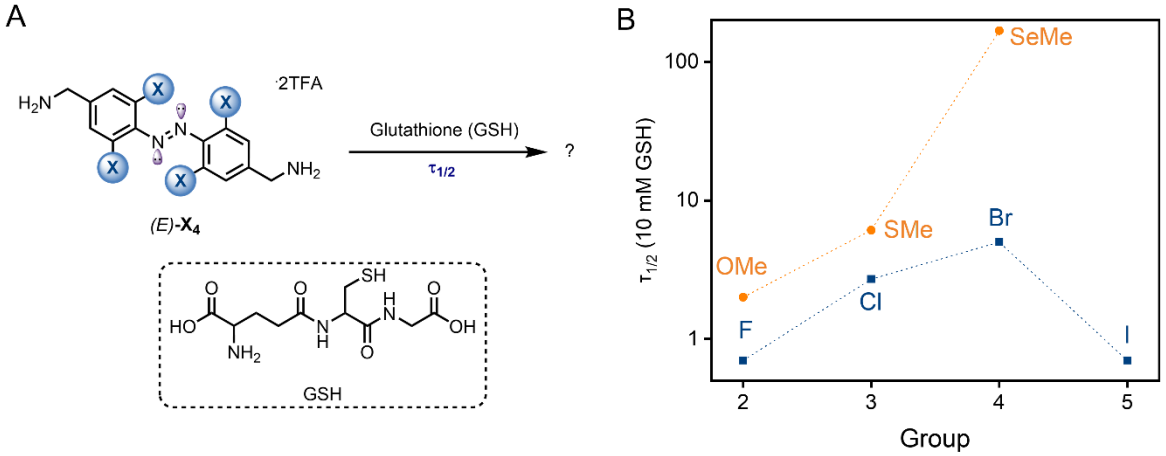


Figure 13. (A) General structure of azobenzenes exposed to GSH (B) $\tau_{1/2}$ of **X_4** derivatives to GSH

been employed in medicinal applications.[32] The selenide derivative may be anomalously stable due to presence of the stable 5-membered chalcogen bonding delocalised π system protecting attack to the N=N bond (note logarithmic scale).

2.7 Chapter Conclusions

Azobenzenes capable of photoswitching in the red to near-IR range represent promising scaffolds for manipulating biological systems with light. This chapter highlights robust periodic trends of ortho-chalcogen and halogen substituted azobenzenes, using extensive photo-physical measurements and solid state structural analysis. In general, the presence of four large atoms ortho to the diazo bond results in more redshifted $n \rightarrow \pi^*$ absorption tails, which are proposed to generally arise from repulsive interactions between the ortho substituent and diazo lone pairs; raising the n orbital energy. The heavier chalcogens unambiguously form internal chalcogen bonds, which results in more planar structures and redshifted transitions.

Meta substituents allow for the fine-tuning of the thermal half-life, while para electron withdrawing groups simultaneously can redshift the E-isomer and decrease the half-life; leading to a library of azobenzenes that can be switched using up to near-IR light, and exhibit half-lives spanning over 7 orders of magnitude. These photoswitches serve as important building blocks for photo-pharmacology, and serve as the basis of the remaining chapters, in which a range of applications including photoswitchable anion transporters and catalysts are presented. In particular, the **Cl_4** and **F_4** scaffolds display a good balance of bi-stability and redshifted switching, whilst **I_4** scaffolds can be used for spatiotemporal control using exclusively red light and thermal decay.

2.8 References

[1] D. B. Konrad, G. Savasci, L. Allmendinger, D. Trauner, C. Ochsenfeld and A. M. Ali, *J. Am. Chem. Soc.*, 2020, **142**, 6538–6547.
[2] M. Dong, A. Babalhavaeji, S. Samanta, A. A. Beharry and G. A. Woolley, *Acc. Chem. Res.*, 2015, **48**, 2662–2670.
[3] E. Merino and M. Ribagorda, *Beilstein J. Org. Chem.*, 2012, **8**, 1071–1090.
[4] A. A. Beharry and G. A. Woolley, *Chem. Soc. Rev.*, 2011, **40**, 4422.
[5] H. M. D. Bandara and S. C. Burdette, *Chem. Soc. Rev.*, 2012, **41**, 1809–1825.
[6] X.-M. Liu, X.-Y. Jin, Z.-X. Zhang, J. Wang and F.-Q. Bai, *RSC Adv.*, 2018, **8**, 11580–11588.

[7] M. Zhu and H. Zhou, *Org. Biomol. Chem.*, 2018, **16**, 8434–8445.
[8] D. Bléger, J. Schwarz, A. M. Brouwer and S. Hecht, *J. Am. Chem. Soc.*, 2012, **134**, 20597–20600.
[9] W.-C. Lin and R. H. Kramer, *Bioconjugate Chem.*, 2018, **29**, 861–869.
[10] C. Zhang, Z. Zhao and M. Kong, *Optik*, 2020, **206**, 163120.
[11] M. Dong, A. Babalhavaeji, M. J. Hansen, L. Kálmán and G. A. Woolley, *Chem. Commun.*, 2015, **51**, 12981–12984.
[12] C. Knie, M. Utecht, F. Zhao, H. Kulla, S. Kovalenko, A. M. Brouwer, P. Saalfrank, S. Hecht and D. Bléger, *Chem. Eur. J.*, 2014, **20**, 16492–16501.
[13] M. Dong, A. Babalhavaeji, C. V. Collins, K. Jarrah, O. Sadovski, Q. Dai and G. A. Woolley, *J. Am. Chem. Soc.*, 2017, **139**, 13483–13486.
[14] J. García-Amorós and D. Velasco, *Beilstein J. Org. Chem.*, 2012, **8**, 1003–1017.
[15] Y. Yang, R. P. Hughes and I. Aprahamian, *J. Am. Chem. Soc.*, 2014, **136**, 13190–13193.
[16] R. Siewertsen, H. Neumann, B. Buchheim-Stehn, R. Herges, C. Näther, F. Renth and F. Temps, *J. Am. Chem. Soc.*, 2009, **131**, 15594–15595.
[17] M. S. Maier, K. Hüll, M. Reynders, B. S. Matsuura, P. Leippe, T. Ko, L. Schäffer and D. Trauner, *J. Am. Chem. Soc.*, 2019, **141**, 17295–17304.
[18] H. Bisle and H. Rau, *Chem. Phys. Lett.*, 1975, **31**, 264–266.
[19] O. Sadovski, A. A. Beharry, F. Zhang and G. A. Woolley, *Angew. Chem. Int. Ed.*, 2009, **48**, 1484–1486.
[20] A. A. Beharry, O. Sadovski and G. A. Woolley, *J. Am. Chem. Soc.*, 2011, **133**, 19684–19687.
[21] S. Samanta, A. A. Beharry, O. Sadovski, T. M. McCormick, A. Babalhavaeji, V. Tropepe and G. A. Woolley, *J. Am. Chem. Soc.*, 2013, **135**, 9777–9784.
[22] S. Samanta, T. M. McCormick, S. K. Schmidt, D. S. Seferos and G. A. Woolley, *Chem. Commun.*, 2013, **49**, 10314.
[23] M. Wegener, M. J. Hansen, A. J. M. Driessen, W. Szymanski and B. L. Feringa, *J. Am. Chem. Soc.*, 2017, **139**, 17979–17986.
[24] S. Samanta, A. Babalhavaeji, M. Dong and G. A. Woolley, *Angew. Chem. Int. Ed*, 2013, **52**, 14127–14130.
[25] A. Antoine John and Q. Lin, *J. Org. Chem.*, 2017, **82**, 9873–9876.
[26] R. Weiss and J. Seubert, *Angew Chem. Int. Ed*., 1994, **33**, 891–893.
[27] M. Yamamura, N. Kano and T. Kawashima, *Heteroat. Chem.*, 2011, **22**, 301–306.
[28] R. Henyecz, G. Keglevich, *Curr. Org. Synth.*, 2019, **16**, 523–545
[29] A. Kerckhoffs, K. E. Christensen and M. J. Langton, *Chem. Sci.*, 2022, **13**, 11551–11559.
[30] K. Srivastava, T. Chakraborty, H. B. Singh and R. J. Butcher, *Dalton Trans.*, 2011, **40**, 4489–4496.
[31] J. Broichhagen, D. H. Woodmansee, D. Trauner and P. Mayer, *Acta Cryst E*, 2015, **71**, o459–o460.
[32] K. Aggarwal, T. P. Kuka, M. Banik, B. P. Medellin, C. Q. Ngo, D. Xie, Y. Fernandes, T. L. Dangerfield, E. Ye, B. Bouley, K. A. Johnson, Y. J. Zhang, J. K. Eberhart and E. L. Que, *J. Am. Chem. Soc.*, 2020, **142**, 14522–14531.
[33] S. Mehrparvar, Z. N. Scheller, C. Wölper and G. Haberhauer, *J. Am. Chem. Soc.*, 2021, **143**, 19856–19864.
[34] M. A. Kienzler, A. Reiner, E. Trautman, S. Yoo, D. Trauner and E. Y. Isacoff, *J. Am. Chem. Soc.*, 2013, **135**, 17683–17686

Chapter 3 – Photoswitchable transmembrane anion transporters

3.1 Stimuli-responsive anion transporters

The field of anion transporters has experienced a burgeoning interest in the last 10-20 years and has become a relatively established area of research; showing promise as potential therapeutics for cystic fibrosis and cancer.[1] However, in a therapeutic context, disrupting ion homeostasis in off-target cells may lead to severe side-effects and potentially fatal consequences,[2] so it is much more attractive to gain precise control of the flow of ions across a lipid bilayer with high spatiotemporal control. Natural ion channels are gated using external stimuli such as ligand or ion binding, light, pH, voltage or mechanical stress,[3] yet synthetic systems mimicking this 'On/Off' activity are extremely rare and remains an ongoing challenge.[4] This section will highlight key examples of stimuli-responsive ion transporters.

3.1.1 Stimuli-responsive carriers without the use of light

The rapid proliferation of cancer cells intrinsically results in higher reactive oxygen species and glutathione levels, which has spurred the development of redox-responsive anion transporters.[5] In 2022, Gale reported Au(III)-complexed pro-carrier **1**, which in the presence of GSH becomes reduced to Au(I) to reveal the active chloride transporter **2**.[6] In the same year,[7] Gabbaï demonstrated that highly charged antimony derivative **3** is cleaved by thiols via a reductive demethylation to form membrane permeable **4**, allowing for high 'On/Off' transport activity. In 2022, Langton and co-workers developed reversible diaryl tellurium-based receptors that only display activity as the Te(IV) species **5**, whereas the Te(II) and Te(VI) species are completely inactive. The main advantage of this system is that it demonstrates the concept of achieving high selectivity within a specific redox window via reversible redox activation.[5] The authors reason that chloride affinity and transport activity is much higher for the Te(IV) telluroxide than the other oxidation states due to much higher binding affinity *via* chalcogen bonding.

In 2014, Buschaert developed the acidic thiosquaramide **8** which is deprotonated pH > 7 and is thus inactive as a transporter, whereas protonation leads to a switch on in transport.[8]

Although these systems offer limited spatiotemporal control due to the challenge of externally perturbing pH in biological systems, these derivatives may potentially exhibit selectivity towards more acidic environments such as lung epithelia and extracellular cancer cells. The first voltage-gated transporter **8** was reported by Gale,[9] which selectively co-transports HCl as **8·HCl⁻** and diffuses back across the membrane as **8⁻**. As a result of the negative charge in both species, application of a negative or positive membrane potential inhibits the diffusion of **8⁻** or **8·HCl⁻** respectively, thus effectively gating anion transport with voltage (Figure 2A).

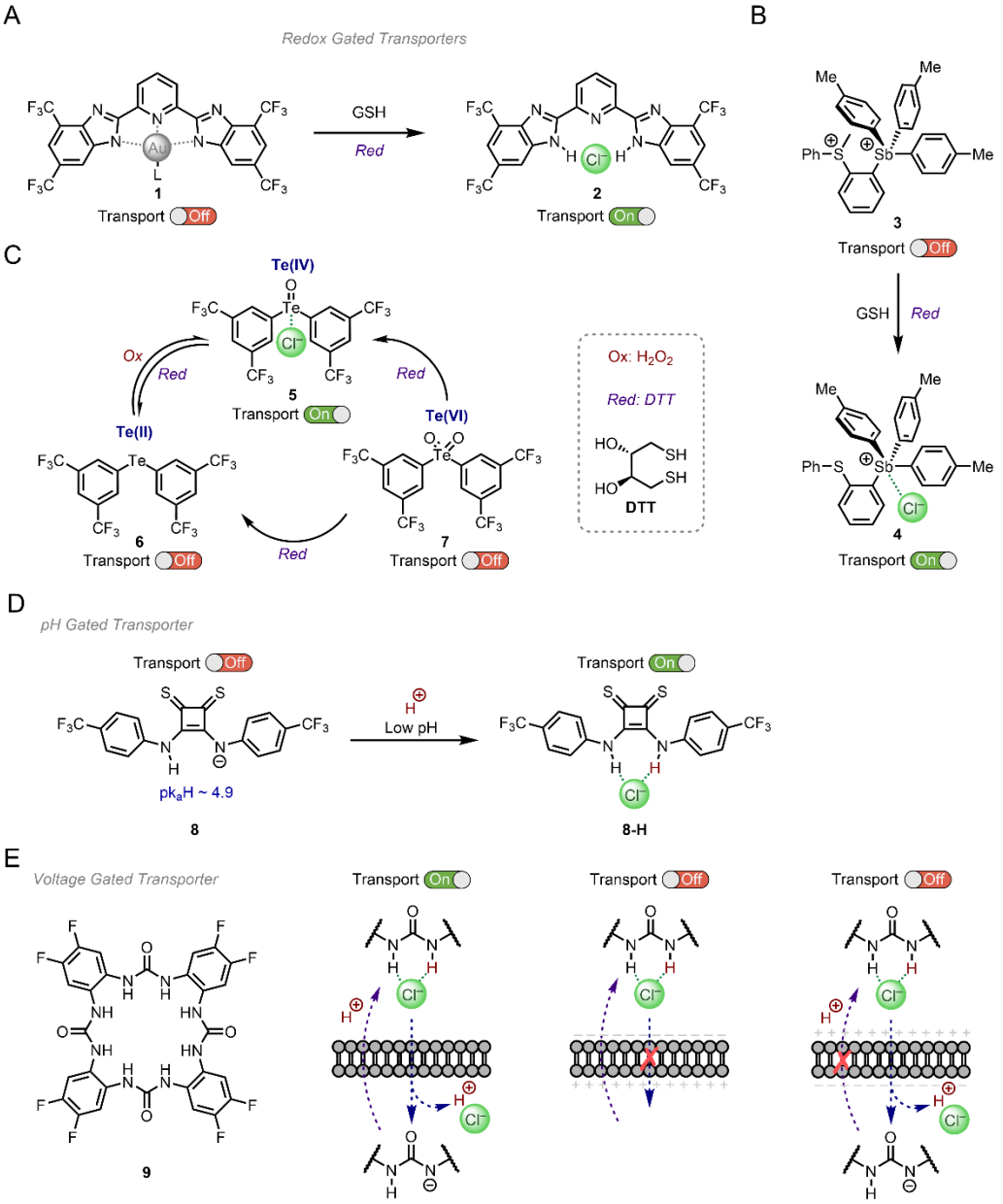


Figure 1: Stimuli-responsive anion transporters without using light. (A)-(C) redox-responsive transporters by (A) Gale[6] (B) Gabbaï[7] (C) Langton[5] (D) pH-responsive transporter by Buschaert[8] (E) Voltage-responsive transporter by Gale[9]

3.1.2 Stimuli-responsive carriers responsive to light

As previously discussed, light represents an attractive stimulus to regulate ion transport due to its non-invasive nature yet high spatiotemporal precision, and lack of wasteful by-products (such as the reduced gold species in **1**). Although limited, a few key examples have been reported (Figure 2). In 2019, Talukdar developed photo-caged transporter **10**, which does not bind or transport chloride.[10] When irradiated with UV light, the o-nitrophenyl group is photo-deprotected to release the active carrier. The authors demonstrated that chloride transport in cancer cells could be switched on by photo-cleavage, leading to increased cytotoxicity.

In the subsequent year, the same group reported azobenzene (*E*)-**12**, which binds and transporters chloride as a 2:1 sandwich complex. As the *E* isomer, a well-defined hydrogen

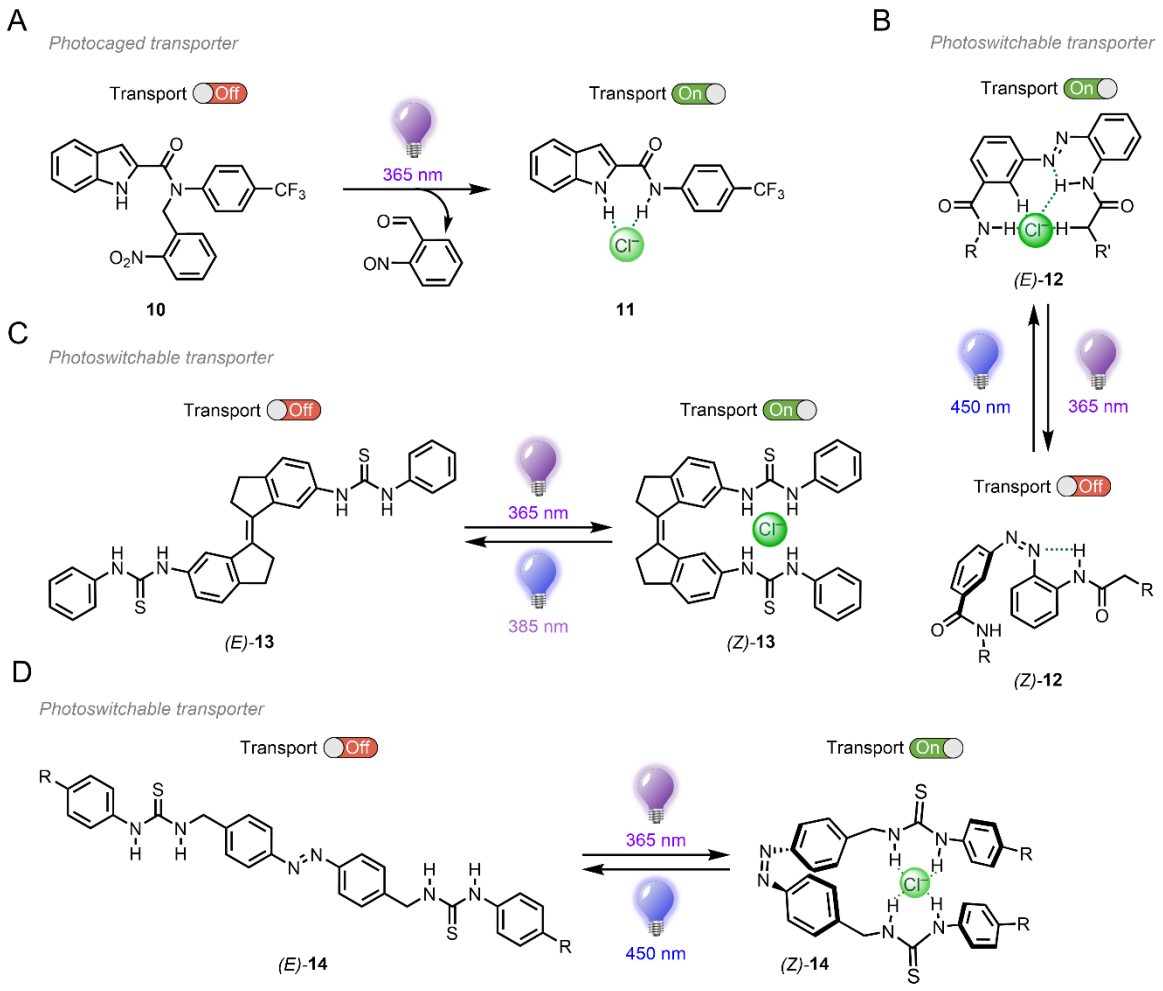


Figure 2. (A) Photocaged transporter by Talukdar[10] (B-C): Photoswitchable transporters by (B) Talukdar[13] (C) Feringa[11] (D) Jeong[12]

bond network allows for favourable binding interactions, whereas (Z)-**12** adopts a non-binding conformation where the key hydrogen bond is suppressed by intramolecular coordination. The authors demonstrate reversible switching using two orthogonal wavelengths of light, allowing high control of 'On/Off' activity.

In 2022, Feringa and co-workers published stiff-stilbene based thiourea **13**, which binds chloride ~ 5-6x more strongly in the *Z* form due to cooperative binding.[11] These derivatives displayed enhancements of chloride transport rates up to >34 x for the Z isomer relative to E, highlighting the importance of molecular geometry and membrane partitioning as well as N-H acidity/binding constant towards achieving efficient transmembrane carriers.

Similarly, Jeong and co-workers developed **14**, which isomerises with UV and blue light to ***(Z)*-14.**[12] ***(Z)*-14** typically exhibited 10-fold enhancements in chloride binding constant and improved transport rates due to increased cooperativity and anion encapsulation. The authors also demonstrate that these compounds were capable of transporting chloride in mammalian cells. However, appreciable background transport was observed in the *trans* "OFF" state during switching experiments.

3.2 Proposed approach towards developing redshifted photoswitchable transporters

Photo-responsive mobile ion carriers that function in lipid bilayers are extremely rare, and synthetic systems with *reversible* photo-control over transport activity in membranes remain elusive. Consequently, there is no general design criteria and knowledge base to guide the development of such systems. Additionally, the current state of-the-art photoresponsive carriers (Figure 2) are activated by UV light, limiting their uses in a biological context due to damage to cellular surroundings and low tissue penetration. Furthermore, redshifted azobenzenes remain highly underexploited in biological applications, and have yet to be incorporated into ion carriers.

We aim to synthesise photoswitchable azobenzene chloride transporters able to be (i) controlled with biologically compatible red light and (ii) switched between well-defined binary

states (i.e. achieve a spike in activity for the *Z* isomer, whilst maintaining zero activity for the *E* isomers at the same concentration, and switch between these states in a reversible fashion using different wavelengths of bio-orthogonal visible light). Chloride transport activities and binding affinities will be determined using HPTS-based vesicle assays and NMR titrations to develop a structure-activity relationship. We also aim to optimise the cooperativity in these systems.

3.2.1 Initial design and synthesis of photoswitchable anion transporter

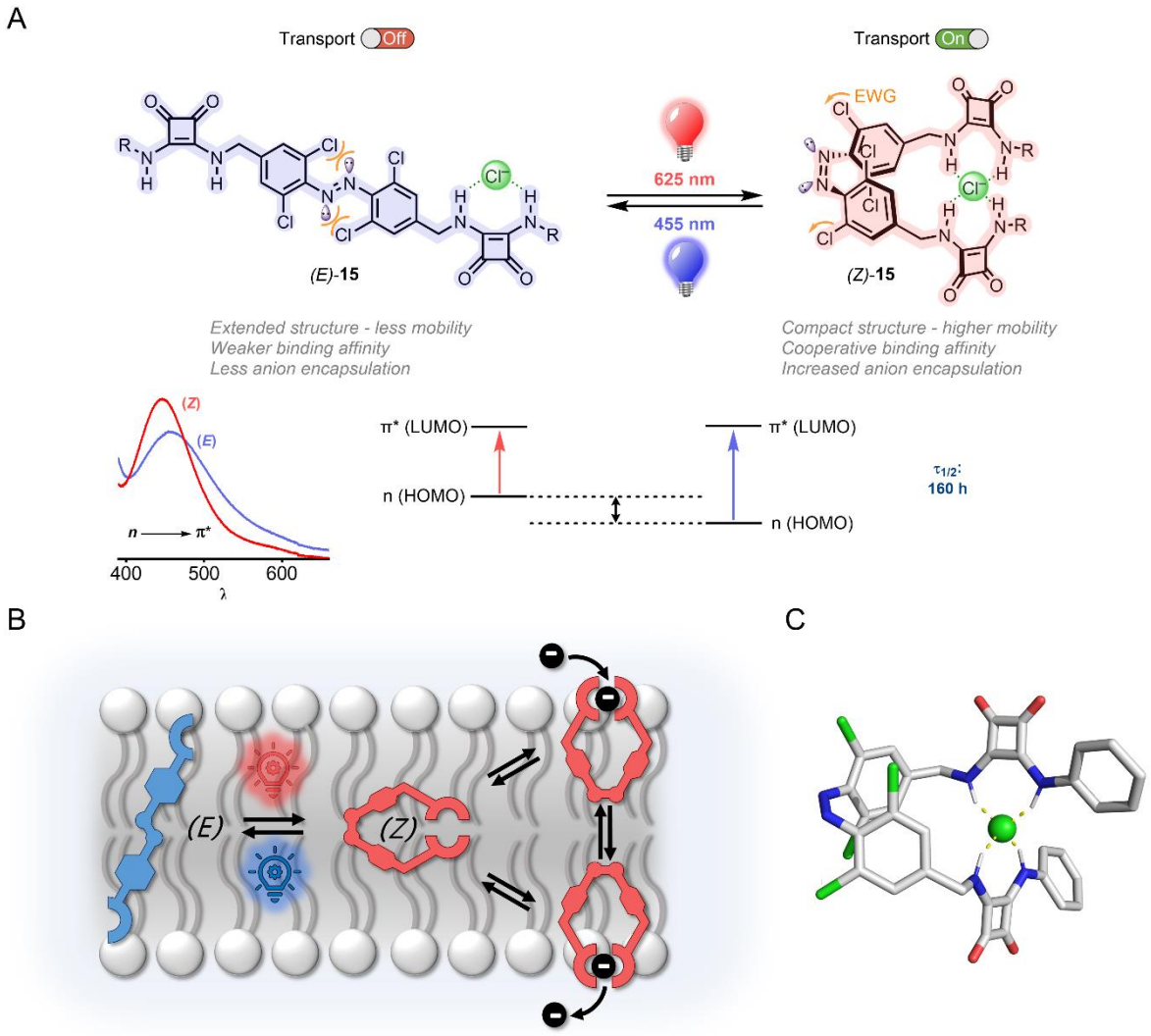


Figure 2. (A) Initial design for photoswitchable anion transporter with key absorption transitions shown. (B) Schematic diagram of photoswitchable anion transport within lipid bilayer (C) Calculated structures of *(Z)*-**15a** chloride complex (MM+ force field, HyperChem).

Our initial design features an azobenzene photoswitch with a **Cl_4** core (Chapter 2) appended to two anion binding squaramides, leading to structure **15** (Figure 2). This allows the formation of the (*Z*)-isomer with high photo-stationary state (PSS) distribution using red light due to well-separated n → π* transitions for both isomers. The chlorine atoms also result in an essentially bistable system by alleviating lone pair repulsions in (Z)-**15** (thermal half-life ~ 1 week), which conveniently allows the analysis of binding and transport properties (Z)-**15** without constant light irradiation. Although not as biocompatible as red light, large quantities (*E*)-**15** may be generated upon irradiation with blue light; facilitating the control of ion transport and binding using orthogonal wavelengths of light (Figure 2B).

As highlighted in chapter 1, efficient anion transporters exhibit strong anion binding affinities and typically benefit from cooperativity and anion encapsulation ('shielding' the highly charged anion from the non-polar environment of the bilayer). Conversely, transporters displaying poor binding affinity and less encapsulation are inefficient transporters, the latter arising from decreased mobility within the bilayer and larger reorganization penalties within the membrane due to hydrophobic interactions.[14] These features, together with the high logP values of the proposed structure, should result in higher activities of the (*Z*) isomer relative to the (*E*) form.

The squaramide R group can be fine-tuned with a modular approach to optimise the On/Off switching behaviour and can be replaced with virtually any receptor if other applications are desired. Finally, the methylene spacer deconjugates the squaramide groups from the azobenzene core, resulting in Z half-lives that are independent of anion concentration (because in conjugated systems anion binding increases electron density on the azobenzene, modifying its photophysical properties.[15] Molecular mechanics modelling confirmed that these geometrical constraints had the potential to lead to cooperative chloride anion binding between both squaramide motifs in the Z isomer (Figure 2C).

The desired derivatives were conveniently prepared by deprotection of **Cl_4-NHBoc** (Chapter 2) with TFA, followed by coupling with a variety of monosquaramides **16a-i** with a range of electron donating, electron-withdrawing and alkyl substituents, providing a varied library to

elucidate the optimal R group for On/Off switching (Figure 4). The monosquaramides were in turn accessed from commercially available amines and dimethyl squarate. The absorption spectra of the derivatives showed that squaramide substitution patterns did not significantly influence the positions of the n → π* bands (Appendix Figure S1). Irradiation of transporter **15f** with LEDs (~0.9 W) at a variety of wavelengths allowed quantification of the wavelength dependence of the photo-stationary states using ^{1}H NMR experiments (Figure 4). Most importantly, irradiation with blue and red light allowed for reversible photoswitching with high PSSs (83% *E* and 77% *Z*, respectively), whereas thermal heating allowed near quantitative conversion to (*E*)-**15**, key for studying both isomers for their anion binding and transport.

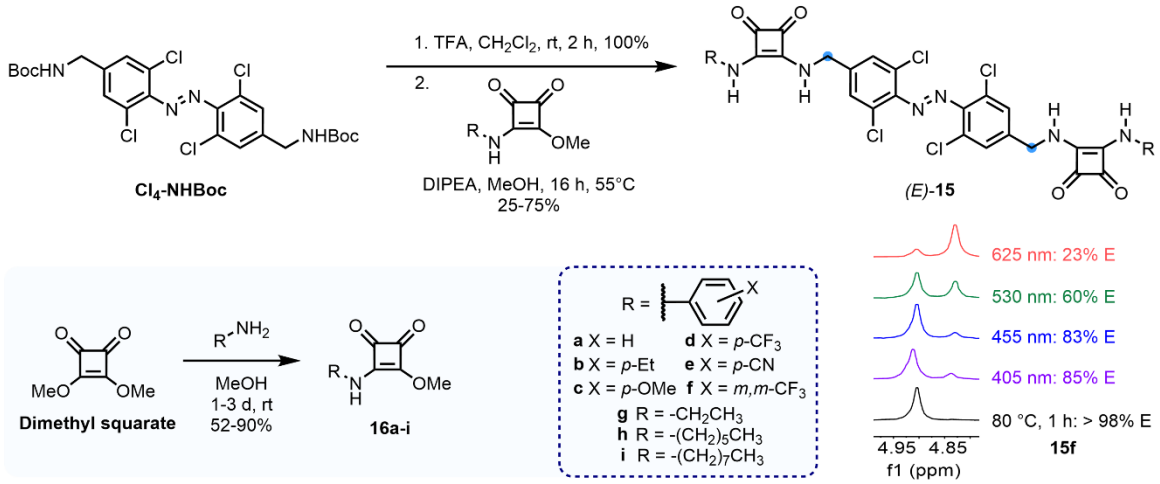


Figure 4. Preparation of photoswitchable anion transporters and PSS of **15f** at various wavelengths as determined by integration of benzylic ^{1}H signals (DMSO-d_6)

3.2.2 NMR titrations and anion binding capabilities of initial scaffold

The anion binding capabilities of **15a-i** were probed via a series of ^{1}H NMR titration experiments conducted in DMSO-d_6 (necessary to fully solubilise the bis-squaramides) by addition of aliquots of tetrabutylammonium chloride and monitoring the binding induced chemical shift perturbations.[16] Where resolved, the squaramide N-H and *ortho* C-H signals were analysed using a global fit procedure through the Dynafit software program,[17] using non-linear least squares analysis to determine the best fit between observed and calculated chemical shifts for all signals (Figure 5; S2-3). To elucidate the (*Z*)**-15** binding constant, the binding constant of the competing minor population of (*E*)**-15** was taken into account.

Table 1. 1:1 association constant for chloride binding in d_6-DMSO. K_1^Z takes into account K_1^E at the photostationary state. Errors at the 95% confidence limit, averaged over at least two titrations

	15a	**15b**	**15c**	**15d**	**15e**	**15f**	**15g**	**15h**
K_1^E (M^{-1})	180 ± 4	144 ± 6	154 ± 6	252 ±3	274 ± 20	278 ± 20	94 ± 2	130 ± 10
K_1^Z (M^{-1})	267 ± 2.5	201 ± 2.5	231 ± 12	346 ± 2	358 ± 12	402 ± 6	142 ± 7	204 ± 21
K_1^Z / K_1^E	1.4	1.4	1.5	1.4	1.3	1.4	1.5	1.5

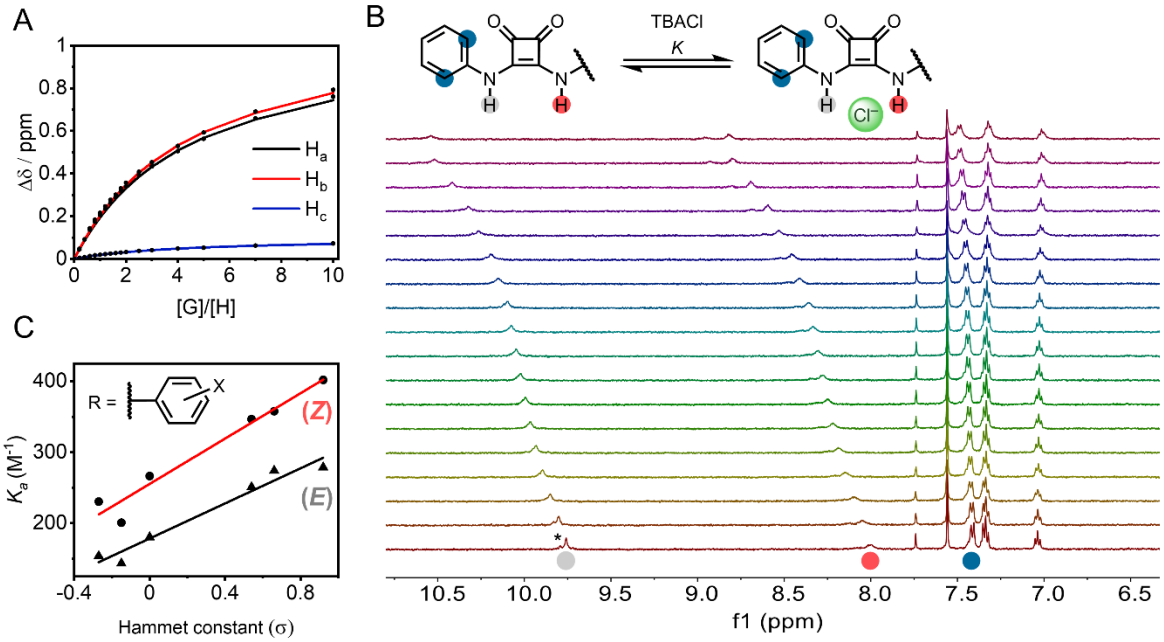


Figure 5. Representative ^{1}H NMR titration with TBACl. G = Guest, H = Host. (A) Chemical shift perturbations for *(Z)*-**15** with (B): Stacked NMR spectrum. *(E)*-**15** peak labelled as * (C) Plot of *K* vs. Hammett parameter σ for **15** aryl derivatives.[18]

In principle, 1:2 binding stoichiometry is possible due to the two identical squaramide receptors. However, the overall observed association constants are weak in DMSO ($K_1^E{}_{obs}$ ~ 10^2; similar for other reported aryl-, alkyl-squaramide receptors in DMSO)[19] and binding of the second equivalent of anion is too weak to be detected, as concluded from the failure to fit the data to 1:2 binding models. This can be rationalised by significant anion-anion repulsion in the 1:2 complex, leading to negligible association of the second anion in this competitive polar solvent. The binding constants are summarised in Table 1.

The affinity of (*Z*)-**15** derivatives for chloride were higher than the analogous (*E*)-**15** isomers, consistent with the predicted cooperativity between squaramides observed in the calculated structure. The ratio of K_Z^1/K_E^1 ~ 1.5 across all substituents indicates that the modest extent of cooperativity between squaramides is independent of the squaramide substituent. The

electron donating or withdrawing nature of the squaramide substituents translated into changes in the absolute binding affinity for chloride for both isomers, with a linear correlation between *K* and Hammett constant obtained for the aryl substituents; confirming that the electronic effect of the substituent significantly influences anion binding affinity (Figure 5C).

3.2.3 Ion transport properties of initial photoswitchable scaffold

Given the modest cooperativity and large structural changes for (*Z*)**-15** derivatives, we sought to evaluate the anion transport capabilities of our library. A well-established method of quantifying chloride exchange across lipid bilayers is the so-called HPTS assay (Figure 6).[20] 8-Hydroxy-1,3,6-pyrenetrisulfonate (HPTS) is a pH-sensitive fluorophore with a pK_a ~ 7.3; where the protonated (HPTSOH) and deprotonated (HPTSO-) forms exhibit unique excitation fluorescence maxima (λ_{ex} = 405 nm and 460 nm respectively) and a fluorescence emission maximum at λ_{em} = 510 nm. The fluorophore is membrane impermeable, and when loaded inside lipid bilayer vesicles, the ratiometric emission intensity of HPTS I_{rel} can be used to monitor changes of internal pH (equation 3.1).[21]

$$I_{rel} = \frac{I_{460}}{I_{405}} \quad (3.1)$$

Typically, 1-palmitoyl-2-oleoyl-sn-glycero-3-phosphocholine large unilamellar vesicles (POPC LUVs, lipid concentration 31 μM), loaded with HPTS (buffered to pH 7.0 in NaCl and HEPES solution) are placed in a cuvette within a fluorescence spectrometer. A transmembrane pH gradient is generated across the membrane by addition of NaOH. Upon addition of an ion carrier in DMSO solution (<0.5% v/v), carrier-mediated ion transport will take place to dissipate the transmembrane pH gradient. Overall charge neutrality is maintained across the bilayer, leading to an increase in internal pH and thus I_{rel}.

The detected increase in HPTS emission over time corresponds to the preferred ion exchange process. If OH^-/Cl^- exchange (blue) dominates over other plausible pathways that can dissipate the applied pH gradient, i.e.Na^+/H^+ exchange (antiport), H^+/Cl^- or Na^+/OH^- co-transport (symport) (light red), a plot of normalised fluorescence over time reports on the rate

of carrier mediated $^{-}$OH/Cl^{-} antiport. Fluorescence intensity is normalised (I_{rel}) by lysing the vesicles with detergent to determine the free fluorophore emission (R_d, theoretical maximum pH dissipation) and calibrating the data to equation 3.2, where R_o is the fluorescence ratio directly prior to transporter addition, and Rt is the fluorescence intensity at a given time *t*. The alternative symport and antiport pathways can be ruled out by other control experiments (for example, Na^+ transport can be ruled out by swapping the metal cation for other alkali earth metals and observing the effect on transport rates), although generally unidirectional ion pair movement (symport) is osmotically disfavoured and thus is unlikely to dominate. [21]

$$I_{rel} = \frac{R_t - R_0}{R_d - R_0} \quad (3.2)$$

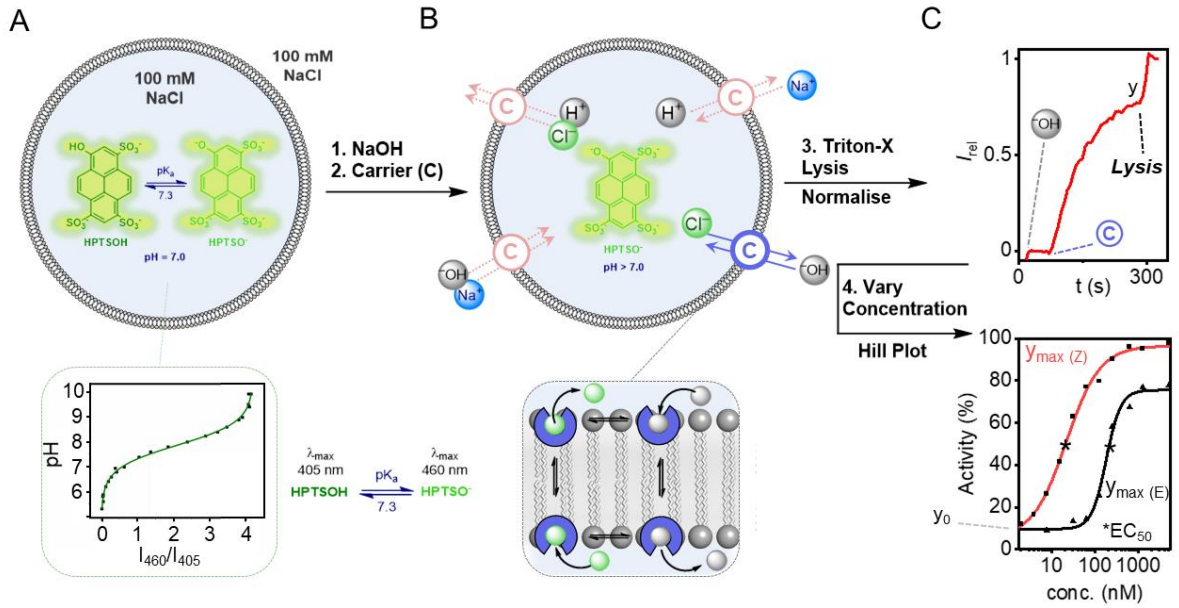


Figure 6. Outline of HPTS assay. (A): Vesicles in NaCl buffer are loaded with pH sensitive dye HPTS. pH curve reproduced from Paxton[22]. (B): Vesicles are subjected to an external base pulse, resulting in a pH gradient across the bilayer. The transporter is added, resulting in transport of ions across the bilayer, in this case proposed as hydroxide influx and chloride efflux. (C) The influx of hydroxide in exchange for chloride results in a change in pH, thus I_{rel}. The vesicles are lysed at the end of the run to normalise data to determine maximal activity at a given concentration (y). The dependence of y on carrier concentration is fitted to the Hill equation, allowing determination of EC_{50}, i.e. transport activity.

Dose–response curves can be generated using this assay by varying the carrier concentration and plotting fractional activities y (maximum fluorescence intensity just prior to lysis). When fitted to the Hill equation (3.3), the dependence of the anion transport activity (y) on the *n*-th power of the carrier concentration (x) can be elucidated, whilst also determining an effective concentration value required to reach 50% activity (EC_{50}):

$$y = y_0 + (y_{max} - y_0) \cdot \frac{x^n}{EC_{50}{}^n - x^n} \quad (3.3)$$

where y is fractional activity at a given concentration, y_0 is the fractional activity in absence of the transporter and y_{max} is the maximum fractional activity reached (with excess transporter). The Hill coefficient n may be interpreted as the number of carrier molecules in the active host-guest complex that facilitates ion transport (in cases where n > 1, given that in such case the active species is not thermodynamically stable).[21] Thus, Hill plots enable quantitative comparison of the relative activities of carriers (EC_{50}) and may provide insight into the binding stoichiometry. The Hill plots for carriers **15a-i** are summarised in Table 2 and Figure 7. Full transport data can be found in Appendix Figure S4.

Table 2. Transport data for carriers **15a-i**. [a] For compounds of low activity, estimated lower bounds for the EC_{50} value are given. [b] For the *Z* isomer, EC $^{Z,PSS}{}_{50}$ indicates apparent value achieved by addition of the 77 : 23 *Z*/*E* PSS mixture. [c] Hill coefficient. [d] Not determined. [e] Poor solubility in DMSO prevented full Hill analysis. [f] Value calculated with *Virtual Computational Chemistry Laboratory.* [23]

		15a	**15b**	**15c**	**15d**	**15e**	**15f**	**15g**	**15h**	**15i**
1	$EC_{50}{}^{E}$ (nM)[a]	181 ± 16	591 ± 341	1020± 477	146 ± 40	232 ± 143	246 ± 121	>5000[e]	204 ± 42	>20,000 [e]
2	$EC_{50}{}^{Z,PSS}$ (nM)[a,b]	22 ± 2	101 ± 18	218 ± 54	42 ± 12	64 ± 13	90 ± 55	432 ± 41	28 ± 2	>20,000 [e]
3	n^{E} [c]	2.6 ± 0.5	0.63 ± 0.1	0.62± 0.1	1.0 ± 0.2	0.62 ± 0.1	0.58 ± 0.1	–[d]	0.8 ± 0.1	–[d]
4	n^{Z} [c]	1.1 ± 0.1	1.0 ± 0.2	0.64 ± 0.1	0.76 ± 0.1	0.74 ± 0.1	0.67 ± 0.1	1.41 ± 0.1	1.2 ± 0.1	–[d]
5	$K_1{}^{Z}$ / $K_1{}^{E}$	3.1	2.8	3.0	2.7	2.6	2.9	3.0	3.1	–[d]
6	$EC_{50}{}^{Z,PSS}$ / $EC_{50}{}^{E}$	8.2	5.9	4.7	3.5	3.6	2.7	>10[e]	7.3	–[d]
7	Log P[f]	6.4 ± 0.4	6.9 ± 0.5	6.3 ± 0.3	6.8 ± 0.2	5.8 ± 0.6	7.1 ± 0.1	5.1 ± 0.3	6.4 ± 0.2	7.2 ± 0.3

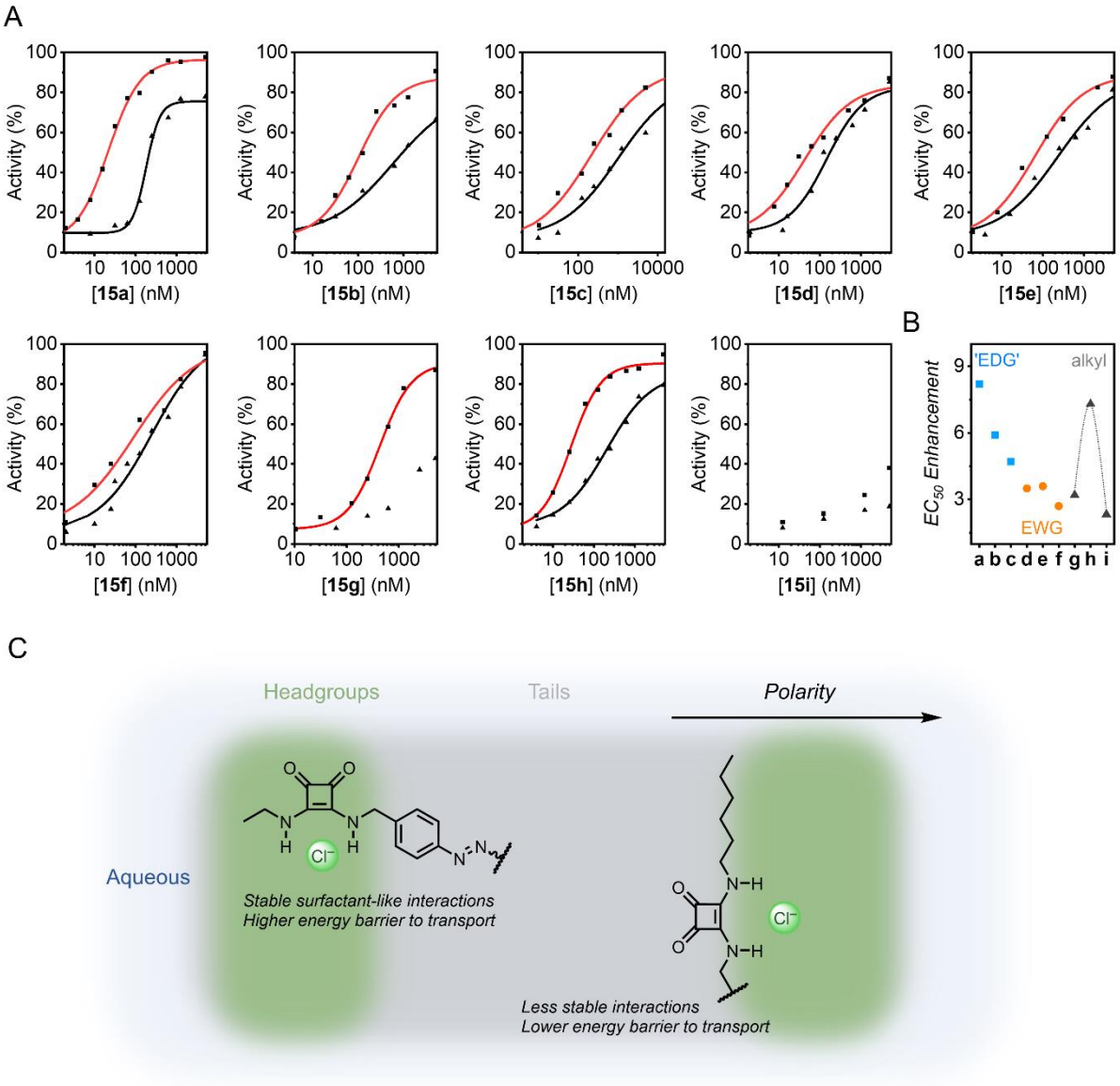


Figure 7. (A) Stacked Hill plots for carriers **15a-i**. (■): (*Z*)-isomers, (▲): (*E*)-isomers, lines: fitted data. (B) Plot of EC_{50} *Z/E* enhancement for carriers **15x** (C) Schematic diagram of potential interactions within the bilayer.

A significant enhancement in activity for the Z-isomers were observed for carriers **15a-i** (Table 2, entry 6; Figure 7B), up to around 8-fold for **15a** (R = phenyl). In general, the enhancement in EC_{50} was larger than the enhancement in binding constant, which was consistently ~1.5 (entry 5). However, there is no obvious correlation between binding strength and transport rates, emphasising the fine balance of lipophilicity, solubility, mobility and molecular shape on transport rates, and these subtle factors are all likely to contribute to the observed transport rates.

It is apparent that the highest enhancements in EC_{50} were observed for the more electron-rich substrates, whereas when R=EWG (**15d-f**), both isomers were relatively efficient transporters, with only ~3-fold enhancement. This may be rationalised by considering that the binding constant for the E isomers is presumably sufficiently high for efficient transport without assistance from the second squaramide, therefore resulting in poorer discrimination between isomers. Additionally, both isomers of **15d-f** were noticeably less soluble and more prone to aggregation than **15a-c** due to stronger intermolecular hydrogen bonding, which could hamper the activity for both isomers by forming non-productive inactive species, leading to poorer differences in EC_{50}. Indeed, with the highest loadings of carrier, overall transport activity started to decrease for these compounds, presumably due to precipitation taking place before successfully reaching the bilayer.

For the alkyl substrates **15g-i**, the largest absolute activities and discrimination between isomers was observed for the hexyl derivative. Interestingly, the log P of **15h** is similar to that of **15a**; perhaps suggesting that the logP and distribution of polarity within the Z-isomer may be optimal for achieving high increases in activity upon isomerisation. Both isomers of octyl derivative **15i** precipitated in the aqueous phase, resulting in poor deliverability for both isomers and thus a poor EC_{50} discrimination. Ethyl derivative **15g** appears to exhibit poor activities for both isomers, perhaps due to formation of stable surfactant-like interactions near the polar headgroups, which may increase the barrier to transport relative to structures incapable of forming these interactions (similar to reports by Davis)[24] (Figure 7C).

The *n* value for the *Z* isomers of the transporters obtained by Hill analysis was typically 1, suggesting a 1:1 binding stoichiometry within the bilayer, consistent with both titration experiments and the molecular mechanics calculations. Conversely, *n* ranged between ~0.6–2.6 for the E-isomers, hinting at a range of competing equilibria taking place depending on the substituent. Hill coefficients below 1 often imply the formation of stable, inactive supramolecular aggregates, which may result in poor deliverability or precipitation of the transporter.[21,25] In general, it is unsurprising that aggregation or higher order complexes are

observed, as both the low polarity environment and two-dimensional confinement within a membrane (which leads to high effective concentrations) enhances intermolecular interactions.[26] However, the high variation in Hill coefficients may also in-part be due to inaccurate data at higher transporter concentrations, where eventually activity is anomalously low due to premature precipitation of the transporter.

A Hill coefficient of ~ 2 in (*E*)**-15a** is indicative of the formation of 2:1 ((*E*)-**15a**$_2$·Cl^-) complex, leading to a steep Hill plot and the requirement for a ternary complex forming for this carrier. This leads to a particularly large difference in activity between both isomers as visually seen in Figure 7A. Although the origin of the large enhancements in activity for the Z isomer were not fully resolved, **15a** was selected for further transport studies

3.2.4 Control experiments

To rule out the possibility of mechanisms other than the postulated $^-OH/Cl^-$ antiport taking place in the HPTS assay, experiments with iso-osmolar replacement of the external anions and cations were conducted with (*Z*)-**15** (Figure 8A-D). The observation of cation independence, and strong anion dependence, confirms that anion transport is the predominant mechanism, consistent with previously reported squaramide anion transporters.[27] Sensitivity towards external anion exchange also provides evidence that changes in HPTS intensity are not a consequence of HPTS release from the vesicles upon addition of the transporters (which would be independent of anion). The absence of activity in the presence of the large hydrophilic gluconate (Glu), where OH^-/Glu^- antiport cannot take place, suggests the transporter predominantly operates via an antiport mechanism.

The HPTS assay was also repeated using dipalmitoylphosphatidylcholine (DPPC) lipids, which adopt a lipid gel phase at 25 °C (Figure 8E-F). At this temperature, no anion transport was observed for **15a**, as diffusion through the membrane in the more ordered gel phase is significantly attenuated. The transport ability of **15a** was restored at 45 °C, above the gel–liquid phase transition temperature (T_c = 41 °C), consistent with the proposed mobile carrier

mechanism.[28] This also rules out alternative formation of a membrane spanning channel structure, whose activity would likely be independent of the lipid phase.

To rule out non-specific vesicle leakage contributing towards the transport kinetic data, vesicles were loaded with the fluorophore calcein, at high concentration (100 mM) at which the fluorescence is collisionally self-quenched (Figure 8G).[29] If the presence of a carrier results an increase in fluorescence (i.e. disappearance of self-quenching), this suggests that

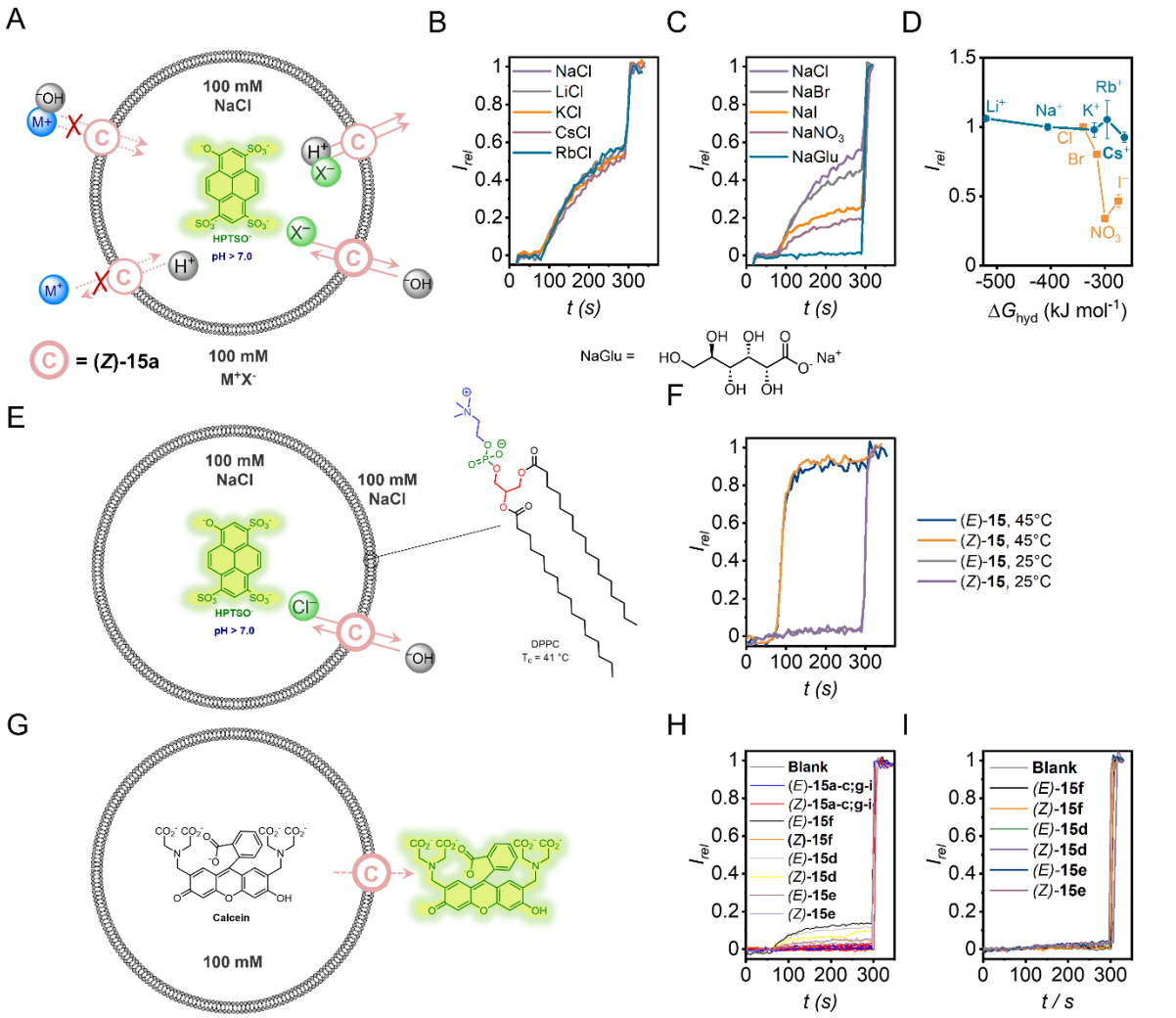


Figure 8. Control experiments. (A) Schematic of possible transport pathways capable of dissipating the applied pH gradient in the HPTS assay. (B-C): Dependence of the activity of (*Z*)-**15** (62.5 nM) on iso-osmolar replacement of extra-vesicular (B) cation and (C) anion. (D) Maximal activity for each ion and its dependence on dehydration energy, normalised relative to the activity for NaCl. (E) Schematic of DPPC assay. (F) Transport data for DPPC assay. (G) Schematic of calcein leakage assay (H) Leakage data at 5 uM concentration. (I) Leakage data at 0.5 uM concentration.

the dye is leaking out of carrier-induced pores, where it is diluted in the external solution. A range of available carriers were tested for their leakage at the maximum concentration used in the HPTS assay (5 µM). In general, no leakage was observed except for **15d-f**, but this significantly diminishes at 500 nM (above the EC_{50} for all compounds; Figure 8H-I). It is possible that the higher order aggregates forming at higher concentrations may also lead to carrier-induced leakage for these compounds (and potentially rationalises the difficulty of accurately determination of Hill coefficients).

3.2.5 In-situ photo-switching experiments within a lipid bilayer membrane

Having established that **15a** was an efficient mobile anion carrier exhibiting a large enhancement in activity upon *E*→*Z* isomerisation, and without triggering vesicle leakage, preliminary in-situ switching studies were conducted using HPTS vesicles and addition of (*E*)-**15a** prior to hydroxide addition (Figure 9A-B)**.** Longer irradiation times with 625 nm light prior to the base pulse resulted in increased transport rates relative to (*E*)-**15a.** At longer irradiation times, transport rates plateaued at ~ half the activity achieved when externally irradiated (*Z*)-**15a** was added (PSS = 77% *Z*)**,** allowing for estimation of the photoconversion within the bilayer by comparing the maximal activity reached of *Z*-**15a** at its PSS. (Figure 9B). UV-vis spectra of vesicles containing **15a** following irradiation with 455 and 625 nm light from LEDs

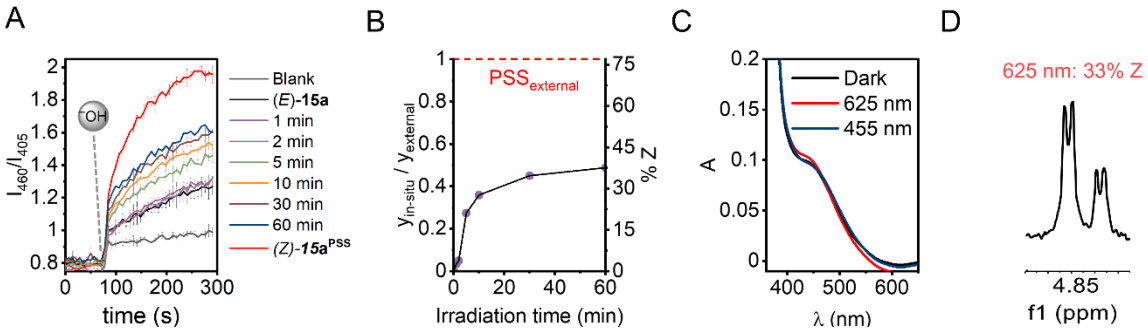


Figure 9. In situ switching experiments. (A) HPTS assay for in-situ (*E*) → (*Z*) switching of (*E*)-**15a** (62.5 nM) with red light for different irradiation times, compared to (*Z*)-**15a** PSS (B) In-situ irradiation time against switching efficiency (PSS) relative to (*Z*)-**15a** PSS (C) Partial UV-vis spectra of 15 mol% **15a** in POPC vesicles following 625 nm red (red line) and 455 nm blue (blue line) irradiation (D) Partial ^{1}H NMR spectrum (3:2 d_6-DMSO/$CDCl_3$) of 15 mol% **15a** in POPC vesicles, following 625 nm irradiation and extraction into $CDCl_3$

confirmed that switching occurred for this system when confined within the bilayer, with distinctive changes in n→π* intensities (Figure 9C). Extraction of these vesicles into deuterated solvent and analysis by ^{1}H NMR revealed a mixture containing ~33% (*Z*)-**15a**, in agreement to the observed transport rates (Figure 9D). The lower PSS could be in-part be due to the lipid bilayer environment resulting in more strongly overlapping *E* and *Z* absorption bands, poorer ability to isomerise within the 2-dimensional bilayer environment, or insufficient light intensity reaching the bilayer due to scattering.

To demonstrate in-situ switching, the commonly employed ion-selective electrode (ISE) chloride-nitrate exchange assay was chosen. [30] This allows for direct measurement of chloride efflux in exchange for nitrate and was chosen to circumvent any issues arising from light from the LEDs used for photoswitching interfering with fluorescence data (Figure 10A). The kinetic profile measures the transport of the rate-limiting chloride anion, rationalised by Hofmeister selectivity arguments. Preliminary studies at 0.5 mol% **15a** relative to lipid showed good 'On/Off' behaviour, where the *E*-isomer was inactive yet significant transport is observed for *(Z)*-**15** (Figure 10B).

Initial experiments revealed that electrode readings were sensitive to light intensity and stirring rates, potentially due to electromagnetic fields interfering with the electrode. Therefore, it was necessary to use a large volume of lipid to ensure that the electrode was not directly exposed to the LED irradiation (Figure 10A), and relatively slow stirring rates. Initial addition of (*E*)-**15a**

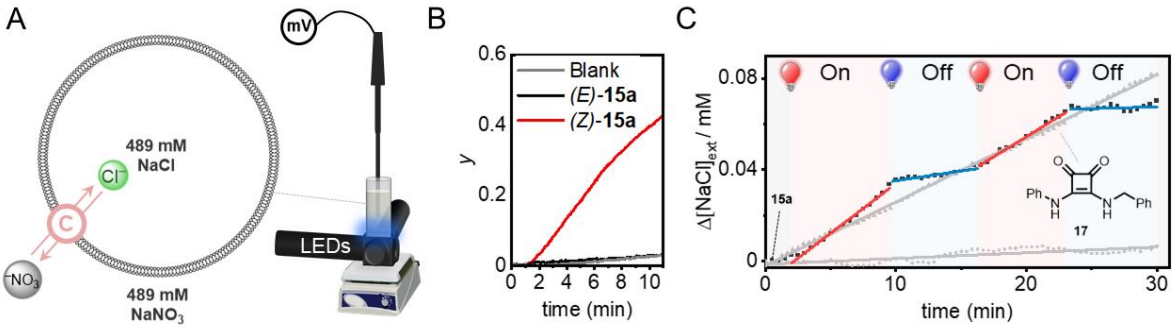


Figure 10. (A) Schematic of the chloride/nitrate exchange ion selective electrode (ISE) assay and experimental set-up. (B) ISE data for (*E*)-**15a** and (*Z*)-**15a** PSS (0.5 mol% relative to lipid). (C): Transport data for **15a** (■), **17** (▲) and DMSO (●) with alternating in situ irradiation

resulted in no observable anion transport (Figure 10C). Constant irradiation with red light (625 nm, ~0.9 W) was used to photo-isomerise the transporter within the membrane, effectively 'switching on' chloride efflux, whilst subsequent irradiation with blue light (455 nm, ~1.1 W) allowed switching 'off' of anion transport. Alternating between red and blue light allowed for reversible on/off switching, thus directly coupling photo-isomerisation with ion transport.

The maximal rate of ion transport following *in situ* photo-isomerisation in the vesicles was ~50% of that achieved by direct addition of (*Z*)-**15a** PSS, consistent with the previous photo-switching studies in membranes (Figures 9A-D). Inactivity under alternating red and blue light irradiation in the absence of **15a** (●); and the lack of switching behaviour for simple squaramide transporter **17** (▲) confirmed the direct role of the azobenzene photoswitch on the reversible transport rates; serving as the first example of fully reversible anion transport using biocompatible wavelengths of light.

3.3 Attempts to improve cooperativity

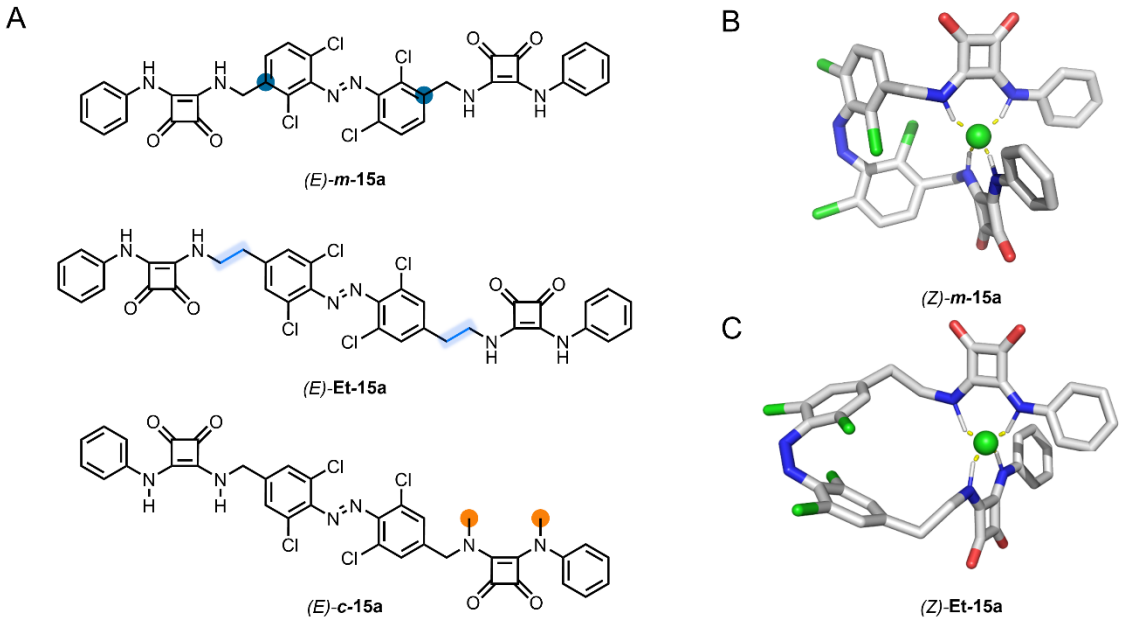


Figure 11. (A) Target Structures (B-C): Calculated structures of *(Z)*-***m*-15a** chloride complex and **Et-15a** chloride complex (MM+ force field, HyperChem).

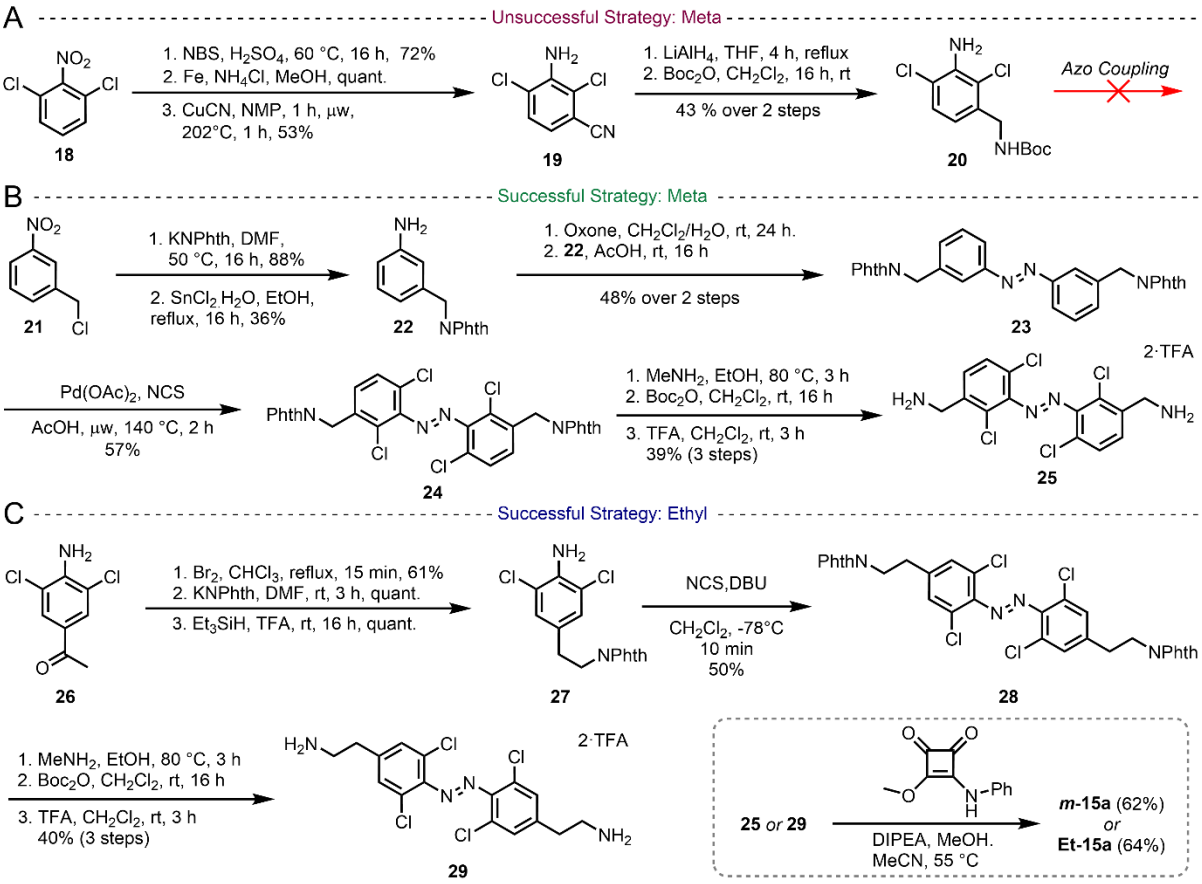
Although **15a** was the first example of reversibly controlling anion transport using a molecular photoswitch, and notably using biocompatible wavelengths of light, there is significant scope

for improvement. In particular, the cooperativity between the receptors was very low (~1.5-fold enhancement upon isomerisation to the Z isomer), whilst (*E*)-**15a** exhibits relatively high background transport activity. To explore the possibility of improving receptors cooperativity, the position of the squaramide linker and spacer length were varied (***m*-15a** and **Et-15a**), and control compound ***c*-15a** were prepared to help dissect the relative importance of cooperativity, aggregation and molecular shape on chloride binding and transport rates in the initial system (Figure 11). The calculated structures *Z* isomers of ***m*-15a** and **Et-15a** both showed promise as scaffolds for cooperatively binding chloride.

3.3.1 Synthesis

Preparation of ***m*-15a** commenced with regioselective bromination of **18**, followed by nitro reduction and cyanation of the aryl bromide to **19** (Scheme 1A). Reduction and subsequent protection afforded **20**, which was subjected to a variety of azo coupling conditions, including NCS/DBU.[31] Unfortunately, this resulted in chlorination of the azobenzene ring, resulting in inseparable mixtures. Therefore, we sought a strategy that commenced with nucleophilic substitution of **21** with potassium phthalimide, followed by nitro reduction to **22** (Scheme 1B). This was converted to **23** using Mills coupling, which was then subjected to C-H activation conditions to afford the $\mathbf{Cl_4}$ derivative **24**.[32] The phthalimide groups were removed using methylamine, but purification of the resulting bis-amine was unsuccessful. The amine was therefore boc-protected, and this derivative which was readily purified by chromatography. The boc groups were quantitively removed with TFA to afford **25**, which was coupled with the phenyl monosquaramide to furnish transporter ***m*-15a**.

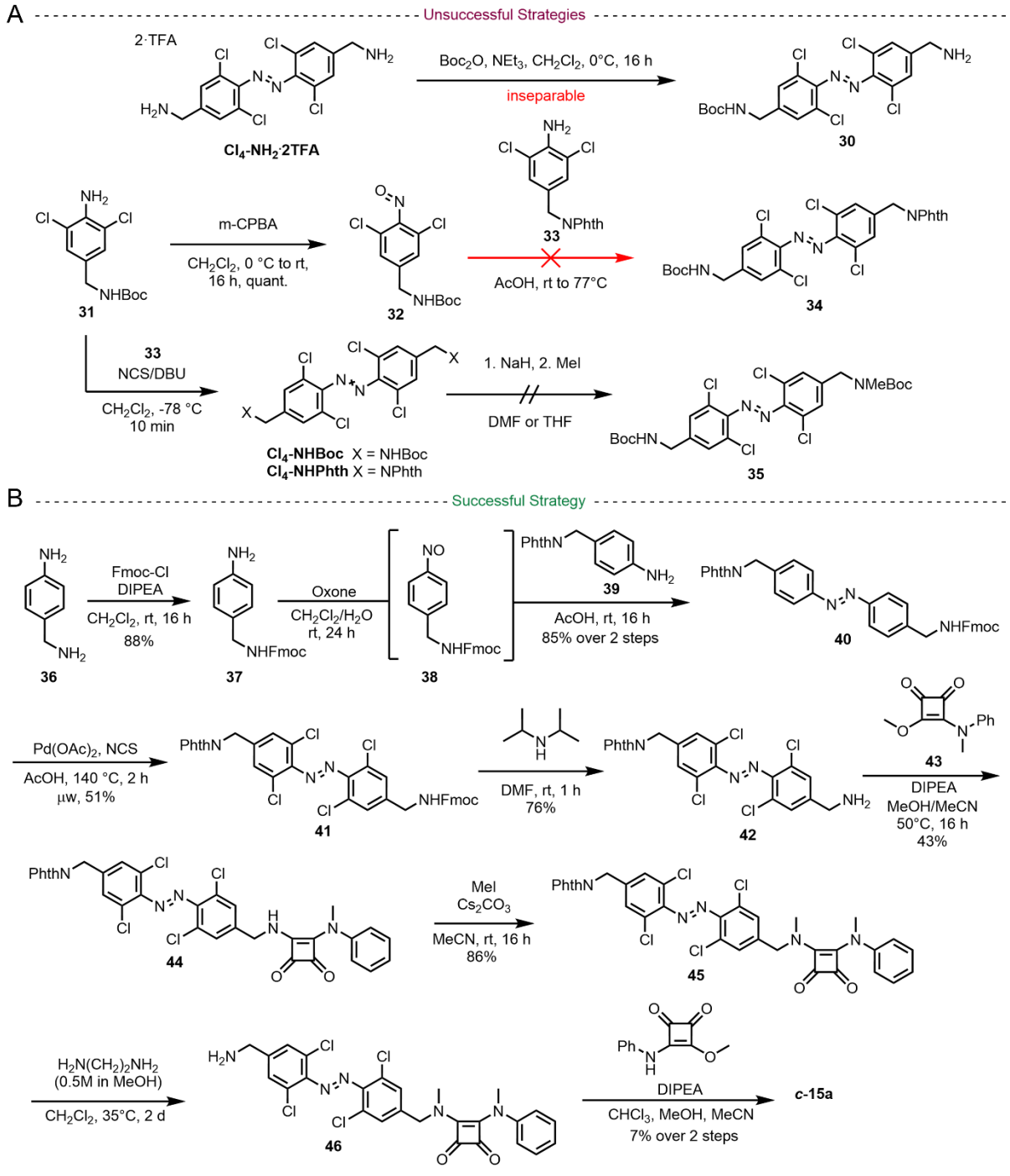
The ethyl spacer derivative was prepared via α bromination from ketone **26**, which was displaced with phthalimide and subsequently reduced to afford the ethyl spaced building block **27** (Scheme 1C). Azo coupling to **28** using NCS and DBU was successful, following by a deprotection-reprotection-deprotection sequence to **29**, similar to the meta derivatives. Finally, squaramide coupling afforded the transporter in good yields.



Scheme 1. Preparation of meta substituted and ethyl-spaced **15a** derivatives.

The initial strategy towards the bis-methylated squaramide derivative ***c*-15a** (Scheme 2A) was by desymmetrising **Cl_4-NH_2.TFA** by mono-boc protection *via* syringe pump, but this afforded inseparable mixtures. Instead, **31** was converted to nitroso **32** and subjected to Mills coupling conditions with **33**, but the sterically hindered diazo bond to generate **34** did not form. Azo coupling with a 1:1 mixture of **31** and **33** in attempts to access **34** in a statistical mixture resulted in homo-coupled products, which may arise from the poor solubility of **34** under these conditions. It was not possible to cleanly isolate **35** by mono-methylation of **Cl_4NHBoc.** Therefore, an unsubstituted azobenzene scaffold containing orthogonal protecting groups was prepared by fmoc protection of **36** to **37**, followed by oxidation to nitroso **38** and Mills coupling with to generate **40** in good yields (Scheme 2B). C-H chlorination of the scaffold was successful affording compound **41**, with both protecting groups surviving the relatively harsh conditions. Selective deprotection to **42** and coupling with methylated squaramide **43** afforded

44, which was methylated under mild conditions to give rise to **45**. Finally, the phthalimide group was removed to **46** and coupled with the phenyl mono-squaramide to generate **c-15a**.



Scheme 2. Preparation of control compound ***c*-15a**.

3.3.2 Anion binding studies and cooperativity

^{1}H NMR titrations with TBACl were conducted in DMSO-d_6 due to solubility constraints (Table 3); analogous to section 3.2.2. The titration data for the **15a** derivatives fit well to a 1:1 chloride binding isotherm, with similar binding constants and behaviour to **15a**. To quantify the chloride binding to a single squaramide derivative; reference compounds **47** and **48** were also prepared to elucidate the binding to one squaramide (K_{ref}) (Figure 12A). Cl^- affinities for **47** and **48** were consistent with the observed (*E*) *K* values for **15a**, ***m*-15a**, **Et-15a** and **c-15a** (Table 1, line 1). Furthermore, both isomers of **c-15a**, in which one of the squaramide binding sites is blocked by methylation, exhibit identical binding constants, further validating the *K* values.

Although the enhancement in binding constant was modest for the new derivatives, the marginal increases upon isomerisation provides evidence that cooperative binding does occur, combined with the data from **c-15a**, **47** and **48.** The intramolecular interaction of the second squaramide binding can be quantified through effective molarity, EM (equation 3.4), which defines the concentration at which intermolecular interactions outcompete the cooperative intramolecular interactions.[33]

$$EM = \frac{{K_{obs}}^Z}{{K_{ref}}^2} \quad (3.4)$$

Table 3. Anion binding and photoswitch properties. 1:1 association constant for chloride binding in d_6-DMSO. K_1^Z takes into account K^E_1 content at the photostationary state. Errors at the 95% confidence limit, averaged over at least two titrations. $K_{ref} = K_{obs}$ (**47**) for compounds **15a**, ***m*-15a**,; $K_{ref} = K_{obs}$ (**48**) for **Et-15a**. PSS determined by ^{1}H NMR integration following irradiation at 625 nm.

	Property	**15a**	***m*-15a**	**Et-15a**	**c-15a**	**47**	**48**
1	K_1^E (M^{-1})	180 ± 4	134 ± 2	102 ± 6	166 ± 18	165 ± 7	130 ± 6
2	K_1^Z (M^{-1})	267 ± 3	183 ± 5	142 ± 2	165 ± 11	—	—
3	K_1^Z / K_1^E	1.5	1.4	1.4	1	—	—
4	EM (mM)	9.81	6.72	8.40	—		
5	K_{ref}EM	1.6	1.1	1.1	—	—	—
6	PSS ratio (*Z* : *E*)	77 : 23	77 : 23	72 : 28	77 : 23	—	—

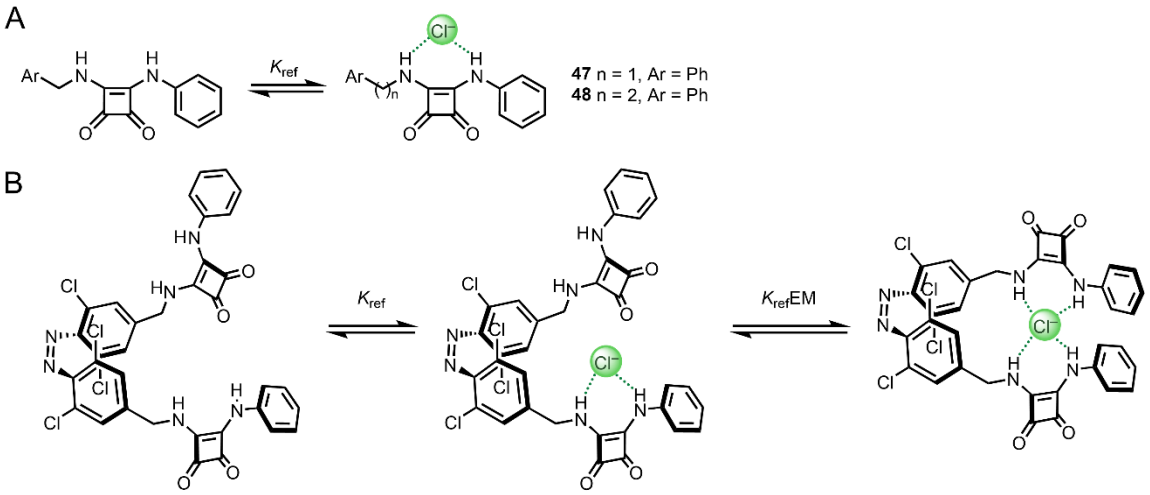


Figure 12. (A) Single site squaramide reference compounds **47** and **48**. K_{ref} is the intermolecular association constant for binding of chloride to one squaramide motif. (B) Schematic of cooperative binding for (*Z*)-**15a** derivatives.

Under the experimental conditions (1 mM receptor), cooperative binding of the second squaramide unit does outcompete intermolecular binding for the **15a** derivatives (EM ~ 10 mM). The product K_{ref}EM quantifies the extent to which the receptor-anion complex containing cooperative intramolecular hydrogen bonds is populated (Table 3, row 5; Figure 12B). The value is relatively low for all receptors, although it is clear that *meta* substitution and ethylene spacing does not improve the cooperativity of the initial system. The generally poor cooperativity for **15a** derivatives may also be a consequence of high desolvation penalties preventing the second binding event K_{ref}EM in this highly competitive solvent.

3.3.3 Ion transport studies

The new compounds were evaluated for their ion transport activities using the HPTS assay. Changing from *para* to *meta* substitution lead to a significant increase in transport rates for both isomers, approaching near picomolar activity for (*Z*)-**m-15a** (Table 4, Figure 13), but only a modest enhancement in activity for the Z isomer was observed (3.3-fold). This is greater than the 1.4-fold enhancement in binding constant, but it should be noted that ion transport is a kinetic effect (dependent not only on binding affinity, but also mobility and ion encapsulation). It is plausible that the modest cooperative binding enhances charge delocalisation of the anion

across more hydrogen bonding motifs, which 'shields' the charge from the apolar membrane more effectively, hence lowering the activation barrier for anion transport. Despite exhibiting an EM of 8 mM, the ethyl-spaced derivative does not appear to exhibit any difference in activity upon isomerisation. This is unexpected, as a bulk concentration of 8 mM equates to an effective concentration of ~ 200 nM when taking into account the confined volume of the vesicle membrane.[34] Thus, below this concentration, we expect cooperativity to take place, which the EC_{50} of both isomers are well below. This suggests that unlike in DMSO solution, the second squaramide may not be involved in binding to the anion within the bilayer.

Table 4. Transport data for **15a** derivatives

Entry	Property	**15a**	***m*-15a**	**Et-15a**	**c-15a**
1	EC_{50}^{E} (nM)[a]	181 ± 16	5.2±0.3	11.2±1.1	138±15
2	EC_{50}^{E} (mol%)[a]	0.58	0.016	0.036	0.44
3	$EC_{50}^{Z,PSS}$ (nM)[a,b]	22 ± 2	1.5±0.1	11.7±1.3	123±18
4	$EC_{50}^{Z,PSS}$ (mol%)[a,b]	0.071	0.005	0.038	0.39
5	n^{E} [c]	2.6±0.5	1.1±0.1	1.0±0.1	1.2± 0.1
6	n^{Z} [c]	1.1±0.1	1.4±0.1	1.2±0.2	1.3± 0.3
7	EC_{50}^{E}/EC_{50}^{Z}	8.2±1.0	3.3±0.3	1.0±0.1	1.2±0.2

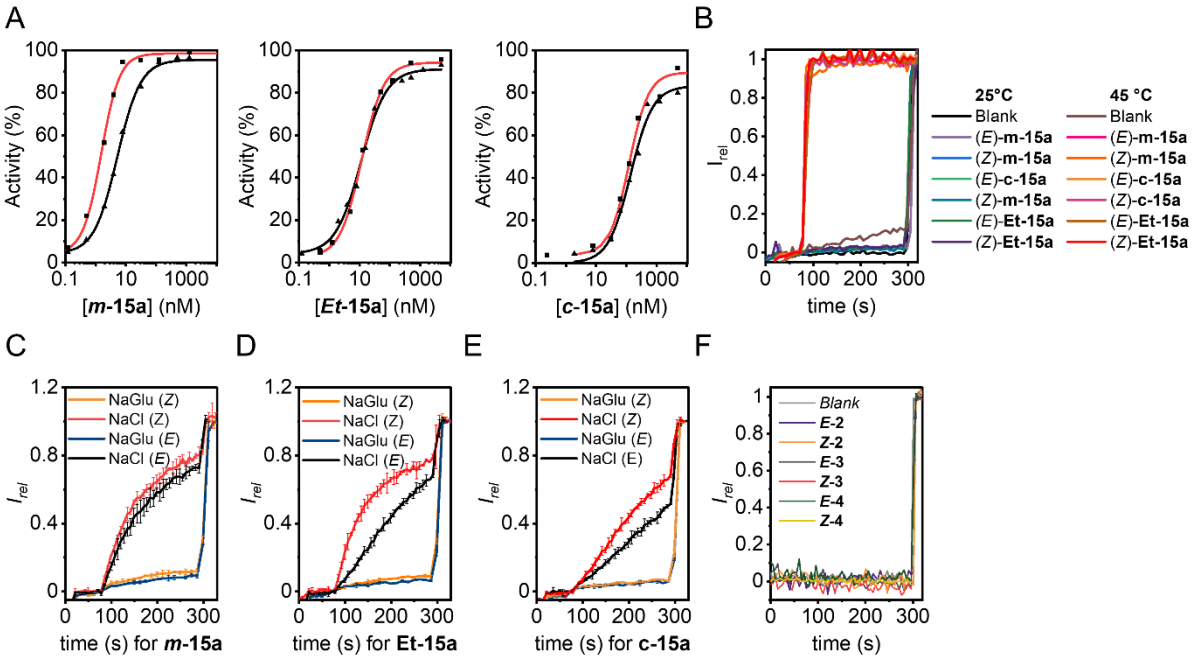


Figure 13. (A) Stacked Hill plots for modified carriers. (■): (*Z*)-isomers, (▲): (*E*)-isomers. lines: fitted data (B) Transport data for DPPC assay (C-E): Dependence of the activity of transporters using 100 mM NaGlu vs 100 mM NaCl near the EC_{50} of carrier (C): (*E*)-***m*-15a** [8 nM] and (Z)-***m*-15a** [4 nM] (D): (*E*)-**Et-15a** [50 nM] and (Z)-**Et-15a** [31 nM] (E): **c-15a** [250 nM] (F) Calcein leakage assay data

Control experiments in DPPC LUVs (Figure 8E) confirmed that a mobile carrier mechanism was operating (Figure 13B), whilst lack of activity when the assays were repeated with iso-osmolar replacement of chloride for hydrophilic gluconate confirmed that anion transport was the dominant process (Figure 13C-E). No significant calcein leakage was observed, suggesting negligible membrane disruption for the studied derivatives (Figure 13F).

It appears that the enhancement in transport is optimal for the initial system **15a**. This may in-part be due to improved cooperativity relative to the meta and ethyl-spaced derivatives, and improved shielding of the anion and bilayer mobility in the more bowl-shaped Z-isomer. Given the relatively diminished activity of (*E*)-**15a** compared to (*E*)-**m-15a,** (*E*)-**Et-15a** and (*E*)-**c-15a,** it is also likely that there are other factors at play. In particular, a modest enhancement in activity for (*E*)-**c-15a** hints at the possibility of (*E*)-**15a** forming higher-order aggregates, which suppresses the transport activity of the E-isomer, whilst the methyl-capped derivatives (*E*)-**c-15a** is less capable of forming these intermolecular hydrogen bonded aggregates.

Chemical shift perturbations of the squaramide NH protons in NMR dilution experiments in DMSO suggest that there is minimal dimerization in this non-polar media, but it was unfortunately not possible to repeat these experiments in less competitive conditions due to poor solubility (Figure 14A). To understand aggregation within the less polar bilayer, molecular dynamics calculations were Z. Bo and F. Duarte, where the stability of (*E*)-**15a** dimers were evaluated by monitoring the average distance between the monomers (Figure 14B).

These experiments revealed that in DMSO, dimers of (*E*)-**15a** dissociated after 10 ns, consistent with the lack of aggregation observed in the NMR dilution experiments. [34] When (*E*)-**15a** dimers are placed within the centre of a POPC membrane, the dimeric species moves to the membrane interface to form lipid head-group interactions, which may in-part outcompete anion binding and suppress transport activity, and contribute to the high EC_{50} enhancements. The notion of a dimeric species binding anions is consistent with the unique Hill coefficient of 2 being observed in the assays, which results in the steeper dose-response curve for (*E*)-**15a.**

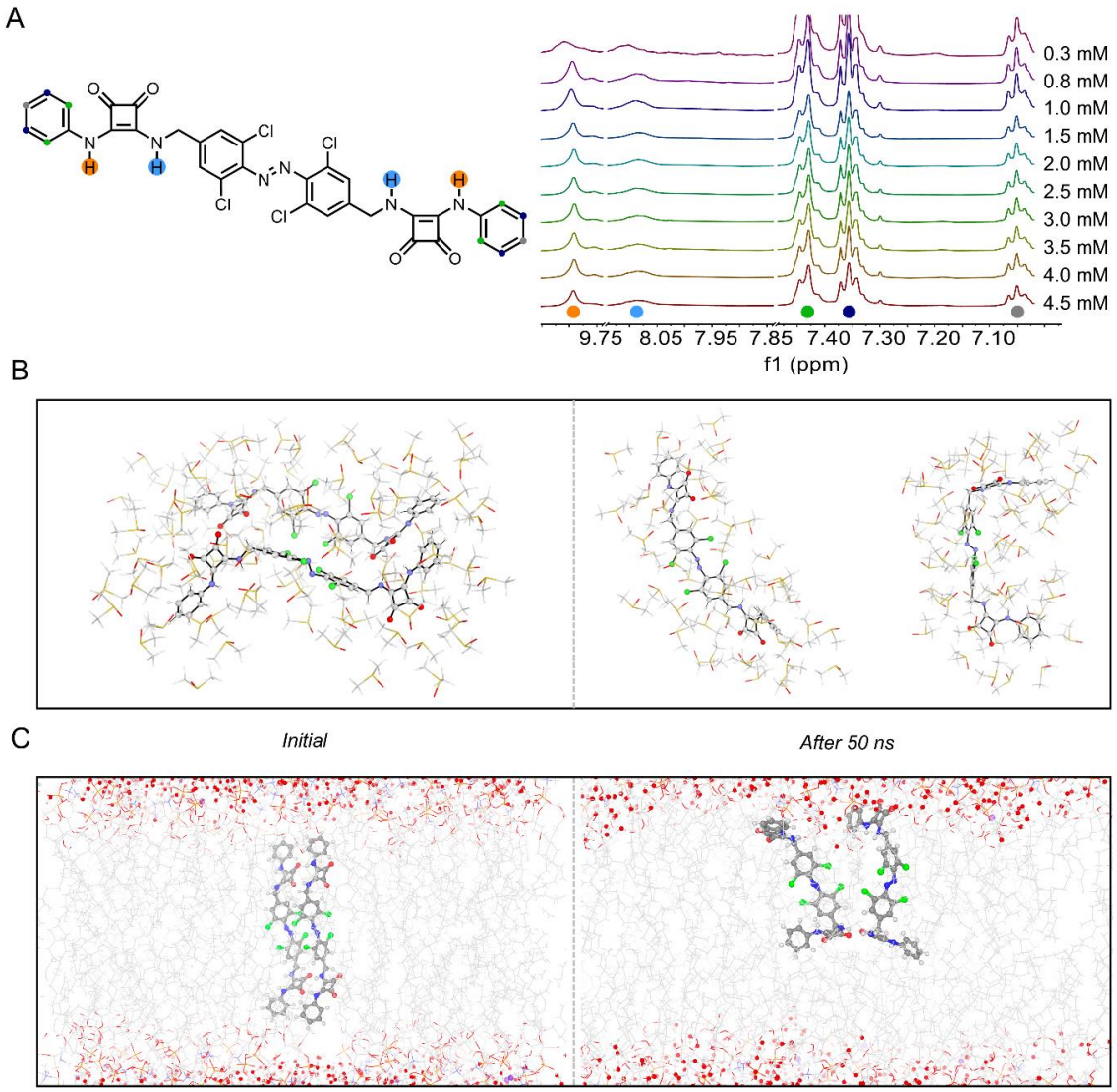


Figure 14. (A) ^{1}H NMR dilution experiments for (*E*)-15a (B-C) Snapshots of explicitly solvated MD simulation in DMSO (B) and a POPC membrane (C). Calculations performed by Z. Bo. [34]

3.4 Chapter conclusions

Disrupting ion homeostasis in off-target cells may lead to severe side-effects and potentially fatal consequences, so it is much more attractive to gain precise control of the flow of ions across a lipid bilayer with high spatiotemporal control in a therapeutic context. In this chapter, we report the first example of a fully reversible photoswitchable anion transporter **15a** using biocompatible wavelengths of light, where the phenyl squaramide substituent exhibited the most promising on/off switching behaviour. We confirmed that chloride/hydroxide antiport was the predominant transport mechanism under the HPTS assay conditions; proceeding *via* a mobile carrier mechanism, and no significant leakage of vesicles was observed. 'On/off'

switching of ion transport in lipid bilayer vesicles was achieved using an ion-selective electrode mounted with LEDs.

Attempts to improve the inherent cooperativity between both squaramides resulted in systems that had poorer enhancements in chloride binding and transport rates upon isomerisation. However, combined with control compounds, this data assisted with the elucidation of the nature of anion binding and extent of cooperativity in the original system. The transport data and MD simulations suggest that the anomalously high discrimination between the (*E*) and (*Z*) states in **15a** originates from (*E*)-1**5a** dimerization within the membrane resulting in diminishing activities, which leads to improved 'On/Off' behaviour in the system due to a steeper dose-responsive curve and the necessity for forming a ternary 2:1 complex with chloride. The less extended bowl-like shape, higher anion encapsulation, and distribution of anion charge due to cooperative anion binding between both squaramide derivatives may also be contributing factors towards good (*Z*)-isomer activity.

3.5 References

[1] J. T. Davis, P. A. Gale and R. Quesada, *Chem. Soc. Rev.*, 2020, **49**, 6056–6086.
[2] J.-B. Kim, *Korean J. Pediatr.*, 2014, **57**, 1–18.
[3] R. S. Hector and M. S. Gin, *Supramol. Chem.*, 2005, **17**, 129–134.
[4] L. E. Bickerton, T. G. Johnson, A. Kerckhoffs and M. J. Langton, *Chem. Sci.*, 2021, **12**, 11252–11274.
[5] A. Docker, T. G. Johnson, H. Kuhn, Z. Zhang and M. J. Langton, *J. Am. Chem. Soc.*, , DOI:10.1021/jacs.2c12892.
[6] M. Fares, X. Wu, D. Ramesh, W. Lewis, P. A. Keller, E. N. W. Howe, R. Pérez-Tomás and P. A. Gale, *Angew. Chem.*, 2020, **132**, 17767–17774.
[7] G. Park and F. P. Gabbaï, *Chem. Sci.*, 2020, **11**, 10107–10112.
[8] N. Busschaert, R. B. P. Elmes, D. D. Czech, X. Wu, I. L. Kirby, E. M. Peck, K. D. Hendzel, S. K. Shaw, B. Chan, B. D. Smith, K. A. Jolliffe and P. A. Gale, *Chem. Sci.*, 2014, **5**, 3617–3626.
[9] X. Wu, J. R. Small, A. Cataldo, A. M. Withecombe, P. Turner and P. A. Gale, *Angew. Chem. Int. Ed.*, 2019, **131**, 15286–15291.
[10] S. B. Salunke, J. A. Malla and P. Talukdar, *Angew. Chem. Int. Ed.*, 2019, **58**, 5354–5358.
[11] S. J. Wezenberg, L.-J. Chen, J. E. Bos, B. L. Feringa, E. N. W. Howe, X. Wu, M. A. Siegler and P. A. Gale, *J. Am. Chem. Soc.*, 2022, **144**, 331–338.
[12] Y. R. Choi, G. C. Kim, H.-G. Jeon, J. Park, W. Namkung and K.-S. Jeong, *Chem. Commun.*, 2014, **50**, 15305–15308.
[13] M. Ahmad, S. Metya, A. Das and P. Talukdar, *Chem. Eur. J.,* 2020, **26**, 8703–8708.
[14] S. J. Edwards, I. Marques, C. M. Dias, R. A. Tromans, N. R. Lees, V. Félix, H. Valkenier and A. P. Davis, *Chem. Eur. J.*, 2016, **22**, 2004–2011.
[15] K. Dąbrowa, P. Niedbała and J. Jurczak, *Chem. Commun.*, 2014, **50**, 15748–15751.

[16] P. Thordarson, *Chem. Soc. Rev.*, 2011, **40**, 1305–1323.
[17] P. Kuzmic, *Anal. Biochem.*, 1996, **237**, 260–273.
[18] Corwin. Hansch, A. Leo and R. W. Taft, *Chem. Rev.*, 1991, **91**, 165–195.
[19] X. Bao, X. Wu, S. N. Berry, E. N. W. Howe, Y.-T. Chang and P. A. Gale, *Chem. Commun.*, 2018, **54**, 1363–1366.
[20] N. Sakai and S. Matile, *J. Phys. Org. Chem.*, 2006, **19**, 452–460.
[21] S. Matile, N. Sakai and A. Hennig, in *Supramolecular Chemistry*, John Wiley & Sons, Ltd, 2012.
[22] W. F. Paxton, D. Price and N. J. Richardson, *Soft Matter*, 2013, **9**, 11295–11302.
[23] I. V. Tetko, J. Gasteiger, R. Todeschini, A. Mauri, D. Livingstone, P. Ertl, V. A. Palyulin, E. V. Radchenko, N. S. Zefirov, A. S. Makarenko, V. Y. Tanchuk and V. V. Prokopenko, *J. Comput. Aided. Mol. Des.*, 2005, **19**, 453–463.
[24] H. Valkenier, C. J. E. Haynes, J. Herniman, P. A. Gale and A. P. Davis, *Chem. Sci.*, 2014, **5**, 1128.
[25] S. Litvinchuk, G. Bollot, J. Mareda, A. Som, D. Ronan, M. R. Shah, P. Perrottet, N. Sakai and S. Matile, *J. Am. Chem. Soc.*, 2004, **126**, 10067–10075.
[26] E. L. Doyle, C. A. Hunter, H. C. Phillips, S. J. Webb and N. H. Williams, *J. Am. Chem. Soc.*, 2003, **125**, 4593–4599.
[27] N. Busschaert, I. L. Kirby, S. Young, S. J. Coles, P. N. Horton, M. E. Light and P. A. Gale, *Angew. Chem. Int. Ed.*, 2012, **124**, 4502–4506.
[28] D. Smith, D. Sheppard, A. Davis, *Chem. Soc. Rev.,* 2007, **36**, 348-357
[29] H. Patel, C. Tscheka and H. Heerklotz, *Soft Matter*, 2009, **5**, 2849–2851.
[30] L. A. Jowett and P. A. Gale, *Supramol. Chem.*, 2019, **31**, 297–312.
[31] A. Antoine John and Q. Lin, *J. Org. Chem.*, 2017, **82**, 9873–9876.
[32] D. B. Konrad, J. A. Frank and D. Trauner, *Chem. Eur. J.*, 2016, **22**, 4364–4368.
[33] C. A. Hunter and H. L. Anderson, *Angew. Chem. Int. Ed.,* 2009, **48**, 7488–7499.
[34] A. Kerckhoffs, Z. Bo, S. E. Penty, F. Duarte and M. J. Langton, *Org. Biomol. Chem.*, 2021, **19**, 9058–9067.

Chapter 4 – Modifications to the receptor

4.1 Attempts to improve the receptor

With a selection of readily functionalisable azobenzene scaffolds and photoswitchable ion transporters in hand, we sought out to modify the nature of the receptor to potentially improve the transport enhancements or introduce further control elements such as pH switchability. Furthermore, we also aimed to explore alternative binding motifs such as crown ethers for alkali metals, and functionalities capable of catalysis to control the rates of chemical reactions in response to light to broaden the scope of these functionalised photoswitches.

4.1.1. Thiosquaramides

Thiosquaramides have recently emerged as pH-switchable chloride receptors, where transport can be switched off at pH > 7 by deprotonation, and switched on at pH < 7 by protonation, leading to potential selectivity towards more acidic environments such as lung epithelia and extracellular cancer cells.[1] When incorporated into our parent photo-switchable transporters, we anticipated that this may lead to a system where dual control of transport using both pH and light is possible, where transport is only switched on at low pH and after irradiation with red light (Figure 1) – allowing higher control of anion transport and the possibility of a molecular 'logic gate' which is only 'on' when exposed to red light and the correct pH.

The initial approach was via the bench-stable cyclopentyl dithiosquarate **3** developed by Rawal.[2] Cyclopentanol and squaric acid were condensed to afford **2**, which was converted into **3** using Lawesson's reagent. Compound **3** was treated with one equivalent of aniline to provide **4**, which was relatively unstable on silica. Treatment of this with freebase azobenzene **Cl_4-NH_2** (chapter 2) lead to an insoluble and impure precipitate, perhaps containing unreactive zwitterion **6**. Therefore, **Cl_4-NH_2** was directly treated with two equivalents of **3** to prepare **7.** The NMR of the product exhibited complex rotameric signals from the azobenzene and cyclopentyl groups. After addition of aniline, a mixture of compounds precipitated with a complex NMR that perhaps contained **1**, but the target mass was not observed by MS. Direct

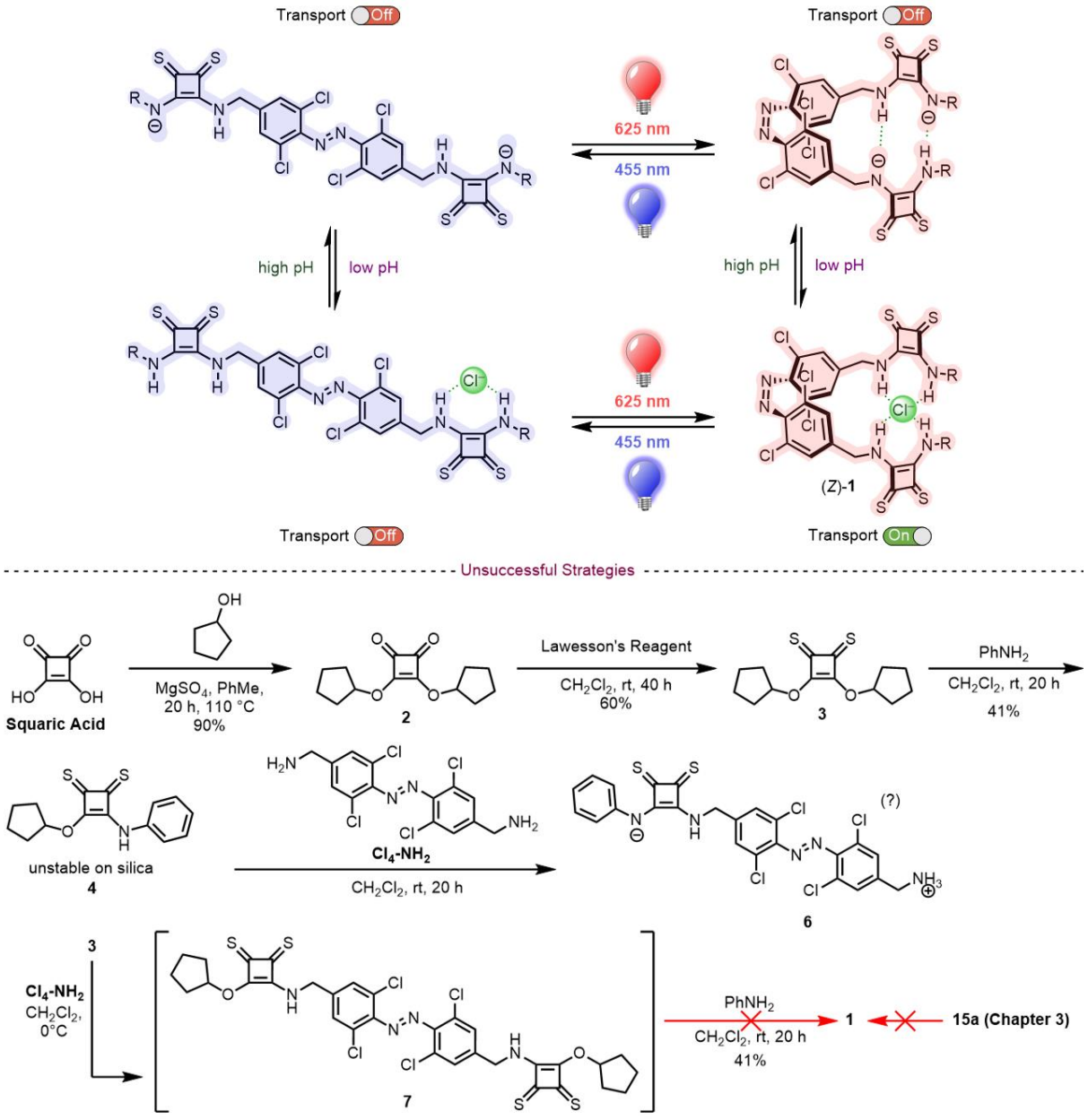


Figure 1. Proposed dual pH/light controllable thiosquaramide **1** and efforts to synthesise **1**.

treatment of (*E*)-**15a** with Lawesson's reagent to afford **1** was not possible due to solubility constraints requiring the use the DMSO and DMF to solubilise **1**, both of which react with Lawesson's reagent. We therefore abandoned the synthesis of **1**.

4.1.2 Thioureas

Hill plots from Chapter 3 support the notion that less acidic receptors performed relatively well in terms of EC_{50} enhancement, presumably because the *E* isomer transports poorly without

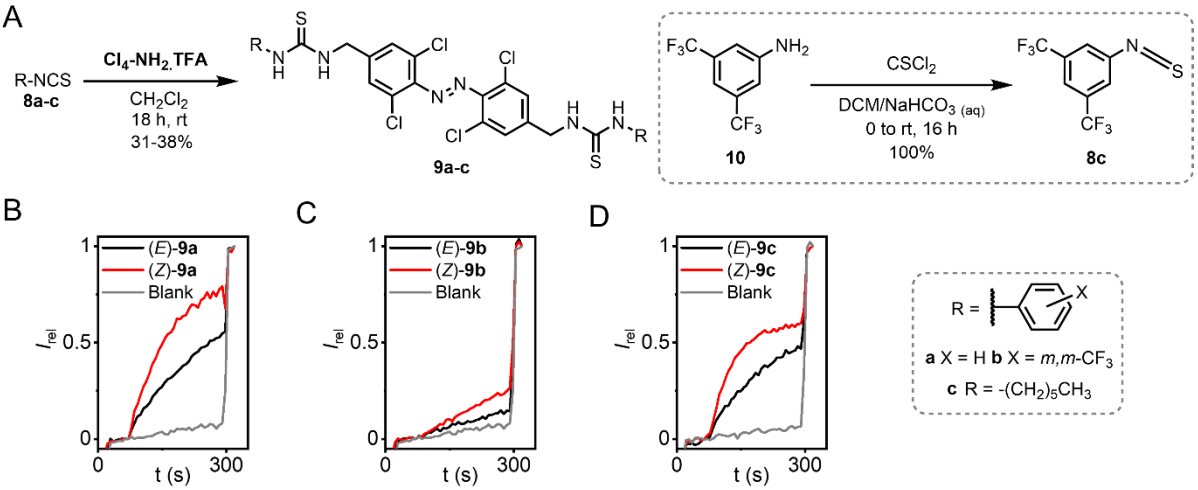


Figure 2. (A) Synthesis of thiourea derivatives (B-C): Preliminary transport data with HPTS assay (B) 625 nM **s** (C) 625 nM **9b** (D) 125 nM **9c**

cooperative assistance from the second receptor. Therefore, we envisaged functionalising the scaffold with thiourea groups, which bind anions more weakly (Figure 2A)[3]. Diamine **Cl_4-NH_2·TFA** (chapter 2) was functionalised with isothiocyanates **8a-c** to provide transporters **9a-c**. **8c** was prepared in one step from aniline **10**. Preliminary HPTS assays revealed that, whilst the Z isomer of each derivatives was more active than the E isomer, the improvement in transport rates between isomers was never as large as observed for the squaramide counterparts, with the largest differences in activity at a given concentration provided in Figure B-D. Therefore, further studies were abandoned.

4.1.3 Iodotriazoles

Iodotriazoles have emerged as potent anion transporters capable of selectively binding and transporting halide anions across lipid bilayers *via* halogen bonding interactions.[4] Simple monodentate iodotriazole carriers have been found to transport anions with multiple carriers per anion, whereas bidentate derivatives with appropriate geometries can form 1:1 complexes with halides.[5] Thus, we reasoned that appendage of an iodotriazole unit to the azobenzene scaffold in **XB-Azo** would allow strong enhancements in binding and transport of anions due to the formation of bidentate interactions in the (*Z*)-isomer (Figure 3A). Molecular mechanics calculations supported the proposed 1:1 binding geometry (Figure 3B).

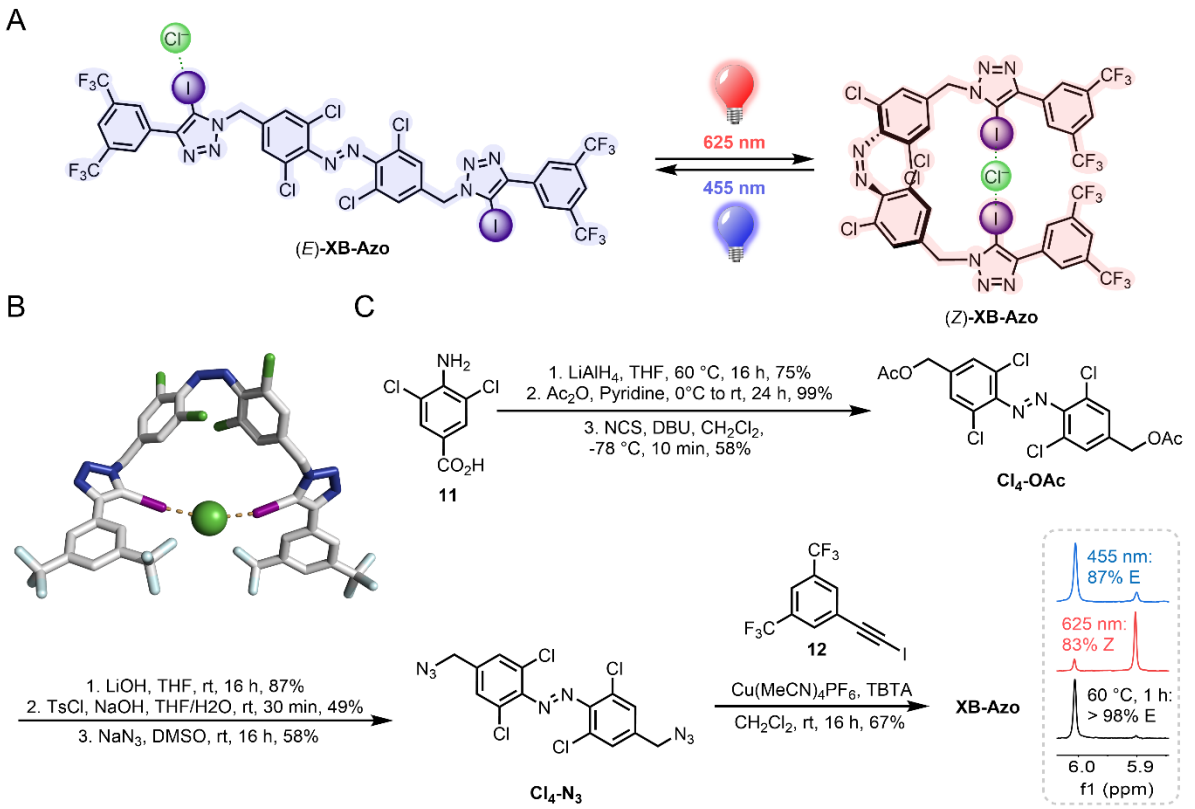


Figure 3. (A) Upon isomerisation, **XB-Azo** is expected to exhibit improved chloride binding and transport rates due to the formation of bidentate halogen bonding interactions. (B) Calculated structure of *(Z)*-**XB-Azo** chloride complex (MM+ force field, HyperChem). (C) Synthesis of **XB-Azo** and partial NMR spectra with PSS in acetone-d_6

To prepare the target compound, acid **11** was reduced to the corresponding alcohol, which was acetyl protected and azo-coupled to afford **Cl_4-OAc**. The acetyl group was removed and the resulting alcohol was tosylated and displaced with sodium azide to provide **Cl_4-N_3**. The azide was subjected to Cu-catalyzed 'click' conditions with iodoalkyne **12** to afford the receptor **XB-Azo** in good yields (Figure 3C). The compound exhibited a high PSS in both switching directions, showing high promise as a photoswitchable anion transporter (Figure 3C).

Preliminary transport studies were conducted using HPTS containing POPC vesicles, analogously to chapter 3. Unfortunately, the transport rates were extremely low, even at high transporter loadings (Figure 4A; 5 mol% i.e. 6 µM, at which squaramide derivatives usually reach 100% activity within seconds). We reasoned this may be a consequence of excessively high lipophilicity, resulting in poor deliverability to the membrane. However, pre-incorporation

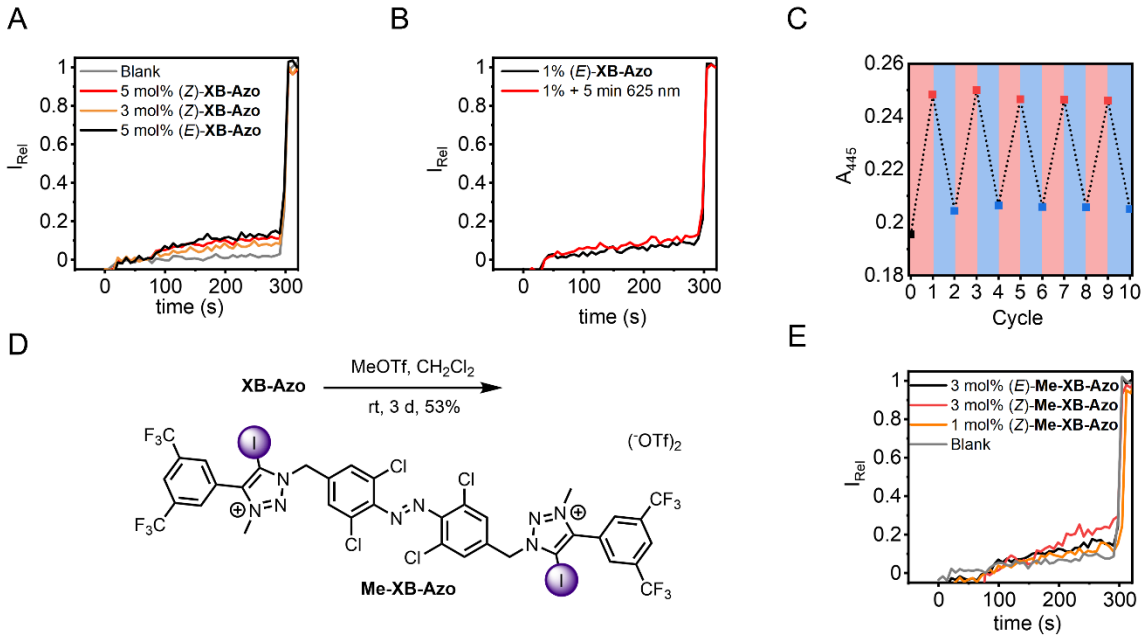


Figure 4. (A-B): HPTS assay kinetic runs for **XB-Azo** derivatives: (A) External Addition (B) Preincorporated (C) Reversible switching of **XB-Azo** in acetone (D) Preparation of methylated derivative **Me-XB-Azo** (E) HPTS assay for **Me-XB-Azo**

of the receptor into the bilayer during vesicle preparation, which should overcome these deliverability issues, still resulted in poor transport rates in the dark or after exposure to 625 nm light (Figure 4B). The photoswitching was fully reversible and could be repeated without detectable fatigue IN solution (Figure 4C). Therefore, the poor transport rates may be due to weak binding affinity to anions, or low mobility within the bilayer due to the relatively large size and molecular weight of **XB-Azo**.

To improve the binding affinity, we prepared methylated cationic analogue **Me-XB-Azo,** by methylating **XB-Azo** with methyl triflate. This derivative should exhibit a more strongly polarised σ-hole interaction,[6] however, poor transport rates were still observed, albeit slightly higher than the parent compound (Figure 4D-E). These results suggest that these structures are perhaps too large or immobile within the bilayer to be efficient anion transporters.

4.2 Halogen bonding-mediated photoswitchable anion catalysis

In addition to their importance in ionophores, halogen bonding motifs are also emerging as important interactions in organocatalysis.[6] We therefore reasoned that **Me-XB-Azo** could be

employed as a photoswitchable halogen bonding catalyst; allowing control of relative reaction rates using light.

4.2.1 Background

As detailed in chapter 1, halogen bonds (XBs) are the Lewis acidic attractive interaction between the electrophilic region of a halogen atom and a Lewis base, and is the functional equivalent of a hydrogen bond donor, although XBs are more hydrophobic in nature, more polarisable, involve larger contacts and are more strongly directional.[7] Recently, this polarising interaction has been exploited to activate a variety of electrophiles. This avoids the use of toxic and air-sensitive transition metals, and may open up novel and unexplored reactivities.

Although iodine has been known as an efficient catalyst for numerous reactions for over a century, the underlying reasons have only recently been attributed to halogen bonding catalysis. For example, 15% I_2 in the presence of **13** and **14** can be used to catalyse challenging hetero Diels-Alder reactions to afford **15** via a formal halogen bonding interaction (Figure 5).[8] The first report of an organic halogen bonding catalyst was used to catalyse the reduction of quinoline **16** using Hanzsch ester and simple perfluoroalkyl iodides.[9] This lead to selective reduction of the pyridine ring to **17**.

Iodotriazolium-based receptors **18** have also been shown to catalyse Friedel-crafts reactions by bromide abstraction of **19** to afford **20**.[10] The authors observed that at least monocationic species were necessary to catalyse these reactions efficiently; having the best balance of halogen bonding strength and solubility in organic media. However, as the abstracted halide is not consumed in this reaction, it is necessary to use 1 equivalent of the halogen bonding catalyst. These issues can be overcome if the nucleophile quenches the liberated halide, as Huber demonstrated with silane **24**, allowing the use of catalyst loadings of **22** as low as 0.5 mol% in the presence of **23**.

Although halogen bonding is often weak towards oxygen based Lewis bases,[11] numerous examples have been shown to catalyse these reactions. For example, catalyst **22** was successfully employed in low loadings to catalyse a Mukaiyama aldol reaction between **26** and **27** to afford **28**.[12] Similarly, bidentate hypervalent iodine catalyst **29** was capable of activating Michael acceptor **30** to react with **31** in a benchmark conjugate addition reaction.[13]

To date, however, there are no reports of photoswitchable halogen bonding catalysts, and only one example of a photoswitchable halogen bonding receptor, although this example was utilized for anion-induced emissive aggregation.[14] Therefore, **XB-Azo** and **Me-XB-Azo** serve as promising scaffolds for exploring this novel concept.

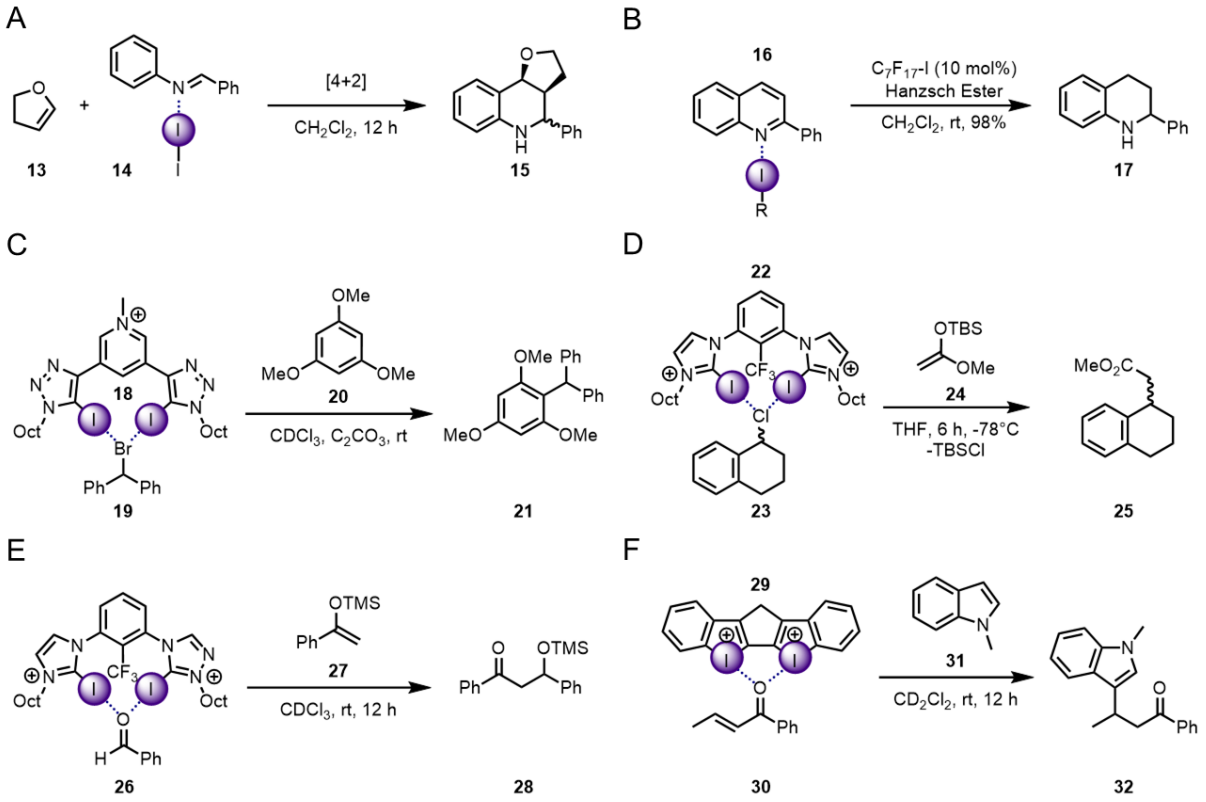


Figure 5. Selected examples of halogen bonding catalysis (A) Activation using iodine (15%) for hetero Diels-Alder reaction (B) Quinoline reduction (C) Halide abstraction (D) Catalytic halide abstraction (0.5 mol% **22**) (E) Mukaiyama aldol reactions (F) Michael addition

4.2.2 Anion binding properties of photoswitchable catalyst XB-Azo

The binding properties of the **XB-Azo** scaffolds were investigated by ^{1}H NMR titrations in acetone-d_6 using a variety of anions as TBA salts (Table 1), by fitting to a 1:1 binding model (analogously to chapter 3). To elucidate the binding constant of a single triazole site, it is necessary to divide the binding constant K_1 by the appropriate statistical factor, i.e. 2, due to the degeneracy of the ditopic binding site (Figure 6A).[15] This arises because there are 2 equivalent ways of initially binding chloride, but only one site to which the anion can be released back to form the free receptor.

The chloride binding affinity for a single 3,5-bistrifluoromethyl aryl-iodotriazole **33** (where the pendant azobenzene group is substituted for n-hexyl; Figure 6B) is K_{ref} = 197 ± 14 M^{-1} in acetone.[4] Dividing the observed binding constant K_1^E by a statistical factor of two provides a binding constant for a single iodotriazole unit = 296 M^{-1}. This suggests that the neighbouring azobenzene leads to a modest enhancement in binding relative to the hexyl derivative, further evidenced by perturbations in chemical shift for the aromatic azobenzene signals upon increasing equivalents of chloride, potentially via anion-π or anion C-H interactions. Since the triazoles in *(E)*-**XB-Azo** are independently involved binding, association of the second 2:1 complex follows $K_2^E = K_1^E/4$ by accounting for the statistical factors.[16]

Binding to the halides decreased in the order $Cl^- > Br^- > I^-$, in line with more charge-dense anions binding more strongly by electrostatic arguments. No binding was observed for oxo-based anions nitrate and sulfate, consistent with previous observations for halogen bonding receptors inherently preferring 'softer' donor atoms.[11]

Table 3. Anion binding of **XB-Azo**. K_1^Z takes into account K_1^E at the PSS. Errors at 95% confidence limit, averaged over at least two titrations. [a] X^- added as the TBA salt in d_6-acetone, 298K. [b] No binding

Anion[a]	$K_{1,}^E$ / M^{-1}	$K_{2,}^E$ / M^{-1}	K^Z / M^{-1}	K^Z/K^E	EM / mM	K_{ref}EM
Cl^-	593±70	148	31607±52	53	360	107
Br^-	311±2	78	4616±45	15	188	30
I^-	108±5	27	677±3	7	232	13
NO_3^-	NB[b]	NB[b]	67±3	-	-	-
HSO_4^-	NB[b]	NB[b]	62±9	-	-	-

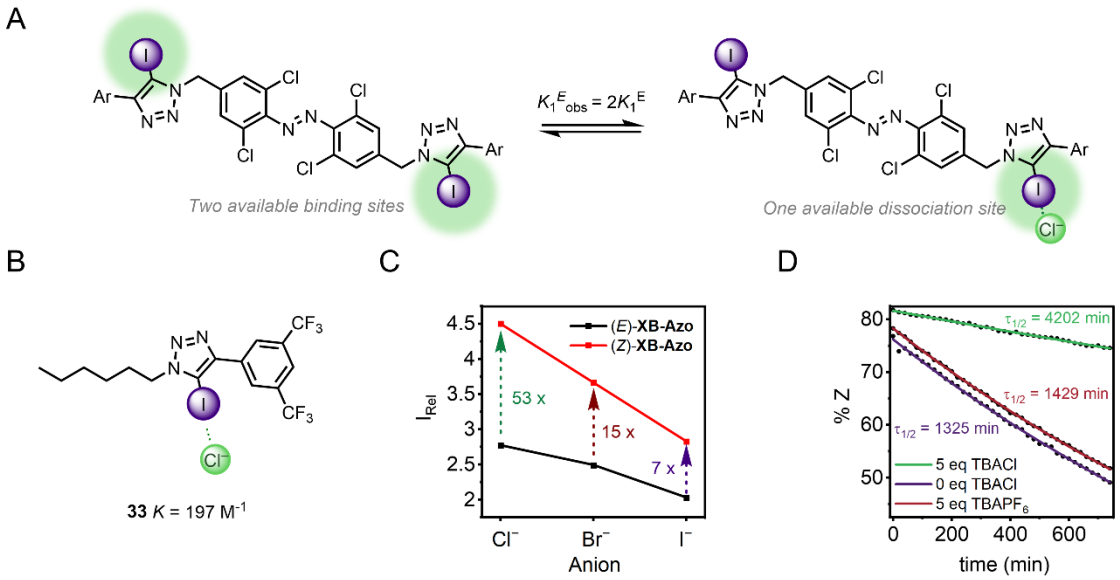


Figure 6. (A) Schematic diagram depicting the origin of the statistical factor of 2 (B) Binding of simple iodotriazole (C) Summary of binding affinity (D) Dependence of half-life of (*Z*)-**XB-Azo** in the presence or of absence of ions (Acetone, 45°C).

Compared to the anion binding studies in Chapter, 3, significant enhancements were observed upon isomerisation, with up to 53-fold increases in binding strength for chloride; the largest observed for switchable receptors incorporating halogen bonding interactions,[14] and among the highest across all known switchable anion receptors (Figure 6C).[17] The effective molarities EM and K_{ref}EM were also elucidated analogously to chapter 3. The large observed values provide evidence for very strong bidentate binding with chelate cooperativity in the Z isomer. The largest enhancements were found for the smaller halides, suggesting a complimentary cavity size for the smaller chloride anion, although this effect may also be electrostatically driven.

The thermal half-life of (*Z*)-XB-Azo was measured in the presence and absence of chloride. A 3-fold enhancement in (*Z*)-isomer $\tau_{1/2}$ relative to the free receptor was observed, whereas this effect is not detected in the presence of a non-coordinating anion; ruling out local charge and polarity effects (Figure 6D). This further points towards strong cooperative binding, and represents a rare example of modulating the thermal half-life of a photoswitch via a supramolecular anion binding event without directly influencing the electronics of the photoswitch (i.e. through direct conjugation of the anion binding site).[18]

We also conducted anion binding studies for **Me-XB-Azo**. As expected, the affinity of the dicationic host for chloride was enhanced relative to the parent system, thus the titrations were performed in the more competitive solvent DMSO-d_6. The increase in binding constant upon *E-Z* isomerisation was maintained, albeit significantly diminished (K_1^E = 349 M^{-1}, K_1^Z = 945 M^{-1}, K^Z/K^E = 2.7). This may be due to charge repulsion in the Z-isomer where cationic binding sites are in close proximity, or a consequence of the second binding event being supressed by the highly solvated receptor. Regardless, these systems exhibit higher cooperativity than their squaramide counterparts from Chapter 3, perhaps due to the inherently lower solvent dependence of halogen bonds relative to hydrogen bonds.[19]

4.2.3 Photoswitchable catalysis

To explore the potential of these systems as photoswitchable halogen bonding catalysts, we employed our systems in a series of benchmark reactions (detailed earlier in Figure 5) and followed the reaction kinetics via ^{1}H NMR. **XB-Azo** was completely inactive in the bromide abstraction reaction under at 1.7 mM concentration (Figure 7B) [10]. Due to solubility constraints in the required solvents ($CDCl_3$ or CD_2Cl_2), we could not study **Me-XB-Azo**. Therefore, we converted the triflate salt to the more soluble **Me-XB-Azo-Bar$^F_4$** (Figure 7A). As a control compound, we also prepared monodentate **c-Bar$^F_4$**, to help elucidate the importance of the photoswitch towards activity. These compounds were tested for the analogous chloride abstraction reaction using benzhydryl chloride **34**, as well as to catalyse a Mukaiyama aldol[12] and Michael addition reaction (Figure 7C-E).[13]

For the bromide abstraction reaction, a ~3-fold rate enhancement was observed for (*Z*)-**Me-XB-Azo-Bar$^F_4$** relative to the (*E*)-isomer. Similarly, we observed a ~2-fold rate enhancement for chloride abstraction. At 0.5 mol% loadings, (*Z*)-**Me-XB-Azo-Bar$^F_4$** generated approximately twice as much Mukaiyama aldol product relative to the (*E*)-isomer within 7 hours. Finally, **Me-XB-Azo-Bar$^F_4$** efficiently catalysed the Michael addition reaction at 10% catalyst loadings, although there was no discernible discrimination between isomers. Perhaps this is due to the

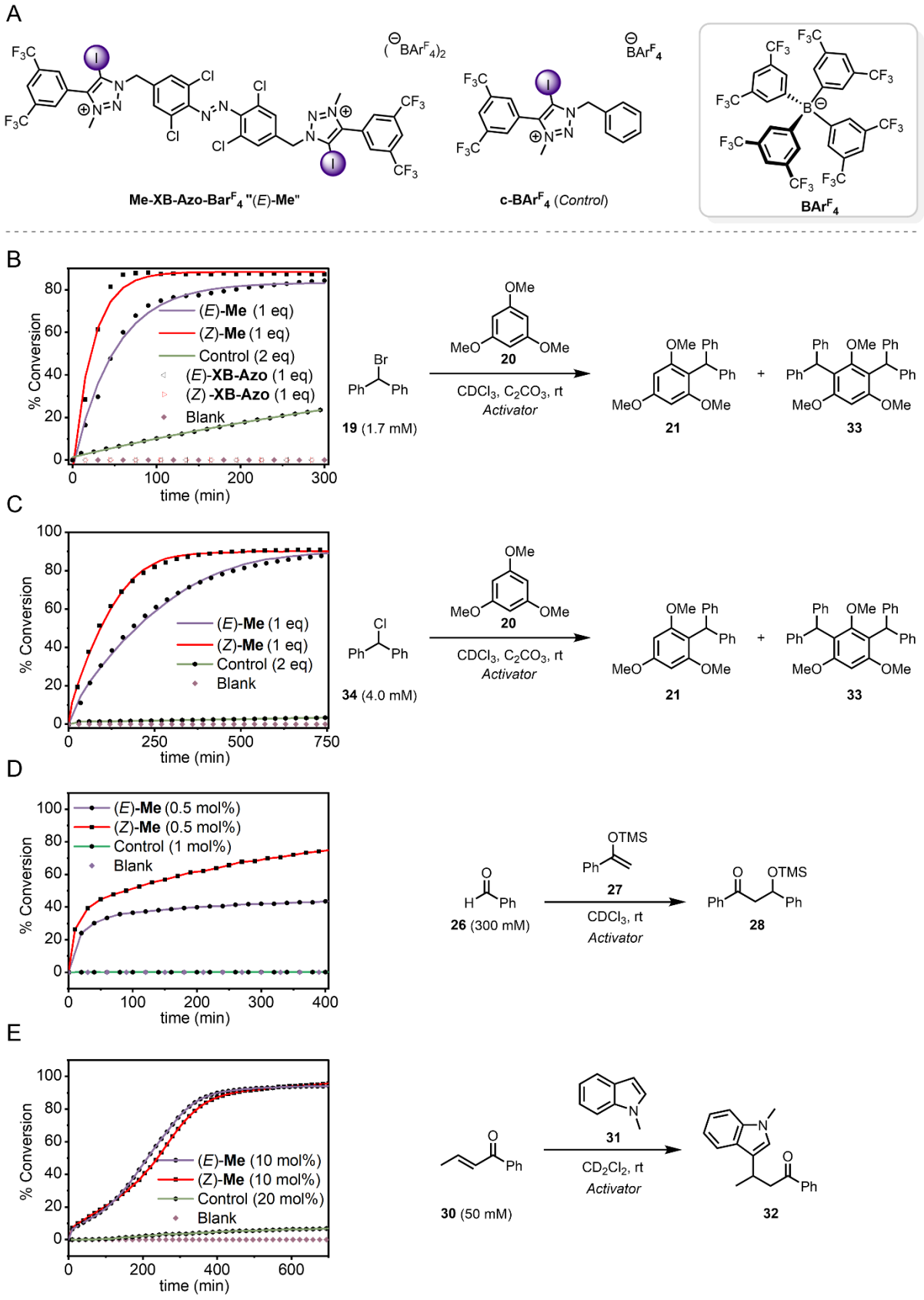


Figure 7. (A) Structure of BAr$^{F}_{4}$ derivatives (B-C): Friedel-Crafts alkylation. Black points = raw data, line = first order rate equation fit (D) Mukaiyama Aldol reaction (E) Michael addition. Data shown in presence and absence of activator for each isomers.

higher steric demands of enone **30**, leading to non-cooperative binding modes for (*Z*)-**Me-XB-Azo-Bar$^{F}_{4}$** and poor discrimination between both isomers.

For each reaction, no background activity was observed in the absence of activator, whilst the presence of two equivalents of control compound **c-Bar$^{F}_{4}$** relative to the photoswitch resulted in significantly diminished activity. It is plausible that the dicationic nature or large hydrophobic size of **Me-XB-Azo-Bar$^{F}_{4}$** is beneficial towards achieving efficient catalysis. Indeed, many high-performing halogen bond catalysts are relatively large, lipophilic structures.[6] Combined, these results highlight that **Me-XB-Azo-Bar$^{F}_{4}$** serves as a promising scaffold for photoswitchable catalysis, and that combining molecular photoswitches with halogen bond donors can open up new applications towards achieving spatiotemporal control of both molecular recognition and catalysis using light.

4.3 Ion pair transport

To further explore the scope of our photoswitches, we envisaged the possibility of appending both anion and cation binding motifs to the azobenzene cores to enable spatiotemporal control of ion pair transport. Synthetic ion pair transporters are exceptionally rare due to the inherent challenge of selectively binding and transporting two unique species across the bilayer within the same receptor, difficulties in unambiguously determining the mechanisms of ion transport,[20] and the fact that ion pair symport is intrinsically osmotically disfavoured.[21] Consequently, there are no known examples of natural products capable of transporting salts across a membrane,[22] and the majority of synthetic ion pair receptors reported to date have typically been employed towards applications in ion recognition and extraction.[23]

4.3.1 Proposed ion pair transporters

Seminal synthetic ion pair transporters **35**-**37** were reported by Jeong,[24] Smith[25] and Sessler[22] (Figure 8A). In the case of **35** and **36**, the key features are crown ether units for alkali metal binding, and hydrogen bond donors to accommodate the chloride. In both cases, the binding units are capable of forming a contact ion-pair between the bound anion and cation, which is expected to lead to ion pair transport. With these

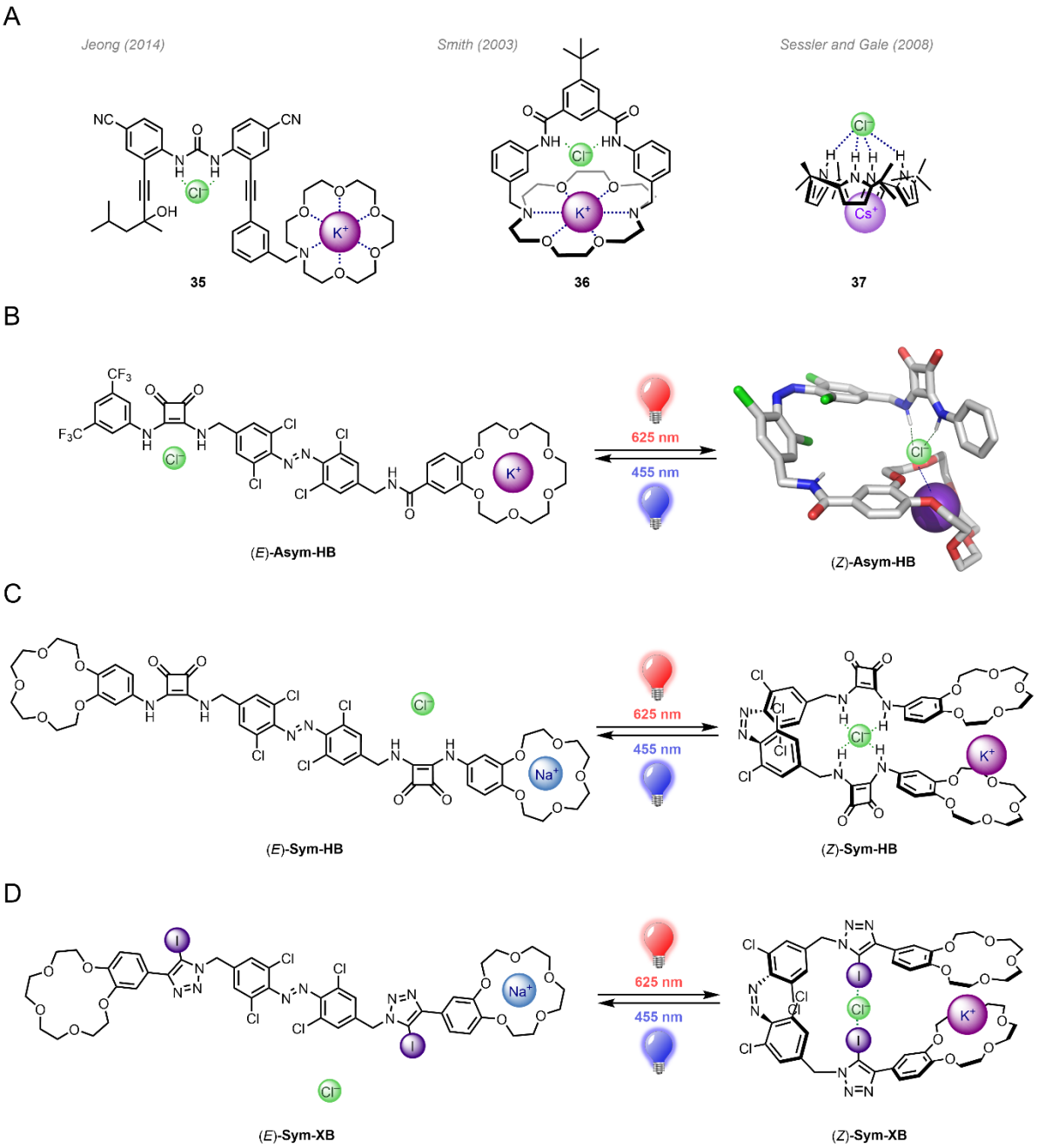


Figure 8. (A) Examples of synthetic ion pair transporters (B-D) Proposed photoswitchable ion pair transporters and calculated structure of (*Z*)-**Asym-HB** (MM+ force field, HyperChem; B)

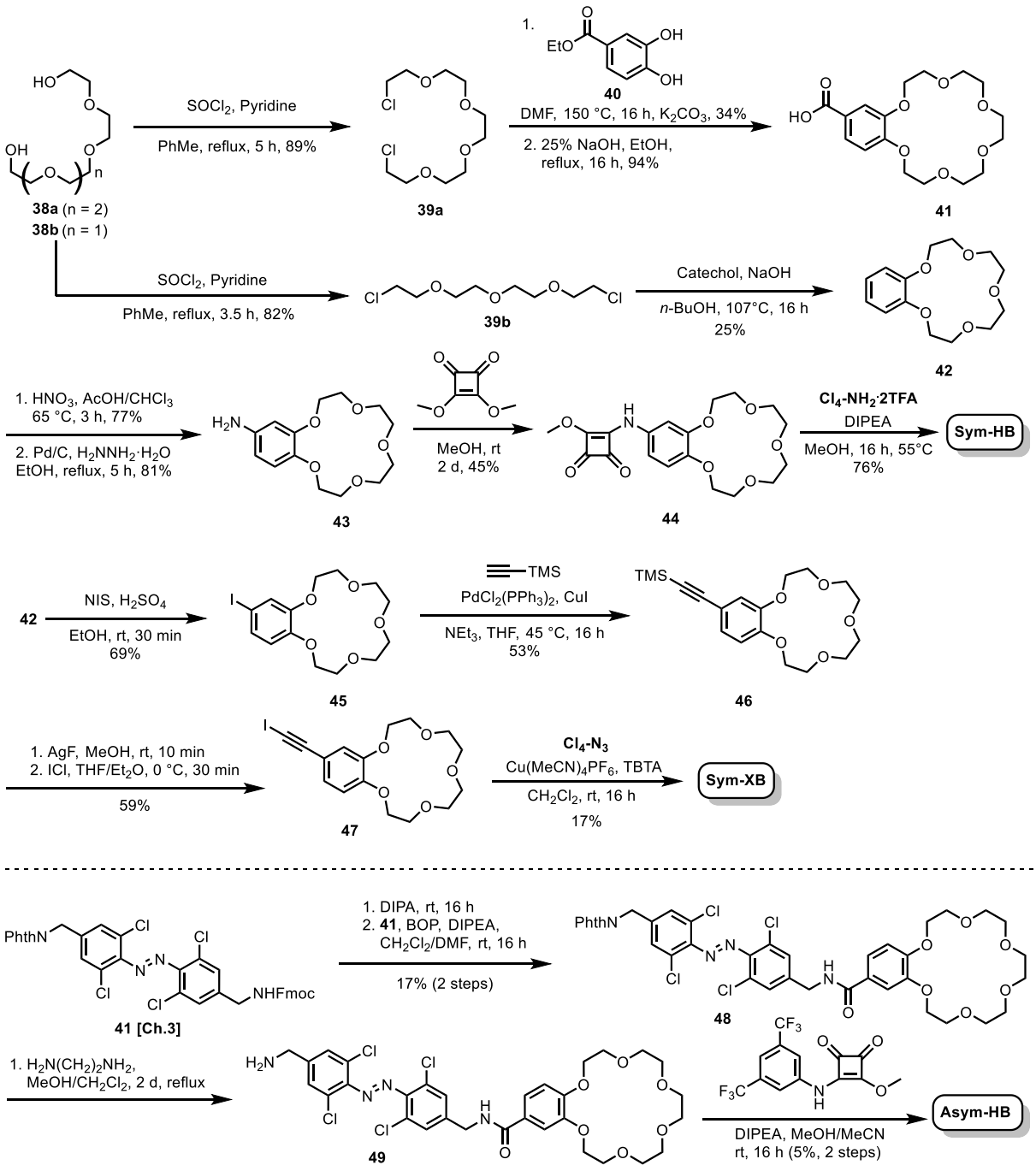
design features in mind, photo-switchable ion pair transporter **Asym-HB** was proposed, where for the (*E*)-isomer, chloride and potassium binding takes place separately, and the charged ions are relatively exposed to the bilayer (Figure 8B). Upon isomerisation, the ions can be brought together to form an ion-pair contact within a more defined pocket, leading to potentially stronger binding and correspondingly, transmembrane transport of ion pairs. It is also conceivable that the (*Z*)-isomer can bind and transport

zwitterionic species such as amino acids, which would not bind as favourably in the (*E*) form.

Sym-HB and **Sym-XB** were designed to merge the core structures of the photoswitchable anion transporters from chapter 3 and photoswitchable catalyst **XB-azo** with crown ether units (Figure 8C-D). In the (*E*)-form, chloride binding will be inherently lower due to monotopic binding, whilst the 15-crown-5 unit is expected to exhibit selectivity towards sodium cations. The longer, extended shape is proposed to lead to slower ion transport. Upon isomerisation, cooperativity between the anion binding units results in stronger chloride binding, whereas formation of a crown ether sandwich complex is expected to facilitate selective potassium binding. Furthermore, the crown ether units are directly conjugated to the anion binding receptor, resulting in improved HB and XB binding strength to the anions due to the electron withdrawing nature of the bound cation.[26] If successful, these systems may be capable of controlling membrane transport of the three most physiological ions (Na^+, K^+, Cl^-) using biocompatible wavelengths of light.

4.3.2 Synthesis of ion pair transporters

The preparation of crown ether building blocks commenced from chlorination of commercially pentaethylene glycol **38a** to generate dichloride **39a**, which was subjected to a macrocyclization with **40**. The ester group was hydrolysed to afford building block **41**. Similarly, tetraethyleneglycol **38b** was chlorinated to give rise to **39b**, which was heated with catechol to generate crown ether **42**. This was nitrated and subsequently hydrogenated to afford aniline **43**, which was coupled to dimethylsquarate to provide novel monosquaramide **44**, ready for coupling to diamine **Cl_4·NH_2** to furnish Sym-HB in good yields. **42** was also iodinated to **45**, and subjected to Sonogashira coupling conditions with TMS acetylene to afford **46**. This was converted to the silver acetylide and subsequently to iodoalkyne **47**, which was subjected to Cu-catalyzed ‘click’ conditions with **Cl_4-N_3** to produce **Sym-XB**.



Scheme 1. Synthesis of ion pair transporters

Finally, **41 [Ch.3]** was deprotected and coupled with **41** to afford **48**, which was deprotected once more and coupled to the monosquaramide to provide **Asym-HB**. The yields were generally low towards **Asym-HB** due to crown ether units streaking during silica gel column chromatography; most likely due to coordination to cations present in the silica and solvents. However, ~1 mg of material was available for preliminary transport studies.

4.3.3 ^{1}H NMR binding studies of ion pair mobile carriers

To elucidate the potassium binding modes and stoichiometries for **Sym-HB** and **Sym-XB**, ^{1}H NMR titrations with $KBar^{F}_{4}$ were performed. Due to solubility constraints, it was necessary to perform titrations in DMSO for **Sym-HB**. Unfortunately, no changes in chemical shift were observed, most likely due to strong solvation of the potassium cation. Gratifyingly, it was possible to conduct binding studies for **Sym-XB** in 50/50 v/v mixture of $CDCl_3$ and MeCN-d_4, which has been previously shown to be a suitable solvent system for observing crown ether sandwich complexes (Figure 9).[27]

The addition of the potassium cation resulted in significant broadening and splitting of proton signals across the entire spectra for both isomers (Figure 9A). This suggests the existence of multiple conformations and potential binding modes. Plots of chemical shift perturbations for (*E*)-**Sym-XB** exhibited sigmoidal binding behaviour with a *Hill coefficient* of 2 and inflexion point at 0.5 equivalents of added potassium and no further changes after 1 equivalent of potassium. This hints at the potential formation of a 2:2

complex, where the existence of parallel or antiparallel diazo bonds within the complex would lead to splitting of proton signals (Figure 9D). This is in agreement with NMR data reported by Howard and co-workers for (bis)crownstilbene derivatives bound as 2:2 cation complexes.[28]

(*Z*)-**Sym-XB** (80% PSS) signals were considerably more complicated to analyse. However, it was possible to extrapolate the chemical shift perturbations for the (*Z*)-crown ether signals, which tailed off around 0.8 equivalents of potassium (Figure 9E). After this point, the (*E*)-isomer signals begin to experience changes in chemical shifts.

This suggests that binding to the (*Z*)-isomer is stronger than that of the (*E*)-isomer, hinting at the formation of a 1:1 sandwich complex. The perturbations in chemical shift of (*Z*) signals was generally in the opposite direction to the (*E*)-isomer for the equivalent proton environment, which is in line with observations by Howard and co-workers observed when comparing 1:1 and 2:2 bis(crown)stilbene complexes with alkali

metals.[28] Overall, these results show promise towards achieving the desired increase in K^+ binding affinity upon isomerisation for **Sym-XB** and structurally related **Sym-XB**.

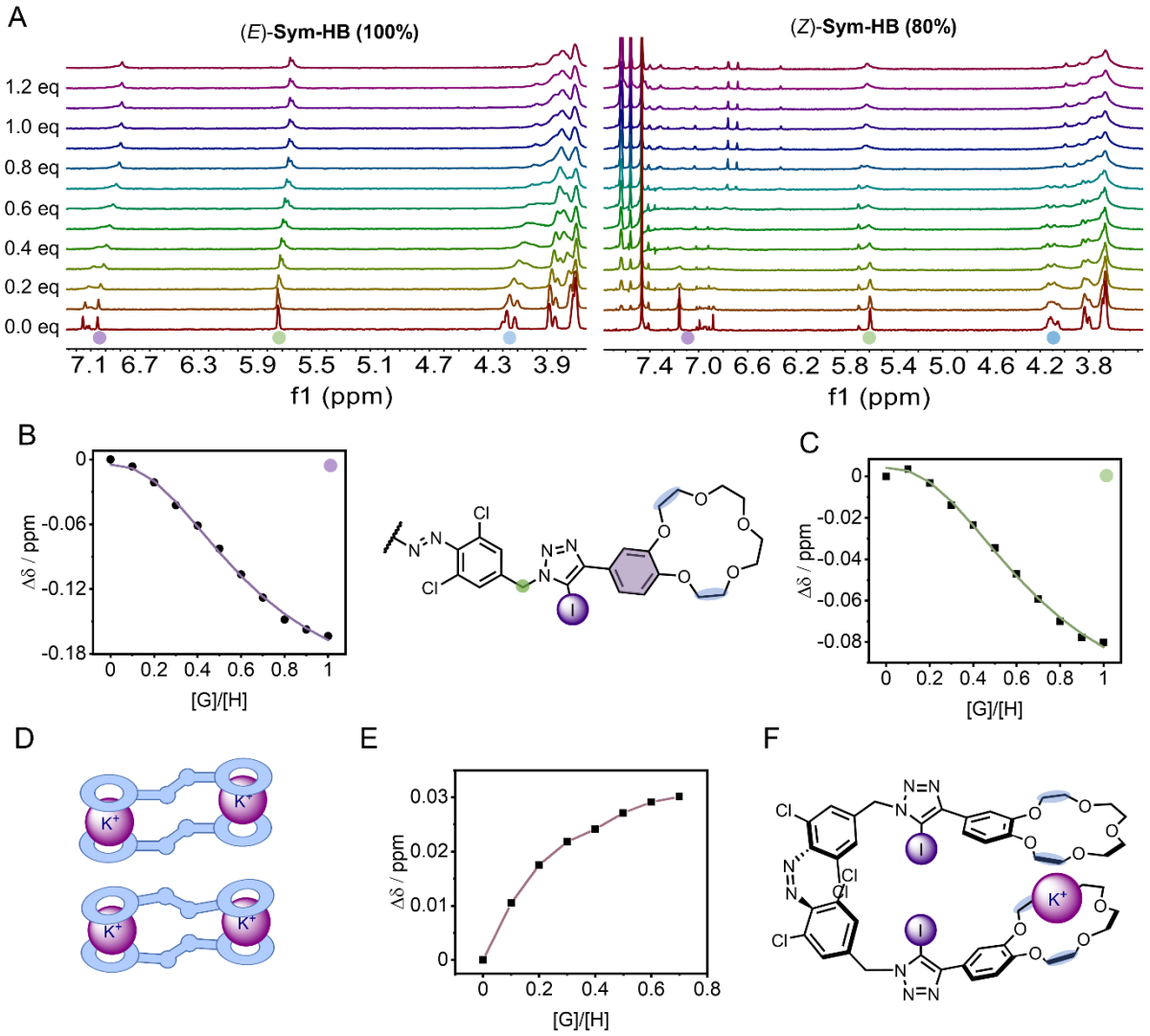


Figure 9. Potassium binding studies for **Sym-XB**. (A) Stacked ^{1}H NMR spectra and key peaks for both isomers – see structure for colour code (B) Chemical shift perturbations for crown ether aryl peak of (*E*)-**Sym-XB** (C) Chemical shift perturbations for benzylic peak of (*E*)-**Sym-XB** (D) Proposed 2:2 binding mode for (*E*)-**Sym-XB** (E) Chemical shift perturbations for crown ether ethylene peaks of (*Z*)-**Sym-XB** (F) Proposed 1:1 binding mode for (*Z*)-**Sym-XB**

4.3.4 Transport studies of ion pair mobile carriers

Preliminary transport studies were conducted using HPTS vesicles (Figure 10), which usually measures the influx of hydroxide in exchange for chloride. In this case, it is most likely that there is a simultaneous influx of hydroxide and cation, although further control experiments would be required to unambiguously prove this. Although a relatively slow transporter relative to simple carriers, both isomers **Asym-HB** successfully perturbed the ion gradients (Figure 10A-C). Both isomers exhibited an inherent preference towards potassium buffers, in line with the expected complementary binding site within the 18-crown-6 unit. However, enhancements in transport rates for the (*Z*)-isomer were less drastic than anticipated, suggesting that the anion and cation binding sites are also both available for binding and transport in the (*E*)-isomer, and the potential contact ion-pair in the (*Z*)-isomer does not significantly improve the transport rates.

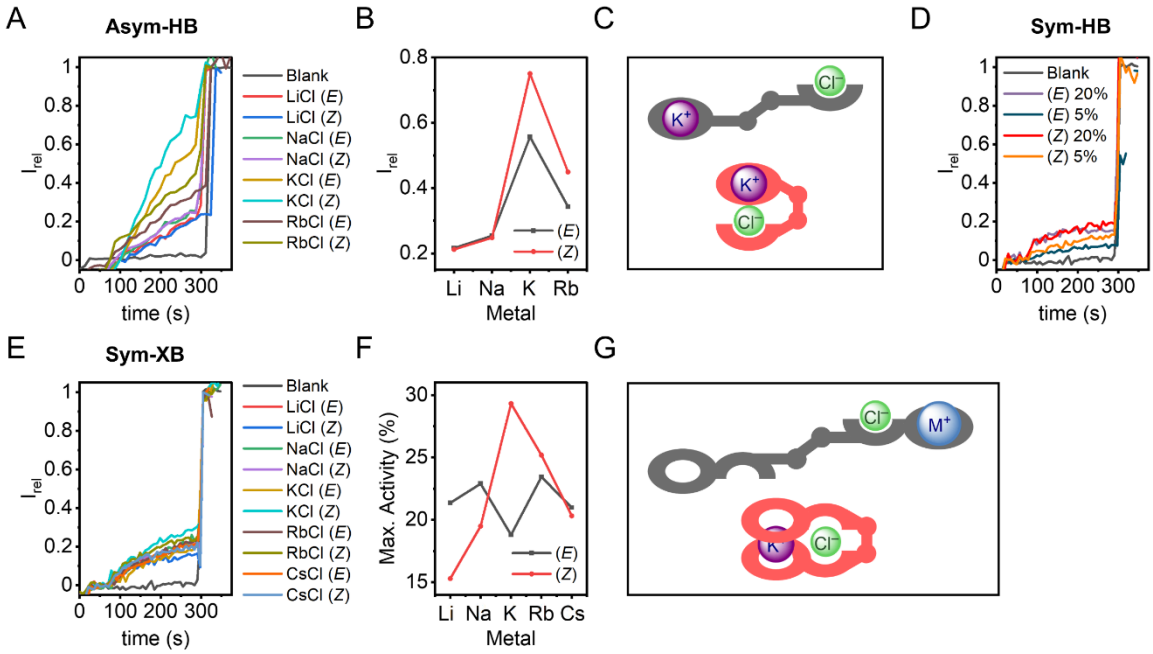


Figure 10. HPTS Assay Data for Ion pair transporters (A) Dependence of the activity of **Asym-HB** (5 mol%) on iso-osmolar replacement of extra-vesicular cation (B) Maximal activity for each ion in the presence of **Asym-HB** (5 mol%) (C) Cartoon representation of ion binding for **Asym-HB.** (D) Dependence of the activity of **Sym-HB** (varying mol%) (E) Dependence of the activity of **Sym-XB** (5 mol%) on iso-osmolar replacement of extra-vesicular cation (F) Maximal activity for each ion in the presence of **Sym-XB** before addition of Triton-X100 (5 mol%) (G) Cartoon representation of ion binding for **Asym-HB.**

Sym-HB did not display significant activity or discrimination between isomers (Figure 10D). Therefore, we turned our attention to **Sym-XB**. **Sym-XB** was significantly less active than **Asym-HB**, but an inherent preference towards potassium was observed for the (*Z*)-isomer, whereas the (*E*)-isomer displayed a minimum at this point. This in agreement with the formation of the proposed sandwich structure in (*Z*)-**Sym-XB** (Figure 10G).

Overall, activities were relatively low. Perhaps this is due to the inherent difficulty of simultaneously bringing two ions across the bilayer, or that the transporters are relatively large species that perform sluggishly as mobile carriers. Another concern may be the nature of the assay, in which hydroxide transport is a key step. If this is the rate limiting step, the results may be an underestimate of the potential MCl transport for these carriers. To rule this out, the lucigenin assay was employed.

Briefly, **lucigenin** (LG) is a fluorescent dye which is quenched with Cl^-, Br^-, I^- and NCS^- anions at relatively high concentrations (~10-100 mM), proposed to arise from the formation of a charge transfer complex (Figure 11A).[29] Therefore, when LG is loaded inside vesicles, transporter-mediated efflux (initial high anion concentration inside vesicles) of these anionic species results in an increase in fluorescence, whereas influx (initial high external anion concentration) of anions lead to a decrease in fluorescence [21] Relative to the HPTS assay, LG kinetic runs have the advantage of directly measuring chloride transport. However, eventual leakage of the more lipophilic LG across the lipid bilayer necessitates that transport experiments are conducted relatively quickly after vesicle preparation.

To measure KX symport, where X = Cl^-, Br^- or I^-, vesicles were internally loaded with LG and 100 mM K_2SO_4, conveniently allowing iso-osmolar replacement of the external Buffer with 200 mM KX (Figure 11B).[30] In principle, sulfate transport is extremely unfavourable due to the high hydrophilicity ($\Delta G_{hydration}$ = −1080 kJ mol^{-1}; −340 kJ mol^{-1}

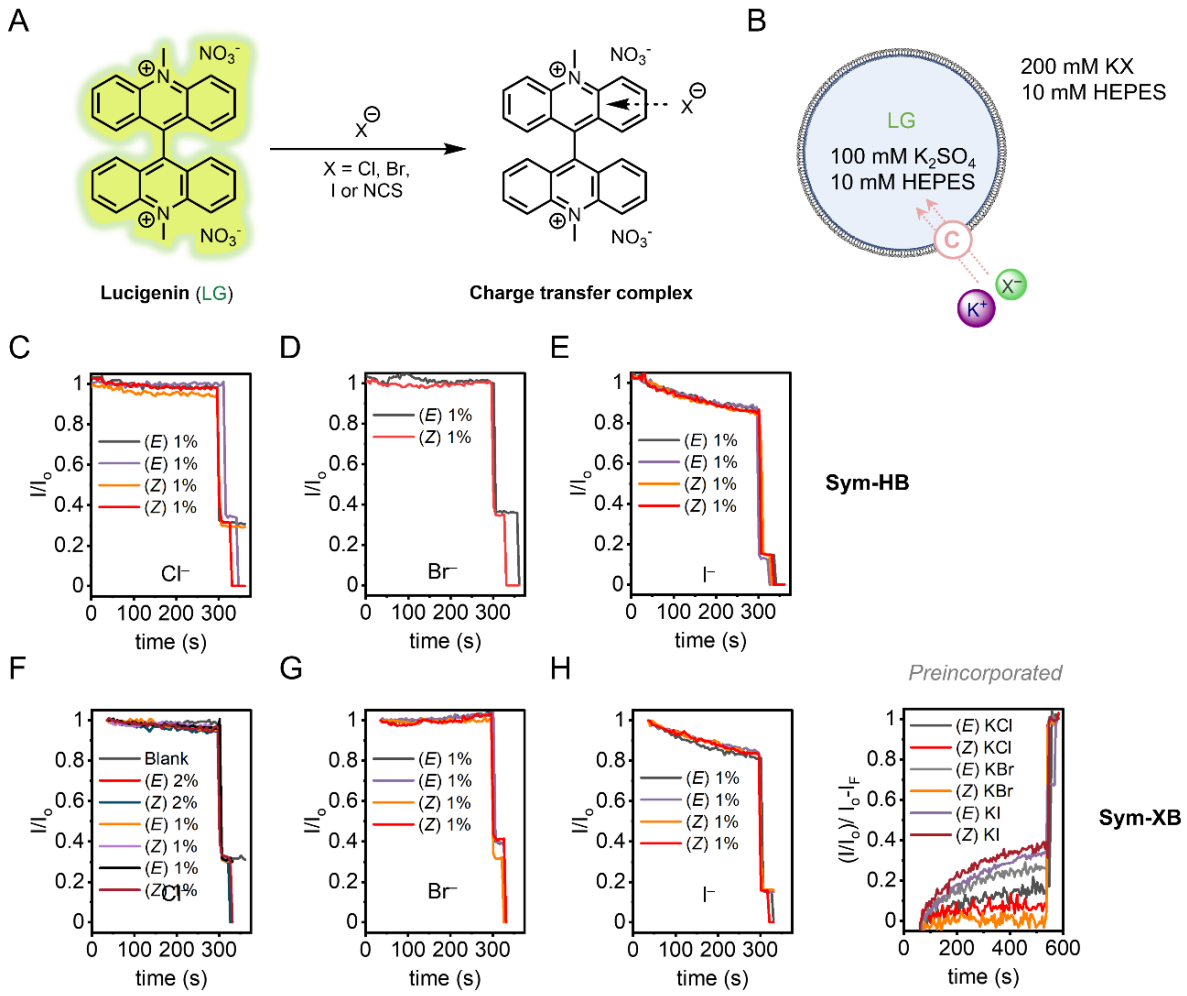


Figure 11. (A) Schematic of anion-induced Lucigenin quenching (B) Lucigenin assay conditions (C-E) Lucigenin transport data with external addition of **Sym-HB** at 1 mol% loading (F-H): Lucigenin transport data with external addition of **Sym-HB** (G) Lucigenin transport data with preincorporated **Sym-HB** (5 mol%)

for chloride),[31] thus under these conditions it is likely that KX symport dominates over X^-/SO_4^{2-} antiport. **Sym-HB** and **Sym-XB** were tested under these conditions, but due to lack of material it was not possible to elucidate the transport properties of **Asym-HB**.

Both isomers of **Sym-HB** did not show significant transport under these conditions for the halides (Figure 11C-E) at 1 mol% loadings, whereas at higher transporter loadings, precipitation occurred. Transport of less hydrophilic I^- was marginally quicker. Similarly, **Sym-XB** exhibited poor activities and discrimination between isomers, although iodide transport was marginally quicker relative to the squaramide **Sym-HB**. To rule out transporter deliverability issues, the assay was repeated with **Sym-XB** pre-

incorporated within the bilayer during vesicle preparation. The transport rates were marginally higher, but irradiation of the samples with 625 nm light did not result in significant enhancements in transport rates. Therefore, these compounds were deemed unsuitable for further ion transport studies.

Although promising in design, the proposed ion pair transporters are relatively large molecules (molecular weight > 1000), which is typically detrimental to transport rates, and may rationalise the poor activity observed for **XB-Azo** (Figure 4). Another factor hampering transport activity could be competitive binding to the zwitterionic phospholipid headgroups and potential hydrophobic interactions between the lipid tails and non-polar azobenzene, as observed by Busschaert and co-workers for compound **50** (Figure 12).[32] If this is the case, it may be necessary increase the distance between the cation and anion binding sites, which leads to even larger, less mobile structures. Indeed, ion pair transporters **35** and **36** (Figure 8) conceivably exhibit geometries where lipid head group binding is less feasible. In principle, **Asym-HB** is less capable of forming these lipid headgroup interactions, so perhaps there is scope in future work to optimise the ion-pair contact in for (*Z*)-**Asym-HB** using molecular modelling and improve the synthetic route towards these derivatives.

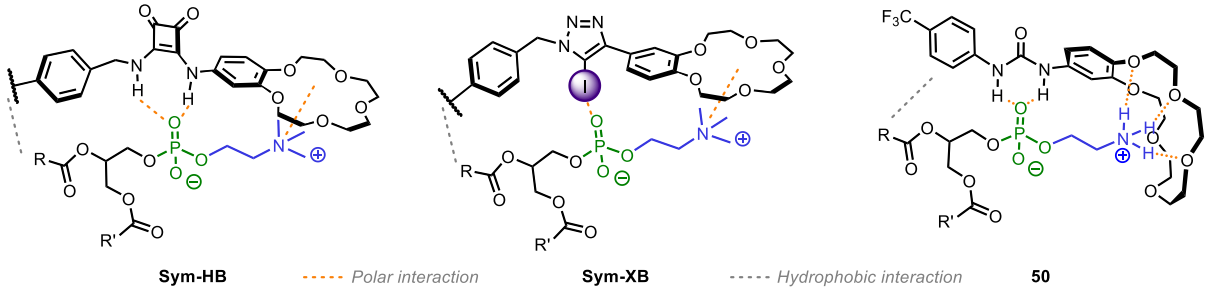


Figure 12. Potential interactions between **Sym-HB** and **Sym-XB** with phospholipids and reported example of phospholipid binding heteroditopic receptor **50**. [32]

4.4 Chapter conclusions and future work

In this chapter, we broaden the scope of our photoswitches by functionalisation with different receptor groups. The thiosquaramide derivatives were too unstable and complicated to synthesise and so were abandoned, whereas thiourea derivatives did

not exhibit improved photoswitchable ion transport activity. Appendage with iodotriazoles resulted in unexpectedly poor transporters, but gratifyingly these systems performed well as photoswitchable anion receptors and catalysts for XB-mediated benchmark reactions. These systems demonstrated, for the first time, that molecular photoswitches with halogen bond donors can open up new applications towards achieving spatiotemporal control of both molecular recognition and catalysis using light.

Finally, a series of heterotopic ion pair receptors were prepared, but these performed poorly under common transport assay conditions. Regardless, these novel ditopic building blocks serve as important scaffolds for potential applications in ion recognition and extraction, and may aid the design of future photoswitchable ion pair transporters.

4.5 References

[1] N. Busschaert, R. B. P. Elmes, D. D. Czech, X. Wu, I. L. Kirby, E. M. Peck, K. D. Hendzel, S . K. Shaw, B. Chan, B. D. Smith, K. A. Jolliffe and P. A. Gale, *Chem. Sci.*, 2014, **5**, 3617–3626.
[2]M. Rombola and V. H. Rawal, *Org. Lett.*, 2018, **20**, 514–517.
[3] S. J. Edwards, H. Valkenier, N. Busschaert, P. A. Gale and A. P. Davis, *Angew. Chem. Int. Ed.,* 2015, **54**, 4592–4596.
[4] L. E. Bickerton, A. J. Sterling, P. D. Beer, F. Duarte and M. J. Langton, *Chem. Sci.*, 2020, **11**, 4722–4729.
[5] L. E. Bickerton, A. Docker, A. J. Sterling, H. Kuhn, F. Duarte, P. D. Beer and M. J. Langton, *Chem. Eur. J*, 2021, **27**, 11738–11745.
[6] R. L. Sutar and S. M. Huber, *ACS Catal.*, 2019, **9**, 9622–9639.
[7] A. Decato, E. A. John and O. B. Berryman, in *Halogen Bonding in Solution*, John Wiley & Sons, Ltd, 2021, pp. 1–41.
[8] J. J. Koenig and M. Breugst, in *Halogen Bonding in Solution*, John Wiley & Sons, Ltd, 2021, pp. 237–268.
[9] A. Bruckmann, M. A. Pena and C. Bolm, *Synlett*, 2008, **2008**, 900–902.
[10] A. Dreger, E. Engelage, B. Mallick, P. D. Beer and S. M. Huber, *Chem. Commun.*, 2018, **54**, 4013–4016.
[11] J. Y. C. Lim and P. D. Beer, *Chem*, 2018, **4**, 731–783.
[12] R. L. Sutar, N. Erochok and S. M. Huber, *Org. Biomol. Chem.*, 2021, **19**, 770–774.
[13] F. Heinen, D. L. Reinhard, E. Engelage and S. M. Huber, *Angew. Chem. Int. Ed.*, 2021, **60**, 5069–5073.
[14] A. Docker, X. Shang, D. Yuan, H. Kuhn, Z. Zhang, J. J. Davis, P. D. Beer and M. J. Langton, *Angew. Chem. Int. Ed.*, 2021, **60**, 19442–19450.
[15] P. Thordarson, *Chem. Soc. Rev.*, 2011, **40**, 1305–1323.
[16] C. A. Hunter and H. L. Anderson, *Angew. Chem. Int. Ed*, 2009, **48**, 7488–7499.
[17] S. J. Wezenberg, *Chem. Commun.*, 2022, **58**, 11045–11058.
[18] K. Dąbrowa, P. Niedbała and J. Jurczak, *Chem. Commun.*, 2014, **50**, 15748–15751.
[19] C. C. Robertson, R. N. Perutz, L. Brammer and C. A. Hunter, *Chem. Sci.*, 2014, **5**, 4179–4183.
[20] L. E. Bickerton, T. G. Johnson, A. Kerckhoffs and M. J. Langton, *Chem. Sci.*, 2021, **12**, 11252–11274.

[21] S. Matile, N. Sakai and A. Hennig, in *Supramolecular Chemistry*, John Wiley & Sons, Ltd, 2012.
[22] C. C. Tong, R. Quesada, J. L. Sessler and P. A. Gale, *Chem. Commun.*, 2008, 6321–6323.
[23] A. J. McConnell, A. Docker and P. D. Beer, *ChemPlusChem*, 2020, **85**, 1824–1841.
[24] J. H. Lee, J. H. Lee, Y. R. Choi, P. Kang, M.-G. Choi and K.-S. Jeong, *J. Org. Chem.*, 2014, **79**, 6403–6409.
[25] A. V. Koulov, J. M. Mahoney and B. D. Smith, *Org. Biomol. Chem.*, 2003, **1**, 27–29.
[26] T. Bunchuay, A. Docker, U. Eiamprasert, P. Surawatanawong, A. Brown and P. D. Beer, *Angew. Chem. Int. Ed.*, 2020, **59**, 12007–12012.
[27] A. Docker, I. Marques, H. Kuhn, Z. Zhang, V. Félix and P. D. Beer, *J. Am. Chem. Soc.*, 2022, **144**, 14778–14789.
[28] S. P. Gromov, A. I. Vedernikov, N. A. Lobova, L. G. Kuz'mina, S. S. Basok, Y. A. Strelenko, M. V. Alfimov and J. A. K. Howard, *New J. Chem.*, 2011, **35**, 724–737.
[29] K. D. Legg and D. M. Hercules, *J. Phys. Chem.*, 1970, **74**, 2114–2118.
[30] G. Grauwels, H. Valkenier, A. P. Davis, I. Jabin and K. Bartik, *Angew. Chem. Int. Ed.*, 2019, **58**, 6921–6925.
[31] Y. Marcus, *J. Chem. Soc., Faraday Trans.*, 1991, **87**, 2995–2999.
[32] S. R. Herschede, H. Gneid, T. Dent, E. B. Jaeger, L. B. Lawson and N. Busschaert, *Org. Biomol. Chem.*, 2021, **19**, 3838–3843.

Chapter 5 – Thesis conclusions and future work

5.1 Summary of thesis

Mobile carrier ionophores are small hydrophobic receptors capable of transporting ions across lipid bilayers, and show high promise as therapeutics for cancer treatment and channelopathies, or as tools for studying ion transport processes.

One promising approach towards overcoming selectivity and drug resistance issues in pharmaceuticals are light-activated drugs, which offer full spatiotemporal control of drug activity. Azobenzenes are the most commonly employed motifs within the field of photopharmacology, as they are easily tuneable, functionalisable, can switch without detectable fatigue, and exhibit large conformational changes. However, UV radiation is required to photo isomerise azobenzenes, which can damage cellular surroundings and exhibits low tissue penetration due to high scattering; limiting its use *in vivo*.

The research described in this thesis involves the preparation of azobenzene scaffolds capable of switching within more deeply penetrating tissues with controlled thermal half-lives. These photoswitches were employed within the context of photoswitchable ion transporters and photoswitchable catalysis.

Chapter 2 described the synthesis of red-shifted azobenzenes functionalised with the heavier chalcogens and halogens, capable of fatigue-resistant photo-switching with red and near IR light. The series exhibited robust periodic trends for the chalcogen and halogen azobenzene series, and exploited intramolecular chalcogen bonding to tune and redshift the absorption maxima; supported by photo-physical measurements and solid-state structural analysis. The series all contained functional handles for further functionalisation for application, and the (*Z*) → (*E*) thermal isomerisation half-life could be tuned over timescales spanning seven orders of magnitude.

In *chapter 3*, a bistable, redshifted azobenzene scaffold was selected as the core for a photoswitchable anion transporter containing two squaramide motifs. Extensive optimisation

of the linker length and squaramide substituents lead to the first example of a fully reversible 'On/Off' photoswitchable anion transporter responding to biocompatible wavelengths of light within synthetic bilayers.

In *chapter 4*, various modifications to the receptor motif were made to broaden the scope of the photoswitches. This lead to the discovery of a photoswitchable anion receptor and catalyst, capable of catalysing numerous benchmark catalysis reactions. A series of photoswitchable ion pair receptors were also prepared, which were found to bind potassium more strongly in the (Z)-form and mildly transported KCl across synthetic bilayers.

5.2 Future work

Over the course of this work, a variety of substitution patterns and receptor types were explored to discover optimal 'On/Off' switching behaviour within the context of synthetic bilayers (*chapters 3-4*). To date, the most promising photoswitchable ion transporter is compound **15a** (*chapter 3*). However, as the thermal half-life is in the order of days, it is necessary to perform (*Z*) → (*E*) isomerisation using blue light, which penetrates tissue significantly more weakly and does not result in full 100% conversion to the (*E*)-isomer (**Figure 1A)**

Therefore, it would be desirable to incorporate a highly redshifted, fast-relaxing azobenzene scaffold within the system (*chapter 2)*. The tetraiodo azobenzene scaffold **I_4-15a** isomerises with deep red light, and exhibits a thermal half-life in the order of minutes, allowing accumulation of the (*Z)* isomer under constant light irradiation whilst relying on thermal decay for back-isomerisation (**Figure 2B**).

Future work would involve preparation of these types of scaffolds and studying their utility as reversible photoswitchable anion transporters; responding to red light only within synthetic bilayers. This work would also demonstrate the utility of the novel photoswitches discovered during this thesis, and serve as an important milestone in employing fast-relaxing azobenzenes within the context of spatial targeting.

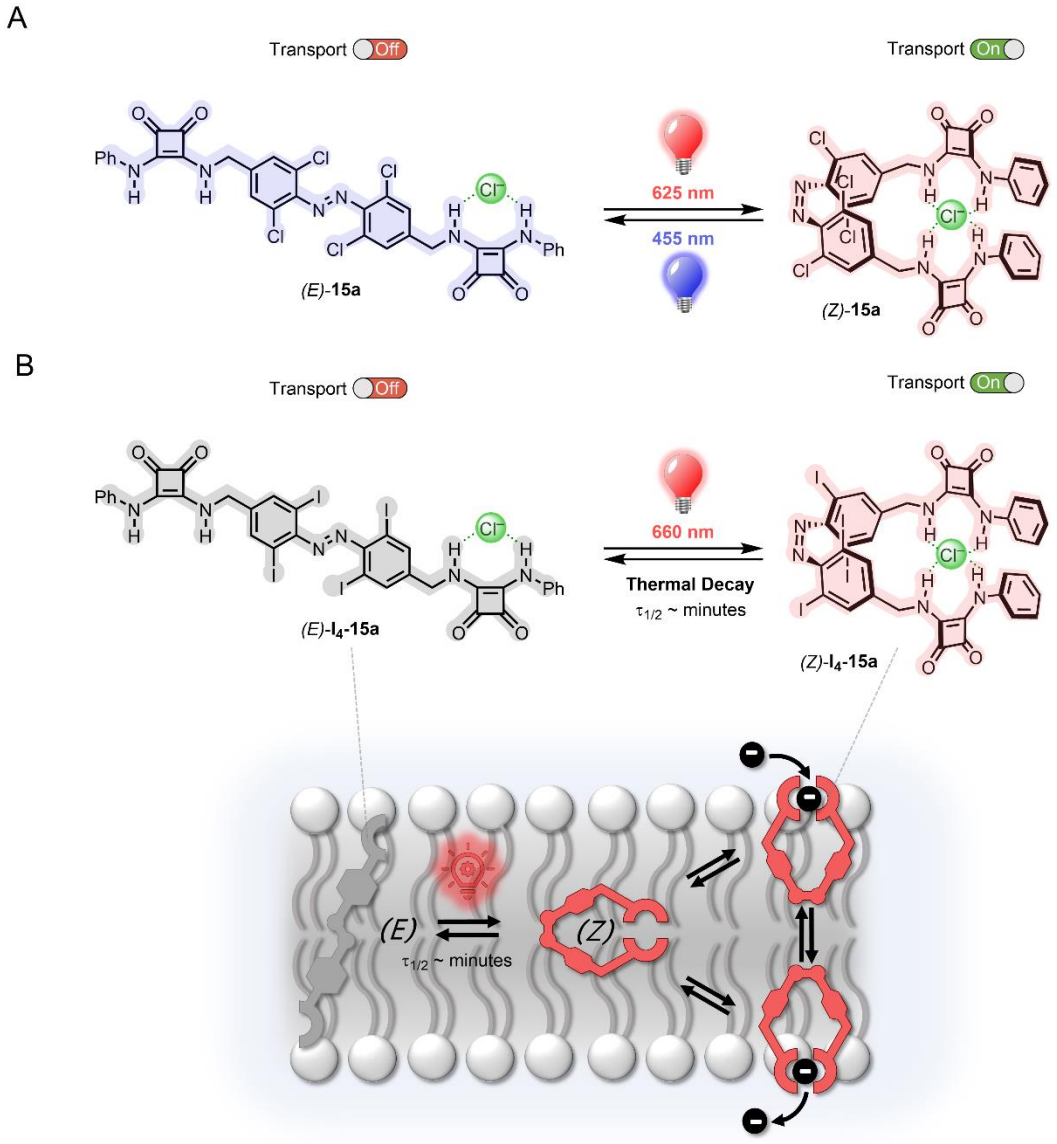


Figure 1. (A) Most promising photoswitchable anion transporter **15a** (B) Outline of future work: fast-relaxing photoswitchable anion transporter responsive to red light.

6.1 Appendix

6.1.1 Materials and methods

All reagents and solvents were purchased from commercial sources and used without further purification. Where necessary, solvents were dried by passing through an MBraun MPSP-800 column and degassed with nitrogen. Triethylamine was distilled from and stored over potassium hydroxide. Column chromatography was carried out on Merck® silica gel 60 under a positive pressure of nitrogen. Where mixtures of solvents were used, ratios are reported by volume. NMR spectra were recorded on a Bruker AVIII 400, Bruker AVII 500 (with cryoprobe), Bruker NEO 600 with broadband helium cryoprobe and Bruker AVIII 500 spectrometers. Chemical shifts are reported as δ values in ppm. Mass spectra were carried out on a Waters Micromass LCT and Bruker microTOF spectrometers. UV-Vis spectra were recorded on a V-770 UV-Visible/NIR Spectrophotometer equipped with Peltier temperature controller and stirrer using quartz cuvettes of 1 cm path length. Experiments were conducted at 25°C unless otherwise stated.

All UV-vis spectra were determined in DMSO solution unless state otherwise. Extinction coefficients were determined by recording a UV-vis spectra for the (*E*) isomer at 10, 20, 30, 40 μM respectively. The absorbance at the maximum of the π - π* transition of the *E*-isomers was plotted against concentration (Beer-Lambert plot) to determine the molar extinction coefficient ε. For each slow relaxing compound, the *E* isomer sample at 40 μM was irradiated with the appropriate wavelength of light to generate the photo-stationary state, and another spectrum was run. This spectrum was normalised to units of ε and overlaid with the dark (100% *E* isomer) spectrum.

Deconvoluted spectra were prepared using Origin Pro 2020b by fitting each λ_{max} to the “Multiple Peak Fit” function.

Photo-irradiation of liquid samples was carried out using Thorlabs high-power mounted LEDs (models M730L4, (NIR, 730 nm), M660L4 (deep red, 660 nm) M625L4 (red, 625 nm); M590L4

(Amber, 590 nm) M530L4 (green, 530 nm); in-house custom built set-ups using optical components supplied by Thorlabs.

Photo-irradiation of liquid samples was carried out using Thorlabs high-power mounted LEDs (models M730L4, (NIR, 730 nm), M660L4 (red, 660 nm) M625L4 (red, 625 nm); M590L4 (Amber, 590 nm); M530L4 (green, 530 nm). Photo-stationary states (PSS) were determined using ^{1}H NMR spectroscopy. For faster relaxing systems, the %Z isomer was extrapolated for t=0 from 1st order exponential decay plots (equation S1) of ^{1}H NMR spectra at known intervals after irradiation of the sample.

Thermal Half- life determination were determined using ^{1}H NMR or UV-Vis spectroscopy. For the **F_4** derivative half-life was determined using UV-vis spectroscopy at elevated temperatures and generating an Arrhenius plot. Slow relaxing systems were evaluated using ^{1}H NMR at room temperature and following the %Z isomer by integration over time. (*Z*) → (*E*) isomerisation for fast relaxing systems were evaluated by UV-Vis spectroscopy by irradiating the sample inside the spectrometer and following a single wavelength for the compound over time.

Data was fitted using Origin Pro using an exponential decay model to determine t_1 (Equation S1). Half-life ($t_{1/2}$) was determined using Equation S2. For **F_4-NHBoc**, the half-life was determined using equation S3.

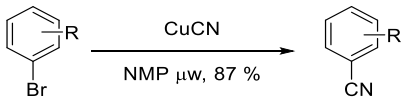
$$y = A_1 e^{\left(\frac{-x}{t1}\right)} \quad (\mathbf{S1})$$

$$T_{1/2} = t_1 ln2 \quad (\boldsymbol{S2})$$

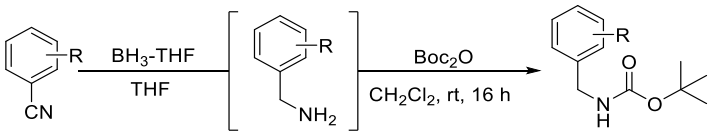
$$k = A_1 e^{\left(\frac{-Ea}{RT}\right)} \quad (\mathbf{S3})$$

6.2.1 Synthetic procedures (Chapter 2)

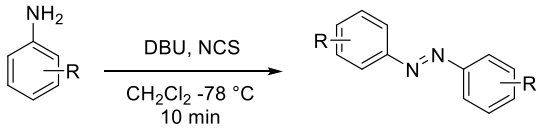
General Procedures



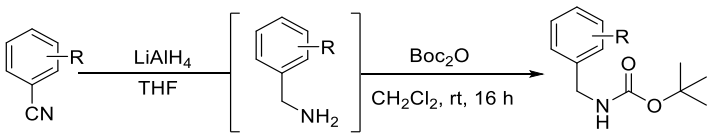
General procedure 1. A suspension of Aryl bromide and copper(I) cyanide in dry NMP (2M wrt. ArBr) was heated under microwave irradiation under N_2. The reaction was poured onto 15% ammonia solution, then extracted with 50:50 Hexane:EtOAc (3 x). The combined organic layers were washed with water (5 x), 5% LiCl solution, then concentrated.



General procedure 2. To a solution of nitrile in THF (0.5M wrt. nitrile) under N_2 was added dropwise 1M BH_3-THF solution at 0°C. The mixture was stirred for the given duration and temperature, then MeOH was added until effervescence stopped, and the resulting mixture was stirred at reflux temperature for 1 h. The solvent was removed *in vacuo* and re-dissolved in EtOAc. The organic layer was washed with water, then brine, then concentrated *in vacuo* to afford crude amine which was immediately dissolved in CH_2Cl_2 (0.5M wrt nitrile). Boc_2O (1M, 1 equiv) was added dropwise to the solution and stirred at rt for 16 h, then solvent removed *in vacuo*.



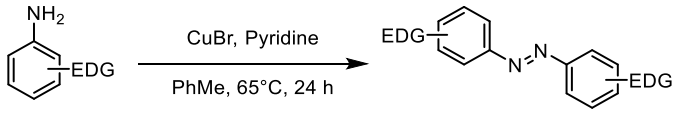
General procedure 3. To a solution of aniline in CH_2Cl_2 (67 mM wrt. aniline) was added DBU (2 eq). The solution was stirred at room temperature for 5 min before being cooled down to −78 °C. NCS (2 eq) was added. The solution was stirred for 10 min at −78 °C before quenching with sat. $NaHCO_3$ solution. The organic layer was separated, washed sequentially with water and 1M HCl, dried over anhydrous sodium sulfate, and concentrated to dryness *in vacuo*.



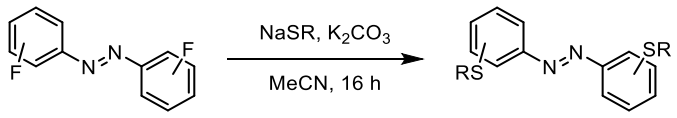
General procedure 4. To a suspension of $LiAlH_4$ (2.2 eq) in dry THF (0.5M) was the nitrile (8.1 g, 43.31 mmol, 1.0 eq) in THF (0.33M) at rt. The suspension was stirred for the given duration and temperature, then cooled to 0°C and diluted in Et_2O (0.67M wrt. Nitrile), then water (1 mL/g $LiAlH_4$), 2.5M NaOH (1 mL/g $LiAlH_4$), and water (3 mL/g $LiAlH_4$) was added dropwise. The suspension was stirred for 15 minutes, and then anhydrous $MgSO_4$ was added. The solution was filtered, and filtrate concentrated. The crude was immediately dissolved in CH_2Cl_2 (0.5M wrt nitrile). Boc_2O (1M, 1 equiv) was added dropwise to the solution and stirred at rt for 16 h, then solvent removed *in vacuo*.



General procedure 5. PIDA (4.66 g, 14.5 mmol, 1.1 eq) was dissolved in dry degassed CH_2Cl_2 (75 mM) under Argon. TMSOTf (5 mL, 2.1 eq) was added. DMAP (2.1 eq) in dry degassed CH_2Cl_2 (150 mM) was added and the yellow solution was stirred for 5 minutes, after which a white precipitate had formed (Weiss reagent). The aniline (1 eq) was added in dry degassed CH_2Cl_2 (150 mM) and the reaction was stirred at reflux temperature under protection from light for 30 minutes, then stirred at room temperature under protection from light for 48 hours. The mixture was filtered, then concentrated.

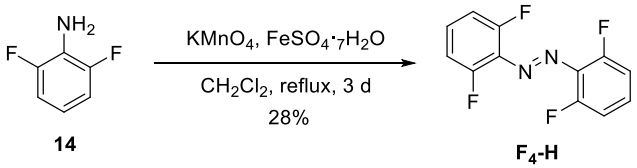


General procedure 6. Aniline (1 eq) was dissolved in toluene (60 mM). Pyridine (2 eq) and CuBr (1 eq) was added and the reaction was stirred under atmospheric air at 65 °C for 24 hours under protection from light, then concentrated.



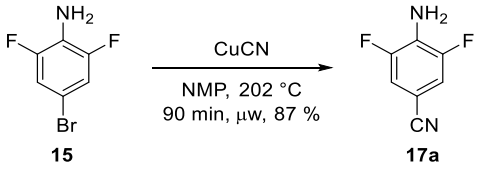
General procedure 7. Fluoroazobenzene (1 eq), thiolate and K_2CO_3 were suspended in MeCN (80 mM) and stirred at rt for 16 hours under N_2 in a sealed microwave vial. The mixture was diluted in CH_2Cl_2, washed with water, then concentrated *in vacuo*.

Synthetic Procedures



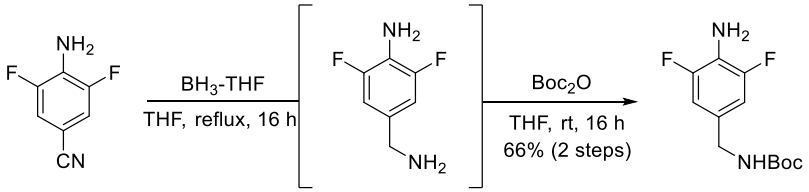
14 **F_4-H**

F_4-H. Prepared according to a modified literature procedure.[1] **14** (8 g, 62.0 mmol) was dissolved in CH_2Cl_2 (300 mL) and a freshly ground mixture of $KMnO_4$ (32 g, 202.5 mmol, 3.27 eq) and $FeSO_4 \cdot 7H_2O$ (32 g, 115 mmol, 1.86 eq) were added. The solution was stirred at reflux temperature for 3 days, filtered through celite, dried over $MgSO_4$, filtered, and concentrated under reduced pressure. The crude residue was purified by column chromatography (dry load, 20% CH_2Cl_2 in hexane) to provide **F_4-H** as an orange solid (2.2 g, 8.66 mmol, 28%). (*E*)-**F_4-H** ^{1}H NMR (400 MHz, $CDCl_3$) δ 7.38 (tt, *J* = 8.4, 5.8 Hz, 2H), 7.11 – 7.03 (m, 4H). Data consistent with that given in the literature. [1]



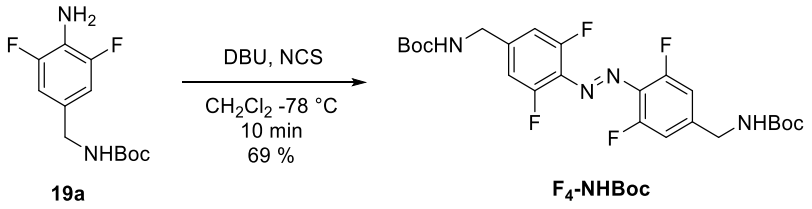
15 **17a**

17a. Prepared according to ***General procedure 1*** from **15** (6.5 g, 31.1 mmol) and CuCN (4.2 g, 146.6 mmol, 1.5 eq) at 202 °C for 90 minutes and purified by silica gel column chromatography (50% CH_2Cl_2 in hexane) to obtain the title compound as a white crystalline solid (4.16 g, 27 mmol, 87%). ^{1}H NMR (400 MHz, Chloroform-d) δ 7.17 (dd, J = 6.0, 2.3 Hz, 2H), 4.29 (s, 2H). Data consistent with that given in the literature.[2]

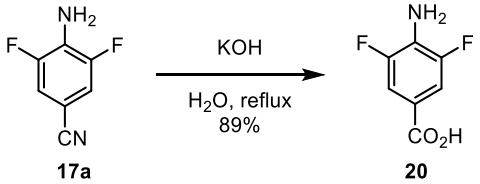


17a **18a** **19a**

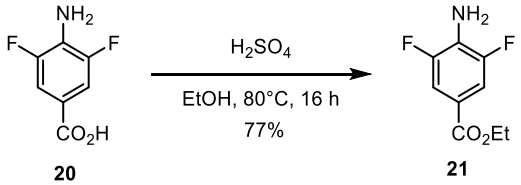
19a. Prepared according to ***General procedure 2*** from **17a** (3.85 g, 25 mmol) and BH_3-THF solution (1M, 100 ml, 100 mmol, 4 eq). The mixture was stirred under reflux temperature for 16 h to afford **18a**. ^{1}H NMR (400 MHz, Acetone) δ 6.97 – 6.77 (m, 1H), 4.29 (s, 1H). ***General procedure 2*** was continued with Boc_2O (5.45 g, 25 mmol, 1 eq), then purified by column chromatography (6:1 hexane-acetone) to afford the title compound as a white solid (4.26 g, 66%). ^{1}H NMR (400 MHz, $CDCl_3$) δ 6.82 – 6.69 (m, 2H), 4.80 (s, 1H), 4.17 (d, *J* = 6.1 Hz, 2H), 3.82 – 3.54 (br s, 2H), 1.46 (s, 9H). ^{13}C NMR (101 MHz, $CDCl_3$) δ 155.85, 151.92 (dd, *J* = 240.8, 8.2 Hz), 128.40 (t, *J* = 7.83 Hz), 122.83 (t, *J* = 16.5 Hz), 109.92 (dd, *J* = 15.1, 7.5 Hz), 79.66, 43.67, 28.35. HRMS-ESI (m/z) Calculated for $C_{12}H_{16}O_2N_2F_2$ $[M+Na]^+$, 281.1072; found 281.1072.



F_4-NHBoc. Prepared according to ***General procedure 3*** from **19a** (303 mg, 1.17 mmol), DBU (350 mg, 2.34 mmol, 2 eq). and NCS (313 mg, 2.34 mmol, 2 eq), and was purified by silica gel flash chromatography (5% EtOAc in CH_2Cl_2) to afford the title compound as an orange solid as a mixture of isomers (205 mg, 402 µmol, 69%). *(E)*-**F_4-NHBoc:** ^{1}H NMR (400 MHz, Chloroform-*d*) δ 6.99 (d, *J* = 10.1 Hz, 4H), 4.99 (s, 2H), 4.35 (d, *J* = 6.4 Hz, 4H), 1.47 (s, 18H). ^{13}C NMR (101 MHz, Chloroform-d) δ 155.95, 155.04 (dd, J = 261.7, 4.53 Hz), 144.60 (m), 130.69 (t, J = 9.8 Hz), 111.14 (d, J = 21 Hz), 80.40, 44.02, 28.50. HRMS-ESI (m/z) Calculated for $C_{24}H_{28}F_4N_4O_4$ $[M+H]^+$, 513.2119; found 513.2119.

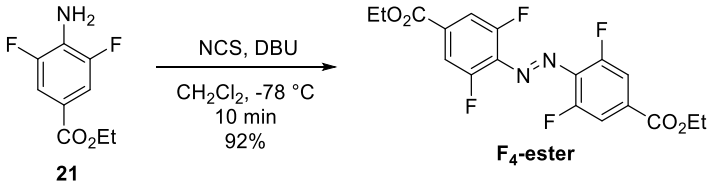


Acid 20. **17a** (2.5 g, 16.2 mmol) was suspended in 25% KOH in water (50 mL) and was stirred at reflux temperature for 16 hours. Then 2N HCl was added until pH 2 was reached, and the precipitate was extracted with EtOAc. The organic layers were washed with brine, then concentrated to afford the title compound as a salmon-pink solid (2.48 g, 14.4 mmol, 89%). ^{1}H NMR (400 MHz, DMSO) δ 12.51 (s, 1H), 7.40 (d, *J* = 7.2, 2.5 Hz, 2H), 6.06 (s, 2H). Data consistent with that given in the literature. [2]

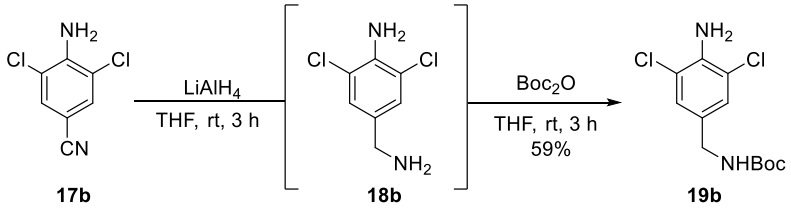


Ester 21. 20 (1 g, 5.78 mmol) was dissolved in EtOH (20 mL). Then sulphuric acid (0.3 mL) was added and the reaction was stirred at 80 °C bath temperature for 16 hours. The reaction

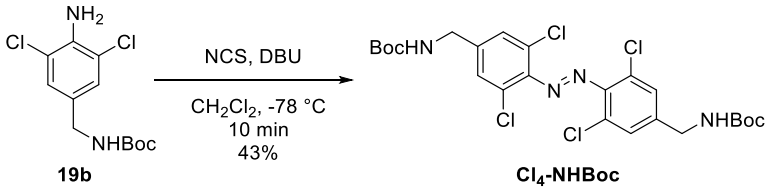
was diluted with CH_2Cl_2 and the organic layer washed with sat. bicarbonate solution. The organic layer was dried then concentrated to afford the title compound as an off-white solid (889 mg, 4.42 mmol, 77%). ^{1}H NMR (400 MHz, $CDCl_3$) δ 7.58 – 7.48 (m, 2H), 4.33 (q, *J* = 7.1 Hz, 2H), 3.72 (br s, 2H), 1.37 (t, *J* = 7.1 Hz, 3H). Data consistent with that given in the literature. [1]



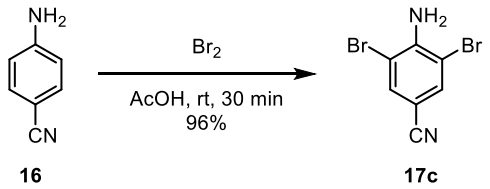
F_4-ester. Prepared according to ***General procedure 3*** from **21** (1.0 g, 5.0 mmol), DBU (1.48 mL, 10.0, 2 eq) and NCS (1.33 g, 10.0 mmol, 2 eq) and was purified by silica gel flash chromatography (50% Hexane in CH_2Cl_2) to afford the title compound as an orange solid (905 mg, 2.49 mmol, 92%. *(E)*-**F_4-ester**: ^{1}H NMR (400 MHz, $CDCl_3$) δ 7.79 – 7.71 (m, 4H), 4.43 (q, *J* = 7.1 Hz, 4H), 1.43 (t, *J* = 7.1 Hz, 6H). Data consistent with that given in the literature. [1]



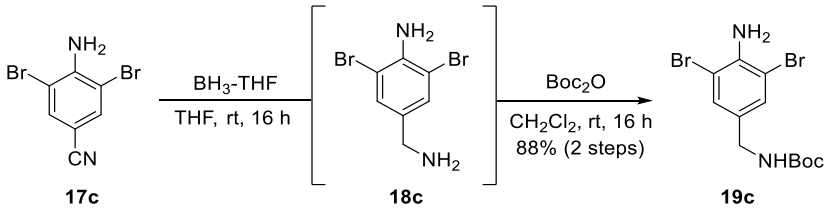
Aniline 19b. Prepared according to ***General procedure 4*** from $LiAlH_4$ (3.62 g, 95.3 mmol, 2.2 eq),**17b** (8.1 g, 43.31 mmol, 1.0 eq). THF (100 mL) was added to break up the thick solids and the mixture was stirred at rt for 3h to afford 18b. ***General procedure 4*** was continued using Boc_2O (8.4 g, 38.5 mmol, 1.05 eq), then was purified by silica gel flash chromatography (18% Acetone in hexane) and recrystallized from Et_2O and petroleum ether to afford the title compound (7.4 g, 3.37 mmol, 59% over two steps). ^{1}H NMR (400 MHz, Chloroform-*d*) δ 7.11 (s, 2H), 4.78 (s, 1H), 4.51 – 4.28 (br s, 2H), 4.15 (d, *J* = 6.0 Hz, 2H), 1.46 (s, 9H). ^{13}C NMR (126 MHz, $CDCl_3$) δ 155.89, 139.37, 129.40, 127.13, 119.70, 79.88, 43.64, 28.35. HRMS-ESI (m/z) Calculated for $C_{12}H_{16}Cl_2N_2O_2$ $[M+H]^+$, 291.0661; found 291.0662.



Cl_4-NHBoc. Prepared according to ***General procedure 3*** from **19b** (3.77 g, 12.9 mmol), DBU (3.95 g, 25.9 mmol, 2 eq) and NCS (3.45 g, 25.9 mmol, 2 eq) and purified by silica gel flash chromatography (1 to 3% EtOAc in CH_2Cl_2) to afford the title compound as a brown solid as a mixture of isomers (1.61 g, 5.55 mmol, 43%). (*E*)**-Cl_4-NHBoc:** ^{1}H NMR (400 MHz, Chloroform-d) δ 7.37 (s, 4H), 4.99 (br s, 2H), 4.32 (d, *J* = 6.2 Hz, 4H), 1.48 (s, 18H) ^{13}C NMR (126 MHz, DMSO-d_6) δ 155.80, 144.97, 144.32, 128.11, 126.13, 78.34, 42.36, 28.16. HRMS-ESI (m/z) Calculated for $C_{24}H_{28}Cl_4N_4O_4$ $[M+H]^+$, 577.0937; found 577.0936.

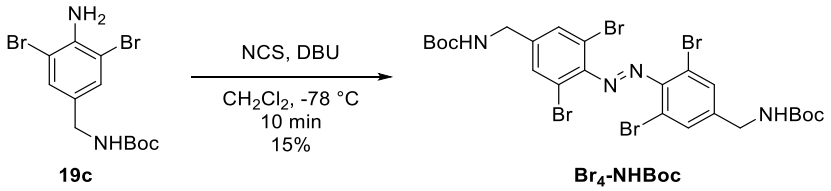


Nitrile 17c. To a solution of **16** (2 g, 16.9 mmol) in AcOH (140 mL) was added Br_2 (1.91 mL, 37.2 mmol, 2.2 eq) dropwise. The reaction was stirred for 30 minutes at room temperature, then poured onto ice water (350 mL). The solid was collected *via* filtration, washed with sodium thiosulfate, then water. The filter cake was dried *in vacuo* to afford the title compound as an off-white solid (4.47 g, 16.2 mmol, 96%). ^{1}H NMR (400 MHz, $CDCl_3$) δ 7.66 (s, 2H), 5.11 (s, 2H). Data consistent with that given in the literature.[4]



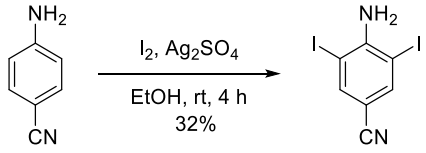
19c. Prepared according to ***General procedure 2*** from **17c** (1 g, 3.6 mmol) and Borane-THF (1M, 14.5 mmol, 14.5 mmol, 4 eq) at rt for 16 hours to afford the intermediate amine **18c**. ^{1}H NMR (400 MHz, $CDCl_3$) δ 7.34 (s, 2H), 4.48 (s, 2H), 3.72 (s, 2H). ***General procedure 2*** was

continued with Boc_2O (790 mg, 3.62 mmol, 1 eq). The resulting residue was purified by silica gel flash chromatography (CH_2Cl_2) to afford the title compound a white solid (1.21 g, 3.17 mmol, 88%). ^{1}H NMR (400 MHz, $CDCl_3$) δ 7.29 (s, 2H), 4.85 (s, 1H), 4.48 (s, 2H), 4.13 (d, *J* = 5.4 Hz, 2H), 1.45 (s, 9H). ^{13}C NMR (101 MHz, $CDCl_3$) δ 155.85, 141.25, 131.03, 130.55, 108.80, 79.85, 43.37, 28.51. HRMS-EI (m/z) Calculated for $C_{12}H_{16}O_2N_2Br_2Na$ $[M+Na]^+$, 402.9450; found 402.9449.



19c **Br$_4$-NHBoc**

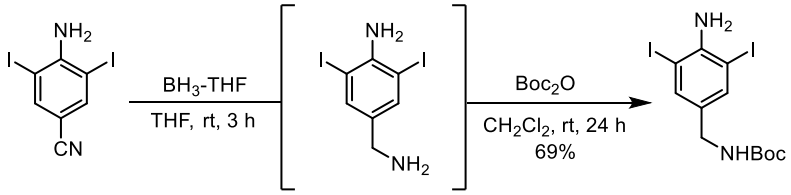
Br$_4$-NHBoc. Prepared according to ***General procedure 3*** from **19c** (211 mg, 555 µmol), DBU (167 µL, 1.11 mmol, 2 eq) and NCS (148 mg, 1.11 mmol, 2 eq) and was purified by silica gel flash chromatography (0 to 1% acetone in CH_2Cl_2) to afford the title compound as an orange solid (31.2 mg, 41.0 µmol, 15%). (*E*)-**Br$_4$-NHBoc:** ^{1}H NMR (600 MHz, $CDCl_3$) δ 7.63 (s, 4H), 4.98 (s, 2H), 4.36 (d, *J* = 6.2 Hz, 4H), 1.51 (s, 18H). ^{13}C NMR (151 MHz, $CDCl_3$) δ 155.76, 147.80, 142.29, 132.04, 116.28, 80.24, 43.26, 28.38. HRMS-EI (m/z) Calculated for $C_{24}H_{29}O_4N_4Br_4$ $[M+H]^+$, 756.8878; found 756.8870.



16 **17d**

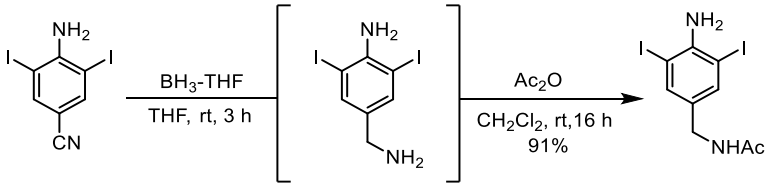
17d. Nitrile **16** (3 g, 25.39 mmol, 1 eq) was added to a mixture of Iodine (12.89 g, 50.8 mmol, 2 eq) and silver (I) sulfate (15.84 g, 50.8 mmol, 2 eq) in EtOH (210 mL). The reaction was stirred vigorously at room temperature for 4 hours. The reaction was filtered over a celite pad, then washed with EtOAc. The filtrate was concentrated, then redissolved in CH_2Cl_2 and subsequently washed with 1N NaOH, then water and dried over magnesium sulfate. The dark brown mixture was dissolved in hot EtOH (120 mL), then filtered. The filtrate was cooled to room temperature. The formed crystals were collected and washed with cold ethanol and

pentane to afford the title compound as brown/purple crystals (3 g, 8.1 mmol, 32%). ^{1}H NMR (400 MHz, $CDCl_3$) δ 7.88 (s, 2H), 5.17 (s, 2H). Data consistent with that given in the literature. [8]



17d **18d** **19d**

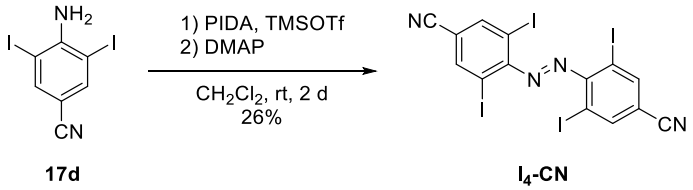
19d. Prepared according to ***General procedure 2*** from **17d** (1 g, 2.7 mmol) and Borane-THF (1M, 10.8 mL, 10.8 mmol, 4 eq) for 3 hours at rt to afford crude **18d**, ^{1}H NMR (400 MHz, $CDCl_3$) δ 7.59 (s, 2H), 4.54 (s, 2H). ***General procedure 2*** was continued using Boc_2O (590 mg, 2.7 mmol, 1.0 eq), then purified by silica gel flash chromatography (70% CH_2Cl_2 in hexane) to afford the title compound as a white solid (818 mg, 1.86 mmol, 69%). ^{1}NMR (600 MHz, $CDCl_3$) δ 7.55 (s, 2H), 4.76 (s, 1H), 4.58 (br s, 2H), 4.11 (d, *J* = 5.8 Hz, 2H), 1.46 (s, 9H). ^{13}C NMR (151 MHz, $CDCl_3$) δ 155.84, 145.54, 138.74, 132.09, 81.37, 79.90, 42.89, 28.54. HRMS-EI (m/z) Calculated for $C_{12}H_{16}N_2O_6I_2$ $[M+H]^+$, 496.9193; found 496.9193.



17d **18d** **22**

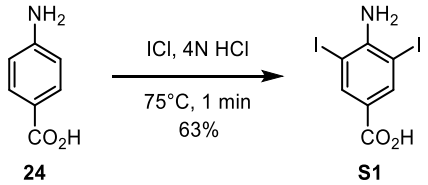
22. Reduction performed according to ***General procedure 2*** from **17d** (600 mg, 1.62 mmol) and Borane-THF (1M, 6.5 mL, 6.5 mmol, 4 eq) for 3 hours at rt to afford the crude **18d**. ^{1}H NMR (400 MHz, $CDCl_3$) δ 7.59 (s, 2H), 4.54 (s, 2H). The off-white solid was redissolved in CH_2Cl_2 (35 mL). Ac_2O (145 µL, 1.54 mmol, 0.95 eq) in CH_2Cl_2 (10 mL) was added dropwise, and the reaction was stirred for 16 hours at room temperature. The reaction was diluted in water, then extracted with CH_2Cl_2. The combined organic layers were concentrated and purified by silica gel flash chromatography (10% Acetone in CH_2Cl_2) to afford the title compound as a white solid (617 mg, 1.48 mmol, 91%). ^{1}H NMR (600 MHz, DMSO) δ 8.22 (t,

J = 6.0 Hz, 1H), 7.52 (s, 2H), 5.00 (s, 2H), 4.03 (d, *J* = 5.9 Hz, 2H), 1.83 (d, *J* = 3.1 Hz, 3H). ^{13}C NMR (151 MHz, DMSO) δ 169.49, 146.28, 138.76, 132.43, 81.88, 40.59, 23.05. HRMS-EI (m/z) Calculated for $C_9H_{11}N_2OI_2$ $[M+H]^+$, 416.8955; found 416.8953.



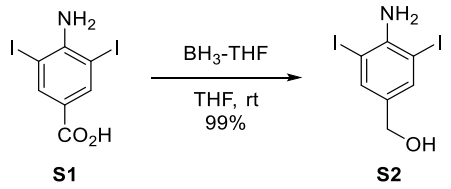
17d **I_4-CN**

I_4-CN. Prepared according to ***General procedure 5*** from PIDA (633 mg, 2.0 mmol, 1.5 eq), TMSOTf (712 µL, 3.9 mmol, 3 eq), DMAP (480 mg, 3.9 mmol, 3 eq) and Nitrile **17d** (500 mg, 1.35 mmol, 1 eq) and purified by silica gel flash chromatography (40% CH_2Cl_2 in hexane) to afford the title compound as a green solid (124 mg, 168.2 µmol, 26%). ^{1}H NMR (600 MHz, $CDCl_3$) δ 8.29 (d, *J* = 0.9 Hz, 4H). ^{13}C NMR (151 MHz, $CDCl_3$) δ 153.11, 143.99, 116.03, 115.13, 89.57. HRMS-EI (m/z) Calculated for $C_{12}H_{16}N_2O_6I_2$ $[M-H]^-$, 735.6620; found 735.6617.



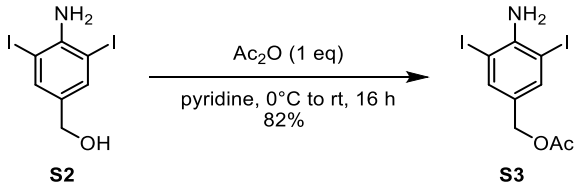
24 **S1**

S1. Prepared according to a modified literature procedure.[9] p-aminobenzoic acid **24** (3.5 g, 25.5 mmol) was dissolved in 12.5 % HCl (150 mL) at 75 °C. Iodine monochloride (15.6 g, 96 mmol, 4 eq) in 12% HCl (20 mL) was added. The reaction was stirred at 75 °C for one minute after which a light brown precipitate had formed. Water (300 mL) was added and a precipitate formed. The solution was allowed to cool to room temperature, and the solid was obtained by filtration. The filter cake was triturated with EtOH (~300 mL until the yellow washings were colourless) to afford the title compound as an off-white solid (6.3 g, 16.2 mmol, 63%). ^{1}H NMR (400 MHz, DMSO) δ 12.66 (s, 1H), 8.12 (s, 2H), 5.75 (br s, 2H). Data consistent with that given in the literature. [10]



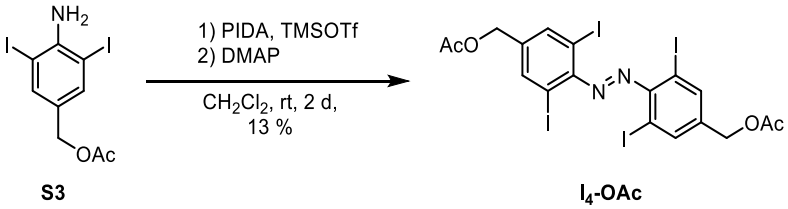
S1 **S2**

Alcohol **S2**. Reduction performed according to ***General procedure 2*** from Acid **S1** (6.3 g, 16.2 mmol) and Borane-THF (49 mL, 49 mmol, 3 eq) at rt for 16 h to afford **S2** as a white solid (6.0 g, 16 mmol, 99%). ^{1}H NMR (600 MHz, $CDCl_3$) δ 7.65 (s, 2H), 4.62 (s, 2H), 4.49 (d, *J* = 5.7 Hz, 2H), 1.55 (t, *J* = 5.89 Hz). ^{13}C NMR (151 MHz, $CDCl_3$) δ 145.82, 138.59, 134.02, 81.32, 63.60. HRMS-EI (m/z) Calculated for $C_7H_8NOI_2$ $[M+H]^+$, 375.8690; found 375.8689.



S2 **S3**

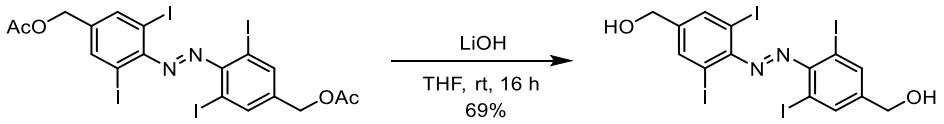
S3. Alcohol **S2** (6.0 g, 16 mmol) was dissolved in pyridine (50 mL). Ac_2O (1.5 mL, 16 mmol, 1 eq) was added dropwise at 0 °C. The reaction was stirred at rt overnight. The solution was concentrated and purified by silica gel flash chromatography (75% CH_2Cl_2 in hexane) to afford the title compound as a white solid (5.5 g, 13.2 mmol, 82%). ^{1}H NMR (600 MHz, $CDCl_3$) δ 7.64 (s, 2H), 4.88 (s, 2H), 4.68 (s, 2H), 2.08 (s, 3H). ^{13}C NMR (151 MHz, $CDCl_3$) δ 170.90, 146.39, 140.02, 128.90, 80.95, 64.45, 21.19. HRMS-EI (m/z) Calculated for $C_{17}H_6I_2$ $[M\text{-}OAc^-]^+$, 357.8584; found 357.8583.



S3 **I_4-OAc**

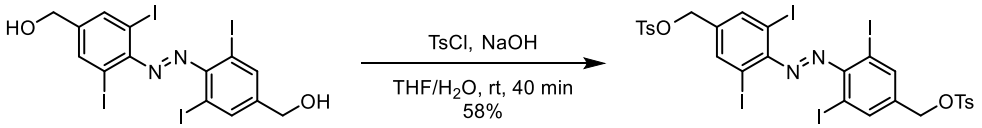
I_4-OAc. Prepared according to ***General procedure 5*** from PIDA (4.66 g, 14.5 mmol, 1.1 eq) TMSOTf (5 mL, 27.7 mmol, 2.1 eq), DMAP (3.38 g, 27.7 mmol, 2.1 eq) and **S3** (5.5 g, 13.2 mmol 1 eq) and was purified by silica gel flash chromatography (70% CH_2Cl_2 in hexane) to afford the title compound as a purple solid (691 mg, 832.6 µmol, 13 % [purity ca 90%]). ^{1}H

NMR (600 MHz, $CDCl_3$) δ 8.00 (s, 4H), 5.07 (s, 4H), 2.16 (s, 6H). ^{13}C NMR (151 MHz, $CDCl_3$) δ 170.67, 149.88, 140.57, 140.06, 90.15, 63.75, 21.06. HRMS-EI (m/z) Calculated for $C_{18}H_{15}N_2O_4I_4$ $[M+H]^+$, 830.7205; found 830.7206.



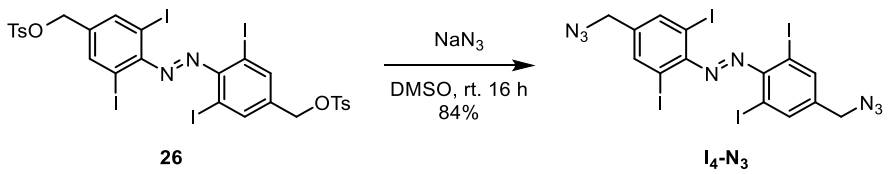
I_4-OAc **I_4-OH**

I_4-OH. I_4-OAc was dissolved in THF (20 mL) under N_2. LiOH (160 mg, 8 eq) in water (2 mL) was added and the reaction was stirred under ambient conditions for 16 hours. The reaction was diluted with CH_2Cl_2 and the organic layer separated and concentrated, then purified by silica gel flash chromatography (5% EtOAc in CH_2Cl_2) to afford the title compound as a purple solid (432 mg, 579 µmol, 69%). ^1H NMR (600 MHz, $CDCl_3$) δ 8.03 (s, 4H), 4.71 (s, 4H), 1.81 (br s, 2H). ^{13}C NMR (151 MHz, $CDCl_3$) δ 149.34, 144.85, 139.23, 90.33, 63.06. HRMS-EI (m/z) Calculated for $C_{14}H_{11}N_2O_2I_4$ $[M+H]^+$, 746.6994; found 746.6992.

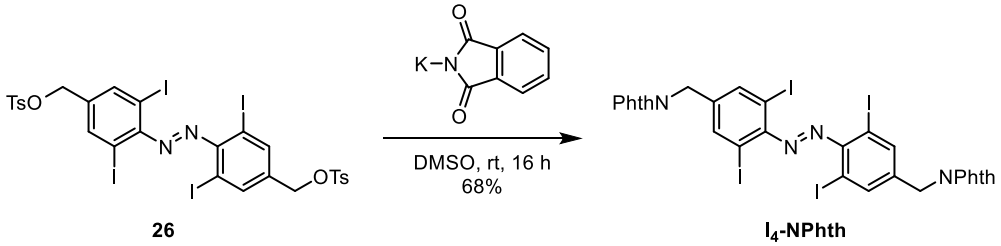


I_4-OH **26**

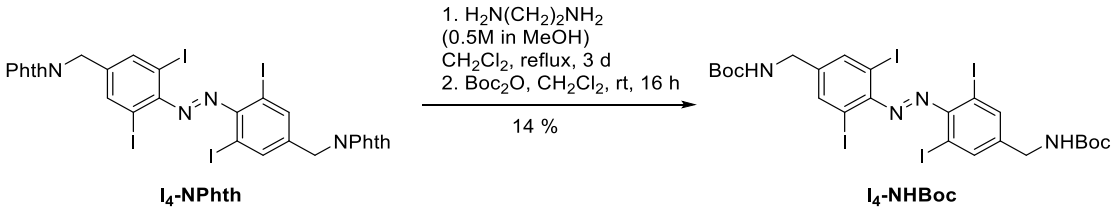
Tosylate 26. I_4-OH (40 mg, 53.6 µmol) was dissolved in 7:3 THF/H_2O (2.5 mL). NaOH (6.5 mg, 161 µmol, 3 eq), then TsCl (31 mg, 161 µmol, 3 eq) was added. The reaction was stirred at rt for 40 minutes under protection from light. The reaction was diluted with CH_2Cl_2, then washed with H_2O (3 x). The organic layer was concentrated, then purified by silica gel flash chromatography (dry load, 30% to 70% CH_2Cl_2 in hexane) to afford the title compound as a purple solid (33 mg, 31.3 µmol, 58%). ^1H NMR (600 MHz, $CDCl_3$) δ 7.82 (d, *J* = 1.0 Hz, 4H), 7.80 – 7.76 (m, 4H), 7.37 – 7.33 (m, 4H), 5.02 (s, 4H), 2.46 (s, 6H). ^{13}C NMR (151 MHz, $CDCl_3$) δ 150.30, 145.54, 140.64, 137.34, 133.12, 130.19, 128.13, 89.85, 68.97, 22.02. HRMS-EI (m/z) Calculated for $C_{28}H_{23}N_2O_6S_2I_4$ $[M+H]^+$, 1054.7171; found 1054.7173.



I_4-N_3. 26 (33 mg, 31 µmol) was dissolved in dry DMSO (0.5 mL) under N_2. Sodium azide (10.2 mg, 156 µmol, 5 eq) was added and the reaction was stirred at rt for 16 hours. Water was added (5 mL) and the reaction was extracted with Et_2O (3 x 10 mL). The combined organic layers were washed with water (3 x 10 mL). The organic layer was concentrated, then purified by silica gel flash chromatography (dry load, 30% CH_2Cl_2 in hexane) to afford the title compound as a purple solid (21 mg, 26.4 µmol, 84%). ^{1}H NMR (600 MHz, $CDCl_3$) δ 7.98 (s, 4H), 4.38 (s, 4H). ^{13}C NMR (151 MHz, $CDCl_3$) δ 149.77, 140.26, 139.55, 90.25, 52.50. HRMS-EI (m/z) Calculated for $C_{14}H_9N_8I_4$ $[M+H]^+$, 796.7123; found 796.7122.

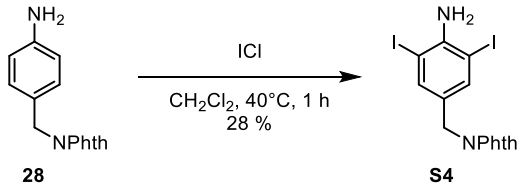


I_4-NPhth. 26 (80 mg, 76 µmol) was dissolved in DMSO (1 mL) under N_2. Potassium phthalimide (56 mg, 303.5 µmol, 4 eq) was added, and the reaction was stirred at room temperature for 16 hours. Water was added, and the solid was collected by filtration, washing with water and then Et_2O. The solid was dried to afford the title compound as a pink solid (52 mg, 51.8 µmol, 68%). ^{1}H NMR (600 MHz, $CDCl_3$) δ 8.06 (s, 4H), 7.92 – 7.87 (m, 4H), 7.78 – 7.73 (m, 4H), 4.79 (s, 4H). ^{13}C NMR (151 MHz, $CDCl_3$) δ 167.74, 149.60, 141.04, 139.94, 134.31, 131.94, 123.66, 90.15, 39.59. HRMS-EI (m/z) Calculated for $C_{30}H_{17}N_4O_4I_4$ $[M+H]^+$, 1004.7423; found 1003.2421.



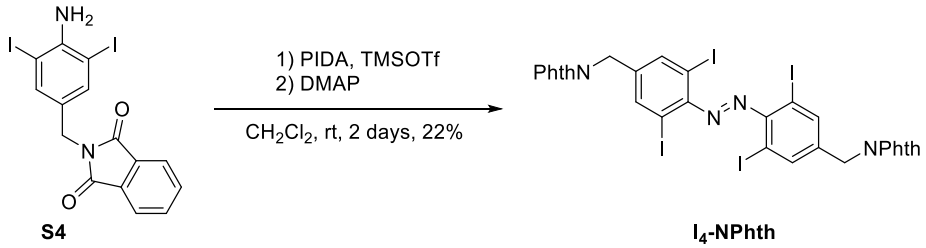
I_4-NPhth **I_4-NHBoc**

I_4-NHBoc. I_4-NPhth (71.7 µmol) was dissolved in CH_2Cl_2 (3 mL). Ethylene diamine (0.5M in MeOH) (1.72 mL, 860 µmol, 12 eq) was added and the reaction was stirred at 40 °C for 3 days. The reaction was concentrated, then redissolved in 1:1 CH_2Cl_2 (5 mL), and Boc_2O (60 mg, 285 µmol, 4 eq) was added. The reaction was stirred for 16 hours at room temperature, then concentrated. The residue was purified by silica gel flash chromatography (dry load, 80% CH_2Cl_2 in hexane) to recover starting material **I_4-NPhth** (22 mg, 22 µmol, 30%). The column was flushed with 2% MeCN in CH_2Cl_2 to afford the title compound as a purple solid (9.7 mg, 10.27 µmol, 14%). ^{1}H NMR (400 MHz, $CDCl_3$) δ 7.93 (s, 4H), 4.94 (s, 2H), 4.30 (d, *J* = 6.3 Hz, 4H), 1.49 (s, 18H). ^{13}C NMR (151 MHz, $CDCl_3$) δ 155.91, 149.25, 143.30, 139.90, 90.44, 80.36, 42.93, 28.54. HRMS-EI (m/z) Calculated for $C_{24}H_{29}N_4O_4I_4$ $[M+H]^+$, 944.8362; found 944.8364.

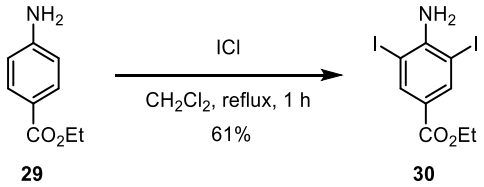


28 **S4**

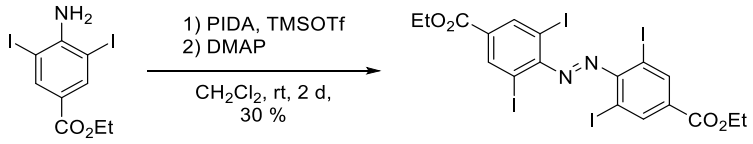
Aniline S4. Phthalimide **28** (880 mg, 3.49 mmol) was dissolved in CH_2Cl_2 (15 mL). Iodine monochloride (1.2 g, 7.33 mmol, 2.1 eq) in CH_2Cl_2 (10 mL) was added. The reaction was stirred at reflux temperature for 1 hour. The mixture was cooled to room temperature and then washed with sodium thiosulfate. The organic layer was dried and concentrated. The crude was purified by silica gel flash chromatography (60 to 80% CH_2Cl_2 in hexane) to afford the title compound as a white solid. (500 mg, 0.99 mmol, 28%). ^{1}H NMR (600 MHz, DMSO) δ 7.89 – 7.86 (m, 2H), 7.86 – 7.82 (m, 2H), 7.61 (s, 2H), 5.09 (s, 2H), 4.56 (s, 2H). ^{13}C NMR (151 MHz, DMSO) δ 167.65, 146.49, 138.69, 134.50, 131.56, 128.69, 123.20, 81.32, 38.87. HRMS-EI (m/z) Calculated for $C_{15}H_{11}N_2O_2I_2$ $[M+H]^+$, 504.8094; found 503.3567.



I_4-NPhth. Prepared according to ***General procedure 5*** from PIDA (351 mg, 1.09 mmol, 1.1 eq), TMSOTf (376 µL, 2.08 mmol, 2.1 eq), DMAP (254 mg, 2.08 mmol, 2.1 eq) and aniline **S4** (500 mg, 1 mmol, 1 eq) and was purified by silica gel flash chromatography (40% to 80% CH_2Cl_2 in hexane) to afford the title compound as a purple solid (108 mg, 107 µmol, 22 %). ^{1}H NMR (600 MHz, $CDCl_3$) δ 8.06 (s, 4H), 7.92 – 7.87 (m, 4H), 7.78 – 7.73 (m, 4H), 4.79 (s, 4H). ^{13}C NMR (151 MHz, $CDCl_3$) δ 167.74, 149.60, 141.04, 139.94, 134.31, 131.94, 123.66, 90.15, 39.59. HRMS-EI (m/z) Calculated for $C_{30}H_{17}N_4O_4I_4$ $[M+H]^+$, 1004.7423; found 1003.2421.

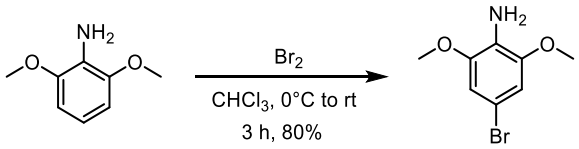


Aniline 30. Benzocaine **29** (2.0 g, 12.11 mmol) was dissolved in CH_2Cl_2 (30 mL). Iodine monochloride (4.91 g, 30.3 mmol, 2.5 eq) in CH_2Cl_2 (20 mL) was added. The reaction was stirred at reflux temperature for 1 hour. The mixture was cooled to room temperature and then washed with sodium thiosulfate. The organic layer was dried and concentrated. The residue was triturated with Et_2O until the purple washings were colourless. The solid was dried to afford the title compound as a white solid (3.1 g, 7.43 mmol, 61 %). ^{1}H NMR (400 MHz, $CDCl_3$) δ 8.30 (s, 2H), 5.05 (s, 2H), 4.32 (q, *J* = 7.1 Hz, 2H), 1.37 (t, *J* = 7.1 Hz, 3H). Data consistent with that given in the literature. [11]



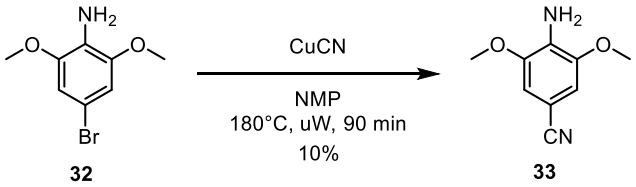
30 **I_4-ester**

I_4-Ester. Prepared according to ***General procedure 5*** from PIDA (3 g, 7.2 mmol, 1.0 eq) TMFOTf (2.73 mL, 15.1 mmol, 2.1 eq), DMAP (1.85 g, 15.1 mmol, 2.1 eq) and ester **30** (1.5 g, 3.6 mmol, 1 eq) and purified by silica gel flash chromatography (40% to 50% CH_2Cl_2 in hexane) to afford the title compound as a purple solid (900 mg, 1.08 mmol, 30 %). ^{1}H NMR (600 MHz, $CDCl_3$) δ 8.65 (s, 4H), 4.42 (q, *J* = 7.1 Hz, 4H), 1.43 (t, *J* = 7.1 Hz, 6H). ^{13}C NMR (151 MHz, $CDCl_3$) δ 163.33, 152.98, 142.06, 133.14, 89.16, 62.16, 14.45. HRMS-EI (m/z) Calculated for $C_{18}H_{15}N_2O_4I_4$ $[M+H]^+$, 830.7205; found 830.7203.



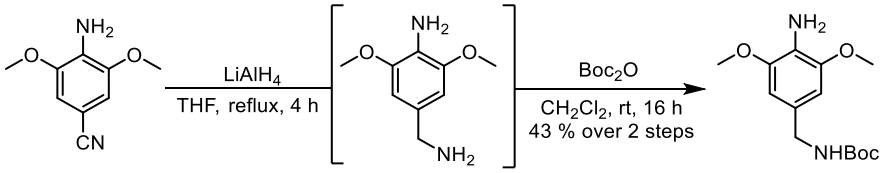
31 **32**

32. Prepared according to a literature procedure.[12] **31** (722 mg, 4.71 mmol, 1.03 eq) was dissolved in $CHCl_3$ (12 mL). Bromine (731 mg, 4.58 mmol, 1 eq) in $CHCl_3$ (12 mL) was added dropwise at 0 °C via a dropping funnel, then allowed to warm to room temperature over 3 hours. The reaction was quenched with aqueous sodium thiosulfate. The organic layer was separated and concentrated. The residue was purified by silica gel flash chromatography (90% CH_2Cl_2 in hexane) to afford the title compound as a white solid (849 mg, 3.67 mmol, 80%). ^{1}H NMR (400 MHz, $CDCl_3$) δ 6.66 (s, 2H), 4.34 – 3.06 (br s, 2H), 3.84 (s, 6H). Data consistent with that given in the literature. [12]



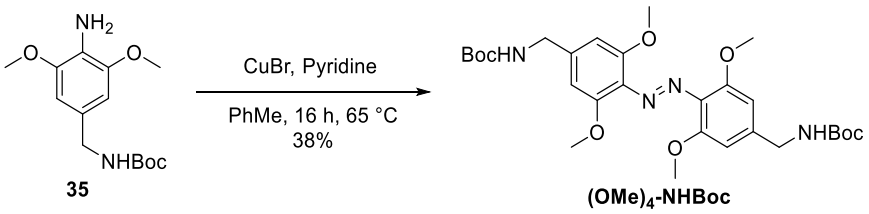
32 33

Nitrile 33. Prepared according to ***General procedure 1*** from **32** (740 mg, 3.19 mmol) and CuCN (571 mg, 6.38 mmol, 2 eq) at 180 °C for 90 min. and purified by silica gel flash chromatography (20% Acetone in hexane) to afford the title compound as a white solid (55 mg, 0.31 mmol, 10%). ^{1}H NMR (600 MHz, $CDCl_3$) δ 6.79 (d, *J* = 1.4 Hz, 2H), 3.87 (s, 6H). ^{13}C NMR (151 MHz, $CDCl_3$) δ 146.28, 131.08, 120.68, 98.14, 56.20. HRMS-EI (m/z) Calculated for $C_9H_{11}O_2N_2$ $[M+H]^+$, 179.0815; found 179.0815.

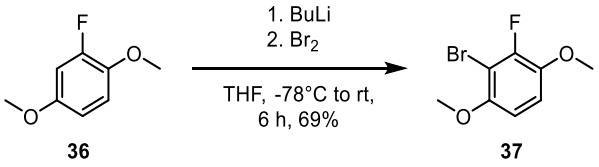


33 34 35

Aniline 35. Prepared according to ***General procedure 4*** from $LiAlH_4$ (75 mg, 2.04 mmol, 7 eq) and **33** (52 mg, 292 µmol, 1.0 eq), at reflux temperature for 16 hours to afford **34.** ^{1}H NMR (400 MHz, $CDCl_3$) δ 6.49 (s, 2H), 3.85 (s, 6H), 3.78 (s, 2H), 3.74 (br s, 2H). ***General procedure 4*** was continued using Boc_2O (60.5 mg, 6.93 mmol, 0.9 eq) in CH_2Cl_2 (15 mL) was was purified by silica gel flash chromatography (2% to 4% Acetone in CH_2Cl_2) to afford the title compound as a white solid (45.5 mg, 159 µmol, 55%). ^{1}H NMR (600 MHz, $CDCl_3$) δ 6.47 (s, 2H), 4.74 (s, 1H), 4.21 (d, *J* = 5.5 Hz, 2H), 3.84 (s, 6H), 1.47 (s, 9H). ^{13}C NMR (151 MHz, $CDCl_3$) δ 156.03, 147.56, 127.95, 124.67, 103.91, 79.49, 56.01, 45.38, 28.58. HRMS-EI (m/z) Calculated for $C_{14}H_{23}O_4N_2$ $[M+H]^+$, 283.1652; found 283.1648.

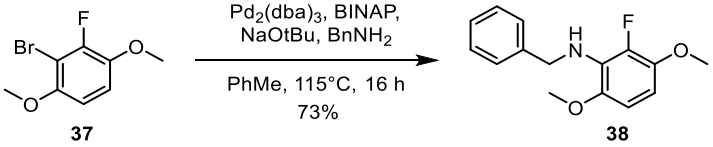


$(OMe)_4$-NHBoc. Prepared according to ***General procedure 6*** with Aniline **35** (43 mg, 152 mmol), Pyridine (25 µL, 304 mmol, 2 eq) and CuBr (22 mg, 152 µmol, 1 eq) and purified by silica gel flash chromatography (6% - 14% Acetone in CH_2Cl_2), to afford the title compound as an orange solid (16 mg, 29 µmol, 38%). ^{1}H NMR (600 MHz, $CDCl_3$) δ 6.58 (s, 4H), 4.90 (s, 2H), 4.30 (d, *J* = 6.0 Hz, 4H), 3.83 (s, 12H), 1.47 (s, 18H). ^{13}C NMR (151 MHz, $CDCl_3$) δ 155.99, 152.60, 140.97, 133.38, 104.30, 79.69, 56.61, 45.12, 28.41. HRMS-EI (m/z) Calculated for $C_{14}H_{23}O_4N_2$ $[M+H]^+$, 561.2919; found 561.2918.

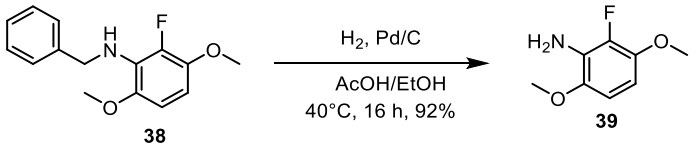


37. A flame-dried 250 mL round-bottom flask equipped with a magnetic stir-bar and a septum was charged with **36** (4.2 g, 25 mmol) and THF (100 mL). The reaction mixture was cooled to –78 °C in a dry ice/acetone bath and n-butyllithium (2.5 M in hexane, 11.3 mL, 26.5 mmol, 1.06 eq) was added dropwise. The reaction mixture was allowed to stir at –78 °C for 1 h, after which time bromine (1.46 mL, 25.5 mmol, 1.02 eq) was added dropwise via syringe and the reaction mixture was allowed to slowly warm up to room temperature for 6 h. The reaction was quenched with 100 mL of sat. $Na_2SO_{3\,(aq)}$. The aqueous and organic phases were separated and the aqueous phase was extracted with EtOAc (2 x 60 mL). The combined organic layers were dried over Na_2SO_4, filtered and concentrated. The crude residue was dissolved in CH_2Cl_2 and filtered through a short plug of silica gel, eluting with 20% CH_2Cl_2 in hexanes. The filtrate was concentrated and the residue was purified via column chromatography on silica gel (5% EtOAc in hexanes) to afford the title compound as white crystals (4.32 g, 17.12 mmol, 68%).

^{1}H NMR (500 MHz, CD_2Cl_2) δ 6.92 (t, *J* = 9.2 Hz, 1H), 6.66 (dd, *J* = 9.1, 2.2 Hz, 1H), 3.84 (s, 3H), 3.84 (s, 3H). Data consistent with that given in the literature.[13]

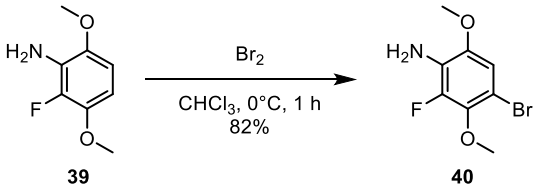


Protected amine 38. Aryl bromide **37** (1.5 g, 6.38 mmol), Pd_2dba_3 (292 mg, 0.32 mmol, 0.05 eq), rac-BINAP (238 mg, 0.383 mmol, 0.06 eq), benzylamine (2.74 g, 25.53 mmol, 4 eq) and sodium *tert*-butoxide (859 mg, 8.93 mmol, 1.4 eq) were added to a 20 mL microwave vial. The solids were purged with N_2 for 30 minutes. Degassed dry toluene (20 mL) was added, the tube was sealed and the reaction was stirred at reflux temperature for 16 hours. The solution was cooled and diluted with CH_2Cl_2 (100 mL). The organic layer was washed with 1M HCl (100 mL). The organic layer was collected and concentrated *in vacuo*. The residue was purified by silica gel flash chromatography (85% CH_2Cl_2 in hexane), to afford the title compound as a yellow oil (1.21 g, 6.38 mmol, 73%). ^{1}H NMR (500 MHz, $CDCl_3$) δ 7.41 – 7.20 (m, 5H), 6.48 (dd, *J* = 8.9, 2.0 Hz, 1H), 6.33 (t, *J* = 8.9 Hz, 1H), 4.51 (d, *J* = 1.8 Hz, 2H), 4.36 (br s, 1H), 3.82 (s, 3H), 3.78 (s, 3H). ^{13}C NMR (126 MHz, $CDCl_3$) δ 144.38 (d, *J* = 7.0 Hz), 153.57 (d, *J* = 238.4 Hz) 143.51 (d, *J* = 10.4 Hz), 128.59, 127.85, 127.70 (d, *J* = 9.5 Hz), 127.22, 104.97 (d, *J* = 3.2 Hz), 101.80 (d, *J* = 1.7 Hz), 56.77, 56.47, 50.74 (d, *J* = 7.8 Hz). HRMS-EI (m/z) Calculated for $C_{15}H_{17}O_2NF$ $[M+H]^+$, 262.1238; found 262.1239

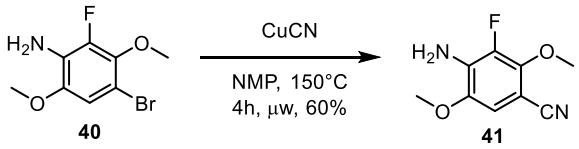


Aniline 39. Benzylamine **38** (600 mg, 2.30 mmol) was dissolved in 1:1 AcOH:EtOH (20 mL). The reaction vessel was evacuated and filled with nitrogen 3 x. Palladium 10% on carbon (570 mg) was added and the reaction was stirred under a hydrogen atmosphere for 16 hours at 40 °C. The reaction was filtered over celite, the filtrate concentrated to afford the title compound as a grey oil (360 mg, 2.1 mmol, 92%). ^{1}H NMR (400 MHz, $CDCl_3$) δ 6.54 – 6.40 (m, 1H), 6.28

(t, *J* = 9.0 Hz, 1H), 3.82 (m, 8H). ^{13}C NMR (101 MHz, $CDCl_3$) δ 142.85 (d, *J* = 6.2 Hz) 142.77 (d, *J* = 9.8 Hz), 141.93 (d, *J* = 236.4 Hz), 125.94 (d, *J* = 12.5 Hz), 104.89 (d, *J* = 3.2 Hz), 100.71, 56.77, 56.27. HRMS-EI (m/z) Calculated for $C_8H_{11}O_2NF$ $[M+H]^+$, 172.0768; found 172.0770

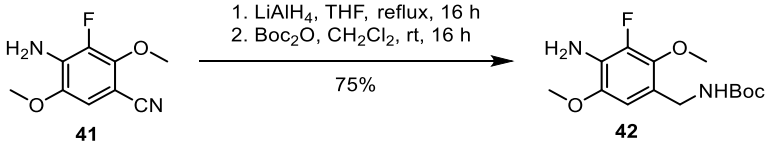


Aryl bromide 40. Aniline **39** (520 mg, 3.04 mmol) was dissolved in $CHCl_3$ (60 mL) and the solution was cooled to 0°C. Bromine (156 µL, 3.04 mmol, 1 eq) in 5 mL $CHCl_3$ was added dropwise and the reaction was stirred at this temperature for 1 hour. Saturated sodium thiosulfate was added and the organic layer was separated and concentrated *in vacuo*. The residue was purified by silica gel flash chromatography (85% CH_2Cl_2 in hexane) to afford the title compound as a grey oil which solidified over time (620 mg, 2.48 mmol, 82%). ^{1}H NMR (400 MHz, $CDCl_3$) δ 6.71 (d, *J* = 2.2 Hz, 1H), 3.86 (d, *J* = 0.8 Hz, 3H), 3.82 (s, 3H), 3.79 (s, 2H). ^{13}C NMR (126 MHz, $CDCl_3$) δ 146.36, 145.08 – 143.83 (m), 140.12 (d, *J* = 12.0 Hz), 125.62 (d, *J* = 13.7 Hz), 109.39 (d, *J* = 2.6 Hz), 102.75 (d, *J* = 3.9 Hz), 61.75 (d, *J* = 3.7 Hz), 56.34. HRMS-EI (m/z) Calculated for $C_8H_{10}O_2NBrF$ $[M+H]^+$, 249.9873; found 249.9875.



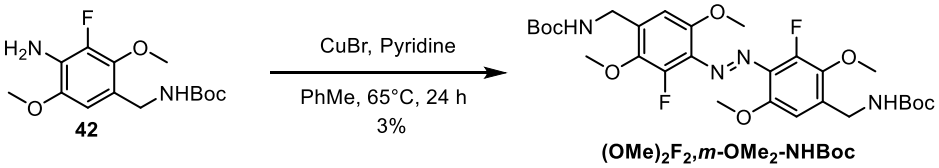
Nitrile 41. Prepared according to ***General procedure 1*** from Bromide **40** (589 mg, 2.36 mmol) and CuCN (316 mg, 3.53 mmol, 1.5 eq) at 150 °C for 4 h and purified by silica gel flash chromatography (75% CH_2Cl_2 in hexane) to afford the title compound as a white solid (620 mg, 2.48 mmol, 82%).^{1}H NMR (400 MHz, $CDCl_3$) δ 6.66 (d, *J* = 1.9 Hz, 1H), 4.30 (s, 2H), 4.02 (d, *J* = 1.7 Hz, 3H), 3.85 (s, 3H). ^{13}C NMR (126 MHz, $CDCl_3$) δ 145.82 (d, *J* = 10.9 Hz), 142.92 (d, *J* = 7.2 Hz), 142.82, (d, *J* = 7.2 Hz), 131.65 (d, *J* = 238.2 Hz), 116.99 (d, *J* = 4.8 Hz), 108.35

(d, *J* = 2.3 Hz), 91.73 (d, *J* = 4.9 Hz), 62.16 (d, *J* = 5.1 Hz), 56.26. HRMS-EI (m/z) Calculated for $C_9H_{10}O_2N_2F$ $[M+H]^+$, 197.0721; found 197.0722.



41 **42**

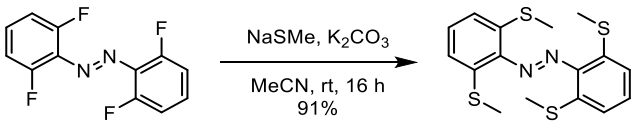
Aniline **42**. Prepared according to ***General procedure 4*** from $LiAlH_4$ (78 mg, 2.1 mmol, 3 eq) and **41** (135 mg, 0.69 mmol). At reflux temperature for 16 hours to afford the intermediate amine. ^{1}H NMR (400 MHz, $CDCl_3$) δ 6.47 (d, *J* = 2.0 Hz, 1H), 3.84 (d, *J* = 1.3 Hz, 3H), 3.80 (s, 3H), 3.73 (s, 2H). ***General procedure 4*** was continued using Boc_2O (135 mg, 0.9 eq) and was purified by silica gel flash chromatography (4% acetone in CH_2Cl_2) to afford the title compound as a white solid (156 mg, 0.52 mmol, 75%). ^{1}H NMR (400 MHz, $CDCl_3$) δ 6.50 (s, 1H), 4.91 (br s, 1H), 4.21 (d, *J* = 6.0 Hz, 2H), 3.84 (d, *J* = 1.3 Hz, 3H), 3.80 (s, 3H), 3.76 (br s, 2H), 1.43 (s, 9H). ^{13}C NMR (101 MHz, $CDCl_3$) δ 155.99, 144.93 (d, *J* = 238.44 Hz), 143.85 (d, *J* = 6.9 Hz), 140.34 (d, *J* = 9.7 Hz), 125.26 (d, *J* = 13.2 Hz), 119.74 (d, *J* = 2.1 Hz), 106.09, 79.38, 61.75 (d, *J* = 5.2 Hz), 56.17, 39.82, 28.53. HRMS-ESI (m/z) Calculated for $C_{14}H_{21}N_2O_4FNa$ $[M+Na]^+$, 323.1378; found 323.1382.



42 **(OMe)$_2$F$_2$,*m*-OMe$_2$-NHBoc**

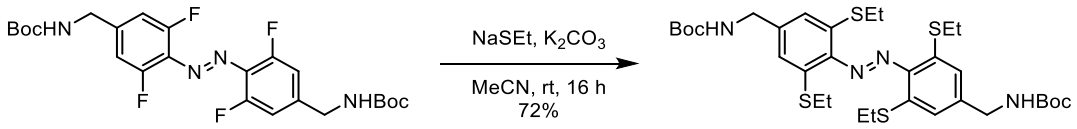
(OMe)$_2$F$_2$,*m*-OMe$_2$-NHBoc. Prepared according to ***General procedure 6*** with **Aniline 42** (154 mg, 520 µmol), Pyridine (125 µL, 1.56 mmol, 3 eq) and CuBr (74 mg, 520 µmol, 1 eq) and purified by silica gel flash chromatography (5% EtOAc, 1 % MeOH in CH_2Cl_2) then further purified by silica gel flash chromatography (50% EtOAc in in hexane) to afford the title compound as an orange solid (5 mg, 8 µmol, 3%). ^{1}H NMR (400 MHz, Acetone) δ 6.99 (d, *J* = 1.8 Hz, 1H), 6.52 (t, *J* = 6.2 Hz, 1H), 4.38 (d, *J* = 6.2 Hz, 2H), 3.90 (s, 3H), 3.85 (s, 3H), 1.44 (s, 9H). ^{13}C NMR (126 MHz, Acetone) δ 156.86, 150.68, 147.27 (d, *J* = 260 Hz), 140.44,

136.66, 133.58, 107.98, 79.11, 62.04, 57.16, 39.52, 28.63. HRMS-ESI (m/z) Calculated for $C_{28}H_{39}N_4O_8F_2Na$ $[M+H]^+$, 597.2730; found 597.2728.



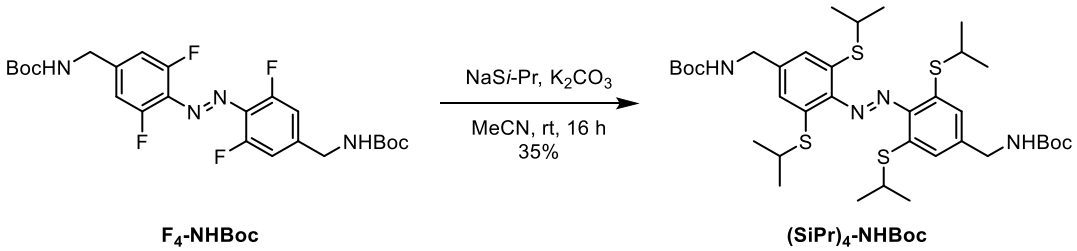
F_4-H **$(SMe)_4$-H**

(SMe_4)-H. Prepared according to ***General procedure 7*** from **F_4-H** (100 mg, 393 µmol), Sodium methanethiolate (200 mg, 3.15 mmol, 8 eq) and potassium carbonate (200 mg, 1.57 mmol, 4 eq) and purified by silica gel flash chromatography (0 to 60% hexane in CH_2Cl_2) to afford the title compound as an orange solid (131 mg, 357 µmol, 91%). ^{1}H NMR (400 MHz, $CDCl_3$) δ 7.27 (t, *J* = 7.9 Hz, 2H), 7.09 (d, *J* = 8.0 Hz, 4H), 2.43 (s, 12H). ^{13}C NMR (101 MHz, $CDCl_3$) δ 145.69, 138.18, 129.67, 120.74, 16.46. HRMS-EI (m/z) Calculated for $C_{16}H_{19}N_2S_4$ $[M+H]^+$, 367.0426; found 367.0424



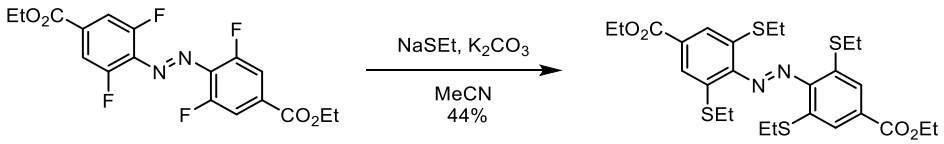
F_4-NHBoc **$(SEt)_4$-NHBoc**

$(SEt)_4$-NHBoc. Prepared according to ***General procedure 7*** from **F_4-NHBoc** (100 mg, 209 µmol), Sodium ethanethiolate (80%, 164 mg, 1.68 mmol, 8 eq) and potassium carbonate (107 mg, 836 µmol, 4 eq) and purified by silica gel flash chromatography (0 to 2% Acetone in CH_2Cl_2) to afford the title compound as an orange solid (96 mg, 141 µmol, 72%). ^{1}H NMR (400 MHz, $CDCl_3$) δ 7.03 (s, 4H), 4.88 (br s, 2H), 4.30 (d, *J* = 6.2 Hz, 4H), 2.91 (q, *J* = 7.4 Hz, 8H), 1.47 (s, 18H), 1.32 (t, *J* = 7.3 Hz, 12H). ^{13}C NMR (126 MHz, $CDCl_3$) δ 155.92, 145.85, 140.17, 137.10, 121.02, 79.74, 28.41, 26.76, 13.40. HRMS-EI (m/z) Calculated for $C_{32}H_{49}O_4N_4S_4$ $[M+H]^+$, 681.2631; found 681.2623



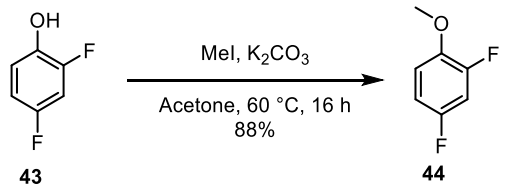
F_4-NHBoc **$(SiPr)_4$-NHBoc**

$(S^iPr)_4$-NHBoc. Prepared according to ***General procedure 7*** from **F_4-NHBoc** (100 mg, 195 µmol), Sodium 2-propanethiolate (90%, 164 mg, 1.56 mmol, 8 eq) and potassium carbonate (100 mg, 780 µmol, 4 eq) and purified by silica gel flash chromatography (0 to 1% Acetone in CH_2Cl_2) to afford the title compound as an orange solid (950 mg, 68 µmol, 35%). ^{1}H NMR (500 MHz, $CDCl_3$) δ 7.17 (s, 4H), 4.88 (s, 2H), 4.31 (d, *J* = 6.1 Hz, 4H), 3.48 (hept, *J* = 6.7 Hz, 4H), 1.48 (s, 18H), 1.27 (d, *J* = 6.6 Hz, 24H). ^{13}C NMR (126 MHz, $CDCl_3$) δ 155.88, 148.52, 139.51, 135.28, 124.44, 79.71, 44.50, 28.40, 22.77. HRMS-EI (m/z) Calculated for $C_{36}H_{57}O_4N_4S_4$ $[M+H]^+$, 737.3251; found 737.3257



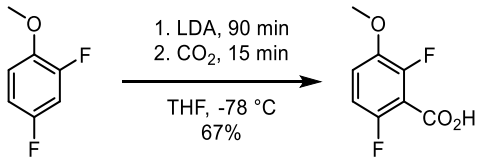
F_4-ester **$(SEt)_4$-ester**

$(SEt)_4$-ester. Prepared according to ***General procedure 7*** from **F_4-ester** (66 mg, 165 µmol), Sodium ethanethiolate (80%, 142 mg, 1.23 mmol, 7.5 eq) and potassium carbonate (150 mg, 0.99 mmol, 6 eq) were suspended in MeCN (3 mL) and purified by silica gel flash chromatography (50 to 70% CH_2Cl_2 in hexane) to afford title compound as a brown solid (41.7 mg, 73.5 µmol, 44%).^{1}H NMR (600 MHz, $CDCl_3$) δ 7.81 (s, 4H), 4.42 (q, *J* = 7.1 Hz, 4H), 3.00 (q, *J* = 7.4 Hz, 8H), 1.42 (t, *J* = 7.1 Hz, 6H), 1.35 (t, *J* = 7.4 Hz, 12H).^{13}C NMR (151 MHz, $CDCl_3$) δ 165.92, 148.84, 137.41, 130.66, 123.30, 61.63, 27.11, 14.47, 13.42. HRMS-EI (m/z) Calculated for $C_{26}H_{35}O_4N_2S_4$ $[M+H]^+$, 567.1474; found 567.1473



43 **44**

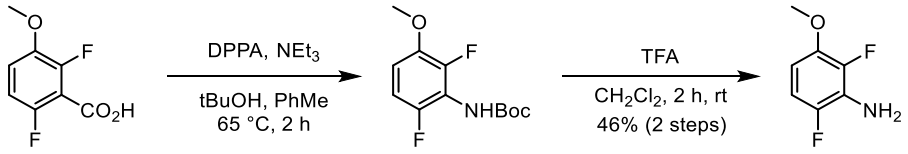
Anisole **44**. Phenol **43** (5.15 mL, 53.81 mmol) was dissolved in Acetone (50 mL). Potassium carbonate (29.8 g, 215.23 mmol, 4 eq) and methyl iodide (7.37 mL, 118.4 mmol, 2.2 eq) was added and the reaction was stirred at 60 °C for 16 hours. The mixture was filtered, then solvent removed *in vacuo*. The residue was dissolved in CH_2Cl_2, then washed with water. The organic layer was dried and concentrated to afford the title compound as a clear oil (6.85 g, 47.5 mmol, 88%). ^{1}H NMR (400 MHz, $CDCl_3$) δ 6.94 – 6.72 (m, 3H), 3.85 (s, 3H). ^{13}C NMR (101 MHz, $CDCl_3$) δ 156.43 (dd, *J* = 240.5, 10.4 Hz), 152.32 (dd, *J* = 248.3, 10.4 Hz), 144.39 (dd, *J* = 10.7, 3.4 Hz), 114.04 (dd, *J* = 9.5, 2.9 Hz), 110.34 (dd, *J* = 22.4, 4.1 Hz), 104.89 (dd, *J* = 27.0, 21.9 Hz). Data consistent with that given in the literature. [14]



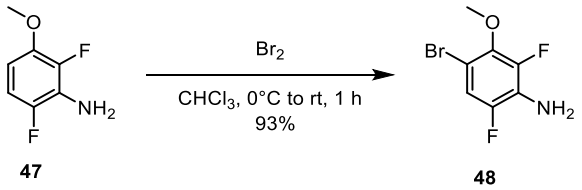
44 **45**

Acid 45. Difluoride **44** (6.85 g, 47.5 mmol) was dissolved in dry THF (50 mL). In a separate flask, BuLi (22.8 mL, 57.04 mmol, 1.2 eq) was added to DIPA (8.72 mL, 61.8 mmol, 1.3 eq) in dry THF (30 mL) at -78 °C. The solution was stirred at 0 °C for 15 minutes, then added dropwise to the solution of **44** at -78 °C. The solution was stirred at this temperature for 90 minutes. Then CO_2 (Dry ice, dried over $CaSO_4$) was bubbled through the mixture for 15 minutes, after which a solid precipitate formed. The reaction was warmed to 0 °C, and 8M HCl was added slowly until pH 1 was reached. The solution was extracted with ethyl acetate (3 × 100 mL). The organic layers were extracted with 5% aq. NaOH (3 × 100 mL). The NaOH extracts were adjusted to pH 1 with HCl and the white solid was filtered, washed with water then dried *in vacuo* to afford the title compound as a white solid (6 g, 31.9 mmol, 67%).^{1}H NMR (400 MHz, $CDCl_3$) δ 10.18 (s, 1H), 7.09 (td, *J* = 9.1, 4.9 Hz, 1H), 6.91 (td, *J* = 9.2, 2.1

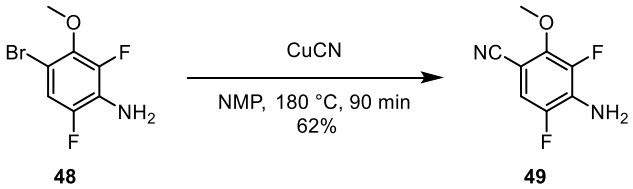
Hz, 1H), 3.90 (s, 3H). ^{13}C NMR (101 MHz, $CDCl_3$) δ 166.51, 154.45 (dd, *J* = 251.7, 4.8 Hz), 151.02 (dd, *J* = 259.4, 5.9 Hz), 144.79 (dd, *J* = 10.9, 3.5 Hz), 118.72 – 116.02 (m), 111.23 (dd, *J* = 23.3, 4.5 Hz), 110.40, 57.27. HRMS-ESI (m/z) Calculated for $C_8H_5O_3F_2$ $[M-H]^-$, 187.0212; found 187.0202.



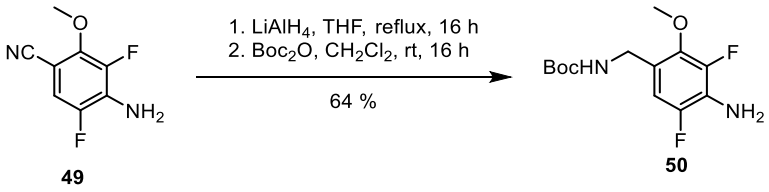
Aniline 47. To a mixture of **45** (4 g, 21.3 mmol), triethyl amine (3.26 mL, 23.4 mmol, 1.1 eq) and tert-butanol (2.22 mL, 1.73 g, 23.4 mmol, 1.1) in toluene (68 mL) was added diphenylphosphorylazide (4.25 mL, 22.32 mmol, 1.05 eq). The reaction was heated at 65 °C for 2 hours. The reaction mixture was evaporated and the residue was dissolved in ethyl acetate (70 mL), washed with sat KH_2PO_4, $NaHCO_3$ and brine, then dried over Na_2SO_4, filtered and evaporated under vacuum to give **46** as white solid. The residue was dissolved in CH_2Cl_2 (70 mL), then trifluoroacetic acid (15 mL) was added, and the reaction was stirred at room temperature for 2 hours. The reaction was dried under a stream of nitrogen, then concentrated *in vacuo*. The pH of the residue was adjusted to pH 8 with a saturated aqueous solution of sodium bicarbonate. The organic layer was separated and the aqueous layer is extracted with CH_2Cl_2 3x. The organic extracts were combined, then purified by silica gel flash chromatography (50% CH_2Cl_2 in hexane) to afford the title compound as a clear oil (1.54 g, 9.68 mmol, 46% [2 steps]. ^{1}H NMR (400 MHz, $CDCl_3$) δ 6.71 (ddd, *J* = 10.2, 9.2, 2.3 Hz, 1H), 6.26 (td, *J* = 9.1, 4.8 Hz, 1H), 3.83 (s, 3H), 3.81 – 3.64 (m, 2H). ^{13}C NMR (101 MHz, $CDCl_3$) δ 146.71 (dd, *J* = 233.4, 5.5 Hz), 144.52 (dd, *J* = 8.9, 2.6 Hz), 141.88 (dd, *J* = 238.7, 6.8 Hz), 124.88 (dd, *J* = 17.6, 13.7 Hz), 109.09 (dd, *J* = 19.7, 3.7 Hz), 100.58 (d, *J* = 8.7 Hz), 56.61. HRMS-APCI (m/z) Calculated for $C_7H_8ONF_2$ $[M+H]^+$, 160.0568; found 160.0565.



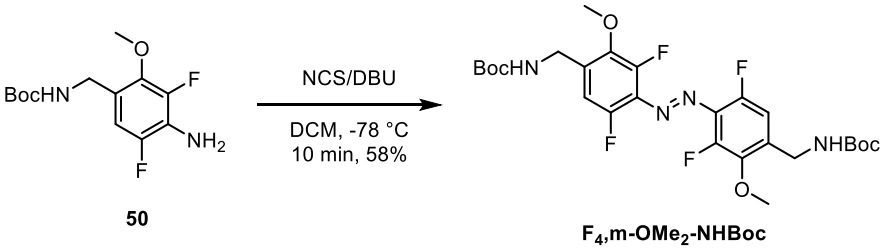
Bromide 48. Aniline **47** (1.44 g, 9.05 mmol) was dissolved in $CHCl_3$ (150 mL). Then bromine (1.45 g, 463.6 µL, 9.05 mmol, 1 eq) in chloroform (30 mL) was added slowly at 0°C. The reaction was allowed to warm up to room temperature over 1 hour, then was quenched with sodium thiosulfate solution. The organic layer was separated, then dried and concentrated to afford the title compound, which was left without further purification as a beige solid (2 g, 8.4 mmol, 93%). ^{1}H NMR (600 MHz, $CDCl_3$) δ 7.01 (m, 1H), 3.89 (t, *J* = 1.1 Hz, 3H), 3.77 (t, *J* = 1.0 Hz, 2H). ^{13}C NMR (151 MHz, $CDCl_3$) δ 147.73 (dd, *J* = 239.6, 7.2 Hz), 145.79 (dd, *J* = 243.1, 8.2 Hz), 142.47 (dd, *J* = 11.5, 3.8 Hz), 124.94 (dd, *J* = 17.3, 14.8 Hz), 114.16 (dd, *J* = 22.4, 3.3 Hz), 102.60 (dd, *J* = 11.1, 3.5 Hz), 61.75 (d, *J* = 4.1 Hz). HRMS-APCI (m/z) Calculated for $C_7H_6ONF_2Br$ $[M+H]^+$, 239.9653; found 240.0649.



Nitrile 49. Prepared according to ***General procedure 1*** with **48** (2.0 g, 8.4 mmol) and CuCN (978 mg, 10.9 mmol, 1.3 eq). at 180 °C for 90 minutes and purified by silica gel flash chromatography (50% CH_2Cl_2 in hexane) to afford the title compound as a white solid (962 mg, 5.22 mmol, 62%). ^{1}H NMR (400 MHz, $CDCl_3$) δ 6.98 (dd, *J* = 9.9, 2.1 Hz, 1H), 4.32 (s, 2H), 4.04 (d, *J* = 2.1 Hz, 3H). ^{13}C NMR (101 MHz, $CDCl_3$) δ 147.51 (dd, *J* = 10.4, 2.6 Hz), 145.98 (dd, *J* = 238.2, 6.8 Hz), 143.32 (dd, *J* = 241.4, 7.8 Hz), 131.08 (dd, *J* = 16.9, 13.8 Hz), 115.83 (t, *J* = 3.9 Hz), 114.05 (dd, *J* = 22.1, 3.1 Hz), 92.09 (dd, *J* = 10.7, 4.9 Hz), 62.18 (d, *J* = 5.7 Hz). HRMS-APCI (m/z) Calculated for $C_8H_7ONF_2$ $[M+H]^+$, 185.0521; found 185.0517.

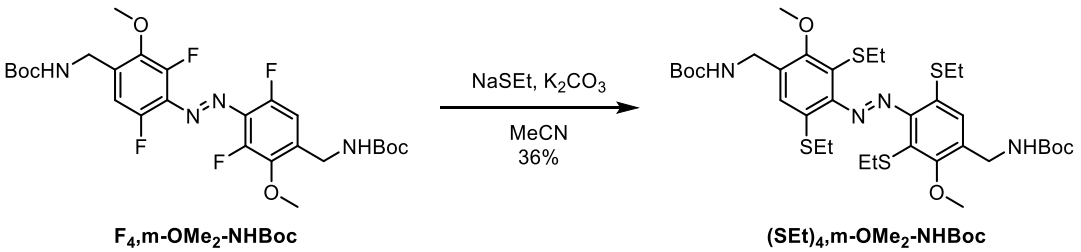


Aniline 50. Prepared according to ***General procedure 4*** from $LiAlH_4$ (705 mg, 15.6 mmol, 3 eq) and **49** (960 mg, 5.21 mmol) at reflux temperature for 16 hours to afford the intermediate amine. ^{1}H NMR (400 MHz, $CDCl_3$) δ 6.75 (dd, *J* = 10.8, 2.3 Hz, 1H), 3.90 (d, *J* = 1.6 Hz, 3H), 3.75 (s, 2H), 3.69 (s, 2H). ***General procedure 4*** was continued using Boc_2O (970 mg, 4.43 mmol, 0.85 eq) and was purified by silica gel flash chromatography (1% acetone in CH_2Cl_2) to afford the title compound as a white solid (966 mg, 3.35 mmol, 64%). ^{1}H NMR (400 MHz, $CDCl_3$) δ 6.74 (d, *J* = 10.7 Hz, 1H), 4.88 (s, 1H), 4.19 (d, *J* = 4.6 Hz, 2H), 3.88 (s, 3H), 3.42 (s, 2H), 1.43 (s, 9H). ^{13}C NMR (151 MHz, $CDCl_3$) δ 155.92, 147.48 (dd, *J* = 236.5, 6.6 Hz), 145.27 (dd, *J* = 241.0, 7.5 Hz), 142.32 (dd, *J* = 9.3, 3.2 Hz), 124.38 (dd, *J* = 17.6, 14.4 Hz), 120.42 (d, *J* = 7.7 Hz), 110.60 – 109.53 (m), 79.61, 61.66, 39.32, 28.54. HRMS-EI (m/z) Calculated for $C_{13}H_{18}F_2N_2O_2Na$ $[M+Na]^+$, 311.1178; found 311.1178.



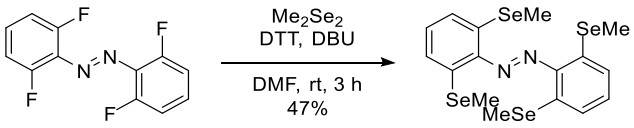
F_4,*m*-OMe_2-NHBoc. Prepared according to ***General procedure 3*** from **50** (966 mg, 3.35 mmol) in CH_2Cl_2 (52 mL), DBU (1 mL, 6.70 mmol, 2 eq) and NCS (902 mg, 6.70 mmol, 2 eq) and the residue was purified by silica gel flash chromatography (1 to 5% acetone in CH_2Cl_2) to afford the title compound as an orange solid (520 mg, 1.94 mmol, 58%). ^{1}H NMR (600 MHz, $CDCl_3$) δ 7.00 (d, *J* = 10.7 Hz, 1H), 4.99 (s, 1H), 4.37 (d, *J* = 6.2 Hz, 2H), 3.99 (d, *J* = 1.5 Hz, 3H), 1.46 (s, 9H). ^{13}C NMR (151 MHz, $CDCl_3$) δ 155.79, 150.75 (d, *J* = 258.0 Hz), 148.50 (d, *J* = 262.2 Hz), 142.31, 136.18, 131.41 (d, *J* = 9.9 Hz), 111.45 – 110.68 (m), 80.04, 61.67 (d,

J = 6.0 Hz), 39.59, 28.38. HRMS-EI (m/z) Calculated for $C_{26}H_{32}F_4N_4O_6Na$ $[M+Na]^+$, 595.2150; found 595.2139.



F_4,m-OMe_2-NHBoc **(SEt)$_4$,m-OMe_2-NHBoc**

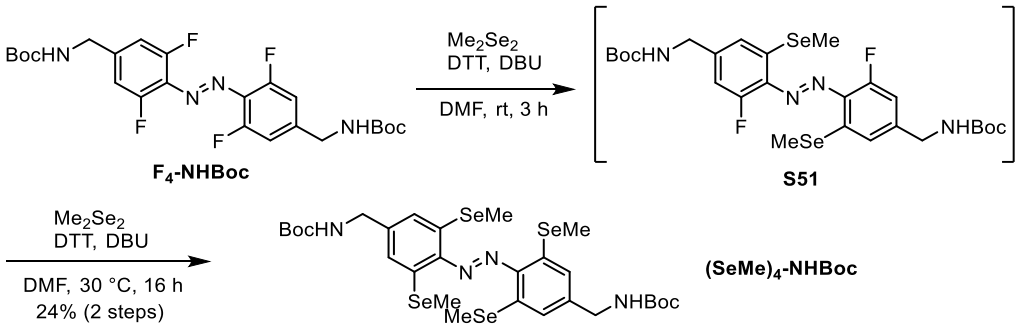
(SEt)$_4$,*m*-OMe_2-NHBoc. Prepared according to ***General procedure 7*** from **F_4,*m*-OMe_2-NHBoc** (100 mg, 174.7 µmol), NaSEt (80%, 147 mg, 1.40 mmol, 8 eq) and K_2CO_3 (97 mg, 0.7 mmol, 4 eq), and the residue was purified by silica gel flash chromatography (1% Acetone in CH_2Cl_2) to afford the title compound as a red solid (36 mg, 63 µmol, 36%).^{1}H NMR (600 MHz, $CDCl_3$) δ 7.35 (s, 2H), 5.03 (t, *J* = 6.3 Hz, 2H), 4.41 (d, *J* = 6.3 Hz, 4H), 3.97 (s, 6H), 2.89 (m, 8H), 1.49 (s, 18H), 1.26 (t, *J* = 7.3 Hz, 6H), 1.13 (t, *J* = 7.4 Hz, 6H). ^{13}C NMR (151 MHz, $CDCl_3$) δ 156.60, 156.05, 152.25, 133.27, 128.78, 127.38, 126.90, 79.77, 60.76, 40.41, 30.03, 28.57, 28.10, 14.95, 13.75. HRMS-EI (m/z) Calculated for $C_{34}H_{53}S_4N_4O_6$ $[M+H]^+$, 741.2842; found 741.2832.



F_4-H **(SeMe)$_4$-H**

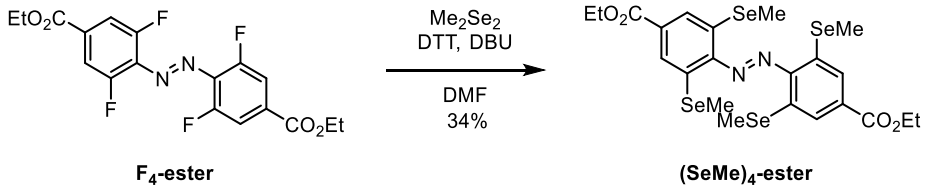
(SeMe$_4$)-H. Dry Dithiothreitol (61 mg, 393 µmol, 2.5 eq) was dissolved in dry DMF (2mL) under N_2 in a sealed tube. Dimethyldiselenide (45 µL, 472 µmol, 3 eq) and degassed DBU (211 uL, 1.42 mmol, 9 eq) was added. The solution was stirred at room temperature for 30 minutes. The solution was transferred via syringe into a separate vial containing **F_4-H** (40 mg, 157 µmol, 1 eq) in Dry DMF (1 mL) under N_2. The reaction was stirred for 3 h at room temperature, then water was added. The organic precipitate was extracted with EtOAc (2x). The combined organic layers were washed with water (2x), then concentrated. The resulting residue was purified by silica gel flash chromatography (40% CH_2Cl_2 in hexane) to afford the title compound

as a sparkly red solid (41 mg, 73 µmol, 47%). ^{1}H NMR (600 MHz, $CDCl_3$) δ 7.24 (d, *J* = 1.4 Hz, 4H), 7.18 (dd, *J* = 8.7, 6.7 Hz, 2H), 2.23 (s, 12H). ^{13}C NMR (151 MHz, $CDCl_3$) δ 148.23, 134.28, 130.02, 124.72, 7.09. HRMS-EI (m/z) Calculated for $C_{16}H_{19}N_2Se_4$ $[M+H]^+$, 554.8219; found 554.8227.



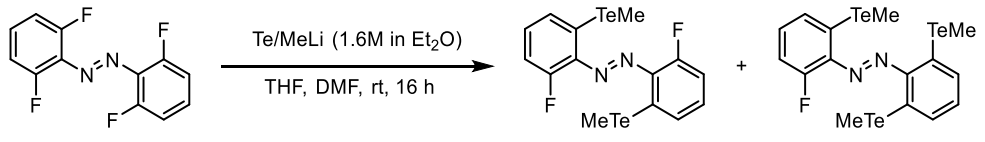
(SeMe$_4$)-NHBoc. Dry Dithiothreitol (53 mg, 341 µmol, 2.5 eq) was dissolved in dry DMF (1.5 mL) under N_2 in a sealed tube. Dimethyldiselenide (33 µL, 472 µmol, 3 eq) and degassed DBU (211 uL, 683 µmol, 5 eq) was added. The solution was stirred at room temperature for 30 minutes. The solution was transferred via syringe into a separate vial containing **F$_4$-NHBoc** (70 mg, 136 µmol, 1 eq) in Dry DMF (1 mL) under N_2. The reaction was stirred for 3 h at rt, after which H_2O was added. The precipitate was extracted with EtOAc (2x). The organic layer was washed with water (2x), then concentrated. The residue was purified by silica gel flash chromatography (100% CH_2Cl_2) to afford the title compound as an orange film (30 mg, 45 µmol, 33%). ^{1}H NMR (400 MHz, $CDCl_3$) δ 7.16 (s, 2H), 7.07 – 7.03 (d, *J* = 10.8, 1.1 Hz, 2H), 4.97 (s, 2H), 4.38 (d, *J* = 6.6 Hz, 4H), 2.22 (s, 6H), 1.48 (s, 18H). Then, dry Dithiothreitol (21 mg, 136 µmol, 3 eq) was dissolved in dry DMF (1 mL) under N_2 in a sealed tube. Dimethyldiselenide (13 µL, 136 µmol, 3 eq) and degassed DBU (27 uL, 181 µmol, 4 eq) was added via syringe. The solution was stirred at room temperature for 30 minutes. The solution was transferred into a separate vial containing **S51** (30 mg, 45 µmol, 1 eq) in Dry DMF (1 mL) under N_2. The reaction was stirred for 16 hours at 30 °C, after which water was added. The organic precipitate was extracted with EtOAc (2x). The combined organic layers were washed with water (2x), then concentrated. The resulting residue purified by silica gel flash chromatography (3% MeCN in CH_2Cl_2) to afford the title compound as an orange solid (27 mg,

45 µmol, 73%) [24% over 2 steps]. ^{1}H NMR (600 MHz, $CDCl_3$) δ 7.12 (s, 4H), 4.90 (s, 2H), 4.33 (d, *J* = 6.2 Hz, 4H), 2.22 (s, 12H), 1.48 (s, 18H).^{13}C NMR (151 MHz, $CDCl_3$) δ 156.08, 147.50, 141.19, 134.58, 123.73, 79.95, 28.56, 7.13. HRMS-EI (m/z) Calculated for $C_{28}H_{40}N_4O_4Se_4$ $[M+H]^+$, 814.9791; found 814.9798.



F_4-ester **$(SeMe)_4$-ester**

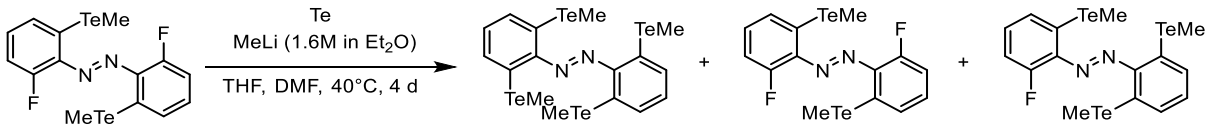
$(SeMe_4)$-ester. Dry Dithiothreitol (125 mg, 810 µmol, 3 eq) was dissolved in dry DMF (2 mL) under N_2 in a sealed tube. Dimethyldiselenide (81 µL, 472 µmol, 3 eq) and degassed DBU (322 uL, 1.42 mmol, 8 eq) was added via syringe. The solution was stirred at room temperature for 30 minutes. The solution was transferred into a separate vial containing **F_4-ester** (100 mg, 270 µmol, 1 eq) in Dry DMF (1 mL) under N_2. The reaction was stirred for 16 hours at room temperature after which a dark purple solution had formed. The mixture was poured into a separating funnel containing Et_2O (20 mL) and water (20 mL). The mixture was shook gently (which turned brown/orange), then the water layer removed. The organic layer was washed with water (2x), then concentrated. The resulting residue was purified by silica gel flash chromatography (10 to 100% CH_2Cl_2 in hexane) to afford the title compound as a brown solid (62 mg, 93 µmol, 34%). ^{1}H NMR (600 MHz, $CDCl_3$) δ 7.89 (s, 4H), 4.43 (q, *J* = 7.1 Hz, 4H), 2.31 (s, 12H), 1.43 (t, *J* = 7.1 Hz, 6H).^{13}C NMR (151 MHz, $CDCl_3$) δ 165.73, 150.35, 134.83, 131.18, 125.89, 61.75, 14.49, 7.50. HRMS-EI (m/z) Calculated for $C_{22}H_{27}N_2O_4Se_4$ $[M+H]^+$, 700.8634; found 700.8637.



F_4-H **Te_2F_2-H** (88%) **Te_3F-H** (4%)

Te_2F_2-H and **Te_3F-H.** Te powder (500 mg, 3.9 mmol) was added to dry THF (10 mL). MeLi (1.6M in Et_2O, 2.4 mL, 4 mmol, 1.2 eq) was added and the solution was stirred at room

temperature for 3 hours. The green/grey suspension was transferred into a separate vial containing **F_4-H** (200 mg, 786 µmol, 0.2 eq) in Dry DMF (3 mL) under N_2. The reaction was stirred for 16 hours at room temperature. The mixture was poured into a separating funnel containing Et_2O (100mL) and water (50 mL). The mixture was shook gently, then the water layer removed. The organic layer was dry loaded onto silica gel, and purified by silica gel flash chromatography (5% Hexane to 10% Hexane in CH_2Cl_2) to afford **Te_2F_2-H** as a sparkly dark purple solid. **Te_3F-H** was obtained with 15% hexane in CH_2Cl_2, then purified further using preparative TLC (15% hexane in CH_2Cl_2). **Te_2F_2-H**: ^{1}H NMR (600 MHz, $CDCl_3$) δ 7.48 (d, *J* = 7.9 Hz, 2H), 7.32 (td, *J* = 7.9, 5.2 Hz, 2H), 7.22 (ddd, *J* = 10.5, 8.0, 1.2 Hz, 2H), 1.96 (s, 6H). ^{13}C NMR (151 MHz, $CDCl_3$) δ 162.58 (d, *J* = 263.7 Hz), 139.50 (d, *J* = 9.9 Hz), 130.82 (d, *J* = 8.4 Hz), 128.40 (d, *J* = 3.8 Hz), 117.43 (d, *J* = 3.6 Hz), 113.13 (d, *J* = 19.8 Hz), -11.09. ^{19}F NMR (377 MHz, $CDCl_3$) δ -113.50. HRMS-EI (m/z) Calculated for $C_{14}H_{12}N_2F_2Te_2OH$ $[M+O+H]^+$, 520.9097; found 520.9094. **Te_3F-H**: ^{1}H NMR (600 MHz, $CDCl_3$) δ 7.47 (d, *J* = 7.6 Hz, 2H), 7.43 (d, *J* = 7.9 Hz, 1H), 7.25 (dd, *J* = 8.0, 5.1 Hz, 1H), 7.15 (t, *J* = 9.1 Hz, 1H), 7.08 (t, *J* = 7.6 Hz, 1H), 2.04 (s, 5H), 1.99 (s, 3H). ^{13}C NMR (151 MHz, $CDCl_3$) δ 160.77 (d, *J* = 261.5 Hz), 153.09, 140.91 (d, *J* = 8.9 Hz), 131.03 (d, *J* = 8.3 Hz), 130.98, 130.09, 129.58 (d, *J* = 8.9 Hz), 121.75, 115.02 (d, *J* = 2.1 Hz), 113.78 (d, *J* = 19.8 Hz), -12.00, -13.99. HRMS-EI (m/z) Calculated for $C_{15}H_{15}N_2FTe_3OH$ $[M+O+H]^+$, 642.8381; found 642.8379.



F_4-H **$(TeMe)_4$-H** (0.7%) **Te_2F_2-H** (57%) **Te_3F-H** (14%)

$(TeMe)_4$-H. Te powder (500 mg, 3.9 mmol) was added to dry THF (10 mL). MeLi (1.6M in Et_2O, 2.4 mL, 4 mmol, 1.2 eq) was added and the solution was stirred at room temperature for 3 hours. The green/grey suspension was transferred into a separate vial containing **Te_2F_2-H** (190 mg, 379 µmol, 1 eq) in Dry DMF (1 mL) under N_2. The reaction was stirred for 48 hours at 40 °C. In a separate flask, Te powder (500 mg, 3.9 mmol) was added to dry THF (10 mL). MeLi (1.6M in Et_2O, 2.4 mL, 4 mmol, 1.2 eq) was added and the solution was stirred at room

temperature for 3 hours. This mixture was added to the solution of **Te_2F_2-H**, and this was stirred for a further 48 hours at 40 °C. The mixture was poured into a separating funnel containing Et_2O (50 mL) and water (30 mL). The mixture was shook gently, then the water layer removed. The organic layer was dry loaded onto silica gel, and purified by silica gel flash chromatography (5% Hexane to 10% Hexane in CH_2Cl_2) to afford **Te_2F_2-H** as a sparkly dark purple solid (108 mg, 215 µmol, 57%). The trisubstituted compound was obtained by silica gel flash chromatography (15% hexane in CH_2Cl_2; 33 mg, 53 µmol, 14%). The tetra substituted compound was isolated using 20% Hexane in CH_2Cl_2, then purified further using preparative TLC (20% Hexane in CH_2Cl_2) to afford **$(TeMe)_4$-H** (2 mg, 2.7 µmol, 0.7%). ^{1}H NMR (400 MHz, CD_2Cl_2) δ 7.43 (d, *J* = 7.7 Hz, 4H), 7.06 (t, *J* = 7.6 Hz, 2H), 2.02 (s, 12H). ^{13}C NMR (151 MHz, CD_2Cl_2) δ 154.04, 131.92, 130.57, 119.75, -14.68. HRMS-EI (m/z) Calculated for $C_{16}H_{18}N_2Te_4OH$ $[M+H+O]^+$, 766.7676; found 766.7682.

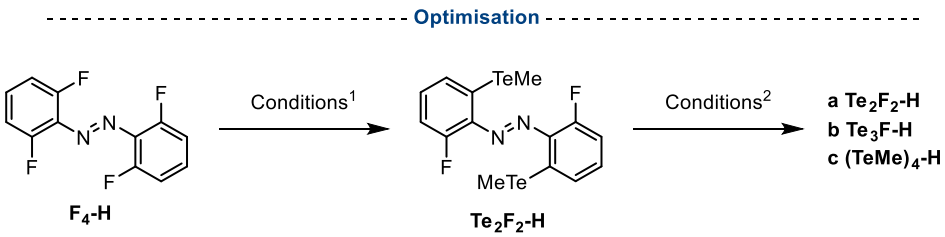
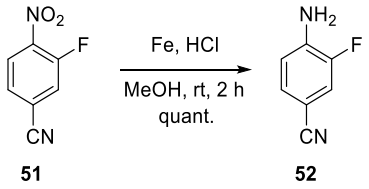


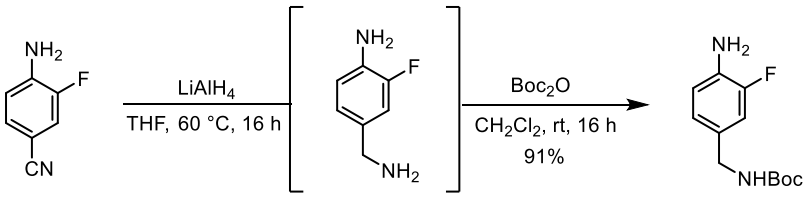
Table S1. Optimisation table for telluro azobenzene derivatives. It was necessary to prepare the tetra telluride step-wise via the ditelluride (conditions 2). Conditions 1 (analogous to Selenolate chemistry) [15] were less successful in generating products

	Conditions[1]	**Yield**
1	Me_2Te_2 (2.5 eq), DTT (2.5 eq), DBU (5 eq), DMF 0.1M, rt, 16 h	**a** 1.4%
2	Me_2Te_2 (2.5 eq), DTT (2.5 eq), DBU (5 eq), DMF 0.1M, **40 °C**, 16 h	No conv.
3	Me_2Te_2 (2.5 eq), DTT (2.5 eq), DBU (5 eq), DMF 0.1M, **30 °C 1 day, 35 °C 1 day**	No conv.
4	Me_2Te_2 (2.5 eq), $NaBH_4$ (5 eq), DMF 0.1M, rt, 16 h	(Decomp)
5	Me_2Te_2 (2.5 eq), DTT (2.5 eq), DBU (5 eq), DMF 0.1M, rt, overnight, **Et_2O/water workup**	**a** 10%
6	Te (5 eq), MeLi (5 eq), THF/DMF, 16 h, Et_2O/water workup	**a** 88% **b** 4%
7	Te (10 eq), MeLi (10 eq), THF/DMF, 16 h , Et_2O/water workup	**a** 49% **b** 10%
	Conditions[2]	**Yield**
8	Me_2Te_2 (3 eq), DTT (3 eq), DBU (4 eq), DMF 0.1M, rt to 40 to 50 to 60 °C	**Yield**
9	Te (10 eq), MeLi (10 eq), THF/DMF, 40 °C, 2 days, then Te (10 eq), MeLi (10 eq), 40 °C, 1 more day.	No conv.



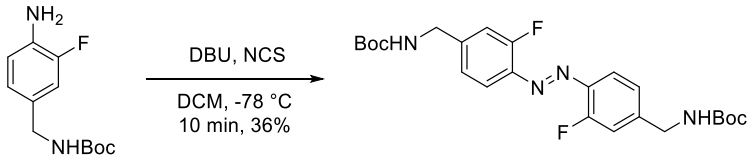
51 52

Aniline 52. Prepared according to a modified literature procedure.[16] Nitro compound **51** (1 g, 6 mmol) was dissolved in MeOH (10 mL), then iron powder (1 g, 18 mmol, 3 eq) was added. HCl (4 mL) was added carefully and the reaction was stirred at room temperature for 2 h. The solution was filtered over celite, then concentrated. The residue was extracted with EtOAc and basified with 10% $NaHCO_3$. The combined organic layer was dried and filtered to afford the title compound (820 mg, 6 mmol, quant). ^{1}H NMR (400 MHz, DMSO) δ 7.50 (dd, *J* = 11.7, 1.9 Hz, 1H), 7.30 (dd, *J* = 8.3, 1.9 Hz, 1H), 6.80 (t, *J* = 8.7 Hz, 1H), 6.24 (s, 2H). Data consistent with that given in the literature. [16]



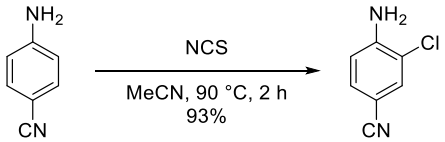
52 53

Aniline 53. Prepared according to ***General procedure 4*** from $LiAlH_4$ (686 mg, 18.1 mmol, 3 eq) and **52** (820 mg, 6 mmol, 1.0 eq) at reflux temperature for 16 h. ***General procedure 4*** was continued using Boc_2O (1.25 g, 5.7 mmol, 0.95 eq) was added and was purified by silica gel flash chromatography (0 to 2% Acetone in CH_2Cl_2) to afford the title compound as a yellow oil (1.32 g, 5.5 mmol, 91%). ^{1}H NMR (400 MHz, $CDCl_3$) δ 6.92 (dd, *J* = 11.6, 1.9 Hz, 1H), 6.87 – 6.79 (m, 1H), 6.71 (dd, *J* = 9.0, 8.1 Hz, 1H), 4.77 (s, 1H), 4.18 (d, *J* = 5.9 Hz, 2H), 3.69 (br s, 2H), 1.45 (s, 9H). ^{13}C NMR (101 MHz, $CDCl_3$) δ 155.94, 151.69 (d, *J* =240.1 Hz) 133.74 (d, *J* =12.9 Hz), 129.83 (d, *J* = 6.4 Hz), 123.73 (d, *J* = 3.7 Hz), 116.98 (d, *J* = 3.79 Hz), 114.73 (d, *J* = 18.7 Hz), 79.49, 43.98, 28.41. HRMS-ESI (m/z) Calculated for $C_{12}H_{18}FN_2O_2$ $[M+H]^+$, 241.1347; found 241.1349.



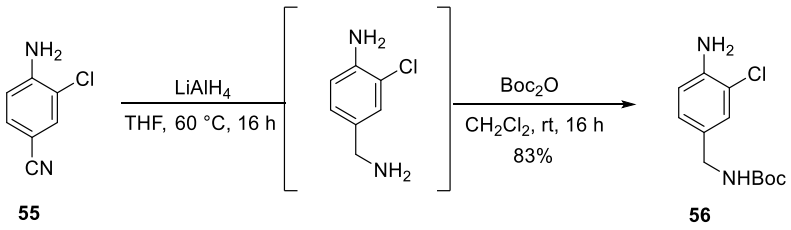
S53 **F_2,*m*-H_2**

F_2,*m*-H_2. Prepared according to ***General procedure 3*** from **53** (415 mg, 1.17 mmol), DBU (516 µL, 3.45 mmol, 2 eq) and NCS (526 mg, 3.45 mmol, 2 eq) and was purified by silica gel flash chromatography (0 to 2% Acetone in CH_2Cl_2) to afford the title compound as an orange solid as a mixture of isomers (150 mg, 315 µmol, 36%). *(E)*-**F_2,*m*-H_2**: ^{1}H NMR (400 MHz, $CDCl_3$) δ 6.96 (dd, *J* = 8.2, 1.7 Hz, 2H), 6.92 – 6.79 (m, 4H), 4.90 (s, 2H), 4.25 (d, *J* = 6.2 Hz, 4H), 1.44 (s, 18H). ^{13}C NMR (151 MHz, $CDCl_3$) δ 160.57 (d, *J* = 258.9 Hz), 156.02, 145.33, 140.01 (d, *J* = 6.8 Hz), 123.14, 118.17, 115.72 (d, *J* = 20.5 Hz), 80.13, 44.17, 28.52. HRMS-ESI (m/z) Calculated for $C_{24}H_{30}F_2N_4O_4$ $[M+H]^+$, 477.2308; found 477.2307.

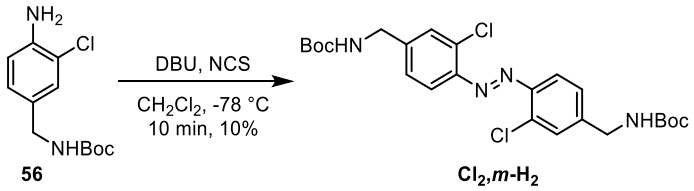


54 **55**

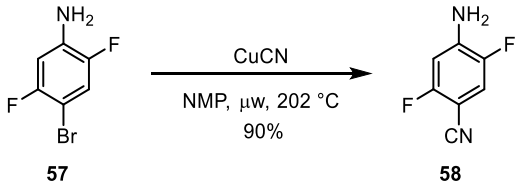
Aniline 55. Nitrile **54** (1 g, 8.5 mmol), then NCS (1.24 g, 9.3 mmol, 1.1 eq) in MeCN (10 mL) were stirred at 90°C for 2 h. The mixture was cooled, concentrated, then dissolved in 50 mL CH_2Cl_2. The organic layer was washed with 5% NaOH, then dried and concentrated to afford the title compound as a beige solid (1.2 g, 7.86 mmol, 93%). ^{1}H NMR (400 MHz, $CDCl_3$) δ 7.53 (d, *J* = 1.8 Hz, 1H), 7.34 (dd, *J* = 8.4, 1.9 Hz, 1H), 6.75 (d, *J* = 8.4 Hz, 1H), 4.55 (s, 2H). Data consistent with that given in the literature. [17]



Aniline 56. Prepared according to ***General procedure 4*** using $LiAlH_4$ (746 mg, 19.66 mmol, 3 eq) and **55** (1 g, 6.55 mmol, 1.0 eq) at reflux temperature for 16 h. ***General procedure 4*** was continued using Boc_2O (1.36 g 6.23 mmol, 0.95 eq) and was purified by silica gel flash chromatography (3% acetone in CH_2Cl_2), to afford the title compound as a white solid (1.4 g, 5.45 mmol, 83%).^{1}H NMR (400 MHz, $CDCl_3$) δ 7.20 (d, *J* = 2.0 Hz, 1H), 7.04 – 6.99 (m, 1H), 6.77 (d, *J* = 8.2 Hz, 1H), 4.77 (s, 1H), 4.47 – 4.18, 4.20 (d, *J* = 5.8 Hz, 2H), 1.48 (s, 9H). Data consistent with that given in the literature. [18]

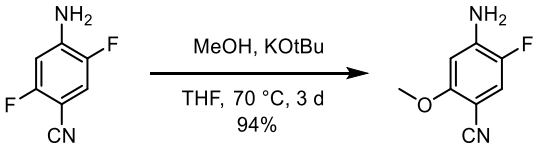


Cl_2,*m*-H_2: Prepared according to ***General procedure 3*** from **56** (1.4 g, 5.45 mmol), DBU (1.63 mL, 10.9 mmol, 2 eq) and NCS (1.46 g, 10.9 mmol, 2 eq) and the residue was purified by silica gel flash chromatography (1% EtOAc in CH_2Cl_2) to afford the title compound as an orange solid (141 mg, 277 µmol, 10%). *(E)*-**Cl_2,*m*-H_2**: ^{1}H NMR (400 MHz, $CDCl_3$) δ 7.74 (d, *J* = 8.3 Hz, 2H), 7.48 (d, *J* = 1.8 Hz, 2H), 7.25 (d, *J* = 8.3 Hz, 2H), 4.97 (s, 2H), 4.36 (d, *J* = 6.2 Hz, 4H), 1.48 (s, 18H). ^{13}C NMR (151 MHz, $CDCl_3$) δ 155.99, 148.04, 144.14, 136.28, 129.40, 126.40, 118.38, 80.16, 44.05, 28.53. HRMS-EI (m/z) Calculated for $C_{24}H_{31}O_4N_4Cl_2$ $[M+H]^+$, 509.1717; found 509.1717



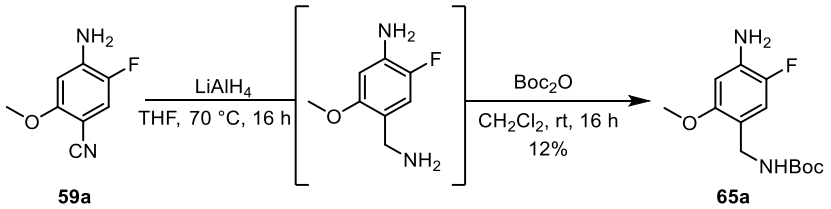
57 58

Nitrile 58. Prepared according to ***General procedure 1*** with Aryl bromide **57** (2.5 g, 12.02 mmol) and CuCN (1.3 g, 13.2 mmol, 1.2 eq) at 202°C for 90 minutes and left without further purification (1.67 g, 10.84 mmol, 90%). ^{1}H NMR (400 MHz, $CDCl_3$) δ 7.17 (dd, *J* = 10.2, 5.7 Hz, 1H), 6.51 (dd, *J* = 9.9, 7.1 Hz, 1H), 4.41 (s, 2H). Data consistent with that given in the literature. [19]



58 59a

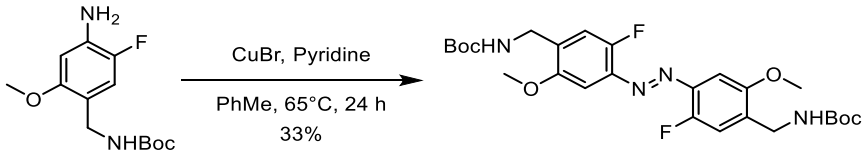
Aniline 59a. To a cooled (0°C) solution of methanol (43 mL) in anhydrous THF (25 ml) under N_2 was added KOtBu (4.8 g, 42.8 mmol, 2 eq). Then **58** (1.65 g, 10.7 mmol) was added to the solution. The reaction mixture was heated to 70°C and stirred for 3 days. The solvent was removed, then diethyl ether was added. The organic phase was washed with saturated bicarbonate solution, dried, then concentrated to afford the title compound as a white solid (1.68 g, 10.1 mmol, 94%). ^{1}H NMR (400 MHz, $CDCl_3$) δ 7.12 (d, *J* = 10.3 Hz, 1H), 6.27 (d, *J* = 7.2 Hz, 1H), 4.28 (s, 2H), 3.84 (s, 3H). Data consistent with that given in the literature. [20]



59a 65a

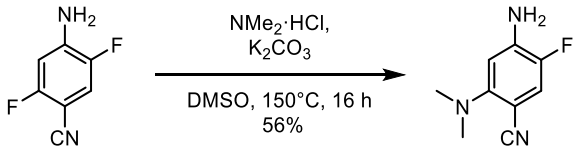
Aniline 65a. Prepared according to ***General procedure 4*** using $LiAlH_4$ (136 mg, 3.58 mmol, 2.5 eq) and **59a** (238 mg, 2.38 mmol, 1.0 eq) at reflux temperature for 16 h to afford the intermediate amine. ***General procedure 4*** was continued using Boc_2O (312 mg, 1.43 mmol, 1.0 eq) and was purified by silica gel flash chromatography (100% CH_2Cl_2), and the pure

fractions were combined to afford the title compound as a white solid (45 mg, 0.17 mmol, 12%). ^{1}H NMR (400 MHz, $CDCl_3$) δ 6.89 (d, *J* = 11.0 Hz, 1H), 6.27 (d, *J* = 7.4 Hz, 1H), 4.94 (s, 1H), 4.15 (d, *J* = 6.0 Hz, 2H), 3.73 (m, 5H), 1.43 (s, 9H). ^{13}C NMR (101 MHz, $CDCl_3$) δ 155.98, 153.99 (d, *J* = 1.9 Hz), 145.61 (d, *J* = 231.2 Hz), 134.10 (d, *J* = 14.2 Hz), 116.95 (d, *J* = 5.2 Hz), 116.24 (d, *J* = 20.4 Hz), 99.97 (d, *J* = 3.2 Hz), 79.30, 55.84, 39.75, 28.55. HRMS-EI (m/z) Calculated for $C_{13}H_{19}O_3N_2FNa$ $[M+Na]^+$, 293.1272; found 293.1271



65a **F_2,*m*-OMe_2**

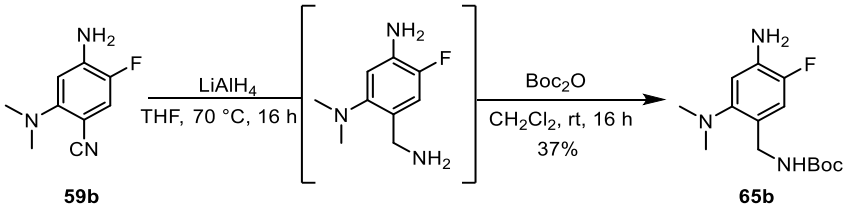
F_2,*m*-OMe_2. Prepared according to ***General procedure 6*** with Aniline **65a** (39 mg, 138 µmol), Pyridine (22µL, 0.28 mmol, 2 eq) and CuBr (20 mg, 137 µmol, 1 eq) and purified by silica gel flash chromatography (5% EtOAc in $CHCl_3$), and the pure fractions were combined to afford the title compound as an orange solid (12.5 mg, 45 µmol, 33%). *(E)*-**F_2,*m*-OMe_2:** ^{1}H NMR (400 MHz, $CDCl_3$) δ 7.21 (d, *J* = 5.9 Hz, 1H), 7.14 (d, *J* = 10.5 Hz, 1H), 4.97 (s, 1H), 4.27 (d, *J* = 6.3 Hz, 2H), 3.82 (s, 3H), 1.40 (s, 9H). ^{13}C NMR (101 MHz, $CDCl_3$) δ 155.87, 155.17 (d, *J* = 228.69 Hz), 153.61 (d, *J* = 1.9 Hz), 139.55 (d, *J* = 7.4 Hz), 133.34 (d, *J* = 7.2 Hz), 117.00 (d, *J* = 22.8 Hz), 98.10, 79.73, 55.96, 39.98, 28.42. ^{19}F NMR (377 MHz, $CDCl_3$) δ -132.84 (s). HRMS-EI (m/z) Calculated for $C_{26}H_{35}O_6N_4F_2$ $[M+H]^+$, 537.2519; found 537.2519



58 **59b**

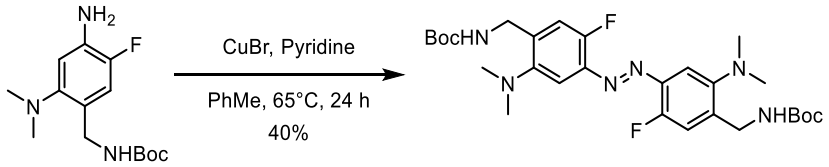
Amine 59b. Nitrile **58** (700 mg, 4.54 mmol) was dissolved in DMSO (15 mL) and, potassium carbonate (1.26 g, 9.08 mmol, 2 eq) and dimethylamine hydrochloride (1.46 g, 18.2 mmol, 4 eq) was added. The reaction was stirred at 80 °C for 16 hours, then for a further 4 hours at 150 °C after which the reaction was 60% complete. The solution was poured onto ice and extracted with Et_2O 5 x. The combined organic layers were washed with water, then

concentrated. The residue was purified by silica gel flash chromatography (100% CH_2Cl_2) to afford the title compound as a white solid (456 mg, 2.54 mmol, 56 %). ^{1}H NMR (400 MHz, $CDCl_3$) δ 7.07 (d, *J* = 10.6 Hz, 1H), 6.22 (d, *J* = 7.7 Hz, 1H), 4.23 (s, 2H), 2.89 (s, 6H). ^{13}C NMR (101 MHz, $CDCl_3$) δ 154.28, 144.52 (d, *J* = 234.6 Hz), 140.11 (d, *J* = 13.4 Hz), 120.00 (d, *J* = 21.4 Hz), 119.56 (d, *J* = 2.1 Hz), 103.87 (d, *J* = 3.6 Hz), 90.19 (d, *J* = 8.1 Hz), 43.53. HRMS-EI (m/z) Calculated for $C_9H_{11}FN_3$ $[M+H]^+$, 180.0937; found 180.0932



59b **65b**

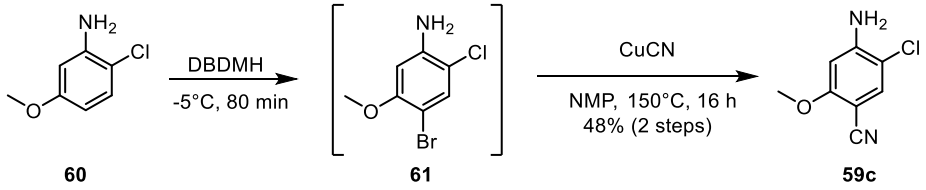
Aniline 65b. Prepared according to ***General procedure 4*** using $LiAlH_4$ (160 mg, 4.18 mmol, 2.5 eq) and **S59b** (300 mg, 4.18 mmol, 1.0 eq) at reflux temperature for 16 h to afford the crude amine and imine intermediate. ***General procedure 4*** was continued using Boc_2O (183 mg, 0.84 mmol, 0.5 eq) and was purified by silica gel flash chromatography (10% EtOAc in CH_2Cl_2 to afford the title compound as a yellow oil (176 mg, 0.62 mmol, 37%). ^{1}H NMR (400 MHz, $CDCl_3$) δ 6.84 (dd, *J* = 11.6, 2.2 Hz, 1H), 6.50 (dd, *J* = 8.3, 1.6 Hz, 1H), 5.24 (s, 1H), 4.23 (d, *J* = 5.9 Hz, 2H), 3.72 (s, 2H), 2.54 (d, *J* = 2.0 Hz, 6H), 1.42 (s, 9H). ^{13}C NMR (101 MHz, $CDCl_3$) δ 156.15, 148.76 (d, *J* = 2.6 Hz), 147.77 (d, *J* = 235.01 Hz), 133.69 (d, *J* = 13.8 Hz), 123.73, 115.37 (d, *J* = 20.0 Hz), 108.49 (d, *J* = 3.9 Hz), 79.16, 40.34, 28.43. HRMS-EI (m/z) Calculated for $C_{14}H_{23}O_2N_3F$ $[M+H]^+$, 284.1769; found 284.1769



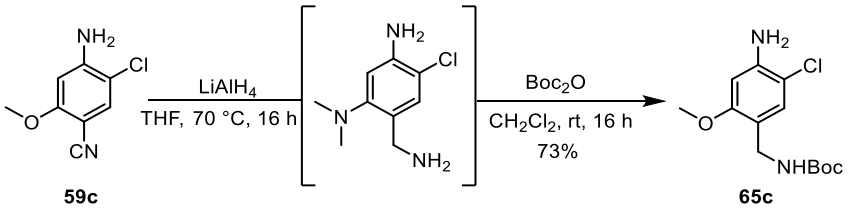
65b **F_2,*m*-$(NMe_2)_2$**

F_2,*m*-$(NMe_2)_2$. Prepared according to ***General procedure 6*** with Aniline **65b** (176 mg, 621 µmol), pyridine (100 µL, 1.24 mmol, 2 eq) and CuBr (89mg, 621 µmol, 1 eq) and purified by silica gel flash chromatography (5% Acetone in CH_2Cl_2), and the pure fractions were combined

to afford the title compound as an orange solid (70 mg, 123 µmol, 40%). (*E*)-**F_2,*m*-(NMe_2)$_2$:** ^{1}H NMR (500 MHz, $CDCl_3$) δ 7.51 (d, *J* = 7.0 Hz, 2H), 7.21 (d, *J* = 11.2 Hz, 2H), 5.18 (s, 2H), 4.46 (d, *J* = 7.4 Hz, 4H), 2.69 (s, 12H) 1.45, (s, 18H). ^{13}C NMR (126 MHz, $CDCl_3$) δ 157.05 (d, *J* = 218.6 Hz), 155.89, 148.68 (d, *J* = 2.5 Hz), 139.77, 139.61 (d, *J* = 7.5 Hz), 116.43 (d, *J* = 21.6 Hz), 108.33, 79.78, 45.03, 40.72, 28.45. HRMS-EI (m/z) Calculated for $C_{28}H_{41}O_4N_6F_2$ $[M+H]^+$, 563.3152; found 563.3148

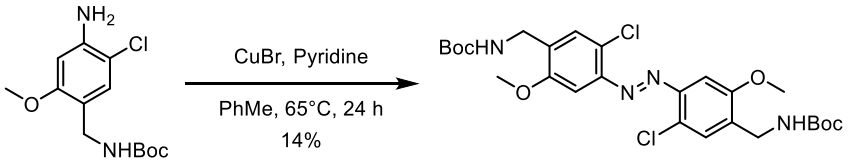


Nitrile 59c. Aniline **S60** (3 g, 19.04 mmol) was dissolved in EtOAc (50 mL). The reaction was cooled to -5 °C and DBDMH was added portionwise over 20 minutes at this temperature. The reaction was stirred at -5 °C for a further hour. Then, the organic layer was washed with K_2CO_3 (2 g) in water (13 mL), then water (20 mL). The organic later was concentrated to afford the intermediate bromide **S61** without further purification. The residue was subjected to ***General procedure 1*** with CuCN (2.56 g, 28.55 mmol, 1.5 eq) at 150°C for 16 h and purified by silica gel flash chromatography (70% CH_2Cl_2 in hexane) to afford the title compound as a white solid (1.67 g, 9.15 mmol, 48%). ^{1}H NMR (400 MHz, DMSO) δ 7.54 (s, 1H), 6.46 (s, 1H), 6.40 (s, 2H), 3.79 (s, 3H). Data consistent with that found in the literature. [21]



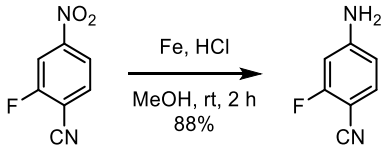
Aniline **65c**. Prepared according to ***General procedure 4*** using $LiAlH_4$ (624 mg, 16.43 mmol, 3 eq) and **59c** (1 g, 5.48 mmol, 1.0 eq) at reflux temperature for 16 h to afford the crude amine. ***General procedure 4*** was continued using Boc_2O (1.11 mg, 5.09 mmol, 0.93 eq) and was purified by silica gel flash chromatography (3% EtOAc in CH_2Cl_2), to afford the title compound

as a white solid (1.14 g, 3.98 mmol, 73%). ^{1}H NMR (400 MHz, $CDCl_3$) δ 7.11 (s, 1H), 6.27 (s, 1H), 4.89 (s, 1H), 4.14 (d, *J* = 5.44 Hz, 2H), 4.02 (s, 2H), 3.76 (s, 3H), 1.44 (s, 9H). ^{13}C NMR (126 MHz, $CDCl_3$) δ 157.09, 155.80, 142.98, 129.93, 118.26, 110.18, 98.64, 79.22, 55.51, 39.66, 28.46. HRMS-ESI (m/z) Calculated for $C_{13}H_{19}ClN_2O_3Na$ $[M+Na]^+$, 309.0975; found 309.0978.



65d **Cl_2,*m*-$(OMe)_2$**

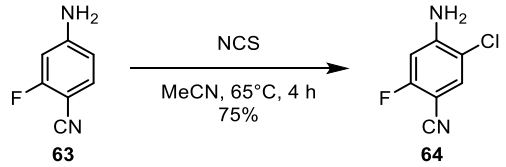
Cl_2,*m*-OMe_2. Prepared according to ***General procedure 6*** with Aniline **65d** (100 mg, 348 µmol), pyridine (56 µL, 0.7 mmol, 2 eq) and CuBr (50 mg, 348 µmol, 1 eq) and purified by silica gel flash chromatography (3% MeCN in $CHCl_3$) then further purified by silica gel flash chromatography (2% MeOH in CH_2Cl_2) to afford the title compound as an orange solid (14 mg, 24.6 µmol, 14%). *(E)*-**Cl_2,*m*-$(OMe)_2$:** ^{1}H NMR (400 MHz, $CDCl_3$) δ 7.45 (s, 2H), 7.33 (s, 2H), 5.02 (s, 2H), 4.34 (d, *J* = 6.3 Hz, 4H), 3.90 (s, 6H), 1.47 (s, 18H).^{13}C NMR (126 MHz, $CDCl_3$) δ 156.59, 155.96, 148.24, 132.80, 130.39, 128.50, 99.39, 79.87, 55.89, 40.05, 28.53. HRMS-ESI (m/z) Calculated for $C_{26}H_{35}Cl_2N_4O_6$ $[M+H]^+$, 569.1928; found 569.1928.



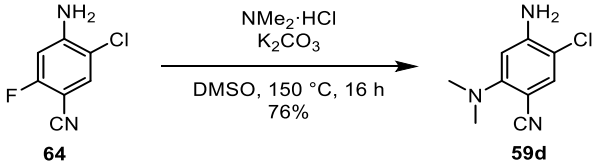
62 **63**

Aniline 63. To a solution of nitro compound **62** (2 g, 12 mmol) in MeOH (20 mL) was added Fe powder (2 g, 36 mmol, 3 eq). Then, concentrated HCl (8 mL) was added dropwise, and the reaction was stirred for 2 hours at room temperature. The reaction was filtered over celite and washed with MeOH. The filtrate was diluted with H_2O, then extracted with EtOAc. The combined organic layer was washed with saturated bicarbonate solution. The organic layer was dried with magnesium sulfate, filtered, then concentrated to afford the title compound as

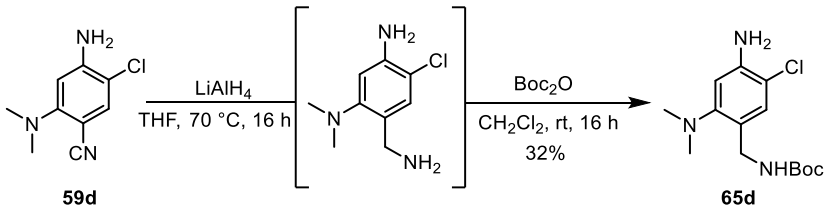
an off-white solid (1.45 g, 10.7 mmol, 88%). ^{1}H NMR (400 MHz, $CDCl_3$) δ 7.34 (dd, *J* = 8.4, 7.2 Hz, 1H), 6.49 – 6.32 (m, 2H), 4.60 – 3.50 (br s, 2H). Data consistent with that given in the literature. [22]



Nitrile 64. Aniline **S63** (1.25 g, 9.18 mmol) was dissolved in MeCN (63 mL). NCS (1.23 g, 9.18 mmol, 1 eq) was added and the reaction was stirred at 65 °C for 4 hours. The reaction was concentrated, then purified by silica gel flash chromatography (7:2:1 Hexane:CH_2Cl_2:EtOAc) to afford the title compound as a white solid (1.18 g, 6.92 mmol, 75%). ^{1}H NMR (400 MHz, $CDCl_3$) δ 7.46 (d, *J* = 6.4 Hz, 1H), 6.51 (d, *J* = 10.3 Hz, 1H), 4.71 (s, 2H). ^{13}C NMR (101 MHz, $CDCl_3$) δ 163.20 (d, *J* = 255.5 Hz), 148.84 (d, *J* = 12.0 Hz), 133.38 (d, *J* = 2.6 Hz), 117.31 – 109.78 (m), 101.71 (d, *J* = 24.5 Hz), 89.80 (d, *J* = 17.6 Hz). HRMS-EI (m/z) Calculated for $C_7H_3N_2FCl$ $[M-H]^-$, 168.9974; found 168.9966

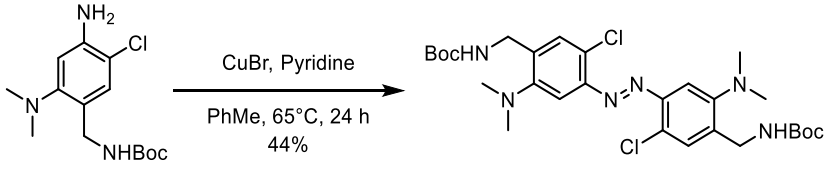


Aniline 59d. Aryl fluoride **64** (130 mg, 0.76 mmol) was dissolved in DMSO (4 mL). Then, dimethylamine hydrochloride (316 mg, 2.29 mmol, 3 eq) and potassium carbonate (615 mg, 7.6 mmol) was added. The reaction was stirred at 150 °C for 16 hours. The mixture was poured onto ice, then extracted with Et_2O 3x. The combined organic layer was washed with water, then concentrated. The residue was purified by silica gel flash chromatography (70% CH_2Cl_2 in hexane to 100% CH_2Cl_2) to afford the title compound as a white solid (114 mg, 0.58 mmol, 76%).^{1}H NMR (400 MHz, $CDCl_3$) δ 7.33 (s, 1H), 6.16 (s, 1H), 4.59 – 4.37 (m, 2H), 2.95 (s, 6H). ^{13}C NMR (101 MHz, $CDCl_3$) δ 155.64, 147.48, 135.11, 119.68, 109.66, 102.12, 91.48, 91.45, 43.08. HRMS-EI (m/z) Calculated for $C_9H_{11}N_3Cl$ $[M+H]^+$, 196.0636; found 196.0636



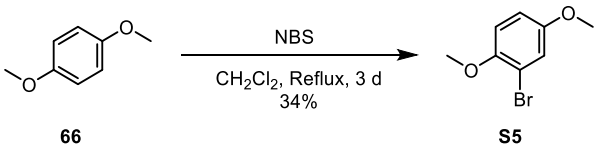
59d **65d**

Aniline 65d. Prepared according to ***General procedure 4*** using $LiAlH_4$ (66 mg, 1.75 mmol, 3 eq) and **59d** (114 mg, 0.58 mmol, 1.0 eq) at reflux temperature for 16 h to afford the crude amine intermediate. ***General procedure 4*** was continued using Boc_2O (64 mg, 0.29 mmol, 0.5 eq) and was purified by silica gel flash chromatography (CH_2Cl_2 to 10% EtOAc in CH_2Cl_2), and the pure fractions were combined to afford the title compound as a yellow oil (56 mg, 0.19 mmol, 32%). ^{1}H NMR (400 MHz, $CDCl_3$) δ 7.12 (s, 1H), 6.49 (s, 1H), 5.10 (s, 1H), 4.26 (d, *J* = 5.8 Hz, 2H), 3.99 (s, 2H), 2.61 (s, 6H), 1.45 (s, 9H). ^{13}C NMR (101 MHz, $CDCl_3$) δ 156.18, 152.21, 142.50, 129.72, 124.21, 113.78, 107.20, 79.39, 44.90, 40.59, 28.56. HRMS-EI (m/z) Calculated for $C_{14}H_{23}O_2N_3Cl$ $[M+H]^+$, 300.1473; found 300.1472



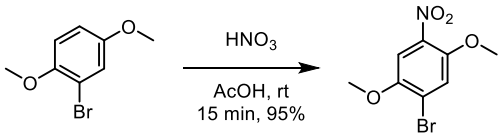
65d **Cl_2,*m*-$(NMe_2)_2$.**

Cl_2,*m*-$(NMe_2)_2$. Prepared according to ***General procedure 6*** with Aniline **65d** (56 mg, 187 µmol), Pyridine (45 µL, 0.56 mmol, 3 eq) and CuBr (27 mg, 187 µmol, 1 eq) and purified by silica gel flash chromatography (2.5% Acetone in CH_2Cl_2), and the pure fractions were combined to afford the title compound as an orange solid (24.5 mg, 41 µmol, 44%). *(E)*-**Cl_2,*m*-$(NMe_2)_2$:** ^{1}H NMR (400 MHz, $CDCl_3$) δ 7.52 (s, 1H), 7.48 (s, 1H), 5.16 (s, 1H), 4.46 (d, *J* = 5.9 Hz, 2H), 2.72 (s, 6H), 1.49 (s, 9H). ^{13}C NMR (151 MHz, $CDCl_3$) δ 156.30, 151.74, 147.98, 138.37, 130.68, 130.22, 108.58, 79.96, 44.77, 40.86, 28.54. HRMS-EI (m/z) Calculated for $C_{28}H_{41}O_4N_6Cl_2$ $[M+H]^+$, 595.2561; found 595.2559



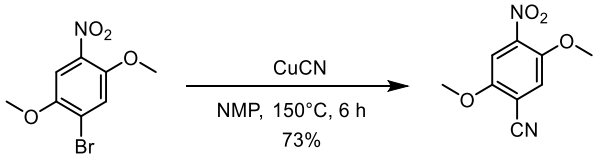
66 **S5**

Bromide S5. Dimethylhydroquinone **66** (8.28 g, 60 mmol) was dissolved in dry CH_2Cl_2 (50 mL). N-bromosuccinimide (11 g, 1.02 eq, 61.2 mmol) was added and the reaction was stirred at 35°C for 3 days. The reaction was concentrated, then purified by silica gel flash chromatography (20% CH_2Cl_2 in hexane). The pure fractions were combined to afford the title compound as a white solid (4.4 g, 20.2 mmol, 34%). ^{1}H NMR (400 MHz, $CDCl_3$) δ 7.13 (dd, *J* = 2.7, 0.6 Hz, 1H), 6.85 – 6.80 (m, 2H), 3.85 (s, 3H), 3.76 (s, 3H). Data matches that give in the literature. [23]



66 **67**

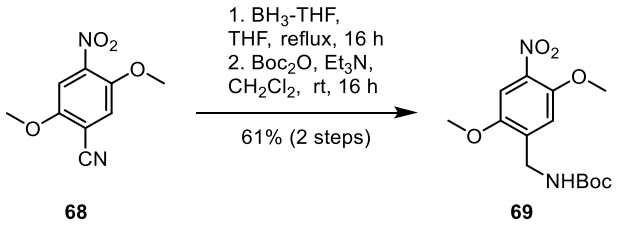
Nitro compound 67. 66 (4.4 g, 20.2 mmol) was suspended in AcOH (10 mL), then nitric acid (1.8 mL) was added. The solution immediately turned yellow and was stirred for a further 15 minutes at room temperature. H_2O (40 mL) was added and the suspension was stirred for 10 minutes. The precipitated solid was collected by filtration, then dried to afford the title compound as a yellow solid (5.03 g, 9.2 mmol, 95%). ^{1}H NMR (400 MHz, $CDCl_3$) δ 7.47 (s, 1H), 7.35 (s, 1H), 3.94 (s, 3H), 3.91 (s, 3H). Data consistent with that given in the literature[24]



67 **68**

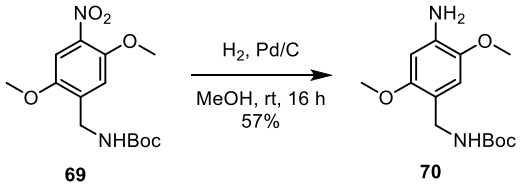
Nitrile 68. Prepared according to ***General procedure 1*** from Bromide **67** (2.5 g, 9.54 mmol) and CuCN (1.71 g, 19.1 mmol, 2 eq) at 150 °C for 6 and purified by silica gel flash chromatography (60% CH_2Cl_2 in hexane) to afford the title compound as a yellow solid (1.44 g, 7.70 mmol, 73%). ^{1}H NMR (400 MHz, $CDCl_3$) δ 7.41 (s, 1H), 7.29 (s, 1H), 3.96 (s, 3H), 3.94

(s, 3H). ^{13}C NMR (126 MHz, $CDCl_3$) δ ^{13}C NMR (126 MHz, $CDCl_3$) δ 154.85, 146.49, 142.72, 118.98, 114.59, 108.75, 106.51, 57.51, 57.12. HRMS-EI (m/z) Calculated for $C_9H_8O_4N_2Na$ $[M+Na]^+$, 231.0376; found 231.0377.



68 **69**

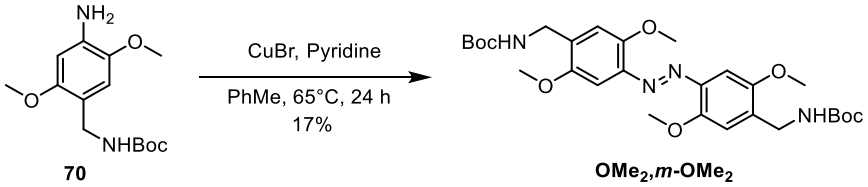
Aniline 69. Prepared according to ***General procedure 2*** with Nitrile **68** (1.4 g, 6.73 mmol) and Borane-THF (1M, 27.6 mL, 27.6 mmol, 6 eq) at reflux temperature for 16 hours to afford the crude amine. ***General procedure 2*** was continued with Boc_2O (1.47g, 6.73 mmol, 1 eq) and Et_3N (1 mL), then purified by silica gel flash chromatography (80% CH_2Cl_2 to 100% CH_2Cl_2) to afford the title compound as a yellow solid. (1.29 g, 4.13 mmol, 61% over two steps). ^{1}H NMR (400 MHz, $CDCl_3$) δ 7.40 (s, 1H), 7.07 (s, 1H), 5.05 (s, 1H), 4.31 (d, *J* = 5.9 Hz, 2H), 3.93 (s, 3H), 3.86 (s, 3H), 1.45 (s, 9H). ^{13}C NMR (126 MHz, $CDCl_3$) δ 155.99, 150.48, 147.89, 138.00, 134.90, 115.10, 107.61, 80.00, 57.27, 56.24, 40.18, 28.52. HRMS-EI (m/z) Calculated for $C_{14}H_{20}O_6N_2Na$ $[M+Na]^+$, 335.1214; found 335.1213



69 **70**

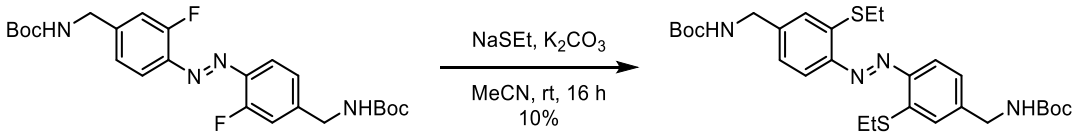
Aniline 70. nitro compound **69** (1.28 g, 4.10 mmol) was dissolved in MeOH (40 mL). The reaction vessel was evacuated and filled with nitrogen 3 x. Palladium 10% on carbon (800 mg) was added and the reaction was stirred under a hydrogen atmosphere for 16 hours. The reaction mixture was filtered over celite, the filtrate was concentrated, then purified by silica gel flash chromatography (5% acetone in CH_2Cl_2) to afford the title compound as light brown solid (665 mg, 2.36 mmol, 57%). ^{1}H NMR (400 MHz, $CDCl_3$) δ 6.76 (s, 1H), 6.39 (s, 1H), 4.95 (s, 1H), 4.20 (d, *J* = 5.8 Hz, 2H), 3.80 (s, 3H), 3.75 (s, 3H), 1.44 (s, 9H). ^{13}C NMR (126 MHz,

$CDCl_3$) δ 156.06, 152.24, 141.02, 136.28, 116.27, 113.30, 99.49, 79.14, 56.42, 55.99, 40.41, 28.61. HRMS-EI (m/z) Calculated for $C_{14}H_{22}O_4N_2Na$ $[M+Na]^+$, 305.1472; found 305.1472



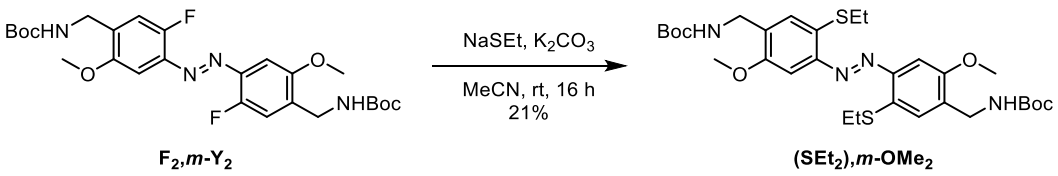
70 **OMe_2,*m*-OMe_2**

OMe_2,*m*-OMe. Prepared according to ***General procedure 6*** with Aniline **S70** (214 mg, 758 µmol), Pyridine (122µL, 1.52 mmol, 2 eq) and CuBr (109 mg, 758 µmol, 1 eq) and purified by silica gel flash chromatography (0.5% MeOH in $CHCl_3$), and the pure fractions were combined to afford the title compound as an orange solid (36 mg, 64 µmol, 17%). *(E)*-**OMe_2,*m*-OMe_2:** ^{1}H NMR (500 MHz, CD_2Cl_2) δ 7.19 (s, 1H), 7.05 (s, 1H), 5.13 (s, 1H), 4.31 (d, *J* = 6.2 Hz, 2H), 3.98 (s, 3H), 3.86 (s, 3H), 1.45 (s, 9H). ^{13}C NMR (126 MHz, CD_2Cl_2) δ 156.20, 152.18, 152.14, 142.18, 132.51, 114.81, 98.94, 79.51, 57.59, 56.17, 28.53. HRMS-EI (m/z) Calculated for $C_{28}H_{41}O_8N_4$ $[M+H]^+$, 561.2919; found 561.2916



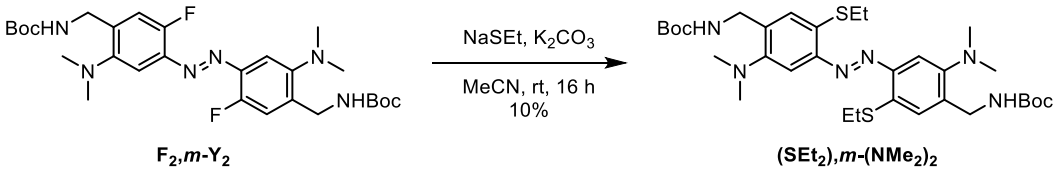
F_2,*m*-Y_2 **(SEt_2),*m*-H**

($SEt)_2$,*m*-H_2. Prepared according to ***General procedure 7*** from **F_2,*m*-H_2** (55 mg, 115 µmol), Sodium ethanethiolate (80%, 49 mg, 461 µmol, 4 eq) and potassium carbonate (32 mg, 230 µmol, 2 eq) were suspended in MeCN (1.5 mL) and purified by silica gel flash chromatography (0 to 0.5% Acetone in CH_2Cl_2) to afford the title compound as an orange solid (6.2 mg, 11 µmol, 10%). *(E)*-**SEt_2,*m*-H_2**: ^{1}H NMR (500 MHz, DMSO) δ 7.51 (d, *J* = 8.2 Hz, 2H), 7.40 (s, 2H), 7.15 (d, *J* = 8.4 Hz, 2H), 7.04 (s, 2H), 4.21 (d, *J* = 6.2 Hz, 4H), 3.04 (q, *J* = 7.3 Hz, 4H), 1.43 (s, 18H), 1.35 (t, *J* = 7.3 Hz, 6H). ^{13}C NMR (151 MHz, DMSO) δ 155.88, 147.36, 144.42, 139.54, 124.10, 123.56, 116.66, 78.02, 43.24, 28.22, 24.45, 13.65. HRMS-EI (m/z) Calculated for $C_{28}H_{41}O_4N_4S_2$ $[M+H]^+$, 561.2564; found 561.2560



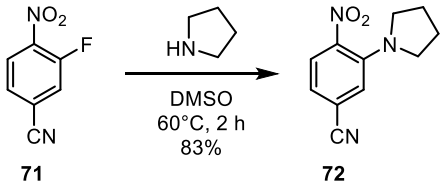
F_2,*m*-Y_2 **(SEt$_2$),*m*-OMe$_2$**

(SEt)$_2$,*m*-OMe$_2$. Prepared according to ***General procedure 7*** from **F_2,*m*-H_2** (70 mg, 130 µmol), Sodium ethanethiolate (80%, 55 mg, 522 µmol, 4 eq) and potassium carbonate (36 mg, 261 µmol, 2 eq) were suspended in MeCN (2 mL) and purified by silica gel flash chromatography (5% EtOAc in CH_2Cl_2) to afford the title compound as an orange solid (21 mg, 27 µmol, 21%). ^{1}H NMR (400 MHz, $CDCl_3$) δ 7.32 (m, 4H), 5.04 (s, 2H), 4.33 (d, *J* = 6.3 Hz, 4H), 3.90 (s, 6H), 3.00 (q, *J* = 7.4 Hz, 4H), 1.46 (s, 18H), 1.36 (t, *J* = 7.4 Hz, 6H). ^{13}C NMR (126 MHz, $CDCl_3$) δ 156.17, 156.01, 150.36, 131.42, 131.29, 128.92, 99.31, 79.62, 55.71, 40.45, 28.57, 27.32, 14.26. HRMS-EI (m/z) Calculated for $C_{30}H_{45}O_6N_4S_2$ $[M+H]^+$, 625.2775; found 625.2774

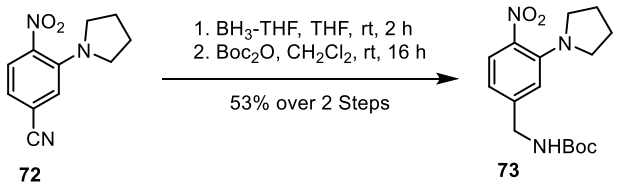


F_2,*m*-Y_2 **(SEt$_2$),*m*-(NMe$_2$)$_2$**

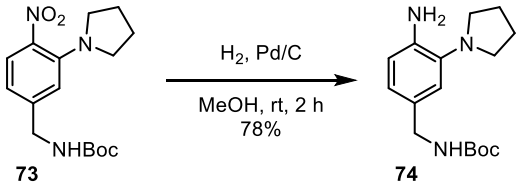
(SEt$_2$),*m*-(NMe$_2$)$_2$. Prepared according to ***General procedure 7*** from **F_2,*m*-H_2** (41.5 mg, 73 µmol), Sodium ethanethiolate (80%, 31 mg, 295 µmol, 4 eq) and potassium carbonate (20.4 mg, 148 µmol, 2 eq) were suspended in MeCN (2 mL) and purified by silica gel flash chromatography (5 to 8% EtOAc in CH_2Cl_2) to afford the title compound as an orange solid (6.7 mg, 10 µmol, 14%). ^{1}H NMR (500 MHz, $CDCl_3$) δ 7.52 (s, 2H), 7.33 (s, 2H), 5.24 (s, 2H), 4.45 (d, *J* = 6.4 Hz, 2H), 3.01 (q, *J* = 7.4 Hz, 4H), 2.71 (s, 12H), 1.38 (t, *J* = 7.4 Hz, 6H). ^{13}C NMR (126 MHz, $CDCl_3$) δ 156.24, 150.37, 149.58, 136.87, 133.57, 127.68, 108.69, 79.53, 44.78, 41.12, 28.45, 26.69, 14.05. HRMS-EI (m/z) Calculated for $C_{32}H_{51}O_4N_6S_2$ $[M+H]^+$, 647.3408; found 647.3405



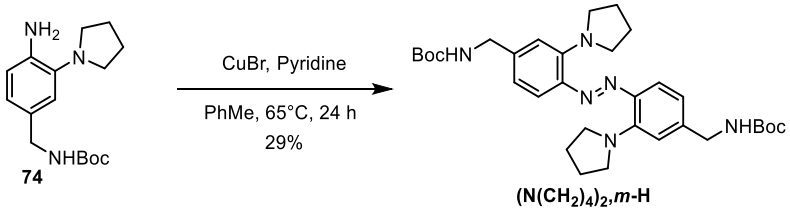
Nitrile 72. To a solution of 3-fluoro-4-nitrobenzonitrile **71** (3 g, 18 mmol) in DMSO (20 mL) was added pyrrolidine (3 mL, 36 mmol, 2 eq); the solution went from colourless to yellow. The yellow solution was stirred at 60 °C for 2 hours. Ice and brine were added to the mixture, and the solid precipitate was extracted with CH_2Cl_2 3x. The organic layer was washed with brine. The solution was concentrated and recrystallized from boiling EtOH to afford the title compound as yellow needle-like crystals (3.26 g, 15 mmol, 83%). ^{1}H NMR (400 MHz, $CDCl_3$) δ 7.73 (d, J = 8.4 Hz, 1H), 7.16 (d, J = 1.6 Hz, 1H), 6.92 (dd, Jz = 8.4, 1.6 Hz, 1H), 3.29 – 3.14 (m, 4H), 2.10 – 1.95 (m, 4H). ^{13}C NMR (101 MHz, $CDCl_3$) δ 141.99, 138.81, 127.47, 120.20, 117.96, 117.65, 116.36, 50.51, 25.79. HRMS-ESI (m/z) Calculated for $C_{11}H_{11}N_3O_2$ $[M+H]^+$, 218.0924; found 218.0926.



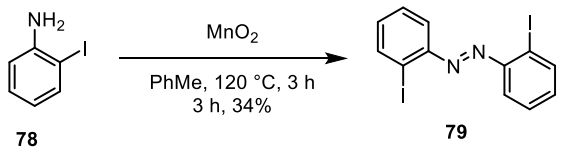
Carbamate 73. Prepared according to ***General procedure 2*** with **72** (1g, 4.6 mmol) and BH_3-THF (1M, 13.8 mL, 13.8 mmol, 3 eq) at room temperature for 16 hours. ***General procedure 2*** was continued with Boc_2O (1.11g, 5 mmol) at rt for 2 hours, then purified by silica gel flash chromatography (50:50 Hexane:CH_2Cl_2 and 6% acetone) to afford the title compound as an orange gum (844 mg, 53% over two steps, 2.4 mmol). ^{1}H NMR (400 MHz, $CDCl_3$) δ 7.70 (d, *J* = 8.4 Hz, 1H), 6.84 – 6.74 (s, *J* =1.7 Hz, 1H), 6.60 (dd, *J* = 8.4, 1.7 Hz, 1H), 4.93 (br s, 1H), 4.28 (d, *J* = 6.2 Hz, 2H), 3.28 – 3.13 (m, 4H), 2.03 – 1.89 (m, 4H), 1.46 (s, 9H). ^{13}C NMR (101 MHz, $CDCl_3$) δ 156.04, 144.71, 143.10, 136.21, 127.38, 114.41, 114.34, 79.97, 50.56, 44.56, 28.50, 25.85. HRMS-ESI (m/z) Calculated for $C_{16}H_{23}N_3O_4$ $[M+H]^+$, 322.1761; found 322.1762.



Aniline 74. Carbamate **73** (820 mg, 2.55 mmol) was dissolved in MeOH (25 mL). The reaction vessel was evacuated and filled with nitrogen 3 x. Palladium 10% on carbon (500 mg) was added and the reaction was stirred under a hydrogen atmosphere for 2 hours. The reaction mixture was filtered over celite, the filtrate was concentrated and purified by silica gel flash chromatography (10% EtOAc in CH_2Cl_2) to afford the title compound as a white solid (580 mg, 2 mmol, 78%). ^{1}H NMR (400 MHz, $CDCl_3$) δ 6.90 (d, *J* = 2.0 Hz, 1H), 6.78 (dd, *J* = 7.9, 2.0 Hz, 1H), 6.67 (d, *J* = 7.9 Hz, 1H), 4.72 (s, 1H), 4.18 (d, *J* = 5.6 Hz, 2H), 3.81 (s, 2H), 3.03 (h, *J* = 2.8 Hz, 4H), 1.92 (h, *J* = 2.8 Hz, 4H), 1.46 (s, 9H). 13C NMR (101 MHz, $CDCl_3$) δ 155.99, 140.56, 137.98, 129.04, 122.81, 118.28, 115.47, 79.33, 50.90, 44.91, 28.57, 24.21. HRMS-ESI (m/z) Calculated for $C_{16}H_{25}N_3O_2$ $[M+H]^+$, 292.2020; found 292.2020.

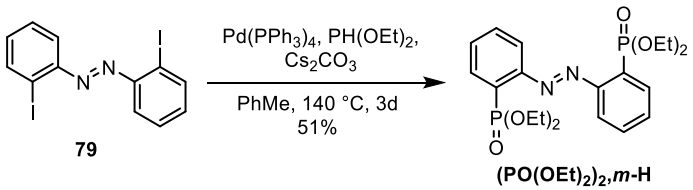


$(N(CH_2)_4)_2$,*m*-H. Prepared according to ***General procedure 6*** using Aniline **74** (138 mg, 628 µmol), Pyridine (101 µL, 1.26 mmol, 2 eq) and CuBr (90 mg, 628 µmol, 1 eq) and purified by silica gel flash chromatography under protection from light (3% Acetone in CH_2Cl_2), and the pure fractions were combined to afford the title compound as a dark red solid (53 mg, 91 µmol, 29%). ^{1}H NMR (400 MHz, $CDCl_3$) δ 7.52 (s, 2H), 6.72 (s, 2H), 6.60 (s, 2H), 4.84 (s, 2H), 4.28 (s, 4H), 3.65 (s, 8H), 1.98 (s, 8H), 1.47 (s, 18H). ^{13}C NMR (101 MHz, $CDCl_3$) δ 155.94, 147.90, 146.71, 141.25, 140.31, 117.35, 115.51, 114.42, 79.45, 52.46, 44.99, 28.46, 25.96. HRMS-EI (m/z) Calculated for $C_{32}H_{47}O_4N_6$ $[M+H]^+$, 579.3653; found 579.3657



78 **79**

Azobenzene **79**. Aniline **78** (1 g, 4.57 mmol) was dissolved in toluene (100 mL). Manganese dioxide (technical grade 70%) (11.34 g, 91.31 mmol, 20 eq) was added and the suspension was stirred at reflux temperature for 3 hours. The mixture was filtered over celite then concentrated. The crude was dry loaded onto silica and purified by silica gel flash chromatography (100% pentane) to afford the title compound as an orange solid (336 mg, 0.77 mmol, 34%). ^{1}H NMR (400 MHz, $CDCl_3$) δ 8.04 (dd, *J* = 7.9, 1.3 Hz, 2H), 7.76 (dd, *J* = 8.0, 1.6 Hz, 2H), 7.46 (ddd, *J* = 8.2, 7.2, 1.3 Hz, 2H), 7.19 (td, *J* = 7.5, 1.6 Hz, 2H). Data consistent with that given in the literature. [25]



79 **(PO(OEt)$_2$)$_2$,*m*-H**

(PO(OEt)$_2$)$_2$,*m*-H Diiodide **79** (100 mg, 230 µmol), caesium carbonate (83 mg, 230 µmol, 1.1 eq), Tetrakis(triphenylphosphine)palladium(0) (14 mg, 11.5 µmol, 0.05 eq) were degassed with N_2 in a microwave vial for 15 minutes. Degassed toluene (1 mL) was added, then diethylphosphite (65 µL, 507 µmol, 2.2 eq) was added and the vial was sealed. The reaction was stirred at 140 °C for 3 days, then concentrated. The crude mixture was purified by silica gel flash chromatography (2% MeOH in CH_2Cl_2) to afford the product as an orange solid (53 mg, 117 µmol, 51%). ^{1}H NMR (600 MHz, $CDCl_3$) δ 8.09 (ddd, *J* = 13.9, 7.6, 1.5 Hz, 2H), 7.93 (ddd, *J* = 8.1, 5.4, 1.2 Hz, 2H), 7.66 (td, *J* = 7.6, 1.3 Hz, 2H), 7.55 (tdd, *J* = 7.5, 3.5, 1.2 Hz, 2H), 4.26 – 4.19 (m, 4H), (4.19 – 4.12 (m, 4H), 1.29 (t, *J* = 7.1 Hz, 12H). ^{13}C NMR (151 MHz, $CDCl_3$) δ 153.89 (d, *J* = 5.2 Hz), 134.35 (d, *J* = 7.4 Hz), 133.55 (d, *J* = 2.6 Hz), 130.88 (d, *J* = 14.1 Hz), 128.85 (d, *J* = 184.3 Hz), 116.67 (d, *J* = 10.4 Hz), 62.39 (d, *J* = 5.6 Hz), 16.50 (d, *J* = 6.5 Hz). HRMS-EI (m/z) Calculated for $C_{20}H_{29}N_2O_6P_2$ $[M+H]^+$, 455.1495; found 455.1497.

6.2.2 UV-Vis spectra (Chapter 2)

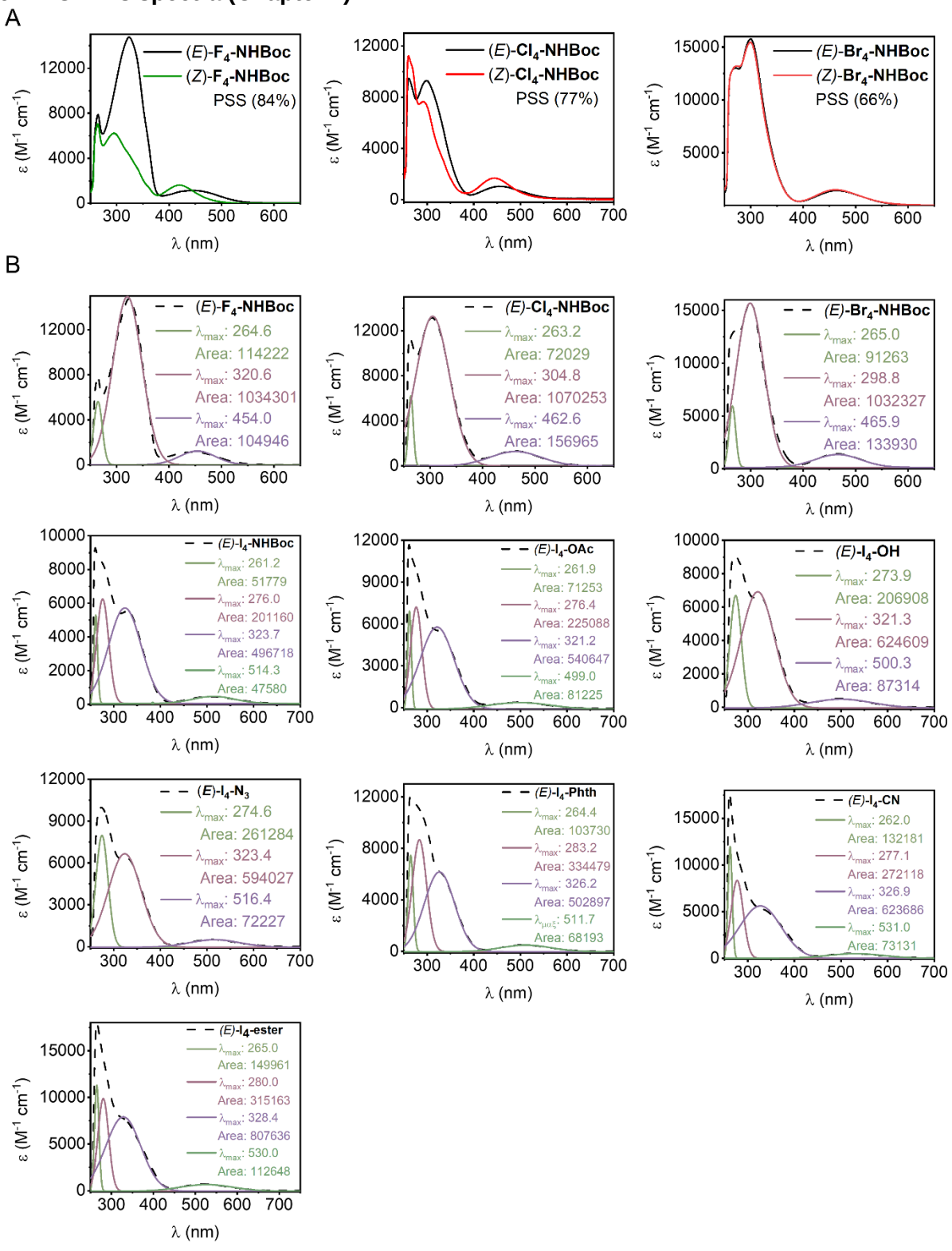


Figure S1. (A) UV-Vis spectra of halogen $\mathbf{X_4}$ derivatives with Z-isomer PSS spectra. (B) Deconvoluted UV-Vis spectra of halogen $\mathbf{X_4}$ derivatives.

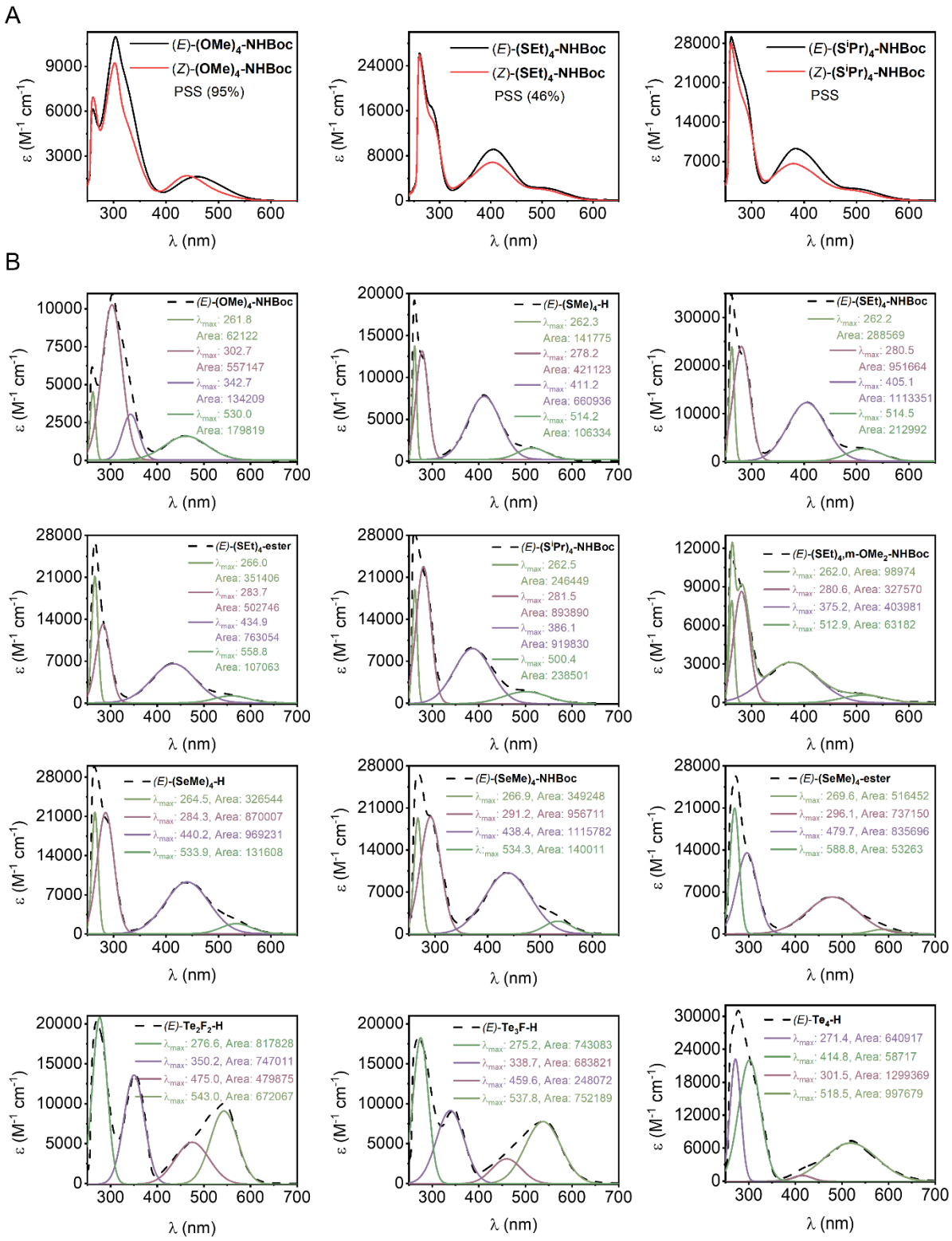


Figure S2. (A) UV-Vis spectra of chalcogen $\mathbf{X_4}$ derivatives with Z-isomer PSS spectra. (B) Deconvoluted UV-Vis spectra of chalcogen $\mathbf{X_4}$ derivatives.

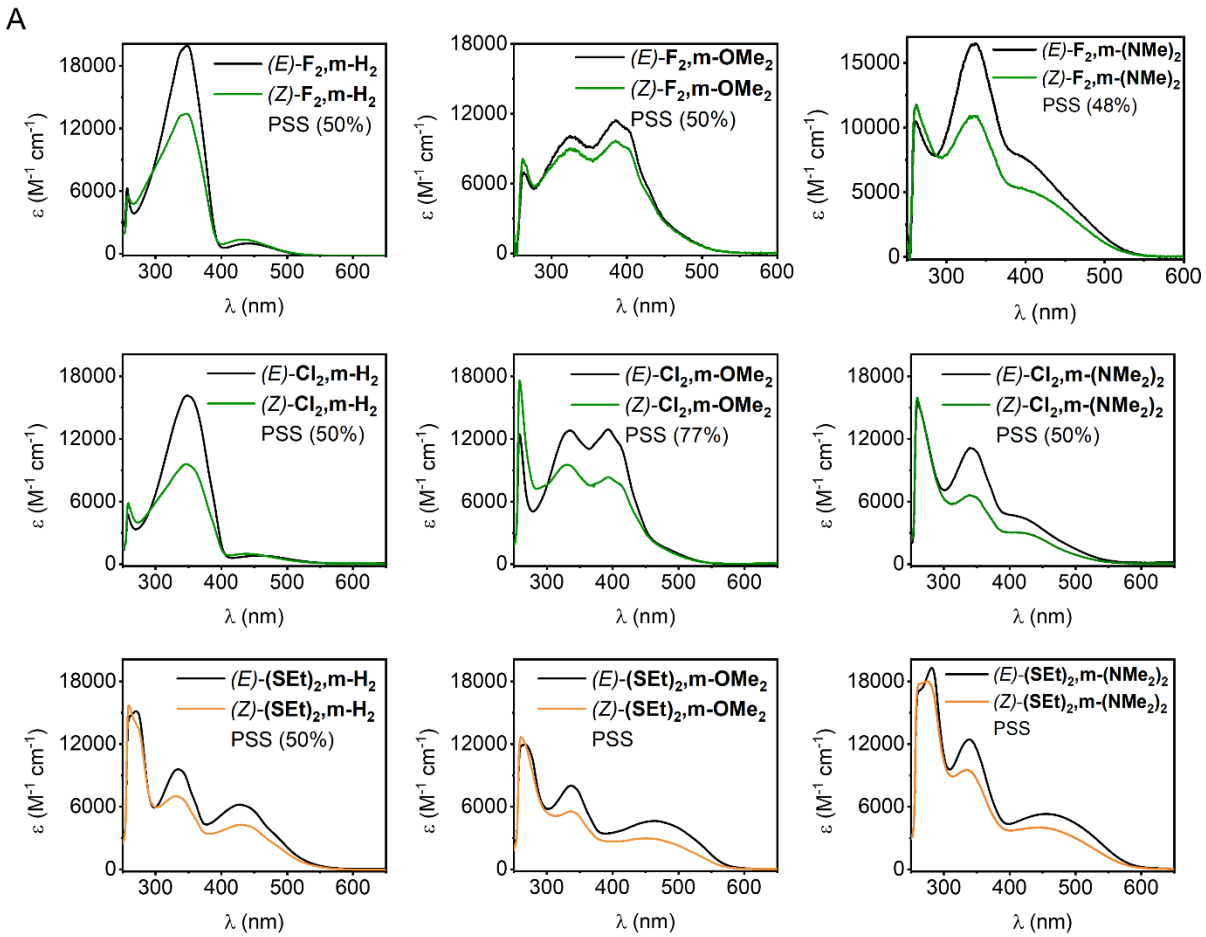


Figure S3. (A) UV-Vis spectra of **X_2Y_2** derivatives with Z-isomer PSS spectra.

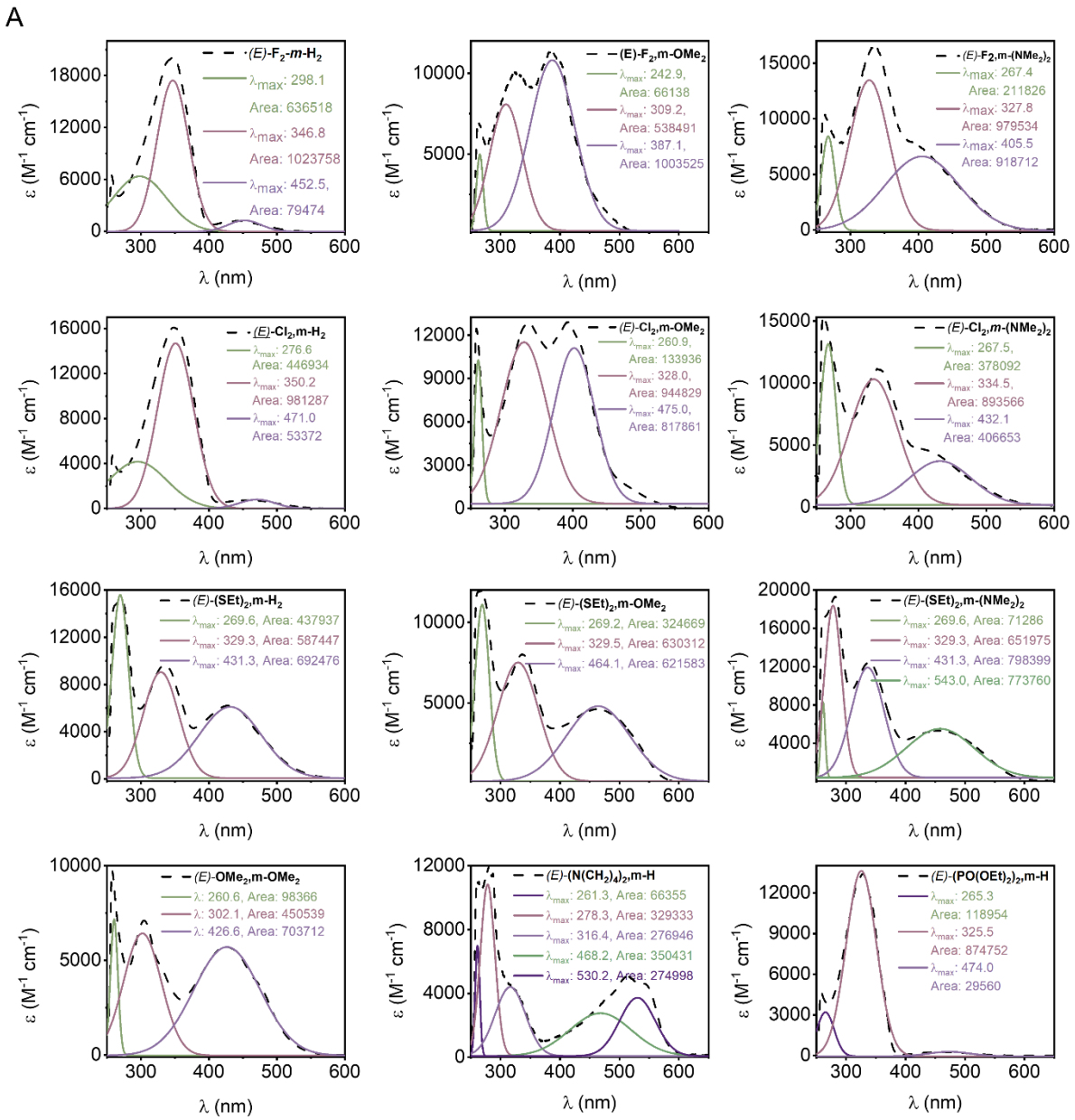


Figure S4. (A) Deconvoluted UV-Vis spectra of $\mathbf{X_2Y_2}$ derivatives with Z-isomer PSS spectra.

6.2.3 Photoswitching: PSS and half-Life determination

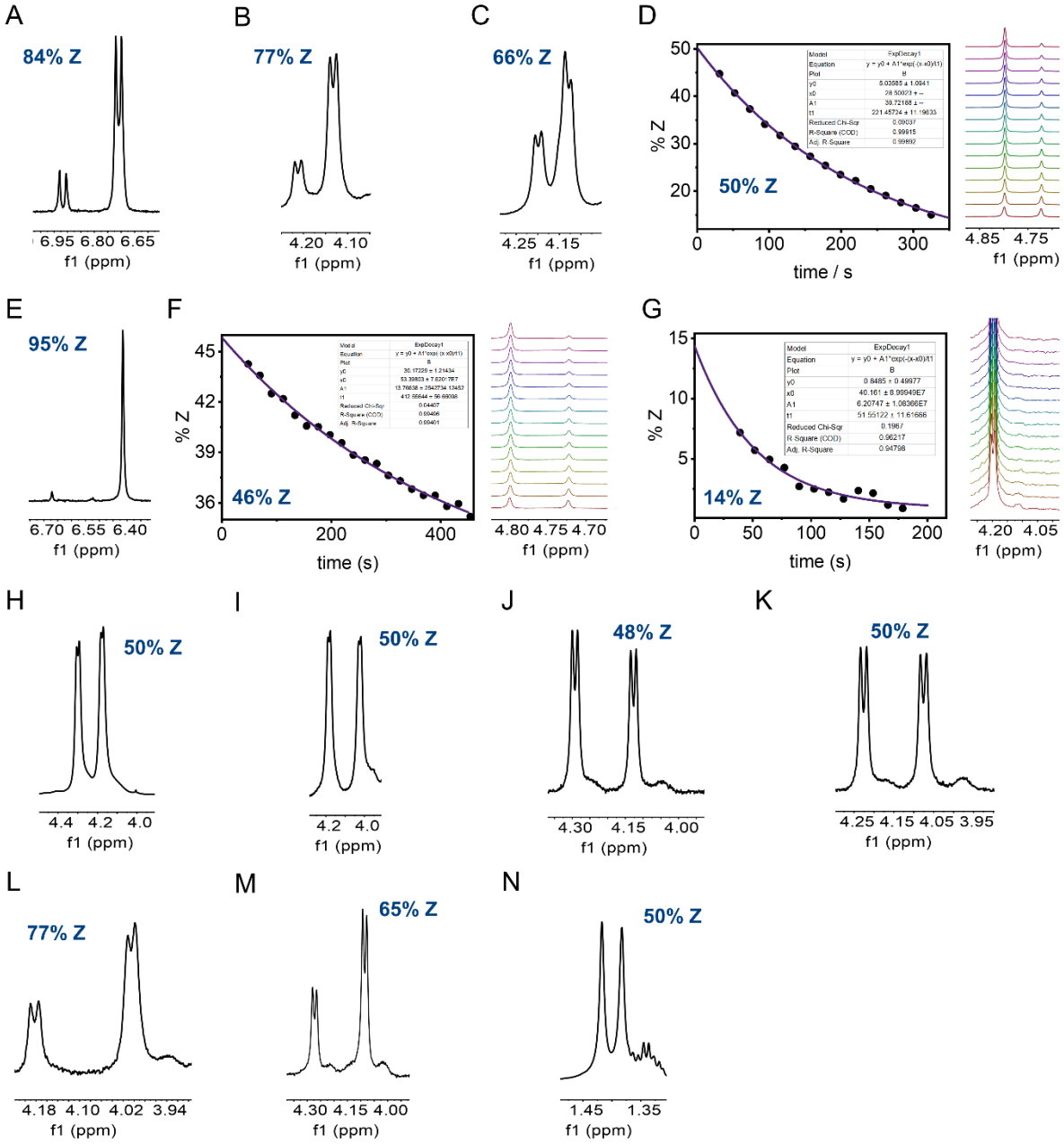


Figure S5. PSS determination for (A) **F_4-NHBoc** [530 nm] (B) **Cl_4-NHBoc** [625 nm] (C) **Br_4-NHBoc** [625 nm] (D) **I_4-NPhth** [660 nm] (E) **$(OMe)_4$-NHBoc** [625 nm] (F) **$(SEt)_4$-NHBoc** [625 nm] (G) **$(SeMe)_4$-NHBoc** [625 nm] (H) **F_2,*m*-H_2** [530 nm] (I) **F_2,*m*-OMe_2** [530 nm] (J) **F_2,*m*-(NMe_2)** [530 nm] (K): **Cl_2,*m*-H_2** [530 nm] (L) **Cl_2,*m*-OMe_2** [530 nm] (M) **Cl_2,*m*-(NMe_2)** (N) **$(SEt)_2$,*m*-H_2** [590 nm]

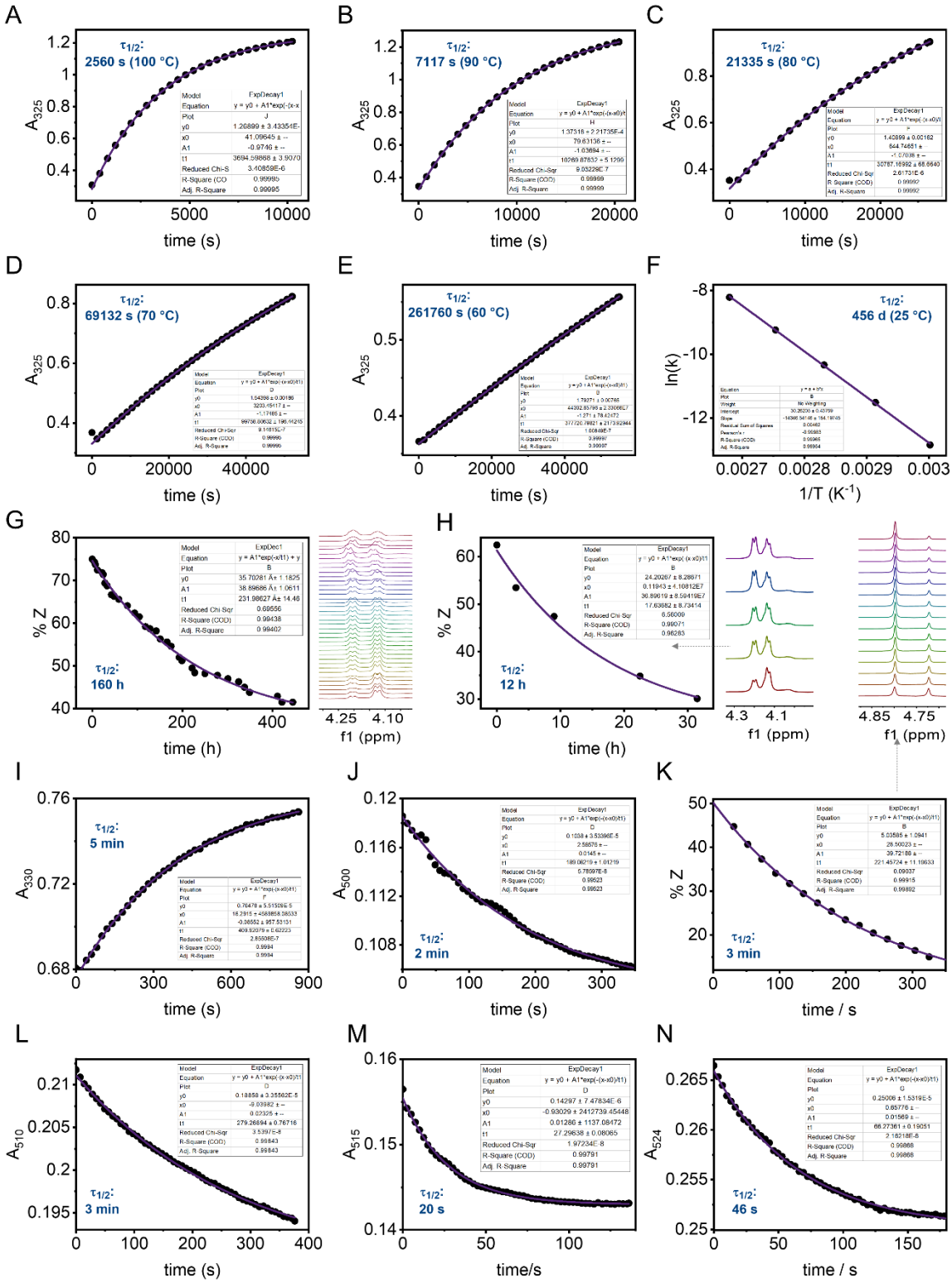


Figure S6. Lifetime plot of halogenated **X_4** derivatives by UV-Vis or ^{1}H NMR. (A-E): **F_4-NHBoc** at variable temperatures after irradiation with 530 nm. (F): Arrhenius plot using data from A-E (G) **Cl_4-NHBoc** with ^{1}H NMR spectra [625 nm] (H) **Br_4-NHBoc** with ^{1}H NMR spectra [625 nm] (I) **I_4-NHBoc** [660 nm] (J) **I_4-OAc** [625 nm] (K) **I_4-NPhth** with ^{1}H NMR spectra [625 nm] (L) **I_4-N_3** [625 nm] (M) **I_4-CN** [660 nm] (N) **I_4-Ester** [660 nm]

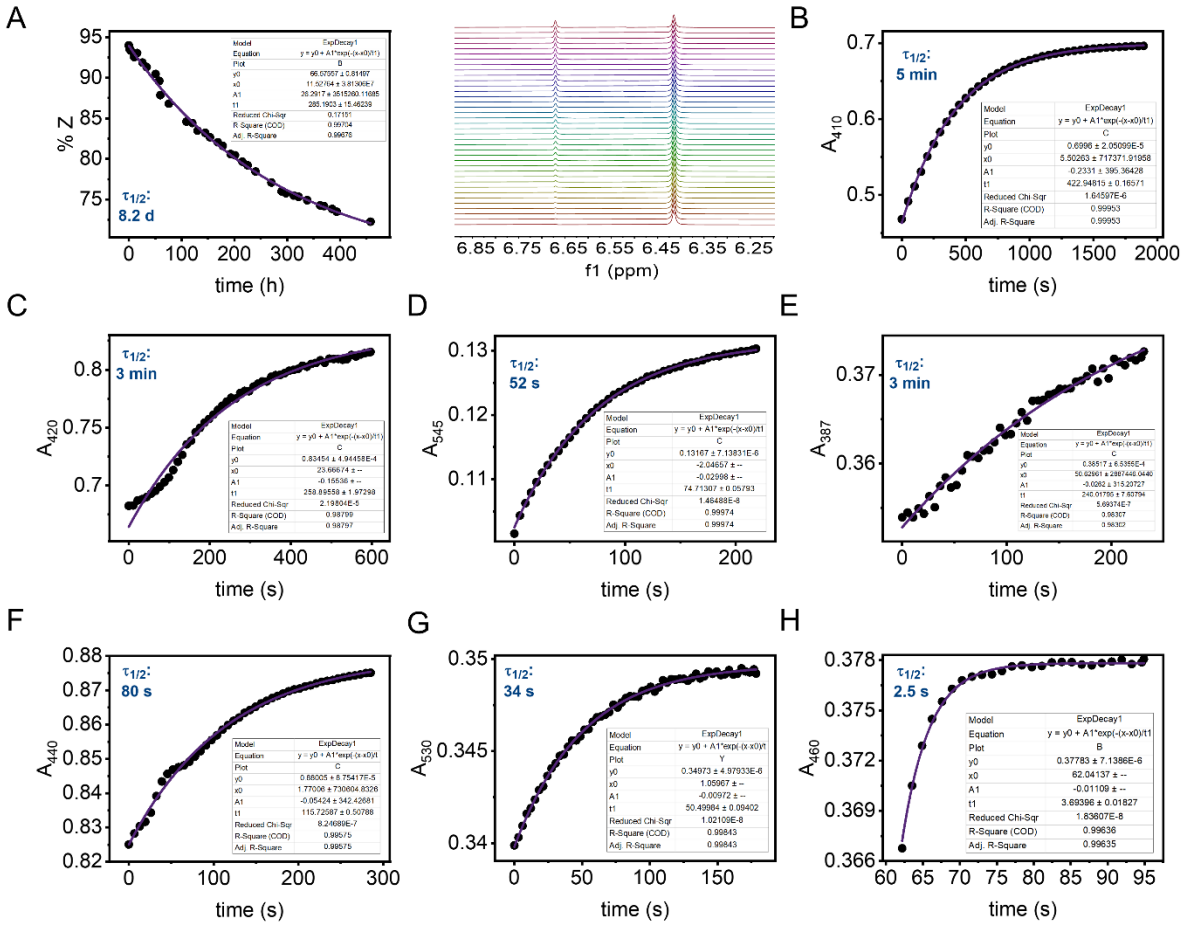


Figure S7. Lifetime plot of chalcogen $\mathbf{X_4}$ derivatives by UV-Vis or ^{1}H NMR. (A): **$(OMe)_4$-NHBoc** with ^{1}H NMR spectra [625 nm] (B) **$(SMe)_4$-H** [625 nm] (C) **$(SEt)_4$-NHBoc** [625 nm] (D) **$(SEt)_4$-ester** [660 nm] (E) **$(SiPr)_4$-NHBoc** [590 nm] (F) **$(SeMe)_4$-H** [625 nm] (G) **$(SeMe)_4$-NHBoc** [625 nm] (H) **$(SeMe)_4$-ester** [660 nm]

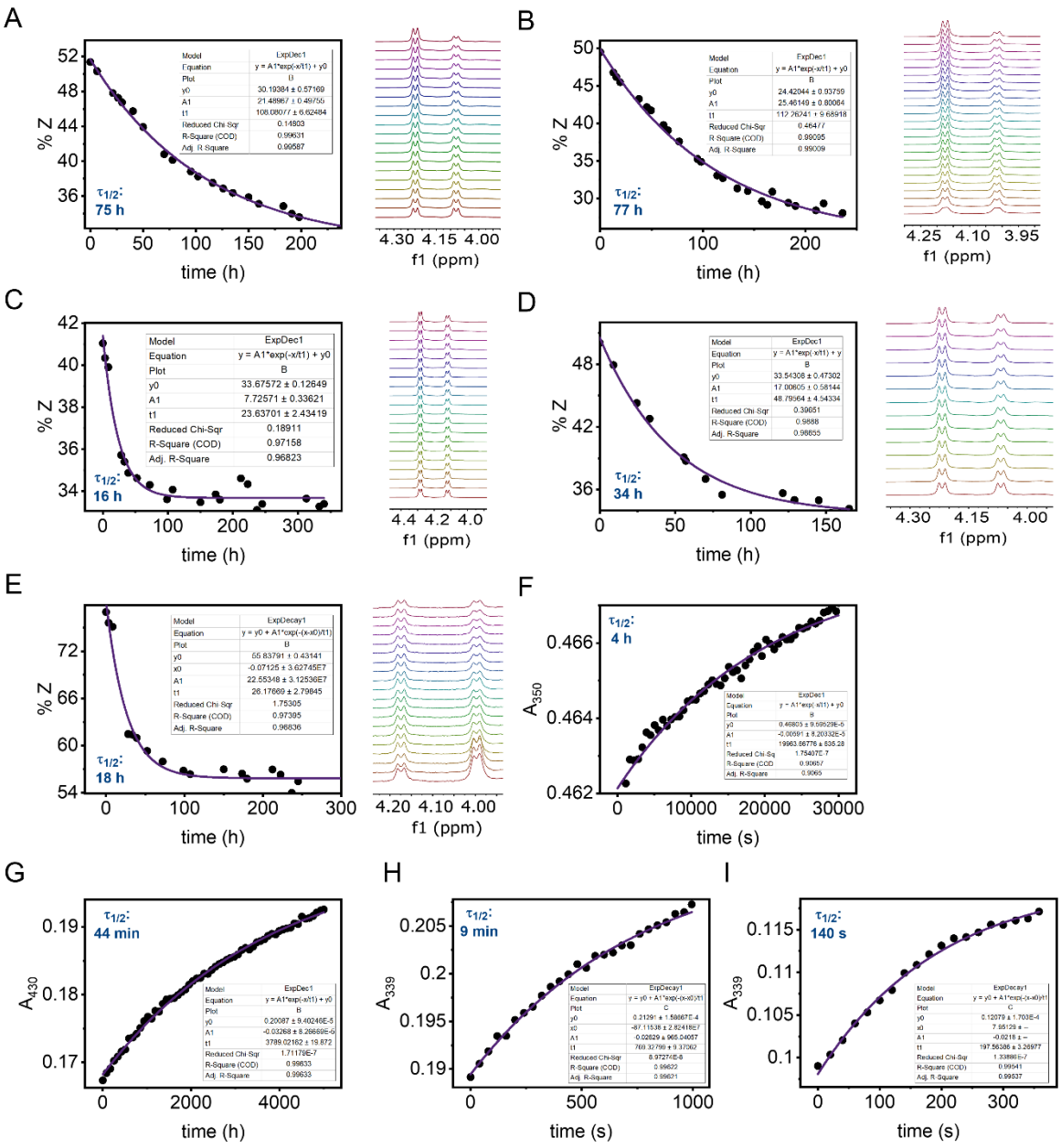


Figure S8. Lifetime plot of **X_2,*m*-Y_2** derivatives by UV-Vis or ^{1}H NMR. (A): **F_2,*m*-H_2** with ^{1}H NMR spectra [530 nm] (B) **F_2,*m*-OMe_2** with ^{1}H NMR spectra [530 nm] (C) **F_2,*m*-(NMe_2)** with ^{1}H NMR spectra [530 nm] (D): **Cl_2,*m*-H_2** with ^{1}H NMR spectra [530 nm] (E) **Cl_2,*m*-OMe_2** with ^{1}H NMR spectra [530 nm] (F) **Cl_2,*m*-(NMe_2)** (G) **$(SEt)_2$,*m*-H_2** [590 nm] (H) **$(SEt)_2$,*m*-OMe_2** [590 nm (I) **$(SEt)_2$,*m*-(NMe_2)** [590 nm]

6.2.4 GSH Stability Studies

A 10 mM reduced glutathione (GSH) solution was prepared in degassed 100 mM sodium phosphate buffer (at least 15 minutes of N_2 bubbled through the buffer solution prior to addition to GSH). The absorption of the solution was measured periodically at 25°C, then fitted to a 1st order exponential decay.

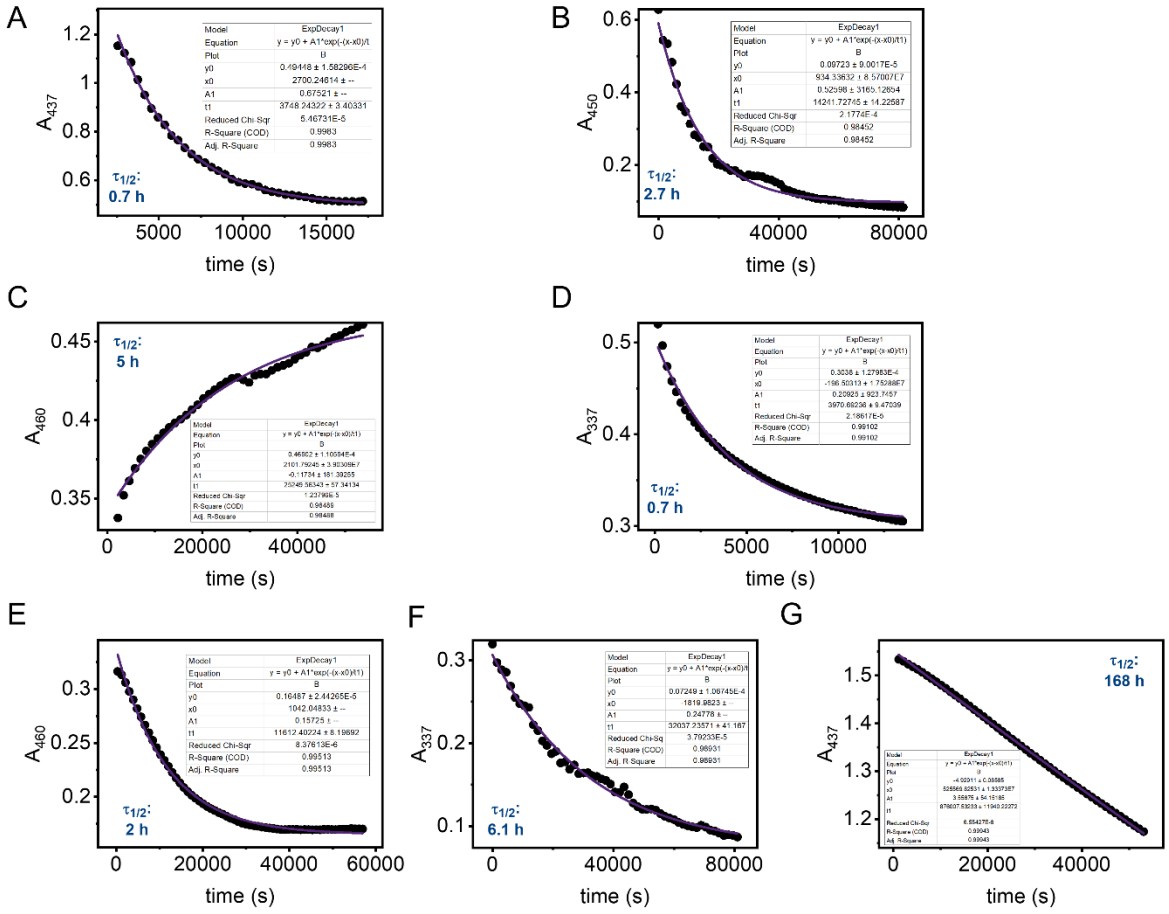


Figure S9. Decomposition of **X_4-CH_2NH_2•TFA** Conditions: 100 mM phosphate buffer containing 10 mM GSH degassed with N_2. T = 298 K. (A) **F_4** (B) **Cl_4** (C) **Br_4** (D) **I_4** (E) **$(OMe)_4$** (F) **$(SEt)_4$** (G) **$SeMe_4$**

6.2.5 Single crystal X-ray diffraction experiments

Crystals were grown by vapour diffusion. Compounds (2-15 mg) were dissolved in minimal amounts of $CDCl_3$, then filtered over cotton into a small vial. The vial was capped and punctured with a small needle, then placed into a larger vial containing pentane or hexane. The vials were stored in the fridge until suitable crystals formed.

Crystal Structure Determination Deposition Number(s) 2196083-92 contains the supplementary crystallographic data for this work. These data are provided free of charge by the joint Cambridge Crystallographic Data Centre and Fachinformationszentrum Karlsruhe Access Structures service www.ccdc.cam.ac.uk/structures."

Single-crystal X-ray diffraction data were collected at 150 K on an Oxford Diffraction(Rigaku) SuperNovae or a Rigaku Synergy-DW diffractometer (EP/V028995/1). In all cases, Cu-Kα (λ = 1.54184 Å) radiation was used and the instrument was equipped with a nitrogen gas Oxford Cryosystems Cryostream unit. A suitable crystal was chosen and mounted on a 200 μm MiTeGen loop using perfluoropolyether oil. The CrysAlisPro software was used for data collection and integration. All structures were solved using SuperFlip and refined using full-matrix least-squares refinement within the CRYSTALS suite. All non-hydrogen atoms were refined anisotropically. The hydrogen atoms were positioned at geometrically sensible positions and refined using a riding model.

Substituent	Dihedral (°)		Average N=N-C-C' Angle (°) (normalised)	Coplanarity (°)	Distance (Å)		Distance (Å) (Average) N···X		N=N (Å)	N=N (°)					
F, ⁰ = H	40.7	40.7	40.7	0	2.760, 2.761	2.747, 2.759	2.761	**2.753**	1.229	179.2	124.6, 125.3	120,120	120,120	120,120	120,120
*F, ⁰ = Br	3.2	3.2	3.2	0	2.655, 2.655	2.635, 2.635	2.655	**2.635**	1.253	180.0	115.2, 115.2	128.8,128.8	116.3,116.3	119.5,119.5	117.4,117.5
Cl, ⁰ = H	79.7	35.2	57.45	44.5	3.229, 2.930	2.990, 2.880	3.080	**2.935**	1.182	180.0	112.9,117.8	120.8,126.7	120.8,115.7	119.9,121.9	119.4,119.1
	126.9	59.3	56.2	67.6	2.962, 3.815	2.916, 3.092	3.389	**3.004**	1.248	176.2	113.6,112.1	124.1, 123.6	118.1,118.0	120.9,120.4	118.9,119.0
	135.0	61.9	53.45	73.1	3.725, 3.096	2.956, 2.928	3.411	**2.942**	1.245	178.0	113.0,112.1	117.9,117.6	124.2,124.3	119.3,118.9	120.7,120.3
Br, ⁰ = CH_2NHBoc	45.8	-134.2	45.8	-88.4	3.031, 3.022	3.030, 3.023	3.027	3.027	1.252	175.6	113.8,113.8	125.2,125.2	117.9,117.9	121.8,121.8	120,120
I, ⁰ = CH_2N_3	48.6	-135.5	46.55	-86.7	3.170, 3.121	3.183, 3.203	**3.146**	3.193	1.260	174.2	111.6,112.6	123.3,123.0	116.1,116.6	124.6,125.5	122.1,122.5
	50.9	-129.4	50.75	-78.5	3.177, 3.254	3.188, 3.078	3.216	**3.133**	1.215	179.5	112.8,116.2	126.5,123.5	115.4,118.4	123.5,122.4	118.8,120.7
I, ⁰ = CO_2Et	50.3	-48.8	49.6	-80.9	3.389, 3.439	3.152, 3.222	3.414	**3.187**	1.249	171.6	114.9,112.9	123.9,123.3	116.6,118.4	124.6,123.1	120.5,118.5
OMe, ⁰ = Br	29.6	-142	33.8	-67.6	2.584, 2.622	2.678, 2.714	**2.603**	2.696	1.252	179.4	116.5,113.6	127.8,125.3	113.8,115.7	117.0,117.6	115.6,115.9
SMe, ⁰ = H	22.4	-150.8	**25.8**	51.8	2.653, 2.686	2.811, 2.814	**2.670**	2.812	**1.268**	**169.9**	115.0,114.1	124.6,124.0	114.6, 115.2	120.8,120.9	116.5,116.2
	152.3	159.5	**24.1**	48.2	2.721, 2.659	2.777, 2.821	**2.690**	2.836	**1.266**	**169.7**	113.5,116.1	124.2,125.9	115.4,113.3	120.8,121.1	115.8,116.2
SEt, ⁰ = CO_2Et	1.0	-1.6	**1.3**	0.3	2.666, 2.666	2.813, 2.813	**2.666**	2.813	**1.275**	**180.0**	116.2, 116.2	126.6,126.6	114.0, 114.0	120.2,120.2	117.1,117.1
SeMe, ⁰ = H	19.5	159.5	**20.0**	47.0	2.739, 2.710	2.885, 2.894	**2.725**	2.890	**1.265**	**170.5**	114.0,115.8	124.4,125.7	115.4,114.1	120.8,121.0	116.1,116.6
	158.0	152.9	**24.55**	49.1	2.670, 2.705	2.917, 2.911	**2.688**	2.914	**1.266**	**169.9**	115.2,114.2	124.2,124.2	115.4,115.7	120.7,120.3	116.8,116.5
SeMe ⁰ = ester	-21.4	160.2	20.6	41.2	2.702, 2.703	2.927, 2.927	2.702	2.927	1.263	175.4	115.1,115.1	125.3,125.3	114.9,114.9	120.6,120.7	117.8,117.8
	-23.2	162.3	20.5	41.0	2.728, 2.728	2.921, 2.921	2.728	2.921	1.261	174.1	115.3,115.3	125.1,125.1	114.8,114.8	120.7,120.7	117.7,117.7
TeMe ⁰ H	158.1	157.3	Av: 23.37 (24.45/22.3)	44.6	2.763,2.838	3.096,3.048	2.800	3.072	1.279	174.6	115.8,114.2	124.3,124.0	114.9,115.5	121.7,122.0	119.1,117.1
	22.2	26.7		48.9 a:46.75	2.792,2.834	3.091,3.060	2.813	3.076	1.265	177.9	115.3,114.0	123.8,123.9	115.1,114.9	122.1,122.2	119.1,117.4

Table S2: Summary of key data from crystal structures

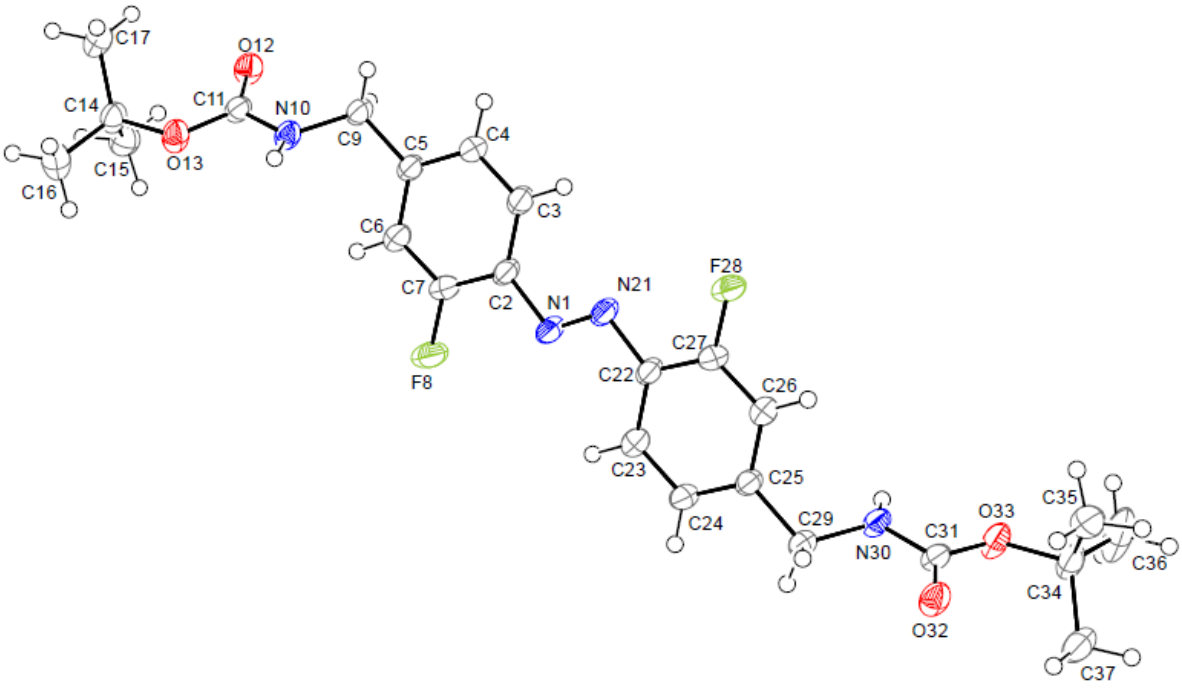


Figure S10. X-ray crystallographic structure of **F_2H_2-NHBoc**.

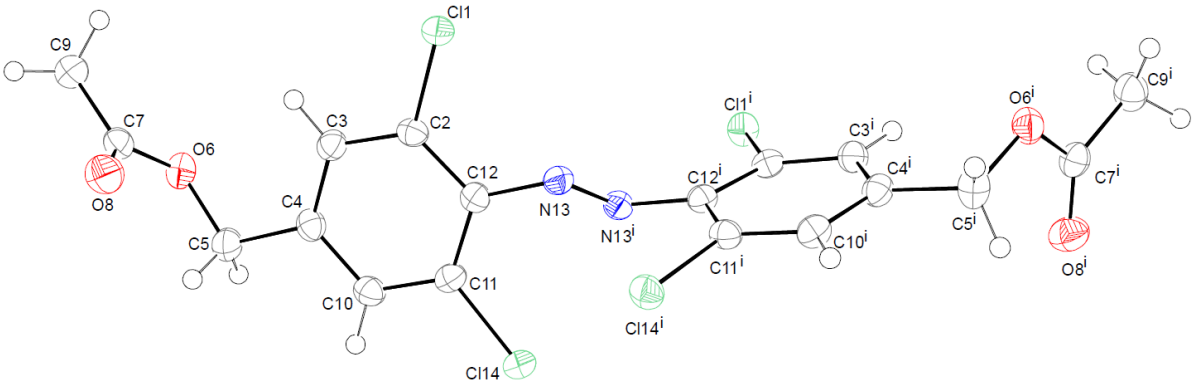


Figure S11. X-ray crystallographic structure of **Cl_4-OAc**.

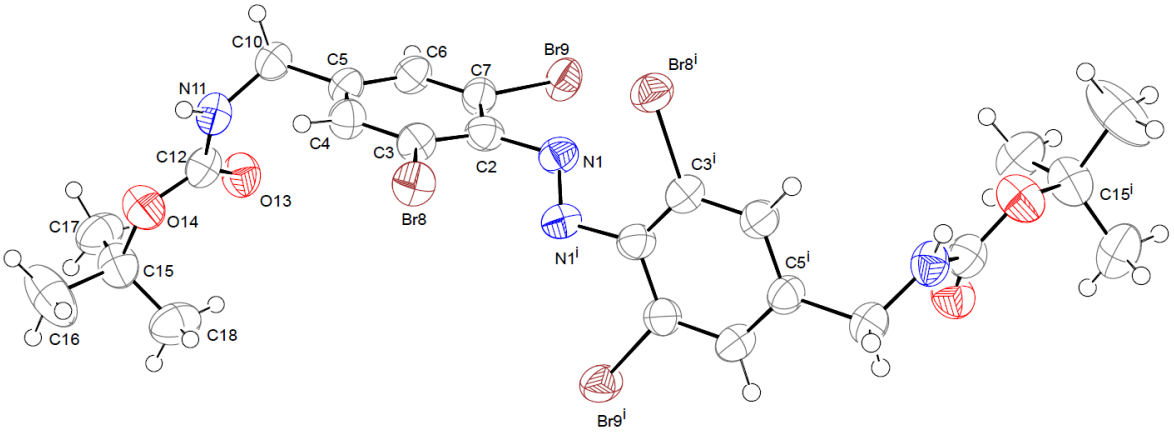


Figure S12. X-ray crystallographic structure of **Br_4-NHBoc**.

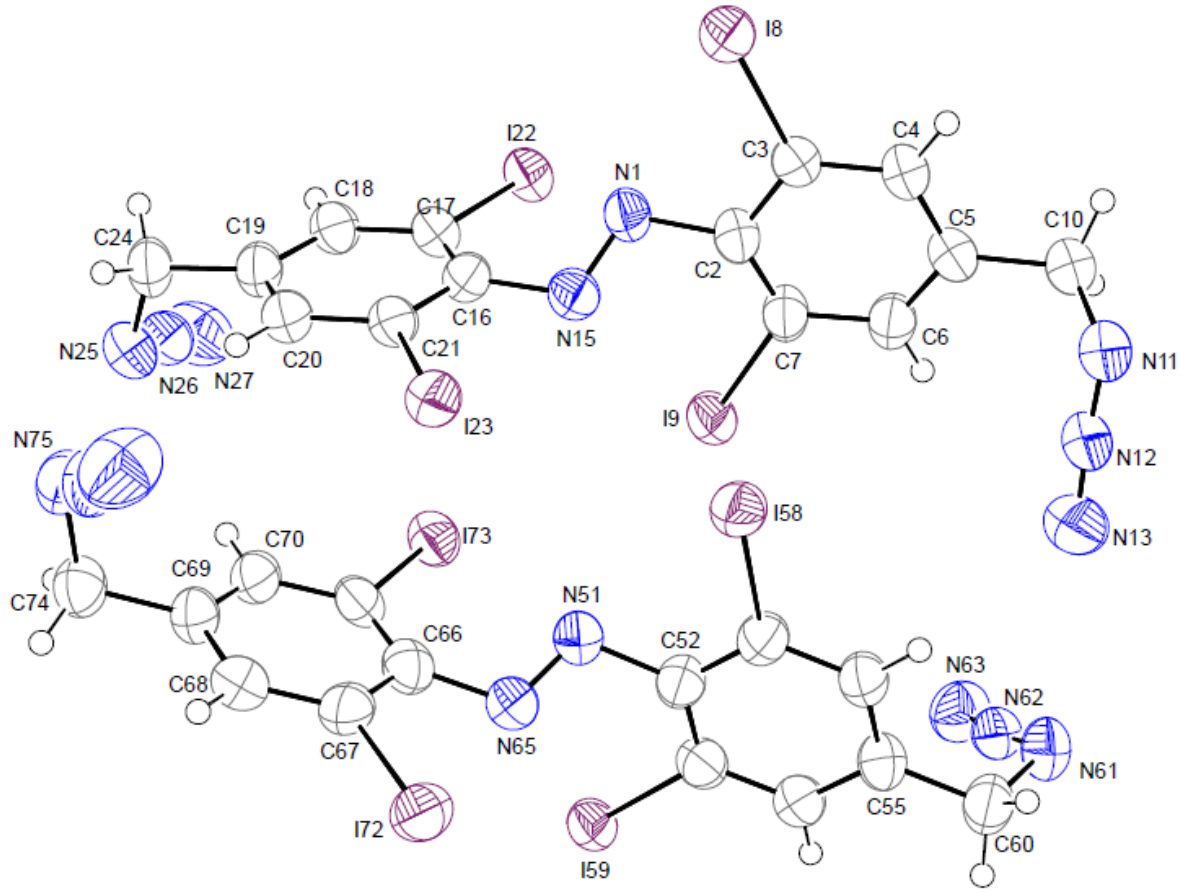


Figure S13. X-ray crystallographic structure of **I_4-N_3**.

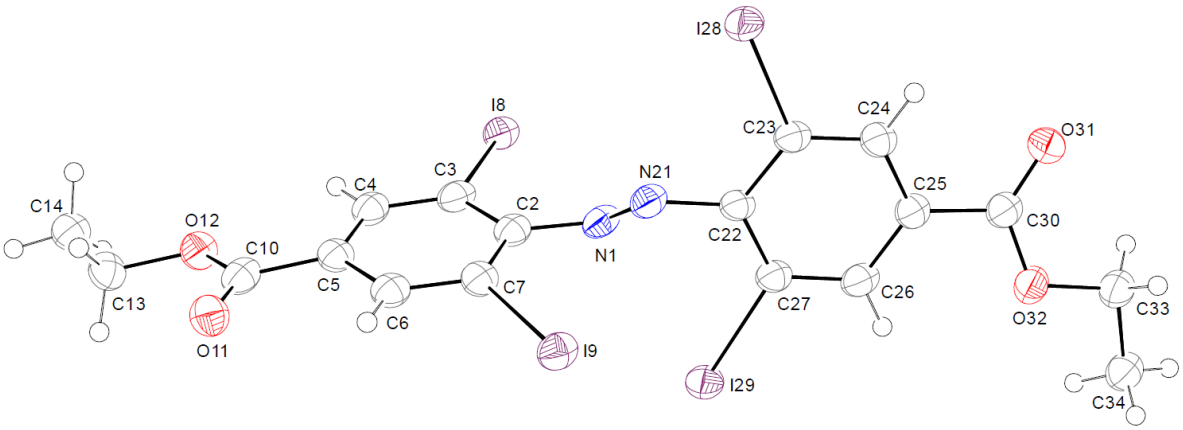


Figure S14. X-ray crystallographic structure of **I_4-Ester**.

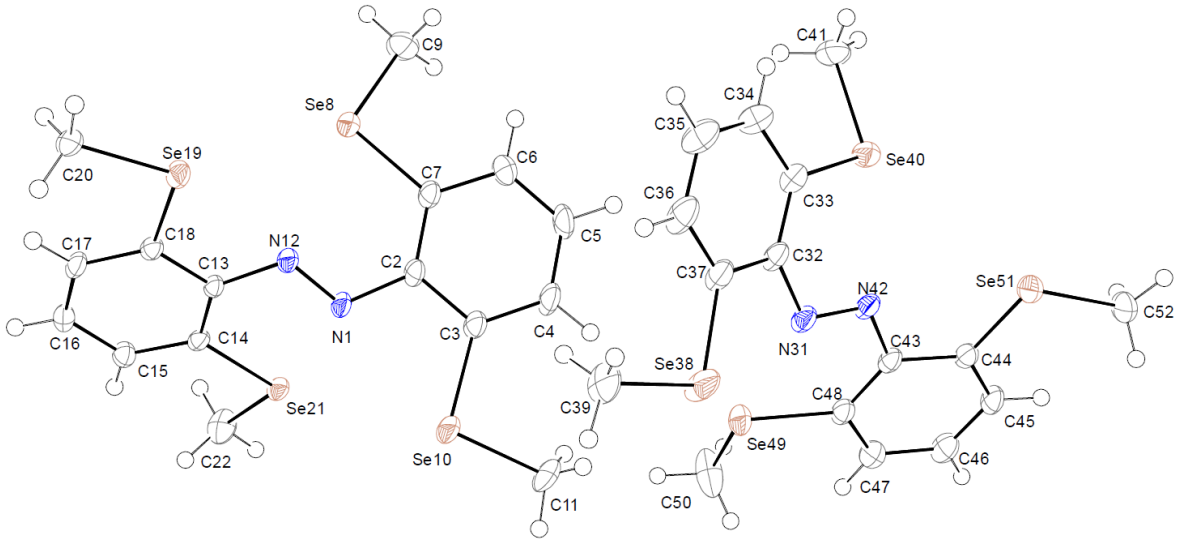


Figure S15. X-ray crystallographic structure of **(SMe_4)-H.**

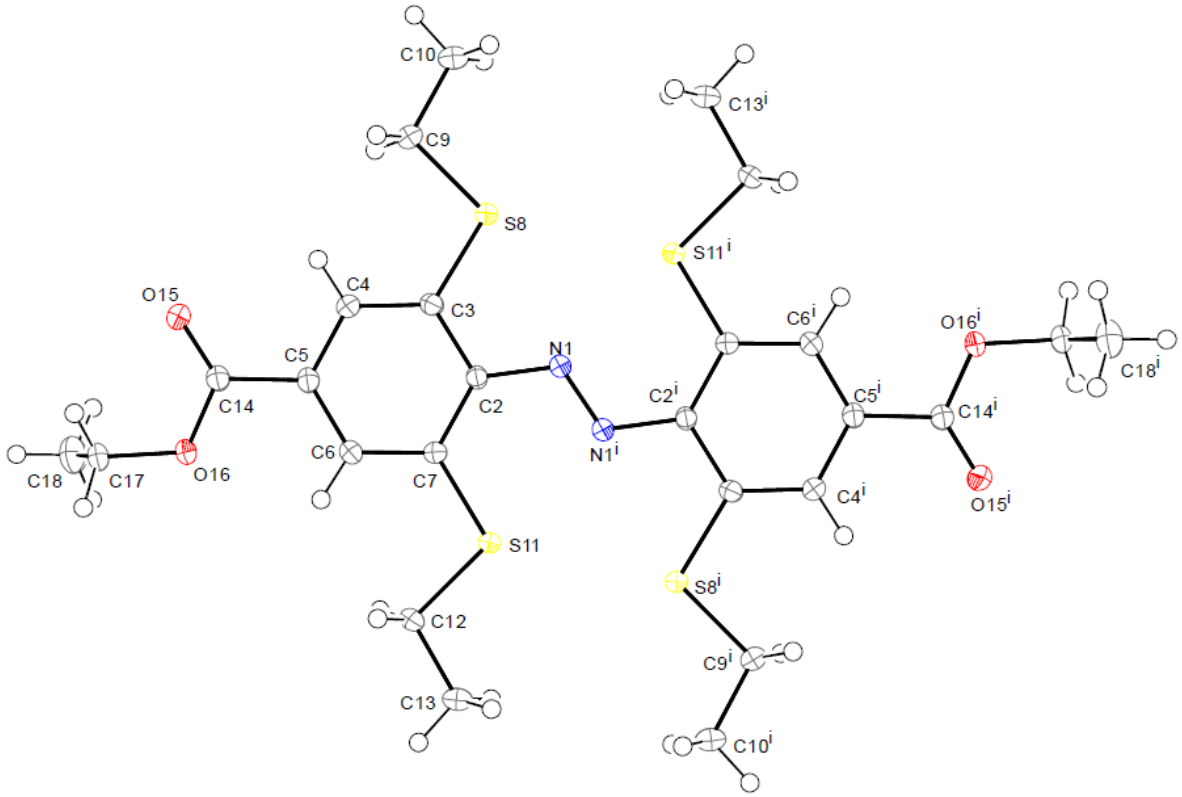


Figure S16. X-ray crystallographic structure of **(SEt$_4$)-ester**

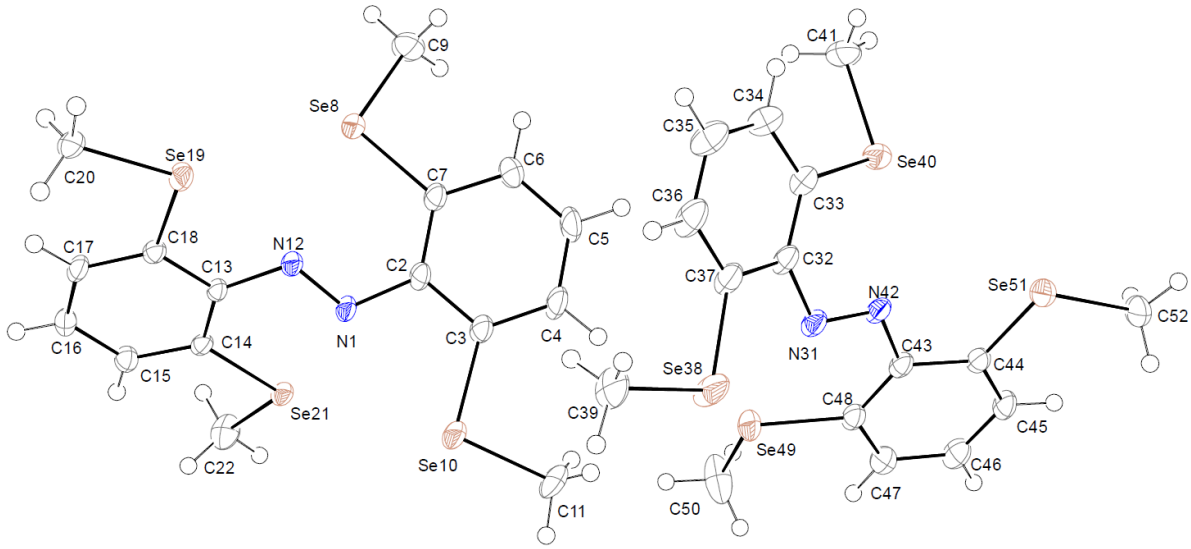


Figure S17. X-ray crystallographic structure of **(SeMe$_4$)-H**.

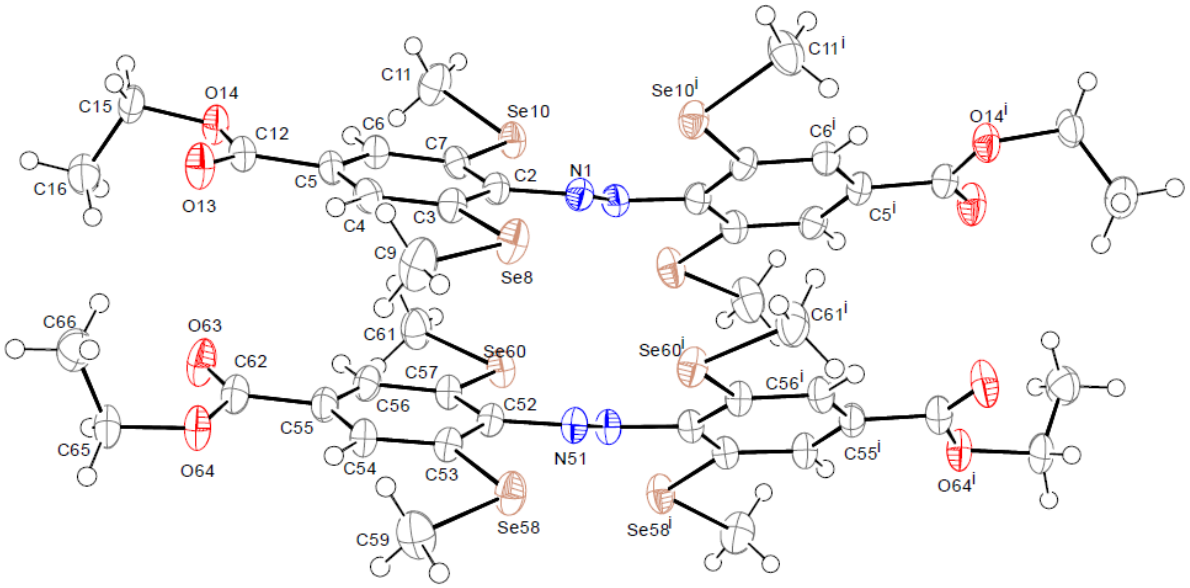


Figure S18. X-ray crystallographic structure of **($SeMe_4$)-ester.**

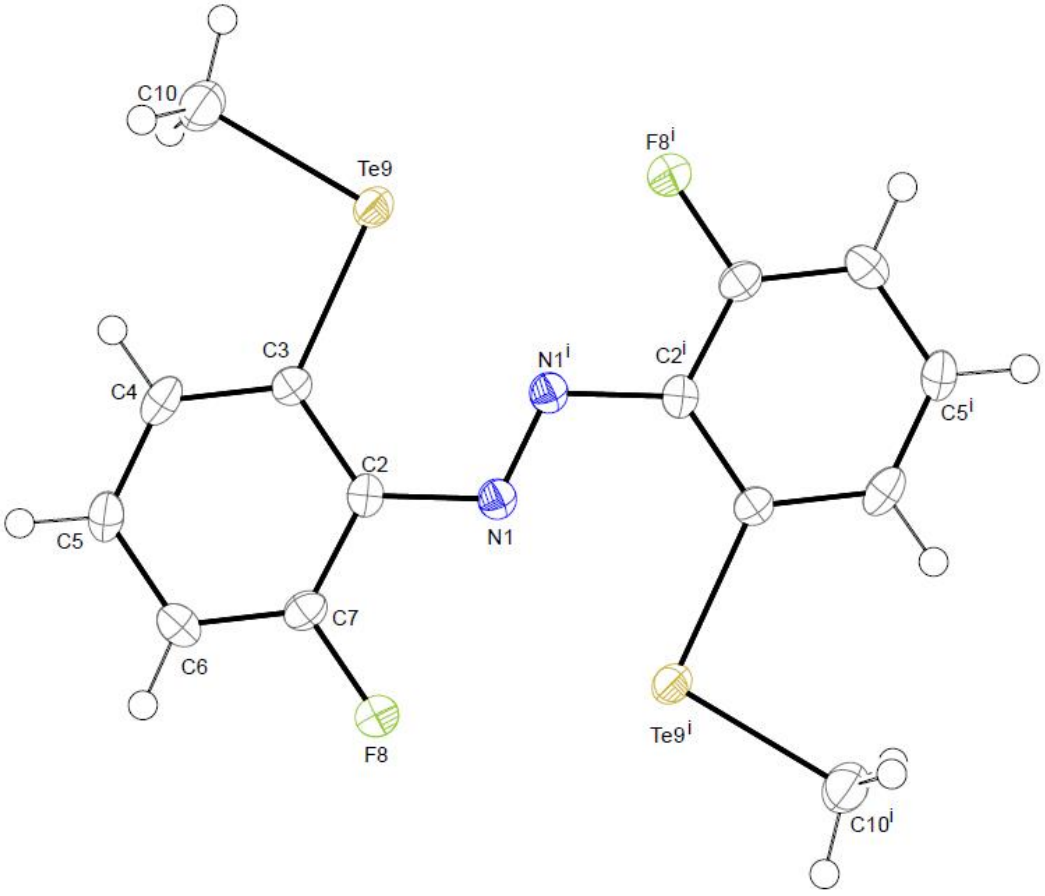


Figure S19. X-ray crystallographic structure of **Te_2H_2-H.**

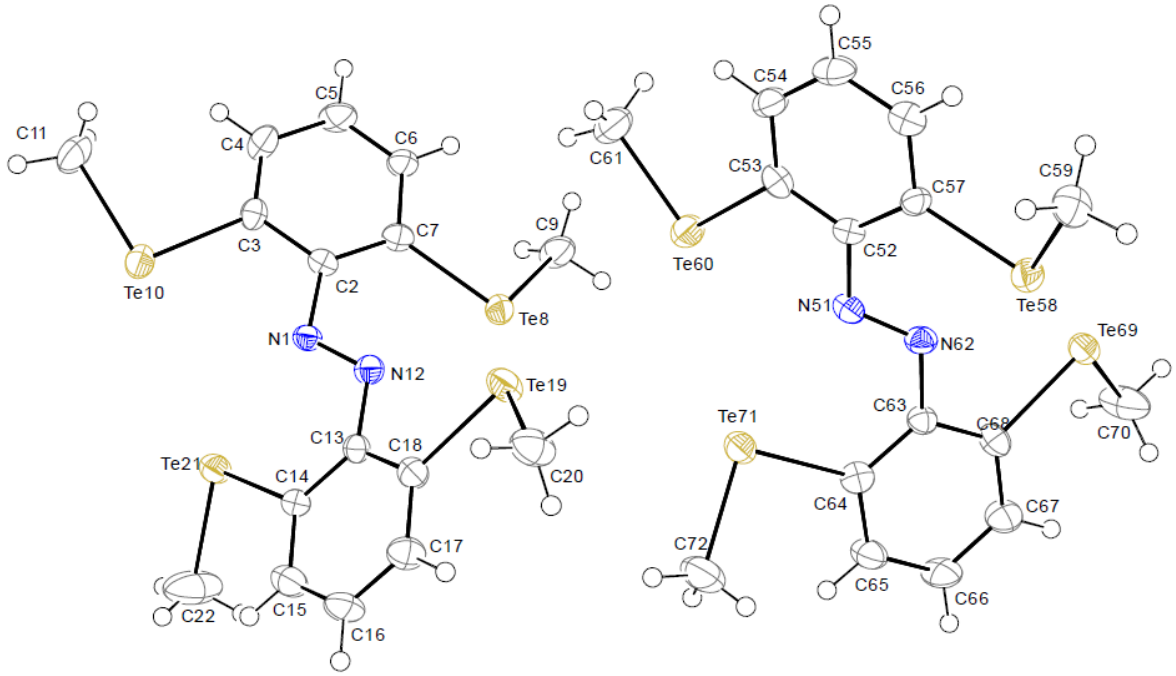


Figure S20. X-ray crystallographic structure of **Te_4-H.**

Table S3. Crystal data and structure refinement for **Br_4-NHBoc**.

Empirical formula	C24 H28 Br4 N4 O4	
Formula weight	756.13	
Temperature	150 K	
Wavelength	1.54184 Å	
Crystal system	Monoclinic	
Space group	I2/a	
Unit cell dimensions	a = 20.6359(4) Å	□= 90°.
	b = 5.18090(10) Å	□= 104.528(2)°.
	c = 27.7349(6) Å	□ = 90°.
Volume	2870.40(10) $Å^3$	
Z	4	
Density (calculated)	1.750 Mg/m^3	
Absorption coefficient	7.147 mm^{-1}	
F(000)	1488	
Crystal size	0.31 x 0.05 x 0.01 mm^3	
Theta range for data collection	4.427 to 76.043°.	
Index ranges	-18<=h<=25, -6<=k<=6, -34<=l<=34	
Reflections collected	13970	
Independent reflections	2983 [R(int) = 0.041]	
Completeness to theta = 74.523°	99.6 %	
Absorption correction	Semi-empirical from equivalents	
Max. and min. transmission	0.93 and 0.23	
Refinement method	Full-matrix least-squares on F^2	
Data / restraints / parameters	2978 / 0 / 164	
Goodness-of-fit on F^2	1.1565	
Final R indices [I>2sigma(I)]	R1 = 0.1031, wR2 = 0.0656	
R indices (all data)	R1 = 0.1044, wR2 = 0.0666	
Largest diff. peak and hole	3.23 and -1.12 e.$Å^{-3}$	

Table S4. Crystal data and structure refinement for **I_4-N_3**.

Empirical formula	C14 H8 I4 N8	
Formula weight	795.89	
Temperature	150 K	
Wavelength	1.54184 Å	
Crystal system	Triclinic	
Space group	P -1	
Unit cell dimensions	a = 11.9316(3) Å	□= 73.159(4)°.
	b = 12.2715(5) Å	□= 73.857(3)°.
	c = 15.2444(7) Å	□ = 79.026(3)°.
Volume	2037.41(14) $Å^3$	
Z	4	
Density (calculated)	2.595 Mg/m^3	
Absorption coefficient	48.188 mm^{-1}	
F(000)	1440	
Crystal size	0.22 x 0.09 x 0.03 mm^3	
Theta range for data collection	3.791 to 76.110°.	
Index ranges	-14<=h<=13, -15<=k<=15, -18<=l<=19	
Reflections collected	20715	
Independent reflections	8417 [R(int) = 0.073]	
Completeness to theta = 73.827°	99.7 %	
Absorption correction	Semi-empirical from equivalents	
Max. and min. transmission	0.24 and 0.01	
Refinement method	Full-matrix least-squares on F^2	
Data / restraints / parameters	8412 / 0 / 469	
Goodness-of-fit on F^2	1.1626	
Final R indices [I>2sigma(I)]	R1 = 0.1252, wR2 = 0.1083	
R indices (all data)	R1 = 0.1306, wR2 = 0.1122	
Largest diff. peak and hole	6.41 and -2.29 e.$Å^{-3}$	

Table S5. Crystal data and structure refinement for **I_4-ester**.

Empirical formula	C18 H14 I4 N2 O4	
Formula weight	829.94	
Temperature	150 K	
Wavelength	1.54184 Å	
Crystal system	Monoclinic	
Space group	P 21/c	
Unit cell dimensions	a = 14.0017(3) Å	□= 90°.
	b = 8.23620(10) Å	□= 104.636(2)°.
	c = 19.1456(4) Å	□ = 90°.
Volume	2136.24(7) $Å^3$	
Z	4	
Density (calculated)	2.580 Mg/m^3	
Absorption coefficient	46.060 mm^{-1}	
F(000)	1520	
Crystal size	0.20 x 0.10 x 0.09 mm^3	
Theta range for data collection	5.058 to 76.433°.	
Index ranges	-17<=h<=17, -10<=k<=8, -23<=l<=23	
Reflections collected	18739	
Independent reflections	4444 [R(int) = 0.050]	
Completeness to theta = 74.904°	99.5 %	
Absorption correction	Semi-empirical from equivalents	
Max. and min. transmission	0.02 and 0.00	
Refinement method	Full-matrix least-squares on F^2	
Data / restraints / parameters	4443 / 0 / 253	
Goodness-of-fit on F^2	1.0359	
Final R indices [I>2sigma(I)]	R1 = 0.0694, wR2 = 0.1752	
R indices (all data)	R1 = 0.0716, wR2 = 0.1791	
Largest diff. peak and hole	4.27 and -1.58 e.$Å^{-3}$	

Table S6. Crystal data and structure refinement for **$(SMe)_4$-H**

Empirical formula	C16 H18 N2 S4	
Formula weight	366.60	
Temperature	150 K	
Wavelength	1.54184 Å	
Crystal system	Monoclinic	
Space group	P 2/n	
Unit cell dimensions	a = 15.1050(2) Å	□= 90°.
	b = 7.88010(10) Å	□= 90.6804(12)°.
	c = 28.9196(3) Å	□ = 90°.
Volume	3442.03(7) $Å^3$	
Z	8	
Density (calculated)	1.415 Mg/m^3	
Absorption coefficient	5.038 mm^{-1}	
F(000)	1535.991	
Crystal size	0.28 x 0.10 x 0.03 mm^3	
Theta range for data collection	3.285 to 76.196°.	
Index ranges	-13<=h<=18, -9<=k<=9, -28<=l<=36	
Reflections collected	24880	
Independent reflections	7138 [R(int) = 0.040]	
Completeness to theta = 74.672°	99.6 %	
Absorption correction	Semi-empirical from equivalents	
Max. and min. transmission	0.86 and 0.46	
Refinement method	Full-matrix least-squares on F^2	
Data / restraints / parameters	7138 / 0 / 397	
Goodness-of-fit on F^2	1.0088	
Final R indices [I>2sigma(I)]	R1 = 0.0418, wR2 = 0.1073	
R indices (all data)	R1 = 0.0486, wR2 = 0.1183	
Largest diff. peak and hole	1.10 and -0.55 e.$Å^{-3}$	

Table S7. Crystal data and structure refinement for **$(SEt)_4$-ester**

Empirical formula	C26 H34 N2 O4 S4	
Formula weight	566.83	
Temperature	150 K	
Wavelength	1.54184 Å	
Crystal system	Triclinic	
Space group	P -1	
Unit cell dimensions	a = 7.2152(2) Å	□= 87.957(3)°.
	b = 8.0923(3) Å	□= 82.964(3)°.
	c = 12.5451(4) Å	□ = 66.841(3)°.
Volume	668.32(4) $Å^3$	
Z	1	
Density (calculated)	1.408 Mg/m^3	
Absorption coefficient	3.561 mm^{-1}	
F(000)	300	
Crystal size	0.25 x 0.09 x 0.02 mm^3	
Theta range for data collection	3.550 to 76.057°.	
Index ranges	-9<=h<=8, -10<=k<=10, -15<=l<=15	
Reflections collected	12330	
Independent reflections	2761 [R(int) = 0.021]	
Completeness to theta = 73.776°	99.7 %	
Absorption correction	Semi-empirical from equivalents	
Max. and min. transmission	0.93 and 0.68	
Refinement method	Full-matrix least-squares on F^2	
Data / restraints / parameters	2761 / 0 / 163	
Goodness-of-fit on F^2	0.9995	
Final R indices [I>2sigma(I)]	R1 = 0.0245, wR2 = 0.0696	
R indices (all data)	R1 = 0.0252, wR2 = 0.0703	
Largest diff. peak and hole	0.40 and -0.27 e.$Å^{-3}$	

Table S8. Crystal data and structure refinement for **$(SeMe)_4$-H**

Empirical formula	C16 H18 N2 Se4	
Formula weight	554.17	
Temperature	150 K	
Wavelength	1.54184 Å	
Crystal system	Monoclinic	
Space group	P 2/n	
Unit cell dimensions	a = 15.5783(2) Å	□= 90°.
	b = 7.94990(10) Å	□= 90.3204(10)°.
	c = 29.5587(3) Å	□ = 90°.
Volume	3660.67(8) $Å^3$	
Z	8	
Density (calculated)	2.011 Mg/m^3	
Absorption coefficient	9.571 mm^{-1}	
F(000)	2111.991	
Crystal size	0.23 x 0.10 x 0.06 mm^3	
Theta range for data collection	5.299 to 76.285°.	
Index ranges	-18<=h<=19, -9<=k<=6, -32<=l<=36	
Reflections collected	38021	
Independent reflections	7607 [R(int) = 0.034]	
Completeness to theta = 74.759°	99.9 %	
Absorption correction	Semi-empirical from equivalents	
Max. and min. transmission	0.56 and 0.27	
Refinement method	Full-matrix least-squares on F^2	
Data / restraints / parameters	7605 / 0 / 398	
Goodness-of-fit on F^2	1.0394	
Final R indices [I>2sigma(I)]	R1 = 0.0250, wR2 = 0.0614	
R indices (all data)	R1 = 0.0266, wR2 = 0.0625	
Extinction coefficient	7.9(9)	
Largest diff. peak and hole	0.79 and -1.29 e.$Å^{-3}$	

Table S9. Crystal data and structure refinement for **$(TeMe)_4$-H**

Empirical formula	C16 H18 N2 Te4	
Formula weight	748.73	
Temperature	150 K	
Wavelength	1.54184 Å	
Crystal system	Monoclinic	
Space group	P 21	
Unit cell dimensions	a = 10.73350(10) Å	□= 90°.
	b = 10.57430(10) Å	□= 95.2723(7)°.
	c = 18.02080(10) Å	□ = 90°.
Volume	2036.69(3) $Å^3$	
Z	4	
Density (calculated)	2.442 Mg/m^3	
Absorption coefficient	44.738 mm^{-1}	
F(000)	1344	
Crystal size	0.03 x 0.03 x 0.005 mm^3	
Theta range for data collection	4.136 to 76.409°.	
Index ranges	-13<=h<=13, -13<=k<=12, -22<=l<=22	
Reflections collected	45376	
Independent reflections	8268 [R(int) = 0.036]	
Completeness to theta = 74.117°	99.9 %	
Absorption correction	Semi-empirical from equivalents	
Max. and min. transmission	0.80 and 0.24	
Refinement method	Full-matrix least-squares on F^2	
Data / restraints / parameters	8268 / 1 / 398	
Goodness-of-fit on F^2	0.9937	
Final R indices [I>2sigma(I)]	R1 = 0.0249, wR2 = 0.0600	
R indices (all data)	R1 = 0.0263, wR2 = 0.0606	
Absolute structure parameter	-0.020(4)	
Largest diff. peak and hole	1.15 and -0.56 e.$Å^{-3}$	

Table S10. Crystal data and structure refinement for **$(SeMe)_4$-ester**

Empirical formula	C22 H26.00 N2 O4 Se4	
Formula weight	698.30	
Temperature	150 K	
Wavelength	1.54184 Å	
Crystal system	Orthorhombic	
Space group	P b c n	
Unit cell dimensions	a = 16.0349(3) Å	□= 90°.
	b = 15.8463(4) Å	□= 90°.
	c = 19.0464(4) Å	□ = 90°.
Volume	4839.57(18) $Å^3$	
Z	8	
Density (calculated)	1.917 Mg/m^3	
Absorption coefficient	7.531 mm^{-1}	
F(000)	2719.987	
Crystal size	0.14 x 0.11 x 0.09 mm^3	
Theta range for data collection	3.922 to 77.501°.	
Index ranges	-20<=h<=10, -18<=k<=19, -23<=l<=23	
Reflections collected	43637	
Independent reflections	5050 [R(int) = 0.050]	
Completeness to theta = 75.176°	99.8 %	
Absorption correction	Semi-empirical from equivalents	
Max. and min. transmission	0.51 and 0.35	
Refinement method	Full-matrix least-squares on F^2	
Data / restraints / parameters	5050 / 0 / 289	
Goodness-of-fit on F^2	1.0194	
Final R indices [I>2sigma(I)]	R1 = 0.0399, wR2 = 0.1076	
R indices (all data)	R1 = 0.0502, wR2 = 0.1190	
Largest diff. peak and hole	1.48 and -0.77 e.$Å^{-3}$	

Table S11. Crystal data and structure refinement for **Te_2F_2-H.**

Empirical formula	C14 H12 F2 N2 Te2	
Formula weight	501.46	
Temperature	150 K	
Wavelength	0.71073 Å	
Crystal system	Monoclinic	
Space group	$P2_1/n$	
Unit cell dimensions	a = 6.4567(7) Å	□= 90°.
	b = 8.6728(9) Å	□= 92.320(9)°.
	c = 13.3795(13) Å	□ = 90°.
Volume	748.61(13) $Å^3$	
Z	2	
Density (calculated)	2.225 Mg/m^3	
Absorption coefficient	3.909 mm^{-1}	
F(000)	464	
Crystal size	0.15 x 0.10 x 0.08 mm^3	
Theta range for data collection	3.450 to 30.490°.	
Index ranges	-9<=h<=9, -12<=k<=12, -18<=l<=18	
Reflections collected	6642	
Independent reflections	2012 [R(int) = 0.066]	
Completeness to theta = 27.727°	99.8 %	
Absorption correction	Semi-empirical from equivalents	
Max. and min. transmission	0.73 and 0.59	
Refinement method	Full-matrix least-squares on F^2	
Data / restraints / parameters	1580 / 0 / 91	
Goodness-of-fit on F^2	1.0063	
Final R indices [I>2sigma(I)]	R1 = 0.0337, wR2 = 0.0580	
R indices (all data)	R1 = 0.0646, wR2 = 0.0707	
Largest diff. peak and hole	2.27 and -2.26 e.$Å^{-3}$	

Table S12. Crystal data and structure refinement for **F_2,H_2-NHBoc**.

Empirical formula	C24 H30 F2 N4 O4	
Formula weight	476.52	
Temperature	150 K	
Wavelength	1.54184 Å	
Crystal system	Triclinic	
Space group	P -1	
Unit cell dimensions	a = 10.1072(7) Å	□= 94.868(6)°.
	b = 11.4012(8) Å	□= 95.841(6)°.
	c = 11.5402(9) Å	□ = 112.726(7)°.
Volume	1208.99(17) $Å^3$	
Z	2	
Density (calculated)	1.309 Mg/m^3	
Absorption coefficient	0.841 mm^{-1}	
F(000)	504	
Crystal size	0.26 x 0.05 x 0.02 mm^3	
Theta range for data collection	3.886 to 77.150°.	
Index ranges	-11<=h<=12, -13<=k<=14, -14<=l<=14	
Reflections collected	12314	
Independent reflections	5019 [R(int) = 0.038]	
Completeness to theta = 72.521°	99.5 %	
Absorption correction	Semi-empirical from equivalents	
Max. and min. transmission	0.98 and 0.88	
Refinement method	Full-matrix least-squares on F^2	
Data / restraints / parameters	5012 / 0 / 307	
Goodness-of-fit on F^2	0.9792	
Final R indices [I>2sigma(I)]	R1 = 0.0509, wR2 = 0.1349	
R indices (all data)	R1 = 0.0760, wR2 = 0.1584	
Largest diff. peak and hole	0.37 and -0.33 e.$Å^{-3}$	

6.2.6 References (Chapter 2 appendix)

[1] D. Bléger, J. Schwarz, A. M. Brouwer, S. Hecht, *J. Am. Chem. Soc.,* **2012**, *134*, 20597-20600.

[2] B. Heinrich, K. Bouazoune, M. Wojcik, U. Bakowsky, O. Vázquez, *Org. Biomol. Chem.,* **2019**, *17*, 1827-1833.

[3] A. Kerckhoffs, M. J. Langton, *Chem. Sci.,* **2020**, *11*, 6325-6331.

[4] K. Khosravi, S. Naserifar, *Tetrahedron* **2018**, *74*, 6584-6592.

[5] M. Dong, A. Babalhavaeji, C. V. Collins, K. Jarrah, O. Sadovski, Q. Dai, G. A. Woolley, *J. Am. Chem. Soc.* **2017**, *139*, 13483-13486.

[6] Y. Takeda, S. Okumura, S. Minakata, *Synthesis* **2013**, *45*, 1029-1033.

[7] S. M. Walter, S. H. Jungbauer, F. Kniep, S. Schindler, E. Herdtweck, S. M. Huber, *J. Fluorine Chem.* **2013**, *150*, 14-20.

[8] B. Latli, R. Kiesling, S. Aßfalg, M. Chevliakov, M. Hrapchak, S. Campbell, N. Gonnella, C. A. Busacca, C. H. Senanayake, *J. Label. Compd. Radiopharm.,* **2016**, *59*, 648-656.

[9] A. R. T. A.I. Vogel, B.S. Furnis, A.J. Hannaford, P.W.G Smith, *Vogel's Textbook of Practical Organic Chemistry*, Prentice Hall, **1989**.

[10] S. V. Khansole, S. B. Junne, M. A. Sayyed, Y. B. Vibhute, *Synth. Commun.,* **2008**, *38*, 1792-1798.

[11] J. Hirschfeld, A. Buschauer, S. Elz, W. Schunack, M. Ruat, E. Traiffort, J. C. Schwartz, *J. Med. Chem.* **1992**, *35*, 2231-2238.

[12] A.-L. Leistner, S. Kirchner, J. Karcher, T. Bantle, M. L. Schulte, P. Gödtel, C. Fengler, Z. L. Pianowski, *Chem. Eur. J.,* **2021**, *27*, 8094-8099.

[13] N. H. Park, E. V. Vinogradova, D. S. Surry, S. L. Buchwald, *Angew. Chem. Int. Ed.,* **2015**, *54*, 8259-8262.

[14] S. T. Gadge, A. Mishra, A. L. Gajengi, N. V. Shahi, B. M. Bhanage, *RSC Adv.,* **2014**, *4*, 50271-50276.

[15] D. Lim, H. Lee, D. Nam, R. Dubey, *Tetrahedron Lett.,* 2011, **52**, 6839-6842

[16] G. L. A. M. N. P. D. K. J. N. S. D. M. K. Sheetal, Glenmark Pharamceuticals SA, **2016**.

[17] M. A. B. Mostafa, R. M. Bowley, D. T. Racys, M. C. Henry, A. Sutherland, *J. Org. Chem.,* **2017**, *82*, 7529-7537.

[18] C. C. Woodroofe, B. Zhong, X. Lu, R. B. Silverman, *J. Chem. Soc., Perkin trans.,* **2000**, 55-59.

[19] S. S. Matikonda, J. M. Fairhall, F. Fiedler, S. Sanhajariya, R. A. J. Tucker, S. Hook, A. L. Garden, A. B. Gamble, *Bioconjug. Chem.* **2018**, *29*, 324-334.

[20] A. A. Estrada, X. Liu, C. Baker-Glenn, A. Beresford, D. J. Burdick, M. Chambers, B. K. Chan, H. Chen, X. Ding, A. G. DiPasquale, S. L. Dominguez, J. Dotson, J. Drummond, M. Flagella, S. Flynn, R. Fuji, A. Gill, J. Gunzner-Toste, S. F. Harris, T. P. Heffron, T. Kleinheinz, D. W. Lee, C. E. Le Pichon, J. P. Lyssikatos, A. D. Medhurst, J. G. Moffat, S. Mukund, K. Nash, K. Scearce-Levie, Z. Sheng, D. G. Shore, T. Tran, N. Trivedi, S. Wang, S. Zhang, X. Zhang, G. Zhao, H. Zhu, Z. K. Sweeney, *J. Med. Chem.,* **2012**, *55*, 9416-9433.

[21] T. Suzuki, K. Iwaoka, N. Imanishi, Y. Nagakura, K. Miyata, H. Nakahara, M. Ohta, T. Mase, *Chem. Pharm. Bull.,* **1999**, *47*, 120-122.

[22] R. L. Mackman, B. A. Katz, J. G. Breitenbucher, H. C. Hui, E. Verner, C. Luong, L. Liu, P. A. Sprengeler, *J. Med. Chem.,* **2001**, *44*, 3856-3871.

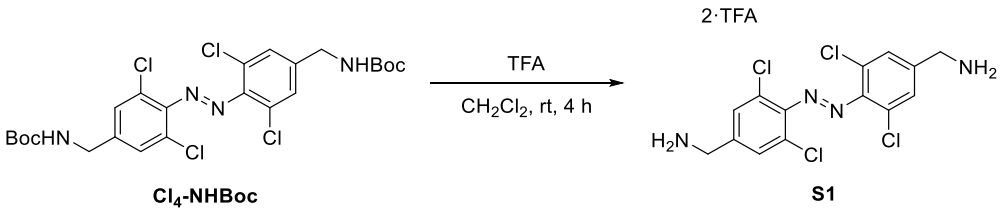
[23] A. Granados, A. Shafir, A. Arrieta, F. P. Cossío, A. Vallribera, *J. Org. Chem.,* **2020**, *85*, 2142-2150.

[24] M. Dong, A. Babalhavaeji, M. J. Hansen, L. Kálmán, G. A. Woolley, *Chem. Commun.,* **2015**, *51*, 12981-12984.

[25] N. Sakai, S. Asama, S. Anai, T. Konakahara, *Tetrahedron* **2014**, *70*, 2027-2033.

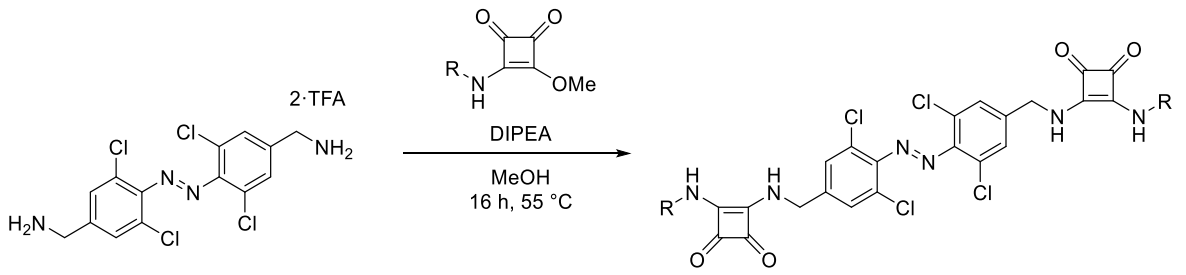
6.3.1 Synthetic procedures (Chapter 3)

Compounds **16a-d and 16f** were prepared according to literature procedures[1-2].

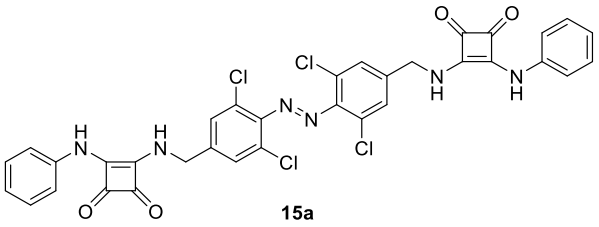


Cl_4-NHBoc **S1**

Amine S1. To a solution of **Cl_4-NHBoc** (2.00 g, 3.46 mmol) in CH_2Cl_2 (40 mL) was added TFA (5 mL). The reaction was stirred at room temperature for 4 hours. The TFA was removed under a stream of nitrogen, then dried *in vacuo* to afford the title compound as a brown solid as a mixture of isomers (2.10 g, 3.46 mmol, 100%). ***E*-5:** ^{1}H NMR (400 MHz, Methanol-d_4) δ 7.74 (s, 4H), 4.23 (s, 4H). ^{13}C NMR (101 MHz, Methanol-d_4) δ 148.73, 137.49, 131.33, 128.58, 42.86. HRMS-ESI (m/z) Calculated for $C_{14}H_{12}Cl_4N_4$ $[M+H]^+$, 376.9889; found 376.9888.

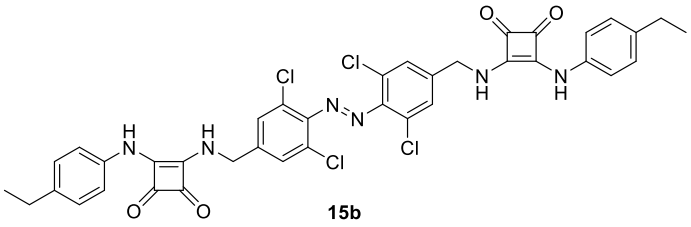


General Procedure 1. Amine **5** (50 mg, 82.5 µmol) was dissolved in MeOH (1 mL). DIPEA (86.2 µL, 0.5 mmol, 6 eq) was added dropwise. Monosquaramide **16a-i** (165 µmol, 2 eq) in MeCN (1 mL) was added, and the solution heated at 55 °C for 16 hours. The reaction was cooled to rt and the solid precipitate was filtered and washed sequentially with MeOH and MeCN, then collected and dried under high vacuum to afford the title compound as an orange/brown solid.



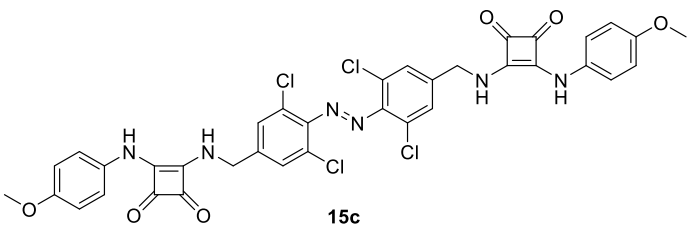
15a

15a. Prepared according to ***General procedure 1*** (31 mg, 44 µmol, 51%). ***E*-15a:** ^{1}H NMR (400 MHz, DMSO-d_6) δ 9.80 (s, 2H), 8.09 (br s, *J* = 6.3 Hz, 2H), 7.74 (s, 4H), 7.43 (m, 4H), 7.34 (m, 4H), 7.04 (t, *J* = 7.3 Hz, 2H), 4.90 (d, *J* = 6.3 Hz, 4H). ^{13}C NMR (126 MHz, DMSO-d_6) δ 183.81, 180.68, 168.50, 164.16, 145.24, 141.98, 138.46, 128.62, 128.32, 126.10, 122.34, 118.06, 45.50. HRMS-ESI (m/z) Calculated for $C_{34}H_{22}Cl_4N_6O_4$ $[M-H]^-$, 717.0373; found 717.0376.



15b

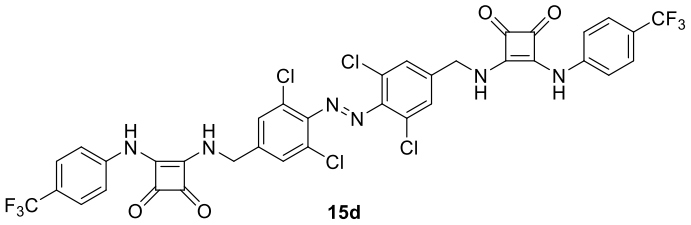
15b. Prepared according to ***General procedure 1*** (39.1 mg, 50.3 µmol, 61%). ***E*-15b:** ^{1}H NMR (400 MHz, DMSO-d_6) δ 9.74 (s, 2H), 8.04 (t, *J* = 5.54 Hz, 1H), 7.74 (s, 4H), 7.33 (d, *J* = 8.25 Hz), 7.18 (d, *J* = 8.25 Hz) 4.90 (d, *J* = 5.54 Hz, 4H), 2.57 (q, *J* = 7.61 Hz, 4H), 1.17 (t, *J* = 7.61 Hz, 6H). ^{13}C NMR (126 MHz, DMSO-d_6) δ 183.79, 180.89, 168.57, 164.36, 145.50, 142.76, 138.43, 136.53, 128.84, 128.57, 126.37, 118.44, 45.78, 27.50, 15.70. HRMS-ESI (m/z) Calculated for $C_{38}H_{30}Cl_4N_6O_4$ $[M-H]^-$, 773.1010; found 773.1017



15c

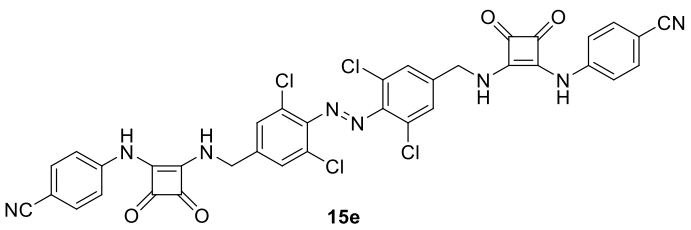
15c. Prepared according to ***General procedure 1*** (32 mg, 44 µmol, 53%). ***E*-15c:** ^{1}H NMR (400 MHz, DMSO-d_6) δ 9.67 (s, 2H), 7.94 (s, 2H), 7.73 (s, 4H), 7.34 (d, *J* = 8.5 Hz, 4H), 6.96

– 6.91 (m, 4H), 4.88 (d, *J* = 6.1 Hz, 4H), 4.80 (s, 1H), 3.74 (s, 6H). ^{13}C NMR (126 MHz, DMSO-d_6) δ 183.23, 180.92, 168.05, 164.34, 155.40, 145.24, 142.14, 131.69, 128.32, 126.11, 119.91, 114.32, 55.06, 45.50. HRMS-ESI (m/z) Calculated for $C_{36}H_{26}Cl_4N_6O_6$ [M-H]$^-$, 777.0584; found 777.0591.



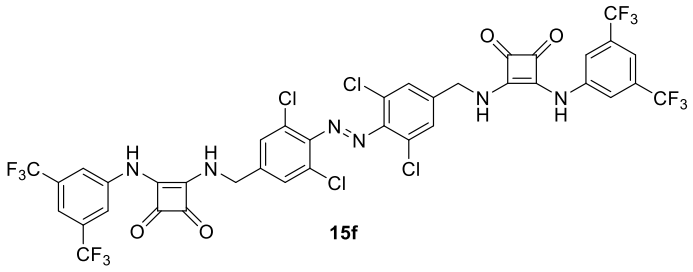
15d

15d. Prepared according to ***General procedure 1*** (34.5 mg, 40.2 µmol, 49%). ***E*-15d:** ^{1}H NMR (400 MHz, DMSO-d_6) δ 10.07 (s, 2H), 8.17 (t, *J* = 5.43 Hz, 1H), 7.75 (s, 4H), 7.69 (d, *J* = 8.69 Hz), 7.60 (d, *J* = 8.69 Hz), 4.91 (d, *J* = 5.43 Hz, 4H). ^{13}C NMR (126 MHz, DMSO-d_6) δ 184.54, 180.62, 169.22, 163.46, 145.31, 142.08, 128.37, 125.92, 124.48 (q, *J* = 271.3 Hz), 122.48 (q, *J* = 32.13 Hz), 117.94, 45.60. HRMS-ESI (m/z) Calculated for $C_{36}H_{20}Cl_4F_6N_6O_4$ [M-H]$^-$, 855.0115; found 855.0107



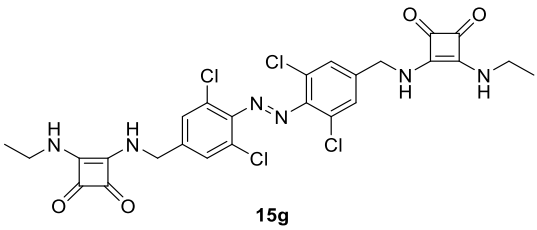
15e

15e. Prepared according to ***General procedure 1*** (40 mg, 52 µmol, 63%). ***E*-15e:** ^{1}H NMR (400 MHz, DMSO-d_6) δ 10.12 (s, 2H), 8.21 (m, 2H), 7.80 (d, *J* = 8.01 Hz, 4H), 7.75 (s, 4H), 7.58 (d, *J* = 8.01 Hz), 4.91 (d, *J* = 4.38 Hz, 4H). ^{13}C NMR (126 MHz, DMSO-d_6) δ 184.71, 180.52, 169.45, 162.98, 145.29, 142.68, 141.68, 132.97, 128.35, 126.09, 118.32, 118.00, 103.86, 45.59. Calculated for $C_{36}H_{20}Cl_4N_8O_4$ [M-H]$^-$, 767.0278, found 767.0301.



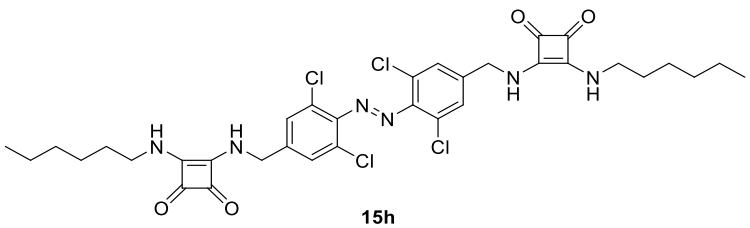
15f

15f. Prepared according to ***General procedure 1*** (34 mg, 46.2 µmol, 70%). ***E*-15f:** ^{1}H NMR (400 MHz, DMSO-d_6) δ 10.37 (br s, 2H), 8.20 (br s, 2H), 8.02 (s, 4H), 7.74 (s, 4H), 7.69 (s, 2H), 4.91 (s, 4H). ^{13}C NMR (101 MHz, DMSO-d_6) δ 184.69, 180.87, 169.42, 162.86, 145.33, 141.80, 140.72, 131.05 (q, *J* = 33.08 Hz), 128.43, 126.12, 122.74 (q, *J* = 274 Hz), 118.03, 114.34, 45.66. HRMS-ESI (m/z) Calculated for $C_{38}H_{18}Cl_4N_6O_4$ $[M-H]^-$, 988.9879; found 988.9863.



15g

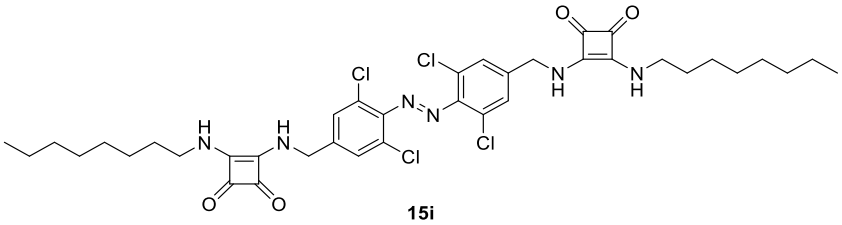
15g. Prepared according to ***General procedure 1*** (34.6 mg, 55 µmol, 67%). ***E*-15g:** ^{1}H NMR (400 MHz, DMSO-d_6) δ 7.87 (br s, 2H), 7.67 (s, 4H), 7.49 (br s, 2H), 4.78 (d, *J* = 6.2 Hz, 4H), 3.52 (m, 4H), 1.16 (t, *J* = 7.2 Hz, 6H). ^{13}C NMR (126 MHz, DMSO) δ 182.76, 182.19, 168.05, 166.90, 145.14, 142.53, 128.27, 126.07, 45.19, 38.01, 15.80. HRMS-ESI (m/z) Calculated for $C_{26}H_{22}Cl_4N_6O_4$ $[M-H]^-$, 621.0384; found 621.0384



15h

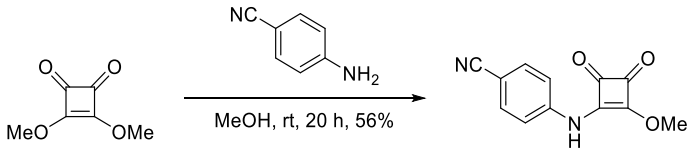
15h. Prepared according to ***General procedure 1*** (50 mg, 68.4 µmol, 83%). ***E*-15h:** ^{1}H NMR (400 MHz, DMSO-d_6) δ 7.83 (br s, 2H), 7.66 (s, 4H), (br m, 2H) 4.79 (d, *J* = 5.54 Hz, 4H), 3.50 (m, 4H), 1.51 (m, 4H), 1.27 (m, 12H), 0.84 (m, 6H). ^{13}C NMR (126 MHz, DMSO-d_6) δ 182.77,

182.16, 168.20, 166.81, 145.10, 142.53, 128.19, 126.05, 45.12, 43.04, 30.21, 30.06, 24.89, 21.25, 12.99. HRMS-ESI (m/z) Calculated for $C_{34}H_{38}Cl_4N_6O_4$ $[M-H]^-$, 733.1625; found 733.1632.



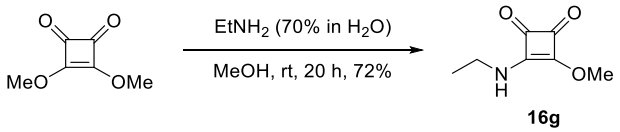
15i

15i. Prepared according to ***General procedure 1*** (55.6 mg, 68.4 µmol, 83%). ***E*-15i:** ^{1}H NMR (400 MHz, DMSO-d_6) δ 7.62 (s, 4H), 4.75 (s, 4H), 3.56 (m, 4H), 1.48 (m, 4H), 1.22 (m, 20H), 0.80 (t, *J* = 6.5 Hz, 6H). ^{13}C NMR (126 MHz, DMSO-d_6) δ 182.79, 182.18, 168.22, 166.84, 145.13, 142.57, 128.22, 126.08, 45.15, 43.07, 30.57, 30.12, 27.98, 27.91, 25.30, 21.34, 13.10. HRMS-ESI (m/z) Calculated for $C_{38}H_{46}Cl_4N_6O_4$ $[M-H]^-$, 789.2251; found 789.2254.



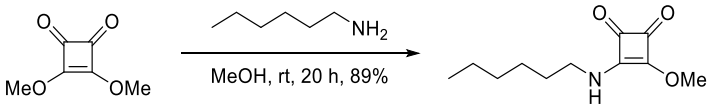
16e

Monosquaramide 16e. To a stirred solution of 3,4-dimethoxy-3-cyclobutene-1,2-dione (100 mg, 0.70 mmol, 1 eq) in methanol (1 mL) was added 4-aminobenzonitrile (87 mg, 0.77 mmol, 1.04 eq) and the mixture stirred for 24 hours at room temperature. The residue was concentrated, dry-loaded onto silica, then purified by silica gel flash chromatography (0% then 10% MeCN in CH_2Cl_2) afford the title compound (90 mg, 0.316 mmol, 56%) as a white solid. ^{1}H NMR (400 MHz, DMSO) δ 11.06 (s, 1H), 7.81 (d, *J* = 8.4 Hz, 2H), 7.53 (d, *J* = 8.3 Hz, 2H), 4.41 (s, 3H). ^{13}C NMR (101 MHz, DMSO-d_6) δ 187.37, 184.65, 180.04, 169.05, 142.33, 133.59, 119.31, 118.96, 105.36, 60.91. HRMS-ESI (m/z) Calculated for $C_{12}H_{10}NO_4$ $[M-H]^-$, 227.0462; found 227.0460.



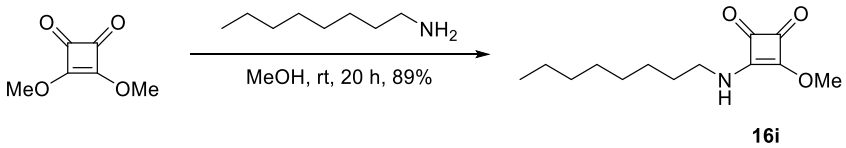
16g

Monosquaramide 16g. To a stirred solution of 3,4-dimethoxy-3-cyclobutene-1,2-dione (100 mg, 0.77 mmol, 1 eq) in methanol (1 mL) was added 70% ethylamine in water (168 µl, 2.11 mmol, 3 eq) and the mixture was allowed to stir at room temperature for 20 hours. The residue was concentrated and purified by silica gel flash chromatography (7% MeCN in CH_2Cl_2) to afford the title compound (73 mg, 0.316 mmol, 72%) as a white solid. The compound exists as two rotamers in DMSO at room temperature in a 3:2 ratio. **Major rotamer:** ^{1}H NMR (400 MHz, DMSO-d_6). δ 8.78 (s, 1H), 4.29 (s, 3H), 3.29 (t, *J* = 6.9 Hz, 2H), 1.13 (t, *J* = 7.0 Hz, 3H). ^{13}C NMR (126 MHz, DMSO) δ 189.05, 182.25, 176.95, 171.89, 60.11, 38.54 15.68. HRMS-ESI (m/z) Calculated for $C_7H_9NO_3$ $[M-H]^-$, 154.0499; found 154.0503.



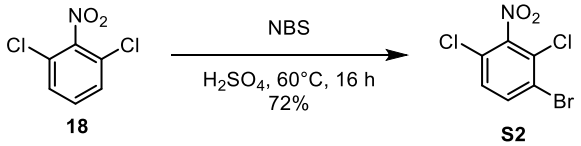
16h

Monosquaramide 16h. To a stirred solution of 3,4-dimethoxy-3-cyclobutene-1,2-dione (100 mg, 0.70 mmol, 1 eq) in methanol (1 mL) was added hexylamine (78.3 mg, 0.77 mmol, 1.1 eq) and the mixture was stirred for 20 hours at room temperature, then concentrated. The residue was purified by silica gel flash chromatography (9% MeCN in CH_2Cl_2) to afford the title compound (133 mg, 0.629 mmol, 89%). The compound exists as two rotamers in DMSO at room temperature in a 3:1 ratio. **Major Rotamer**: ^{1}H NMR (400 MHz, Chloroform-d) δ 6.26 (br s, 1H), 4.41 (s, 3H), 3.46 – 3.36 (m, 2H), 1.60 (m, 2H), 1.39 – 1.25 (m, 6H), 0.95 – 0.83 (m, 3H), ^{13}C NMR (101 MHz, Chloroform-d) δ 189.85, 182.88, 177.72, 172.29, 60.56, 45.11, 31.36, 30.57, 26.09, 22.58, 14.06. HRMS-ESI (m/z) Calculated for $C_{11}H_{17}NO_3$ $[M-H]^-$, 210.1136; found 210.1133.



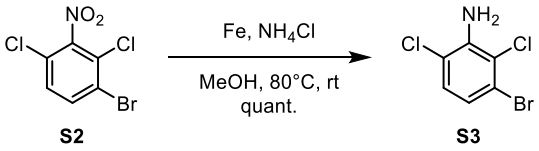
16i

Monosquaramide 16i. To a stirred solution of 3,4-dimethoxy-3-cyclobutene-1,2-dione (100 mg, 0.70 mmol, 1 eq) in methanol (1 mL) was added octylamine (100 mg, 0.77 mmol, 1.1 eq) and the mixture was allowed to stir at room temperature for 20 hours, then concentrated. The residue was concentrated and purified by silica gel flash chromatography (10% MeCN in CH_2Cl_2), to afford the title compound as a white solid (100 mg, 0.629 mmol, 52%). The compound exists as two rotamers in DMSO at room temperature in a 4:1 ratio. **Major Rotamer:** ^{1}H NMR (400 MHz, Chloroform-d) δ 6.61 (br s, 1H), 4.40 (s, 3H), 3.41 (m, 2H), 1.61 (m, 2H), 1.29 (m, 10H), 0.87 (t, *J* = 6.7 Hz, 3H). δ ^{13}C NMR (101 MHz, Chloroform-d) δ 189.72, 183.02, 177.73, 172.32, 60.62, 45.13, 31.86, 30.65, 29.24, 29.18, 26.44, 22.73, 14.18. HRMS-ESI (m/z) Calculated for $C_{13}H_{21}NO_3$ $[M-H]^-$, 240.1596; found 240.1594.

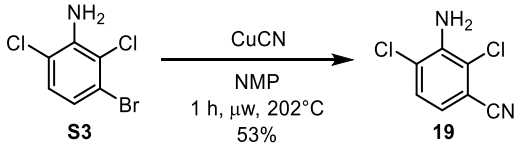


18 **S2**

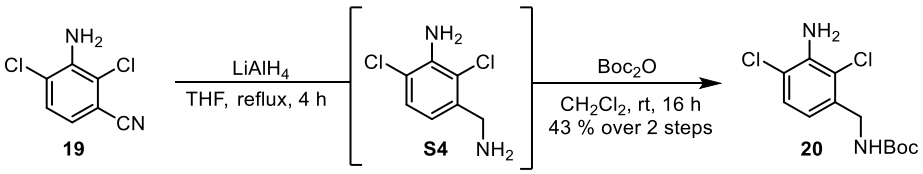
Aryl bromide S2. Prepared according to a modified literature procedure.[3] To a stirring solution of **18** (3.93 g, 20.5 mmol) in concentrated sulphuric acid (110 mL) under inert atmosphere was added N-bromosuccinimide (3.64 g, 20.5 mmol) at rt and the resulting suspension was heated to 60 °C and stirred for 16 h. The reaction was poured into ice water (100 mL) and extracted with EtOAc (2 x 100 mL). The organic layers were concentrated then recrystallized from hexane to afford the title compound as white crystals (4.0 g, 14.8 mmol, 72%). ^{1}H NMR (400 MHz, DMSO) δ 8.11 (d, *J* = 8.9 Hz, 1H), 7.79 (d, *J* = 8.8 Hz, 1H). Data consistent with that given in the literature. [3]



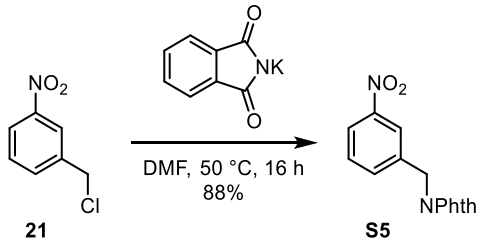
Aniline S3. To a solution of **S2** (4.0 g, 14.77 mmol) in MeOH (100 mL) equipped with a large stirring bar was added Fe powder (4.12 g, 73.83 mmol, 5 eq) and ammonium chloride (3.95 g, 73.83 mmol, 5 eq). The suspension was stirred vigorously at 80 °C (bath temperature) for 4 hours. The solution was filtered over celite and the filtrate was concentrated *in vacuo* to afford the title compound as a white solid (3.55 g, 14.74 mmol, 100%). ^{1}H NMR (400 MHz, $CDCl_3$) δ 7.05 (d, *J* = 8.6 Hz, 1H), 6.95 (d, *J* = 8.6 Hz, 1H), 4.61 (br s, 2H). ^{13}C NMR (101 MHz, $CDCl_3$) δ 141.64, 128.16, 121.84, 121.41, 119.85, 118.33. HRMS-ESI (m/z) Calculated for $C_6H_4Cl_2NBr$ $[M+H]^+$, not found under any conditions.



Nitrile 19. In a microwave vial was added **S3** (3.5 g, 14.53 mmol) and CuCN (1.69 g, 18.89 mmol, 1.3 eq). The vial was purged with N_2 for 10 minutes. Then, 20 mL degassed NMP was added, the tube was sealed and reaction was heated to 202 °C under microwave irradiation for 1h. The reaction was cooled, poured over ice water ammonia solution and extracted with 50:50 hexane:EtOAc 3x. The combined organic layers were sequentially washed with water and 5% LiCl solution, then concentrated. The resulting residue was purified by silica gel flash chromatography (50% CH_2Cl_2 in hexane) to afford the title compound as a white solid (1.44 g, 7.70 mmol, 53%, 90% purity). ^{1}H NMR (400 MHz, $CDCl_3$) δ 7.28 (d, *J* = 8.3 Hz, 1H), 7.00 (d, *J* = 8.3 Hz, 1H), 4.72 (br s, 2H). ^{13}C NMR (101 MHz, $CDCl_3$) δ 141.48, 128.27, 124.07, 122.11, 121.06, 116.06, 112.33. HRMS-EI (m/z) Calculated for $C_7H_4Cl_2N_2$ 185.9752; found 185.9748

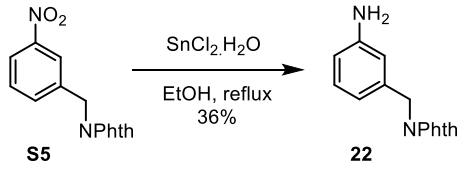


Carbamate 20. To a suspension of $LiAlH_4$ (733 mg, 19.25 mmol, 2.5 eq) in dry THF (40 mL) was added **19** (1.44 g, 7.70 mmol, 1.0 eq) in THF (60 mL). The suspension was stirred at reflux temperature for 4 hours. The reaction mixture was cooled, diluted in Et_2O (150 mL), then water (730 µL), 2.5M NaOH (730 µL), and water (2 mL) was added dropwise. The suspension was stirred for 15 minutes, and then anhydrous $MgSO_4$ was added (Fieser work-up). The solution was filtered, then concentrated to afford crude **S4** without further purification (1.35 g). ^{1}H NMR (400 MHz, $CDCl_3$) δ 7.13 (d, *J* = 8.2 Hz, 1H), 6.68 (d, *J* = 8.2 Hz, 1H), 4.50 (br s, 2H), 3.84 (s, 2H), 1.85 – 1.72 (br s, 2H). **S4** was dissolved in CH_2Cl_2 (25 mL), then Boc_2O (1.51 g, 6.93 mmol, 0.9 eq) in CH_2Cl_2 (15 mL) was added dropwise. The reaction was stirred at room temperature for 16 h. The reaction was concentrated, then purified by silica gel flash chromatography (80% CH_2Cl_2 in hexane) to afford the title compound as a white solid (734 mg, 3.32 mmol, 43%). ^{1}H NMR (400 MHz, $CDCl_3$) δ 7.15 (d, *J* = 8.3 Hz, 1H), 6.71 (d, *J* = 8.3 Hz, 1H), 4.92 (s, 1H), 4.33 (d, *J* = 6.0 Hz, 2H), 1.45 (s, 9H). ^{13}C NMR (126 MHz, $CDCl_3$) δ 155.85, 140.38, 135.78, 127.49, 118.81, 118.76, 118.10, 79.85, 42.86, 28.53. HRMS-ESI (m/z) Calculated for $C_{12}H_{16}Cl_2N_2O_2$ $[M+Na]^+$, 313.0481; found 313.0481.

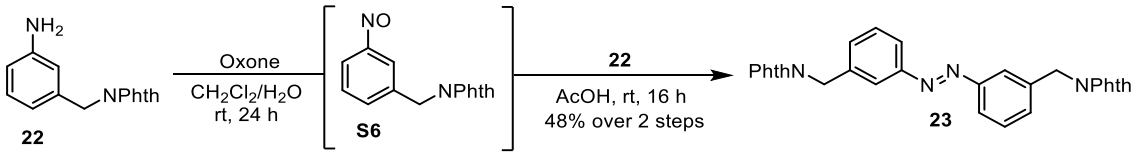


Phthalimide S5. Prepared according to a modified literature procedure.[4] 3-nitrobenzyl chloride **21** (2 g, 11.7 mmol) was dissolved in DMF (10 mL). Potassium phthalimide (2.27 g, 12.2 mmol, 1.05 eq) was added and the reaction was stirred at 50 °C for 16 hours. The DMF was removed *in vacuo* at 70 °C. To the residue was added water (15 mL) and EtOAc (4 mL)

and the biphasic mixture was stirred vigorously for 30 minutes. The precipitated solid was filtered, washed with EtOAc and dried to afford the title compound as a white solid (2.9 g, 10.27 mmol, 88%). ^{1}H NMR (400 MHz, $CDCl_3$) δ 8.28 (t, *J* = 2.0 Hz, 1H), 8.14 (ddd, *J* = 8.2, 2.3, 1.1 Hz, 1H), 7.91 – 7.85 (m, 2H), 7.79 – 7.73 (m, 3H), 7.51 (t, *J* = 7.9 Hz, 1H), 4.94 (s, 2H). Data consistent with that given in the literature. [4]

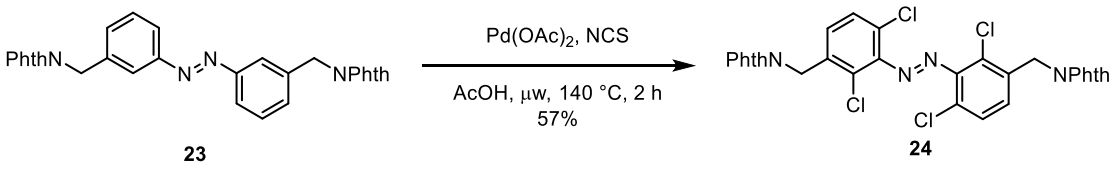


Phthalimide 22. Prepared according to a modified literature procedure.[4] **S5** (2.9 g, 10.25 mmol) was dissolved in EtOH (50 mL). $SnCl_2.H_2O$ (9.2 g, 41 mmol, 4 eq) was added and the reaction was stirred at reflux temperature for 16 hours. The mixture was concentrated and suspended in 60 mL 4N NaOH and 40 mL EtOAc and the biphasic mixture was stirred vigorously for 30 minutes at 0 °C. The precipitated solid was filtered, washed with EtOAc and dried to afford a solid, which was recrystallised from MeCN to afford the title compound light green crystals (930 mg. 10.3 mmol, 36%). ^{1}H NMR (400 MHz, $CDCl_3$) δ 7.84 (dd, *J* = 5.5, 3.1 Hz, 2H), 7.73 – 7.67 (m, 2H), 7.09 (t, *J* = 7.8 Hz, 1H), 6.82 (dt, *J* = 7.6, 1.3 Hz, 1H), 6.75 (t, *J* = 2.0 Hz, 1H), 6.58 (ddd, *J* = 8.0, 2.4, 1.0 Hz, 1H), 4.75 (s, 2H), 3.65 (s, 2H). Data consistent with that given in the literature. [4]



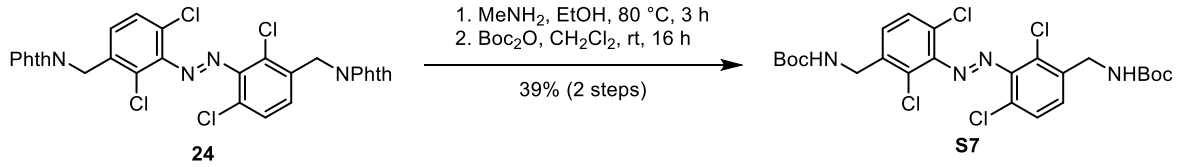
Azobenzene 23. A solution of **22** (650 mg, 2.58 mmol) in CH_2Cl_2 (50 mL) was treated with a solution of Oxone® (7.6 g, 23 mmol, 9.0 equiv.) in H_2O (50 mL) at 23 °C. The resulting biphasic reaction mixture was stirred vigorously at room temperature for 24 hours. The phases were separated and the aqueous phase was extracted with CH_2Cl_2. The combined organic extracts were washed sequentially with a 1M aqueous hydrochloric acid solution (50 mL), saturated

aqueous sodium bicarbonate solution (50 mL), and H_2O (50 mL). The washed organic layer was treated with **22** (780 mg, 8.37 mmol, 1.2 equiv.) and AcOH (40mL). The CH_2Cl_2 was then removed under reduced pressure at 35 °C and the solution was stirred overnight. The AcOH was then removed under reduced pressure. The residue was purified by flash silica gel chromatography (CH_2Cl_2) to yield the title compound as an orange solid as a mixture of isomers (620 mg, 1.24 mmol, 48%). *(E)*-**23:** ^{1}H NMR (400 MHz, $CDCl_3$) δ 7.96 (t, *J* = 1.9 Hz, 2H), 7.89 – 7.83 (m, 4H), 7.80 (dt, *J* = 7.9, 1.5 Hz, 2H), 7.74 – 7.69 (m, 4H), 7.54 (dt, *J* = 7.7, 1.5 Hz, 2H), 7.45 (t, *J* = 7.7 Hz, 2H), 4.95 (s, 4H). ^{13}C NMR (126 MHz, $CDCl_3$) δ 168.15, 152.96, 137.59, 134.17, 132.24, 131.24, 129.58, 123.61, 123.50, 122.11, 41.49. HRMS-ESI (m/z) Calculated for $C_{30}H_{20}N_4O_4$ $[M+H]^+$, 501.1557; found 501.1556



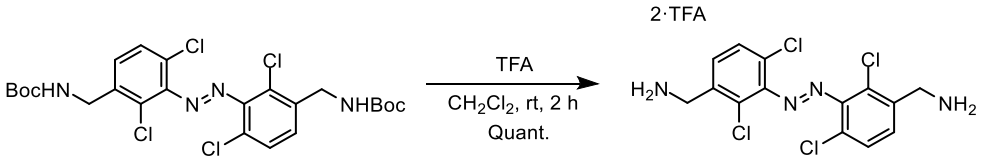
23 **24**

Azobenzene 24. Azobenzene **23** (300 mg, 0.6 mmol, 1.0 eq), NCS (400 mg, 3 mmol, 5.0 eq) and $Pd(OAc)_2$ (16.15 mg, 72 µmol, 0.10 eq) were suspended in degassed AcOH (6 mL) under a N_2-atmosphere in a microwave vial. The tube was sealed and the reaction was heated to 140 °C under microwave irradiation for 2h. The dark red solution was cooled, concentrated and redissolved in CH_2Cl_2. The organic layer was washed with water, then concentrated *in vacuo*. The brown oil was purified by silica gel flash chromatography (8% acetone in 1:1 hexane:CH_2Cl_2) to afford the title compound as an orange solid as a mixture of isomers (220 mg, 0.34 mmol, 57%). *(E)*-**24**: ^{1}H NMR (400 MHz, $CDCl_3$) δ 7.90 (dd, *J* = 5.5, 3.1 Hz, 4H), 7.79 – 7.75 (m, 4H), 7.39 (d, *J* = 8.5 Hz, 2H), 7.23 (d, *J* = 8.4 Hz, 2H), 5.05 (s, 4H). ^{13}C NMR (126 MHz, $CDCl_3$) δ 167.80, 148.00, 134.35, 133.98, 131.93, 129.04, 128.85, 126.81, 125.55, 123.66, 39.32. HRMS-ESI (m/z) Calculated for $C_{30}H_{16}Cl_4N_4O_4$ $[M+Na]^+$, 658.9823; found 658.9816



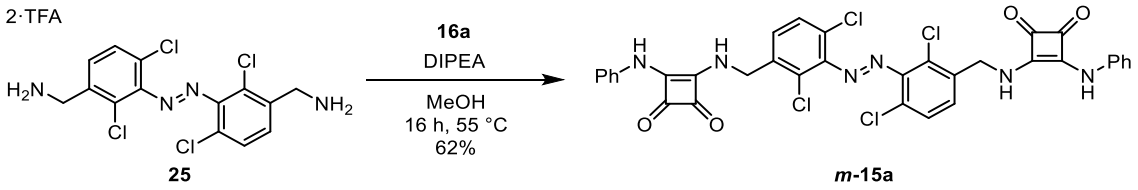
24 **S7**

Azobenzene S7. Phthalimide **24** (210 mg, 329 µmol) was dissolved in 33% $MeNH_2$ solution in ethanol (5 mL). The reaction was stirred to reflux temperature for 3 h. The solvent was removed *in vacuo*. The resulting residue was dissolved in CH_2Cl_2 (5 mL). To this was added Boc_2O (163 mg, 744 µmol, 2.2 eq) in CH_2Cl_2 (5 mL). The reaction was stirred at rt for 16 h and the solvent was then removed *in vacuo*. The residue was purified by silica gel flash column chromatography (1.5% EtOAc in CH_2Cl_2) to afford the title compound as an orange solid as a mixture of isomers (76 mg, 131 µmol, 39 %). **S7**: ^{1}H NMR (400 MHz, $CDCl_3$) δ 7.38 (d, *J* = 8.3 Hz, 2H), 7.33 (d, *J* = 8.5 Hz, 2H), 5.00 (s, 2H), 4.39 (d, *J* = 6.4 Hz, 4H), 1.39 (s, 18H). ^{13}C NMR (126 MHz, $CDCl_3$) δ 155.75, 147.89, 137.07, 129.62, 129.16, 126.86, 125.23, 80.03, 42.39, 28.40. HRMS-ESI (m/z) Calculated for $C_{24}H_{28}Cl_4N_4O_4$ $[M+H]^+$, 577.0937; found 577.0933.

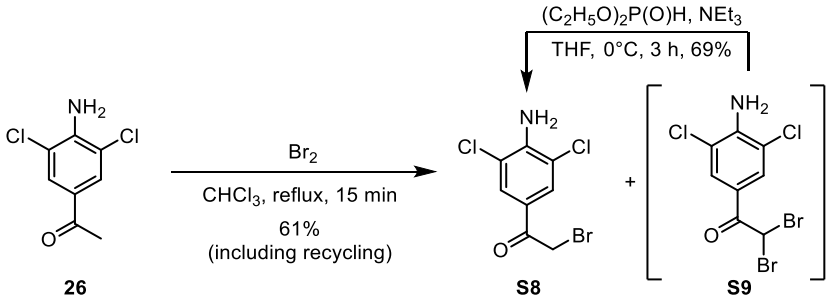


S7 **25**

TFA salt 25. To a solution of **S7** (60 mg, 104 µmol) in CH_2Cl_2 (1 mL) was added TFA (133 µL). The reaction was stirred at room temperature for 2 hours. The TFA was removed under a stream of nitrogen, then dried *in vacuo* to afford the title compound as an orange solid (63 mg, 104 µmol, 100%). ***(E)*-25:** ^{1}H NMR (400 MHz, MeOD) δ 7.72 (d, J = 8.4 Hz, 2H), 7.63 (d, J = 8.4 Hz, 2H), 4.39 (s, 4H). ^{13}C NMR (126 MHz, MeOD) δ 147.83, 131.92, 131.12, 129.80, 127.55, 126.85, 39.93. HRMS-ESI (m/z) Calculated for $C_{14}H_{12}Cl_4N_4$ $[M+H]^+$, 376.9889; found 376.9890.

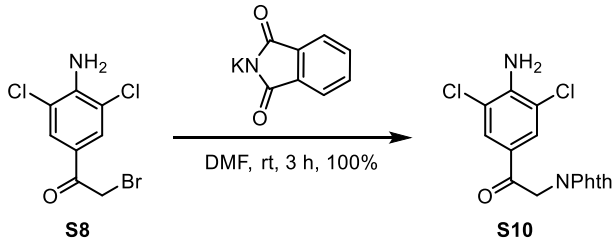


m*-15a**. Prepared according to ***General procedure 1 using **25** (23 mg, 37 µmol), DIPEA (40 µL, 0.23 mmol, 6 eq), **16a** (15.2 mg, 75 µmol, 2 eq) to afford the title compound as an orange solid (16.8 mg, 23.4 µmol, 62%). *(E)*-***m*-15a:** ^{1}H NMR (400 MHz, DMSO) δ 9.81 (s, 2H), 8.14 (s, 2H), 7.78 (d, *J* = 8.4 Hz, 2H), 7.65 (d, *J* = 8.5 Hz, 2H), 7.44 (d, *J* = 8.1 Hz, 4H), 7.35 (t, *J* = 7.7 Hz, 4H), 7.04 (t, *J* = 7.2 Hz, 2H), 5.01 (s, 4H). ^{13}C NMR (126 MHz, DMSO) δ 183.84, 180.74, 168.91, 164.22, 146.87, 138.86, 137.32, 130.42, 129.86, 129.39, 125.72, 124.31, 122.87, 118.18, 44.96. HRMS-ESI (m/z) Calculated for $C_{34}H_{22}Cl_4N_6O_4$ $[M-H]^-$, 717.0373; found 717.0376.



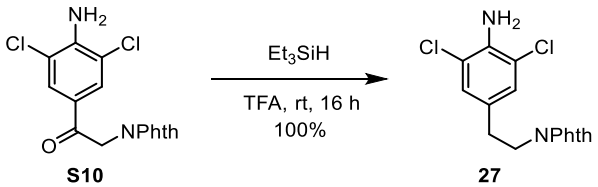
Bromide S8 and S9. To a solution of compound **26** (5 g, 24.5 mmol) in $CHCl_3$ (100 mL) was added Br_2 (1.64 mL, 31.85 mmol, 1.3 equiv) dropwise with vigorous stirring. The reaction was stirred at reflux temperature for 15 min and then cooled to rt. 10 % sodium thiosulphate solution was added dropwise until the reaction mixture had lost its brown colour. The reaction mixture was then neutralised with 10% $NaHCO_3$ solution. The organic layer was concentrated, then purified by silica gel column chromatography (50% Hexane in CH_2Cl_2) to afford **S8** and **S9** as white solids. Compound **S8** (2.92 g, 10.3 mmol, 42%): ^{1}H NMR (400 MHz, d_6-DMSO) δ 7.87 (s, 2H), 6.58 (s, 2H), 4.76 (d, *J* = 1.3 Hz, 2H). Data consistent with that given in the literature. [5] Compound **S9** (2.47 g, 6.8 mmol, 28%): ^{1}H NMR (400 MHz, $CDCl_3$) δ 7.98 (s, 2H), 6.53 (s,

1H), 5.13 (s, 2H). Data consistent with that given in the literature. [6] To improve the yield of desired compound **S8**, isolated compound **S9** was dissolved in THF (15ml) and cooled to 0°C. A solution of diethyl phosphite (879 µL, 6.8 mmol, 1 equiv) and NEt_3 (1.05 mL, 7.48 mmol, 1.1 equiv.) in THF (6 ml) was added dropwise with vigorous stirring. The reaction was brought to rt and stirred for 3 h. 200 mL ice water was poured into the reaction mixture. The precipitate was collected and dried by vacuum filtration to afford 1.33 g of **S8** (Total yield: 4.25 g, 15.9 mmol, 61.3%).



S8 **S10**

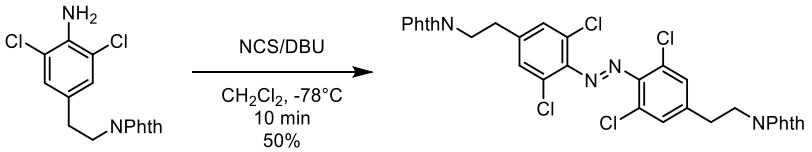
Phthalimide S10. To a solution of **S8** (4.25 g, 15.0 mmol) in DMF (20 mL) was added potassium phthalimide (3.34 g, 16.5 mmol, 1.1 equiv). The reaction was stirred at rt for 3 h. 300 mL of ice water was added to form a precipitate, which was isolated by vacuum filtration then dried to afford the title compound as a white solid (5.2 g, 15.0 mmol, quant.). ^{1}H NMR (400 MHz, d_6-DMSO) δ 7.96 (s, 2H), 7.95 – 7.88 (m, 4H), 6.65 (s, 2H), 5.13 (s, 2H). ^{13}C NMR (126 MHz, d_6-DMSO) δ 188.49, 167.56, 146.39, 134.80, 131.57, 128.70, 123.37, 122.27, 117.46, 43.87. HRMS-ESI (m/z) calculated for $C_{16}H_{10}Cl_2N_2O_3^+$ $[M+H]^+$, 349.0141; found 349.0141.



S10 **27**

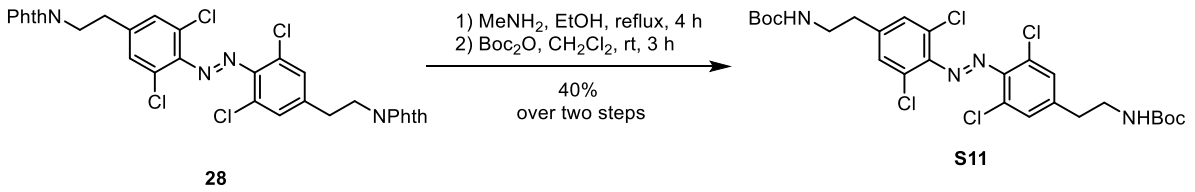
Aniline 27. To a solution of compound **S10** (6.00 g, 17.2 mmol) in TFA (50 mL) at 0°C was added dropwise triethylsilane (6.86 mL, 43.0 mmol, 2.5 equiv) under a nitrogen atmosphere with vigorous stirring. The reaction was warmed to rt and stirred for 16 h. The mixture was

diluted with 200 mL of water and brought to pH 9 by the addition of 10% NaOH solution (~ 100 mL) to form a precipitate, which was isolated by vacuum filtration then dried to afford the title compound as a white solid (5.76 g, 17.2 mmol, quant.). ^{1}H NMR (400 MHz, DMSO) δ 7.87 – 7.79 (m, 4H), 7.05 (s, 2H), 5.30 (s, 2H), 3.75 (t, *J* = 7.0 Hz, 2H), 2.77 (t, *J* = 7.0 Hz, 2H). ^{13}C NMR (101 MHz, DMSO) δ 167.71, 139.46, 134.47, 131.44, 128.16, 127.28, 123.06, 118.00, 38.68, 32.13. HRMS-ESI (m/z) calculated for $C_{16}H_{13}Cl_2N_2O_2^+$ $[M+H]^+$, 335.0349, found 335.0350.



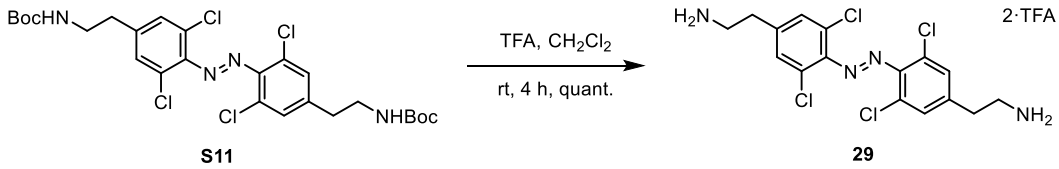
27 **28**

Protected azobenzene 28. To a solution of **27** (3.82 g, 11.4 mmol) in CH_2Cl_2 (150 mL) was added DBU (3.40 mL, 22.8 mmol, 2 equiv). The solution was stirred at rt for 5 min before being cooled to −78°C. *N*-chlorosuccinimide (3.04 g, 22.8 mmol, 2 equiv) was added. The solution was stirred at −78°C for 10 min before quenching by addition of saturated sodium bicarbonate solution (150 mL). The organic layer was washed with water (5 x 150 mL) and 1 M HCl (150 mL), dried over anhydrous $MgSO_4$ and concentrated *in vacuo*. The residue was purified by silica gel flash column chromatography (CH_2Cl_2) to afford the title compound as an orange brown solid as a mixture of isomers (1.89 g, 2.84 mmol, 50%): (*E*)**-28** ^{1}H NMR (500 MHz, $CDCl_3$) δ 7.87 (dd, *J* = 5.5, 3.1 Hz, 4H), 7.75 – 7.73 (m, 4H), 7.37 (s, 4H), 3.98 – 3.94 (m, 4H), 3.05 – 2.99 (m, 4H). ^{13}C NMR (126 MHz, $CDCl_3$) δ 168.20, 146.30, 140.63, 134.29, 132.07, 129.93, 127.72, 123.57, 38.50, 33.92. HRMS-ESI (m/z) calculated for $C_{32}H_{21}Cl_4N_4O_4^+$ $[M+H]^+$, 665.0317; found 665.0306.



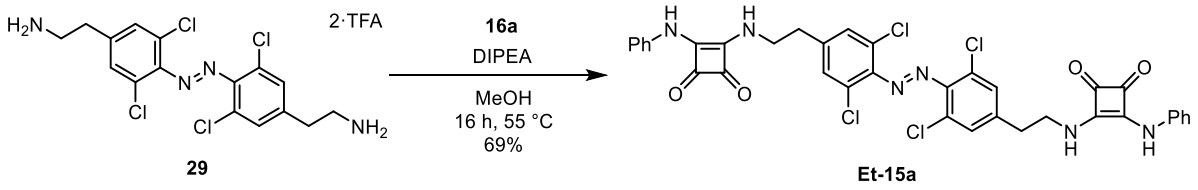
28 **S11**

Protected diamine S11. Compound **28** (400 mg, 600 µmol) was dissolved in 33% $MeNH_2$ solution in ethanol (9.6 mL). The reaction was stirred under reflux temperature for 4 h. The solvent was removed *in vacuo*. The resulting residue (243 mg) was dissolved in CH_2Cl_2 (10 mL). To this was added Boc_2O (122 mg, 557 µmol) in CH_2Cl_2 (10 mL). The reaction was stirred at rt for 3 h and the solvent was then removed *in vacuo*. The crude was purified by silica gel flash column chromatography (10% EtOAc in CH_2Cl_2) to afford the title compound as an orange solid as a mixture of isomers (146 mg, 240.78 µmol, 40 %): (*E)*-**S11:** ^{1}H NMR (400 MHz, $CDCl_3$) δ 7.29 (s, 4H), 4.58 (s, 2H), 3.40 (q, *J* = 6.7 Hz, 4H), 2.83 (t, *J* = 6.7 Hz, 4H), 1.45 (s, 18H). ^{13}C NMR (126 MHz, $CDCl_3$) δ 155.90, 146.11, 141.94, 129.92, 127.65, 79.79, 41.41, 35.54, 28.51. HRMS-ESI (m/z) calculated for $C_{26}H_{32}Cl_4N_4O_4Na^+$ $[M+Na]^+$, 629.1042; found 629.1037.

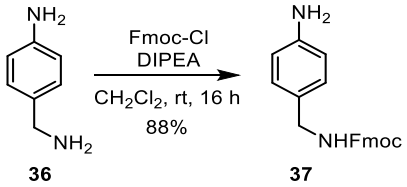


S11 **29**

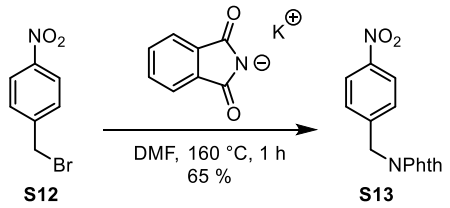
TFA Salt 29. To a solution of **S11** (70 mg, 115 µmol) in CH_2Cl_2 (1.6 mL) was added TFA (0.2 mL). The reaction was stirred at rt for 4 h. The TFA and solvent were removed by evaporation under a stream of nitrogen and then dried under high vacuum to afford the title compound as an orange salt (73 mg, 115 µmol, quant.). (*E*)-**29**: ^{1}H NMR (400 MHz, CD_3OD) δ 7.51 (s, 4H), 3.22 (d, *J* = 7.4 Hz, 4H), 3.00 (t, *J* = 7.4 Hz, 4H). HRMS-ESI (m/z) calculated for $C_{16}H_{17}Cl_4N_4Na^+$ $[M+H]^+$, 407.0173; found 407.0173.



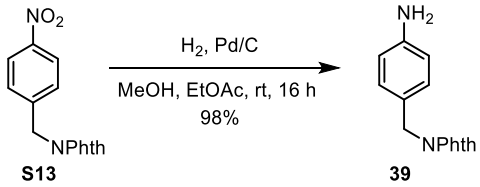
Et-15a. Prepared according to ***General procedure 1*** using **29** (23 mg, 39 µmol), DIPEA (40 µL, 0.23 mmol, 6 eq), monosquaramide **16a** (15.6 mg, 77 µmol, 2 eq to afford the title compound as an orange solid (20 mg, 39 µmol, 69%). (*E*)-**Et-15a:** ^{1}H NMR (400 MHz, DMSO-d_6) δ 9.67 (br s, 2H), 7.66 (s, 4H), 7.57 (s, 2H), 7.39 (d, *J* = 6.7 Hz, 4H), 7.32 (t, *J* = 7.8 Hz, 4H), 7.02 (t, *J* = 7.3 Hz, 2H), 3.94 (s, 4H), 3.01 (t, *J* = 6.9 Hz, 4H). ^{13}C NMR (126 MHz, DMSO) δ 184.55, 180.97, 169.57, 164.24, 145.34, 143.28, 139.40, 130.81, 129.81, 126.63, 123.14, 118.54, 44.62, 36.33. HRMS-ESI (m/z) Calculated for $C_{36}H_{26}Cl_4N_6O_4$ $[M-H]^-$, 745.0697; found 745.0690



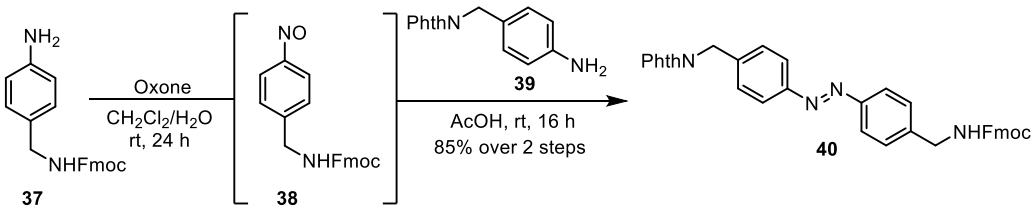
Fmoc building block 37. Prepared according to a modified literature procedure.[9] 4-aminobenzylamine **36** (550 mg, 4.5 mmol, 1 eq) and DIPEA (0.78 mL, 4.5 mmol, 1 eq) were dissolved in CH_2Cl_2 (50 mL). Fmoc-Cl (1.16 g, 4.5 mmol, 1 eq) in CH_2Cl_2 (10 mL) was added dropwise at 0 °C. The reaction was stirred at room temperature for 16 hours, after which a white precipitate had formed. The organic layer was washed with water, then concentrated *in vacuo*. The crude was purified by silica gel flash chromatography (dry load, 10% EtOAc in CH_2Cl_2) to afford the title compound as a white solid (1.37 g, 4.0 mmol, 88%). ^{1}H NMR (400 MHz, Chloroform-d) δ 7.75 (d, *J* = 7.56 Hz, 2H), 7.58 (d, *J* = 7.40 Hz, 2H), 7.39 (t, *J* = 7.34 Hz, 2H), 7.29 (t, *J* = 7.30 Hz, 2H), 7.21 (t, *J* = 6.96 Hz, 1H), 7.05 (d, *J* = 8.10 Hz, 2H), 6.62 (d, *J* = 8.34 Hz, 2H), 5.01 (s br, 1H), 4.42 (d, *J* = 7.18 Hz, 2H), 4.24 (s, 2H), 3.72 (br s, 2H). Data consistent with that given in the literature. [9]



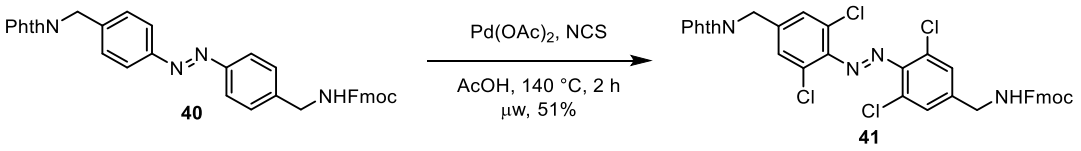
Phthalimide S13. Prepared according to a modified literature procedure.[8] **S12** (7 g, 32.40 mmol) was dissolved in DMF (45 mL). Potassium phthalimide (6.3 g, 34 mmol, 1.05 eq) was added and the reaction was stirred at reflux temperature for 1 h. The reaction was cooled, and ice water was added. The filtrate was dissolved in hot EtOAc (300 mL), and allowed to recrystallize for two days at room temperature in a 500 mL flask. The solid was collected and washed with cold EtOAc to afford the title compound as white crystals (5.9 g, 20.9 mmol, 65%). ^{1}H NMR (400 MHz, $CDCl_3$) δ 8.22 – 8.15 (m, 2H), 7.88 (dd, *J* = 5.4, 3.1 Hz, 2H), 7.75 (dd, *J* = 5.5, 3.1 Hz, 2H), 7.62 – 7.56 (m, 2H), 4.93 (s, 2H). [8]



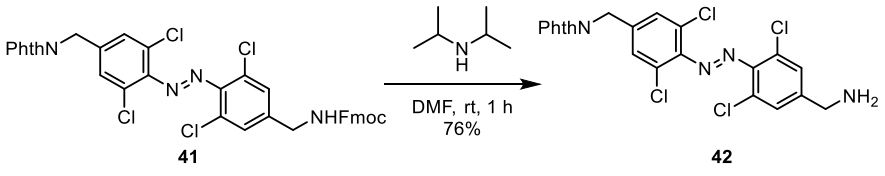
Phthalimide 39. Nitro compound **S13** (3 g, 22.0 mmol) was dissolved in 40% MeOH in EtOAc (160 mL). The reaction was placed under nitrogen, then 10% Pd/C (300 mg) was added. The reaction was stirred under H_2 atmosphere for 16 hours at rt. The mixture was filtered over celite, then concentrated to afford the title compound as a white solid (2.3 g, 21.7 mmol, 98%). ^{1}H NMR (400 MHz, DMSO) δ 7.92 – 7.79 (m, 4H), 6.98 (d, *J* = 8.4 Hz, 2H), 6.48 (d, *J* = 8.4 Hz, 2H), 5.04 (s, 2H), 4.56 (s, 2H). Data consistent with that given in the literature. [7]



Azobenzene 40. A solution of **37** (855 mg, 2.77 mmol, 1.4 equiv.) in CH_2Cl_2 (50 mL) was treated with a solution of Oxone® (5.43 g, 17.84 mmol, 9.0 equiv.) in H_2O (50 mL) at 23 °C. The resulting biphasic reaction mixture was stirred vigorously at room temperature for 24 hours, after which the organic layer turned green. Subsequently, the phases were separated and the aqueous phase was extracted with CH_2Cl_2 (2 x 50 mL). The combined organic extracts were washed sequentially with a 1M aqueous hydrochloric acid solution (50 mL), saturated aqueous sodium bicarbonate solution (50 mL), and H_2O (50 mL). The washed organic layer was treated with **37** (500 mg, 1.98 mmol, 1.0 equiv.) and AcOH (40 mL). The CH_2Cl_2 was removed under reduced pressure at 35 °C and the solution was stirred for 16 hours. The AcOH was removed under reduced pressure. The residue was purified by flash silica gel chromatography (CH_2Cl_2 to 1% Acetone in CH_2Cl_2) to yield the title compound as an orange solid (1.0 g, 1.69 mmol, 85%). (*E*)**-40**: ^{1}H NMR (400 MHz, $CDCl_3$) δ 7.91 – 7.80 (m, 6H), 7.79 – 7.74 (m, 2H), 7.72 (dd, *J* = 5.5, 3.1 Hz, 2H), 7.64 – 7.54 (m, 4H), 7.43 – 7.34 (m, 4H), 7.31 (t, *J* = 7.5 Hz, 2H), 5.15 (br t, *J* = 6.2 Hz, 1H), 4.92 (s, 2H), 4.50 (d, *J* = 6.7 Hz, 2H), 4.45 (d, *J* = 6.2 Hz, 2H), 4.23 (t, *J* = 6.7 Hz, 1H); ^{13}C NMR (126 MHz, $CDCl_3$) δ 168.13, 156.60, 152.27, 152.12, 143.99, 141.66, 141.49, 139.34, 134.25, 132.21, 129.48, 128.22, 127.84, 127.20, 125.13, 123.60, 123.37, 123.34, 120.14, 66.84, 47.46, 44.89, 41.44. HRMS-ESI (m/z) Calculated for $C_{37}H_{28}N_4O_4$ $[M+H]^+$, 593.2183; found 593.2180

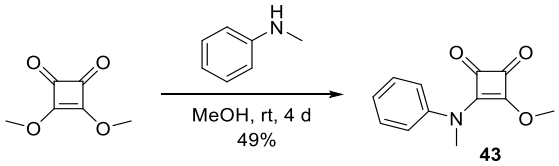


Azobenzene 41. This reaction was split into three 1 g batches due to microwave vial size restrictions. **40** (1 g , 1.69 mmol, 1.0 eq), NCS (1.13 mg, 8.44 mmol, 5.0 eq) and $Pd(OAc)_2$ (46 mg, 0.2 mmol, 0.12 eq) were dissolved in degassed AcOH (17 mL) under a N_2-atmosphere in a 20 mL microwave vial. The tube was sealed and reaction was heated to 140 °C under microwave irradiation for 2h. The dark red solution was cooled, concentrated and redissolved in CH_2Cl_2. The organic layer was washed sequentially with sat. aq. NaCl and phosphate buffer (pH 7), and then concentrated *in vacuo*. The three batches were combined and purified by silica gel flash chromatography (CH_2Cl_2) to afford the title compound as a dark red solid as a mixture of isomers (1.96 g, 2.68 mmol, 51% [~90% purity]). (*E*)**-41:** ^{1}H NMR (400 MHz, $CDCl_3$) δ 7.88 (td, *J* = 5.3, 2.2 Hz, 2H), 7.76 (dd, *J* = 5.4, 3.1 Hz, 2H), 7.74 – 7.62 (m, 2H), 7.58 (d, *J* = 6.2 Hz, 2H), 7.53 (s, 2H), 7.45 – 7.31 (m, 4H), 7.26 – 7.15 (m, 2H), 5.21 (br t, *J* = 6.6 Hz, 1H), 4.84 (s, 2H), 4.62 – 4.41 (m, 1H), 4.38 (d, *J* = 6.6 Hz, 2H), 4.22 (t, *J* = 6.7 Hz, 1H). ^{13}C NMR (126 MHz, $CDCl_3$) δ 167.73, 156.24, 147.60, 147.13, 145.69, 143.31, 141.06, 138.44, 134.36, 131.91, 129.49, 129.17, 128.33, 128.24, 128.07, 128.03, 125.44, 123.67, 120.09, 66.59, 47.24, 43.89, 40.35. HRMS-ESI (m/z) Calculated for $C_{37}H_{24}Cl_4N_4O_4$ $[M-H]^-$, 729.0624; found 729.024

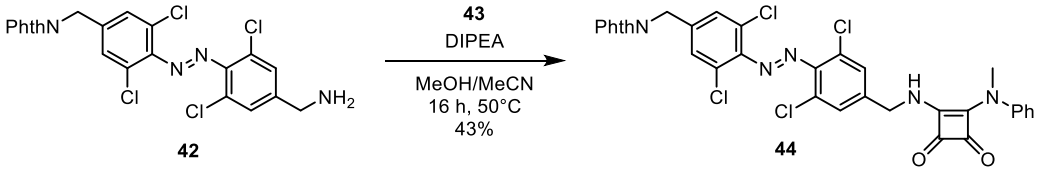


Amine 42. 41 (1.1 g, 1.51 mmol) was dissolved in DMF (8 mL). Diisopropylamine (341 µL, 1.96 mmol, 1.3 eq) was added, and the reaction was stirred at room temperature for 1 hour, after which a precipitate had formed. The DMF was azeotropically removed under reduced pressure with toluene. The residue was purified by silica gel flash chromatography (100:3:1 CH_2Cl_2:MeOH:NEt_3) to afford the title compound as a dark red solid as a mixture of isomers

(580 mg, 1.14 mmol, 76%), which is used immediately in the next step. (*E*)**-42:** ^{1}H NMR (400 MHz, $CDCl_3$) δ 7.92 – 7.85 (m, 2H), 7.79 – 7.72 (m, 2H), 7.52 (s, 2H), 7.44 (s, 2H), 4.84 (s, 2H), 3.91 (s, 2H). HRMS-ESI (m/z) Calculated for $C_{22}H_{14}Cl_4N_4O_2$ $[M+H]^+$, 506.9944; found 506.9943

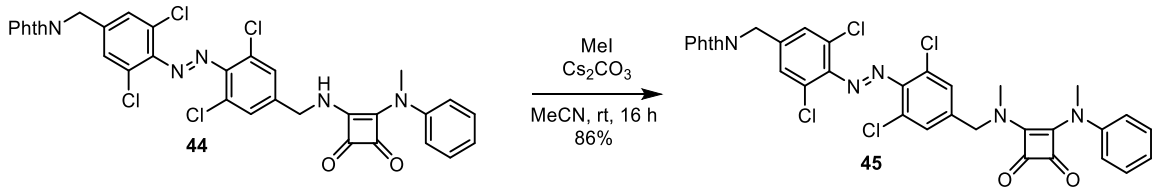


Monosquaramide 43. To a stirred solution of dimethylsquarate (100 mg, 0.70 mmol, 1 eq) in methanol (1 mL) was added N-methylaniline (68 µL, 0.7 mmol, 1 eq) and the mixture was allowed to stir at room temperature for 90 hours. The reaction was concentrated and purified by silica gel flash chromatography (6 % MeCN in CH_2Cl_2) to afford the title compound as a white solid (75 mg, 0.345 mmol, 49%).^{1}H NMR (400 MHz, $CDCl_3$) δ 7.46 – 7.38 (m, 2H), 7.33 – 7.27 (m, 1H), 7.20 – 7.13 (m, 2H), 4.52 – 4.19 (br s, 3H), 3.73 (s, 3H). ^{13}C NMR (126 MHz, $CDCl_3$) δ 189.00, 184.58, 177.99, 170.78, 141.56, 129.16, 127.17, 123.14, 60.75, 39.39. HRMS-ESI (m/z) Calculated for $C_{12}H_{11}NO_3$ $[M+H]^-$, 218.0812; found 218.0810

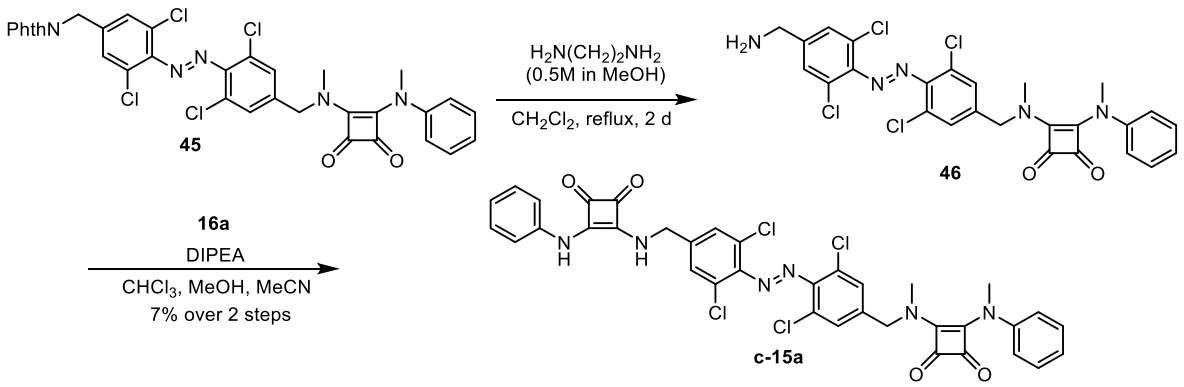


Squaramide 44. 42 (580 mg, 1.14 mmol) and **43** (272 mg, 1.26 mmol, 1.1 eq) were dissolved in MeOH (10 mL) and MeCN (5 mL). DIPEA (437 µL, 2.51 mmol, 2.2 eq) was added. The reaction was stirred at 50 °C for 6 hours. The reaction was concentrated, then purified by silica gel flash chromatography (5% to 8% MeCN in CH_2Cl_2) to afford the title compound as an orange solid as a mixture of isomers (270 mg, 0.49 mmol, 43%). (*E*)**-44:** ^{1}H NMR (400 MHz, $CDCl_3$) δ 7.92 – 7.86 (m, 2H), 7.78 – 7.73 (m, 2H), 7.52 (s, 2H), 7.50 – 7.45 (m, 2H), 7.37 – 7.30 (m, 1H), 7.28 (s, 2H), 7.15 – 7.10 (m, 2H), 4.84 (s, 2H), 4.80 (d, *J* = 6.6 Hz, 2H), 4.29 (t, *J* = 6.5 Hz, 1H), 3.80 (s, 3H). ^{13}C NMR (126 MHz, $CDCl_3$) δ 184.52, 184.29, 167.88, 166.79,

165.86, 147.19, 147.05, 141.48, 140.27, 138.78, 134.52, 132.02, 130.08, 129.66, 128.44, 128.03, 127.84, 127.56, 123.82, 123.13, 47.14, 40.48, 39.17. HRMS-ESI (m/z) Calculated for $C_{33}H_{21}Cl_4N_5O_4$ $[M+H]^+$, 692.0420; found 692.0416

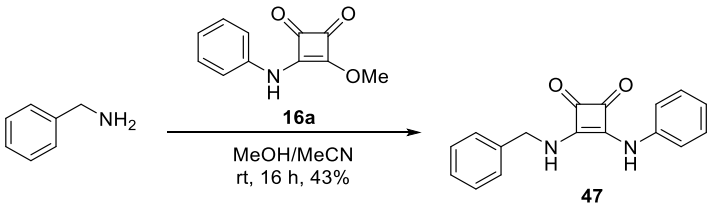


Squaramide 45. 44 (270 mg, 390 µmol) was dissolved in MeCN (5 mL). Cs_2CO_3 (950 mg, 2.29 mmol, 7.5 eq) and MeI (364 µL, 5.84 mmol, 15 eq) were added, then stirred vigorously for 16 hours at room temperature. The reaction was concentrated, then diluted in CH_2Cl_2 and washed with water to remove salts. The organic layer was concentrated and purified by silica gel flash chromatography (7% Acetone in 50:50 CH_2Cl_2:PhMe) to afford the title compound as an orange solid as a mixture of isomers (236 mg, 333 µmol, 86%). (*E*)**-45:** ^{1}H NMR (400 MHz, $CDCl_3$) δ 7.92 – 7.86 (m, 2H), 7.79 – 7.73 (m, 2H), 7.54 (s, 2H), 7.39 (t, *J* = 7.7 Hz, 2H), 7.27 (s, 2H), 7.21 (t, *J* = 7.6 Hz, 1H), 7.12 – 7.07 (m, 2H), 4.85 (s, 2H), 4.71 (s, 2H), 3.80 (s, 3H), 2.30 (s, 3H). ^{13}C NMR (126 MHz, $CDCl_3$) δ 186.00, 185.29, 170.45, 167.87, 166.88, 147.27, 147.07, 144.70, 138.81, 138.32, 134.52, 132.02, 130.13, 129.67, 128.76, 128.00, 127.86, 126.51, 123.83, 122.03, 54.72, 40.48, 39.49, 38.79. HRMS-ESI (m/z) Calculated for $C_{34}H_{23}Cl_4N_5O_4$ $[M+H]^+$, 706.0577; found 706.0577



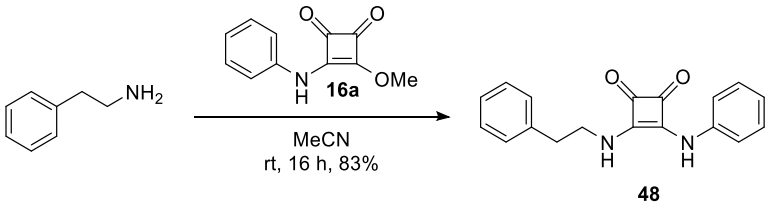
Control compound c-15a. Phthalimide **45** (80 mg, 113 µmol) was dissolved in CH_2Cl_2 (4 mL). Ethylene diamine (0.5M in MeOH) (1.36 mL, 680 µmol, 6 eq) was added, and the reaction was

stirred at 43 degrees bath temperature for 48 hours. The reaction was concentrated *in vacuo* (do not exceed 40 °C). The orange residue was purified by flash-column chromatography (5% MeOH in CH_2Cl_2) to afford 12 mg (20.8 µmol) of intermediate amine **46**. ^{1}H NMR (400 MHz, $CDCl_3$) δ 7.48 – 7.43 (s, 2H), 7.42 – 7.37 (m, 2H), 7.29 (s, 2H), 7.24 – 7.19 (m, 1H), 7.12 – 7.08 (m, 2H), 4.72 (s, 2H), 3.93 (s, 2H), 3.82 (s, 3H), 2.31 (s, 3H). The residue was immediately dissolved in 1:1 MeOH/$CHCl_3$ (0.5 mL) and DIPEA (7 µL, 41.6 µmol, 2 eq) was added. Monosquaramide **16a** (4.22 mg, 20.8 µmol, 1 eq) in MeCN (0.5 mL) was added, and the reaction was stirred at 55 °C for 16 hours. The reaction was cooled to rt and the solid precipitate was filtered and washed sequentially with MeOH and MeCN, then collected and dried under high vacuum to afford the title compound as an orange solid as a mixture of isomers (6.2 mg, 7 µmol, 7% over 2 steps). *(E)***-c-15a:** ^{1}H NMR (400 MHz, DMSO) δ 9.81 (s, 1H), 8.12 (s, 1H), 7.75 (s, 2H), 7.68 (s, 2H), 7.47 – 7.41 (m, 2H), 7.39 – 7.28 (m, 6H), 7.21 – 7.16 (m, 1H), 7.04 (tt, *J* = 7.3, 1.2 Hz, 1H), 4.90 (d, *J* = 5.5 Hz, 2H), 4.78 (s, 2H), 3.68 (s, 3H), 2.24 (s, 3H). ^{13}C NMR (126 MHz, DMSO) δ 186.02, 184.51, 184.01, 180.81, 170.82, 168.80, 166.24, 164.33, 145.68, 145.49, 144.31, 142.74, 140.18, 138.87, 129.40, 129.35, 129.17, 128.85, 126.40, 126.31, 125.37, 122.83, 121.61, 118.23, 53.25, 45.80, 38.33, 38.12. HRMS-ESI (m/z) Calculated for $C_{36}H_{26}Cl_4N_6O_4$ $[M-H]^-$, 745.0697; found 745.0687.



Control 47. Benzylamine (17 mg, 158 µmol) was dissolved in MeOH (0.5 mL). **16a** (21 mg, 104 µmol, 1.0 eq) dissolved in MeCN (1.5 mL) was added, and the reaction was stirred at room temperature, after which a white precipitate had formed. The solid precipitate was filtered and washed sequentially with MeOH and MeCN, then collected and dried under high vacuum to afford the title compound as a white solid (19 mg, 68 µmol, 43%). ^{1}H NMR (500 MHz, DMSO) δ 9.64 (s, 1H), 8.01 (s, 1H), 7.45 – 7.37 (m, 6H), 7.33 (m, 3H), 7.02 (t, *J* = 7.4 Hz, 1H),

4.82 (s, 2H). ^{13}C NMR (126 MHz, DMSO) δ 184.00, 180.36, 168.83, 163.78, 138.96, 138.45, 129.35, 128.75, 127.69, 127.63, 122.68, 118.01, 47.20. HRMS-ESI (m/z) Calculated for $C_{17}H_{15}N_2O_2$ $[M+H]^+$, 279.1128; found 279.1130.



Control 48. Phenethylamine (24 µL, 189 µmol, 1.1 eq) was added to **16a** (35 mg, 172 µmol, in MeCN, and the reaction was stirred at room temperature for 16 hours. The solid precipitate was filtered and washed sequentially with MeOH and MeCN, then collected and dried under high vacuum to afford the title compound as a white solid (42 mg, 143 µmol, 83 %). ^{1}H NMR (500 MHz, DMSO) δ 9.63 (s, 1H), 7.64 (s, 1H), 7.40 (d, *J* = 8.0 Hz, 2H), 7.32 (t, *J* = 7.6 Hz, 4H), 7.27 (d, *J* = 7.4 Hz, 2H), 7.23 (t, *J* = 7.2 Hz, 1H), 7.02 (t, *J* = 7.3 Hz, 1H), 3.87 (m, 2H), 2.90 (t, *J* = 7.1 Hz, 2H). ^{13}C NMR (126 MHz, DMSO) δ 184.00, 180.31, 169.14, 163.54, 138.97, 138.38, 129.33, 128.82, 128.45, 126.38, 122.58, 117.97, 44.91, 36.88. HRMS-ESI (m/z) Calculated for $C_{18}H_{15}N_2O_2$ $[M+H]^+$, 291.1139; found 291.1140.

6.3.2 UV Vis spectra (Chapter 3)

All UV-vis spectra were determined in DMSO solution, analogously to chapter 2. Spectra are summarised below:

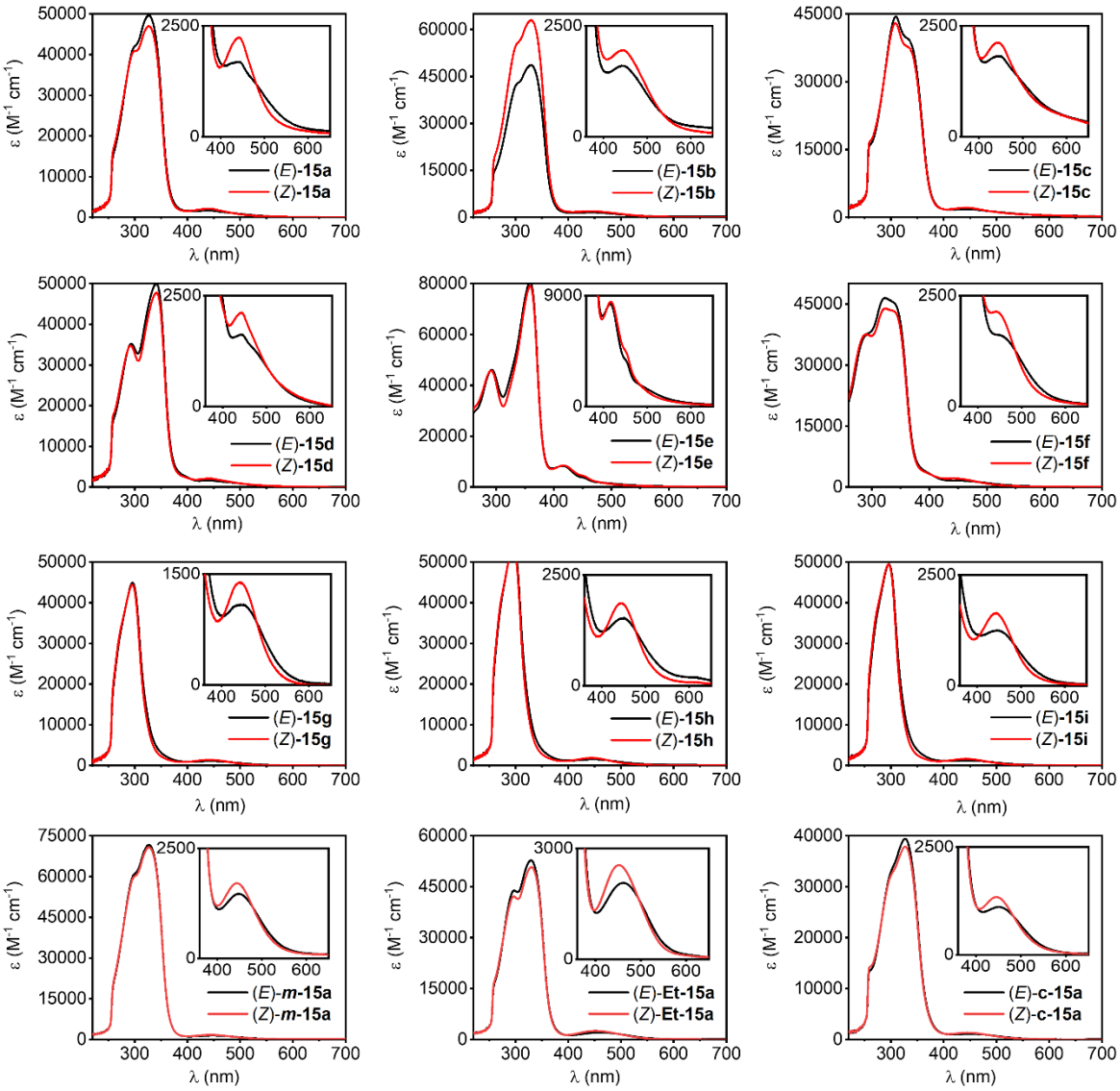


Figure S1. (A) UV-Vis spectra of **15** derivatives with Z-isomer PSS spectra (77%)

6.3.3 NMR titration experiments (Chapter 3)

All binding constants were measured by ^{1}H NMR titrations in a Bruker AVIII 500 spectrometer at 500 MHz and 298 K. The host was dissolved in d_6-DMSO and added at 1 mM concentration and a known volume (0.5 mL) added to the NMR tube. Known volumes of guest (TBACl) in d_6-DMSO were added, and the spectra were recorded after each addition. The chemical shifts of the host spectra, where resolved, were monitored as a function of [G]. The data was analysed using a global fit procedure for all three data sets simultaneously in the Dynafit software program,[10] using non-linear least squares analysis to obtain the best fit between observed and calculated chemical shifts. In all experiments the association of guest and host was fast on the NMR timescale (Figure 5, Table 1, Table 3)

***E* isomer:** Chloride binding to a dark-adapted (*E*)-**15** derivative sample (>99% *E*) was determined by NMR titration analysis in d_6-DMSO as described above, fitting excellently to a 1:1 binding model:

$$(E)\textbf{-15} + Cl^- \overset{K_1^E}{\rightleftharpoons} (E)\textbf{-15}\cdot Cl^-$$

Binding of a second equivalent of chloride, to form a 1:2 host:guest complex, was not observed in DMSO, as inferred from the failure to fit the data to 1:2 binding models, presumably due to inter-anion repulsion in the 1:2 complex, leading to negligible association of the second anion.

***Z* isomer:** A 1 mM sample of in d_6-DMSO was irradiated with red light until the PSS was reached, before the titration experiment was conducted as described above. The PSS ratio was maintained throughout the titration for all derivatives. The binding constants were obtained by fitting the data, using a global fit procedure, to the following equilibria where K_1^E is fixed, and obtained from the previous titration with the *E* isomer.

$$(E)\textbf{-15} + Cl^- \overset{K_1^E}{\rightleftharpoons} (E)\textbf{-15}\cdot Cl^-$$
$$(Z)\textbf{-15} + Cl^- \overset{K_1^Z}{\rightleftharpoons} (Z)\textbf{-15}\cdot Cl^-$$

[(*E*)-**15**] + [(Z)-**15**] = 1 mM; [(*Z*)-**15**] = 0.77 mM; [(*E*)-**15**] = 0.23 mM

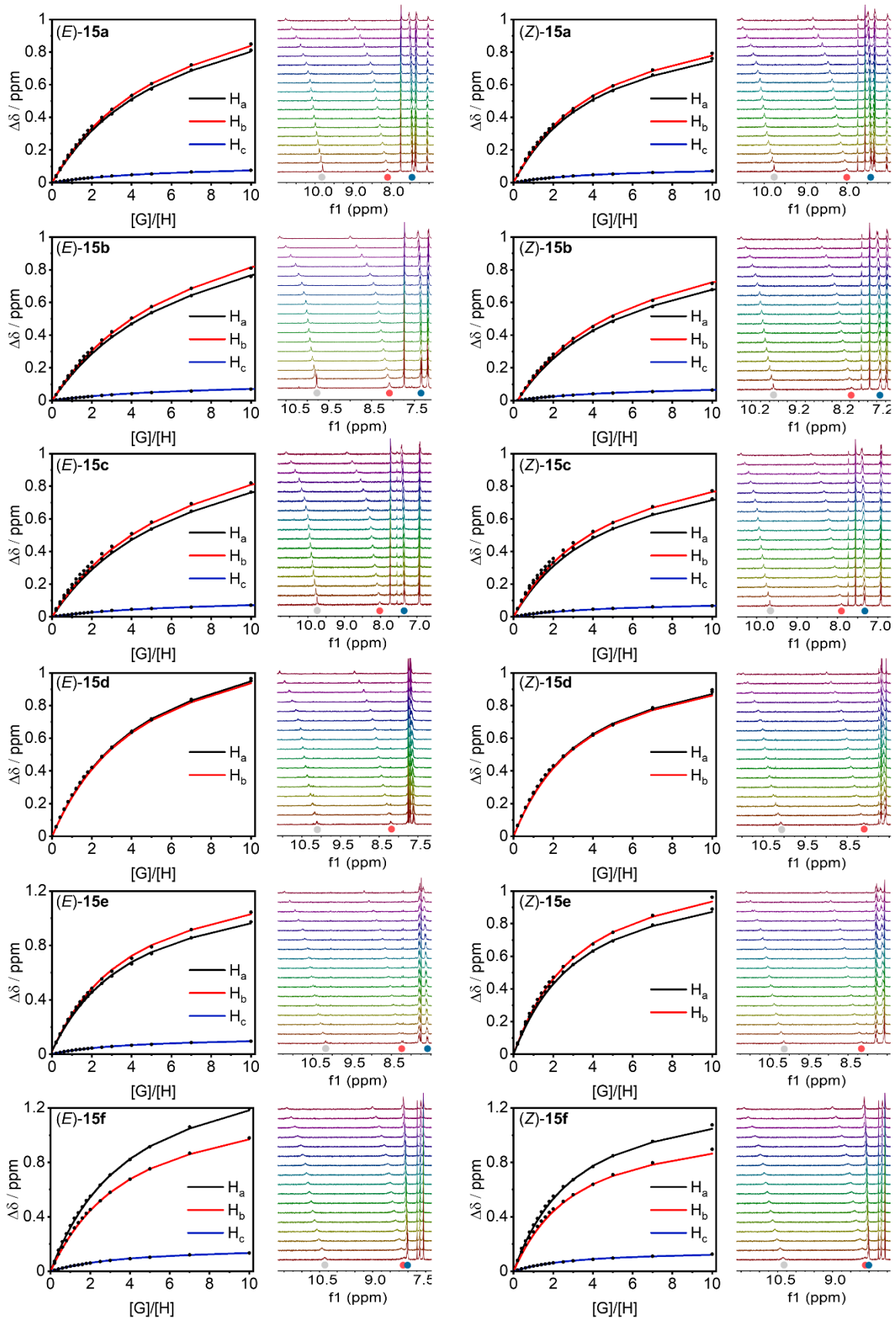


Figure S2. Plots of chemical shift changes and stacked ^{1}H NMR spectra for NMR titrations (part 1)

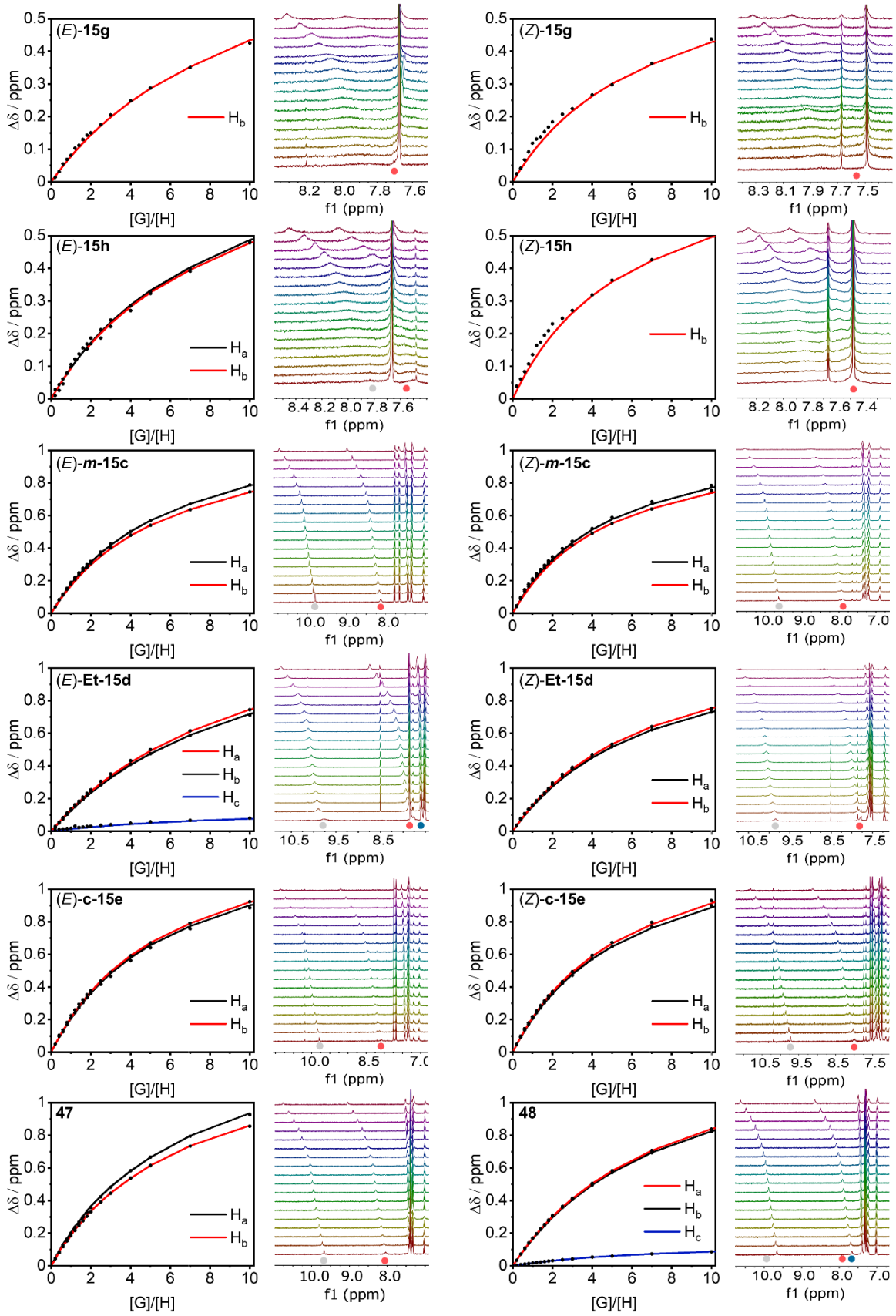


Figure S3. Plots of chemical shift changes and stacked ^{1}H NMR spectra for NMR titrations (part 2)

6.3.4 Anion transport studies (Chapter 3)

6.3.4.1 Vesicle preparation

A thin film of lipid (1-palmitoyl-2-oleoyl-*sn*-3-phosphatidylcholine POPC, egg-yolk phosphatidylglycerol EYPG or dipalmitoyl phosphatidylcholine DPPC) was formed by evaporating a chloroform solution under a stream of nitrogen gas, and then under high vacuum for 6 hours. The lipid film was hydrated by vortexing with the prepared buffer (100 mM NaCl, 10 mM HEPES, 1 mM 8-Hydroxypyrene-1,3,6-trisulfonic acid trisodium salt (HPTS), pH 7.0). The lipid suspension was then subjected to 5 freeze-thaw cycles using liquid nitrogen and a water bath (40°C), followed by extrusion 19 times through a polycarbonate membrane (pore size 200 nm) at rt. Extrusion was performed at 50°C in the case of DPPC lipids. Extra-vesicular components were removed by size exclusion chromatography on a Sephadex G-25 column with 100 mM NaCl, 10 mM HEPES, pH 7.0. Final conditions: LUVs (2.5 mM lipid); inside 100 mM NaCl, 10 mM HEPES, 1 mM HPTS, pH 7.0; outside: 100 mM NaX (X = Cl for standard experiments), 10 mM HEPES, pH 7.0. Vesicles for the sodium gluconate assay were prepared by the same procedure, substituting NaCl for NaGluconate in the buffer solution.

6.3.4.2 Transport assays with HPTS

In a typical experiment, the LUVs containing HPTS (25 μL, final lipid concentration 31.3 μM) were added to buffer (1950 μL of 100 mM NaCl, 10 mM HEPES, pH 7.0) at 25°C under gentle stirring. A pulse of NaOH (20 μL, 0.5 M) was added at 20 secs to initiate the experiment. At 80 s the test transporter (various concentrations, in 5 μL DMSO) was added, followed by detergent (25 μL of Triton X-100 in 7:1 (v/v) H_2O-DMSO) at 300 secs to calibrate the assay. The fluorescence emission was monitored at λ_{em} = 510 nm (λ_{ex} = 460/405 nm). The fractional fluorescence intensity (I_{rel}) was calculated from equation (S1), where R_t is the fluorescence ratio at time *t*, (ratio of intensities 460 nm / 405 nm excitation) R_0 is the fluorescence ratio at time 77 s, and R_d is the fluorescence ratio after the addition of detergent.

$$I_{rel} = \frac{R_t - R_0}{R_d - R_0} \quad \textbf{(3.2)}$$

The fractional fluorescence intensity (I_{rel}) at 290 s just prior to lysis, defined as the fractional activity *y*, was plotted as a function of the ionophore concentration (*x* / μM). Hill coefficients (*n*) and EC_{50} values were calculated by fitting to the Hill equation (S2) equation,

$$y = y_0 + (y_{max} - y_0).\frac{x^n}{EC50^n + x^n} \qquad (\mathbf{3.3})$$

where y_0 is the fractional activity in the absence of transporter, y_{max} is the fractional activity in with excess transporter, *x* is the transporter concentration in the cuvette.

For each compound as the *E* and Z isomer, Hill plots were fitted to at-least 8, and up to 12 data points spanning the required concentration range, and each individual concentration was repeated at-least twice and averaged (>16 independent measurements per isomer); **Figure 7A; Figure 12A**)

Experiments with DPPC lipids were conducted in the same way. For elevated temperature studies, the sample was equilibrated at 45°C (using the Peltier temperature controller) for 5 minutes prior to initiating the experiment (Figure 8E-F; 12B; Table 2, Table 4).

6.3.4.3 Ion selectivity assay (Figure 8B-D; Figure 12C-E)

Ion transport selectivity was explored by using a previously reported external ion exchange assay.[11-13] This assay allows for comparison of the relative transport rates in the presence of varying external cation and anions, using a consistent batch of vesicles across all experiments. This removes inconsistencies associated with preparation of different batches of vesicles containing different salt solutions, and has previously been shown to provide equivalent selectivity trends to those obtained from permeability ratios obtained from black lipid membrane (BLM) studies.[11-12] These experiments were carried out by adding the POPC vesicle solution (prepared as above) to buffer (100 mM MX, 10 mM HEPES, pH 7.0), where M = Li, Na, K, Rb (X = Cl), and X = Cl, Br, I, NO_3 (M = Na). In the case of NaI buffer, 5 mM $Na_2S_2O_3$ was added.

6.3.4.4 Transport data with HPTS

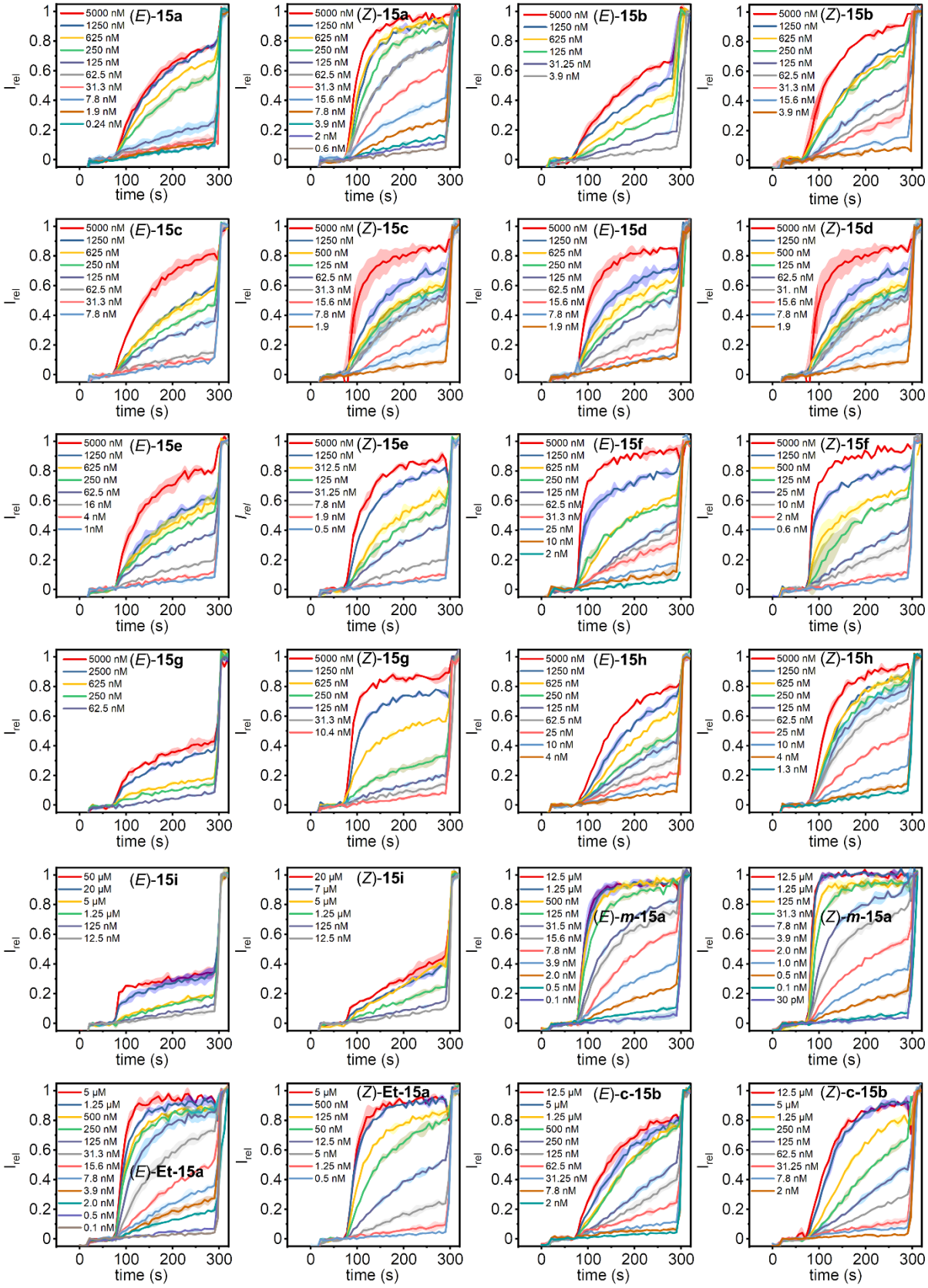


Figure S4. Transport kinetics data using HTPS assay for **15** derivatives. Error bars (s.d.) shown as glow. Hill analysis and plots found in main text.

6.3.4.5 Calcein leakage assay (Figure 8G, 12F)

POPC vesicles were prepared containing calcein (Internal buffer: 100 mM NaCl, 10 mM HEPES, 100 mM calcein, pH 7.0. External buffer: 100 mM NaCl, 10 mM HEPES, pH 7.0). Each transport experiment was carried out as follows; the calcein-containing POPC vesicles (25 μl, 2.5 mM) were suspended in the external buffer (1925 μL, 100 mM NaCl, 10 mM HEPES, pH 7.0) at 25°C and gently stirred. At 60 s, the carriers were administered in 5 μL DMSO. The assay was calibrated at 250 s with detergent (25 μL of Triton X-100 in 7:1 (v/v) H_2O-DMSO). The time-dependent change in fluorescence intensity (λ_{ex} = 490 nm, λ_{em} = 520 nm) was monitored, and normalised according to Equation S3.1:

$$I_{rel} = \frac{I_t - I_0}{I_{max} - I_0} \qquad \textbf{(S3.1)}$$

where $I_0 = I_t$ before transporter addition, $I_{max} = I_t$ after lysis.

6.3.4.6 ISE assay vesicle preparation

A thin film of lipid (1-palmitoyl-2-oleoyl-*sn*-3-phosphatidylcholine POPC, was formed by evaporating a chloroform solution under a stream of nitrogen gas, and then under high vacuum for 6 hours. The lipid film was hydrated by vortexing with the prepared buffer (489 mM NaCl, buffered to pH 7.0 with 5 mM sodium phosphate salts) The lipid suspension was then subjected to 9 freeze-thaw cycles using liquid nitrogen and a water bath (25°C), followed by extrusion 21 times through a polycarbonate membrane (pore size 200 nm) at rt. Extra-vesicular components were removed by size exclusion chromatography on a Sephadex G-25 column with 489 mM $NaNO_3$, buffered with phosphate salts to pH 7.0. After collecting, the vesicles were diluted to 30 mL in 489 mM $NaNO_3$/pH 7.0 phosphate buffer. Final conditions after dilution: LUVs (1 mM lipid); inside: 489 mM NaCl, buffered to pH 7.0 with 5 mM sodium phosphate salts; outside: 489 mM $NaNO_3$, buffered to pH 7.0 with 5 mM sodium phosphate salts. Lipids are used within 24 hrs, and stored in the fridge between experiments. Stocks were warmed to room temperature prior to use.

UV-vis of the vesicle samples containing **15a** following red and blue light irradiation (JASCO V-770 UV-Visible/NIR Spectrophotometer, using a 60 mm integrating sphere to reduce light loss from scattering, scanning 400-700 nm), revealed, as for solution studies, increased intensity of the n→π* transition of **15a** at 440 nm with red light irradiation, which was reversed with blue light (Figure 9C). This provided evidence for *in-situ* switching of (*E*)-**15a** in the membrane using the same LUV conditions used for the ion transport assay. This was confirmed by an additional NMR experiment, in which following red-light induced photo-switching the sample was extracted into $CDCl_3$, diluted with d_6-DMSO and the spectrum recorded (**Figure 9D**). This provides an estimate for the extent of photo-switching when carried out in the vesicles used for the ISE assay, which was found to be ~45 % of that achieved in DMSO solution (65:35 *E*:*Z*).

6.3.4.7 Electrode calibration

The chloride selective electrode (Thermo Scientific™ Orion™ ionplus® Sure-Flow® Solid State Combination ISE) was soaked in 1000 ppm chloride for extended periods (>1 hr) until readings were stable. Before each run, the electrode was calibrated by recording the potential of known chloride concentrations. The readings (mV) were converted to chloride activity using the modified Nernst equation **S3.2**, where *y* is chloride activity, *x* is potential (mV) and *a* and *b* are parameters to be determined and c=0.

$$y = a - b\ln(x + c) \qquad \textbf{(S3.2)}$$

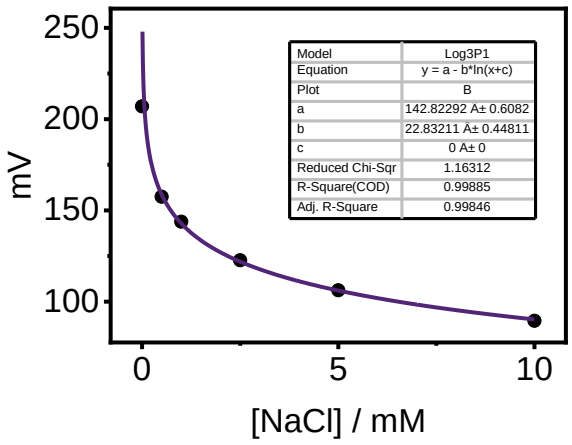


Figure S5. ISE calibration curve

6.3.4.8 Transport assays with ISE (Figure 9F)

Vesicle suspensions (1.5 mL, 1 mM lipid) were added to a 17 mm diameter vial, and gently stirred. The transporter (1 mM stock solution) was added in DMSO (7.5 μL, 0.5 mol% relative to lipid) after 60s, and the voltage was monitored over time, and converted to chloride concentration using **equation S3.2**.

Vesicle suspensions (4.5 mL, 1 mM lipid) were added to a 17 mm vial, and gently stirred. The electrode is placed as high as possible into solution, to avoid interference with any incoming light from the LEDs (Fig. 9E, Fig. S5). For each run, the electrode is held at the same angle, stirring rate held constant (300 rpm), and calibration curves using **equation S3.2** are made before and after each run to ensure consistency. The electrode must not be disturbed during the run (vibrations, movement etc).

Transporter **15a** as the dark-adapted *E* isomer or control squaramide **47** is added as a 1 mM stock solution in DMSO (22.5 μL, 0.5 mol% relative to lipid) at 60s and voltage was monitored over time. Light was continually irradiated as follows: red at 2 minutes, blue at 9 minutes, red at 16 minutes, blue at 23 minutes (Figure 9G). Results were calibrated with **equation S3.2**.

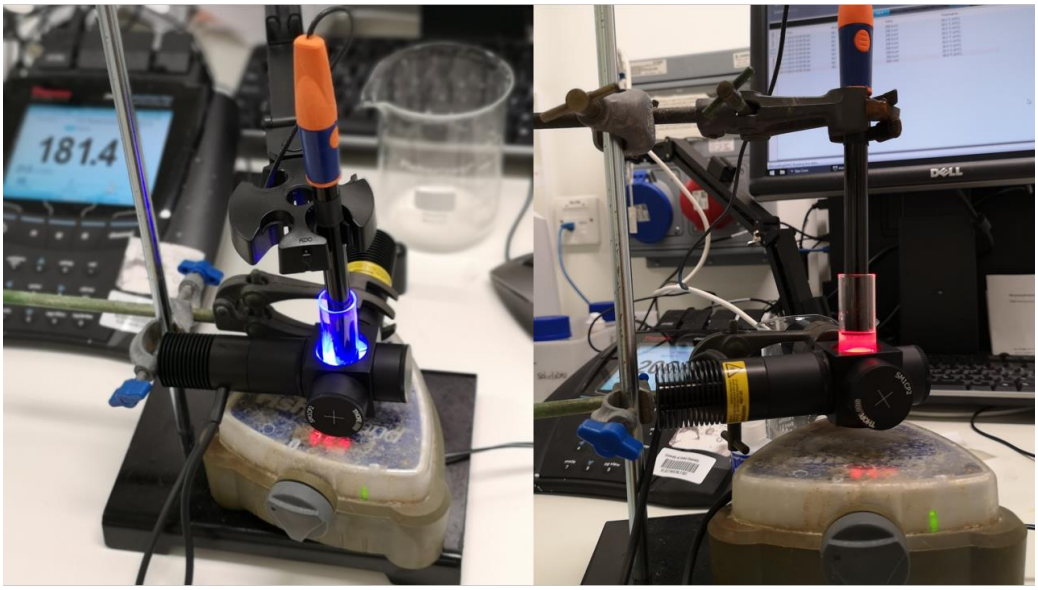


Figure S5. Experimental setup for ISE.

6.3.5 References (Chapter 3 appendix)

[1] Dai, L.; Su-Xi, C; *Adv. Synth. Cat.,* **2011**, 13, 2137–2141

[2] Yang, C.; Wang, J.; Liu, Y.; Ni, X.; Li, X.; Cheng, J.; *Chem. Eur. J.,* **2017,** 23, 5488–5497

[3] ASSEMBLY BIOSCIENCES, INC.; L. Li, L. D. Arnold, D. Lee, S. Reddy WO2018/169907, 2018, A1

[4] VICHEM CHEMIE KUTATÓ KFT.; GREFF, Zoltán; VARGA, Zoltán; KÉRI, György; NÉMETH, Gábor; ÖRFI, László; SZÁNTAI KIS, CsabaWO2011/77171, 2011, A1

[5] G. Yan, L. Hao, Y. Niu, W. Huang, W. Wang, F. Xu, L. Liang, C. Wang, H. Jin and P. Xu, *Eur. J. Med. Chem.*, 2017, **137**, 462-475.

[6] A. González-Antuña, I. Lavandera, P. Rodríguez-González, J. Rodríguez, J. I. García Alonso and V. Gotor, *Tetrahedron*, 2011, **67**, 5577-5581.

[7] Mahlooji, I.; Shokri, M.; Manoochehri, R.; Mahboubi-Rabbani, M.; Rezaee, E.; Tabatabai, S. A., ***353*** (8), 2000052.

[8] Tran-Hoang, N.; Kodadek, T., *ACS Comb. Sci.,* 2018, ***20*** (2), 55-60.

[9] M. A. Lucherelli, J. Raya, K. F. Edelthalhammer, F. Hauke, A. Hirsch, G. Abellán, A. Bianco, *Chem. Eur. J.,* 2019, **25**,13218-13223

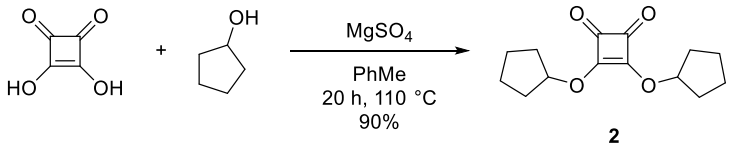
[10] P. Kuzmič, *Anal. Biochem.*, 1996, **237**, 260–273.

[11] Sakai N, Houdebert D, Matile S. *Chem. Eur. J.* **2003**, 9, 223–232

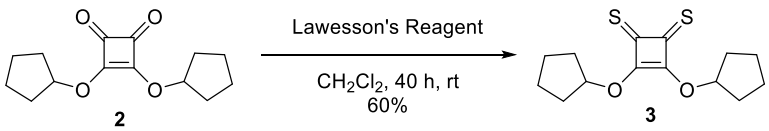
[12] Sakai, N.; Matile, S.; *J. Phys. Org. Chem.* **2006**, 19, 452–460

[13] Ren, C.; Chen, F.; Ye, R.; Ong, Y. S.; Lu, H.; Lee, S. S.; Ying, J. Y.; Zeng, H.; *Angew. Chem. Int. Ed.* 2019, 58, 8034-8038

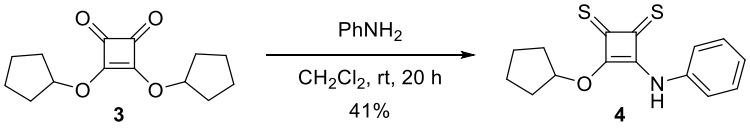
6.4.1 Synthetic procedures (Chapter 4)



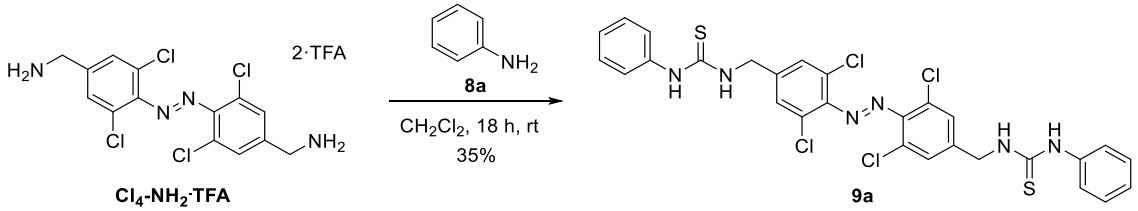
Dione 2. A suspension of squaric acid (4.56 g, 17.54 mmol, 1.0 equiv) in PhMe (13 mL) was treated with cyclopentanol (10.6 mL, 114 mmol, 6.5 equiv) and anhydrous $MgSO_4$ (7 g). The resulting mixture was stirred at reflux temperature for 20 h. The suspension was filtered, washed with MeOH, and the filtrate concentrated. The residue was purified by silica gel flash chromatography (0 to 1% MeOH in CH_2Cl_2) to afford the title compound (3.95 g, 90%) as a white solid. ^{1}H NMR (400 MHz, $CDCl_3$): δ = 5.54 (tt, J = 5.3, 2.5 Hz, 2H), 1.96 (m, 8H), 1.81 (m, 4H), 1.68 (m, 4H). Data consistent with that given in the literature.[1]



Dithione 3. To a suspension of Lawesson's reagent (3.70 g, 9.15 mmol, 1.0 equiv) in dry CH_2Cl_2 (40 mL) was added **2** (2.29 g, 9.15 mmol, 1.0 equiv). The reaction was stirred for 40 h. The reaction mixture was filtered, concentrated to roughly half the original volume, and immediately wet loaded onto silica, then purified by silica gel flash chromatography (70% Hexane in CH_2Cl_2) to afford the title compound (1.546 g, 60%) as an orange solid. ^{1}H NMR (400 MHz, $CDCl_3$): δ = 6.06 (m, 2H), 2.02 (m, 8H), 1.86 (m, 4H), 1.70 (m, 4H). Data consistent with that given in the literature. [1]

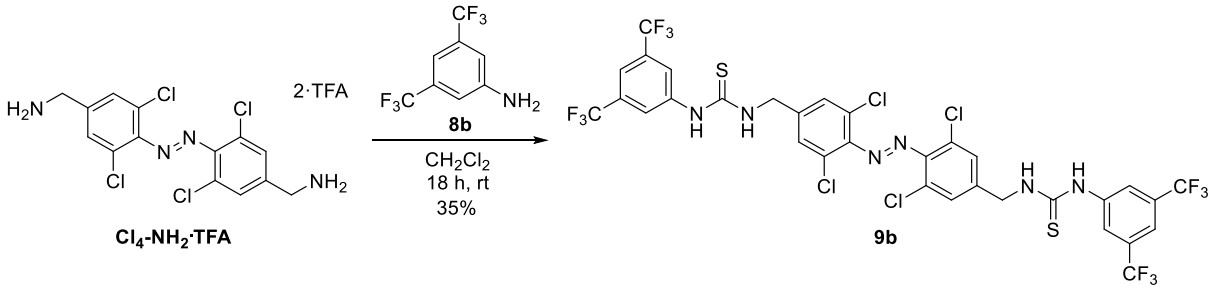


Monothiosquaramide **4**. To a solution of **3** (339 mg, 1.2 mmol, 1.2 equiv) in dry CH_2Cl_2 (3 mL) was added aniline (91 µL, 1.0 mmol, 1.0 equiv) and the resulting solution was stirred for 20 h, during which time a yellow precipitate appeared (diaryl thiosquaramide byproduct). The suspension was then loaded directly onto column and quickly purified by silica gel flash chromatography (50% Hexane in CH_2Cl_2) to afford the title compound (118 mg, 0.41 mmol, 41%) as an orange solid. 1H NMR (400 MHz, DMSO-d6): δ = 11.59 (s, 1H), 7.40 (m, 4H), 7.26 (m, 1H), 6.47 (m, 1H), 1.94 (s, 4H), 1.66 (s, 4H). Data consistent with that given in the literature. [1]

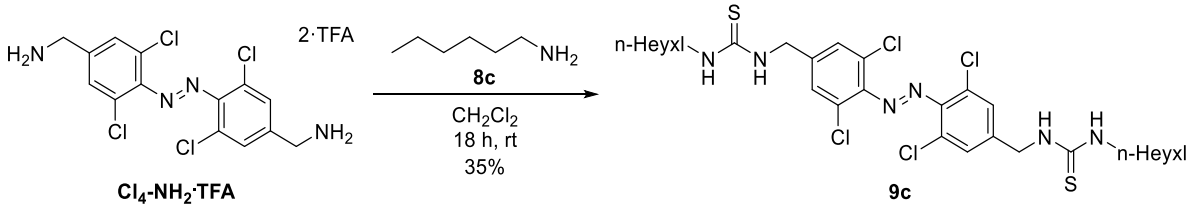


Thiourea 9a. Cl_4-NH_2·TFA (50 mg, 92.5 µmol) was suspended in CH_2Cl_2 (1 mL). NEt_3 (77 µL, 0.55 mmol, 6 eq) was added to form a brown solution. Phenyl isothiocyanate (24 µL, 222 µmol,

2.4 eq) was added and the reaction was stirred for 18 hours. The precipitated solid was filtered, washed with MeOH and dried to afford the title compound as a light brown solid (18 mg, 32.4 mmol, 35%). (*E*)-**9a**: ^{1}H NMR (400 MHz, DMSO-d6) δ 9.82 (s, 2H), 8.32 (d, 2H, J = 7.9 Hz), 7.62 (s, 4H), 7.45 – 7.38 (m, 4H), 7.35 (t, J = 7.9 Hz, 4H), 7.19 – 7.12 (m, 2H), 4.80 (d, J = 5.8 Hz, 4H). ^{13}C NMR (126 MHz, DMSO-d_6) δ 182.60, 147.24, 146.46, 145.16, 140.33, 130.31, 129 .96, 127.52, 126.19, 125.95, 125.17, 47.24. HRMS-ESI (m/z) Calculated for $C_{28}H_{22}Cl_4N_6S_2$ $[M-H]^-$, 623.0369; found 623.0356.

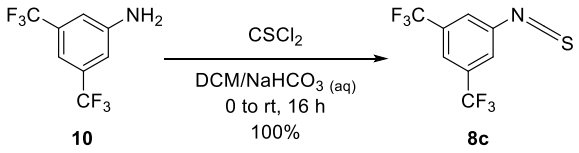


Thiourea 9b. Cl_4-NH_2·TFA (50 mg, 92.54 µmol) was suspended in CH_2Cl_2 (1 mL). NEt_3 (77 µL, 0.55 mmol, 6eq) was added to form a brown solution. **8b** (34 µL, 222 µmol, 2.4 eq) was added and the reaction was stirred for 40 hours. The solution was concentrated *in vacuo*. The residue was purified by silica gel flash chromatography (50% EtOAc in hexane) to afford the title compound as an orange solid (21 mg, 28.7 µmol, 31 %). (*E*)-**9b**:^{1}H NMR (400 MHz, DMSO-d_6) δ 10.37 (br s, 2H), 8.80 (br s, 2H), 8.27 (s, 4H), 7.78 (s, 2H), 7.65 (s, 4H), 4.85 (s, 4H). ^{13}C NMR (126 MHz, DMSO-d6) δ 181.40, 145.15, 143.13, 141.73, 130.67 (q, *J* = 32.68 Hz), 128.52, 126.16, 123.70 (q, *J* = 272.68 Hz), 122.51, 116.63, 45.92. HRMS-ESI (m/z) Calculated for $C_{32}H_{18}Cl_4F_{12}N_6S_2$ $[M-H]^+$ 918.9667, found 918.9687.

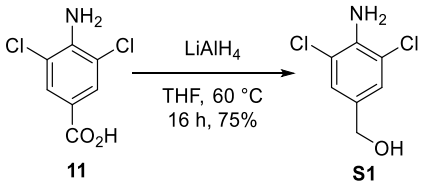


Thiourea 9c. Cl_4-NH_2·TFA (50 mg, 92.54 µmol) was suspended in CH_2Cl_2 (1 mL). NEt_3 (77 µL, 0.55 mmol, 6 eq) was added to form a brown solution. **9c** (34 µL, 222 µmol, 2.4 eq) was

added and the reaction was stirred for 40 hours. The solution was concentrated *in vacuo* and residue purified by silica gel flash chromatography (50% EtOAc in hexane) to afford the title compound as an orange solid (23.7 mg, 23.4 µmol 38%). (*E*)-**9c**:^{1}H NMR (400 MHz, Chloroform-*d*) δ 7.42 (s, 4H), 6.02 (d, *J* = 5.7 Hz, 4H), 4.80 (d, 5.7 Hz, 4H), 3.46 – 3.26 (m, 4H), 1.61 (m, 4H), 1.34 – 1.26 (m, 12H), 0.88 (m, 6H). ^{13}C NMR (126 MHz, DMSO-d_6) δ 182.41, 144.77, 143.99, 128.06, 125.91, 54.76, 45.20, 30.88, 28.46, 25.87, 21.94, 13.78. HRMS-ESI (m/z) Calculated for $C_{28}H_{38}Cl_4N_6S_2$ $[M-H]^-$, 661.1270; found 661.1279.

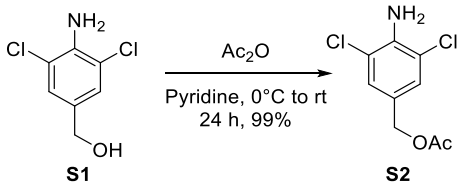


8b. $NaHCO_3$ (293.31 mg, 3.49 mmol, 4 eq) was dissolved in distilled water (1.4 mL). CH_2Cl_2 (1.4 mL) and **10** (200 mg, 0.873 mmol, 1 eq) were added. The biphasic solution was cooled to 0 °C and thiophosgene (0.1 mL, 1.31 mmol, 1.5 eq) was added dropwise. The solution was vigorously stirred over 16 hours. This was diluted with CH_2Cl_2 (15 mL), washed with brine (15 mL), then dried and concentrated to afford the title compound (233 mg, 0.859 mmol, 98%) as a yellow oil. ^{1}H NMR (400 MHz, Chloroform-d) δ 7.76 (qt, J = 1.4, 0.7 Hz, 1H), 7.66 – 7.64 (m, 2H). Rf = 0.85 (silica gel, 5:1 hexane:EtOAc). Data consistent with that given in the literature.[2]



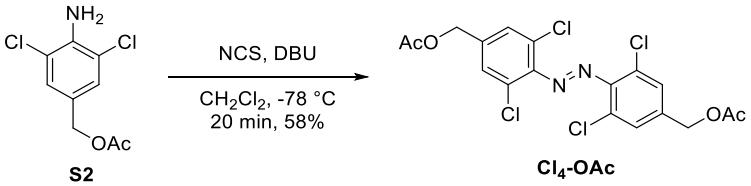
Compound S1: $LiAlH_4$ (4.60 g, 121.2 mmol, 2.5 equiv.) was suspended in dry THF (143 mL) under nitrogen. Acid **11** (10.0 g, 48.5 mmol) was suspended in dry THF (100 mL) and this was added to the solution of $LiAlH_4$ over 15 mins at 0 °C. The reaction mixture was then heated at 60 °C for 16 h, resulting in a colour change from brown to grey. The reaction mixture was diluted with ether (200 mL) and cooled to 0 °C. 5 mL water was added dropwise, then 5 mL NaOH was added dropwise before adding a further 15 mL water, resulting in a light brown

suspension (Fieser workup). The reaction mixture was stirred for 15 minutes, then $MgSO_4$ was added. The solids were filtered under vacuum and the filtrate concentrated. The residue was purified by silica gel flash chromatography (50% EtOAc in hexane) to afford the title compound as a yellow solid (6.99 g, 36.4 mmol, 75%). ^{1}H NMR (400 MHz, $CDCl_3$) δ 7.20 (s, 2H), 4.54 (s, 2H), 4.43 (br s, 2H), 1.59 (br s, 1H) Data consistent with that given in the literature.[3]



S1 **S2**

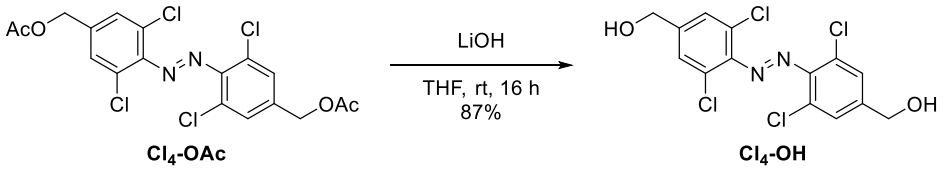
Compound S2: To a solution of **S1** (4.45 g, 23.2 mmol) in pyridine (15 mL) was added acetic anhydride (2.19 mL, 32.3 mmol, 1 eq). The reaction mixture was stirred at 0 °C and allowed to warm to rt before stirring for 24 h. The product was extracted into EtOAc (20 mL) and the mixture was washed with water (2 ×20 mL) and HCl (15 mL), then dried over $MgSO_4$. The solvent was removed *in vacuo* afford the title compound as a yellow oil (5.41 g, 23.1 mmol, 99%). ^{1}H NMR (400 MHz, $CDCl_3$) δ 7.20 (s, 2H), 4.93 (s, 2H), 4.75 – 4.14 (m, 2H), 2.08 (s, 3H). ^{13}C NMR (101 MHz, $CDCl_3$) δ 170.90, 140.28, 128.44, 126.14, 119.46, 65.25, 21.15. HRMS-ESI (*m/z*) for $[M+H]^+$, $C_9H_{10}Cl_2NO_2^+$: calculated 231.9938; found 231.9931.



S2 **Cl_4-OAc**

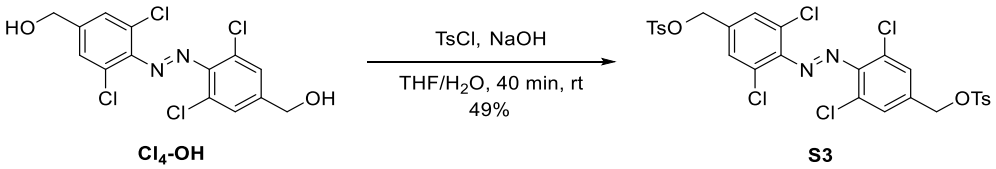
Cl_4-OAc: To a solution of **S2** (4.32 g, 18.5 mmol) in CH_2Cl_2 (290 mL) was added DBU (5.63 g, 37.0 mmol, 2 equiv.) with stirring at rt for 5 mins. NCS (4.92 g, 36.9 mmol, 2 equiv.) was added at -78 °C and the reaction mixture was stirred for 20 mins at -78 °C with occasional brief sonication, before quenching by addition of saturated $NaHCO_3$ (250 mL). The dark orange reaction mixture was washed with water (3 × 250 mL) and 1 M HCl (250 mL). The organic layer was concentrated *in vacuo* and was purified by silica gel flash chromatography

(30% Hexane in CH_2Cl_2) to afford the title compound as an orange solid as a mixture of isomers (2.48 g, 5.34 mmol, 58%). (*E*)-**Cl_4-OAc**: ^{1}H NMR (400 MHz, $CDCl_3$) δ 7.45 (s, 4H), 5.10 (s, 4H), 2.16 (s, 6H). ^{13}C NMR (101 MHz, $CDCl_3$) δ 170.59, 147.20, 138.58, 128.82, 127.67, 64.33, 20.99. HRMS-ESI (*m/z*) for $[M+H]^+$, $C_{18}H_{15}Cl_4N_2O_4^+$: calculated 464.9751; found 464.9751.



Cl_4-OAc **Cl_4-OH**

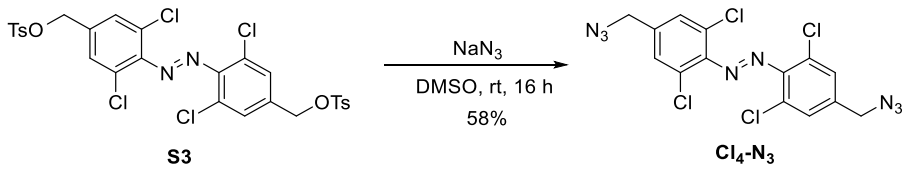
Cl_4-OH: To a solution of **Cl_4-OAc** (2.48 g, 5.3 mmol) in THF (20 mL) was added LiOH (632.7 mg, 26.4 mmol, 5 equiv.) in water (5 mL). The reaction mixture was stirred at rt for 16 h and monitored by TLC before diluting in DCM (100 mL) and washing with water (3 × 100 mL). The solvent was removed *in vacuo*, then was purified by silica gel flash chromatography (3% MeOH in CH_2Cl_2) to afford the title compound as an orange solid as a mixture of isomers (1.76 g, 4.63 mmol, 87%). (*E*)**-Cl_4-OH**: ^{1}H NMR (400 MHz, Acetone) δ 7.61 (t, *J* = 0.8 Hz, 4H), 4.79 – 4.73 (m, 4H), 4.66 (dd, *J* = 6.3, 5.4 Hz, 2H). ^{13}C NMR (101 MHz, Acetone) δ 147.21, 146.60, 128.07, 127.65, 62.94. HRMS-ESI (*m/z*) for $[M+H]^+$, $C_{14}H_{11}Cl_4N_2O_2^+$: calculated 380.9540; found 380.9541.



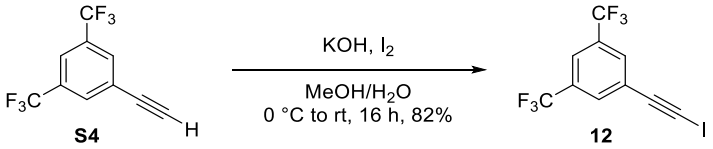
Cl_4-OH **S3**

Tosylate S3. Cl_4-OH (173 mg, 455 µmol) was dissolved in 7:3 THF/H_2O (20 mL). NaOH (91 mg, 2.28 mmol, 5 eq) was added. Then TsCl (261 mg, 1.37 mmol, 3 eq) was added. The reaction was stirred at room temperature for 40 minutes. The reaction was diluted with CH_2Cl_2, then washed with H_2O (3x). The organic layer was concentrated, then purified by silica gel flash chromatography (dry load, 50% to 100% CH_2Cl_2 in hexane) to afford the title compound as an orange solid as a mixture of isomers (154.3 mg, 223 µmol, 49%). (*E*)**-S3**: ^{1}H NMR (400

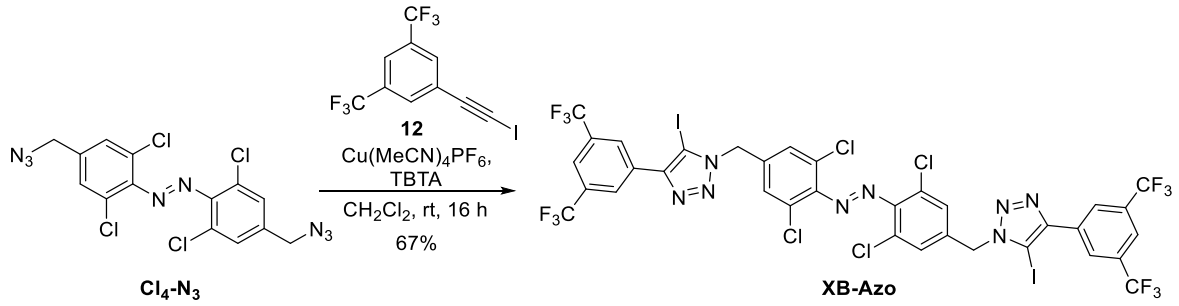
MHz, $CDCl_3$) δ 7.81 – 7.76 (m, 4H), 7.35 (dd, *J* = 8.0, 5.0 Hz, 4H), 7.30 (s, 4H), 5.06 (s, 4H), 2.45 (s, 6H). ^{13}C NMR (151 MHz, $CDCl_3$) δ 147.67, 145.59, 135.96, 133.08, 130.14, 129.00, 128.14, 127.69, 69.53, 21.83. HRMS-ESI (m/z) Calculated for $C_{28}H_{22}N_2O_6S_2Cl_4$ $[M+H]^+$, 688.9717; found 685.4355.



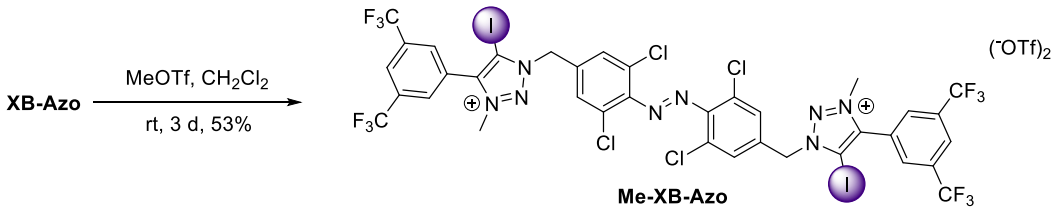
Cl_4-N_3. Tosylate S3 (150 mg, 218 µmol) was dissolved in dry DMSO (3.5 mL) under N_2. Sodium azide (71 mg, 1.09 mmol, 5 eq) was added and the reaction was stirred at room temperature for 16 hours. Water was added (5 mL) and the reaction was extracted with Et_2O (3x 10 mL). The combined organic layers were washed with water (3 x 10 mL) then dried with $MgSO_4$. The organic layer was concentrated and left without further purification to afford the title compound as an orange solid (54 mg, 126 µmol, 58%). (*E*)**-Cl_4-N_3**: ^1H NMR (400 MHz, $CDCl_3$) δ 7.43 (s, 4H), 4.41 (s, 4H). ^{13}C NMR (126 MHz, $CDCl_3$) δ 147.26, 138.19, 128.79, 128.00, 53.34. HRMS-ESI (m/z) Calculated for $C_{14}H_9Cl_4N_8$ $[M+H]^+$, 428.9699; found 428.9700.



12. Prepared according a literature procedure.[3] **S4** (165 mg, 0.69 mmol) and KOH (185 mg in 0.5 mL H_2O, 1.73 mmol, 2.5 eq) was stirred in MeOH (4 mL) at 0°C for 10 mins. Iodine (361 mg, 0.76 mmol, 1.1 eq) was added and the reaction mixture was allowed to warm to rt and stirred overnight. The reaction was diluted with water (25 mL) and the product was extracted with ethyl acetate (2 x 25 mL). The organic layer was dried with $MgSO_4$, then concentrated to afford a yellow oil (206 mg, 0.56 mmol, 82%).^1H NMR (400 MHz, $CDCl_3$) δ 7.87 (s, 2H), 7.81 (s, 1H). ^{19}F NMR (377 MHz, $CDCl_3$) δ -63.22. Data consistent with that given in the literature.[4]

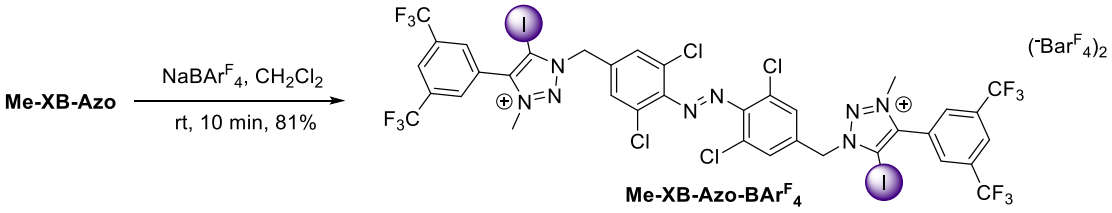


XB-Azo. Cl_4-N_3 (53 mg, 123 µmol), Iodoalkyne **12** (180 mg, 492 µmol, 4 eq), Tris((1-benzyl-4-triazolyl)methyl)amine [TBTA] (13 mg, 24.6 µmol, 0.2 eq) and $Cu(MeCN)_4PF_6$ (9 mg, 24.6 µmol, 0.2 eq) were placed in a flask and purged with N_2. Degassed CH_2Cl_2 (3 mL) was added and the reaction was stirred at room temperature overnight. The mixture was diluted with CH_2Cl_2, then washed with ammonia / EDTA solution. The organic layer was concentrated and the residue was purified by silica gel flash chromatography (dry load, 50% to 70% CH_2Cl_2 in hexane) to afford the title compound as an orange solid as a mixture of isomers (95 mg, 82 µmol, 67%). (*E*)-**XB-Azo**: ^{1}H NMR (600 MHz, $CDCl_3$) δ 8.49 (s, 4H), 7.92 (s, 2H), 7.43 (s, 4H), 5.71 (s, 4H). ^{13}C NMR (151 MHz, $CDCl_3$) δ 148.06, 147.74, 136.15, 132.26 (q, *J* = 33.5 Hz), 128.92, 128.34, 127.39 (m), 124.21, 123.30 (q, *J* = 272.8 Hz), 122.54 (m), 77.68, 53.22. ^{19}F NMR (377 MHz, $CDCl_3$) δ -62.96. HRMS-ESI (m/z) Calculated for $C_{34}H_{13}N_8F_{12}Cl_4I_2$ $[M-H]^-$, 1156.7896; found 1156.7876.

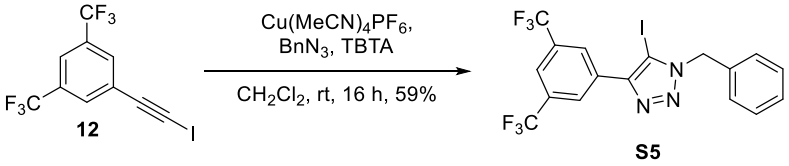


Me-XB-Azo. To a suspension of **XB-Azo** (25 mg, 21.6 µmol) in dry CH_2Cl_2 (1 mL) under N_2 in a sealed tube was added methyl triflate (7 µL, 64.8 µmol, 3 eq). The reaction was stirred under protection from light for 3 days. Then, Et_2O (10 mL) was added, and the precipitate was collected *via* filtration. The solid was collected and dried to afford the title compound as an orange solid (17 mg, 11.4 µmol, 53%). *(E)*-**Me-XB-Azo**: ^{1}H NMR (400 MHz, DMSO) δ 8.59 (s, 2H), 8.41 (s, 4H), 7.86 (s, 4H), 6.20 (s, 4H), 4.32 (s, 6H). ^{13}C NMR (151 MHz, DMSO) δ 146.53,

144.32, 135.95, 131.59 (m), 131.31 (d, *J* = 33.4 Hz), 129.95, 126.45, 125.97 (m), 125.66, 122.81 (d, *J* = 273.2 Hz), 95.75, 55.19, 40.05. ^{19}F NMR (377 MHz, DMSO) δ -61.28, -77.75. HRMS-ESI (m/z) Calculated for $C_{36}H_{20}N_8F_{12}Cl_4I_2$ $[M]^{2+}$, 593.9214; found 593.9197

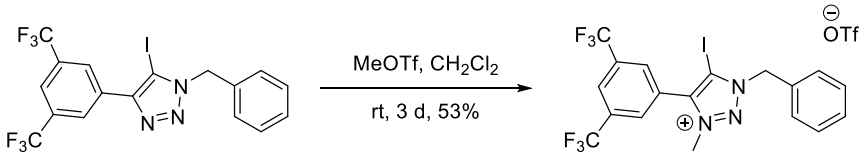


Me-XB-Azo-BAr$^F_4$. Me-XB-Azo (50 mg, 33.6 µmol) was suspended in CH_2Cl_2 (2 mL). NaBAr$^F_4$ (59.62 mg, 67.3 µmol, 2 eq) was added, and the mixture turned into an orange solution, which was stirred for a further 10 minutes. The reaction was diluted with CH_2Cl_2 (20 mL). The organic layer was washed with water twice, then dried and concentrated to afford the title compound as a sparkly orange solid (79 mg, 27.1 µmol, 81%). %). (*E*)-**Me-XB-Azo-BAr$^F_4$**: ^{1}H NMR (400 MHz, CD_2Cl_2) δ 8.35 (s, 2H), 7.94 (s, 4H), 7.71 (br s, 24H), 7.63 (s, 4H), 7.55 (q, *J* = 1.4 Hz, 12H), 5.83 (s, 4H), 4.32 (s, 6H). ^{19}F NMR (377 MHz, CD_2Cl_2) δ -62.81, -63.54.



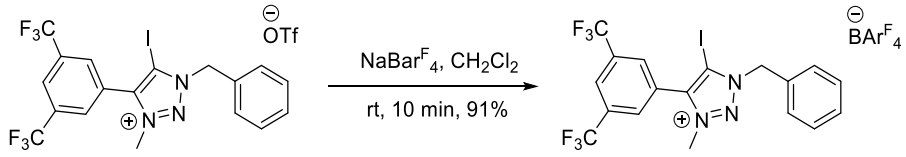
S5. Benzyl azide (165 µL, 1.32 mmol, 3 eq), Iodoalkyne **12** (160 mg, 440 µmol, 1 eq), [TBTA] (45 mg, 85 µmol, 0.2 eq) and $Cu(MeCN)_4PF_6$ (31 mg, 85 µmol, 0.2 eq) was placed in a flask and purged with N_2. Degassed CH_2Cl_2 (5 mL) was added and the reaction was stirred at room temperature for 16 hours. The mixture was diluted with CH_2Cl_2, then washed with ammonia / EDTA solution. The organic layer was concentrated and the residue was purified by silica gel flash chromatography (10% Acetone in hexane) to afford the title compound as a white solid (170 mg, 342 µmol, 78%). ^{1}H NMR (600 MHz, $CDCl_3$) δ 8.48 (d, *J* = 1.7 Hz, 2H), 7.89 (s, 1H), 7.40 – 7.34 (m, 3H), 7.34 – 7.30 (m, 2H), 5.71 (s, 2H). ^{19}F NMR (377 MHz, $CDCl_3$) δ -62.95.

^{13}C NMR (151 MHz, $CDCl_3$) δ 147.63, 133.95, 132.51, 132.17 (d, *J* = 33.4 Hz), 129.20, 128.92, 128.00, 127.35 (q, *J* = 3.7 Hz), 123.35 (q, *J* = 272.8 Hz), 122.25 (h, *J* = 3.8 Hz), 77.42, 54.81. HRMS-ESI (m/z) Calculated for $C_{17}H_{11}F_6IN_3$ $[M+H]^+$, 497.9896; found 497.9883.



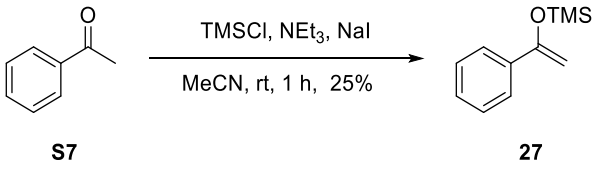
S5 **S6**

S6. To a suspension of **S5** (100 mg, 201.13 µmol) in dry CH_2Cl_2 (1 mL) under N_2 in a sealed tube was added methyl triflate (65 µL, 603 µmol, 3 eq). The reaction was stirred for 2 days. Then, Et_2O (10 mL) was added, and the precipitate was collected *via* filtration. The solid was collected and dried to afford the title compound a white solid (68 mg, 103 µmol, 53%). ^{1}H NMR (600 MHz, DMSO) δ 8.54 (s, 1H), 8.43 (d, *J* = 1.7 Hz, 2H), 7.53 – 7.43 (m, 5H), 6.04 (s, 2H), 4.26 (s, 3H). ^{19}F NMR (377 MHz, DMSO) δ -61.34, -77.77. ^{13}C NMR (151 MHz, DMSO) δ 144.21, 132.40, 131.76 (m), 131.33 (q, *J* = 33.8 Hz), 129.16, 129.10, 128.45, 125.89, 125.81, 122.87 (d, *J* = 273.2 Hz), 94.76, 57.04, 40.05. HRMS-ESI (m/z) Calculated for $C_{18}H_{14}N_3F_6I$ $[M]^+$, 513.0068; found 513.0131



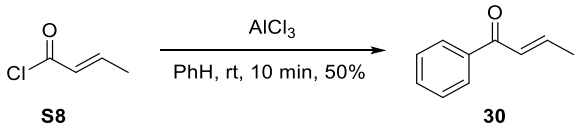
S6 **c-BAr$^F_4$**

c-BAr$^F_4$. S6 (31 mg, 46.9 µmol) was suspended in CH_2Cl_2 (3 mL). NaBAr$^F_4$ (41.5 mg, 46.9 µmol, 1 eq) was added, resulting in a colourless solution which was stirred for a further 10 minutes. The reaction was diluted with CH_2Cl_2 (20 mL). The organic layer was washed with water twice, then dried and concentrated to afford the title compound as a sparkly white solid (96 mg, 43.9 µmol, 91%). ^{1}H NMR (600 MHz, $CDCl_3$) δ 8.26 (s, 1H), 7.89 (s, 2H), 7.68 (dt, *J* = 5.5, 2.4 Hz, 6H), 7.49 (s, 3H), 7.47 (t, *J* = 7.3 Hz, 1H), 7.41 (t, *J* = 7.3 Hz, 2H), 7.36 (d, *J* = 7.5 Hz, 2H), 5.62 (s, 2H), 4.10 (s, 3H). ^{19}F NMR (377 MHz, $CDCl_3$) δ -62.40, -63.17.



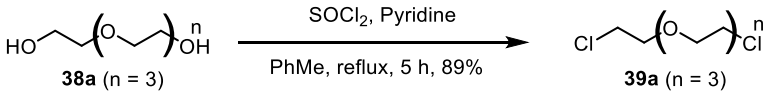
S7 **27**

27. Prepared according to a modified literature procedure.[5] To a mixture of acetophenone **S7** (0.97 mL, 8.32 mmol), triethylamine (1.45 mL, 10.4 mmol, 1.25 eq) and TMSCl (1.32 mL, 10.4 mmol) in dry acetonitrile was added NaI (1.56 g, 1.25 eq) under nitrogen. The reaction was stirred at room temperature for 1 hour. The reaction was poured onto pentane (20 mL) and ice water (20 mL). The organic layer was concentrated, then quickly purified by silica gel flash chromatography (petroleum ether) to afford the title compound as a clear oil (400 mg, 2.08 mmol, 25%). ^{1}H NMR (500 MHz, $CDCl_3$) δ 7.61 (dd, *J* = 7.2, 1.8 Hz, 2H), 7.37 – 7.27 (m, 3H), 4.93 (d, *J* = 1.6 Hz, 1H), 4.45 (d, *J* = 1.7 Hz, 1H), 0.29 (s, 9H). Data consistent with that given in the literature. [5]



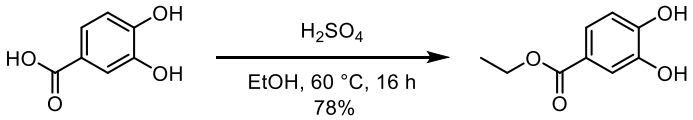
S8 **30**

30. Prepared according to a modified literature procedure.[6] **S8** (6.50 g, 62.2 mmol, 1 eq) was suspended in benzene (18.0 mL) and $AlCl_3$ (13.6 g, 101 mmol, 1.62 eq) was added while cooling. The mixture was stirred for 10 minutes at rt and was quenched by pouring into a mixture of 1 M HCl (100 mL) and ice (100 mL). The aqueous layer was extracted with CH_2Cl_2 (3 × 50 mL) followed by washing with 1 M NaOH (30 mL) and drying over Na_2SO_4 yielded the crude product after removal of the solvent. The organic layer was concentrated and the residue was purified by silica gel flash chromatography (3% EtOAc in pentane) to afford the title compound as a clear oil (4.6 g, 31.3 mmol, 50 %).^{1}H NMR (400 MHz, $CDCl_3$) δ 7.97 – 7.88 (m, 2H), 7.58 – 7.50 (m, 1H), 7.50 – 7.42 (m, 2H), 7.08 (dq, *J* = 15.5, 6.8 Hz, 1H), 6.91 (dq, *J* = 15.3, 1.6 Hz, 1H), 2.00 (dd, *J* = 6.8, 1.6 Hz, 3H). Data consistent with that given in the literature.[6]



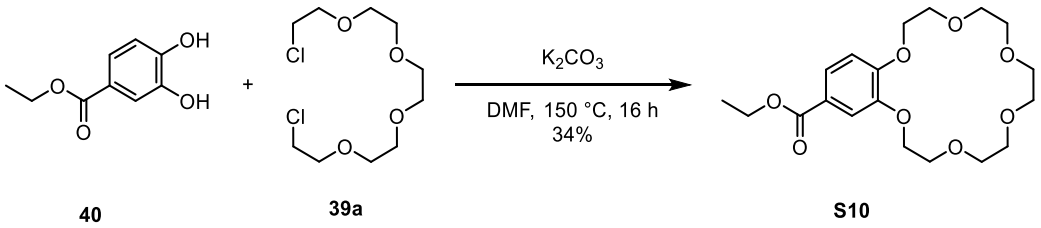
38a (n = 3) **39a** (n = 3)

Dichloride 39a. Prepared according to a modified literature procedure.[7] Pentaethylene glycol **38a** (4.86 g, 20 mmol) was dissolved in dry toluene (30 mL). Dry pyridine (4.1 mL, 51 mmol, 2.5 eq) was added, then thionyl chloride (3.7 mL, 51 mmol, 2.5 eq) in dry toluene (4 mL) was added dropwise. The reaction was stirred at reflux temperature for 5 hours. The reaction was concentrated, then partitioned between EtOAc and water. The organic layer was dried and concentrated to afford the title compound which was left without further purification (5.01 g, 18.2 mmol, 89%). ^{1}H NMR (400 MHz, $CDCl_3$) δ 3.76 (td, *J* = 5.9, 0.7 Hz, 4H), 3.70 – 3.65 (m, 12H), 3.63 (td, *J* = 5.9, 0.6 Hz, 4H). Data consistent with that given in the literature. [7]



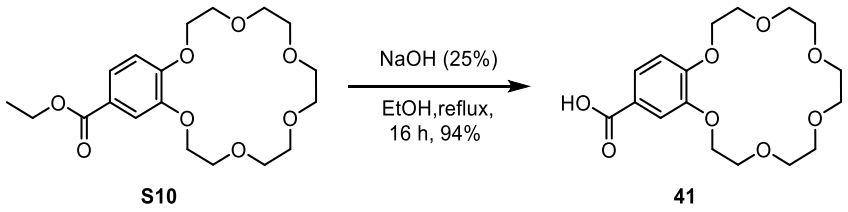
S9 **40**

40. Prepared according to a modified literature procedure.[7] **S9** (10 g, 64.9 mmol) was dissolved in EtOH (100 mL). H_2SO_4 (2 mL) was added dropwise at 0 °C. The reaction was stirred at 60 °C for 16 hours, after which the reaction was concentrated. EtOAc (200 mL) was added, and the organic layer was washed with sat. $NaHCO_3$ (150 mL), then brine (150 mL). The organic layer was dried over Na_2SO_4, then concentrated under vacuum to afford the title compound as a white solid (9.27 g, 50.9 mmol, 78%). ^{1}H NMR (400 MHz, $CDCl_3$) δ 7.70 (d, *J* = 2.0 Hz, 1H), 7.58 (dd, *J* = 8.4, 2.0 Hz, 1H), 6.92 (d, *J* = 8.3 Hz, 1H), 6.27 (s, 1H), 6.00 (s, 1H), 4.35 (q, *J* = 7.1 Hz, 2H), 1.38 (t, *J* = 7.1 Hz, 3H). Data consistent with that given in the literature. [7]



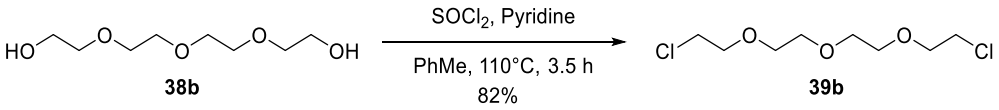
40 **39a** **S10**

Crown ether **S10**. Prepared according to literature procedure. [7] Potassium carbonate (4.55 g, 32.94 mmol, 2 eq) was suspended in anhydrous DMF under N_2 at 150 °C. Diol **40** (3.0 g, 16.47 mmol, 1 eq) and dichloride **39a** (4.53 g, 16.47 mmol, 2 eq) were added. The reaction was stirred at this temperature for 16 hours. The reaction was cooled, concentrated *in vacuo*, and then redissolved in CH_2Cl_2. The organic layer was washed with bicarbonate solution twice, then concentrated. The brown residue extracted with hot hexane. The combined hexane layers were recrystallized from hexane twice to afford the title compound as a white solid (2.15 g, 5.6 mmol, 34%). ^{1}H NMR (400 MHz, $CDCl_3$) δ 7.66 (dd, *J* = 8.4, 2.0 Hz, 1H), 7.55 (d, *J* = 2.0 Hz, 1H), 6.86 (d, *J* = 8.5 Hz, 1H), 4.34 (q, *J* = 7.1 Hz, 2H), 4.23 – 4.16 (m, 4H), 3.97 – 3.90 (m, 4H), 3.78 (ddt, *J* = 5.0, 3.5, 1.3 Hz, 4H), 3.75 – 3.70 (m, 4H), 3.69 (s, 4H), 1.37 (t, *J* = 7.1 Hz, 3H). Data consistent with that given in the literature. [7]

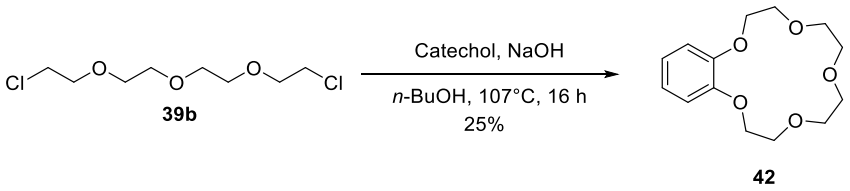


S10 **41**

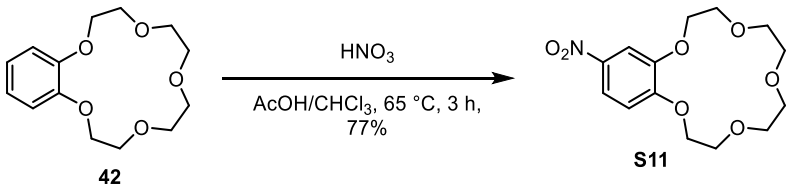
41. Prepared according to literature procedure.[7] Ester **S10** was suspended in EtOH (8 mL), then 25% NaOH (8 mL) was added. The reaction was stirred at reflux temperature for 6 hours. The solvent was removed, then dissolved in water (6 mL). HCl was added until the pH was 3, after which a precipitate formed. The solid was collected and dried to afford the title compound as a white solid (1.35 g, 3.79 mmol, 94%). ^{1}H NMR (400 MHz, DMSO) δ 12.64 (s, 1H), 7.54 (dd, *J* = 8.4, 2.0 Hz, 1H), 7.43 (d, *J* = 2.0 Hz, 1H), 7.04 (d, *J* = 8.5 Hz, 1H), 4.22 – 4.04 (m, 4H), 3.76 (dt, *J* = 6.8, 2.6 Hz, 4H), 3.61 (dd, *J* = 6.2, 3.2 Hz, 4H), 3.55 (dd, *J* = 6.4, 2.9 Hz, 8H). Data consistent with that given in the literature. [7]



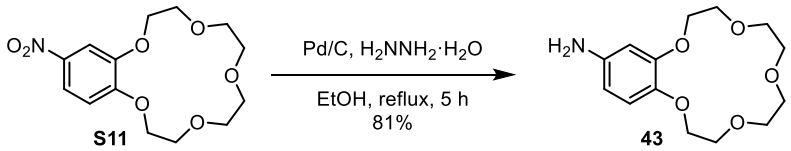
39b. Prepared according to literature procedure.[7] **38b** (17 mL (19.1 g), 98.5 mmol) was dissolved in toluene (150 mL). Pyridine (20 mL, 246.2 mmol, 2.5 eq) and $SOCl_2$ (20 mL, 246.2 mmol, 2.5 eq) was added and the reaction was stirred at 110 °C for 3.5 hours. The reaction mixture was concentrated, then the residue was partitioned between EtOAc (200 mL) and water (200 mL). The organic layer was dried, then concentrated to afford the title compound as a brown oil (18.6 g, 80.5 mmol, 82%). ^{1}H NMR (400 MHz, $CDCl_3$) δ 3.79 – 3.74 (m, 4H), 3.68 (br s, 8H), 3.66 – 3.61 (m, 4H). Data consistent with that given in the literature. [7]



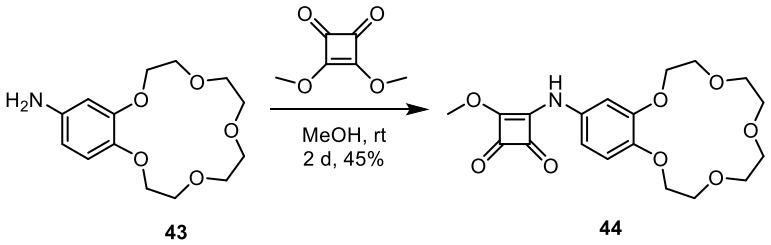
42. Prepared according to literature procedure.[8] Catechol (8.83 g, 80.5 mmol) was suspended in *n*-BuOH (140 mL). NaOH (6.72 g, in 22 mL H_2O) was added whilst stirring. Dichloride **39b** (18.6 g, 80.5 mmol, 1 eq) was added dropwise. The reaction was stirred at 107 °C for 16 hours. The reaction was cooled, and conc. HCl was added (3 mL). The reaction was filtered, and washed with MeOH (100 mL) and filtrate was concentrated. The residue was extracted with boiling hexane (10 x 100 mL). The combined hexane fractions were concentrated, then recrystalised from boiling heptane (200 mL). The obtained crystals were collected via filtration, washed with heptane, then dried to afford the title compound as a white solid (5.4 g, 20.13 mmol, 25%). ^{1}H NMR (400 MHz, $CDCl_3$) δ 6.93 – 6.85 (m, 4H), 4.14 (dd, *J* = 5.6, 3.3 Hz, 4H), 3.96 – 3.88 (m, 4H), 3.76 (s, 8H). Data consistent with that given in the literature.[8]



S11. Prepared according to literature procedure.[8] **42** (333 mg, 1.24 mmol) was dissolved in Chloroform (9 mL) Then nitric acid (70%, 2.6 mL, 43.4 mmol, 35 eq) in AcOH (6.7 mL) was added dropwise, and the reaction was stirred at 65 °C for 3 h. The solution was diluted with water, then extracted with chloroform. The organic layer was washed with water 3 x. The organic layer was dried andconcentrated to afford the title compound as a yellow solid (300 mg, 0.96 mmol, 77%). ^{1}H NMR (400 MHz, $CDCl_3$) δ 7.88 (dd, *J* = 8.9, 2.7 Hz, 1H), 7.72 (d, *J* = 2.6 Hz, 1H), 6.86 (d, *J* = 8.9 Hz, 1H), 4.20 (q, *J* = 4.0 Hz, 4H), 3.93 (q, *J* = 4.4 Hz, 4H), 3.81 – 3.71 (m, *J* = 3.6, 2.9 Hz, 8H). Data consistent with that given in the literature.[8]

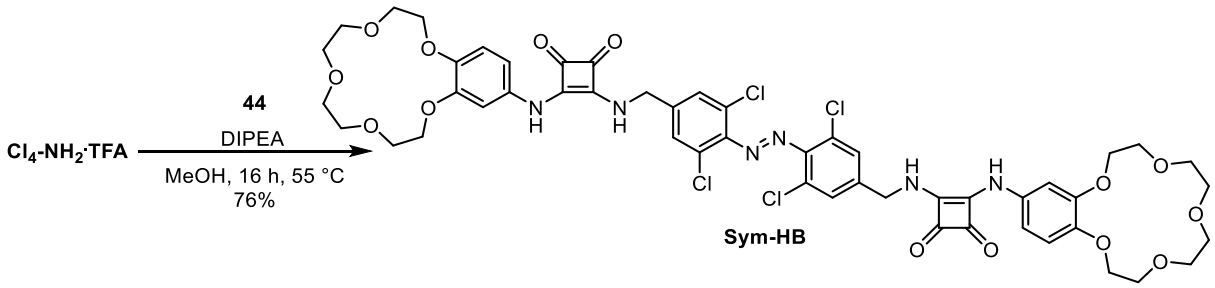


43. Prepared according to literature procedure.[8] **S11** (300 mg, 0.96 mmol) and Pd/C (10% loading, 50 mg) and ethanol (7 ml) were mixed together. Then, hydrazine monohydrate (3 ml) was added and the reaction was stirred at reflux temperature for 5 h. The residue was filtered over celite, then the solvent was removed *in vacuo*. The crude product was redissolved in CH_2Cl_2 and the organic layer dried over $MgSO_4$. The solvent was removed to afford the title compound as a light yellow oil (220 mg, 0.78 mmol, 81%). ^{1}H NMR (400 MHz, $CDCl_3$) δ 6.73 (d, *J* = 8.4 Hz, 1H), 6.28 (d, *J* = 2.6 Hz, 1H), 6.21 (dd, *J* = 8.4, 2.6 Hz, 1H), 4.11 – 4.04 (m, 4H), 3.92 – 3.85 (m, 4H), 3.75 (s, 8H). Data consistent with that given in the literature.[8]



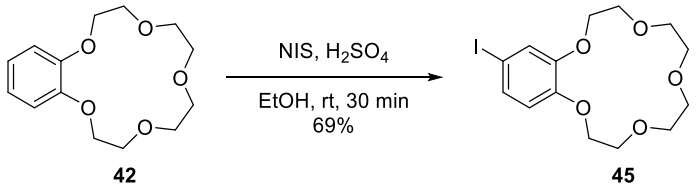
43 **44**

Squaramide **44**. Crown ether aniline **43** (220 mg, 0.78 mmol) and dimethyl squarate (110 mg, 0.78 mmol, 1 eq) were mixed in MeOH (2.7 mL). The reaction was stirred at room temperature for 48 hours, after which a solid precipitate had formed. The suspension was cooled using ice, then filtered. The filter cake was washed with Et_2O and hexane. The solid was collected and dried to afford the title compound as a white solid (140 mg, 0.36 mmol, 45%). ^{1}H NMR (400 MHz, DMSO) δ 10.62 (s, 1H), 7.04 (br s, 1H), 6.92 (d, *J* = 8.6 Hz, 1H), 6.81 (br s, 1H), 4.36 (s, 3H), 4.02 (q, *J* = 4.6 Hz, 4H), 3.81 – 3.72 (m, 4H), 3.65 – 3.57 (m, 8H). ^{13}C NMR (151 MHz, DMSO) δ 188.09, 183.81, 177.91, 168.58, 148.78, 145.45, 131.61, 114.45, 111.85, 106.50, 70.44, 70.41, 69.85, 69.71, 68.97, 68.88, 68.65, 68.26, 60.44. HRMS-ESI (m/z) Calculated for $C_{19}H_{23}NO_8Na$ $[M+Na]^+$, 416.1321; found 416.1309.



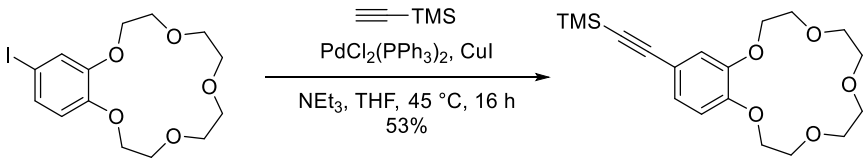
Sym-HB. **Cl_4-NH_2·TFA** (50 mg, 82 µmol) was dissolved in MeOH (1 mL). DIPEA (86 µL, 0.49 mmol, 6 eq) was added dropwise. Monosquaramide **44** (22.5 mg, 165 µmol, 2 eq) in MeCN (1mL) was added, and the solution was heated at 55 °C for 16 hours. The reaction was cooled to rt and the solid precipitate was filtered and washed sequentially with MeOH and MeCN, then collected and dried under high vacuum to afford the title compound as an orange solid (69 mg, 63 µmol, 76%). (*E*)-**Sym-HB**: ^{1}H NMR (400 MHz, DMSO) δ 9.74 (s, 2H), 7.96 (s, 2H), 7.73 (s, 4H), 7.16 (s, 2H), 6.92 (d, *J* = 8.6 Hz, 2H), 6.78 (dd, *J* = 8.5, 2.5 Hz, 2H), 4.98 – 4.76 (m, 4H), 4.02 (q, *J* = 5.1 Hz, 8H), 3.75 (q, *J* = 4.6 Hz, 8H). ^{13}C NMR (176 MHz, DMSO) δ

183.50, 181.21, 168.29, 164.23, 149.21, 145.46, 144.54, 142.80, 132.67, 128.84, 126.33, 115.00, 110.49, 105.32, 70.44, 70.39, 69.89, 69.69, 69.12, 68.95, 68.67, 68.08, 45.77. HRMS-ESI (m/z) Calculated for $C_{50}H_{51}N_6O_{14}Cl_4$ $[M+H]^+$, 1099.2212; found 1099.2228.



42 **45**

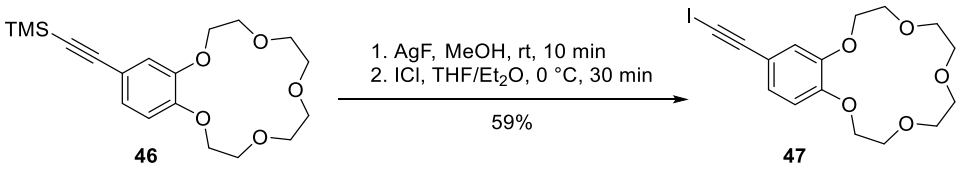
45. Prepared according to literature procedure.[9] **42** (5.2 g, 19.4 mmol) was dissolved in EtOH (32 mL). Sulfuric acid (1.5 mL) was added dropwise with cooling (10-15 °C). N-iodosuccinimide (4.37 g, 19.4 mmol, 1 eq) was added portionwise. The orange solution was stirred for 30 minutes under ambient conditions. 3% Sodium sulphite (150 mL) was added and the pH adjusted to 7 with Na_2CO_3. The precipitate was collected via filtration and washed with water (10 mL). The residue was recrystalised from boiling heptane to afford the title compound as a white solid (5.3 g, 13.4 mmol, 69%). ^{1}H NMR (400 MHz, $CDCl_3$) δ 7.20 (dd, *J* = 8.4, 2.1 Hz, 1H), 7.13 (d, *J* = 2.0 Hz, 1H), 6.61 (d, *J* = 8.4 Hz, 1H), 4.13 – 4.06 (m, 4H), 3.93 – 3.86 (m, 4H), 3.74 (q, *J* = 2.0 Hz, 8H). Data consistent with that given in the literature. [9]



45 **46**

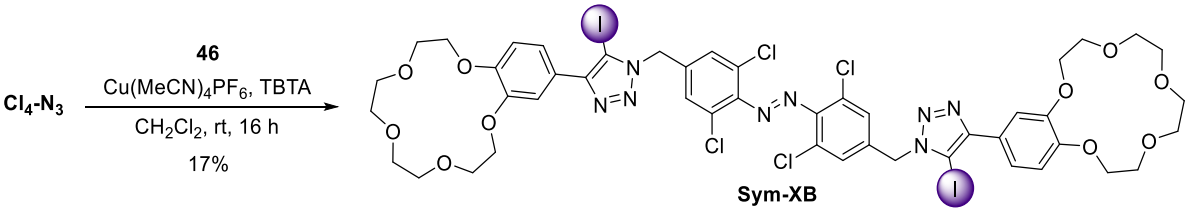
46. Prepared according to literature procedure.[9] **45** (600 mg, 1.52 mmol), CuI (15 mg, 78 µmol, 0.05 eq), Bis(triphenylphophine)palladium(II) dichloride (30 mg, 296.5 µmol, 0.2 eq) were placed in a degassed, dry tube under Argon and was purged for 15 minutes. Then, degassed THF (10 mL), dry triethylamine (630 µL, 4.57 mmol, 3 eq) was added. Finally, TMS acetylene (540 µL, 3.81 mmol, 2.5 eq) was added and the reaction was stirred at 45 °C for 16 hours. The reaction was concentrated, then purified by silica gel chromatography (6% MeOH in CH_2Cl_2) to afford the title compound as a brown oil (295.7 mg, 0.806 mmol, 53%). ^{1}H NMR

(400 MHz, $CDCl_3$) δ 7.05 (dd, *J* = 8.3, 1.9 Hz, 1H), 6.96 (d, *J* = 1.9 Hz, 1H), 6.76 (d, *J* = 8.3 Hz, 1H), 4.16 – 4.08 (m, 4H), 3.93 – 3.86 (m, 4H), 3.75 (s, 8H), 0.23 (s, 9H). Data consistent with that given in the literature. [9]



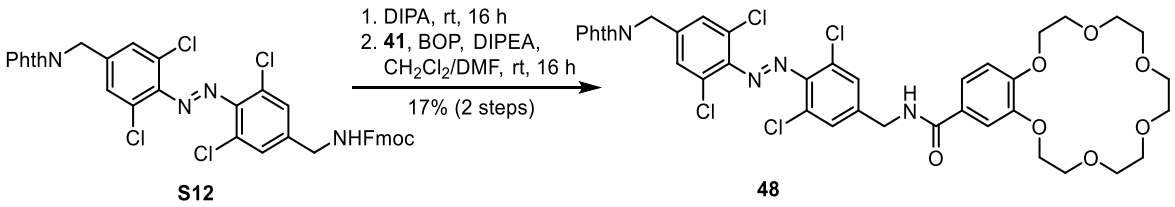
46 **47**

47. **46** (370 mg, 1.02 mmol) was dissolved in MeOH (5 mL). AgF (142 mg, 1.12 mmol, 1.1 eq) in MeOH (20 mL) was added under protection from light. the reaction was stirred in the dark for 10 minutes under ambient conditions. The precipitate was concentrated under rotary evaporation (35 °C water temperature). Then dry THF (15 mL) was added and ICl (173 mg, 1.07 mmol, 1.05 eq) in Et_2O (5 mL) was added at 0 °C. The reaction was stirred at this temperature for 30 minutes, then diluted in CH_2Cl_2 (50 mL), and filtered over celite. The solution was concentrated, then quickly purified by silica gel chromatography (3% MeOH in CH_2Cl_2) to afford the title compound as a yellow solid (250 mg, 0.60 mmol, 59%). ^{1}H NMR (400 MHz, $CDCl_3$) δ 7.01 (dd, *J* = 8.3, 2.0 Hz, 1H), 6.93 (dd, *J* = 8.1, 2.0 Hz, 1H), 6.76 (d, *J* = 8.3 Hz, 1H), 4.11 (td, *J* = 7.6, 3.8 Hz, 4H), 3.90 (p, *J* = 4.1 Hz, 4H), 3.75 (d, *J* = 3.8 Hz, 8H). ^{13}C NMR (101 MHz, $CDCl_3$) δ 150.24, 148.60, 126.28, 117.52, 116.06, 113.19, 94.20, 71.26, 71.25, 70.56, 70.53, 69.54, 69.53, 69.03, 68.89, 4.03. HRMS-ESI (m/z) Calculated for $C_{16}H_{20}IO_5$ $[M+H]^+$, 419.0350; found 419.0343.



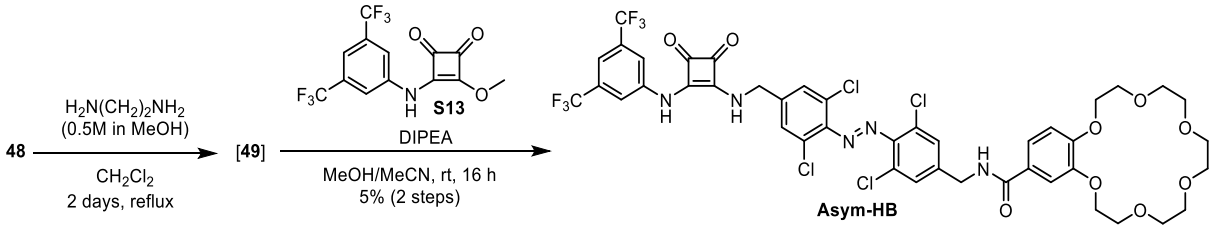
Sym-XB. TBTA (19 mg, 34.9 µmol, 0.5 eq) and $Cu(MeCN)_4PF_6$ (11 mg, 34.9 µmol, 0.5 eq) were placed in a flask and purged with N_2. Degassed CH_2Cl_2 (1 mL) was added the reaction was stirred for 10 min. Then **Cl_4-N_3** (30mg, 69.76 µmol), **46** (120 mg, 279 µmol, 4 eq) in degassed CH_2Cl_2 (1 mL) was added and the reaction was stirred at room temperature

overnight. The mixture was diluted with CH_2Cl_2, then washed with ammonia / EDTA solution. The organic layer was concentrated and the residue was purified by silica gel flash chromatography (1 to 3 to 5 to 10% MeOH in CH_2Cl_2) to afford the title compound as an orange solid (14.7 mg, 11.6 µmol, 17%). (*E*)-**Sym-XB**: ^{1}H NMR (600 MHz, $CDCl_3$) δ 7.52 (dd, *J* = 8.1, 2.0 Hz, 2H), 7.50 (d, *J* = 2.0 Hz, 2H), 7.40 (s, 4H), 6.95 (d, *J* = 8.2 Hz, 2H), 5.66 (s, 4H), 4.25 – 4.16 (m, 8H), 3.93 (dt, *J* = 6.2, 3.4 Hz, 8H), 3.77 (td, *J* = 4.2, 1.8 Hz, 16H). ^{13}C NMR (151 MHz, $CDCl_3$) δ 150.60, 149.80, 149.20, 147.55, 136.75, 128.84, 128.19, 123.10, 120.58, 113.69, 113.30, 76.07, 71.28, 71.25, 70.63, 70.62, 69.66, 69.64, 69.14, 69.09, 53.00. HRMS-ESI (m/z) Calculated for $C_{46}H_{46}N_8O_{10}Cl_4I_2Na$ $[M+Na]^-$, 1289.0043; found 1289.0033.



48. S12 (250 mg, 0.34 mmol) was dissolved in DMF (3 mL). Diisopropylamine (80 µL, 0.45 mmol, 1.3 eq) was added, and the reaction was stirred at room temperature for 16 hours, after which a precipitate had formed. The DMF was azeotropically removed under reduced pressure with toluene. The residue was purified by silica gel flash chromatography (100:3:1 CH_2Cl_2:MeOH:NEt_3) to afford the intermediate amine with ~ 90% purity: ^{1}H NMR (400 MHz, $CDCl_3$) δ 7.92 – 7.85 (m, 2H), 7.79 – 7.72 (m, 2H), 7.52 (s, 2H), 7.44 (s, 2H), 4.84 (s, 2H), 3.91 (s, 2H). The residue was dissolved in 4 mL 4:1 CH_2Cl_2:DMF, after which BOP (144 mg, 0.325 mmol, 0.95 eq), DIPEA (131 µL, 0.75 mmol, 2.2 eq) and crown ether **41** (104 mg, 0.29 mmol, 0.85 eq) was added under N_2. The reaction was stirred overnight at room temperature, then concentrated and purified by preparative TLC (10% MeOH in CH_2Cl_2) to afford the title compound as an orange solid (50 mg, 59 µmol, 17%). ^{1}H NMR (500 MHz, $CDCl_3$) (*E*)-**48**: δ 7.90 – 7.84 (m, 2H), 7.76 – 7.72 (m, 2H), 7.51 (s, 2H), 7.46 – 7.42 (m, 1H), 7.40 (s, 2H), 7.33 (d, *J* = 8.2 Hz, 1H), 6.84 (d, *J* = 8.2 Hz, 1H), 6.76 (br s, 1H), 4.83 (s, 1H), 4.60 (d, *J* = 5.3 Hz, 1H), 4.24 – 4.12 (m, 4H), 3.97 – 3.87 (m, 4H), 3.81– 3.71 (m, 4H), 3.73 – 3.63 (m, 8H).^{13}C

NMR (126 MHz, $CDCl_3$) δ 167.73, 167.11, 151.98, 148.75, 147.12, 146.46, 141.42, 138.43, 134.36, 131.88, 129.48, 128.54, 127.69, 127.55, 126.56, 123.67, 120.08, 113.02, 112.43, 70.91, 70.86, 70.76, 70.69, 70.68, 70.61, 69.50, 69.42, 69.09, 68.92, 42.80, 40.35. HRMS-ESI (m/z) Calculated for $C_{39}H_{36}N_4O_9Cl_4Na$ $[M+Na]^+$, 869.1105; found 869.1089.



Asym-HB. 48 was dissolved in CH_2Cl_2 (1 mL). Then ethylene diamine (0.5M in MeOH, 328 µL, 164 µmol, 6 eq) was added and the reaction was stirred at reflux temperature for 2 days in a sealed tube. The residue was concentrated, then purified by preparative TLC (10% MeOH in CH_2Cl_2) to afford the intermediate amine **49**. This was dissolved in 50 : 50 MeOH : MeCN (0.5 mL) and DIPEA (5 µL, 27 µmol, 1 eq), and **S13** (3 mg, 9 µmol, 0.33 eq) in MeCN (0.5 mL) was added. The mixture was stirred for 16 hours at rt, then dissolved in CH_2C_{l2} (10 ml). The organic layer was washed with H2O, then concentrated and purified by preparative TLC (10% MeOH in CH_2Cl_2) to afford the title compound. (*E*)-**Asym-HB**: 1H NMR (500 MHz, Acetone) δ 9.63 (s, 1H), 8.20 (s, 1H), 8.04 (s, 2H), 7.83 (s, 1H), 7.59 (s, 2H), 7.50 (s, 2H), 7.47 – 7.43 (m, 2H), 6.92 (dd, J = 8.8, 2.1 Hz, 1H), 4.92 (s, 2H), 4.54 (d, J = 6.1 Hz, 2H), 4.08 (dt, J = 8.9, 4.2 Hz, 4H), 3.76 (dq, J = 6.9, 2.3 Hz, 4H), 3.61 – 3.55 (m, 4H), 3.51 (t, J = 4.7 Hz, 4H), 3.48 (d, J = 2.0 Hz, 4H). HRMS-ESI (m/z) Calculated for $C_{43}H_{36}N_5O_9Cl_4F_6$ $[M+H]^+$, 1022.1155; found 1022.1148.

6.4.2 NMR titrations (Chapter 4)

All binding constants were measured by ^{1}H NMR titrations in a Bruker AVIII 500 spectrometer at 500 MHz and 298 K. Receptor **XB-Azo** was dissolved in d_6-acetone (Receptor **Me-XB-Azo** in DMSO-d_6) and added at 1 mM concentration and a known volume (0.5 mL) added to the NMR tube. Known volumes of guest (X^-, added as the TBA salt) in d_6-acetone or DMSO-d_6 were added, and the spectra were recorded after each addition. Samples were prepared and analysed analogously to chapter 3.

For cation binding studies of **Sym-XB**, samples were prepared in 0.5 mL in a 50/50 v/v/ mixture of $CDCl_3$ and MeCN-d_4, and known volumes of $KBAr^F_4$ were added in a 50/50 v/v/ mixture of $CDCl_3$ and MeCN-d_4. For cation binding studies of Sym-XB, the analogous experiment was performed in DMSO-d_6. No binding was observed (Figure S1).

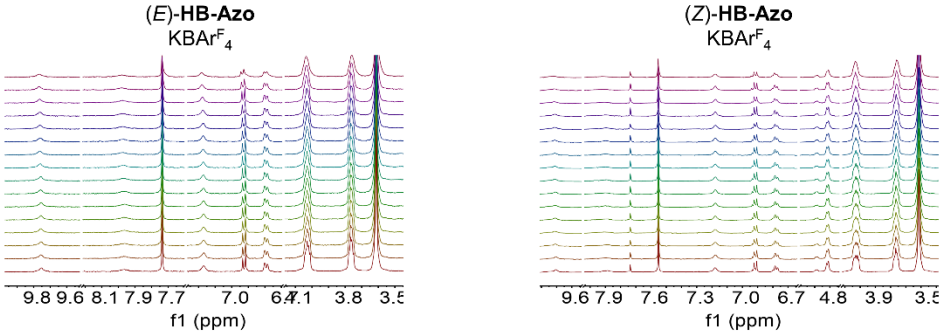


Figure S1. Plots of chemical shift changes and stacked ^{1}H NMR spectra for NMR titrations of **HB-Azo**

Plots for **XB-Azo** can be found in the main text (Figure 8).

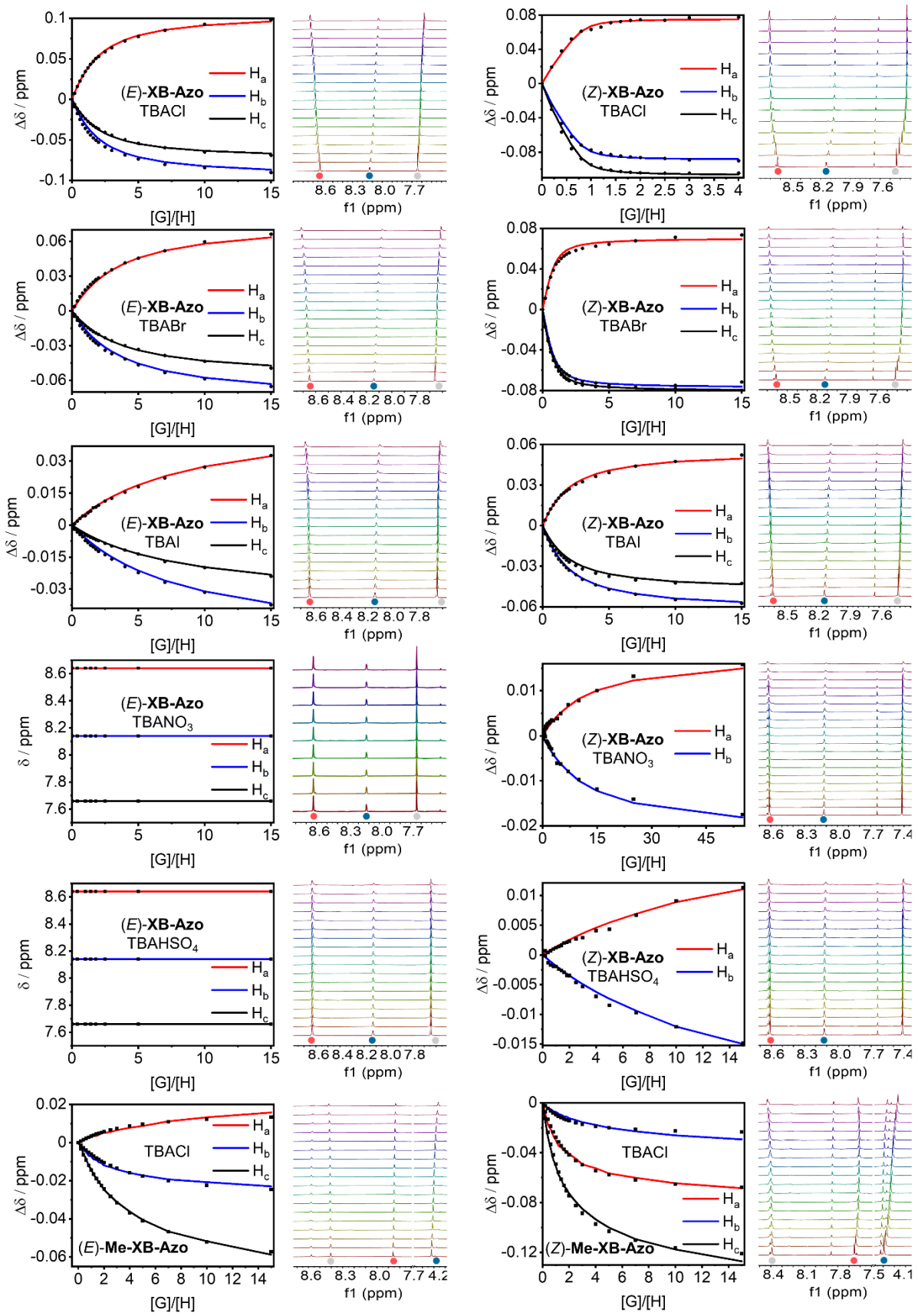


Figure S2. Plots of chemical shift changes and stacked ^{1}H NMR spectra for NMR titrations

6.4.3 Anion transport studies (Chapter 4)

Transport assays with HPTS vesicles (Figure 3D-E; Figure 9) were performed analogously to chapter 3.

6.4.3.1 Lucigenin transport assays (Figure 10)

Vesicle preparation

A thin film of lipid POPC (or POPC + 5 mol% **XB-Azo**) was formed by evaporating a chloroform solution under a stream of nitrogen gas, and then under high vacuum for 6 hours. The lipid film was hydrated by vortexing with the prepared buffer (100 mM K_2SO_4, 10 mM HEPES, 1 mM 10,10′-Dimethyl[9,9′-biacridine]-10,10′-diium dinitrate (Lucigenin), pH 7.0). The lipid suspension was then subjected to 5 freeze-thaw cycles using liquid nitrogen and a water bath (40°C), followed by extrusion 19 times through a polycarbonate membrane (pore size 200 nm) at rt. Extra-vesicular components were removed by size exclusion chromatography on a Sephadex G-25 column with 100 mM K_2SO_4, 10 mM HEPES, pH 7.0. Final conditions: LUVs (8.22 mM lipid); inside 100 mM K_2SO_4, 10 mM HEPES, 1 mM HPTS, pH 7.0; outside: 200 mM NaX, 10 mM HEPES, pH 7.0.

Transport assays with Lucigenin

In a typical experiment, the LUVs containing Lucigenin (50 μL, final lipid concentration 206 μM) were added to buffer (1950 μL of 200 mM NaX, 10 mM HEPES, pH 7.0) at 25°C under gentle stirring. At 40 s the test transporter (various concentrations, in 5 μL DMF) was added, followed by detergent (25 μL of Triton X-100 in 7:1 (v/v) H_2O-DMSO) at 300 secs to calibrate the assay. The fluorescence emission was monitored at λ_{em} = 505 nm (λ_{ex} = 430 nm). The relative intensity (I_{rel}) was calculated from equation (S4.1), where I_t is the fluorescence ratio at time *t*, (ratio of intensities 460 nm / 405 nm excitation) I_0 is the fluorescence ratio at time 40 s.

$$I_{rel} = \frac{I_t}{I_0} \qquad \textbf{(S4.1)}$$

6.4.4 ^{1}H NMR kinetics Studies (Chapter 4)

Bromide Abstraction reaction:

1 mg Cs_2CO_3 was added in the NMR tube, then 400 µL (2.5 mM) of **Me-XB-Azo BAr$^F_4$** (Pre-heated at 70 degrees for 1 h or PSS at 625 nm) or **c-BAr$^F_4$** in $CDCl_3$ and 100 µL (10 mM) 1,3,5-trimethoxybenzene was added. Finally, 100 µL (10 mM) benzhydryl bromide solution was added and mixed by inversion. The samples were directly transferred and submitted to the NMR spectrometer and ^{1}H NMR were recorded in 15 minute intervals. The conversion was determined by integration of the methoxy signals (3.77 ppm) of 1,3,5-trimethoxybenzene against the two methoxy signals (3.80 ppm and 3.58 ppm) in the product ((2,4,6-trimethoxyphenyl)methylene)dibenzene. The twofold substitution occurred and ((2,4,6-trimethoxy-1,3-phenylene)bis(methanetriyl))tetrabenzene (methoxy signals at 3.41 ppm and 3.03 ppm) was formed as minor product (ca. 13% for both isomers)

Chloride abstraction reaction.

3 mg Cs_2CO_3 was added in the NMR tube, then 200 µL (12 mM) of **Me-XB-Azo BAr$^F_4$** (Pre-heated at 70 degrees for 1 h or PSS at 625 nm) or **c-BAr$^F_4$** in $CDCl_3$ and 200 µL (12 mM) 1,3,5-trimethoxybenzene was added. Finally, 200 µL (12 mM) benzhydryl chloride solution was added and mixed by inversion. The samples were directly transferred and submitted to the NMR spectrometer and ^{1}H NMR were recorded in 15 minute intervals The conversion was determined analogously to the bromide abstraction. Two-fold substitution occurred and ((2,4,6-trimethoxy-1,3-phenylene)bis(methanetriyl))tetrabenzene (methoxy signals at 3.41 ppm and 3.03 ppm) was formed as minor product (ca. 6% for both isomers)

Mukaiyama Aldol Reaction.

Catalyst (0.5 mol% **Me-XB-Azo BAr$^F_4$** or 1 mol% **c-BAr$^F_4$**) was added to an NMR tube. The NMR tube was purged with N_2, then degassed, dry $CDCl_3$ (0.5 mL) was added. Benzaldehyde (10.2 µL, 0.1 mmol) was added to it under N_2. The silyl enol ether (30 µL, 0.15 mmol) was added to it and ^{1}H NMR were recorded in 15 minute intervals. Conversions were determined

based on the consumption of aldehyde through the measurement of integration of the aldehyde proton relative to that of TMS signal of the product.

Michael addition reaction

To a new NMR tube, freshly prepared stock solutions of the respective catalyst (200 µL, 0.1 eq. 15 mM), 1- methylindole (200 µL, 1 eq., 150 mM) and β-trans-crotonophenone (200 µL, 1 eq., 150 mM) in deuterated methylene chloride were added, tube sealed and the NMR tube shaken. Afterwards, ^{1}H-NMR experiments were performed periodically every 15 minutes at room temperature. Conversions were determined based on the consumption of β-trans-crotonophenone (signal at 1.99 ppm) vs. the formation of product (signal at 1.42).

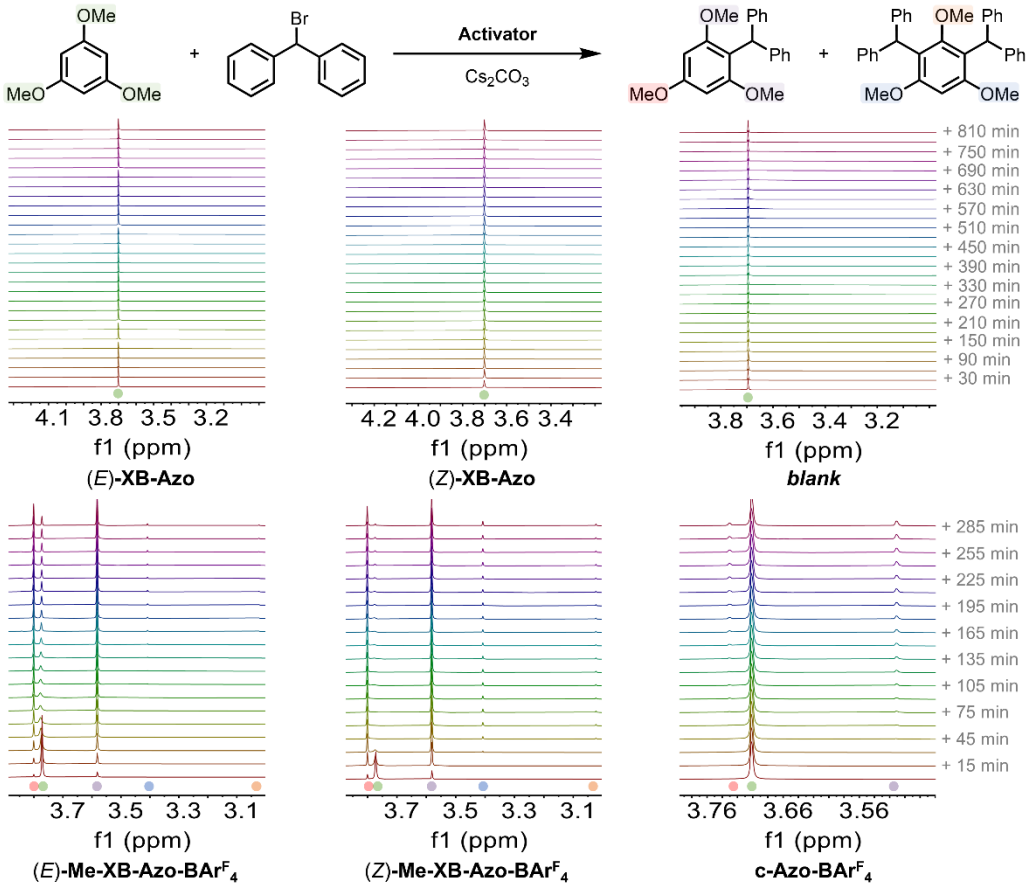


Figure S3. Stacked plot of the ^{1}H NMR kinetic experiments for bromide abstraction

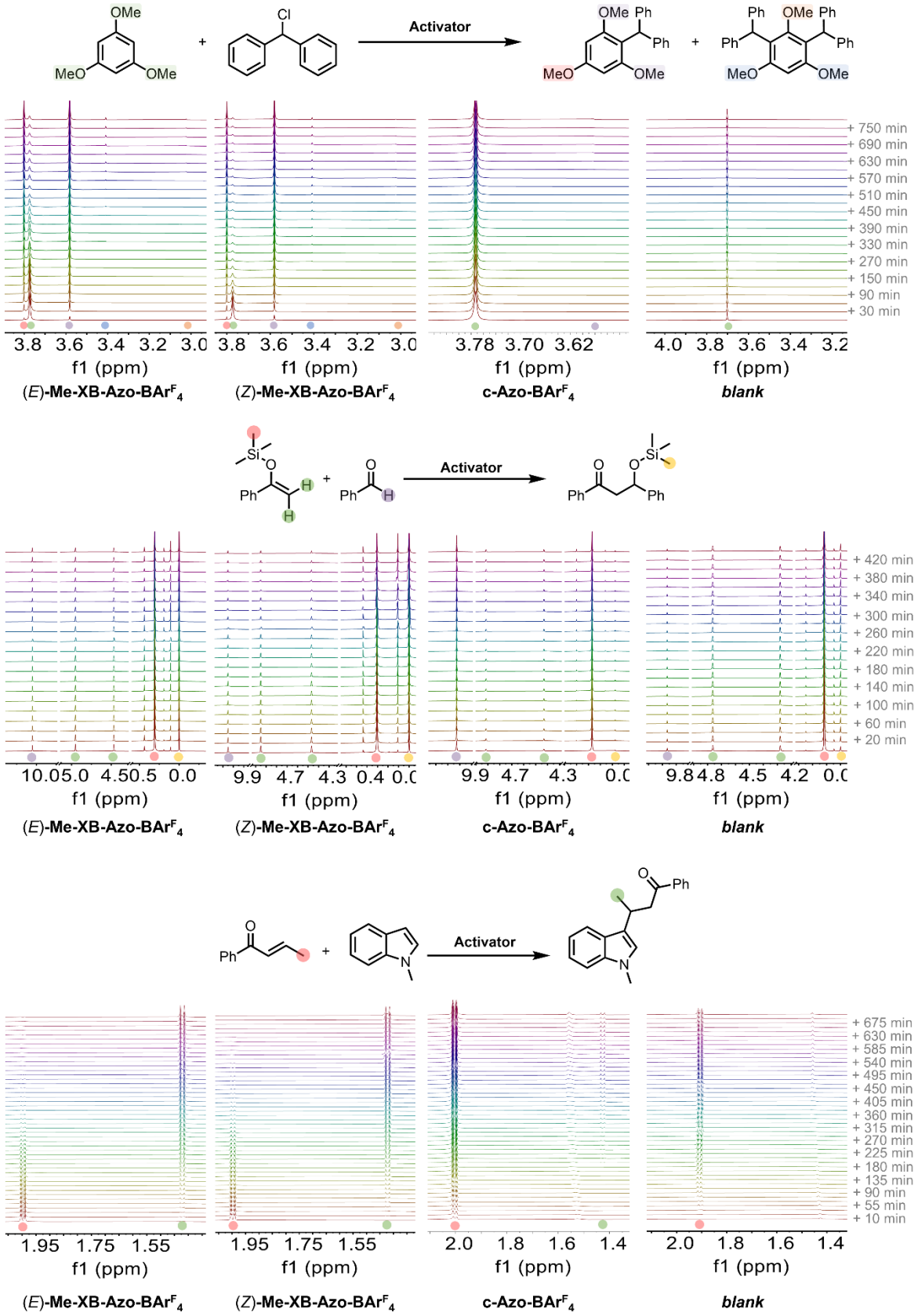


Figure S4. Stacked plot of the ^{1}H NMR kinetic experiments for (A) chloride abstraction, (B) Mukaiyama aldol reaction and (C) Michael addition

6.4.5 References (Chapter 4 appendix)

[1] M. Rombola and V. H. Rawal, *Org. Lett.*, 2018, **20**, 514–517.
[2] S. Ferla, M. Bassetto, F. Pertusati, S. Kandil, A. D. Westwell, A. Brancale and C. McGuigan, *Biorg. Med. Chem. Lett.*, 2016, **26**, 3636–3640.
[3] J. L. Neumeyer, W.-Y. Zhang, V. Bakthavachalam, Y. Gao and W. L. White, *Heterocycles*, 1994, **39**, 19.
[4] L. E. Bickerton, A. J. Sterling, P. D. Beer, F. Duarte and M. J. Langton, *Chem. Sci.*, 2020, **11**, 4722–4729.
[5] P. Cazeau, F. Duboudin, F. Moulines, O. Babot and J. Dunogues, *Tetrahedron*, 1987, **43**, 2075–2088.
[6] F. Heinen, D. L. Reinhard, E. Engelage and S. M. Huber, *Angew. Chem. Int. Ed.*, 2021, **60**, 5069–5073.
[7] J. Rey, F. C. García and J. M. García, *React. Funct. Polym.*, 2011, **71**, 948–957.
[8] T. Bunchuay, A. Docker, U. Eiamprasert, P. Surawatanawong, A. Brown and P. D. Beer, *Angew. Chem. Int. Ed.*, 2020, **59**, 12007–12012.
[9] S. V. Klyatskaya, E. V. Tretyakov and S. F. Vasilevsky, *Russ. Chem. Bull.*, 2001, **50**, 868–873.
[10] P. Kuzmic, *Anal. Biochem.*, 1996, **237**, 260–273.